Binder Stability and Powder\Binder Interaction in Three Dimensional Printing

by

James Frederic Bredt

S.B., Materials Science and Engineering, MIT, 1982;
S.M., Mechanical Engineering, MIT, 1987.

Submitted to the Department of Mechanical Engineering
in Partial Fulfillment of the Requirements for the Degree of

Doctor of Philosophy

at the

Massachusetts Institute of Technology

January 1995

Signature of Author _____
Department of Mechanical Engineering
February 10, 1995

Certified by _____
Emanuel M. Sachs
Associate Professor of Mechanical Engineering
Laboratory for Manufacturing and Productivity
Thesis Supervisor

Accepted by _____
Ain A. Sonin
Chairman of Graduate Committee

Binder Stability and Powder\Binder Interaction in Three Dimensional Printing

by

James Frederic Bredt

Submitted to the Department of Mechanical Engineering
on Jan. 1, 1995
in partial fulfillment of the requirements for the degree of
Doctor of Philosophy in Mechanical Engineering

Abstract

Three Dimensional Printing is a process for building solid shapes directly from a CAD model. Material is formed by deposition of a liquid adhesive binder into dry powder through an ink-jet printhead. The fidelity of rendering three dimensional shapes depends on the size of primitive features formed by the interaction of the binder jet with the powder.

A materials system was developed for printing ceramic shell molds. The binder was based on colloidal silica and was used to bond aluminum oxide powder. The performance of the binder was characterized in terms of its drying rate and the chemical reaction that leads to its transformation into a solid gel. This gel remains fixed in the bed of powder until subsequent heat treatment, during which the silica in the gel fuses to the powder grains, resulting in a porous ceramic material suitable for metal casting.

The formation of features was found to be a process of capillary migration of the binder through the powder followed by transformation of the binder into gel. The time for gel formation was found to be very much longer than the time for capillary equilibration. It was concluded that the distribution of binder in primitive features was determined by an equilibrium between moist powder comprising the features and dry powder surrounding them. Dry powder surrounding the features exerts a characteristic suction on the moisture present in the features, with causes binder to from saturated regions into surrounding powder until the pressures are equalized.

A model was developed to predict the equilibrium fluid content of primitive features from measurements of the capillary characteristics of the powder. Experimental measurements were taken of the capillary characteristics of the powders which were used to calculate predictions of the equilibrium fluid content in primitive features. The 30 μm powder that is currently used in the ceramic shell process was found to have a pore size of 6-10 μm, depending on the packing density. The equilibrium saturation varied from approximately 60% of the available pore space when the powder packing was below 35%, and approached 90% as the powder packing approached 50%. Different powders were tested, and they were found to behave in a manner that agreed with the model, except in the case of a class of blended powders. These powders contained fractions of powder with two widely different grain sizes and they were found to increase greatly in packing density upon printing. Although they did not conform with he model, it was found that this "bimodal" powder formed into features with very smooth surfaces. For the other powders tested, the packing density did not change significantly, and the fluid within primitive features was found to fill between 60% and 95% of the available pore space.

Thesis Committee: Dr. Emanuel M. Sachs, Chairman;
Dr. Michael J. Cima; Dr. T. Alan Hatton

Acknowledgment

This thesis is dedicated to my mother and father, who never stopped believing in me, and Libby Shaw, who stood by me through the whole process.

It would be impossible to list all those who helped me through this project. I would like to especially thank:

Ely Sachs, the rock holding the Three Dimensional Printing project together.

My thesis committee (Profs. Sachs, Michael Cima, and T. Alan Hatton) for helping guide me

David Brancazio and James Serdy who put the fruits of my research to practice, helped with crucial observations, and were generally great to work with.

The students of the Three Dimensional Printing Project, without whose work over the past five years, this thesis could not have existed. I am very grateful for direct assistance in sharing observations, but the more importantly for companionship and the feeling that we were all working together to make something much greater than any of us could conceive.

Tara Arthur
Won Bang
Scott Borland
Jain Charnnarong
Seth Close
Alain Curodeau
Mark Eichler
Tailin Fan
Bugra Giritlioglu
Jason Grau
Honglin Guo
Haeseong Jee
Satbir Khanuja
Anne Kohnen
John Lee
Steve Michaels
Daniel Nammour
Chris Richardson
David Robinson
Mike Rynerson
Christopher Shutts
Chris Stratton
Earl Sun
Hon Tang
Gail Thornton
Ben Wu
Ed Wylonis
Jae Yoo

I would like to thank those especially who contributed photographs, designs, data, or labor that were used in the preparation of this document. These were Tim Anderson, Tara Arthur, Scott Borland, Dave Brancazio, Alain Curodeau, Jain Charnnarong, Mark Eichler, Marcos Esterman, Tailin Fan, Tiina Hameenanttila, Chris Harris, Satbir Khanuja, Alan Lauder, John Lee, Steve Michaels, Jim Serdy, Chris Shutts, and Hon Tang.

The editors and publishers of VooDoo Magazine for giving me a precious outlet.

All the support staff, too numerous to list, but especially Fred Cote who has been a valuable friend.

Biographical Sketch

Jim Bredt came to MIT in 1978 as a freshman. For his undergraduate work, he studied Materials Science under Prof. Merton Flemings, where he developed an appreciation for metal casting and sculpture. While doing his Master's work under Prof. George Chryssolouris, he taught a classes in moldmaking and casting.

His professional career between degrees included a period as C.E.O. of Cryoelectro Associates, Inc., and Director of R&D at Axiomatics Corp. It was during this period that he learned a practical knowledge of chemistry and a healthy respect for safety.

Throughout his MIT career, he drew cartoons which were published in a variety of student journals: The Legend of Fred (1980-82 in Link, and 84-87 in The Tech) The Final Exam (VooDoo, 1990-92) and Twenty-First Century Romance (VooDoo, 93-95.) Among his other publications are The First and Second Laws, a Cartoon Introduction to Classical Thermodynamics (1987, Dept of Materials Science) and a number of books he illustrated, most notably Geometric Measure Theory by Frank Morgan, (Acad. Pr., 1989) and Mathematical Modeling in the Social and Biological Sciences by Edward Beltrami (Jones & Bartlett, 1993.)

He has appeared on television as a Human Spotlight in the 4th annual Ig-Nobel Prize Awards Ceremony.

He has always been fascinated by geometry, three dimensional rendering, and manufacturing. The Three Dimensional Printing Project was, for him, the culmination of a life's preparation. He is a co-inventor on several improvement patents in the process, and a number of papers. The one closest to his research topic was: "CAD-Casting: Direct Fabrication of Ceramic Shells and Cores by Three Dimensional Printing," Manufacturing Review, **5** (2) 6/92. He intends to pursue a career in Rapid Prototyping. He is presently employed as Chief Materials Scientist at Z Corporation in Cambridge, MA.

Table of Contents

List of Figures

Chapter 1. Introduction

Chapter 2. The Colloidal State

Chapter 3. Colloidal Silica

Chapter 4. Development of Colloidal Silica for Three Dimensional Printing

Chapter 5. Capillary Migration in Porous Materials: Foundations and Review of the Literature

Chapter 6. Feature Formation in Three Dimensional Printing

Chapter 7. Experimental Characterization of Powder Pore Structure

Chapter 8. Experimental Measurement of Binder Saturation in Single Printed Lines

Chapter 9. Variation of Process Conditions

Chapter 10. Conclusions

Appendix A. Thermodynamics and Capillary Phenomena

Appendix B. Geometric Model of an "Ink-Bottle" Pore

Appendix C. Meniscus Instability in Networks of Ink-Bottle Pores

Appendix D. The Physics of Our Printhead

Appendix F. Material Specifications

Appendix G. Schematic of 1:4 Switching Circuit for Printing at Low Binder Dose

List of Variables

a = (in general) the radius of a spherical particle

a_1, a_2 = the radii of two particles (2.45)

A = Hamaker's constant (2.44,45)

$A_{feature}$= cross-sectional area of a single line primitive

A_{liquid} = binder dose per unit length (area) in a single line primitive

A_{powder}= powder dose per unit length (area) in a single line primitive

$[a_{Ag}]$ = activity coefficient of silver ions in solution

α = electrostatic polarizability of a particle (2.21,22,23)

b = major half-axis of a crack (3.1)

B = distance between two particles

β = an angle of scattered light

$c(x)$ = concentration as a function of linear position

c_i = concentration in mol/liter of species i.(2.55)

c.c.c. = critical coagulation concentration

c.m.c. = critical micelle concentration of a surfactant

cosq = possible misprint of $\cos\theta$.

C = mean curvature of a fluid meniscus

$Ca = \frac{\eta u}{\sigma}$ = "capillary number" = ratio of viscous forces to surface tension forces

C_e = compression index (a constant for consolidation of a porous material)

d = the differential operator

$d_{est'd} = \sqrt{\frac{4A_{powder}}{\pi f_{powder}}}$ = diamter of a line feature estimated from weight measurements.

d_{grain} = mean grain size of a powder.

d_{line} = diameter of a single line primitive

d_{occl} = diameter measured optically (by occlusion)

D = diffusion coefficient

D_{ion} = diffusion coefficient for an electrolyte ion

$D_M = \frac{P_B k_{rel}}{\eta \Lambda (1 - f_{powder})}$ = moisture diffusivity

Δ = a change in some quantity

∂ = the fractal dimension of a structure

δ = bias on diameter measurement from optical measurement

DEDMAB = dodecylethyldimethylammonium bromide

E_C = critical fracture energy

e = electronic charge

ε_0 = electrostatic permittivity of free space

ε = electrostatic permittivity of a medium

erfc = complementary error function

f = (in general) volume fraction of a single phase in some region

f_{crit} = "critical" volume fraction at which particles touch

f_{floc} = volume fraction of flocs of particles (by hydrodyn. radius)

f_{liquid} = volume fraction of liquid in a region

$f_{particle}$ = volume fraction of particles in a dispersion

f_{powder} = volume fraction of powder in a region.

$(1-f_{powder})$= porosity of a region of powder.

f_x, f_y, f_{xx}, f_{yy}, f_{xy} = derivatives of a function f(x,y), e.g. $f_x = df/dx$, $f_{xy} = d^2f/dxdy$

F = (in general) a force

$F_{l/l}$ = Friction coefficient for a liquid droplet in a liquid (2.2)

$F_{s/l}$ = Drag force on a spherical particle in a liquid medium(2.1,2,13)

$Fr = \dfrac{u^2\rho}{ga\Delta\rho}$ = Froude number = (kinetic energy)/(gravitational energy)

ϕ = angle inside the corner of a pore

G = Gibbs' function

g = (in general) a body force, or gravity, in particular.

$\dot{\gamma}$ = strain rate of a liquid

$\bar{\dot{\gamma}}$ = mean strain rate in a liquid

H = enthalpy

h = a vertical height, esp. in a gravitational field

η = viscosity of a liquid (e.g. binder)

η' = viscosity of the liquid in the droplets of an emulsion

η_{medium} = viscosity of a liquid suspension medium

$\eta_{suspension}$ = apparent viscosity of a suspension

i, j = generic indices

i = relative index of refraction between particles and medium in a suspension

$i_{particle}$ = index of refraction of particlesd in a suspension

i_{medium} = index of refraction of a suspending medium.

I = scattered light intensity

I_0 = incident light intensity

I_{90} = intensity of light scattered 90° w.r.t. source.

I_T = transmittedlight intensity

J = Leverett's function

J = (in general) a flux, esp. of material though a control surface

J_0 = Particle flux trough a capture surface for combined Brownian and shear flow.

J_B = particle flux through a capture surface due to Brownian motion

J_H =particle flux through a capture surface with an energy barrier

J_γ = particle flux though a capture surface due to deformation of the suspending medium.

k_B = Boltzmann's constant = 1.3805×10^{-23} J/atom-K

k(S)= hydraulic permeability (a function of saturation) (chapters 5,6,and after)

k_{rw} = relative permeability of a wetting fluid in an unsaturated porous medium

k_{sat} = hydraulic permeability of a saturated porous medium

K = pore curvature: $K = \dfrac{-P_c}{\sigma_{LV}\cos\theta}$

$K_{drainage}(S)$= pore curvature during drainage of a wetting fluid at intermediate saturation S

K_{50} = pore curvature in drainage of a sample at 50% saturation

K_{90} = pore curvature in drainage of a sample at 90% saturation $\approx K_{NW}$

K_{NW} = critical curvature for a pore (or network) during drainage of a wetting fluid

K_W = critical curvature for a pore (or network) during imbitition of a wetting fluid

κ = reciprocal Debye length

L = length, e.g of a tube or distance between two planes

L_{line} = total length of a sample of single line primitives

Λ = pore size distribution parameter

λ = wavelength

$\dot{m}$ = mass flow rate of binder through the printhead

m = (in general) mass of a particular entity

m_P = bouyant weight of a particle in a suspension

M' = mass per unit length of a single line primitive

μ , μ_0 = chemical potentials (2.11,12)

n = a number or the number of entities in a set, esp. number of particles in an aggregate.

$n_{collision}$ = mean number of particle collisions in a tube of a given length

N_A = Avogadro's number = 6.022×10^{23} atom/mole

N_0 =number per unit volume of primary particles in a dispersion

N_P = the number per unit volume of independent particles in a dispersion

$N_{x=0}$ =number per unit volume of particles at some reference position

p (e.g., in pH) = difference in log concentration of a species w.r.t. a standard state

P_{ATM} = atmospheric pressure

P_B = "bubble pressure" of a porous material saturated with fluid

P_C = capillary pressure

$Pe = \frac{\dot{\gamma}a}{D}$ = Peclet number: ratio between deformation rate and diffusion rate.

P_i = Pressure of a fluid in a region at an intermediate state (e.g. during drainage)

P_0 = suction pressure of dry powder for a fluid

π = the number 3.14159....

PEG=PEO=POE = polyethylene glycol = polyethylene oxide = polyoxyethylene

ΔP = excess hydraulic pressure within a partiallly saturated feature

ψ_0 = surface electic potential on a particle

$\psi(r)$ = electric potential as a function of radius from the center of a particle

ψ_S = Stern potential

q(r) = charge density

Q = volumetric flow rate in a tube

r = (in general) a radius, e.g. of a capillary, or a radial coordinate

r(t) = radial dimension as a function of time

r_0 = intial radius of a circular region

r_1 and r_2 = principal radii of curvature of a surface

r_H = Hydrodynamic radius

r_{tube}^{opt} = optimum tube radius

R = universal gas constant = 8.314 J/mole-K

R_{NW} = characteristic radius for a pore during drainage of a wetting fluid

R_{pore} = mean pore radius of a porous medium

R_W = characteristic radius for a pore during imbitition of a wetting fluid

R_{90} = Rayleigh ratio

ρ_{appar} = apparent density of a single line primitive (from optical measurements)

ρ_{bed} = bulk density of the powder bed.

ρ_{floc} = hydrodynamic density of an aggrgate (floc) of particles

ρ_{liquid} = density of some liquid, esp. binder.

ρ_{H_2O} = density of water = 1.00 g/ml at 25°C

ρ_{Hg} = density of mercury = 13.53 g/ml at 25°C

ρ_{medium} = density of a suspending medium

$\rho_{particle}$ = density of a particle in a liquid suspension

ρ_{powder} = density of the substance comprising the powder in the powder bed

$\rho_{suspension}$ = bulk density of a dispersion of particles in a liquid medium

ρ_{true} = density of lines calculared from mean diameter.

s = entropy

S = saturation = fraction of pore volume occupied by liquid.

S* = equilibrium saturation within a feature.

S_{bulk} = binder saturation in a bulk part composed of many printed lines

$S_e = (S - S_{wo}) / (1 - S_{wo})$= "effective" saturation

$S_{local} = \frac{A_{liquid}}{A_{powder}} \frac{f_{powder}}{(1 - f_{powder})}$ = local saturation in a small vicinity of powder

S_{wo} = "irreducible wetting saturation" of a porous material

σ_{Hg} = surface tension of mercury = 485 dyn/cm

σ_{LV} = interfacial tension between liquid phase and a vapor phase = "liquid surface tension"

σ_{MAX} = historical maximum compressive stress in a consolidated porous material

σ_{SL} = the interfacial tension between a liquid phase and a solid phase.

σ_{SV} = surface energy of a solid

σ_Y = yield stress

t = time

t_K = a characteristic time for capillary equilibration

t_R = a characteristic time for rapid coagulation

t_s = 90% settling time of a damped oscillator

$t_{1/2}$= a characteristic time for the number of particles in a colloid to decrease by half

t_{70}= a characteristic time for a floc with 70 particles to aggregate

T = absolute temperature

T = turbidity

τ_Y = shear strength

θ = contact angle between liquid meniscus and solid surface

θ_{adv} = contact angle of an advancing meniscus

θ_{rec} = contact angle of a receding meniscus

TEA = triethanolamine

TMAH = tetramethylammonium hydroxide

u = (in general) velocity of a fluid

u_1 = sedimentation velocity of a single particle

u_{conc} = sedimentation velocity of a particle in a concentrated suspension

u_n = sedimentation velocity of a floc of n particles

v = (in general) volume of a quantity of fluid

v_i - Volume of a gas bubble in a tensiometer at an intermediate stage.

v_0 = initial volume of a gas bubble in a tensiometer

v_{pore} = the volume of the pores within a given control volume

V = (in general) a potential energy function between two particles in a suspension

V_A = van er Waals potential energy between two particles (attractive)

V_R = repulsive potential energy function

V(r) = potential energy of a particle with respect to another

V_{MAX} = maximum of potential energy V(r)

V_x = fast-axis printhead velocity

W_{line} = total weight of a sample of single line primitives

W_0 = initial weight of a powder sample

$W'_{Al_2O_3}$ = weight/unit length of alumina in a single line feature

W'_{SiO_2} = weight/unit length of silica in a line feature

ΔW = weight gain of a porous sample after imbibition of a wetting fluid

(wt.fr.) = weight fraction, e.g. silcia particles in binder.

ω_n = natural frequency of an undamped oscillator

x = (in general) a distance

x(t) = (in general) a displacement over a distance

Δy = line spacing in 3-D Printed pattern

z_i = charge number of species i

Δz = layer thickness in 3-D Printed pattern

Chapter 1. Introduction

1.1 Process Description

The term "rapid prototyping" refers to a number of processes used to manufacture appearance models and functional prototypes that share a number of general characteristics. The chief characteristic is that all rapid prototyping processes are additive. Three dimensional objects are usually built up in a sequence of cross-sections. This gives the process the greatest amount of access to the geometric features of the object during the build, and reduces the three-dimensional fabrication process to a sequence of two-dimensional laminations. This characteristic excludes most machining processes, especially CNC milling unless the milling operation is used to generate thin layers that are subsequently laminated. Lamination depends on an adhesive: either a filler material is bonded with an adhesive or the part is formed entirely from the adhesive, which is caused to undergo a phase change for at least a brief period during the forming process. A third general characteristic of rapid prototyping processes is that the interface to a CAD system is relatively direct: the conversion from a CAD model into patterns for laminations is not a lot more complicated than the classical "scan conversion" by which images are processed for display on a computer screen. In contrast to this interface, CNC milling involves a large amount of calculations for material removal strategies, tool paths, and tool width compensations.

Three Dimensional Printing is a rapid prototyping process developed at the Laboratory for Manufacturing and Productivity at MIT. Data from a CAD model is used to calculate a sequence of cross sections. Parts are formed from a combination of granulated powder and a liquid **binder**. The powder is contained in a rectangular build box with a movable bottom, or piston. The binder is dispensed by an ink-jet printhead that travels over the powder bed. In a typical machine cycle a layer of powder, usually about 200 μm in thickness, is spread by a levelling mechanism onto the upper surface of the body of powder in the build box: the **powder bed**. Binder is printed to bond the the powder into a cross-section of the part being built. The piston is indexed downward by one layer thickness to make room for a new layer.

This layer-by-layer process repeats until the part is completed. The sequence of operations is shown in figure 1.1. The unbound powder temporarily supports unconnected

portions of the component as the structure is built. After heat treatment, the unbound powder is removed, leaving the completed part. The only geometric restriction on the forms that can be produced is the necessity for loose powder to be shaken out of hollow spaces.

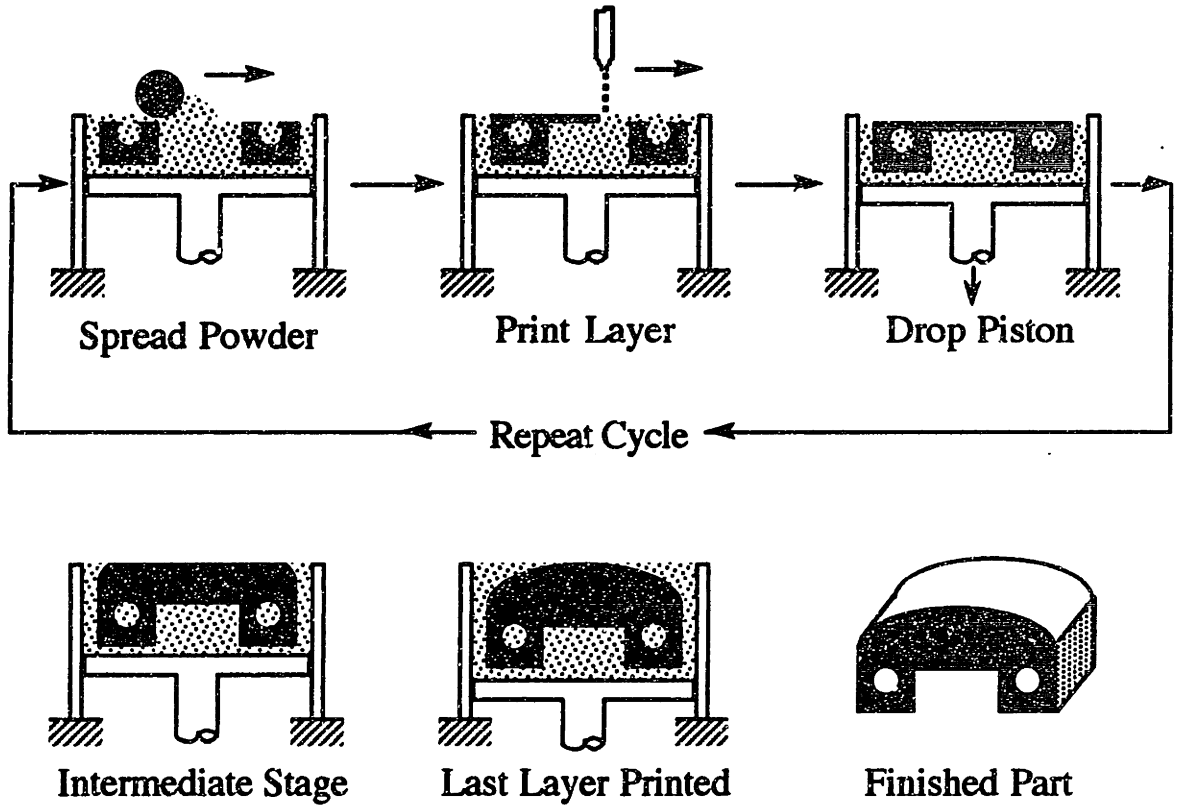

Figure 1.1 Sequence of Operations in Three Dimensional Printing.

The process can potentially be applied to any form of powdered material and any fluid binder. The filler materials that are currently under development are aluminum oxide, fused silica, stainless steel, tungsten, and silicon carbide. For more detailed descriptions of these materials, see theses by Paul Williams, Marcos Esterman, Steve Michaels, and Alan Lauder. Two binders are primarily used for these materials: colloidal silica for the ceramics and Acrysol® latex emulsion for the metals. There has also been some work with alumina suspensions for printing into alumina powder, and making metal dispersions in organic media (See MS thesis of Matthew Galla).

1.2 Three Dimensional Printing of Ceramic Shells

The primary effort in the five-year history of the project has been in the development of printing hardware and a process for producing ceramic shell molds for metal casting. The prospect of building ceramic shells directly from CAD models is very attractive. Cores, cavities, surface texture, filters, and structures that control heat transfer can be designed into a part and formed in a single operation [Sachs, E., et. al. "CAD-Casting: Direct Fabrication of Ceramic Shells and Cores by Three Dimensional Printing", Manufacturing Review 5 2 (6/92), pp. 118-126.] Designs can be iterated without the need to fabricate expensive tooling. This reduces the time and cost of development of castings and permits new products to be brought to market sooner, and with more product variety. The process also offers greater diversity of products that can be produced economically in small runs.

Illustrated below are a few examples of parts produced by the ceramic shell 3-D Printing process. This process utilizes colloidal silica to bond aluminum oxide powder. This combination of materials was selected to closely approximate the material produced by the slurry-dipping process that is conventionally used in industry. [Rusher]

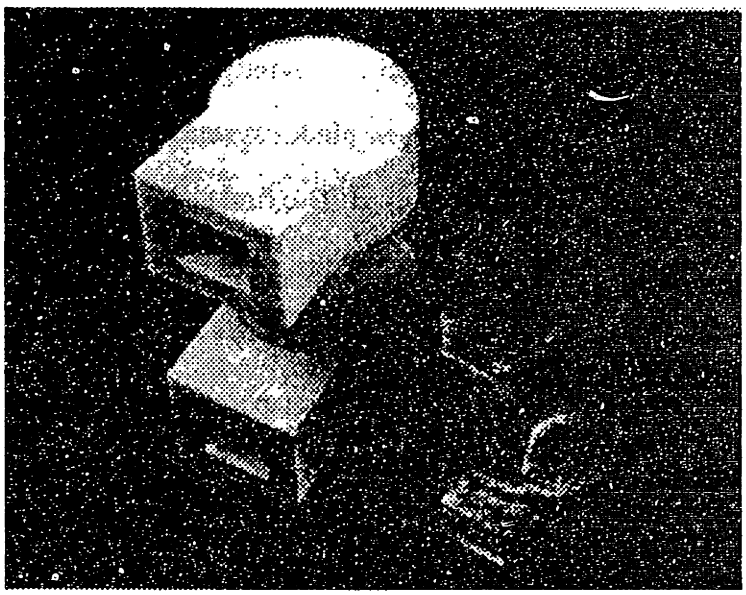

Figure 1.2 Shell and casting for a turbine blade. Blade is hollow, and the shell was printed with a core that integral with the rest of the structure. This demonstration part was cast in Sn-Pb.

Figure 1.3. Rocker arm cast in a 3-D Printed shell. Note some surface defects caused by the lamination of the shell. (Al)

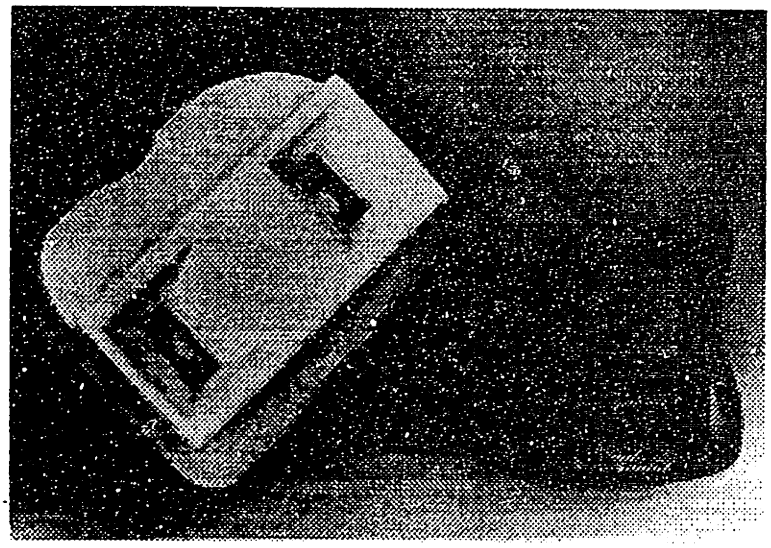

Figure 1.4. Shell and casting of an orthopedic knee implant. (Co-Cr)

To obtain a material that has sufficient mechanical strength to survive subsequent handling and processing, It is necessary to join the grains of powdered filler material with a sufficient quantity of binder solids. In the case of colloidal silica binder and alumina powder, roughly 4 to 10 vol.% of the part must be silica from the binder for it to have adequate strength. The liquid binder is mostly water, and the powder bed becomes supersaturated if the volume of liquid exceeds the pore volume of the bed, which can vary from 40% to 75% of the bed volume, depending on the properties of the powder. For

more discussion of the strength issues in ceramic shell molds, see MS theses by Marcos Esterman and Richard Yu.

Two aspects of dimensional control and surface finish are shown in the following two micrographs. In the first image, the surface of the orthopedic casting in figure 1.4 has been magnified to show the stairstepping defects that arise from the finite width of printed lines grouped in a square raster pattern. The size of the stairsteps is determined by the feature size obtained by the process which is governed by the volume of binder dispensed per unit length of printhead travel and the degree to which binder spreads in the powder from the area of impact.

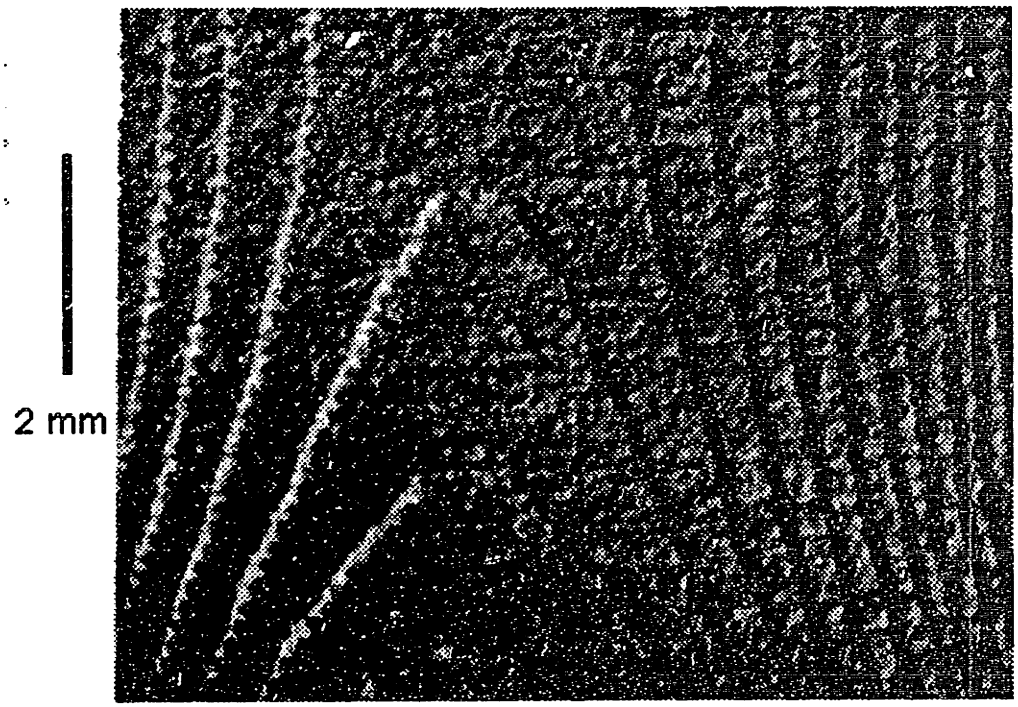

Figure 1.5. Magnified view of casting in figure 1.4 showing surface defects arising from rasterization and lamination of layers, known collectively as **stairstepping**. (M = 15x)

While certain strategies are under development to minimize the stairstepping defect and obtain smooth surfaces on larger parts, the feature size also determined the smallest scale on which useful structures can be defined. The "normal" feature size for the current ceramic shell process is approximately 200 μm, but considerable variation is possible with small modifications to machine parameters. This property was studied in detail in this research. Figure 1.6 below shows the surface of a casting made in a 3-D Printed mold.

The surface is populated with arches about 1mm tall that were cast into wormhole-like cavities in the printed ceramic. These were produced by Alain Curodeau to study adhesive bonding. To produce castings with combinations of smooth and textured surfaces demands the greatest possible control of feature size.

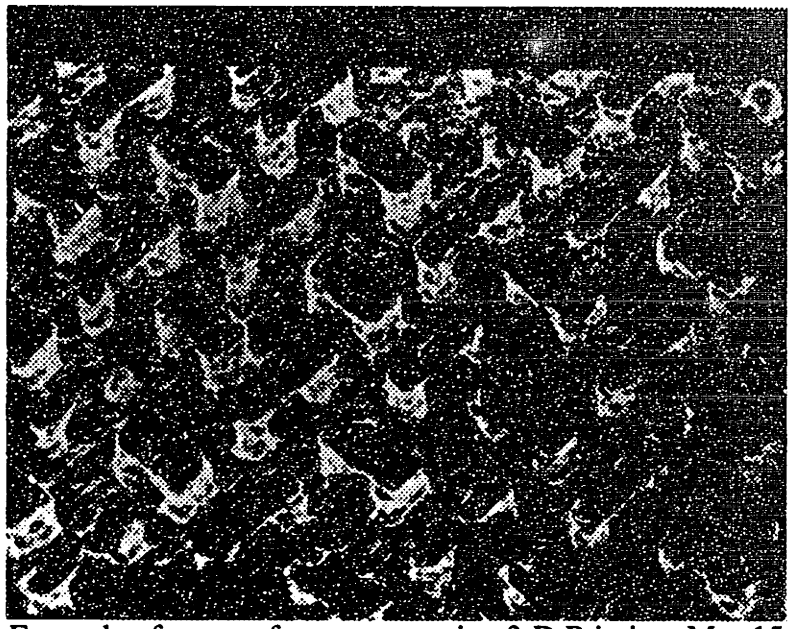

Figure 1.6 Example of cast surface texture using 3-D Printing, M = 15x (Sn-Pb) Casting by Alain Curodeau.

1.3 Printhead Technology

The process of three dimensional printing imposes an elaborate set of requirements on a colloidal dispersion. It must be a well-dispersed, stable fluid that is inert with respect to the printhead materials and have a sufficient volume fraction of solids. The viscosity must be low enough that it can be forced through the nozzle at the desired rate. It must be stable with respect to the very large transient shear rate that is encountered in jet formation, avoid excessive wear to the orifice when passing through it, and it must present a stable meniscus to the outside surface of the nozzle. Once the liquid encounters the powder bed, the stability requirement is suddenly reversed: the solids from the suspension must deposit on powder grains and join them together. Thus the dispersion must be stable, yet not so stable that conditions that exist in the powder bed do not cause it to flocculate or gel and stick to powder grains.

In ink-jet printing there are two major classes of printheads: continuous jet and drop- on-demand. In continuous jet, the fluid is pumped steadily through the orifice, and

the velocity profile is constant over time. In drop-on-demand printing, fluid is pumped through the orifice in a stepwise manner when a particular droplet is needed. It has been found [Williams, P., MS Thesis] that the continuous-jet approach is the most compatible with the colloidal binders because the steady flow of the jet reduces the tendency of the material to dry on the printhead, leading to nozzle failure. Accordingly, a considerable amount of effort has been devoted to the development, control, and maintenance of continuous-jet technology for 3-D Printing of colloidal dispersions. [See MS theses of David Brancazio and Alain Curodeau] This thesis represents a segment of this work: the development and characterization of colloidal silica binder for this process which took place between the fall of 1990 and the spring of 1993.

A description of the general characteristics of the printheads used in the project is given in appendix D.

1.4 Powder\Binder Interaction

The printhead is swept over the powder bed at a rate of approximately 1.5 m/sec. The binder is formed into a stream of droplets approximately 80 μm in diameter which travel downwards at about 10 m/sec. The droplets remain in free flight for about 2×10^{-3} sec before impacting the powder bed at a spacing of about 20 μm. Several droplets overlap one another, and merge to form a linear stripe across the powder. The suite of events leading to the formation of a linear primitive feature are shown in figure 1.7, below.

It has been demonstrated in high-speed photographs made by Tailin Fan that the liquid binder resolves itself into a cylindrical shape in about 10^{-3} sec after impact. Once the liquid comes substantially to rest in the powder, the primary driving force for further movement is capillary attraction which can exert its influence until some mechanism causes the binder solids to be immobilized. One such mechanism could be drying of the liquid vehicle in the binder, but in practice, chemical means are used to solidify the binder at a rate which can be controlled uniformly throughout the powder bed. The distance across which liquid can migrate depends on the fluid mechanics of porous media and the kinetics of the solidification mechanism.

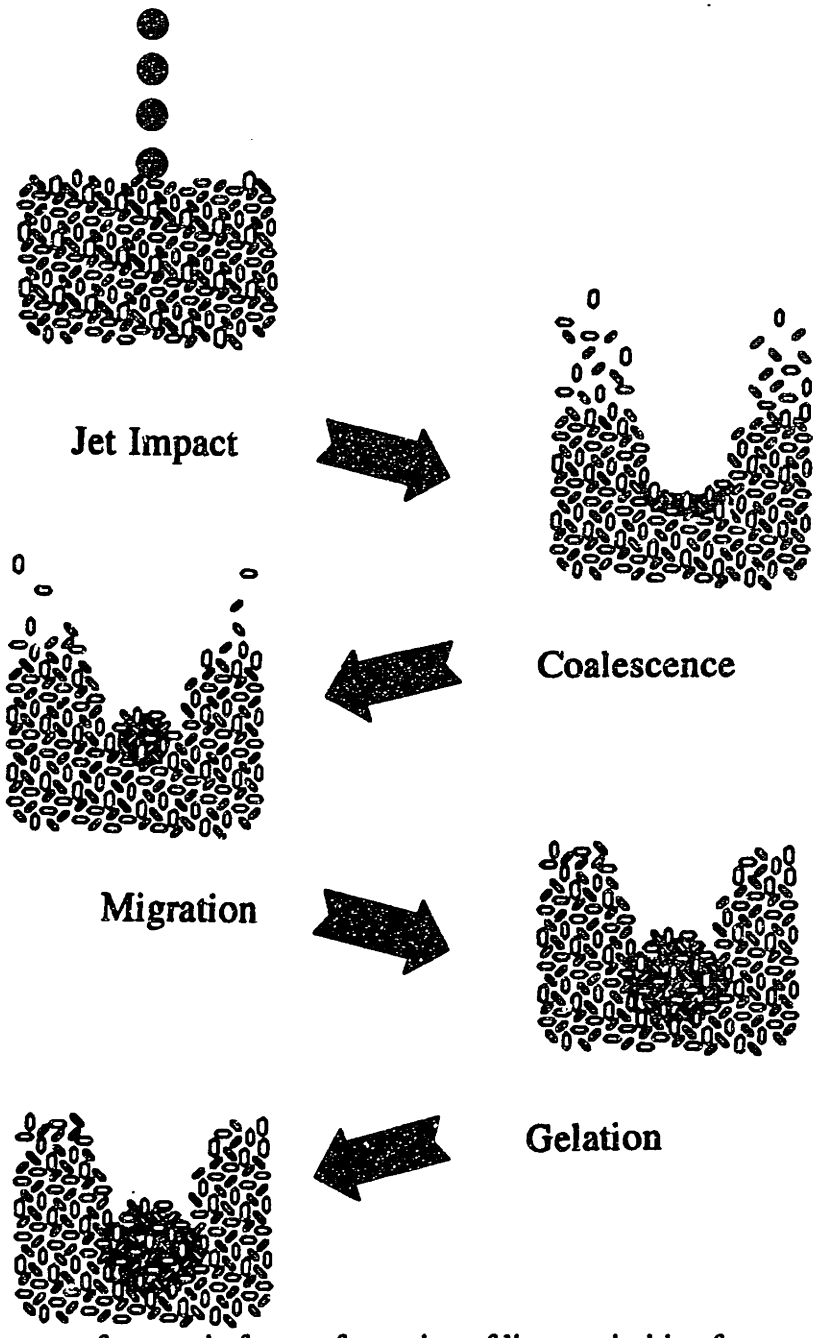

Figure 1.7 Sequence of events in feature formation of linear primitive features in 3-D Printing.

A single line feature is shown in the electron micrograph below. It is a generally cylindrical concretion of powder and binder solids left behind after heat treatment. Individual grains of powder can be clearly distinguished. Irregularities of the surface are approximately the same scale as the grain size of the powder, and deviations from straightness can be attributed in various cases to irregularities in printhead motion,

inhomogeneities in the powder bed, and mechanical distortion of the material during drying.

Figure 1.8 SEM micrograph of a single line feature. Binder: colloidal silica, formula "B" 86 µm droplets, 1.2 cc/min, 1.65 m/sec printhead speed. Powder: 30 µm alumina, Norton # 7920. This corresponds to "normal" printing conditions.
M = 175 x. Bar is 200 µm.

Figure 1.9 Section of a binder stripe across sintered powder. M ≈ 400 x. Lamellar shape of alumina grains is evident. Silica glass is light gray splat in center of image. Dimension bar is 50 µm.

The disposition of silica in powder is shown above. The image in figure 1.9 is a section perpendicular to the axis of printhead motion of a strip of binder printed onto powder that had been sintered to lock its structure and remove the effects of powder rearrangement.

An approximate time line showing the relationship between migration rate and solidification rate is shown below. The impact event can be easily shown (see section 6.6.1) to be finished well before capillary migration takes place. Assuming that some capillary migration takes place before binder can solidify, the timing of the solidification phenomenon determines the distance through which capillary migration can possibly carry the liquid from the point of impact. To develop an understanding of feature formation to control the important parameters, it is necessary to study both the kinetics of solidification and the fluid mechanics of binder in powder.

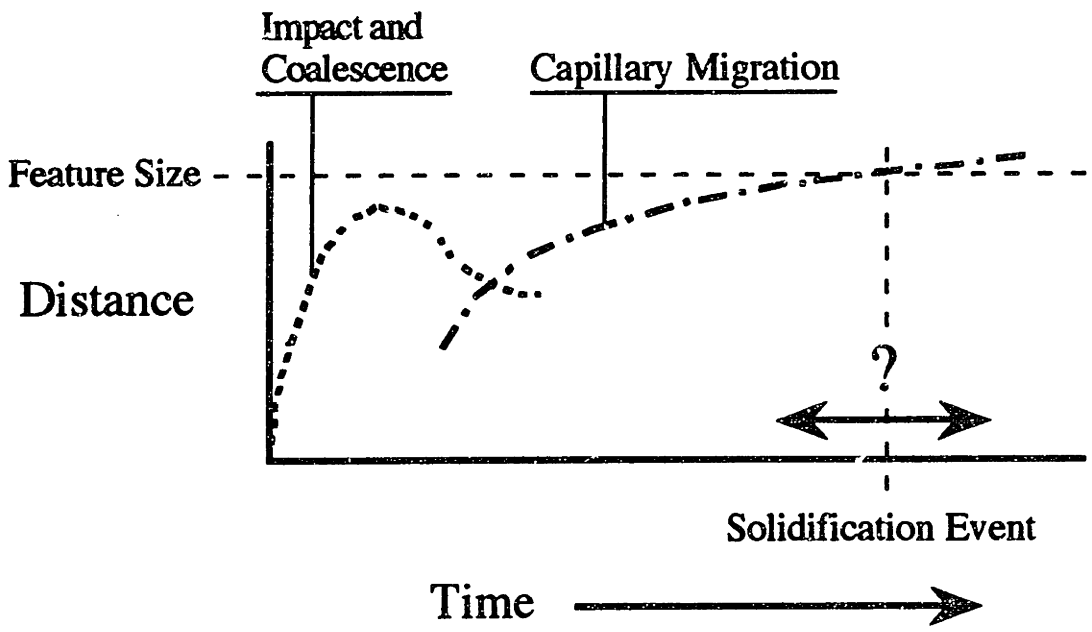

Figure 1.10 Approximate time line for feature formation. Feature size is determined by a competition between the capillary attraction of binder for powder and the kinetics of solidification of the binder.

Alan Lauder, in his MS thesis, began the work of characterizing the interaction of binder and powder in the formation of "primitive" elements from which 3-D Printed parts are composed. Part of this thesis continues this work, and some of the experimental methods described here are an attempt to get around some of the difficulties Lauder

encountered in measuring the size, shape, and density of these primitive features. Since the interaction between powder and binder depends as much cn the structure of the powder bed as it does on the properties of the binder, a theoretical background was needed to find the most important properties to address, both in the modelling of the behavior of the process, and to identify the aspects that should be controlled.

1.5 Organization of this Thesis

To understand the process of feature formation in Three Dimensional Printing, the dynamics of binder solidification and the capillary characteristics of the powder\binder interaction are studied independently. In the course of this research, it was necessary to develop a binder recipe that was compatible with the printing hardware, had a robust and rapid gelation mechanism, and was essentially nontoxic.

A detailed review of colloid science in Chapter 2 and review of the physical chemistry of silica in Chapter 3 are very detailed so that the reader with little background in materials science can develop sufficient familiarity with the concepts, not only to understand the content of this work, but to extend it and further advance 3-D Printing as a process. Chapter 4 describes the experiments that led to the development of a robust binder formula and measurements of the kinetics of its solidification mechanism.

At the conclusion of of the first half of this thesis, the silica binder that is presently used at M.I.T. is presented and its functional properties and limitations are discussed. When the binder was introduced to the process in the spring of 1993, it became evident that the rate of capillary migration in the powder was very much faster than any external mechanisms (e.g. chemically triggered coagulation or drying) could act to bring it to a halt.

In Chapter 5, a review of the literature is given on capillary phenomena in porous material. Background on capillarity in general can be found in Appendix A. Calculations of the rates over which phenomena act that influence feature formation are collected at the beginning of Chapter 6. A model for feature formation is developed in Chapter 6 based on a balance of capillary pressure between a partially saturated feature and the dry powder surrounding the feature. A theoretical background including models for pores and pore structure is given in Appendices B and C. The experimentation on the capillary properties of the materials used are discussed in Chapter 7. These measurements were used to derive

estimates of the volume fraction of the pore space (saturation) filled by binder in primitive features at equilibrium with their surroundings.

Chapters 8 and 9 discuss measurements of the size and density of 3-D Printed features. "Primitive" features are defined as linear concretions (e.g. in figure 1.8) that form during a complete pass of the printhead over the powder bed. In Chapter 8, results are discussed that describe the 3-D Printing process using materials and techniques that characterize the "ordinary" ceramic shell process: "Normal" binder as developed in the first half with only slight modifications in composition and "normal" powder which has a mean grain size of 28 - 30 μm and whose morphology is described in John Lee's MS thesis as "lamellar". In Chapter 9, the results of process variations are discussed. These variations include changing the jet diameter, modifying the acid content of the powder, and using powders with unusual characteristics. The numerical data is given in Appendix E.

Chapter 2. The Colloidal State

2.0 Introduction

In Three Dimensional Printing, grains of a powdered filler material are bonded by an adhesive dispensed through an ink-jet printhead. For the purposes of building ceramic shell molds, the materials of choice are determined by the technology: colloidal silica is practically the only suitable material to use as a binder for the ceramic powder. For other applications, other adhesives can be considered. In order to form mechanically strong bonds between powder particles, it is necessary that about 6 - 10% of the material comprising the finished part be in the form of welds between powder grains. If the welds are composed of adhesive dispensed by the printhead, then it is necessary that the liquid binder contain roughly the same percentage (6-10% by volume) of solids. Few inorganic substances are soluble to this degree, and polymer solutions at these concentrations are excessively viscous. For these practical reasons, the solids carried by the binder must necessarily be dispensed as a dispersion of solid particles in a liquid carrier.

Certainly the connection between Three Dimensional Printing and ordinary printing makes a connection between binder and printing ink an obvious one, except that printing inks contain substances that color the ink (e.g. carbon black or copper phthalocyanine) and contribute little mechanical strength to the dried ink. By contrast, most of the structural materials used in 3-D Printing are stiff or elastic, and are usually transparent or off-white at the very deepest. Nevertheless, the same considerations involved in the formulation of paints and inks are significant for 3-D Printing. There are numerous books discussing paint chemistry. See, for example, [Parfitt]; [Myers, R.]; or [Parker]. Additionally, there are references specifically dealing with ink-jet inks: [Leach and Pierce]; [Gregory]; and [Ashley, Edds & Elbert]. Soluble "Direct" dyes are preferred for ink-jet inks: these are strong enough that black ink contains about 5% solids or less in solution.

This chapter contains a basic review of colloid science for the ink technologist. After classifying different types of colloids, the hydrodynamics of particulate suspensions are discussed in some detail. Features like the Brownian diffusivity and its consequences are explained, as well as dynamic effects that bear on the transport of particulate suspensions in tubing. The mixing of fluids of different densities in transport is described

in terms of the Froude number (Sect. 2.2.3 .) The rate of aggregation of Brownian particles and the statistics of stability are described and the aggregation of particles in shear flow is considered in the derivation of an optimum tubing sized for transporting particulate suspensions. (Section 2.2.9)

The classical mechanisms that stabilize colloidal suspensions are described. The balance between Van der Waals attraction and coulombic repulsion is discussed to introduce the method used to calculate the stability of colloidal silica.

2.1 Terminology and General Properties.

2.1.1 Major Classes of Colloids

A **colloid** is a suspension of particles in a fluid whose thermal agitation is sufficient to keep them permanently suspended against gravity. The term **sol** describes a system of solid particles in a liquid. India ink is such a sol of carbon black in water. An **emulsion** is a suspension of liquid droplets dispersed in an immiscible liquid. Mayonnaise is a classic example of this. A **foam** is a gas dispersed in a liquid, and an **aerosol** is a solid or liquid dispersed in a gas. (See [Hunter] p.3 for other designations.) In this work, the fluid dispersing medium will be referred to by a variety of names. The phase that is discontinuous in the sol is the **dispersed phase**, but will ordinarily be referred to as the **particles**. The terms **medium** or **vehicle** or simply **fluid** will, unless otherwise stated, refer to to suspending medium of a sol. Most of the sols that will be considered are aqueous, but the term **water** where it appears will be used exclusively for the chemical H_2O in pure or nearly pure form.

There are two fundamentally different types of colloids, distinguished by the interaction of the particles with the supporting medium. A **lyophilic** colloid is defined as one in which the free energy of the system decreases when the particles are dispersed. In a **lyophobic** colloid the free energy increases with dispersion. Thus, if the particles are more strongly attracted to the vehicle than to each other, the system is lyophilic. Furthermore, if the vehicle is water, sols care **hydrophilic** and **hydrophobic**: Sodium alginate is a classic example of a hydrophilic sol, also called a hydrosol. Natural rubber latex is an example of a hydrophobic sol. There exist several materials for which the free energy change on dispersion can be positive or negative under different conditions (e.g. pH). There is no good term for these materials, although the principal object of this study, colloidal silica, should be considered a member of this group.

Table 1 below gives some general properties that distinguish the two principal classes of colloids. Colloidal silica is a special case of a generally hydrophobic sol that exhibits some hydrophilic properties (properties 1,2,and 5, below).

Lyophilic	Lyophobic
1. High concentrations of disperse phase frequently stable.	Only low concentrations of disperse phase stable without steric stabilization

The upper limit concentration for lyophobic sols is determined by the physical phenomena that prevents the particles from spontaneously aggregating.

2. Unaffected by small amounts of electrolytes. "Salted out" by large amounts.	Very easily precipitated by electrolytes

Since lyophilic colloids are stabilized primarily by solubilization, the presence of other solutes affects the solvency of the medium. The effect on lyophobic colloids comes from the coulombic interactions with ions in solution.

3. Stable to prolonged dialysis	Unstable to prolonged dialysis

This is a filtration technique for extracting small solute molecules from the sol. The lyophobic colloids are unstable because small amounts of electrolytes adsorb to otherwise neutral particles to form charged layers. Particles with acid or base surface groups that can dissociate are able to self-ionize, so they are an exception to this rule. Colloidal silica is one of these.

4. Residue after desiccation will take up medium spontaneously.	Irreversibly coagulated on desiccation

The surfaces of lyophilic particles attract the dispersing medium strongly. Lyophobic particles are more strongly attracted to each other than to the medium.

5. Coagulation gives gel or jelly	Coagulation gives definite granules

Lyophilic colloids are usually composed of tangled molecules which form a network when crosslinked. Lyophobic colloids always have discrete particles that form aggregates. An exception is when a lyophobic colloid has a very heavy solids loading and particles coagulate to form a space-filling network.

Lyophilic	Lyophobic
6. Usually gives weak Tyndall beam	Very marked light scattering.

Light is scattered strongly by dense particles in lyophobic colloids. The Tyndall beam is the light that is scattered perpendicular to the light source. Lyophilic colloidal particles are frequently diffuse and swollen with solvent so their index of refraction is generally much closer to that of the suspending medium.

7. Surface tension generally lower than dispersion medium	Surface tension not affected

Surface-active molecules generally form lyophilic colloids; most lyophilic sols are surface active to some degree. Lyophobic particles are inert unless treated with surfactants.

8. Viscosity frequently much higher than that of medium	Viscosity only slightly increased.

In lyophilic colloids, the molecules are frequently long chains that are solvated and tangled together. Lyophobic particles only affect the viscosity by surface friction on the compact particles.

Table 2.1 (copied from [Hunter] p.7)

The particle size in a colloid ranges from a few nanometers up to a micron. Frequently the particle size is expressed as a surface area per unit weight. This is because particle sizes are usually determined by measuring the mass of a gas adsorbed on the surface. The gas (e.g. N_2 just above its condensation point) covers a fixed area per unit weight. The vapor pressure of the adsorbed material varies with the pore curvature according to the Kelvin equation (discussed in Appendix A, section A.8.)

Lyophobic colloids are thermodynamically unstable, and under thermal agitation particles will eventually collide and adhere by Van der Waals attraction (see, for example, [Hunter] ch. 4.) Ultimately, particles aggregate into groups that exceed colloidal dimensions. This is generically referred to as **coagulation.** Small, dense groups are called **aggregates**, while porous, diffuse groups are called **flocs**. In the end state, if the particles remain separate, the material is **flocculated** or **aggregated** but if the particles form a continuous, solid network, it is a **gel**. If the gel exudes the clear liquid phase, it is called **syneresis** or **coacervation**. This phenomenon can be observed in cheese, which gradually sweats whey out through the pores in its surface. Many food additives prevent this from happening in some products: ice cream, which is composed of lyophobic milk-fat

particles that are aggregated by freezing, is stabilized by addition of a lyophilic colloid like the polysaccharide Carrageenan. (See, for example, [Gums and Stabilizers])

2.1.2 Other Useful Chemical Classes

Surfactants are substances that possess **surface activity**. These materials are preferentially attracted to phase boundaries between immiscible materials. Their molecular structure is **amphiphilic**: one end of the molecule has a polar, or hydrophilic **head**, and the other has a nonpolar, hydrophobic **tail**. (see [Myers, D.]) There exists a very broad spectrum of surfactants with a wide variety of characteristics. Many are used as **dispersants**, or stabilizing agents for lyophobic colloids. Others are **wetting agents** which lower the surface tension of water without being strongly amphiphilic. **Detergents** are specialized to dispersing oils or oily particles in water. Still others are **coagulants**: they reduce the stability of a sol. Solutions of surfactants commonly form a type of lyophilic colloid called a **micelle**. A micelle is a condensed phase of the surfactant that forms when the surfactant concentration exceeds the **critical micelle concentration** (c.m.c.) There are several chemical classes of surfactants: the most common are **anionic**: a salt consisting of an amphiphilic anion and a soluble cation, such as sodium. Sodium dodecyl sulfate is a common example. For **cationic** surfactants, the charges on the amphiphile and counterion are reversed. **Nonionic** surfactants are amphiphilic without having a salt on the hydrophilic end. They usually have polyethylene oxide as the hydrophile and an aliphatic/aromatic group or polypropylene oxide as the hydrophobe. Another class is **zwitterionic**: changing from cationic to anionic as pH is varied. For a detailed classification of commercial products and their applications, see [Nelson], pp. 71-110.

The term **latex** (or sometimes **latice**) is used for dispersions of organic polymers. The word derives from the latin for "milk". Although the original latex is natural rubber, polyisoprene, the most common synthetic materials are dispersions of polystyrene or acrylic ([Hunter] 17) and are sometimes called **resins**. These are manufactured by polymerization of an emulsion of monomer. (see [Blackley]) Paint resins include a very wide variety of polymers (see, for example, [Parker] 241-271.)

Gum is a generic term for hydrophilic polysaccharides originally derived from plants. Polysaccharides are polymers derived from sugars and encompass an amazing variety of properties. Cellulose is composed entirely of glucose, is insoluble in water and

has good mechanical properties. Gum arabic is ionic, water soluble, and functions as a colloid stabilizer (e.g. india ink.). Heparin is a powerful dispersant used in surgery as a blood anticoagulant. Chitin is a structural material used by insects, and chitosan is a chemically modified form that is a potent coagulating agent. Sodium alginate is used widely as a thickener because it is easily crosslinked by calcium. (See [Hirst]) Starch, like cellulose, is a polysaccharide composed primarily of glucose monomers but linked together differently from cellulose in a way that makes it accessible to metabolic break-down. Besides a food, it is used very widely as an adhesive.

2.2 Hydrodynamics of Colloids and Suspensions

A colloidal dispersion can consist of hard particles, liquid droplets, micelles, or soluble polymers. Each of these have different hydrodynamic characteristics especially when shear flow is considered. While some consideration will be given to each, the greatest attention will be paid to to suspensions of solid particles in a liquid because of its importance to Three Dimensional Printing.

2.2.1 Friction Coefficient

The particle size of colloidal dispersions ranges from one micrometer down to about 10 nm. The flow in the vicinity of particles of this scale is inertia-free, so the Stokes-Einstein solution can be applied to derive the fluid interaction with individual particles.

The drag force (also called the **friction coefficient** , see [Hunter], p.134) on a solid spherical particle immersed in an inviscid, inertia-free liquid is

$$F_{s/l} = -6\pi a u_1 \eta_{medium} \qquad 2.1$$

where η_{medium} is the viscosity of the liquid medium, a is the particle radius, and u_1 is the relative velocity between the particle and the bulk of the liquid. For an emulsion consisting of spherical liquid drops with viscosity η', the drag force is reduced by the factor ([Probstein], p. 109)

$$F_{l/l} = \frac{2}{3}\frac{\eta_{medium} + \frac{3}{2}\eta'}{\eta_{medium} + \eta'} F_{s/l} \qquad 2.2$$

In the limiting case of air bubbles in the fluid this factor approaches 2/3. As $\eta' \rightarrow \infty$ (for solid particles) the factor approaches unity.

2.2.2 Sedimentation Velocity

There exists an impressive theoretical foundation to deal with nonspherical particles. For the purposes of this study, it is sufficient to define the **hydrodynamic radius** which is the radius of a spherical particle having the same drag characteristic as a given nonspherical particle. One method for determining the hydrodynamic radius is to measure the settling velocity of particles in a suspension. This velocity can be calculated by equating the buoyant weight of a particle with the drag force and solving for the terminal velocity:

$$u_1 = \frac{2}{9} \frac{ga^2}{\eta_{medium}} \left(\rho_{particle} - \rho_{medium}\right) \qquad 2.3$$

where g is defined generally as a body force, including the inertial force in a centrifuge. For fluid droplets, the velocity is increased by the factor given above. In the limiting case of a spherical air bubble with negligible density and viscosity, $u_1 = \frac{ga^2 \rho_{medium}}{3\eta_{medium}}$.

Particles settling through a liquid medium do not interact with each other until the volume fraction of particles exceeds about 0.15 ([Hunter], 529). At loadings above that level, the settling becomes slower due to the interactions of the flow fields of the particles. An empirical correction, known as the Richardson-Zaki correlation ([Probstein], 134) is

$$u_{conc} = u_1 \left(1 - f_{particle}\right)^{4.7} . \qquad 2.4$$

where $f_{particle}$ is the volume fraction of particles in the medium, also called the **solids loading**. Sedimentation under these conditions is called hindered sedimentation, and this equation cannot reflect the behavior of very dense suspensions approaching the critical loading. [German] (p. 168) recommends replacing the solvent viscosity in equation 2.3 above with the viscosity of the suspension . As the solids loading approaches the critical loading, the viscosity becomes infinite and the settling speed vanishes.

2.2.3 Stratification

In a monodisperse suspension of noncolloidal particles, the particles settle at the same rate, so a suspension that has been permitted to settle for a period of time will have three zones: a clear region containing essentially no particles on the top surface, a cake of settled particles on the

bottom, and a body of suspension with its composition essentially unchanged separating the two. The disposition of these regions reflects some of the properties of the colloid, and bears some discussion.

The bulk density of the clarified fluid is less than that of the suspension, and has a lower viscosity. These differences permit stratified flow in a settling suspension. This will be discussed in greater detail below, but for illustration, consider the Boycott effect: A suspension is observed to settle more rapidly in an inclined tube than in a vertical tube. The lighter clarified fluid can rise along the upper wall of the tube and collect in a pool on the upper surface. Particles settle away from the upper wall proportional to the sine of the angle of the tube with respect to the vertical.

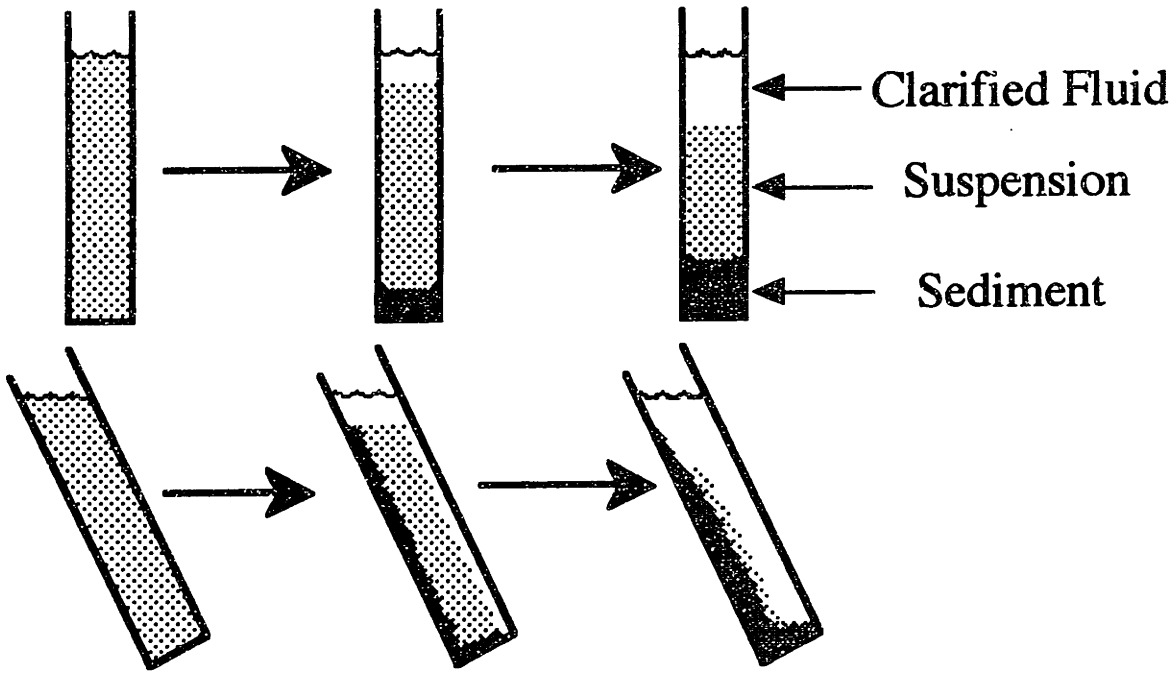

Figure 2.1 The Boycott effect describes how suspensions settle substantially faster in a tilted tube than in a vertical tube. The effect is primarily geometrical, but clarified fluid also tends to pipe upwards along the downward-facing wall of the tilted tube.

In ink-jet printing, colloidal suspensions are transported through tubing from a reservoir to a printhead. It is almost unavoidable that some tubing will be used to carry the colloid and the pure solvent as a rinse solution at different times. If the denser colloid is mixed with the pure suspending medium, the displacing fluid must have a sufficient kinetic energy to carry off a pool of the residual fluid. For fluid moving with velocity u in a tube of radius r, the Froude number is defined as the ratio between kinetic energy and gravitational potential energy:

$$Fr = \frac{u^2 \rho_{medium}}{(\rho_{suspension} - \rho_{medium})gr} \qquad 2.5$$

Fr >> 4 ([Probstein] p.47) is necessary for the two fluids to mix thoroughly and allow one to purge the other from a line when the fluids are switched. In a fluid system operating with a low Froude number, the two fluids cannot mix hydrodynamically, and so residual fluid can only be dispersed by diffusion. The consequences of this can be very inconvenient. If the printhead is disconnected from its feed tubing after insufficient purging, there will remain traces of the binder in both the head and the tubing. These traces can dry and aggregate to particles that can clog the head. In the first two years of the 3-D Printing Project, this was overwhelmingly the most common nozzle failure mechanism. This problem is alleviated somewhat by the ability to cross-flush the printheads, which allows a high fluid velocity to be established in the tubing without having to squeeze the fluid at high rate through the nozzles.

2.2.4 Sediment Volume

The sediment that collects at the bottom of a container consists of particles from the suspension packed at their critical loading f_{crit}. The critical loading is the packing density at which the particles form a self-supporting bed with fluid filling all of the pores. For a well-dispersed suspension, the volume fraction of solids in the sediment can vary from 0.45 to 0.8, depending on the geometry of the particles and the distribution of particle sizes ([German], 138). The volume fraction of the sediment with respect to the total volume of the original suspension will be $f_{particle}/f_{crit}$. If the particles are flocculated, the flocs have a hydrodynamic radius that is much larger and a bulk density that is much lower than the ultimate particles. Illustrated below are flocs of gold particles of varying dimensions.

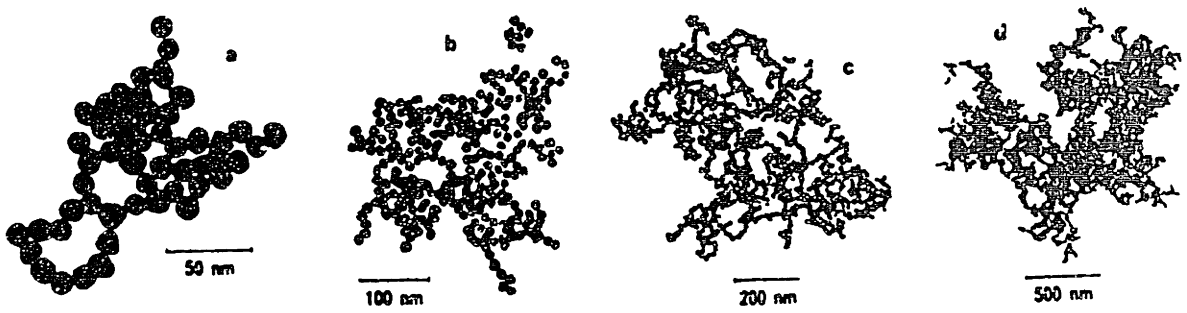

Figure 2.2 Transmission electron micrographs of clusters of gold particles [Feder], p.38.

Matsuchita (in [Avnir], p.173) reports that flocs in aggregated colloidal particles generally have a **fractal dimension** of $\partial \approx 1.75$ to 2.0. [Feder] (pp.38-40) discusses results for aggregates of colloidal silica particles, $\partial = 2.12 \pm 0.05$. This leads to the relation

$$r_H \propto a\, n^{1/\partial} \qquad 2.6$$

where R_H is the hydrodynamic radius of a floc, n is the number of particles of radius a. From this, we can derive an expression for the floc density:

$$(\rho_{floc} - \rho_{medium}) = \frac{a^3 n(\rho_{particle} - \rho_{medium})}{r_H^3} \propto n^{1-3/\partial} \qquad 2.7$$

since the settling velocity goes as $r_H^2(\rho_{particle} - \rho_{medium})$ (eqn 2.3), the settling velocity for flocs should vary as

$$\frac{u_n}{u_1} = \frac{an}{r_H} \propto n^{1-3/\partial} = n^{0.53} \text{ for colloidal silica.} \qquad 2.8$$

The flocs act as independent particles in suspension, and the volume fraction of the suspension can be redefined in terms of the hydrodynamic volumes of the flocs:

$$f_{floc} \propto n^{-1+3/\partial} f_{particle} \propto n^{0.42} \text{ for colloidal silica.} \qquad 2.9$$

The volume fraction of primary particles in the binder presently used for 3-D Printing is 0.17. This implies that when the flocs contain approximately 70 particles, the flocs will overlap to form a "gel."

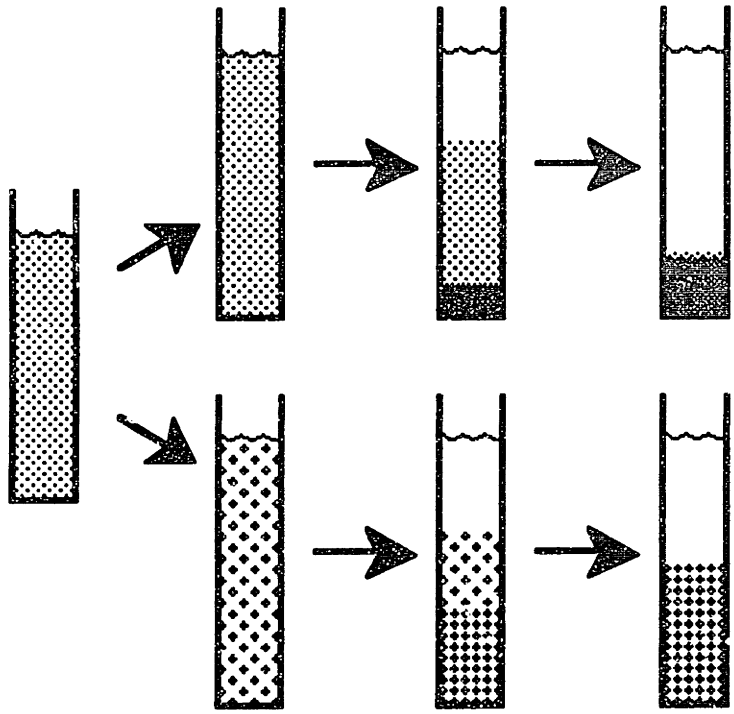

Figure 2.3 Difference in sediment volume for flocculated and unflocculated suspensions. The settling rates for the two samples are not the same: the flocculated material settles much faster.

The settling rate of flocculated material is higher than the well-dispersed colloid, and the volume fraction of the sediment with respect to the original suspension will ultimately be f_{floc}/f_{crit}. Flocs generally contain hundreds or thousands of particles, so the sediment can easily be ten times bulkier in flocculated material than in well-dispersed material. The sediment volume increases with floc size until $f_{floc} = f_{crit}$ at which point the flocculated suspension will be self-supporting and could more properly be called a gel.

In a well-dispersed colloid with particles ≤100 nm, the settling velocity will be so low that the turbulence induced by handling is sufficient to maintain the integrity of the dispersion. The difference between this extreme and the other, in which the material is so severely flocculated that it does not settle, is easily recognized: gelled material is highly thixotropic, or shear-thinning, since weak bonds form between individual flocs on standing but are easily broken under shear. Also in gelled material, the flocs slowly consolidate, exuding a clarified solution that accumulates slowly on the top.

2.2.5 Brownian Motion

In 1822, Robert Brown observed the chaotic motion of pollen grains suspended in water. This phenomenon occurs because colloidal particles participate in the equipartition of the kinetic energy of the molecules in the system. The particles have a mean kinetic energy of ½kT and this allows them to climb against gravitational sedimentation to attain an equilibrium distribution derived by Perrin in 1909*:

$$\frac{N_P}{N_{z=0}} = \exp\left(\frac{-m_P g x}{k_B T}\right). \qquad 2.10$$

* (This was one of the first direct measurements of Boltzmann's constant, k_B, from which Avogadro's number, $N_A = R/k_B$ can be calculated where R is the universal gas constant.)

where m_P is the particle's buoyant weight and x is the vertical distance between concentrations n and $N_{x=0}$. The quantity (k_BT/m_Pg) gives a characteristic height to which Brownian motion is capable of carrying particles in a given system Over this height, the particle concentration decreases by a factor of e= 2.718... the is the **1/e height** given below in table 2.2. For particles of order 100 nm and larger, this distance is much smaller than dimensions of ordinary containers. Colloids with particles in this range are only metastable, and must be agitated to stay in suspension. Colloidal silica of 100 nm particle size is just at the limit where thermal cycling and periodic handling are sufficient to maintain the integrity of the suspension.

The sedimentation equilibrium described above can be visualized as a balance between the gravitational potential mg and the chemical potential defined by

$$\mu = \mu_0 + k_B T \ln\left(\frac{N_P}{N_{z=0}}\right) \qquad 2.11$$

where μ_0 is the chemical potential (per particle) at a standard state and $N_{x=0}$ is the particle concentration at the standard state. With a chemical potential defined for colloidal particles, one can define the driving force for particle diffusion as a gradient in chemical potential (Hunter, 56):

$$\nabla\mu = {}^{k_B T}\!/_{N_P}\ \nabla N_P \qquad 2.12$$

this quantity, with units of energy per unit length, is equivalent to a force on the particles pressing from high concentration to low concentration. With the particles free to diffuse through the fluid, this force is opposed by the hydrodynamic drag

$$F = -6\pi a u_1 \eta_{medium} = {}^{-k_B T}\!/_{N_P}\ \nabla N_P \qquad 2.13$$

The particle flux is given by $J = N_P u_1$. A diffusion coefficient is defined by Fick's first law:

$$J = -D\nabla N_P \qquad 2.14$$

Accordingly,

$$D = \frac{k_B T}{6\pi a u_1 \eta_{medium}} \qquad 2.15$$

[Hunter 50-61] has a very good exposition of this concept.

The Brownian diffusivity of colloidal particles can also be derived from purely statistical considerations. This was done by Einstein in 1905, and equation (2.15) is called the Einstein-Smoluchowski equation. (This is regarded as one of the earliest experimental verifications for the existence of molecules as discrete particles. Three other papers that Einstein published in 1905 introduced the special theory of relativity, the energy equivalence of matter ($E = mc^2$), and the quantum mechanical foundation of the photoelectric effect. The last of these papers won Albert the 1921 Nobel prize in physics.)

Shown below are calculations for representative systems.

material	density g/cm^3	particle diam, μm	particle mass, g	settling vel. cm/sec	1/e diff'n height, cm	diffusivity cm^2/sec
amorph.silica	2.19	0.01	1.15×10^{-18}	6.48×10^{-9}	67.15	4.35×10^{-7}
amorph.silica	2.19	0.1	1.15×10^{-15}	6.48×10^{-7}	6.72×10^{-2}	4.35×10^{-8}
alumina	3.97	0.5	2.6×10^{-13}	4.04×10^{-5}	2.2×10^{-4}	8.7×10^{-9}
polystyrene	1.04	1	5.45×10^{-13}	2.18×10^{-6}	2×10^{-3}	4.35×10^{-9}
iron	7.86	1	4.12×10^{-12}	3.73×10^{-4}	1.2×10^{-5}	4.35×10^{-9}

Table 2.2 Dynamic properties of colloidal particles in aqueous medium at 25°C. The 1/e height is defined above in the discussion of equation 2.10.

The relative stability of these systems with respect to gravitational sedimentation is expressed by comparing the sedimentation velocity and the diffusion height. A settling velocity of 1.2×10^{-6} cm/sec corresponds to a rate of 1 mm per day. This is probably the upper limit that can be stirred by ambient noise and does not require special agitation. [Shaw, D., 204] The diffusion height expresses the range through which Brownian motion all by itself is capable of redistributing particles. If this distance is smaller than a characteristic dimension of the fluid container, the colloid will be incapable of homogenizing itself if, for example, it is mixed with pure solvent and not stirred thoroughly. For large colloidal particles, the diffusivity can be exceedingly slow. The time for 100 nm particles to diffuse a mean distance of 30 cm in the absence of gravity is about 650 years.

2.2.6 Model for Interparticle Spacing

When evaluating additives for a colloidal dispersion, it is important to consider a characteristic dimension which expresses the mean distance between adjacent particles.

The distance B between particles corresponds approximately to the diameter of a spherical region of fluid occupied by that particle. Particles of radius a have a volume of $\frac{4\pi}{3}a^3$ and occupy a sphere of fluid with diameter $\frac{4}{3}(2a + B)^3$. If B approaches 2a, the packing of particles resembles a 12-coordinated close-packed lattice. At a theoretical maximum of $f_{crit} = \frac{\pi}{3\sqrt{2}} \approx 0.7405$, all of the particles touch. The volume of the spherical region occupied by a particle, $\frac{4}{3}(2a + B)^3$, is therefore approximately equal to 0.7405 times the total volume. The volume fraction can be expressed as follows:

$$\frac{8a^3}{(2a + B)^3} \approx \frac{f_{particle}}{.7405} \qquad 2.16$$

and

$$\frac{B}{a} \approx -2 + 1.8094\, f_{particle}^{-1/3} \quad \text{for } 0 < f_{particle} < f_{crit} . \qquad 2.17$$

A graph of this function is shown below.

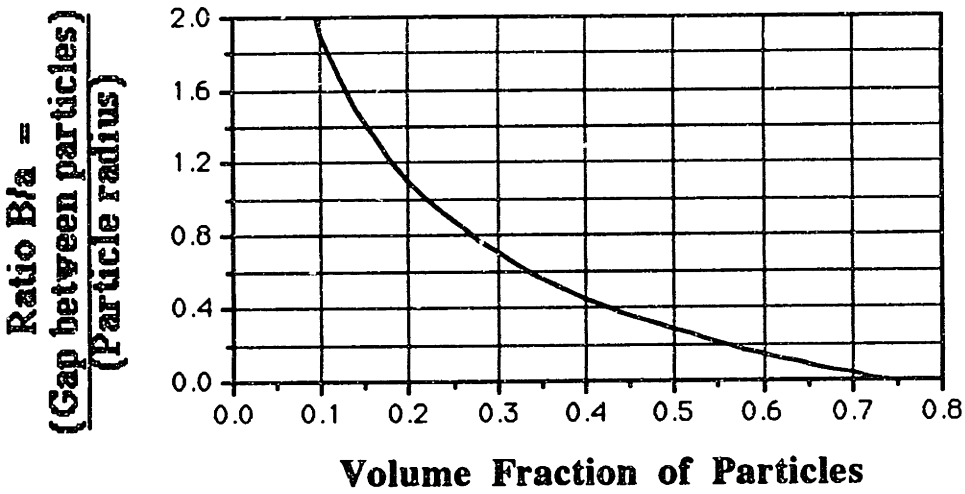

Figure 2.4 Distance between particles expressed as a ratio to the particle radius, as a function of the volume fraction of particles in a sol.

In an actual colloid, the particles move around at random. Each particle will be coordinated with 12-14 other particles, and the spacing is probably uniformly distributed between zero and about 2B. At any given time, the distance to the nearest particle is likely to be 15 - 20% of the mean particle spacing. For 100-nm colloidal silica at 50 wt.% ($f_{particle}$=0.33) the nearest particle would only be 5 nm or so away from any given particle.

Although this expression is only approximate, its accuracy is highest as the solids loading increases. The close-packed arrangement minimizes the energy of the lattice if there is a repulsive force between particles.

2.2.7 Viscosity of Suspensions

In 1956, at the end of his career, Einstein calculated the energy dissipation by viscous forces in a dilute suspension contained in simple shear (Couette) cell:

$$\frac{\eta_{suspension}}{\eta_{medium}} = 1 + \tfrac{5}{2} f_{particle} \qquad 2.18$$

where $\eta_{suspension}$ is the apparent viscosity of the suspension with volume fraction $f_{particle}$ in the limit for dilute suspensions with $f_{particle} < 0.15$. For fluid droplets with a viscosity η', Taylor found the expression [Probstein, 128]

$$\frac{\eta_{suspension}}{\eta_{medium}} = 1 + \left(\frac{\frac{5}{2}\eta' + \eta_{medium}}{\eta' + \eta_{medium}} \right) f_{particle} \cdot \qquad 2.19$$

While these expressions accurately describe dilute dispersions, it is the viscosity of concentrated dispersions that varies more significantly with composition. [German p 157] suggests a model of the form

$$\frac{\eta_{suspension}}{\eta_{medium}} = \left(1 - \frac{f_{particle}}{f_{crit}} \right)^{-n} \qquad 2.20$$

where f_{crit} is the critical solids loading and n is an exponent chosen to fit the data. The requirements for a model are that $\eta_{suspension}$ goes to infinity as the critical solids loading and approach the Einstein equation in the limit as f approaches zero. The critical solids loading is the volume fraction at which the particles achieve a random dense packing and the solvent fills the intersticies. He recommends a value of 2.0 for n, although this only approaches the Einstein equation as $f_{particle} \rightarrow 0$ if $f_{crit} = 0.8$.

The rheological behavior of concentrated dispersions is really much more complicated than these models would suggest. The viscosity must depend on the particle shape and the characteristics of the boundary layers surrounding the particles. As the volume fraction approaches the critical loading, all of the deformation is concentrated in the thin films of solvent separating the particles. Under these conditions, small amounts of surfactants can have profound effects, both by modifying the viscosity of the surface layers and by altering the critical loading.

[German ch. 6] devotes an entire chapter to discussing the rheology of dispersions. Besides monodisperse suspensions, he devotes considerable attention to bimodal spherical dispersions, nonspherical particles, and agglomerated particles.

[Iler 360-364] discusses the viscosity of colloidal silica in detail. There are several phenomena that can contribute to an increase in viscosity. The presence of adsorbed water on the silica surface increases the effective diameter of particles: this tends to increase the viscosity of a dispersion of fine particles over the viscosity of one of coarser particles at the same solids loading. Flocculation increases the viscosity by forming low density

aggregates that have a higher effective solids loading than the unflocculated material , discussed above in section 2.2.4. Colloidal particles normally have a diffuse layer of electrolyte ions attracted to them. This ion atmosphere pins down the solvent more closely to the particle surfaces and increases their effective diameters. This effect is most significant for small particles 10 nm and smaller.

2.2.8 Light Scattering in Colloids

Colloidal particles can be as large as the wavelength of light, but can be considerably smaller. The smallest particles scatter light even though their size is very much smaller than the wavelength of light. The phenomenon is known as the Tyndall effect (after John Tyndall, a Victorian physicist of [illegible] diverse accomplishments) and was modelled by Lord Rayleigh (an equally interesting figure) with the following equation for a dilute suspension of nonabsorbing particles with number concentration N_P :

$$\frac{I}{I_0} = \frac{8N_P v_{irr} \pi^4}{\lambda^4 r^2}\left(\frac{\alpha}{4\pi\varepsilon_0}\right)^2 \left(1+\cos^2\beta\right) \qquad 2.21$$

where I is the intensity at a distance r and angle β of the scattered light from a volume v_{irr} of the sample, I_0 is the intensity of unpolarized incident light of wavelength λ and α is the polarizability of a sphere:

$$\alpha = 4\pi\varepsilon_0 a^3 \frac{i^2-1}{i^2+2} \quad ; \quad i = \frac{i_{particle}}{i_{medium}} \qquad 2.22$$

where a is the radius of the sphere of refractive index $i_{particle}$ suspended in a medium of refractive index i_{medium}. [Hunter, 72]

This is classical electrodynamics and is derived assuming that the particle is immersed in an oscillating electric field which induces a dipole moment on the particle. The polarizability of a sphere becomes $\alpha = 4\pi\varepsilon_0 a^3$ if the sphere is conductive.

The scattered light intensity varies with angle and falls as r^2 because it disperses radially from the sample. It is conventional to measure the scattered light intensity at right angles to the incident beam and the Rayleigh ratio R_{90} is defined as:

$$R_{90} = \frac{I_{90} r^2}{I_0} = \frac{8 N_p v_{in} \pi^4}{\lambda^4} \left(\frac{\alpha}{4\pi\varepsilon_0} \right)^2 \quad \text{[Hunter, 151]} \quad 2.23$$

As particles become larger and approach the wavelength of the incident light, a theory developed by Mie can be applied, but it is exceedingly complicated. By examining the Rayleigh model, it is possible to extract qualitative information about the optical properties of colloids.

The intensity of scattered light varies as a^6 for small particles, and the general trend is that larger particles scatter much more light than smaller particles. Shorter wavelengths are scattered very much more than longer wavelengths. This dependence serves as a basis to explain why the sky is blue. Sunsets appear red because blue light is scattered out of the direct beam, and the presence of particles in the atmosphere causes the red color to intensify, because the larger dust particles are very much more efficient scatterers than air molecules. This effect causes the interesting optical phenomenon observed on a leaky printhead. The silica binder is normally dyed blue, but it appears red if it is illuminated from behind. For 100 nm silica at 17.5% solids loading , 3 mm drips elicit the common exclamation: "What's that red stuff leaking out of the printhead?"

Light scattered from an incident beam decreases the transmitted intensity. The total quantity of light for small particles scattered is found by integrating Rayleigh's model for all angles:

$$T = \frac{16\pi}{R_{90}} \quad 2.24$$

The intensity of the transmitted beam is given by an equation analogous to Beer's law for an absorbing medium:

$$-\frac{dI}{dx} = TI \quad 2.25$$

$$\frac{I_T(x)}{I_0} = \exp(-Tx) \quad 2.26$$

where T is the turbidity of the colloid and x is the sample thickness [Hunter, 153].

For a given colloid, the quantity na^3 is proportional to the mass of particles in the suspension. The turbidity of a Rayleigh-scattering colloid is proportional to na^6. Since the mean particle size increases for the same mass if the colloid is flocculated, it follows that the turbidity of a flocculated colloid is very much greater than for a well-dispersed colloid with the same solids loading. This phenomenon is used as a basis for detecting the state of dispersion of a colloid [Hunter, 152] and was a major experimental technique used to develop a robust colloidal silica formula for Three Dimensional Printing (sect 3.4.)

This phenomenon is amply illustrated in egg white, which is a well-dispersed molecular hydrocolloid in its native form, but coagulates to a gel when cooked. A somewhat less extreme example is the property of paint that its color becomes less brilliant when it dries. Pigment particles both absorb and scatter light. The paint flocculates on drying, so the pigment scatters more and light doesn't penetrate as deeply into the paint film. The light absorption of each particle remains constant, so the thinner surface layer penetrated by light can absorb less light. The perceived color of a paint film is a result of the particles absorbing different wavelengths differently, but visible light is scattered more uniformly across the wavelengths. A higher scattering efficiency leads to the paint looking "whiter".

2.2.9 Kinetics of Coagulation

Lyophobic particles in a suspension adhere when they collide. There exist a number of mechanisms for preventing particle collision, discussed below, but when these mechanisms are insufficient, then the rate of aggregation of particles is determined by the mechanisms by which the particles are brought together. The two most important processes are Brownian motion and shear flow. These are called **perikinetic** and **orthokinetic** mechanisms, respectively.

a. Perikinetic Coagulation

In a quiescent colloid, particles are subject to Brownian motion. The rate of aggregation was first derived by von Smoluchowski in 1916 by calculating the rate at which Brownian particles pass through a spherical surface of radius 2a [Hunter 441]

$$J_S = 8\pi DaN_0 \qquad 2.27$$

where D is the Brownian diffusivity of particles with radius a, and N_0 is the concentration of dispersed primary particles at time t = 0. Pairs of particles form doublets, and we assume that every other particle is a potential target. The rate of particle doublet formation is the flux given above times $N_0/2$ and the number of independent particles decreases as particles merge:

$$\left.\frac{dN_P}{dt}\right|_{t=0} = \frac{-4k_BT}{3\eta_{medium}} N_0^2 \qquad 2.28$$

which is frequently used to derive an expression for the characteristic time for the particle concentration to drop by half [Hunter, 442]:

$$t_R = \frac{3\eta_{medium}}{4k_BT\,N_0} \qquad 2.29$$

In water at 25°C, the characteristic time is

$$t_{\frac{1}{2}} \approx \left(\frac{2x10^{11}}{N_0}\right) \text{seconds} \qquad 2.30$$

if N_0 is expressed in particles/cm^3. For a colloid with 100 nm diameter particles and a volume fraction of 0.175, $N_0 = 3.3 \times 10^{14}$, so the characteristic coagulation time is roughly 0.6 msec.

This expression is of limited use, since it only describes the onset of coagulation. Larger aggregates diffuse more slowly in the medium, and the distance separating aggregates increases with their size. The hydrodynamic radius of a floc containing n particles has been shown above (eqn. 2.6) to be

$$r_H \propto a\, n^{1/\partial} \qquad 2.31$$

and the diffusivity varies accordingly:

$$D = \frac{k_BT}{6\pi r_H \eta_{medium}} \propto n^{-1/\partial} \qquad 2.32$$

The fractal geometry of aggregation has been simulated by computer models. (see, for example, Meakin, P., in [Avnir 131-160.] The net result is that the mean cluster size $n = \left(\frac{N_0}{N_P}\right)$ increases more slowly than the rate suggested by eqn. (2.30) as time progresses.

When a repulsive force exists between colloidal particles, a smaller fraction of particle encounters result in doublet formation. A stability ratio is defined as a ratio between J_S, the Smoluchowski rate and J_H, the rate for the hindered system [Hunter, 443].

$$\frac{J_S}{J_H} = 2a\int_{2a}^{\infty} \exp\left(\frac{V(r)}{k_B T}\right)\frac{dr}{r^2} \qquad 2.33$$

where V(r) is a potential energy barrier between particles which is variable with the radial distance, r, from the particle center, caused by, e.g. coulombic repulsion between particles. A somewhat more convenient expression [Shaw,D., 202] is

$$\frac{J_S}{J_H} \approx \frac{1}{2\kappa a}\exp\left(\frac{V_{MAX}}{k_B T}\right) \qquad 2.34$$

where κ is the reciprocal of the thickness of the ionic atmosphere surrounding the particles in a charge-stabilized colloid, and is generally on the order of 1 nm^{-1}. (This is discussed in much in section 2.3.4.b.). The rate of doublet formation in a hindered system is proportional to J_H, the particle flux.

Equations (2.3.3) and (2.3.4) reflect the statistical mechanics of Brownian motion. The mean kinetic energy of a spherical colloidal particle is $\frac{3}{2}k_B T$ and the Boltzmann factor $\exp\left(\frac{-V_{MAX}}{k_B T}\right)$ expresses the probability that a particle will be able to scale an activation energy barrier V_{MAX}. If the energy barrier is on the order of 25 $k_B T$, the stability ratio is ~ 10^9. This is approximately the stability of pure colloidal silica at pH 5.5 where its stability is a minimum (Figure 3.11.)

b. Orthokinetic Coagulation

When the fluid medium in a colloid is in motion, shear flow can bring particles into contact at a rate that can exceed the Smoluchowski rate. The flux of particles through a "capture surface" of radius 2a in a shear field has been derived [Van de Ven, p.386]; [Poitanin]:

$$J_\gamma = (\tfrac{32}{3})\dot{\gamma}a^3 N_0 \qquad 2.35$$

where $\dot{\gamma}$ is the strain rate in the fluid.

The particle flux increases rapidly with particle size, whereas the diffusion rate of particles decreases with increasing particle size. Thus, orthokinetic effects become much more significant that perikinetic effects in large-particle colloids. Following Smoluchowski's derivation of the initial rate of particle doublet formation,

$$\left.\frac{dN_P}{dt}\right|_{t=0} = (3\frac{2}{3})\dot{\gamma}a^3N_0^2 \qquad 2.36$$

The volume fraction of particles in a suspension is proportional to a^3N_0 so at constant solids loading, the rate of particle collisions is proportional to N_0, the number of particles in the suspension. This number varies as a^{-3} at constant solids loading, so it can be seen that there is a great advantage to use sols with a small number of large particles, both in the perikinetic case (eqn. 2.28) and in the orthokinetic case (eqn. 2.36)

There have been a number of studies published in recent years on the aggregation of colloids in shear and extensional flows for example, [Russel & Schowalter]; [Clark & Flora]; [Melrose & Heyes]; and [Wong et. al.]. Many of these treatments discuss the breakup of flocs in the shear. Fractal aggregates are held together by very fragile backbones, so as they increase in size, they cannot support the hydrodynamic forces in the shear flow. This results in an equilibrium size of flocs that decreases with increasing shear rate, and depends on the strength of particle-particle bonds.

When a potential energy barrier exists between particles, the situation becomes a bit more complicated ([Van de Ven, Ch. 5] goes into it in gory detail.) At very high shear rates, the electrolytic boundary layers (sect. 2.3.4) are stripped from the particles. At the moderate shear rates that pertain in Poiseuille flows, one can assume that the stability ratio defined above for perikinetic flocculation also applies to this phenomenon: i.e. the ratio between the perikinetic and orthokinetic aggregation rates are the same for a stabilized sol is the same as the "rapid" case described here. The degree to which this effect is significant is expressed by the Peclet number, $Pe = \frac{\dot{\gamma}a^2}{D_{ion}}$, which must be smaller than unity in order for the ions comprising the stabilizing layers to keep up with the particles.

c. Optimization with Respect to Shear Flow

The printhead usually demands a fixed volume of fluid per unit time. If one wishes to minimize the combined effects of orthokinetic and perikinetic flocculation for a given length of tube, it is possible to find an optimum tube dimension. The total flux of particles through the capture surface of a given particle at t=0 is

$$J_0 = 8\pi DaN_0 + 3\frac{1}{3}\dot{\gamma}a^3N_0 \qquad 2.37$$

where N_0 is the total number of primary particles in a well-dispersed sol. The total number of particle interactions while a given particle is transported through a tube of length L is given by

$$n_{collision} = \frac{J_0 N_0 L}{2\bar{u}} \qquad 2.38$$

where $\bar{u}$ is the mean velocity of fluid in the tube. This is actually an upper bound, considering that J_0 is the particle flux for the perfectly dispersed colloid with the highest possible concentration of independent particles. Assuming laminar flow in a circular tube, the mean strain rate of the fluid is

$$\bar{\dot{\gamma}} = \frac{8\bar{u}}{3r} . \qquad 2.39$$

The printhead demands a fixed flow rate: $Q = \pi r^2 \bar{u}$ which permits substitution of $\bar{u}$ in terms of r, the radius of the tube. Combining these expressions,

$$\frac{n_{collision}}{La^3N_0^2} = \frac{4\pi^2 Dr^2}{a^2 Q} + \frac{128}{9r} . \qquad 2.40$$

This expression shows that the rate of particle collisions is proportional to the volume fraction a^3N_0 times the number of particles N_0, and times the tube length. There is an obvious advantage to minimizing the length of tubing in a system to decrease the particle interaction time. The expression (2.40) can be solved for an optimum tube diameter for minimum particle interaction in laminar flow:

$$\frac{d}{dr}\left(\frac{n_{collision}}{La^3N_0^2}\right)_{constQ} = \frac{8\pi^2 Dr}{a^2 Q} - \frac{128}{9r^2} = 0 \qquad 2.41$$

$$r_{tube}^{opt} = \sqrt[3]{\frac{16a^2Q}{9\pi^2 D}} = a\sqrt[3]{\frac{32\eta Q}{3\pi kT}} . \qquad 2.42$$

Substituting the following values

$a = 10^{-5}$ cm;

$D = 4.35 \times 10^{-8}$ cm^2/sec for 100 nm silica;

$Q = .02$ cm^3/sec for one nozzle;

one obtains $r_{tube}^{opt} = 0.0202$ cm or about 1/64" i.d. for the optimum tube. For multiple jets, the optimum radius scales as the cube root of the number of jets, so the optimum tube

i.d.for 8 jets is about 1/32". The time spent in the tubing, however, is actually quite small compared to the time spent in the filters.

The optimum diameter varies in proportion to the particle size in the suspension. It is most likely that one is concerned about flocculated particles colliding with one another to form flocs that will clog the filters. If the critical filter in the system is the "last-chance" filter leading to the printhead, and its pore size is 5 μm, then one is most concerned about the collisions between 1-2 μm flocs. The optimum tube diameter under this consideration is 10-20 times larger than that calculated for 100 nm particles: 2-4 mm i.d. for one nozzle, and twice that for eight nozzles. This optimum tube diameter is independent if the number of the particles in the suspension.

From the point of view of the hardware designer, it is more likely that the consideration of the Froude number discussed in section 2.2.3 above will override concern over the rate of flocculation. If the colloid is so unstable that one must worry about its coagulation during transport, than one clearly has big stability problems. It is shown in Appendix D, section D.1, that the deformation that occurs in as the liquid passes through the orifice is insignificant, even though the instantaneous maximum shear rate is impressively large.

2.3 Stability of Colloids

2.3.1 General Considerations

In ink-jet printing, the technologist is concerned with maintaining the stability of a colloid for months of storage and flow through the fluid system; up to the instant the ink passes out through the printhead. After that instant, the colloid can lose its stability and solidify in a convenient time. Stability is thus a dual concern: first maintaining it and subsequently destroying it in a controlled and reproducible way.

There exist three primary mechanisms for stabilizing a dispersion of colloidal particles [Hunter, 453]. For lyophilic colloids, an enthalpic or entropic interaction between the particle and the solvent guarantees thermodynamic stability. For a substance such as sodium alginate, this interaction is called "solubility" but for other members of the class, such as surfactant micelles, this term is not general enough. For lyophobic colloids, two additional phenomena engender an energy barrier between particles that provides a kinetic

form of stability: not absolute, but effective over reasonable time scales. These phenomena are electrical repulsion and steric stabilization. For colloidal silica, which exhibits characteristics of both lyophilic and lyophobic sols, all three mechanisms are available.

2.3.2 Lyophilic Colloids: Solubilization

A lyophilic (solvent-loving) colloid is one that can be reversibly solidified, e.g. by drying down, and redispersed by adding solvent. There are a number of different classes of materials that fall into this category. Soluble polymers are quite common, and depending on the solubility of the chains, they can exist either as low-viscosity dispersions of discrete particles or high-viscosity solutions of tangled chains. Surfactant micelles constitute another broad class of lyophilic colloids. In biology, hydrophilic colloids are legion. Colloidal silica exhibits some properties of hydrophilic colloids, especially in its resistance to precipitation by electrolytes, and the fact that stable dispersions can be prepared with rather high volume fractions of solids (up to 0.33) without recourse to other stabilizing mechanisms (sects. 3.2.1, 3.2.2).

There are two (and possibly more) ways to discuss the phenomenology of solubilization in water. As a mechanic, it is most appealing to describe it in terms of forces and displacements. Water is a strongly polar molecule and coordinates itself around charged bodies in such a way that the electric field is screened from other ions. There is also **hydrogen bonding**, a quantum mechanical attraction between protons in certain molecules and electronic orbitals in other molecules. Ice is held together by hydrogen bonds, and it accounts for the attraction between water and proton-rich substances such as glycerol. Both of these mechanical forces contribute to the attraction between water molecules and solute molecules. When the attraction between solute and water is larger than the attraction of solute for itself, solubility occurs.

As an alternative to thinking in terms of forces, one can begin with the criterion that the free energy of a system is at a minimum when it is at equilibrium. Free energy can be divided into an enthalpic contribution and an entropic contribution. Enthalpy is associated with definite forces of attraction between molecules while entropy is associated with disorder in the system.

This division is expressed in the Gibbs equation:

$$dG = dH - T\,ds = 0 \text{ at equilibrium} \qquad 2.43$$

The solubilization phenomenon can be understood qualitatively by considering a few examples. Cellulose is a polysaccharide consisting of glucose molecules linked into chains of 400 or more units [Hirst p. 9] The molecules exhibit strong hydrogen bonding between chains and form a somewhat crystalline network of microfibrils in a plant structure. Unlike glucose itself, which is exceedingly soluble, unmodified cellulose is quite insoluble because water cannot penetrate the strongly bonded structure. Amylose (starch) is similarly a polymer of glucose, but the chain linkage is different with the result that the substance is less crystalline. This material is much easier to dissolve because water can penetrate between the chains, and the enthalpic interaction between water molecules and the hydroxyl groups on the sugar units can be expressed.

Many salts are very soluble and it follows that when readily ionized functional groups exist on a molecule, its solubility is enhanced. Sodium is especially well hydrated in water and salts containing it dissociate readily. Strong acid groups such as SO_4^{-2} are very common in polymeric surfactants, often used in combination with aromatic/aliphatic polymeric backbones. Soluble ionic polymers are called **polyelectrolytes**. Myers (p.28) outlines a family of derivatives of dodecane: Dodecane, dodecanol and dodecanoic acid are all practically insoluble in water, but the sodium salt of dodecanoic acid is reasonably soluble: "a classic soap". Dodecanoate is precipitated at low pH, but if the acid group is stronger, as in sodium dodecyl sulfate, a versatile detergent is obtained.

Sodium dodecyl sulfate ionizes in water, yielding a strongly hydrated sodium ion and the amphiphilic anion, which is attracted to the water surface. When the concentration of detergent exceeds the critical micelle concentration, the hydrophobic tails cluster together in the center of a micelle and the hydrophilic heads stud the surface, presenting an attractive face to the water which surrounds it. The critical micelle concentration represents a balance between the attractive (enthalpic) forces between surfactant molecules in a micelle and the entropy change when the micelle dissociates and the molecules comprising it are dispersed.

Polyethylene oxide (POE) is a synthetic polymer that is soluble in water. The oxygen atoms in the ether linkages are polar enough to hydrogen bond to water molecules. This polymer is used as a coagulant for colloidal silica (sect. 3.5). It is also used as the hydrophilic head for most nonionic surfactants, e.g. Triton X-100.

Polymers that are essentially insoluble in the solvent can form hydrophilic colloids. Rohm & Haas' product, "Acrysol" is a polymer that is insoluble at low pH, and is sold as a low viscosity colloid which is redispersible after drying. ("ACRYSOL® Thickeners and Rheology Modifiers" Rohm&Haas flyer #23A24) As the pH is raised, the polymer becomes soluble and it greatly increases the viscosity of the medium. These polymers are derivatives of polyacrylic acid, which is a weak acid in water. At low pH, the acid is unionized and as a consequence, it is much less soluble in water that when it is ionized. The sol is stored at low pH and the polymer is condensed into tight colloidal particles. If the pH is raised, the acid groups begin to ionize and the polymer chains become more soluble. They unwind into the solution and increase the viscosity up to 40,000 cP for a 5% solution.

[Iler 373] describes colloidal silica as a hydrophilic sol. The differences in character between colloidal silica and more "classic" hydrophobic colloids may partially justify this assertion, but from the point of view of ink-jet technology, colloidal silica cannot be treated exactly as such. Hydrophilic sols can be dried and redispersed with ease. Such is not true for colloidal silica except when the silica is sterically stabilized. Since the ability to redisperse dried material is crucial in cleaning of ink-jet printheads, a great deal of care must be taken in selecting additives for the silica system used in 3-D Printing.

The interaction between water and silica is exceedingly complicated, and although considerable effort has been devoted to analyzing it, as yet it is not fully understood. A combination of ionization, hydrogen bonding, and physical and chemical adsorption gives colloidal silica a greater stability than more "ordinary" hydrophobic colloids such as polystyrene latex. This stability can be further enhanced by the same phenomena that stabilize hydrophobic colloids.

2.3.3 Lyophobic Colloids: Dispersion Forces

The principal attractive force between colloidal particles is the molecular attraction of van der Waals. It is also called **London** or **dispersion force**. The origin of the force is coulombic attraction, but it affects bodies with no net charge. The phenomenology of dispersion forces can be described with a statistical argument as follows: Since all atoms are composed of separate particles with concentrated positive and negative charges, they possess a net dipole moment at any instant in time. This moment continually fluctuates, but from instant to instant this dipole is capable of inducing a dipole moment in other atoms that

are located nearby. The distance through which this force has effect is determined by the speed of light and the rate at which the dipole fluctuates. The net force is always attractive and diminishes rapidly with distance.

The potential energy has been derived for bodies of various geometries (see [Hunter 183], for example) and the most useful for the purposes of modelling colloids are those for two parallel plates and for two spheres:

$$\text{for plates,} \quad V_A = \frac{-A}{12\pi B^2} \qquad 2.44$$

$$\text{for spheres,} \quad V_A = \frac{-A}{6B}\left(\frac{a_1 a_2}{a_1 + a_2}\right) \qquad 2.45$$

where B is the separation between the two surfaces and a_1 and a_2 are the radii of the spherical particles. A is the **Hamaker constant** for the system, which is a function of the materials comprising the particles and the medium separating them. [Hunter, 222] tabulates selected values. For amorphous silica in water, $A = 8.49 \times 10^{-21}$ J, and for alumina in water, $A = 5.32 \times 10^{-20}$ J. The Hamaker constant is related to the index of refraction of the particles in the sense that a virtual photon is the carrier of the force. Since amorphous silica has a smaller index than alumina, its Hamaker constant is smaller. Metals, which effectively have infinite indices of refraction, ought to have very high Hamaker constants [Hunter, 220] but experimental data does not support this conclusion [Shaw, D., 190.]

2.3.4 Lyophobic Colloids: Charge stabilization

a. Charge Determination

When an ionic compound is placed in contact with an electrolytic solution its surface comes to electrochemical equilibrium with the solution. The equilibrium is expressed as a balance between the surface electric potential and the chemical potential of ions in solution in the electrolyte. An example discussed in many textbooks regards a sol of silver iodide. [Parfitt p. 100] explains that cations are more strongly hydrated than anions, so most sols tend to be negatively charged. [Hunter 360-373] has a very clear description of silver iodide sols. In the AgI system, Ag^+ is more soluble, and a net negative charge results on the solid particles, owing to an excess of I^- on the AgI surface. The ions Ag^+ and I^- are the **charge-determining ions**. The emf on the surface of the

particle is called the Galvani potential. This potential is equal to zero at a particular Ag^+ ion concentration, **the isoelectric point**. This is the solution composition at which the surface concentrations of Ag^+ and I^- are identical. The electrochemical potential of the particles with respect to the solution is predicted very accurately in this case by the Nernst equation:

$$\psi_0 = \frac{k_B T}{ze} \Delta \ln\left[a_{Ag^+}\right] \qquad 2.46$$

$$= -25.7 \text{ mV } \Delta \text{pAg at } 25°C. \qquad 2.47$$

where $z = 1$ = valence of Ag, e = the electronic charge, and Δ pAg is the difference in log concentration with respect to the isoelectric point. (analogous to pH). The concentration of either silver or iodide can be adjusted by adding a salt containing the ion of interest and an indifferent counterion (which does not react with the AgI surface). The potential of the particles varies logarithmically with the concentration of charge-determining ions.

For particles of silver halide, the condition of zero net charge corresponds to equal concentrations of cations and ions on the surface. Metallic surfaces (except gold) in contact with water usually acquire a coating of metal oxide. Ionic oxides (including ceramics) can hydrolyze according to the reaction

$$M_xO_y + wH_2O \rightarrow M_xO_{y-w}(OH)_{2w} \qquad 2.48$$

causing the attachment of hydroxyl groups to the particle surface. The substance could be acidic or basic, depending on the nature of the cation. The surface will exchange ions with the solution by the following two reactions:

$$M_xO_{y-w}(OH)_{2w} + OH^- \leftrightarrow H_2O + \left[M_xO_{y+1-w}(OH)_{2w-1}\right]^- \qquad 2.49$$

$$M_xO_{y-w}(OH)_{2w} + H_3O^+ \leftrightarrow H_2O + \left[M_xO_{y-1-w}(OH)_{2w+1}\right]^+ \qquad 2.50$$

where the bracketed formulas represent surface sites that have acquired an electric charge. If the metal oxide tends to be acidic, reaction (2.49) will predominate over reaction (2.50) if the oxide is basic, the opposite will be true. Clearly, the concentrations of charged sites at equilibrium depend on the concentration of OH^- and H_3O^+ ions in the solution.

For an overwhelming number of aqueous colloids, H_3O^+ and OH^- ions are charge determining, so the surface charge depends on the pH of the solution. The reaction on a silica surface leading to the formation of negative charges is illustrated in figure 3.9. The

isoelectric point for an aqueous oxide. The isoelectric point for an aqueous oxide is the pH at which there are equal numbers of positive and negative charges on the surface, as determined by the equilibria (2.49), (2.50) and

$$H_3O^+ + OH^- \leftrightarrow 2H_2O. \qquad 2.51$$

Other organic molecules contain ionic functional groups, the most famous of which are proteins, which contain various concentrations carboxylic acid (-COOH) and amine (-NH_2) functional groups at varying depths within the coiled molecule. The former are acidic, the latter basic, and each have a characteristic free energy of ionization. Depending on how easily they communicate with the surrounding electrolyte (some groups can be buried very deeply in a coiled molecule) they will ionize at different pH, and the molecular charge is determined by the difference between the number of positively and negatively charged functional groups.

Substances that do not contain ionizable functional groups can acquire surface charge by adsorbing ionic molecules on their surface. Ionic surfactants such as sodium dodecyl sulfate are a favorite choice. The surface charge is here determined by the free energy of adsorption and the surfactant concentration.

b. Electrostatics

When colloidal particles carry a coulombic charge, they repel each other. The electric field in a stable system extends further into the surrounding space than the van der Waals attraction. This repulsion creates an energy barrier that particles must overcome before they can come in contact and form an aggregate. Maxwell-Boltzmann statistics guarantee that some fraction of particles will have enough kinetic energy to overcome any energy barrier, so a charge stabilized sol is only metastable. Nevertheless, the energy barrier can be sufficiently high to enable the sol to survive for years, even centuries.

The electric field engendered by surface charge is modified by the presence of ions that are not located directly on the particle surface. There is usually a layer of chemically adsorbed ions on a particle's surface which lowers the potential within a few Å to a potential of $\psi_S < \psi_0$. ψ_S is the **Stern potential**. Electrolyte ions in solution form a second **diffuse layer** that is attracted to the particle. The electric field is screened out by this layer of ions, and electrostatic forces between colloidal particles diminish more rapidly

with the separation between the particles than they would in vacuo. The space around a colloidal particle is sometimes referred to as the **double layer** because it consists of a layer of ions adsorbed on the particle surface and a second, diffuse layer of solvated ions. The magnitude of the surface charge is estimated by measuring the potential of the hydrodynamic surface of the particles. This potential is called the **zeta potential**. The measurement can be made by determining the electrophoretic mobility of the particles, once the hydrodynamic radius has been determined independently. Zeta potentials exceeding 20-30 mV are typical in electrostatically stabilized colloids.

A popular model for the electric field in the diffuse layer is the Poisson-Boltzmann equation [Hunter 331]

$$\nabla^2\psi(r) = \frac{-q(r)}{\varepsilon} \qquad 2.52$$

where q(r) is the density of electrolyte ions at a distance r from the center of the particle and ε is the permittivity of the medium. Debye and Huckel derived an approximate solution for $(ze\psi_S /k_BT) << 1$:

$$\psi(x) = \psi_S \exp(-\kappa x) \text{ for parallel plates,} \qquad 2.53$$

and

$$\psi(r) = \frac{\psi_S}{(r/a)}\exp[-\kappa(r-a)] \text{ for spherical particles of radius a.} \qquad 2.54$$

where ψ is the electric potential and κ is a parameter with dimension (length)$^{-1}$ that depends only on temperature and electrolyte concentration.

$$\kappa = \left(\frac{e^2 \sum c_i z_i^2}{\varepsilon k_B T}\right)^{1/2} \qquad \text{[Hunter 332]} \qquad 2.55$$

$$= 3.288 \text{ nm}^{-1} \sqrt{I} \text{ for aqueous solutions at 25°C.} \qquad 2.56$$

where I is the ionic strength of the solution, $I = \frac{1}{2}\sum c_i z_i^2$, c_i being the ionic concentration in mol/liter and z_i being the charge, considering only the ions with charge opposite to the particles. The quantity $1/\kappa$ is called the **Debye length**, and corresponds approximately to the thickness of the double layer.

When two particles approach one another, the diffuse layers overlap. For low values of ψ_S , the potential energy of two flat plates separated by a distance $B >> \kappa^{-1}$, is (Hunter 408)

$$V_R = 2\varepsilon\kappa\psi_S^2 \exp(-\kappa B) \quad . \qquad 2.57$$

More accurate expressions are available (see, for example, [Hunter Ch. 7]) The purpose here is to approximate the mutual repulsion between charged particles surrounded by diffuse layers. For a given system , the stability is primarily governed by the surface charge on the particles (as it affects ψ_S) and the ionic strength (as it affects κ). The magnitude of V_R is ~20kT for a well-stabilized (though still metastable) colloid.

c. The Deryaguin Approximation

The expression (2.57) above applies to flat plates. It can be used to calculate the potential energy of two spheres by the Deryaguin approximation [Hunter, 192]

$$V(B)^{sphere} = \pi a \int_H^\infty V(L)^{plate} dL \qquad 2.58$$

where $V(L)^{plate}$ is a potential energy function define for two flat plates and is expressed in units of [energy/unit area]. Two spheres of radius a approach a distance B from one another and various points around the curved surface are at various distances larger than B from the nearest point on the other particle. The assumptions that are necessary are $a >> B$ and $V(L)^{plate}$ is negligible at distances $L \geq a$. (This approximation is used in section 2.2.2 below to derive the potential energy barrier due to adsorbed water on the silica surface)

Using the expression (2.57) as V^{plate}, one can estimate V^{sphere}:

$$V_R^{sphere} \approx 2\pi a \varepsilon \varphi_S^2 \exp(-\kappa B) \qquad 2.59$$

the potential energy of two 100 nm diameter spherical particles at a separation of $B = \kappa^{-1}$ in water ($\varepsilon = 80\ \varepsilon_0$) is approximately 5.1×10^{-20} J if the Stern potential is ±25 mV (see sect. 2.2.4). At 25 °C, this is about 12 $k_B T$. If κ^{-1} is large enough that the Hamaker force is negligible at this distance, this is a reasonable estimate of the energy barrier separating the particles.

2.3.5 Total Potential Energy

The potential energy functions are additive. In an electrostatically stabilized colloid, the potential energy function is

$$V_{tot} = V_A + V_R. \qquad 2.60$$

where V_R is the potential energy from electrostatic repulsion and V_A is the potential energy from van der Waals attraction. Shown below is a potential energy diagram for a stable colloid. If V_{tot} is positive at some value of B, then there is a positive energy barrier for particles to climb before the shorter-range dispersion force can draw them together. The mean kinetic energy of each particle is $\frac{3}{2}k_BT$.

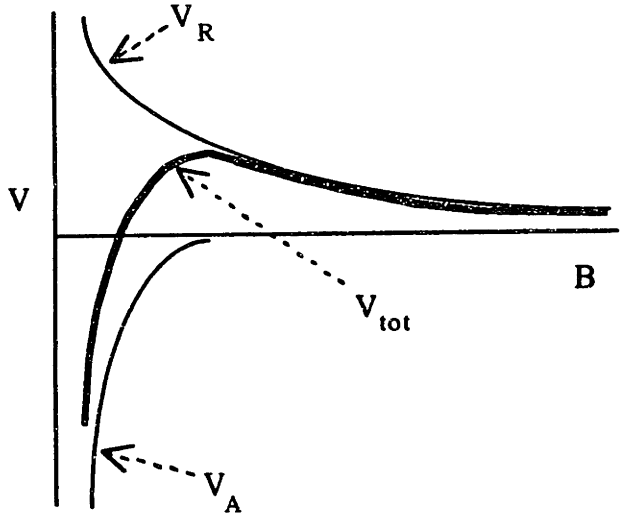

Figure 2.5 Addition of potential energy terms in the field surrounding a colloidal particle. (For a potential energy curve of mica plates in water, see figure 3.15.)

For further discussion of potential energy curves see [Shaw, D.], Ch. 8.

If the ionic strength of the aqueous medium is high, the diffuse layer surrounding the particles becomes compressed and collisions between particles become more likely. Workers in the field have defined the **critical coagulation concentration** (c.c.c.) of electrolyte at which coagulation is observed. Because of the statistical nature of particle collisions, the c.c.c. measured will depend on the time scale over which the observation is

made; however the differences across reasonable time scales make only small errors in the measured value. The point of instability of the colloid occurs when both

$$V_{tot} = 0 \quad \text{and} \quad \frac{dV_{tot}}{dB} = 0 \quad \text{at the same point.} \qquad 2.61$$

from equation (2.45) $\frac{dV_A}{dB} = -\frac{V_A}{B}$ and from equation (2.59) $\frac{dV_R}{dB} = -\kappa V_R$ giving $\kappa B=1$. (see [Shaw, D.,197] By substituting appropriate expressions for κ as a function of salt concentration, it is possible to solve for the critical coagulation concentration of a given colloid.

It has been measured experimentally and predicted theoretically (the Schultze-Hardy rule, see [Hunter, 420]) that the c.c.c varies as z^{-6}. A trivalent ion such as Al^{+++} is expected to be 729 times as effective at coagulating a sol as Na^{+}. In general, this is borne out by experiment.

When a hydrophobic colloid does not carry enough charge in its pure state, the zeta potential can be increased by adding an ionic surfactant. The hydrophobic tail of the surfactant is attracted to the particle surface and the ionic head contributes surface charge.

One notable exception to Schultze-Hardy rule is colloidal silica (sect. 2.3.3). The critical coagulation concentrations for silica are very much higher than theory would predict, and they do not change in a predictable way with changes in zeta potential [Allen & Matijevic]; [Iler, 375]. Silica becomes increasingly stable with respect to electrolytes as the zeta potential approaches zero. This is due to water molecules adsorbing on the silica surface and forming a steric barrier to particle collision (Sect. 2.2.2)

2.3.6 Lyophobic Colloids: Steric Stabilization

A lyophobic colloidal dispersion can be stabilized by the addition of a substance, often a lyophilic colloid, that prevents the lyophobic particles from touching each other. Most frequently, the additive forms an adsorbed layer on the surface of the particles. One of the most versatile materials consists of an amphiphilic block copolymer of polyethylene oxide and polypropylene oxide. [Nelson 105] By varying the lengths of the blocks, the hydrophilicity of the PEO and hydrophobicity of the PPO can be tailored to a wide variety

of requirements. If ionic functional groups are incorporated to the polymer, the charge of the particles can be enhanced, causing **electrosteric** stabilization.

In a more general sense, the presence of a steric stabilizer adds an energy barrier to the collision of particles. In the case of a strongly adsorbed hydrophilic polymer on the surface of the particles, the sol becomes hydrophilic.

Osmosis plays a very important role in steric stabilization. When a surfactant is adsorbed on colloidal particles, the medium is excluded from the lyophilic chains when two particles approach one another. Osmotic pressure drives the solvent back, forcing the particles apart. Frequently the stabilizing additive is a lyophilic polymer with limited solubility in the vehicle. As two colloid particles approach each other, the molecules of the stabilizing additive are attracted to the space between the solid particles because it represents a volume with less solvent. This is called **depletion stabilization** and is a mechanism that is apparent in mayonnaise.

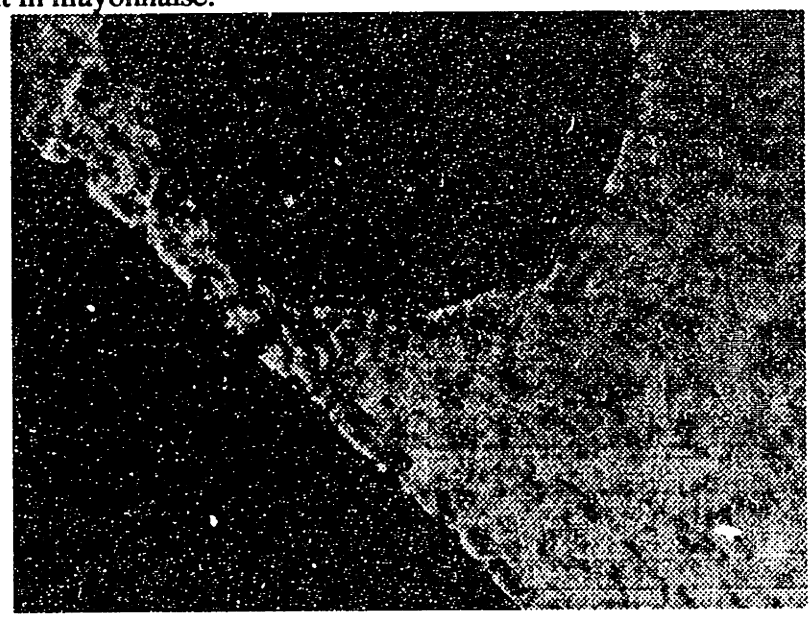

Figure 2.6 Electron Micrograph of mayonnaise.[McGee, 360] Dark semicircle on top is a 4-μm droplet of oil, and triangle lower right is a much larger oil droplet. Egg protein molecules are gray patches in the region separating the droplets. The egg protein is repelled slightly by the aqueous solvent in which it is dispersed. The space between the oil droplets is solvent-poor, so the protein tends to cluster in that space; hence the oil droplets are prevented from merging.

The correct steric stabilizer for a particular system must be chosen with great care, since the amphiphilic character needed depends on the surface energy of the particles in the

solvent. The degree of surface coverage is critical. Since the stabilizing additives are of limited solubility, the dispersions are rather sensitive to effects such as temperature and the presence of other solutes in the vehicle.

A sterically stabilized dispersion can be flocculated by dilution. If there exists just enough amphiphile in the solution to completely coat the particles, dilution reduces this concentration, thereby exposing hydrophobic surfaces on the particles. In the case of polymeric stabilizers, the uncovering effect could lead to bridging of polymer from particle to particle, resulting in a form of flocculation that may be reversible.

In colloidal silica, the steric stabilizer is the medium itself (sect. 2.2.2). For this reason, the sol is normally considered hydrophilic. This is not strictly true because properly hydrophilic colloidal particles attract the solvent more strongly than than they attract each other. Such is not the case with silica. Although water is strongly attracted to the silica surface, the particles adhere if they touch, the solvent attraction notwithstanding.

2.4 Conclusion

The reader should now have a good enough understanding of the basic principles of colloid science to understand the peculiarities of colloidal silica, covered in the following chapter. In particular, the reader is cautioned that colloidal silica exhibits ALL of the stabilization mechanisms for both hydrophilic and hydrophobic colloids in a way that sets it apart from both classes.

Chapter 3. Colloidal Silica

3.0 Introduction

Colloidal silica has quite unusual properties for a dispersion of inorganic particles in water. As a commercial product, it is quite stable and can be prepared with quite high solids loading: quite sufficient for Three Dimensional Printing. These dispersions can be made to coagulate irreversibly with small amounts of the right chemical additives. The rate at which this coagulation takes place can be highly variable, and the control of this phenomenon is an important aspect in determining the time scales over which features form. It was shown in the previous chapter (section 2.2.9.a) that in a quiescent dispersion, the rate of particle aggregation is primarily determined by the diffusivity of the particles in the medium, and the mean distance between the particles. In colloidal silica, the stabilization mechanisms that are active reduces the probability that particles stick to one another when they collide. This causes the rate of aggregation to be highly variable, even for sols that have been destabilized.

In the development of binder for Three Dimensional Printing, it is necessary to immobilize the binder solids in the powder in a time that is less than the time between layers. If this does not occur, significant quantities of liquid binder can migrate into unprinted powder. This phenomenon is known as "bleeding" and is discussed in detail in section 6.4. A relatively rapid mechanism is desired, both to inhibit the migration of binder during feature formation, and because the build rate of 3-D Printers can be dramatically high if printheads are used with multiple jets. At present, there exist only two 3-D Printing machines that are outfitted with a single jet printhead, and roughly four times that many with multiple-jet printheads.

A great deal of the information in this chapter has been culled from one book: The Chemistry of Silica by Ralph K. Iler. The Kirk-Othmer Encyclopedia of Chemical Technology, 3d Ed., Vol. 20, pp. 748-817, ("Silica") gives a very good condensed overview. The beginning of this chapter is a celebration of the chemical diversity of silica chemistry. After describing the physical properties of forms of pure silica, the stability of colloidal silica is discussed in detail. The hydrophilic characteristics of the silica surface at its isoelectric point lead to stabilization by several monolayers of adsorbed water. The

potential energy is estimated from the heat of hydration of silica gel, and the estimate compared favorably with measurements taken with mica sheets in water (sect. 3.2.2.) A more qualitative discussion of the evolution of silica stability at higher pH follows, with data for the zeta potential as a function of pH.

Various mechanisms by which colloidal silica is coagulated are described at the end of this chapter, mostly in the context with what can be found in the literature, with a few qualitative observations obtained in this study.

3.1 Forms of Silica

Silica has the chemical formula SiO_2. Its molecular weight is 60.086. Silicon and oxygen are the most abundant elements in the earth's crust with silica comprising 59% by weight. Quartz, pure crystalline silica is the second most abundant mineral, the most abundant being feldspar $(K,Na,Ca)(Si,Al)_4O_8$; which contains silica as its primary constituent. Nine tenths of the minerals in the earths crust are silicates: chemical combinations of silica and other inorganic oxides. One very important example is kaolinite, the classical clay mineral, which has the ideal formula $Al_2(Si_2O_5)(OH)_4$. [Kingery, Bowen, & Uhlmann, p.6] Colloidal silica used in 3-D Printing consists of particles of amorphous, mostly pure SiO_2 dispersed in water. The distinctions between the various major forms of silica are described below.

3.1.1 General Structure, Silicates

Silicon is ionized to a charge of +4 and accepts two charges of -2 on each oxide. Unlike CO_2, which is π-bonded, silicon is only capable of forming single σ bonds with the much larger oxide ions. The ionic radius of the oxide anions is 1.38 Å while the silicon cation has a radius of 0.26 Å [Kingery, Bowen, & Uhlmann p.58]. The result is an ideal network-forming molecule. Each silicon ion bonds to four neighboring oxide ions, and each oxide bridges two different silicon ions. The structural element of the network is a tetrahedral block consisting of SiO_4^{2-} tetrahedra with oxide ions at the corners and silicon cations buried at the centers.

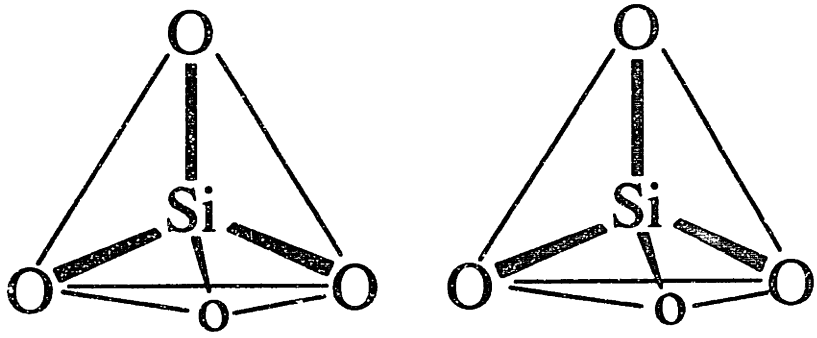

Figure 3.1 Silicate tetrahedra. (Stereoscopic)

Like CO_2, silica is a weak acid, and reacts with more basic oxides to form silicates. The stoichiometry of the compound determines the degree to which the silicate tetrahedra must share oxide ions to maintain charge neutrality. For example, in the mineral zircon, $ZrSiO_4$, the tetrahedra are completely detached: this is an **orthosilicate**. Chrysotile, the principal type of asbestos, is $Mg_3Si_2O_5(OH)_4$ and belongs to the amphibole family, with a structure consisting of two parallel chains of tetrahedra, linked at the corners. Pyroxene is a single-chained silicate: jadeite is an example. In kaolinite, the silicate ions are coordinated into a two-dimensional sheet, laminated to a similar sheet of $AlO(OH)_2$ octahedra. Stress from the size mismatch between these two structural elements prevents kaolin from forming large grains, resulting in the fine particles characteristic of clay. In muscovite, the classic mica, two silica planes sandwich a plane of alumina, and the sandwiches are separated be weak layers of potassium ions. [Kingery, Bowen, & Uhlmann, 70-80]. Zeolites are complex aluminosilicates in which the structural elements arrange themselves in long tubes around alkalai or alkaline earth cations. Obsidian is a naturally occurring glass found in lava flows. Perlite is hydrated obsidian, and can be popped like popcorn at 850°C. [Encyclopaedia Britannica, 1964 ed., Vol. 20, "Silicon"]

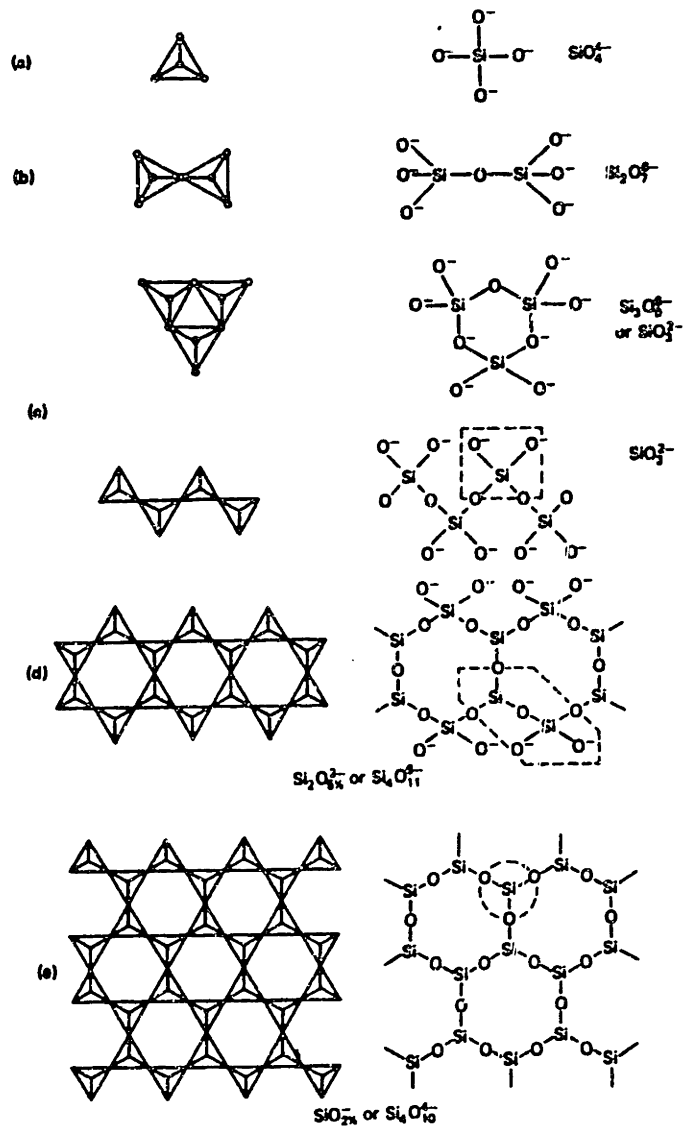

Figure 3.2 Coordination of silica tetrahedra in various silicates.
(a.) Orthosilicate; (b.) Pyrosilicate; (c.) Cyclic Trimer and Pyroxene; (d.) Amphibole; (e.)Sheet [Kirk-Othmer Vol. 20, p.751]

3.1.2 Silica

In pure silica, only traces of foreign elements are present, so the silicate tetrahedra must share all corners with other tetrahedra. While the structural diversity of pure silica is insufficient to build entire planets, as is the case with silicates, these exists a rich menagerie of forms.

Pure silica is very resistant to chemical attack. It resistant to all acids except those containing fluorine. At room temperature, aqueous hydrofluoric acid attacks most forms of silica, converting it to fluorosilicate, SiF_6^{2-}, which is soluble in water. Strong alkalais, especially KOH and NaOH, dissolve silica by forming soluble alkalai orthosilicate. The rate of attack in these cases is limited by the diffusivity of the active agent in the silica network, and varies with the density of the silica structure. Silica can be reduced to silicon by hydrogen, carbon, and several reactive metals at temperatures high enough to give a substantial reaction rate. Silicon falls between aluminum and zinc in the electrochemical series.

Silica reacts with chlorine at elevated temperatures to form $SiCl_4$. This is a very interesting chemical that forms the basis of many chemical syntheses. A liquid at room temperature, $SiCl_4$ has a very high vapor pressure and reacts rapidly with water vapor to yield stoichiometric quantities of "fumed" SiO_2 and HCl. The reaction with alcohols yields silicate esters, such as tetraethyl orthosilicate (TEOS) by reaction with ethanol. TEOS is a popular source reagent for silica because it hydrolyzes slowly, at a rate that is controllable by pH, to yield silica gel that is easily dehydrated.

Silica has a special affinity for water. The surface of silica is entirely coated with oxide ions, which hydrolyze readily to form hydroxyl groups. Liquid water spreads spontaneously on amorphous silica surfaces, and all glass exposed to air typically has several molecular layers of water adsorbed onto it. The energetics of hydration of the silica surface is one of the few cases that has actually been studied in detail, and this subject is treated in greater detail below (see section 3.2.2). In spite of this strong affinity, silica is practically insoluble in water under ordinary conditions. In pure water at pH 7 at room temperature the solubility of quartz is about 10 ppm and amorphous silica it is about 100 ppm . It is sufficient at high temperatures and pressures to cause problems in steam turbines: at 330°C under pressure the solubility is 0.07 wt.%, and as high as 62 wt % in steam at 1050°C and 9500 atm.[Kirk-Othmer Vol. 20 pp. 754-5]

a. Crystalline Silica.

Quartz at room temperature consists of a space-filling network of SiO_4 tetrahedra, linked at the corners, in a slightly deformed trigonal lattice. The asymmetry makes quartz piezoelectric, optically active, and enantiomorphic (right-handed in the northern

hemisphere, left-handed in the southern hemisphere.) Granulated quartz is called sand. Quartzite is consolidated sand. Flint and chert are microcrystalline forms of silica. Impurities cause coloration, e.g. in amethyst and rose quartz. Opal is a pseudocrystalline arrangement of hydrated amorphous silica particles. Cat's eye contains inclusions of rutile (TiO_2); aventurine contains mica. Agate is microcrystalline silica that has been deposited in successive thin layers. Diatomite is microcrystalline biogenic silica. The density of crystalline quartz is 2.65 g/cc and its thermal expansion coefficient is anisotropic, varying from 9 to 14 x 10^{-6}/°C depending on crystal orientation [Kingery, Bowen, & Uhlmann 594.]

As silica is heated from room temperature, it passes through a number of structural transformations, with concomitant changes in volume, thermal expansion, and physical properties. At 574°C, quartz inverts from "low" to "high" quartz, which possesses a symmetric hexagonal structure and a slightly negative thermal expansion coefficient. At 867°C, quartz changes to tridimite, with a 15% increase in volume. These transformations make silica very unstable mechanically, and accounts for explosive fracturing of concrete and granite when exposed to heat. At 1470°C, tridimite changes to cristobalite with little alteration of volume. Finally, cristobalite melts at 1723°C. The transformations from one form to another are relatively slow, and metastable phases can be frozen into a sample at temperatures well outside of the region of stability. Thus, high-silica refractories are formed from tridimite and cristobalite which is quenched to room temperature. Other forms have been discovered that are stable at high pressures, notably coesite and stishovite, both of which are found in meteorite craters.

Silica is physiologically inert. Prolonged exposure to crystalline silica dust causes silicosis, a disabling pulmonary disease common to miners and ceramic artists.

b. Amorphous Silica.

If silica is melted and cooled, or if it is precipitated from a solution, a form of silica results which does not possess long-range crystallographic order. This is **amorphous silica**, vitreous silica, silica glass, or sometimes fused quartz or quartz glass. There exist subtle arguments in favor of amorphous silica being distinct from undercooled molten silica, but they are beyond the scope of this discussion. The density of amorphous silica is 2.19 g/cc, and its thermal expansion coefficient is exceedingly small: 5 x 10^{-7} /°C up to its softening point.

The stiffness of fused silica is 73 GPa, its shear modulus is 31 GPa, and its Poisson ratio is 0.17. The strength of amorphous silica fibers has been measured in excess of 1.3 GPa; fully 60% of its theoretical strength. The strength of ceramics in normal practice is usually determined by the largest flaw present in the structure, and the strength of the structure determined through fracture mechanics. A flame-drawn fiber decreases in strength by roughly a factor of ten merely by touching it with a finger. Accordingly, a more realistic strength measure is the critical fracture energy, E_C, which is 3.7 J/m^2 in air at 40% relative humidity. [Kirk-Othmer, vol. 20,p 789] The yield strength of a silica glass sample is given by:

$$\sigma_Y = \sqrt{\frac{E_C \sigma_{SV}}{b}} \qquad 3.1$$

where σ_{SV} is the surface energy of the glass, and b is the major half-axis of the largest elliptical crack. [Kingery, Bowen, & Uhlmann, p. 785.]

X-ray diffraction reveals that amorphous silica lacks any long-range order to its structure, although short-range ordering ~2nm resembles cristobalite [Kirk-Othmer vol. 20, p. 784]. This structure is represented schematically below.

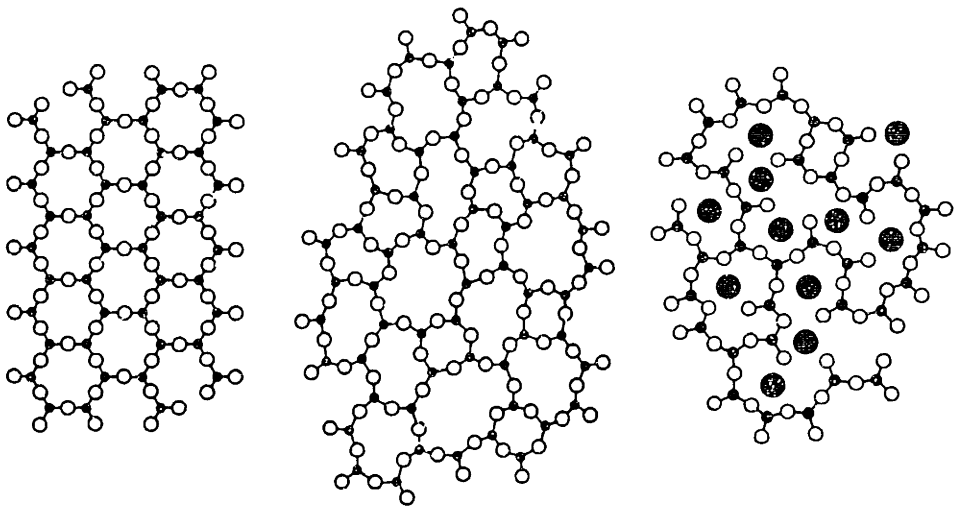

a. b. c.

Figure 3.3 Structural disorder in glass. (a.) Ordered crystalline form; (b.) Glassy network of same composition; (c.) Glass composition containing alkalai network modifiers. •=Si^{+4}; ○=O^{-2}; ●=Na^{+} [Kingery, Bowen, & Uhlmann, p. 97]

Amorphous silica does not have a clearly defined melting point: it exhibits an approximately exponential dependence of viscosity on reciprocal temperature [Kingery, Bowen, & Uhlmann, p. 759]. It has a "softening" point of 1400-1500 °C, and an "annealing" point of 1000-1100°C. At the processing temperatures for silica glass, silica is appreciably volatile. It disproportionates to the gaseous phases silicon monoxide and O_2. On cooling in air, SiO rapidly reoxidizes to form a smoke of amorphous silica.

The thermal characteristics of amorphous silica make it an ideal material for laboratory glassware and as a bonding material for ceramic shell molds because of its impressive resistance to thermal shock. Fused quartz laboratory glassware is relatively expensive: it must be blown with a hydrogen/oxygen torch at 2000°C, but it can be quenched from red heat in cool water without cracking. Since silica forms compounds with most inorganic oxides, it is very well suited as a cementing agent for other ceramic powders. The compound mullite, $2Al_2O_3$-SiO_2 forms at the interface between silica and alumina and lowers the surface energy of the phase boundary. Silica and alumina form a eutectic with a melting point of about 1600°C, which is actually a eutectic between mullite and silica.

Amorphous silica is metastable: the crystalline form has a standard free energy of formation about 1.5 kcal/mole lower [Iler p. 6]. At room temperature, the mobility of atoms is so small that the material cannot spontaneously recrystallize in any reasonable amount of time. To form amorphous silica from molten silica, it is necessary to cool the liquid at a rate fast enough that the impurities which are always present do not have sufficient time to nucleate macroscopic crystals. For pure silica, this rate must be faster than .01 °C/sec. When glass-forming additives are present, the critical cooling rate is larger. For Na_2O - $2SiO_2$, the cooling rate must be 5 °C/sec or faster. [Kingery, Bowen, & Uhlmann, p. 350] If amorphous silica is held at temperatures above 1000°C for prolonged periods, it will **devitrify**, or crystallize, with accompanying destruction of its mechanical properties. The rate of devitrification is expressed as a diffusive growth rate around heterogeneous nuclei, and reaches a maximum of $20\mu m/min^{1/2}$ between 1500°C and 1700°C. Impurities greatly accelerate this rate: traces of alkalai from fingerprints are particularly destructive to high-temperature silica glassware. Fractions of a percent alkalai increase the devitrification rate 20-30 times. [Kirk-Othmer, vol. 20, p. 785] Water of hydration in the silica structure increases the rate of devitrification by increasing the self-diffusivity of the material.

Amorphous silica is especially hydrophilic. This can be explained qualitatively by noting the similarity between the short-range structure of amorphous silica and water. [Iler 637]and [Kingery, Bowen, & Uhlmann, p.96] compare the amorphous silica surface to that of cristobalite. The structure of cristobalite is shown below. It is cubic with silicate tetrahedra arrayed in a way similar to the zinc blende structure. The unit cell dimension is 7.16 Å.

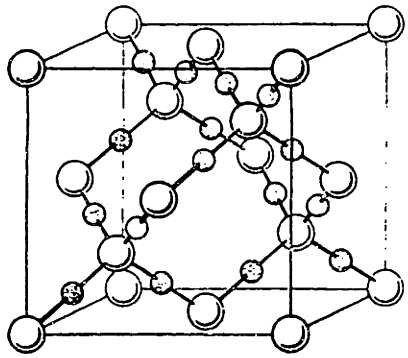

Figure 3.4 Structure of cristobalite. [Kingery, Bowen, & Uhlmann 73]

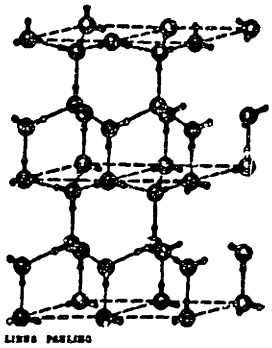

Figure 3.5 Structure of ice. Picture attrib. to Linus Pauling. [Encyclopaedia Brittanica, 1964 ed., vol. 12, "Ice"] (Note six-membered rings in both structures)

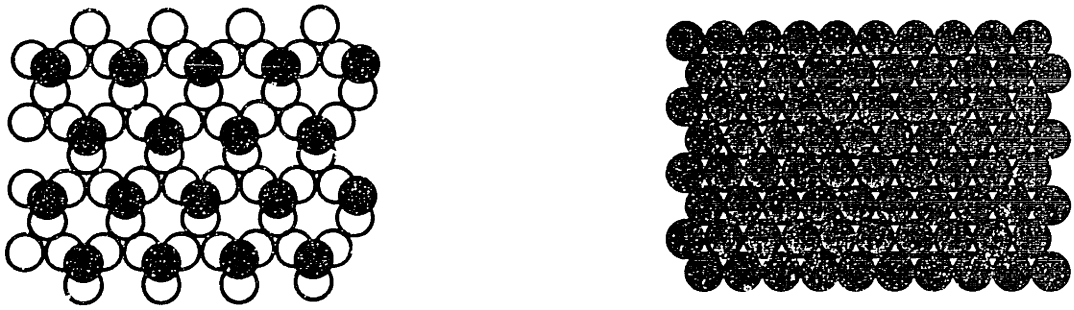

a. b.

Figure 3.6 Projection in close-packed direction of (a.) cristobalite and ice; (b.) alumina. ● = Top layer of oxide ions; ○ = Second tier of oxides.

The spacing between oxygen atoms in this structure is $\sqrt{3}/4$ times the unit cell spacing, or 3.10 Å. In the direction that most closely resembles the close-packed direction, the arrangement is tetrahedral. Liquid water has a short-range structure that resembles ice, which is hexagonal and has a spacing between oxygen atoms of 2.76 Å. The hydrogen bonding in ice causes the water molecules to group themselves in tetrahedral structural elements analogous to, and with almost the same spacing of, the tetrahedral silicate elements comprising silica. This network results in a structure with large voids. By contrast, the oxygen atoms in alumina are nearly close-packed, and the close-packed surface bears little resemblance to the structure of water, even though the spacing between adjacent oxygen atoms is approximately the same in all cases.

Amorphous silica is biologically inert, like crystalline silica. Dust of amorphous silica is substantially less dangerous than crystalline silica with regard to silicosis probably because of its higher solubility.

3.1.3 Glass

When silica is melted together with other ionic solids, the softening point of the material is reduced to a level where it can be formed into useful objects at a reasonable working temperature. The most common additives are oxides of sodium, calcium, boron, potassium, magnesium, and aluminum. A typical window glass contains (by weight) 72% SiO_2, 8% CaO, 14% Na_2O, 4% MgO, and traces of various other additives [Kingery, Bowen, & Uhlmann, p. 109] and has a softening point around 700°C. The thermal expansion coefficient of soda-lime glass is about 10 times higher than that of fused silica, with accompanying decrease in thermal shock resistance.

Alkalai oxides, especially sodium and potassium, modify the structure of silica by allowing a fraction of the doubly-bonded oxide ions to dangle from the network. This opens up the structure, lowering the viscosity and self-diffusivity of the melt at a given temperature. Addition of 5 wt.% potassium oxide to glassy silica is sufficient to decrease its viscosity by five orders of magnitude [Kingery, Bowen, & Uhlmann, p. 764]. The binary phase diagram for Na_2O-SiO_2 is shown below. There exists a deep eutectic with a composition of 72 wt.% SiO_2 which melts at about 800°C. This eutectic accelerates the melting of mixtures of silica and soda because the eutectic forms at the joints between silica and soda grains. The viscosity of the melt decreases exponentially with increasing

temperature and increasing alkalai content. Several stoichiometric compounds exist, and these are the phases that form when a commercial glass devitrifies. The compound devitrite, $Na_2Ca_2Si_3O_9$ is especially common in glass processing.

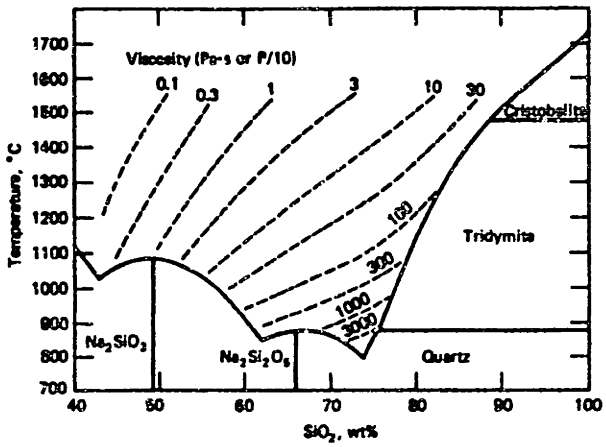

Figure 3.7 Phase diagram of the Na_2O-SiO_2 system and viscosity of sodium silicate melts. (Note: 1 cP = .001 Pa-s) (From PQ Corp.) [Kirk-Othmer Vol. 20, p.865]

Porcelain is of particular commercial importance. It is made from mixture of various minerals, primarily composed of Al_2O_3 and SiO_2, but with other important components. The components are partially fused during firing, and the mixture forms a eutectic of a glassy phase with some insoluble crystalline phase that toughens the material.

3.1.4 Soluble Silicates

Glasses can be formed in a continuous range of compositions. If a sufficient fraction of alkalai is used to form the glass it will be soluble in water. Sodium silicate, Na_2SiO_3, is a stoichiometric compound that is rather difficult to quench into a glass, but it dissolves readily in water. It is commonly called **water glass**, and is used primarily as a flame retardant. Sodium silicate is produced with molar ratios SiO_2:Na_2O ranging from 1.6 to 3.9. [Iler 119] Other bases will dissolve silica, too, including the organic base tetramethylammonium hydroxide (TMAH; [Iler, 116]; see sect. 3.4.3.d)

It is tempting to picture an aqueous solution of sodium silicate as a very low temperature glass containing oxides of silicon, sodium, and hydrogen. It is far more illuminating, though, to note that silica is the anhydrous form of silicic acid, H_4SiO_4, of which sodium silicate is the salt with soda. Although silicic acid has never been isolated as a pure substance, Iler treats it as a chemical species in solution. Silicic acid is a "weak"

acid, so sodium silicate is alkaline. At low pH, the acid is unionized and sparingly soluble. At high pH, above 10.7, the acid is ionized to silicate ion $H_3SiO_4^-$, and is very soluble. [Iler 47] For Na_2O-$2SiO_2$, a solution containing about 33 wt% SiO_2 can be prepared.

3.1.5 Colloidal Silica

The form of silica that is of special interest in Three Dimensional Printing is an aqueous dispersion of spherical particles of amorphous silica with particles ranging in size from 5 nm to 100 nm. It is also called **silica sol**. It has been available as a commercial product since the early 1950's, and its uses range from suspending medium in ceramic shell slurries to stiffening of corrugated cardboard to manufacture of apple juice. The properties of the product used in this research are given in Appendix F.

The exotic properties of colloids are treated in detail elsewhere, only a brief summary of the properties will be discussed here.

Colloidal silica is available commercially with solids loading up to 50 wt.% (33vol.%) and unlike silicate solutions, the viscosity remains quite low over the full range of stability. It is a milky or opalescent liquid with a specific gravity that depends on the silica content:

$$\rho_{suspension} = 1 + f_{particle}\left(\rho_{particle} - 1\right) \qquad 3.2$$

and

$$f_{particle} = \frac{(wt.fr.)}{\rho_{particle} - (wt.fr.)\left(\rho_{particle} - 1\right)} \qquad 3.3$$

where $f_{particle}$ is the volume fraction of silica in the sol and $\rho_{particle}$ is 2.19 for amorphous silica. It is most convenient, in the long run, to treat the silica content in terms of the volume fraction, and this convention will be adhered to throughout.

Colloidal silica is manufactured from sodium silicate with a molar ratio (Na_2O:SiO_2) of 1:3.25 [Iler 119.] After neutralizing the base with a mineral acid (H_2SO_4 is common) the salt is removed by a combination of dialysis and ion exchange. This process results in a supersaturated solution of silicic acid (H_4SiO_4) which polymerizes by **condensation**, liberating a water molecule for every silica unit added to the polymer. By

adjusting such conditions as the temperature, silica and salt concentrations and pH, the nucleation and growth of silica particles can be controlled to produce sols with varying particle sizes and solids loadings.

An alternative process uses tetraethyl orthosilicate as a source of silica and silicic acid is generated through hydrolysis. This process is not used on a large scale in industry, but is used widely in laboratories. TEOS is a convenient source of very pure silica since it can be purified by distillation.

Colloidal silica is typically shipped with a pH of about 10 and a trace of added sodium, typically 0.5 to 1.0% as Na2O. The sodium is added to speed the strengthening of the silica bonds in ceramic shells during heat treatment.[DuPont Co, LUDOX product literature] The ceramic shell industry is a major consumer of the product and influences the product formulation. Other users, e.g. apple juice manufacturers, are less concerned with the presence of small amounts of ionic additives. [Dave Catone, Nyacol Corp., private communication] The casting industry prefers to use sols with particle sizes of 10-20 nm because these give shells with the best strength. [Rusher]

3.1.6 Silica Gel

When colloidal silica is dried past the point of stability, or if its pH is adjusted to between 5 and 7 for a period of time, or some chemical (e.g. salt or an appropriate polymer) is added, the silica particles adhere to one another and a solid, space-filling network can be obtained. This material has a soft, slightly springy feel to it, and is therefore called a **gel**. Colloidal silica is gelled in 3-D Printed material to immobilize the silica inside the printed regions and to keep it from bleeding into unprinted regions. Although it would gel during normal drying, it is preferable to form a gel by some chemical means whose rate can be more easily controlled.

Dried silica gel can be prepared with a bulk density ranging from 0.1 to 0.8 g/cc. It is highly porous, absorbant, and is widely used as a catalyst because of its large specific surface area, which can range from 200 to 700 m^2/g.[Kirk-Othmer, vol. 20, p. 768] Gels are formed from soluble silicates, aqueous colloidal silica of from hydrolyzed organosilicates (e.g. TEOS) and dried to remove the solvent, which initially saturates the pores. If the solvent is removed by normal evaporation, the capillary pressure becomes high enough to crack and distort the network. This is called a **xerogel**, and constitutes the

major volume of silica gel available. In another process, considerably more expensive, the gel is placed in a pressure vessel and raised to the critical point of the solvent. The solvent can then be extracted with no capillary suction, and the resultant gel reflects more closely the network formed by the initial coagulation. Gels with exceedingly low density can be produced: so low that the air permeating the pores weighs more than the solid skeleton. This type of gel is called an **aerogel** and has not yet found wide application.

Silica gel is very hygroscopic, and retains water in its pores up to 300°C. Beginning at 700°C, the primary particles begin to sinter together, resulting in a gradual strengthening of the network. Water that is retained at this point is chemisorbed. Up to 1000°C, there is little change in gel volume, and it will retain some chemisorbed water up to that temperature.[Kirk-Othmer, vol. 20, p. 775] Above that temperature, the gel converts to cristobalite or silica glass. The presence of impurities, particularly alkalai metals, accelerates devitrification.[Iler, 544-549]

Colloidal silica is available commercially in a number of forms: Ludox HS-30 from Dupont is a colloid with a particle size of 10 nm, and a solids loading of 16 vol.% (30 wt.%) Nyacol 830 is an equivalent product. Nyacol 9950 is a product with 100 nm particles and a 50% by weight (33vol.%) silica. All these products have approximately 1% Na_2O and are shipped with a pH of about 8. Ludox DI is a colloidal silica product without the added Na_2O. Ludox AM is a colloidal silica that has been treated to coat the particles with alumina. Because of the higher isoelectric pH of alumina, these sols are positively charged at low pH and are stable for acidic slurries [DuPont, LUDOX product literature]

3.1.7 Pyrogenic Silica

This is a form of amorphous silica that is commonly called **fumed silica**. It is most often made by reacting $SiCl_4$ with water vapor. The material formed has a very low density, and has a much higher purity than silica gel, which usually contains traces of coagulant. It is used as a filler in plastics.

3.1.8 Biogenic Silica

Diatomite is up to 94% pure silica isolated by aquatic micro-organisms, principally diatoms, and piled up in sediments over the ages. Also called diatomaceous earth, it is very

porous, owing to the spiny structure of the microorganisms. It is used as a filtration medium, an insulating material, and as a polishing media, especially in toothpaste.

3.2 The Special Case of Colloidal Silica, a Lyo-Ambivalent Colloid

Colloidal silica formed by the polymerization of aqueous silicic acid, $Si(OH)_4$ is amorphous in structure, but is not chemically pure: it incorporates traces of water trapped there by the condensation reaction [Iler, 632] The polymerization is called condensation because it liberates water. The converse process is called **hydrolysis**.

The stability of colloidal silica is variable with pH, with a metastable range between pH ~1 and 4; a stability minimum at pH 5-7, and total stability above pH 8. Above pH 10-11, silica becomes soluble and acts like a buffering salt. This is illustrated schematically below.

The chemical properties of colloidal silica are determined by the silica surface, which is profoundly influenced by the reactions between silica and water in the aqueous suspending medium.

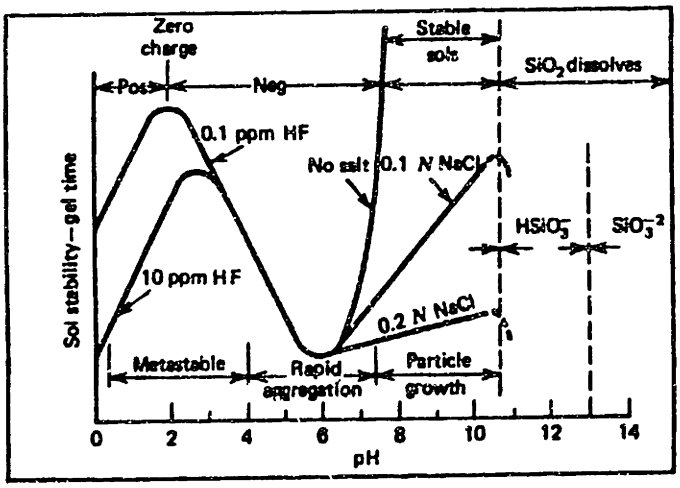

Figure 3.8 Effects of pH in aqueous colloidal silica. The minimum in stability is a result of catalytic action of OH^- combined with a low surface charge at intermediate pH. [Iler, 367]

3.2.1 The Hydrophilic Silica Surface

Since colloidal silica is formed by condensation, the silica is fully hydrated. Studies have shown that some colloidal silica preparations are microporous: the particles are pitted with cavities that provide more surface sites than would be available on a smooth, spherical particle [Tadros & Lyklema]. The atomic spacing of amorphous silica suggests that its surface resembles cubic cristobalite. The structure of cristobalite incorporates a great deal of hollow space in the octahedral sites, and in amorphous silica there is a distribution of cavity sizes. On the molecular scale, perhaps the distinction between a microporous surface and a disordered hollow lattice is meaningless.

A dehydrated silica surface reacts slowly with water to form hydroxylated silica. [Iler 645] The Si-O-Si bond is called siloxane while the Si-O-H bond is called a silanol. Water that is adsorbed by this mechanism is said to be **chemisorbed**. This reaction is showed below.

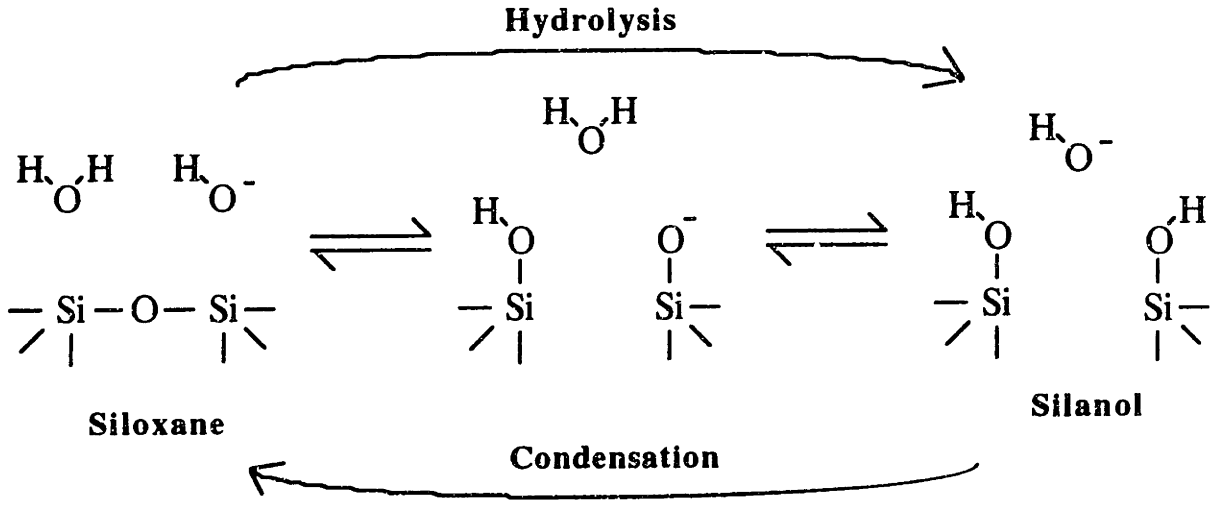

Figure 3.9 Hydrolysis of a silica surface. Bond length not to scale, dangling bonds assumed to be joined to body of silica particle

The hydrolysis of the siloxane bond is catalyzed by the presence of hydroxide in the surrounding solution.[Iler 355] In the intermediate state, a negative charge is formed on the surface. At the isoelectric point, the surface concentration of negative charges must be exceedingly low, so the rate of condensation is slow. Iler uses this as an argument to explain the high degree of stability of colloidal silica at its isoelectric point: if two particles with fully hydroxylated surfaces come together, there are no SiO^- surface groups present to

react and form siloxane bridges between particles. The surface charge density as a function of pH is shown in figure 3.18.

Unlike the covalent siloxane bond, the silanol group is strongly polar, and attracts water by hydrogen bonding. The difference in hydrophilicity can be expressed by a difference in the heat of wetting of silica gels that have been carefully dried of all but chemisorbed water. For silica gel with a pure silanol surface, the heat of wetting is about 150-200 erg/cm^2, while for a siloxane surface it is 117-130 erg/cm^2. Whether or not these values can be related to a difference in surface energy is uncertain, but the difference in affinity for water can be judged qualitatively. Hydroxyl groups populate the silica surface at a density of approximately 4.6/nm^2 [Iler 637]. This is conveniently close to the density of a fully hydroxylated (111) surface of cristobalite.

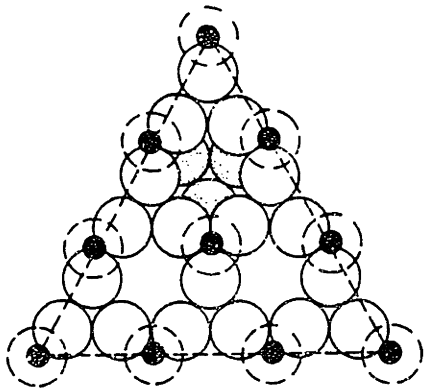

Figure 3.10 Atomic arrangement on the (111) surface of cristobalite. This is the direction of the cube diagonal in figure 3.4. Large circles = oxygen atoms; small circles = silicon atoms; dashed circles = hydroxyl groups. 4.55 hydroxyl groups/nm^2 [Iler 637]

In colloidal silica at the isoelectric point (pH 1-2) virtually all of the silicon atoms at the surface are hydroxylated. As the pH is raised above the isoelectric point, hydroxyl ions in solution react with silanol groups to leave negatively charged sites on the particle surface. Data by [Bolt] suggests that the charge density does not reach very significant values until pH 7, and even at very high pH only 10% or 20% of the silanol groups become ionized. (See figure 3.18) Between the isoelectric point and a pH where the surface charge is high enough to repel particles from one another, there are sufficient negatively charged sites on the silica surface to form siloxane bonds between colliding particles. Accordingly, the gel stability passes through a minimum.

The rate of gel formation in colloidal silica is discussed by [Iler 368] and the graph below gives some representative data for 14 nm colloidal silica. The rate of gelation at the point of minimum stability is so very much slower than the Smoluchowski rate for that particle size, it suggests that another mechanism is active which stabilizes colloidal silica. There is strong evidence that this phenomenon is the physical adsorption of water to the silica surface.

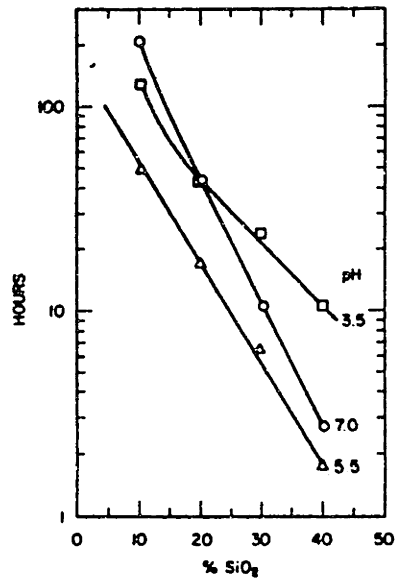

Figure 3.11 Gel time vs. silica content for colloidal silica at various pH. [Iler, 368]

3.2.2 Hydration Energy as Interparticle Repulsion Potential

The process by which water is adsorbed onto a surface without chemical reaction is called physical adsorption, or **physisorption**. Silanol groups present a very attractive surface for the electron-rich oxygen atoms in water. [Iler 627,630] presents various data that suggest the energy of adsorption is between 25 and 40 kJ/mole. Water is adsorbed in two or more monolayers with little decrease in binding energy [Iler 627, 650-653.]

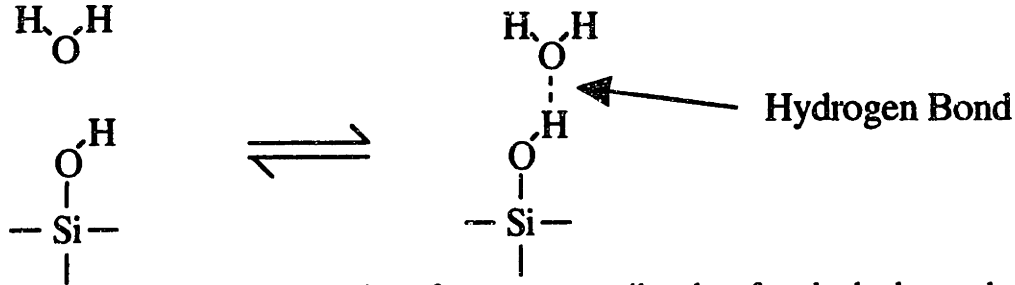

Figure 3.12 Physical adsorption of water onto a silanol surface by hydrogen bonding (see section 2.3.2)

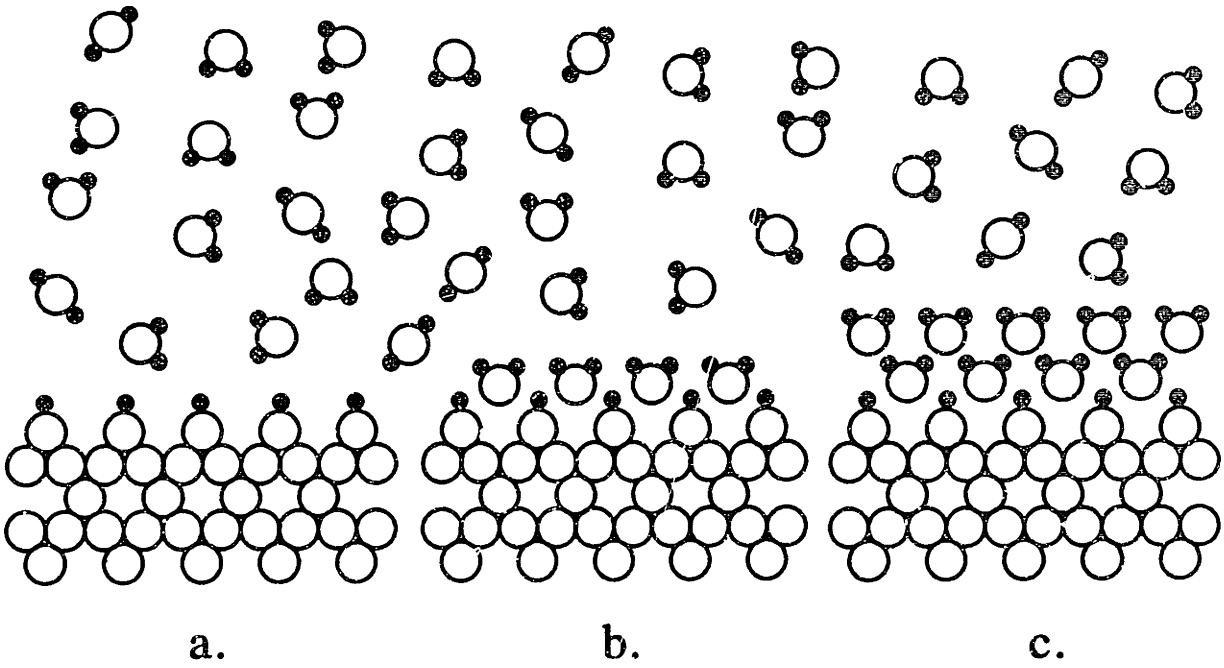

Figure 3.13 Adsorption of water on hydroxylated silica. Open circles: oxygen; filled circles: hydrogen. Lattice shown corresponds to cristobalite (111) plane with hydroxylated surface. Spatial density of water molecules is to scale only in the vaguest possible sense.

Water must be desorbed in order for particles to touch. If two particles each have two layers of adsorbed water, the combined film is approximately 1.0 nm thick. If we assume that water populates the surface of each silica particle with a density corresponding to the density of silanol groups, then the surface concentration is 7.5×10^{-6} mol/monolayer-m^2. Taking the conservative value of 25 kJ/mole as the binding energy, this leads to a surface energy of 0.2 J/m^2 or 2×10^{-19} J/nm^2 per monolayer of water desorbed. For four monolayers piled to a depth of 1 nm, the energy required to desorb is 8×10^{-19} J/nm^2.

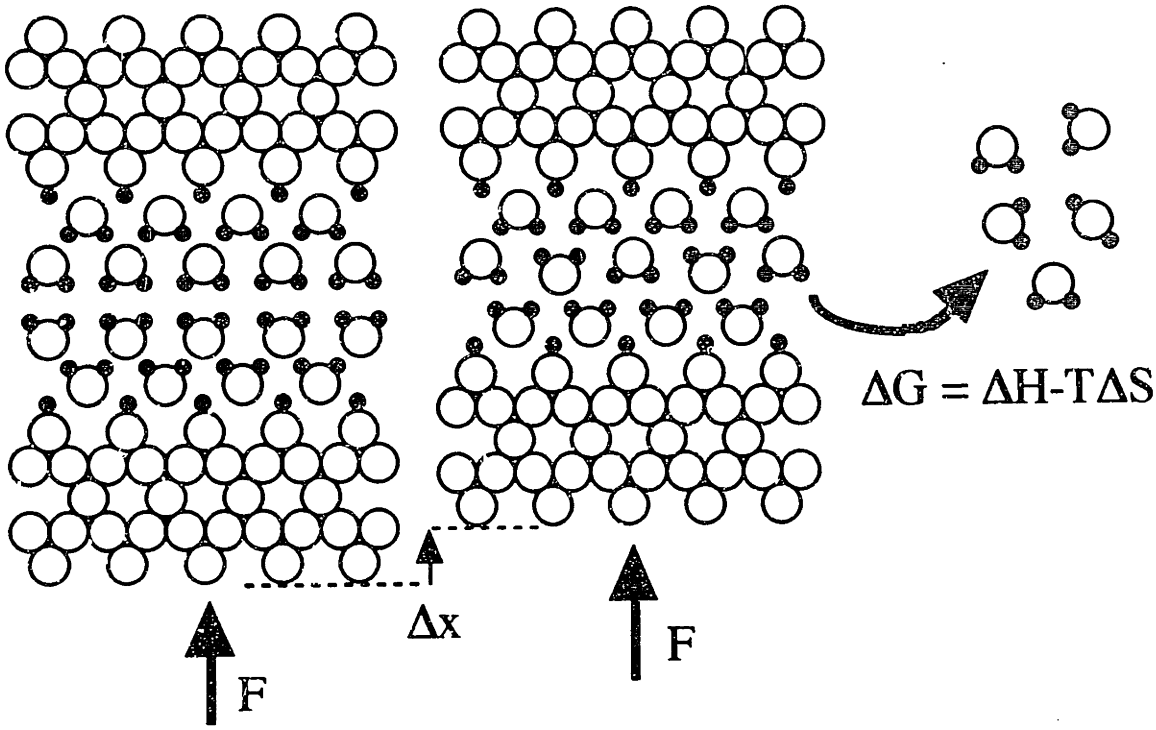

Figure 3.14 Desorption of water as hydroxylated silica surfaces approach one another. The work done is FΔx and that serves to increase the free energy of the desorbed water.

Each monolayer of water is roughly 2.5 Å thick and should be desorbed in a stepwise manner as the surfaces approach. To calculate the potential energy of approaching spherical particles, the Deryaguin approximation can be used [Hunter, 191] (sect. 3.3.4.c):

$$V(B)^{sphere} = \pi a \int_H^\infty V(L)^{plate} dL \qquad 2.58$$

this integral can be evaluated approximately by assuming that the water is desorbed gradually as the spheres come together. This leads to the linear approximation:

$$V_R^{plate} = 8 \times 10^{-19} (1\text{-}L) \ J/nm^2 \quad \text{for } 0 < L < 1nm \qquad 3.4$$

$$= 0 \quad \text{for } L > 1 \text{ nm.} \qquad 3.5$$

where L is expressed in nanometers. For particles with a radius of 50 nm, the repulsive potential is approximately

$$V_R^{sphere} = 6.3 \times 10^{-17} (1\text{-}B)^2 \ J \quad \text{for } 0 < B < 1nm \qquad 3.6$$

$$= 0 \quad \text{for } B > 1 \text{ nm.} \qquad 3.7$$

To put this energy barrier in perspective, recall that k_BT is 4.1×10^{-21} J at 25°C .

Israelachvili observed the repulsive force from adsorbed water on mica. A graph from this reference is shown below. It can be seen that the repulsive force exceeds the magnitude of 0.2 J/m^2 (200 mN/m) for three out of four distinct adsorbed monolayers. One might well wonder how it is possible for silica to coagulate at all.

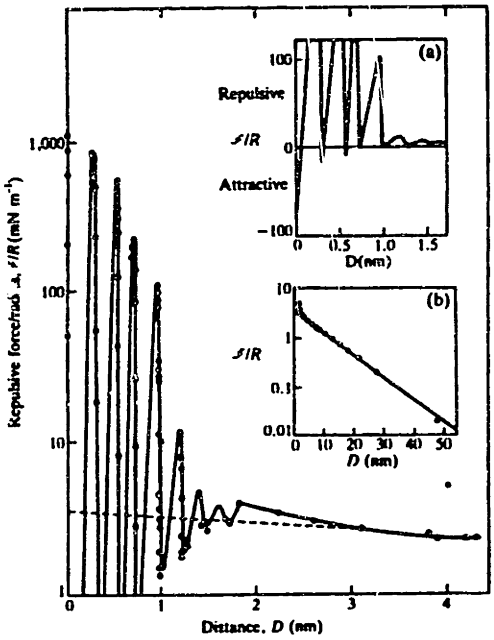

Figure 3.15 Detailed structure of the hydration force between mica plates in .001 M KCl at very short distances. Note: "radius" in the vertical axis is the radius of curvature of the bent mica sheets used in this experiment. This is consistent with equation 2.58. (Israelachvili and Pashley, Nature, **306**, 249) [Hunter 439]

It is probably very rare to have a colloidal silica sample that is pure enough to actually exhibit this characteristic. [Hunter 35-36] describes the elaborate techniques for obtaining water of sufficient purity to study colloid science in a "scientific" fashion. Commercial colloidal silica contains about 0.5-1.0% sodium hydroxide. [Iler 375] describes how cations, especially sodium, can exchange for protons in hydroxylated silica and form bridges through the adsorbed water on neutral particles (see sect. 3.3.4.)

3.2.3 Destabilization at Neutral pH

Hydroxyl ions are potential-determining for silica. As the pH increases above the isoelectric point, the hydroxylated silica surface becomes populated by negative charges. This tends to reduce the ability of the surface to hydrogen bond [Iler, 658] and thereby reduces the potential barrier created by adsorbed water. Apparently, the presence of a small concentration of negative charges on the silica surface is sufficient to disrupt the structure

of the adsorbed water. The surface concentration of OH^- ions is shown below as a function of pH and salt concentration. In the range of pH 5.5 to 7.0, the charge density is negligible, especially at low salt concentrations, and so cannot provide much electrostatic stabilization. This is the range of the stability minimum (see figs. 3.8 and 3.11) but the stability even in this range is still quite substantial (The stability ratio is on the order of 10^{10}) (sect. 3.2.9)

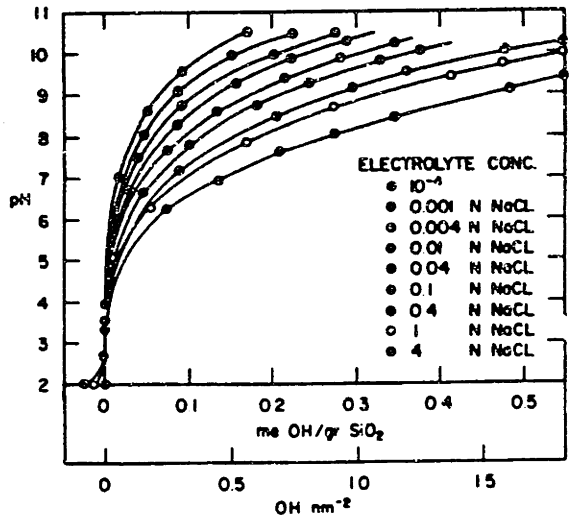

Figure 3.16 Surface charge density on colloidal silica particles as a function of pH and at different salt concentrations.[Bolt]

3.2.4 Charge Stabilization at High pH

A quantitative measure of charge stabilization is obtained by measuring the zeta potential. The zeta potential is the electric potential at the plane of shear between a colloidal particle and the surrounding medium. The zeta potential was measured from the electrokinetic sonic amplitude in a sample of Nyacol 9950 colloidal silica with a particle size of 100 nm on a machine built by Matec Applied Sciences of Hopkinton, MA. The electrokinetic sonic amplitude is an oscillating electric potential caused by an ultrasonic vibration in a suspension of charged particles. Because the particles have a different density from the surrounding medium, they lag behind a sound wave while the solvated ion shells move in step with the sound wave. This induces a net dipole in the electrolyte which is picked up by electrodes in the cell.

Results from two runs are graphed below. Values of 20-30 mV are typical for charge-stabilized colloids. It was shown above that 100-nm particles at 25 mV potential

have a potential energy barrier of about 12 kT at room temperature. At pH 5-6, it can be seen that the zeta potential is about half that, and since the potential energy barrier goes as ψ^2 (eqn 2.55), the barrier is only 3 kT at the stability minimum. If the hydration layer is disrupted at this pH, then the loss of stability could be explained.

As the pH is increased past 8, the zeta potential becomes high enough alone to make the sol stable.

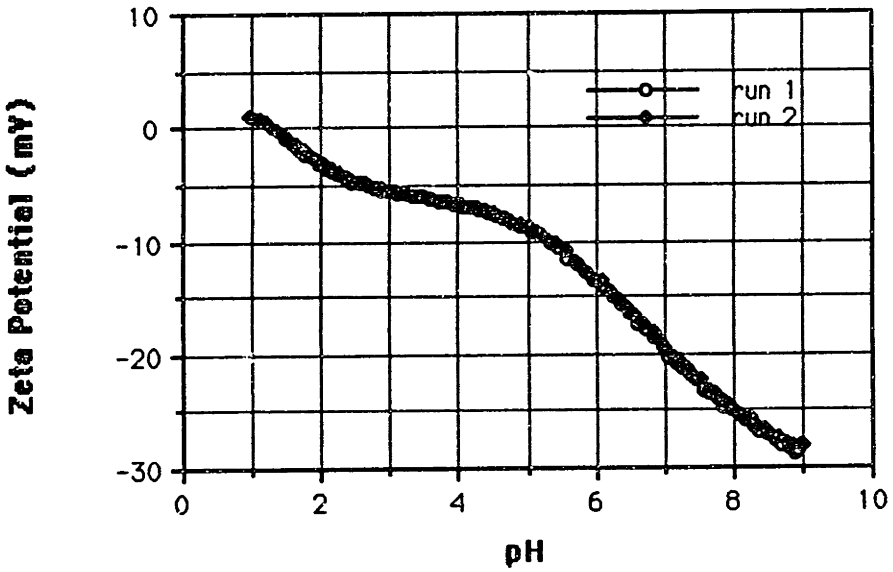

Figure 3.17 Zeta potential of Nyacol 9950 vs. pH at room temperature in water. Measured by electrokinetic sonic amplitude in a Matec (Hopkinton, MA) analyzer.

3.3 Coagulation in Colloidal Silica

The mechanisms that stabilize colloidal silica prevent particles from coming into contact. It follows that mechanisms that bring particles into contact will cause coagulation.

3.3.1 Drying

By removing the solvent that separates the particles in a colloid, particles interact more frequently, and the electrostatic fields of particles begin to overlap. The Debye layer thickness is constant for a given ionic strength, so colloids with smaller particles can be expected to become unstable at lower solids loadings than ones with larger particles because the spacing between smaller particles is less at a given solids loading. This is borne out by experiment pller 325.] For Three Dimensional Printing, silica with the

highest stability is needed, so the largest commercially available particle size is used. Nyacol 9950 with a 100 nm particle size has a solids loading of 50% by weight (33% by volume) from Nyacol Corp., Ashland, MA.

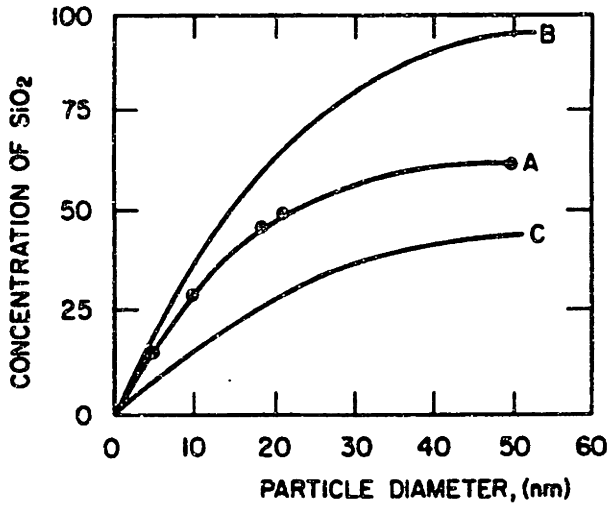

Figure 3.18 Maximum concentration vs. particle size in stable colloidal silica sols at pH 9.5. Curve A: weight percent; B: grams SiO_2 per 100 ml of sol; C: volume percentage of SiO_2. [Iler, 325]

The mechanics of dried unmodified colloidal silica are somewhat undesirable. The capillary pressure in the drying film becomes very large and leads to compression of the gel. Dried gel from colloidal silica cracks and curls off most flat surfaces. This is less of a problem when the material is used as a binder for ceramic particles because the intricate surface geometry localizes the deformation. Cracking is observed in the gel on the scale of the powder particle size, but macroscopic cracking is less prevalent. Iler recommends mixing particle sizes to localize the shrinkage.

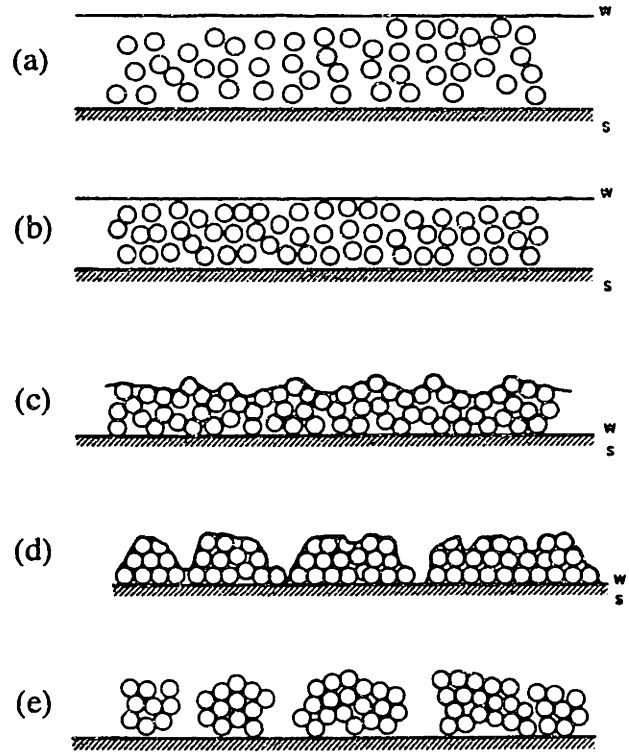

Figure 3.19 Drying of a film of colloidal silica. a. Sol; b. flocculated concentrated sol; c. gel compression by water surface tension; d. gel fracture by shrinkage; e. Loose, dried flakes of silica gel. W: water surface; S: solid substrate. [Iler, 371]

Figure 3.20 SEM Micrograph of 3-D Printed material. Silica gel bridging three particles show some cracking due to gel shrinkage. Photo courtesy of Jain Charnnarong. M≈2500x

3.3.2 Freezing

If a colloidal silica sol freezes, ice crystals force the silica particles into a more confined space, and the sol will coagulate by the same mechanism as when it dries. The literature on LUDOX recommends adding alcohol to colloidal silica, with precautions about establishing the correct pH to maintain stability. The addition of ethylene or propylene glycol as a humectant also prevents freezing, but the small percentages used do not lower the freezing point by very much.

3.3.3 Electrolytic Coagulation

The presence of electrolytes tends to increase the surface charge on colloidal silica while simultaneously decreasing the surface potential. The net result is a decrease in sol stability with increasing ionic strength. One phenomenon that has received considerable study is the pH-dependence of the stability with respect to electrolytes. [Allen and Matijevic] report data for the coagulation of Ludox HS (210 m^2/gm) by electrolytes. This should be compared with AgI, a "classic" hydrophobic sol.

	[Allen & Matijevic]	Overbeek [Hunter, 95]
Sol Charge	Silica (Ludox HS) negative	Silver Iodide negative
c.c.c. (Na^+, mol/lit)	1 (pH 7) .012 (pH 10)	0.14 (indep. of pH)
c.c.c (Al^{+3}, mol/lit)	0.05 (pH 3.4) 2×10^{-4} (pH 4)	7×10^{-5}

Table 3.1 Critical coagulation concentrations for Na^+ and Al^{+3} with SiO_2 and AgI.

The variation of c.c.c. of aluminum with pH can partly be attributed to the hydrolysis of the Al^{+3} ion, and precipitation as $Al(OH)_3$. In general, colloidal silica is most stable with respect to electrolytes as the pH approaches the isoelectric point. Since the charge on the particles decreases as the isoelectric point is approached, the effect on the double layer by electrolytes has less significance. Instead, the attraction of water molecules to the silica surface (with adsorbed cations) becomes more significant, and the less hydrophilic the adsorbed species, the less stable the sol.

[Iler 375-378] postulates that strongly hydrated cations such as sodium can bridge from one particle to another. This might be the mechanism that defeats the seemingly unassailable potential barrier created by physisorbed water. The bridging sites created by adsorbed alkalai ions would breach the hydration layers and provide points of adhesion between particles without the need to overcome the enormous potential barrier (sect. 3.2.2).

While the concentrations of electrolytes that cause coagulation in colloidal silica are reasonably well documented, the mechanisms involved are still the subject of much debate. Hydrolyzable cations such as Al^{+3} tend to coagulate silica at a concentration and pH just below the level at which the substance would precipitate by itself [Allen & Matijevic]. When polyvalent cations are specifically adsorbed on the surface of colloidal silica particles, the positive charges provide points of attachment for other negatively charged particles. This is different from conventional hydrophobic colloids; the addition of electrolytes to them cause compression of the double layer without specifically discharging the surface [Iler, 381].

3.3.4 Ion-Exchange: Tetramethylammonium (TMA+)

Historically in Three Dimensional Printing of colloidal silica, tetramethylammonium hydroxide (TMAH) was added to raise the pH of the silica in an attempt to gain stability. [Iler 376] cites results that describe TMA+ as a powerful coagulant at pH 7.5 but provides steric stabilization at pH 9-10 at high concentrations because the large cations coat the silica surface. He lists the critical coagulation concentration for TMA+ to be .01 mol/lit. at pH 7.5. This was measured experimentally in the coagulation studies described below (sect 4.4.2.)

Colloidal silica (Nyacol 830) with a particle size of 8 nm and a solids loading of 16 vol % was originally used. TMAH was added so the liquid phase had a concentration of 0.39 mol/l . Assuming 4.5 SiOH sites per nm^2, the specific surface area of Nyacol 830 is 325 m^2/g, so there are 5.2×10^{23} sites per liter, or a molarity of SiOH surface of about 0.87 mol/l. This composition was not sufficiently stable for 3-D Printing, so Nyacol 9950 with a particle size of 100 nm and a specific surface area of 3 m^2/g was used at the same solids loading and the same TMAH content. The number of TMA+ ions per silanol site increased from 0.5 to 50, and the sol was substantially more stable but did not have

sufficiently long shelf life to be entirely satisfactory. The silica acted as an acid, gradually lowering the pH of the aqueous medium until the loss of surface charge was sufficient to allow the particles to aggregate. Also, TMAH was found to react adversely with other additives.

3.3.5 Hydrogen-Bonding to Polymers

The adsorption of polyethylene glycol to silica at low pH has received some study. Iler describes how adsorbed cations reduce the efficiency of hydrogen bonding. Polyethylene glycol is water soluble and the oxygen atoms in the ether linkages are very electron-rich and hydrogen-bond to surface silanois. See also [Maltesh & Somasundaran].

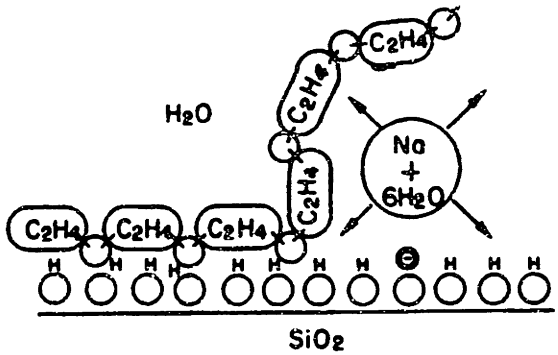

Figure 3.21 Hydrogen bonding of polyethylene glycol to hydroxylated silica. [Iler, 658]

Polymer chains that are long enough to bridge from one particle to another can coagulate silica. Polyethylene glycol (PEG) is currently used as the coagulant in the present formulation of colloidal silica binder. It was found that PEG concentrations as low as 100 ppm were sufficient to coagulate silica at pH below 7.5. The development of this formula is discussed in detail below (sect. 4.4.5). The coagulation mechanism is illustrated below. At high pH, the negative charge sites on the silica surface repel the electron-rich ether oxygen of the polymer. If the pH is lowered somewhat, protons combine with the negatively charge sites and neutralize them. These protons attract the ether oxygen in the polymer, and the polymer becomes adsorbed onto the silica surface. If there is a very high concentration of polymer present, the particles will become entirely coated, and the silica becomes sterically stabilized. If the polymer concentration is relatively low however, chains can bridge from one particle to another, causing the sol to coagulate. This is a form of depletion flocculation discussed in section 2.3.6, above.

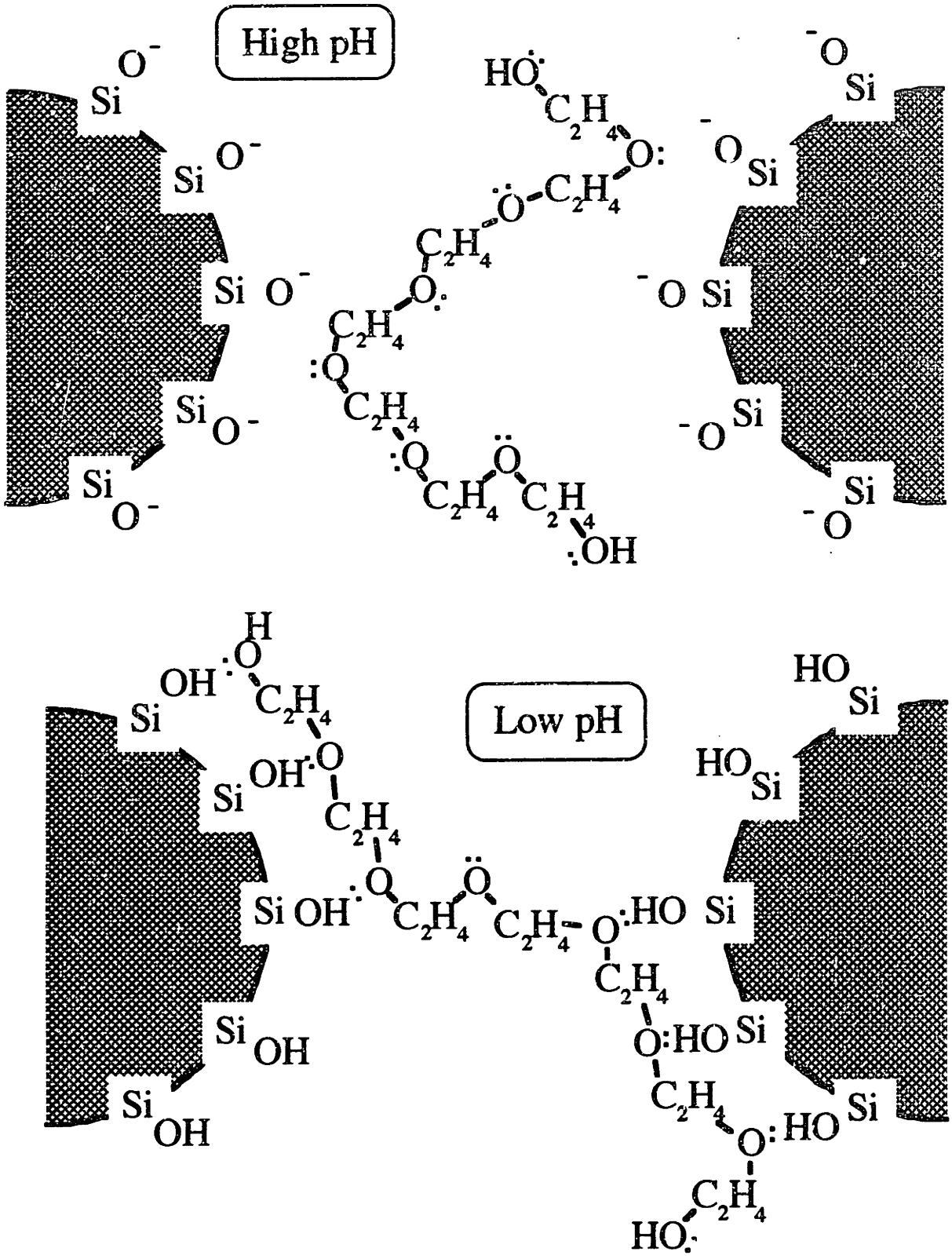

Figure 3.22 Coagulation of silica by polyethylene glycol.

3.3.6 Heterocoagulation

If a positively charged sol is mixed with a negatively charged sol, the mixture will coagulate very rapidly. The positively charged particles stick the negatively charged particles together, forming a space-filling network as rapidly as the particles come together. A colloid of alumina below the isoelectric point of alumina (about pH 5) will have a positive charge on the particles. Colloidal silica can be made positively charged to make it compatible with alumina at low pH by reacting it with an aluminum salt. This is done to make Ludox AM. The reaction must be done very carefully, otherwise the sol coagulates (sect.4.4.2)

3.3.7 Surfactants

a. Anionic Surfactants

Anionic surfactants do not affect the stability of unmodified colloidal silica. Since the surface of silica is primarily hydrophilic, the hydrophobic tail of the surfactant is not attracted. Many anionic surfactants are precipitated by silicate, $HSiO_3^-$, that is always present in colloidal silica. Nonionic surfactants do nothing to enhance silica stability either. If they contain polyethylene oxide, they can coagulate silica by hydrogen bonding. Cationic surfactants react rapidly with colloidal silica and cause coagulation. These phenomena will be discussed in the context of coagulation mechanisms, below. Although useless as stabilizing agents, surfactants are useful in ink-jet printing as wetting agents and detergents. Their inactivity with silica is a positive benefit to the technologist.

b. Cationic Surfactants

A cationic surfactant possesses a positively charged ionic "head" and a nonpolar "tail". Negatively charged silica particles attract the hydrophilic ends of the surfactant, causing the hydrophobic tails to be oriented outward from the particle surfaces. This causes the silica surface to become hydrophobic, erasing the substantial stabilizing effect of adsorbed water, even at very low concentrations of surfactant (sect. 4.4.2.) At concentrations above the critical micelle concentration, the cationic micelles function just

like positively charged colloidal particles, coagulating the sol by heterocoagulation, described above (Iler 388-390)

c. Nonionic Surfactants

Most nonionic surfactants, e.g. Triton X-100, contain a chain of polyethylene oxide as the hydrophilic group. At high pH, this polymer does not associate with colloidal silica. As the pH is lowered past 7.5, the polymer adsorbs onto the silica surface, and the hydrophobic tails of the surfactant cause the silica particles to become hydrophobic. If the concentration of the surfactant is relatively high, the colloid will again be restabilized as a hydrophobic colloid, but at intermediate concentrations, the sol will coagulate.

This property suggests a method for testing the nature of surfactants. If an unknown surfactant is added to a solution of a known ionic surfactant, e.g. sodium dodecyl sulfate, it will precipitate if it is oppositely charged (cationic, in this example.) If it does not precipitate, it might either be anionic or nonionic. Adding a small amount to colloidal silica at neutral pH will distinguish between the two: anionics will have no effect, and nonionics will coagulate the sol.

3.3.8 Cationic Polymers

A soluble polymer with cationic groups is effectively a cationic hydrophilic colloid, and the coagulation mechanism is really the same as the heterocoagulation mechanism described above. Since soluble polymers can have very long chains, however, their ability to coagulate anionic colloids is very much greater than a cationic hydrophobic sol. Polymer chains can stretch between particles more easily, particularly if the molecular weight is high enough to give chain lengths on the order of the particle size. If an excess of polymer is added to the sol, the particles can become coated, and the sol stabilized sterically by the polymer. Such a sol would be rapidly coagulated on dilution.[Iler, 385-388; 393-396] Cationic polymers that were found to coagulate silica at very low concentrations are polyethylene imine and chitosan.

3.3.9 Esterification

The hydroxylated silanol surface is slightly acidic (because it can dissociate to yield a hydrogen ion) and can form an ester linkage with alcohol groups on organic molecules.

[Iler 412,689] discusses the reaction between dried silica gel and alcohols. It is not clear whether alcohols actually react with the silanol surface in aqueous suspension, but the association between silica and certain water-miscible organic solvents, especially t-butanol and acetone leads to very rapid coagulation. Polyvinyl alcohol reacts slowly with colloidal silica. There has been some development work to use it as a reinforcing agent (LUDOX SK) but in general, PVA is incompatible with colloidal silica.

3.4 Conclusion

The combination of insolubility with extreme hydrophilicity gives colloidal silica some very special properties that distinguishes it from other colloids. Like a hydrophobic colloid, silica is only metastable over most of the range of pH, but it is very much more stable than more ordinary hydrophobic colloids owing to the strong affinity of water for the silica surface. Colloidal silica at low pH is stabilized by adsorption of water, and at high pH is is stabilized electrostatically. It passes through a minimum of stability in the intermediate range, but this "minimum" is still very much more stable than most hydrophobic colloids.

In seeking a mechanism for coagulation to design into a binder formulation, there are a wide variety of mechanisms available. Many schemes that are ordinarily used to stabilize hydrophobic colloids tend to destabilize colloidal silica. The addition of nonionic surfactants is the most striking instance, but the addition of bases to raise the surface charge can also degrade the stability of the sol. These mechanisms formed the basis of the binder technology developed in the next chapter for Three Dimensional Printing.

The next chapter describes the experimental program that was followed in the development of colloidal silica binder for Three Dimensional Printing. Most of the techniques developed in this study can be applied to other colloidal materials, so these procedures should be of interest to the technologist. For the purposes of modelling feature formation in 3-D Printing, the measurement of the rate of coagulation of the chosen formula is crucial.

Chapter 4. Development of Colloidal Silica for Three Dimensional Printing

4.0 Introduction

One of the most difficult ways to study the physical properties of a binder used in Three Dimensional Printing is to operate a Three Dimensional Printer. Useful information is usually only gained when some part of the system fails because of the binder, and when that happens, the search for knowledge usually must take the back seat to the desire to return the machine to service. It is far more fruitful to simulate the dominant failure mechanisms on the benchtop in a way that are accessible to analysis. At the time this research was entered into, the dominant printhead failure mechanisms were drying of the binder on the nozzle and the clogging of the nozzle by solid material in the binder feed. Large (50 μm) solid particles could find their way into the binder if the sol was allowed to dry on tube fittings when connections were broken, and they could also form by gradual flocculation of the sol if its stability were not high enough.

Once a gelation mechanism is selected, the rate at which this phenomenon can be made to occur must be measured and compared to the rate of capillary migration in the powder. If the gelation rate is rapid enough to compete with capillary migration, then the feature size will be sensitive to local variations of coagulation rate, e.g. from segregation of the coagulant in the powder.

A series of experiments were done to test the limits of stability of colloidal silica. The stability requirements for binders in 3-D Printing are briefly reviewed. The product selected was Nyacol 9950 because of its high inherent stability (sect. 3.3.1.) First, compositions containing a humectant (ethylene glycol) were tested to measure the time a nozzle could sit idle and still form a jet. These data were used to fix the level of this additive in future formulations. It was found later that ethylene glycol has negligible effect on the stability of colloidal silica with added base (sect. 4.4.4.)

The main body of the experiments in this section were measurements to determine the coagulation threshold for a number of additives. The goal was to find a formula that possessed a high stability and long shelf-life, but incorporated a robust mechanism by

which the sol could be coagulated as desired in the powder bed. It was decided that the coagulation be triggered by a change in pH, specifically by a concentration of about 0.5% citric acid in the powder. The first series was performed to find a good organic base to hold the pH of the sol in the range of 9-10 which is both the range of maximum stability of the sol (see fig. 3.8) and is most compatible with stainless steel and nickel printhead components. It was found that all the bases tested destabilized the sol to some extent, so the decision was made on the basis of accelerated age testing and considerations of volatility on drying. The choice was to use triethanolamine (TEA) at a concentration of about 0.02 mol/l in the aqueous phase (sect. 4.4.3.)

Further coagulation studies were done to explore the interesting interaction between colloidal silica and polyethylene glycol (PEG) (sect.4.4.5). This additive was chosen as the primary coagulant and a series of experiments were done to find the appropriate concentration and molecular weight. A composition of colloidal silica, TEA and PEG was characterized in more detail to measure the rate of gelation around the critical pH (sect. 4.5.1) and the diffusivity of citric acid (sect. 4.5.2) in the gel to determine the kinetics of solidification of printed features in the power bed. Finally, the shear strength of the gel was measured in a simple apparatus.

4.1 Technological Requirements for the Stability of Colloidal Dispersions

The textbooks on colloidal chemistry typically discuss the critical coagulation concentration in the context of colloid stability, in particular with the Schultze-Hardy rule for electrolytes [Hunter, 94-97], [Hiemenz, 431]. From a technological standpoint, the state of dispersion of a colloid profoundly affects its properties. In paper manufacturing, wood pulp must initially be well dispersed to form a dense slurry and flocculated prior to the collection of the pulp into sheets. In slip casting, a deflocculant is added to the clay slip to permit a greater amount of solid to be suspended in the dispersion [Kingery,Bowen, & Uhlmann, p. 386.] Paint pigments settle to form a dense cake at the bottom of the can which is hard to stir up into suspension. The pigment is usually flocculated, settles into a weak, fluffy cake, and is more easily stirred into suspension.[Jefferies, 399]

Iler goes on at great length [Iler, ch. 5] on the properties and processing of silica gel. There exists a large body of research on the coagulation and adsorption behavior of

silica, and it is not the purpose of this work to expand the scientific knowledge of this phenomenon.

The requirements of Three Dimensional Printing are that the material dispersed in the liquid component be stable with respect to the fluid delivery system and immobilize in the powder after printing. The immobilization can be provided by drying, but it is convenient to coagulate the sol with a chemical additive to the powder. The uniformity of this can be controlled more easily than airflow and temperature over the powder bed. With chemical additives, the timing and bond strength can be adjusted within certain limits.

The fluid handling system in a 3-D Printer consists of a reservoir, tubing, various fittings and valves, a printhead, and sometimes (but not always) a pump. [Blackley 61-65] has quite a good discussion of pumping technology for latex, which is directly applicable to colloidal silica. All pumping mechanisms that rely on sliding members are to be avoided. This excludes all piston, vane and gear pumps. The sliding action tends to trap particles in the shear zone, causing the material to flocculate. Acceptable designs include centrifugal pumps, screw pumps, and diaphragm pumps. Apparently, the shearing that occurs in the check valves of the diaphragm pump does not cause the same difficulty as the shearing action of the teeth of a gear pump. Blackley does not mention peristaltic pumps, but these are also acceptable for handling colloids, since the pumping is done by pinching a stationary tube. Peristaltic pumps and diaphragm pumps are most commonly used in 3-D printers: Positive-displacement pumps are more convenient at the low flow rates needed by the printhead.

Metals used in construction pose a potential threat from corrosion. In general, nickel and stainless steel are the most widely used in printhead manufacture. These materials are most stable at a pH in the range of 9.5 to 10.5, and that is fortuitously the region of greatest stability of colloidal silica. Precious metals that do not oxidize (e.g. gold and platinum) are of course acceptable, as are materials such as titanium and niobium that form a dense passive coating. To find out whether other materials are compatible it is necessary to consult a Pourbaix diagram. Materials that are to be avoided: carbon steel, aluminum, brass, copper, and zinc used by themselves, have corrosion products that cause the silica to coagulate. If metals are combined, there is the added problem that galvanic couples will cause electric current to flow in the sol. The particles, being negatively charged, will be attracted to the anode of the couple and form a solid deposit.

In continuous jet printheads, the droplet charging circuit causes a current to flow between the printhead and the droplet stream. The current is on the order of 3×10^{-8} amperes which in an orifice plate might distributed in a ring approximately 10 μm around the circumference of the orifice. This has an area of about 1.5×10^{-5} cm^2. This current density of 2×10^{-3} A/cm^2 is fairly low, but could cause some etching if the plate were not made cathodic. The easiest way to visualize the polarization is to imagine that one wishes to push electrons from the jet into the plate. Accordingly, the charging cell must be negative, and the droplets will have a net positive charge. The to deflect the droplets, it is necessary to include a high voltage cell to establish the deflection field. It must be assumed that the cell will occasionally short-circuit through an electrolyte i.e. optimistically, during cleaning; pessimistically, during flooding. The more positive electrode (the one away from which the positive droplets are deflected) will be subject to much more corrosion than any other component, so it should be thick enough to accommodate this. This is covered in greater detail in Appendix D.

Most plastics that are compatible with alkaline chemicals seem to be acceptable for handling colloidal silica. Polypropylene, polyethylene, Teflon, Delrin, Viton, Nylon, PMMA, PVC,EPDM rubber, butyl rubber, and Silicone have all been used for some time with no observed problems. Some types of epoxy, in prolonged contact with colloidal silica, seems to exude an oily organic residue.

The process history of binder in use runs roughly as follows. After mixing, the binder should be stable for at least a few months on the shelf or in the reservoir. Binder is usually driven from the reservoir to the printer by gas pressure. Helium is preferred, because of its low solubility in water. Compressed air can be used if the liquid is isolated from the gas by an impermeable bladder. After passing through a number of fittings and a length of tubing, the fluid passes through some filters. A pore size of 5 μm is necessary to catch dust, sediment, and algae that would clog the printhead. The necessity to filter to a pore size fine than that has not adequately been demonstrated. After passing through the primary filters, the fluid passes a number of other fittings, most notably, a "switching" valve that is used to change the fluid supply to the printhead from binder to a rinsing solution. The dynamics of mixing of fluids of different densities downstream of this valve have been discussed elsewhere (sect. 2.2.3) . After passing through a flexible length of tubing that carries the binder to the printhead, the fluid passes through a "last-chance" filter with a small displacement and a roughly 5 μm pore size to catch "boulders" and travels directly to the printhead.

Binder that passes out though the nozzles of the printhead mostly lands in the collection gutter on the printhead and must be carried off by a secondary fluid pumping system. With multijet printheads, it is essential to recycle the binder. Thus, it is necessary to collect the binder without permitting it to dry or become too diluted with rinse solution, repressurize it, and return it to the reservoir. This is the stage at which a mechanical pump must be used.

To define the binder stability in terms of the operations just described, the binder must be stable on prolonged standing, under moderate shear in tubing and filtration, miscible with the rinse solution, able to survive the brief but enormous deformation that occurs in the vicinity of the nozzle (See derivation, Appendix D) the drying effect of the impact on the catcher surface, and the action of the pumping mechanism. One additional requirement is very important in a research environment: the binder must dry slowly and be easy to clean up. This last requirement drove the binder design more than anything else, because in the early period of the project, most of the problems with printhead reliability were due to difficulties with keeping the plumbing clean and free of particles. With a more mature technology, the slow drying rate reduces catcher buildup and the humectants also seem to inhibit distortion of the printed part in the powder bed.

The experiments to test the binder properties were done to converge on a convenient, robust, and nontoxic formula that would guarantee long-term operation of 3-D Printers with a minimum of wasted effort. The acquisition of scientific knowledge was not a priority in this process, so many of the experiments were highly qualitative. The results presented in this section are given approximately in chronological order, and occupied most of the academic year 1992-93. The climax of this program was the introduction of a binder, Formula "B", in March, 1993. As of this writing, this formula has been used with little modification for 21 months. Problems that have been encountered with this formula have been primarily resulting from a tendency to foam, and a slight tendency to form satellite droplets during jet breakup.

4.2 Experimental Program

4.2.1 Humectant study

To retard drying of binder ethylene glycol, later switched to propylene glycol, was used as a humectant. For experimental work on ink-jet inks, see [Gendler & Sporer]. In this paper, evaporation rates of ethylene glycol solutions were measured, and the pressure required to form a jet was measured as a function of standing time. Simple experiments were done to find the proper amount to add: Colloidal silica with various amounts of glycol were placed in syringes with nozzles attached, jetted, and allowed to stand for increasing times until the jet could not be reformed. The volume fraction of colloidal silica used is about half the maximum solids loading for the particle size used (100 nm) so the sol can actually dry down a fairly long way before it coagulates. The small body of liquid that can sit at a quiescent nozzle can dry pretty quickly, so a small amount of humectant can provide a dual purpose: To retard the drying of the fluid at the nozzle, and to create an osmotic pressure that will cause water to diffuse from the fluid behind the orifice to the exposed surface.

4.2.2 Coagulation Experiments

To ensure that silica is immobilized in the powder bed after printing, the binder is coagulated in the powder. These experiments were done to characterize coagulation mechanisms and determine their limits. Ultimately, a reliable mechanism was found that was somewhat reversible, facilitating cleaning of printer components. The mechanism is also robust, meaning that it can tolerate substantial deviations in composition, and clues the operator to critical problems with a pH indicator that changes color when the binder is out of the region of greatest stability.

These experiments were carried out in test tubes. Initially, reagents were added to colloidal silica and the onset of gelation was determined by tipping the tube. A more reliable technique, based on light scattering, was used extensively for most of this series.

4.2.3 Accelerated Shelf-Life Testing

Samples of binder with different bases were held at elevated temperature for a period of time and the evolution of the pH was recorded.

4.2.4 Gel Growth Rate

After measuring the time for solidification in homogeneous mixtures, a cell was constructed to measure the rate of growth of binder gel in contact with coagulant solutions. The purpose of these measurements was to determine the rate at which the binder is immobilized in the powder bed. This determines the time that is available for fluid migration in the pore space between powder grains.

4.2.5 Gel Strength

The shear strength of the binder gel was measured in a simple jig. This was to be a precursor to a more detailed study of green strength and a treatment of part distortion.

4.3 Humectant Study

4.3.1 Experimental Procedure

An important performance issue for a binder is its drying rate. In the event of a loss of pressure in the fluid lines leading to the printhead, a robust formula should be able to form a jet after the printhead has been left standing for the time necessary to replace some tube fitting or filter on the system. When the binder collects in the catcher, it is important that the binder not dry to form a crust.

The following binder formulas were mixed to give 176.8 ml of liquid containing 15 vol.% silica with various fractions of ethylene glycol as a humectant:

Vol.% glycol in liquid phase	Nyacol 2050 ml	ethylene glycol ml	dist. water ml
50	100	88.4	19.7
25	100	44.2	63.8
10	100	17.7	90.3
5	100	8.8	99.2
2.5	100	4.4	105.6

Table 4.1 Formulas for colloidal silica mixtures containing a humectant.

Nozzles were constructed using electroformed nickel orifice plates with 50 μm orifices obtained from Veco. The plates were disc-shaped and had a thickness of 25 μm and a diameter of 2.54 mm. They were attached to 15-Ga. blunt stainless syringe needles with epoxy. The binder samples were dispensed from 3-cc disposable syringes to which the needles were attached. After a jet was formed initially by pressing on the syringe plunger, the jet was stopped, the nozzle wiped off to remove excess liquid, and placed horizontally on a shelf. After a planned period had elapsed, another attempt was made to form the jet. If successful, the nozzle was wiped and allowed to stand for a longer time. The relative humidity was approximately 40% through the test, and the ambient temperature was 75°F.

4.3.2 Results

The results for the experiments are shown below. Error bars have been drawn between the longest time a nozzle stood without clogging to the time it stood when it clogged. The real time to clog is assumed to have fallen somewhere between the limits. For compositions with less than 10% glycol, the time to clog varied between two and sixteen minutes. For 10% glycol, the time to clog varied from 30 min to one hour. At 25% glycol, the nozzles could stand for several days before clogging. The nozzle with 50% glycol in the liquid phase was unclogged after standing 19 days.

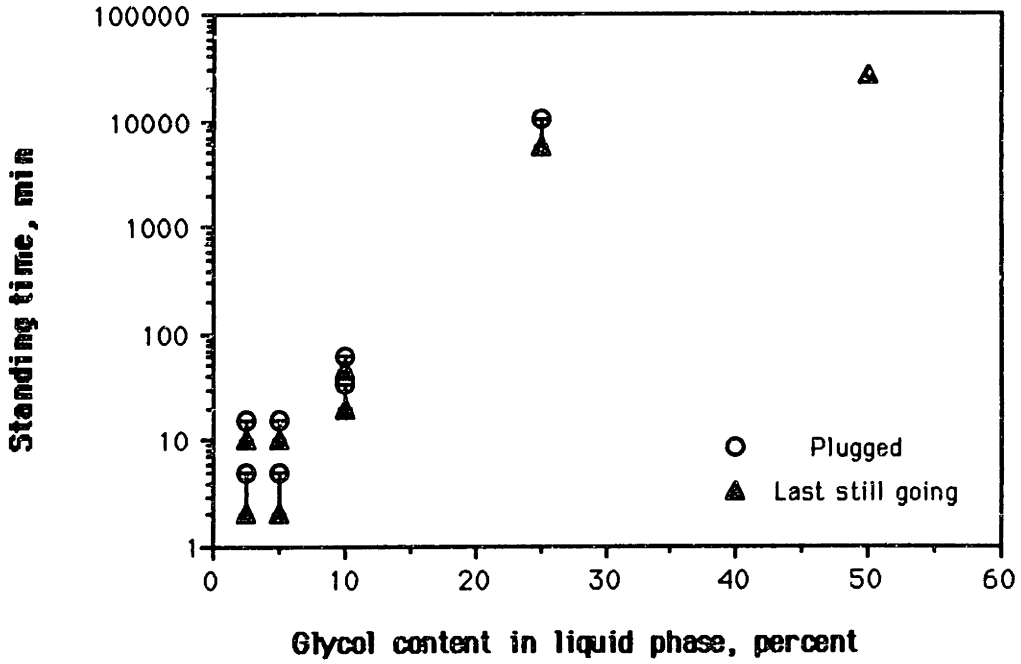

Figure 4.1 Time to clog vs. humectant content in 15 vol.% colloidal silica. Humectant content expressed as volume percentage with respect to the liquid phase of the dispersion.

For the purposes of binder design, the value of 10% glycol was taken to be a minimum desirable humectant content (in the liquid phase) for a robust binder. The standing time of 30-60 min was judged to be sufficient for printhead service. If the printhead was required to stand longer, it would need to be flushed or wiped off to restart.

After this formula began to run for long periods on 3-D Printing machines, it was found that this material had a slight tendency to build up on the catcher. Since the glycol content was actually the minimum necessary to pass the (somewhat arbitrary) test performed above, it seemed appropriate to increase the fraction of glycol in the formula. This was attempted once, but this caused a larger problem at that time with satellite droplets, so it was decided to address the buildup by better electronic synchronization of the computer control with the jet breakup.

To calculate the weight percentage of glycol in the binder, the 10% by volume in the liquid phase, which itself is 87.5% of the total volume of the sol. Accordingly, the volume percentage must be 8.75% of the volume sol. The sol has a density of 1.2 and glycol has a density of 1.1, so the weight percentage of the glycol in the sol is
(1.1 x 8.75%)/1.2 = 8.0%.

4.4 Coagulation Studies

4.4.1 Experimental Methods

Historically, colloidal silica has been been coagulated in the powder bed by changing its pH with citric acid. This system was chosen very early in the program, before a detailed knowledge of colloidal silica had been obtained on the project. The overriding concerns at the time were that the powder additives be nontoxic and easily mixed in the powder. The basic system that was developed consisted of a mixture of colloidal silica and a base which, on mixing with the acid in the powder bed, turned to a salt and initiated coagulation.

The basic procedure for measuring a critical coagulation concentration is to take a set of test tubes filled with a colloid, add the coagulant in question in different concentrations, and find the lowest concentration that initiates coagulation. [Hiemenz, 431] suggests that coagulation can be conveniently detected by waiting a fixed period of time

after the addition and turning over the test tubes to see if the material has solidified. While this method is marginally reliable, a more sensitive method was developed based on light scattering.

A photometer was built which sent a red laser beam from a diode laser through a 1-cm square sample cuvette and onto a photocell. The general layout is illustrated below.

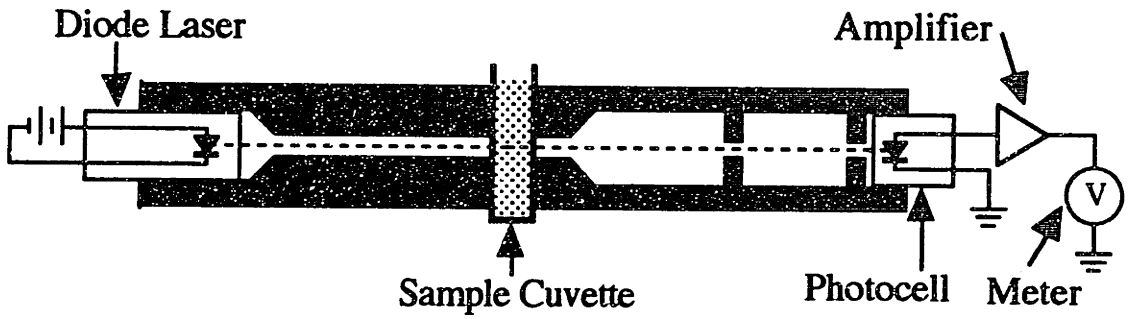

. Figure 4.2 Photometer for qualitative determination of coagulation.

Cuvettes were obtained with a sample volume of 4 ml. In a typical experiment, a series of cuvettes were filled with 2 ml of colloidal silica and 2 ml of coagulating solution. The volume fraction of the colloidal silica was reduced by half, and the concentration of the coagulant was similarly reduced by half. Thus, when colloidal silica with a volume fraction of silica of 17.5% was found to coagulate with a .08 mol/l solution of citric acid, for example, it was really an 8.75 vol.% colloid coagulated by an 0.04 mol/l solution. This complication makes it somewhat inconvenient to express the coagulation threshold in terms of concentration.

There are two ways of dealing with coagulation concentrations. Depending on the mechanism, it makes more sense either to express the coagulation concentration with respect to the liquid medium or with respect to the suspended solids. For example, if a sol is coagulated by addition of a salt which causes the double layers of the particles to collapse, the concentration of salt in the bulk solution is the relevant quantity. On the other hand, if coagulation is caused by adsorption of a chemical species on particle surfaces, clearly the concentration with respect to the particles is relevant. The complication arises because the addition of a coagulant solution to a sample of colloid causes both the coagulant and the particles to be diluted. Since the binder is not diluted when it mixes with coagulant in the powder bed, it is important to account for the dilution in the experiment in the best

way possible. When the coagulation was triggered by a change in pH, the pH was measured for each sample, and the turbidity plotted as a function of pH.

For the turbidity tests, colloidal silica (Nyacol 9950) with a 100 nm particle size and a volume fraction of 0.175 was used consistently. A control sample was prepared for each test in which the colloid was diluted by half with water. The turbidity of this sample was used as a reference and the turbidities of the test samples were normalized with respect to his sample. This was to make the measurements insensitive to changes in laser intensity and amplifier gain. It was found that the uncoagulated colloid transmitted only about 1% of the laser light, but the photocell was sensitive enough to quantitatively measure transmission 10-100 times less in coagulated samples. The method was insensitive to whether or not the liquid had turned to a solid, but considering the small pore size of the powder bed, flocs on the order of a few microns in size would be trapped as effectively as if the material was fully gelled.

4.4.2 Critical Coagulation Measurements for Silica with TMAH

Before the turbidity meter was developed, measurements were made on mixtures of Nyacol 9950 and tetramethylammonium hydroxide. The base was chosen early in the project because it is a strong base, it burns out of the gel on firing, and it is mentioned in Iler. In particular, on page 359, he discusses a preparation that can be dried and redispersed. As an approach to dealing with catcher buildup, having a binder that would redisperse itself would allow subsequent applications of binder to remove deposits left behind from before. Reagent grade TMAH was obtained as a 25 wt.% solution from Johnson Matthely. The standard composition of binder at that time was Nyacol 9950 diluted to 16vol.% silica, and the mixture contained 10% by weight of the TMAH solution. This composition was named "Binder A" by Adam Cohen of Soligen. The molarity of TMAH was accordingly 0.39 mol/l in the liquid phase.

a. Method

Solutions containing fractions of TMAH solution varying from 10% down to nothing were tested with a variety of coagulants. 2-ml samples of the sol were mixed with 2-ml coagulant solutions, and the gelation of the mixture was determined by shaking the tube. Solutions with gradually increasing coagulant concentration were used in a series

until a threshold was observed, below which the coagulation did not occur over a period of several minutes. The results are given below: the concentrations given are the concentrations in the test solutions before mixing with the colloid, of the lowest composition causing coagulation.

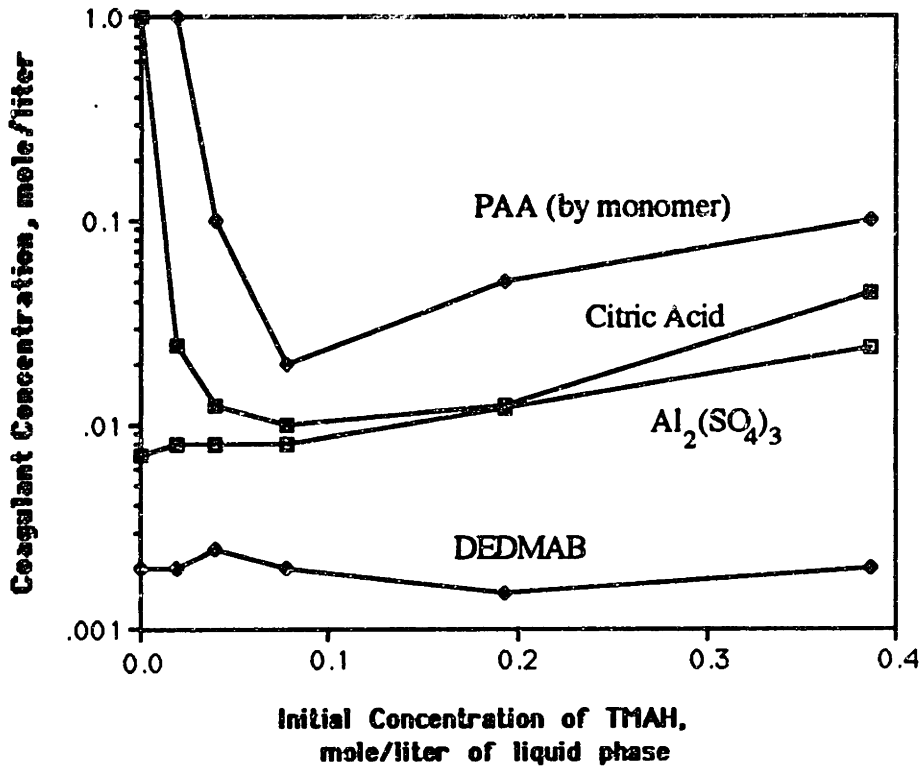

Figure 4.3 Coagulation concentrations for a variety of coagulants in Nyacol 9950, 17 vol% silica containing various concentrations of tetramethylammonium hydroxide. PAA = polyacrylic acid (MW 2000); DEDMAB = dodecylethyldimethylammonium bromide.

b. Discussion

The acid additives were the most variable in their ability to coagulate the mixtures. At high base concentration, the positive slope of the two curves indicates that the acid was neutralizing the base, and the quantity of acid necessary depended on the quantity of base and the number of acid groups on the acid. Citric acid has three acid groups per molecule while PAA has one per monomer, so its molar efficiency is three times higher in this regime. At low base concentrations, the mixture became more resistant to acid addition. When no base was present at all, the sol would not coagulate at all up to a concentration of 1 mol/l of citric acid. This increased stability at with little base reflects the increase in stability of silica at low pH (see figure 3.8)

Aluminum sulfate was found to coagulate the sol more uniformly across the concentration of base, as did the cationic surfactant dodecylethyldimethylammonium bromide. These chemicals were considered for a time as powder additives. Aluminum salts were rejected because they would not burn out and might hamper powder removal. The cationic soap DEDMAB appeared particularly attractive because it would be universally effective as a coagulant for negatively charged colloids and help lubricate the powder to give a higher packing density. In the end, it was decided to stick with citric acid because it would be easier to monitor the acid content by pH measurements and it was fairly well established in practice at that time. (Soligen, the licensee of the ceramic shell process was then sourcing large quantities of powder and blending it all with citric acid)

The citric acid composition was traditionally between 0.2% and 0.5% by weight in aluminum oxide powder. The reagent grade citric acid was hydrated, with a molecular weight of 210 g/mol. Alumina powder used typically packs to a density of about 1600 g/l, with a pore volume fraction of 0.6. If a bed containing 0.5% citric is completely saturated with binder, 3.2 grams of citric acid comes in contact with 600 ml of binder. The molarity of the acid is about 0.063 mol/l of binder, or 0.077 mol/l of liquid. It was decided that this should be well past the critical concentration for coagulation to ensure that the system would tolerate a fair amount of segregation of the citric acid in the powder. the TMAH concentration in the final formula (Binder "A") was 0.39 mol/l, so the citric acid concentration in the powder bed was roughly twice the minimum amount needed to neutralize the base.

4.4.3 Base Selection

a. Formulation

Since it was chosen to coagulate silica sol by lowering its pH, it was necessary to select an appropriate base that gave the binder the best properties. A group of four "fugitive" bases were chosen to test: TMAH, ammonia, morpholine, and triethanolamine (TEA). The first series of experiments were to measure the pH-dependence of the coagulation as a function of base concentration. TMAH was historically used, and the other three are discussed by Blackley. Ammonia [Blackley, 182-3] is the primary stabilizer for natural rubber, and the others are mentioned [Blackley 137] as solubilizers for proteins.

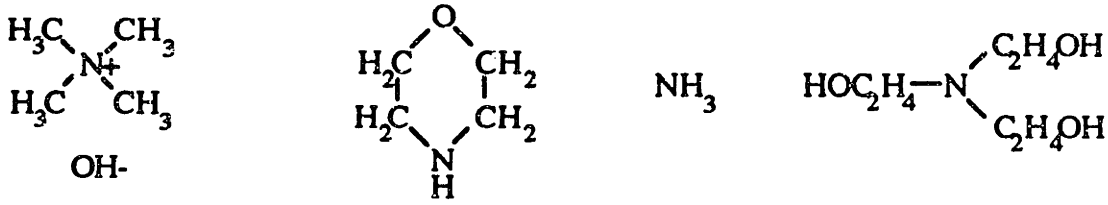

Figure 4.4 Organic bases considered for binder formulation.

TMAH was available as a 25 wt.% solution and ammonia as a 50 wt.% solution. TEA and morpholine were available as pure chemicals. Following the practice to mix binder solutions as weight percentages of base in the sol, five stock solutions were mixed using each base, each containing 0.5%, 1%, 2%, 5% and 10% by weight of the base (or solution) and 17.5% by volume of silica. The molarity of each base was different, but this method made it easier to keep track of the formulas. Additionally, a control containing no base was mixed. The weights of Nyacol 9950, water, and base to make 100 ml of sol with 17.5% solids are given below:

wt.% base in sample	Nyacol 9950 grams	Water grams	Base grams
0.0	77.0	44.0	0.0
0.5	77.0	43.4	0.6
1.0	77.0	42.8	1.2
2.0	77.0	41.6	2.4
5.0	77.0	38.0	6.1
10.0	77.0	31.9	12.1

Table 4.2 Formulas for silica samples used in coagulation experiments.

There is a small error in this method: The densities of the various bases used varied from 1.00 for morpholine to 1.12 for TEA. The 10% TEA sample had a maximum solids loading of 17.7%. This roughly 1% error was considered negligible.

The molecular weights of each base, figuring in the excess water of the aqueous solutions, were as follows: TMAH: 364; ammonia: 70, morpholine: 87; TEA: 149. The molarities of the respective bases in each sample is given below.

wt.% base in sample	TMAH mol/l	ammonia mol/l	morpholine mol/l	TEA mol/l
0.5	0.02	0.10	0.08	0.05
1	0.04	0.21	0.17	0.10
2	0.08	0.42	0.33	0.20
5	0.20	1.04	0.84	0.49
10	0.40	2.08	1.67	0.98

Table 4.3 Molarities of base solutions used in coagulation experiments.

To handle the large number of measurements to be made, the transmission photometer described above was developed and used for all subsequent coagulation studies. Because the turbidity depends on solids loading as well as the state of the dispersion, care was taken to assure the the solids loading of all the samples was the same: initially 17.5 vol.% and diluted to 8.75 vol.% on addition of coagulant.

b. Coagulation Measurements by Light Scattering

For each test, seven 2-ml samples were be placed in a row of cuvettes. There were (7x5=35) samples for each of the four bases, and a group of 7 containing no base. To each tube in a row, 2 ml of solution containing 0.00, 0.02, 0.04, 0.10, 0.20, 0.40, or 1.00 mol/l citric acid was added. The sample with no acid and no base was used as a control, and all of the measured turbidities were normalized with respect to that of this sample. The experiment was set up so that the acid and base would both be diluted by the same amount. In regards to the change in pH, the effect is almost the same as if the dilution did not occur. If, for example, a 1 mol/l solution of HCl is added to a 1 mol/l solution of NaOH, the acid neutralizes the base, and the final concentration of NaCl is 0.5 mol/l. When the effects of ionic strength are considered (as, for example, in examining the coagulating power of tetramethylammonium) the dilution must be figured in.

The pH of each sample was measured with a Cole-Parmer digital pH meter after mixing with the acid and measuring the turbidity. The transmittance data are plotted with respect to sample pH for each base below.

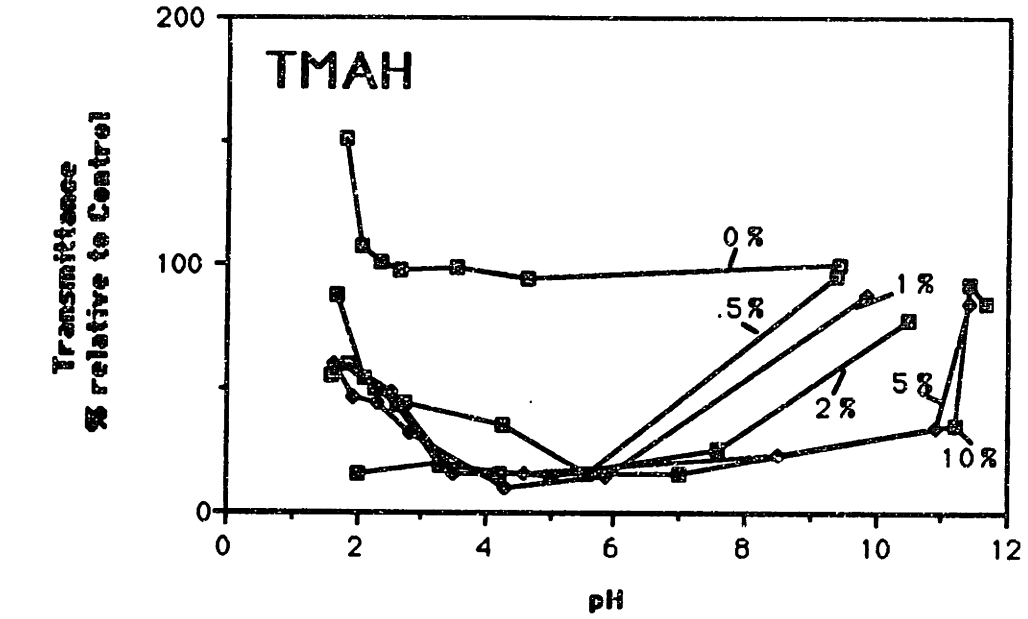

a.

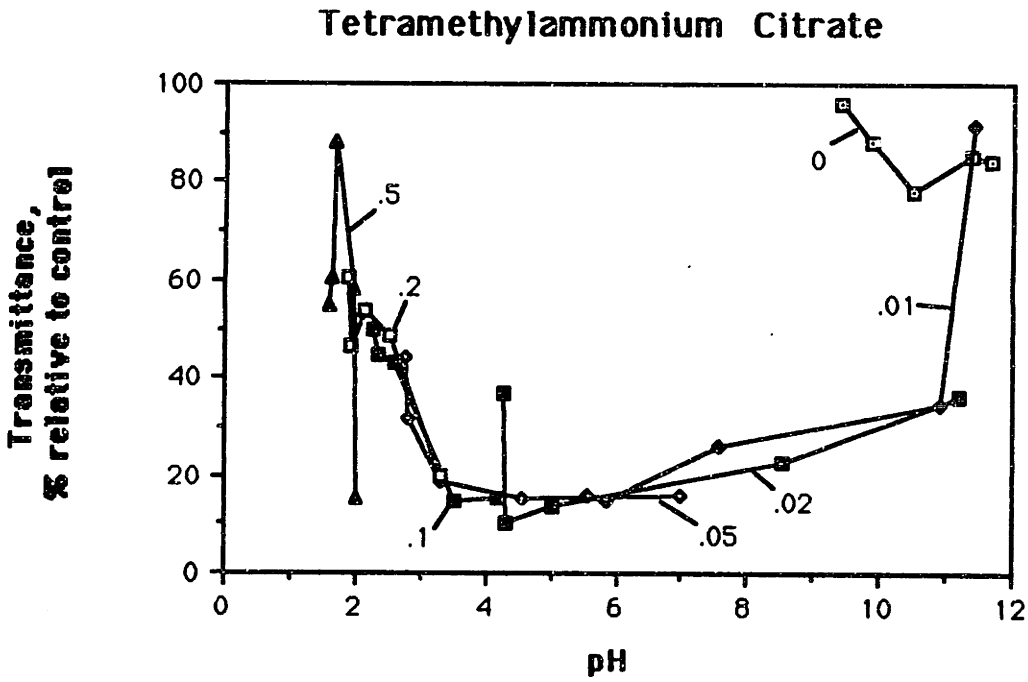

b.

Figure 4.5 Transmittance data for colloidal silica 8.75% silica by volume, with added TMAH. (a.) Lines of constant base content. Percentages given are weight percentages of the 25 wt% stock solution in the 17.5 vol.% binder sample before dilution with citric acid solution. (b.) Lines of constant citric acid concentration. Numbers given are molarities of citric acid after dilution in the sol, and correspond roughly to the concentration of the salt tetramethylammonium citrate.

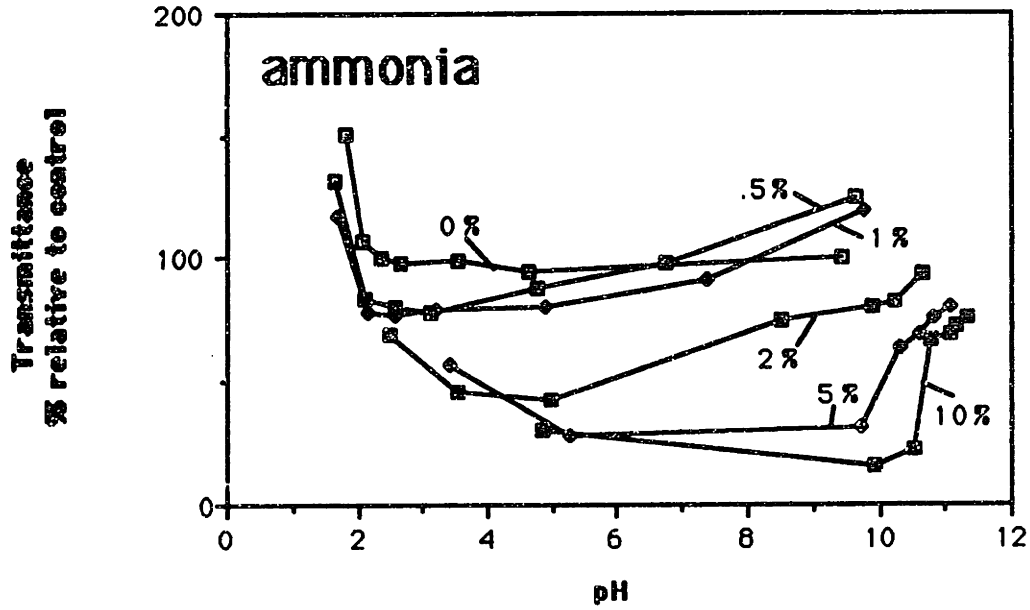

a.

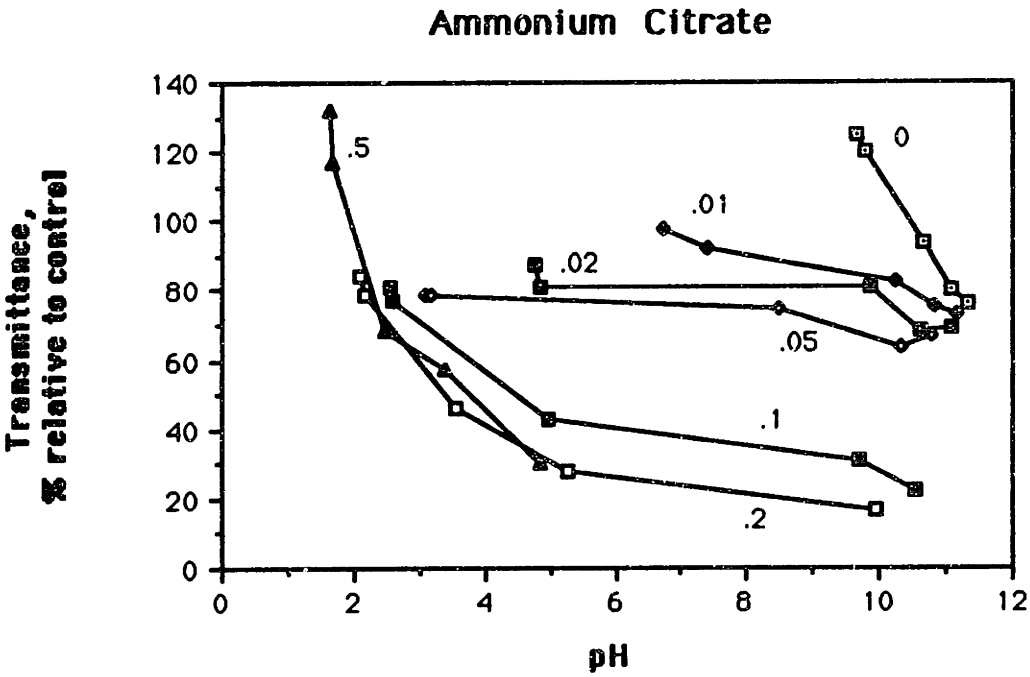

b.

Figure 4.6 Transmittance data for colloidal silica 8.75% silica by volume, with added ammonia. (a.) Lines of constant base content. Percentages given are weight percentages of 50wt% stock solution in the 17.5 vol.% binder sample before dilution with citric acid solution.(b.) Lines of constant citric acid concentration. Numbers given are molarities of citric acid after dilution in the sol, and correspond roughly to the concentration of the salt ammonium citrate.

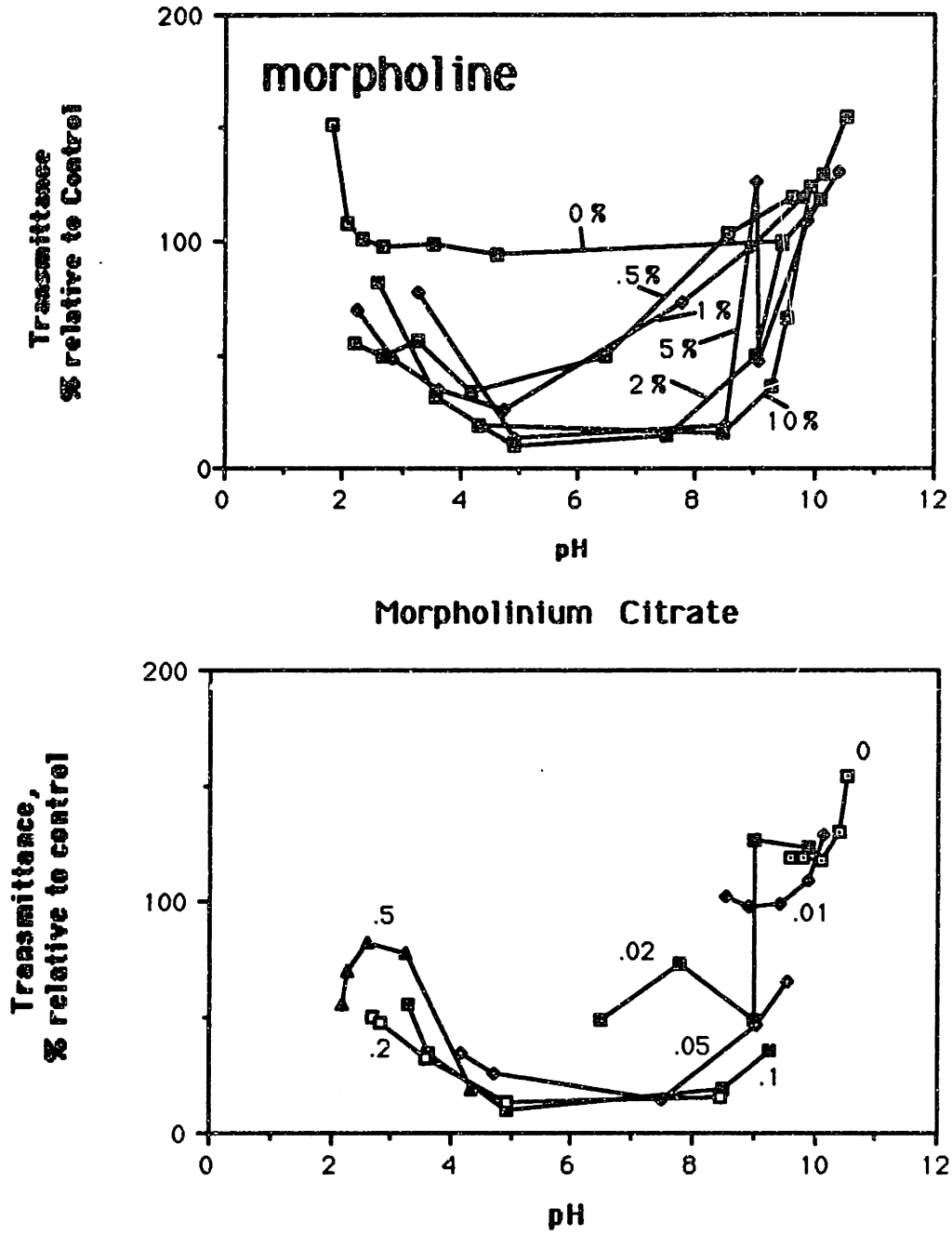

Figure 4.7 Transmittance data for colloidal silica 8.75% silica by volume, with added morpholine. (a.) Lines of constant base content. Percentages given are weight percentages of the reagent in the 17.5 vol.% binder sample before dilution with citric acid solution. (b.) Lines of constant citric acid concentration. Numbers given are molarities of citric acid after dilution in the sol, and correspond roughly to the concentration of the salt morpholinium citrate.

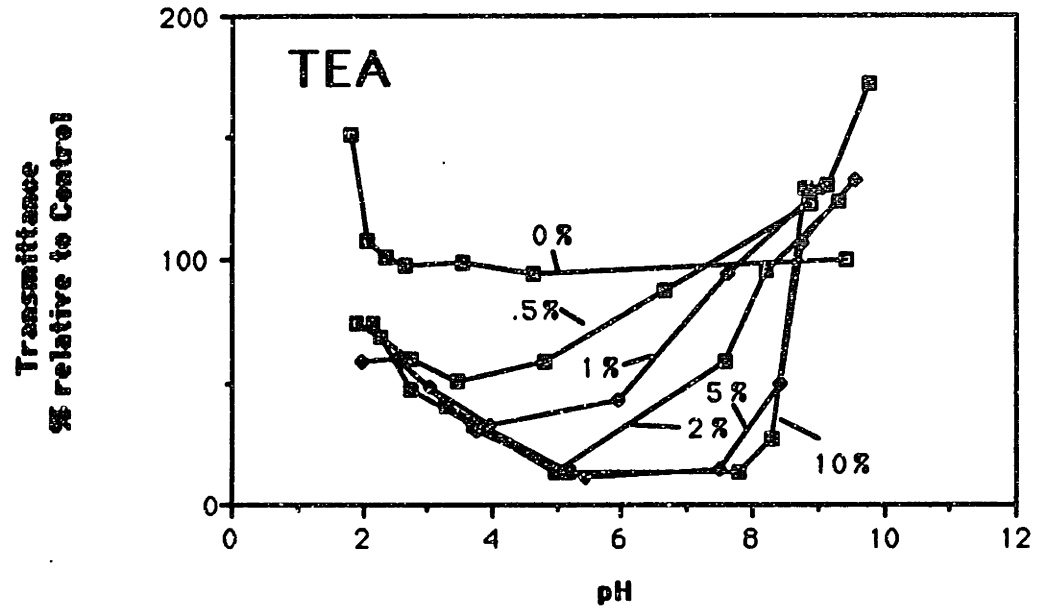

a.

Triethanolammonium Ctirate

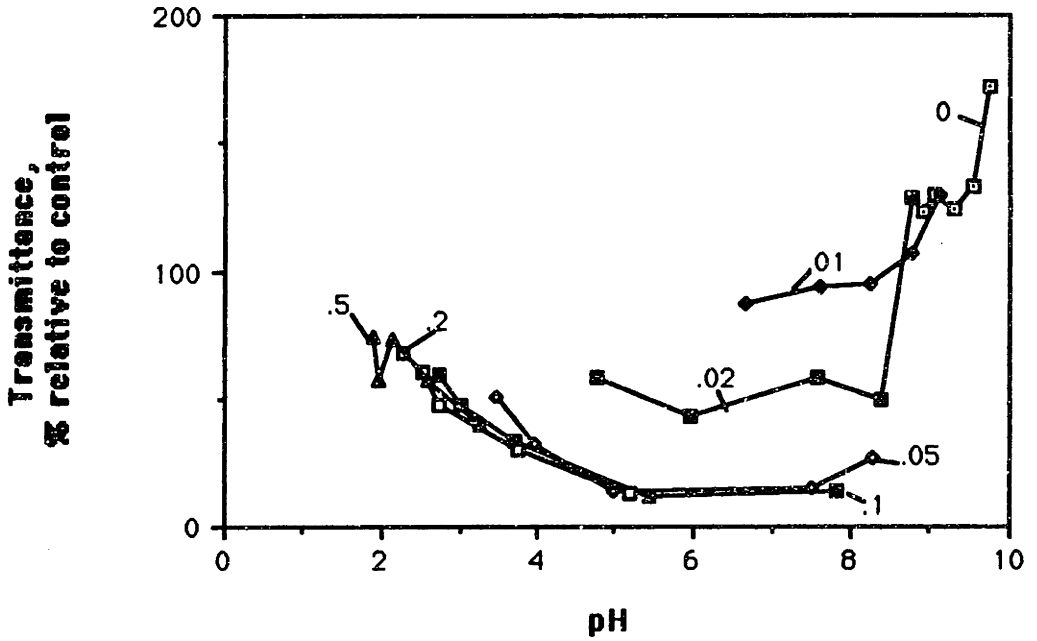

b.

Figure 4.8 Transmittance data for colloidal silica 8.75% silica by volume, with added TEA. (a.) Lines of constant base content. Percentages given are weight percentages of the reagent in the 17.5 vol.% binder sample before dilution with citric acid solution. (b.) Lines of constant citric acid concentration. Numbers given are molarities of citric acid after dilution in the sol, and correspond roughly to the concentration of the salt TEA citrate.

c. Discussion of Light Scattering Results

These results, by themselves, are not sufficient to choose a base to add to colloidal silica. There are, however, some interesting features to these curves. Low transmittance implies that the liquid was flocculated (see sect. 2.2.8). Most samples with intermediate transmittance were still liquid. The samples with no acid added are the most basic. The graphs labelled "a" are lines of constant cation concentration, and the graphs labelled "b" are lines of constant anion concentration.

The curve for the samples with no added base (labelled 0% on all four "a" graphs) shows quite conclusively that citric acid by itself cannot coagulate colloidal silica over the relatively short duration of these experiments (a few minutes). The increase in transmittance at the lower limit of pH is probably due to the concentrated citric acid increasing the index of refraction of the liquid medium, make it closer to that of silica.

The bases added did not "stabilize" the binder at all, rather, they provided a mechanism for the sol to coagulate as the base was neutralized. All compositions were fairly well dispersed before the addition of acid and their tendency to coagulate at a given pH increased with ionic strength. The coagulating effect of the neutralized base can be seen most clearly in the plots labelled "B" at constant salt concentration. The coagulating power of TMAH is clearly evident in these results: the dilution of this base in the stock solution was the highest, but it was capable of coagulating silica even at the least concentration (After dilution, it was 0.01 molar, agreeing with Iler; see sect. 3.3.4) at pH 5.5. After TMAH, both morpholine and TEA seemed to have about the same coagulating power: approximately 0.05 mol/l (after dilution) at pH 5. Ammonia was quite a feeble coagulant, only causing the transmittance to drop to the bottom at 0.2 mol/l after dilution.

The entire family of curves exhibits increasing stability as the pH decreases past 5. This is consistent with the fact that silica loses its surface charge at lower pH, and becomes stabilized by hydration. The presence of salt (as the citrate of the base) clearly has some effect on the stability of the sol at low pH, but this effect diminishes as the isoelectric point (pH 1) is approached. The restabilization at low pH could be a severe problem in 3-D Printing if the powder is segregated, or if the citric acid is distributed in coarse granules. If a region of powder contains a large excess of acid, the binder might not coagulate in a

reasonable amount of time, and pools of liquid, besides being sources of bleeding, could cause the part to distort inhomogeneously.

d. Accelerated Age Testing

The stability of the four bases was also tested with respect to age, using the same samples of binder. Each mixture was baked for 14 hours at 75°C in tightly capped bottles. This treatment was designed to simulate storage at 30°C for about two months. The coagulation experiments in section 4.4.3.b. (immediately above) were performed on the aged samples. The change in pH between the freshly mixed samples and the aged samples is shown below.

TMAH exhibited the largest change in pH, probably due to dissolution of silica from the particles in the sol (see sect. 3.1.4). This agrees with qualitative observations of the slow decay of 10% TMAH binder that was formerly used for printing: over several months, the sol deposited a sediment, and the pH was observed to decay over the same period.

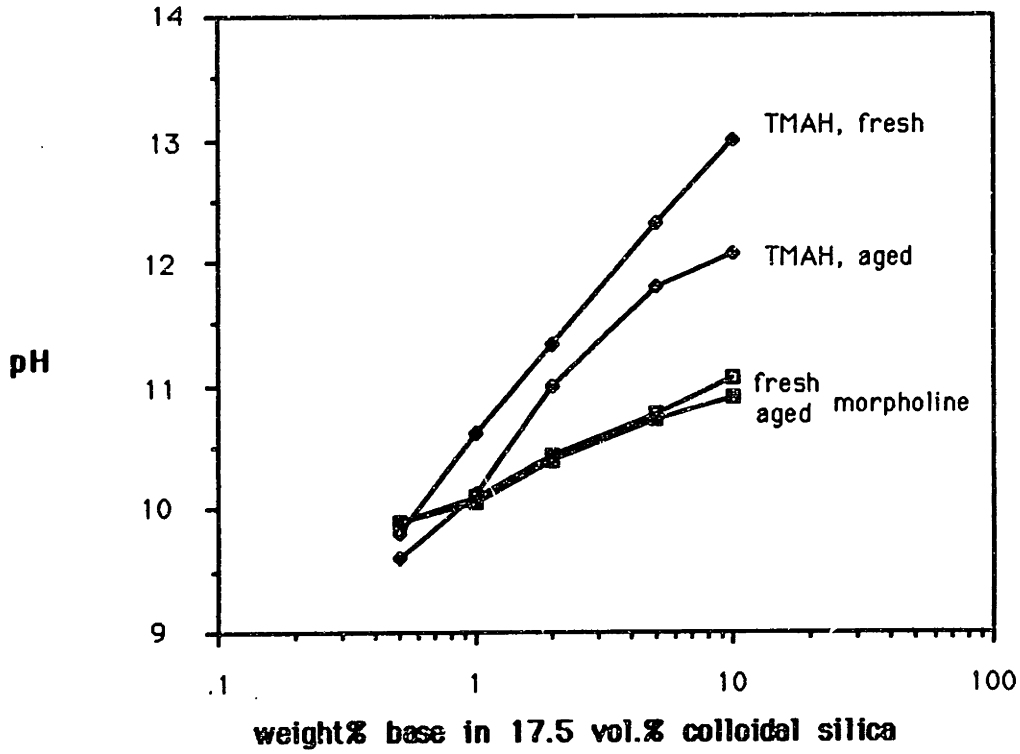

Figure 4.9 pH change for TMAH and morpholine after baking at 75°C 14 hrs.

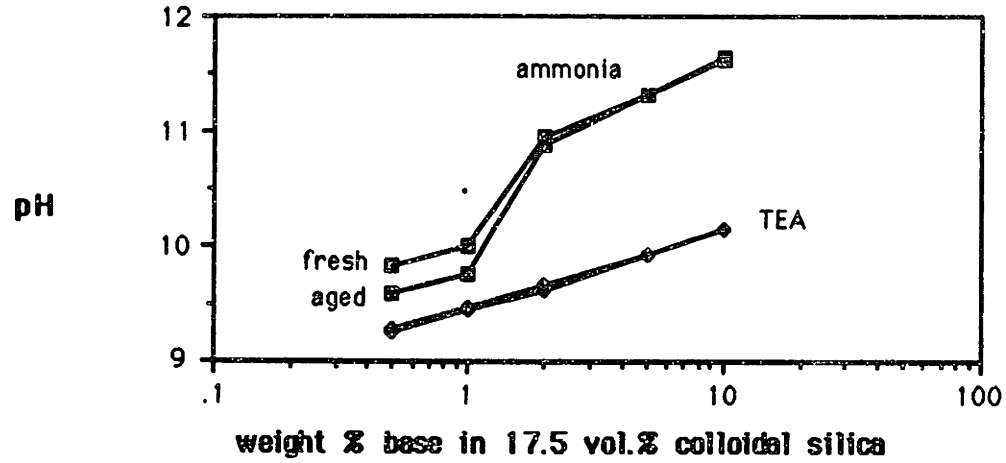

Figure 4.10 pH change for ammonia and TEA after baking at 75°C for 14 hours.

The sols with ammonia also declined in pH for the lowest concentrations. These could have been the result of the ammonia precipitating the solubilized silicate from the solution. [Iler p.137] discusses the coagulation of sodium silicate by ammonia, and since this sol contains about 1% soda,(see sect. 3.1.5) it could also be expected to have about the same quantity of silicate $\left(HSiO_3^-\right)$ present in solution.

e. Conclusion: Selection of Base for Colloidal Silica

The bases morpholine and TEA appeared to be quite stable during the accelerated aging. The two had about the same ability to coagulate silica, and both are liquids at room temperature. When binder dries, it is desirable that the base not evaporate out of the gel. This permits the gel to be redispersed when water is added back. This greatly aids cleaning of printhead components and prevents the formation of a solid crust on dried tube fittings. Morpholine has a boiling point of 130°C, white TEA has a boiling point listed as 278°C. Of the four bases tested, the conclusion was that TEA was the best one to use to raise the pH of binder.

4.4.4 Effects of Glycol and Methanol on Coagulation

The use of ethylene glycol as a humectant had previously been established: It was necessary to find out whether its presence had any significant effect on the stability of colloidal silica with added base. A set of 11 samples, all with 17.5 vol.% silica were mixed, one containing no organic additives, and ten containing 3% total additive,

distributed among ethylene glycol, methanol, and TEA (for example, sample #2 contained 2% MeOH and 1% Gly; #5 had 1% each of MeOH,Gly,and TEA; #10 had 3% TEA.).

These samples were divided into 4-ml cuvettes as before, and citric acid solution were added in the same fashion as the test previously described. The turbidity of the samples is plotted vs. measured pH below.

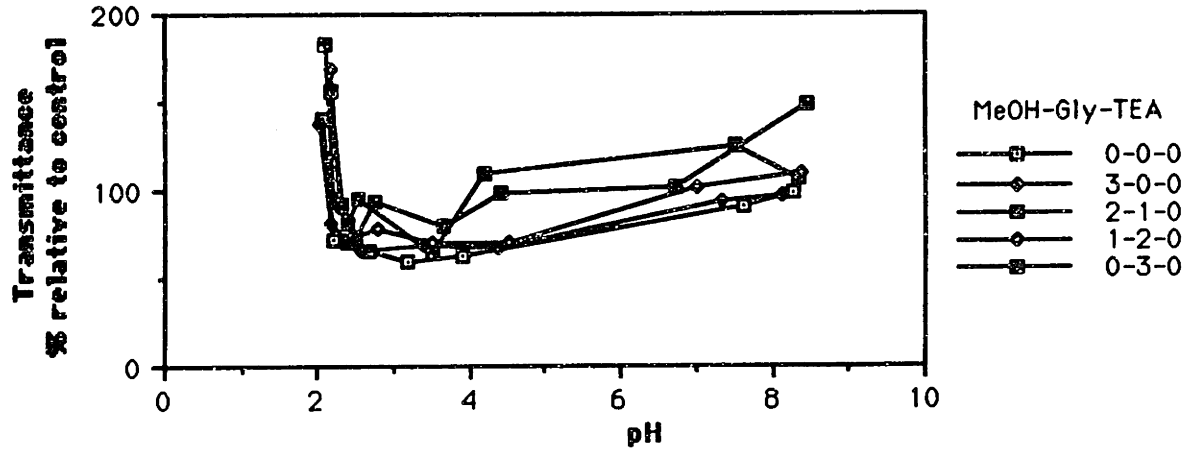

Figure 4.11 Turbidity vs. pH for binder containing methanol and ethylene glycol.(3% total)

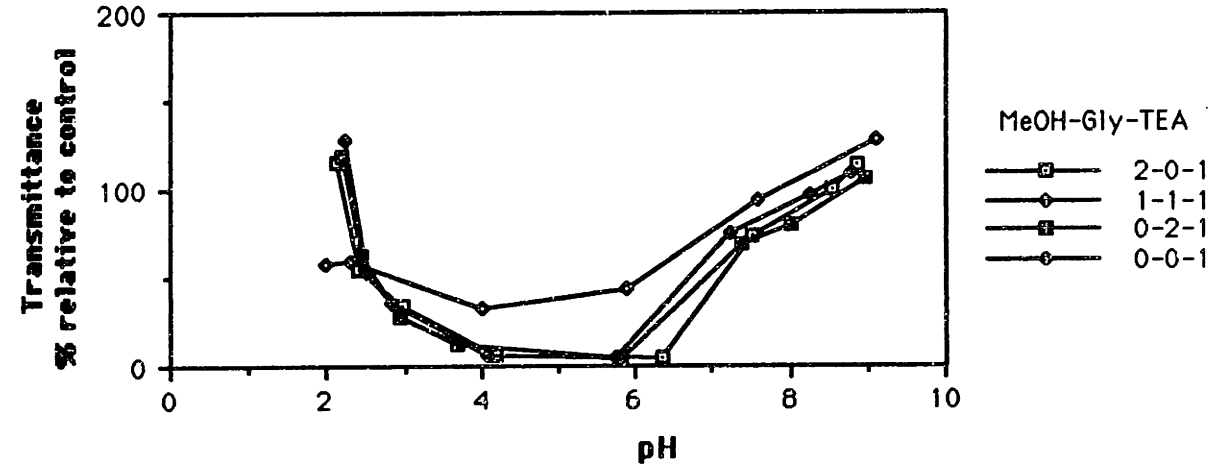

Figure 4.12 Turbidity vs pH for binder containing 1% TEA with glycol and methanol.

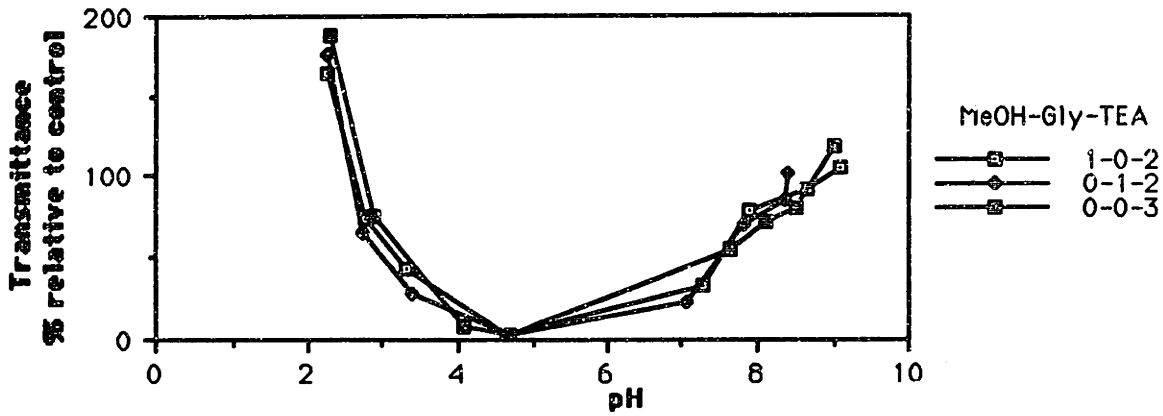

Figure 4.13 Turbidity vs. pH for 2% TEA with 1% MeOH or 1% glycol and 3% TEA.

In figure 4.12, the data for 1% TEA with no organic additives has been translated from figure 4.8, above. It seems possible that there is a slight enhancement of the coagulating power of TEA when the other additives are present, but the effect is subtle. For all practical purposes, it can be concluded that ethylene glycol and methanol have no significant effect on the coagulation of colloidal silica by triethanolamine.

4.4.5 Coagulation by Polyethylene Glycol

During this period, we became aware of the special affinity of polyethylene glycol for colloidal silica(see sect. 3.3.5). The data graphed below was collected in 17.5% colloidal silica with 2% TEA added. While these data compare somewhat favorably with the behavior of 2% TEA without PEG (see, for example, figure 4.12) they do not tell the entire story. Binder with 2% TEA and no PEG remained liquid across the entire range of pH, while the mixtures containing PEG solidified to a thick, buttery gel which could be reliquified if the pH was raised again.

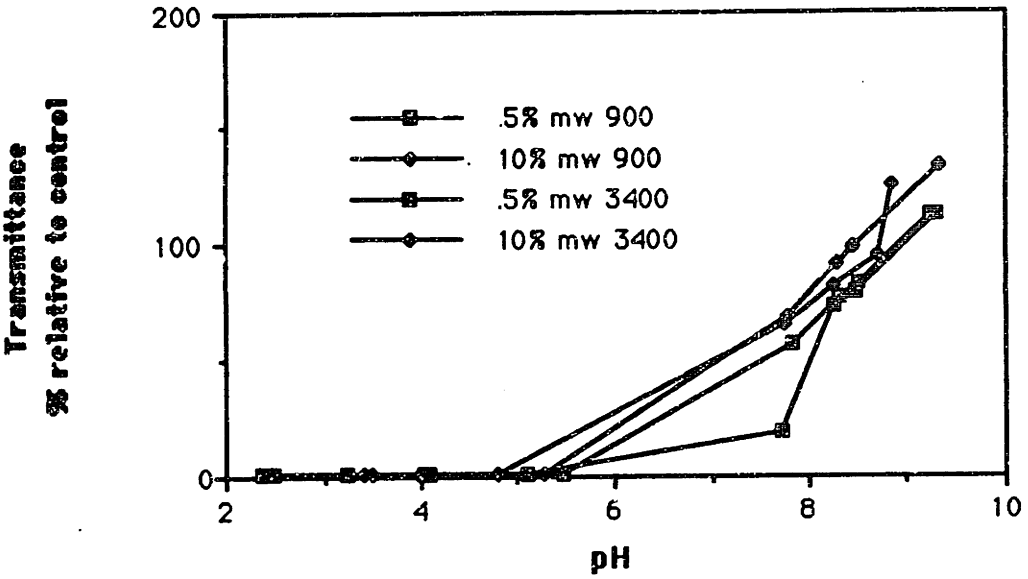

Figure 4.14 Turbidity vs. pH for 17.5 vol.% silica with 2% TEA and added PEG.

The range between pH 6 and pH 8 is the critical range, so the next study took colloidal silica with the standard silica content and 2% TEA and varied the content and molecular weight of the added PEG. A constant amount of citric acid was added: 2 ml of .04 mol/l solution was added to 2 ml of the binder. The pH after the addition was approximately 7.5 in all cases. The turbidities of these samples are plotted with respect to PEG content in figure 4.15, below. Since the PEG is assumed to associate with the silica particles, the effect of dilution can be ignored because the ratio between PEG and SiO_2 remains the same.

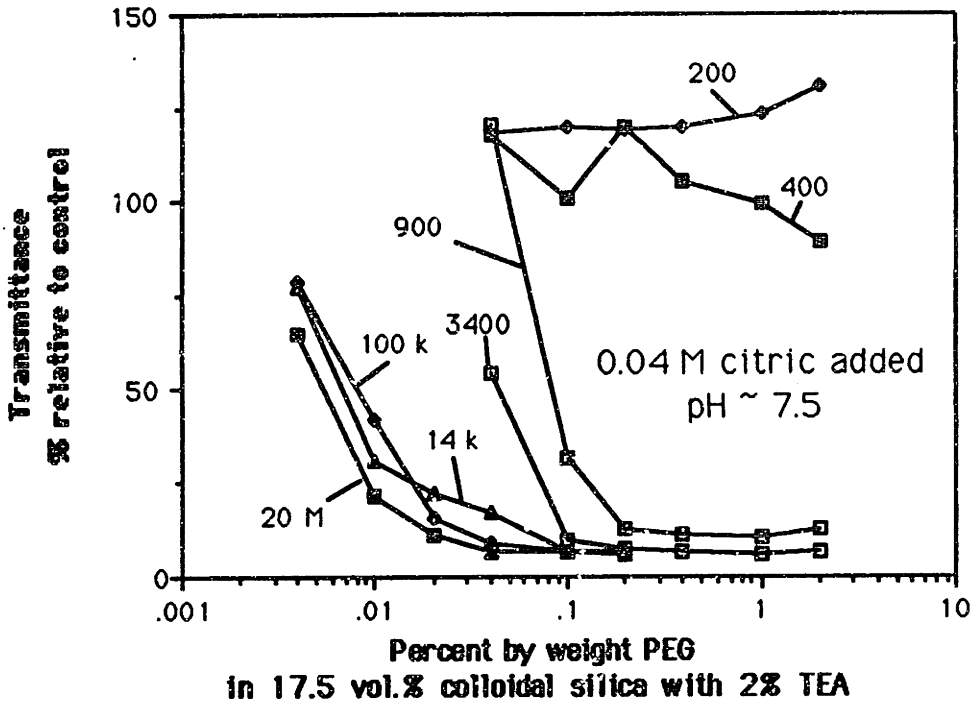

Figure 4.15 Turbidity vs. PEG content for 17.5 vol.% colloidal silica, 2% TEA after addition of a similar volume of 0.40 mol/l citric acid. Numbers associated with each curve is the molecular weight of the polymer.

4.5 Characterization of PEG-Coagulated Binder Formula

4.5.1 Threshold pH and Gelation Rate

Based on this data, a binder formula consisting of Nyacol 9950 with 17.5% by volume of silica, 6 wt.% ethylene glycol, 2 wt.% TEA, and 0.1% PEG (MW 3400) was tested to mea , the time to coagulate in a narrow pH range. The composition of 8% by weight total glycol was calculated at the end of section 4.3.2. TEA acts as a humectant as well asa base, so it was counted in the total. This was the precursor to the formula that was named "Binder B" by Adam Cohen of Soligen. Citric acid solutions with .026, .028, .032, and .036 mol/l were added to samples of this binder in equal volumes. The effect of dilution in these tests can be ignored, because the coagulation mechanism is not directly related to the ionic strength. The time to gel was measured in a manner similar to that described by [Hiemenz p.431.] A set of tubes with identical compositions were mixed at the same time. After successive intervals, one of the tubes would be inverted to see if the liquid had solidified. Several data points for each composition were collected, with the exception of the lowest pH point, where the gelation time of 1 ± 0.5 sec was simply a qualitative estimate. These data are shown in figure 4.16, below.

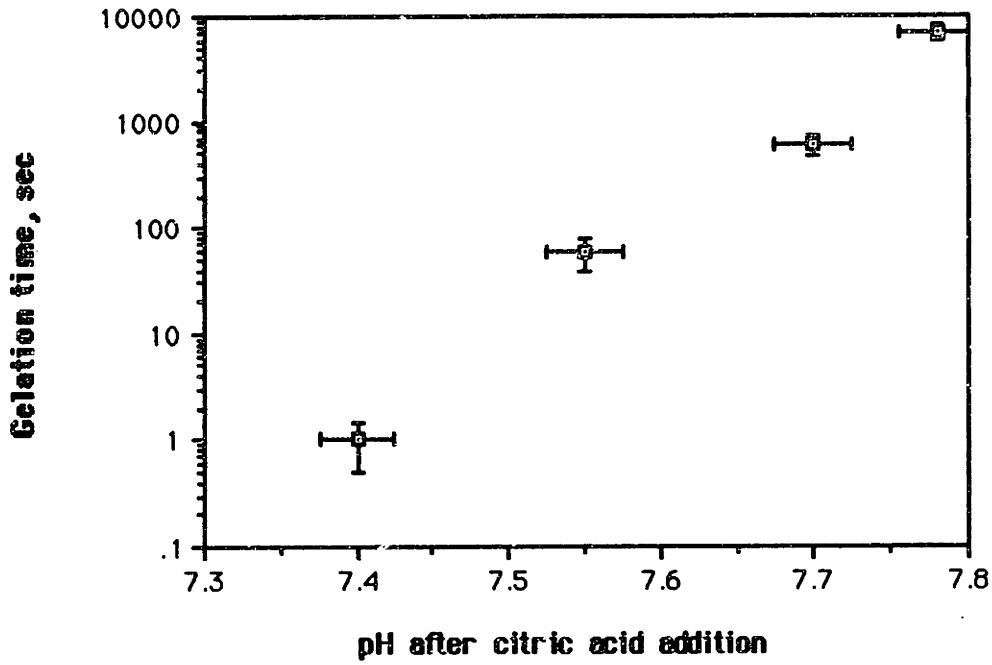

Figure 4.16 Gelation time vs. pH for Binder "proto-B".

This very sharp solidification threshold corresponds in pH pretty closely to the color transition in the indicator dye Thymol Blue. This composition of binder was titrated with citric acid and the colors of .1% added Thymol Blue were noted approximately.

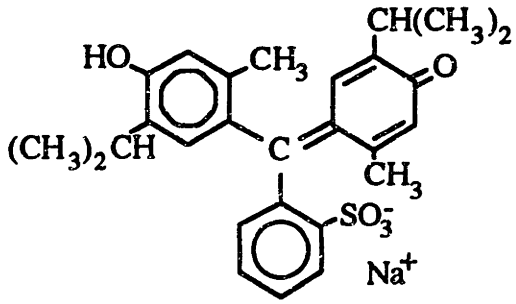

Figure 4.17 Thymol Blue (sodium salt)

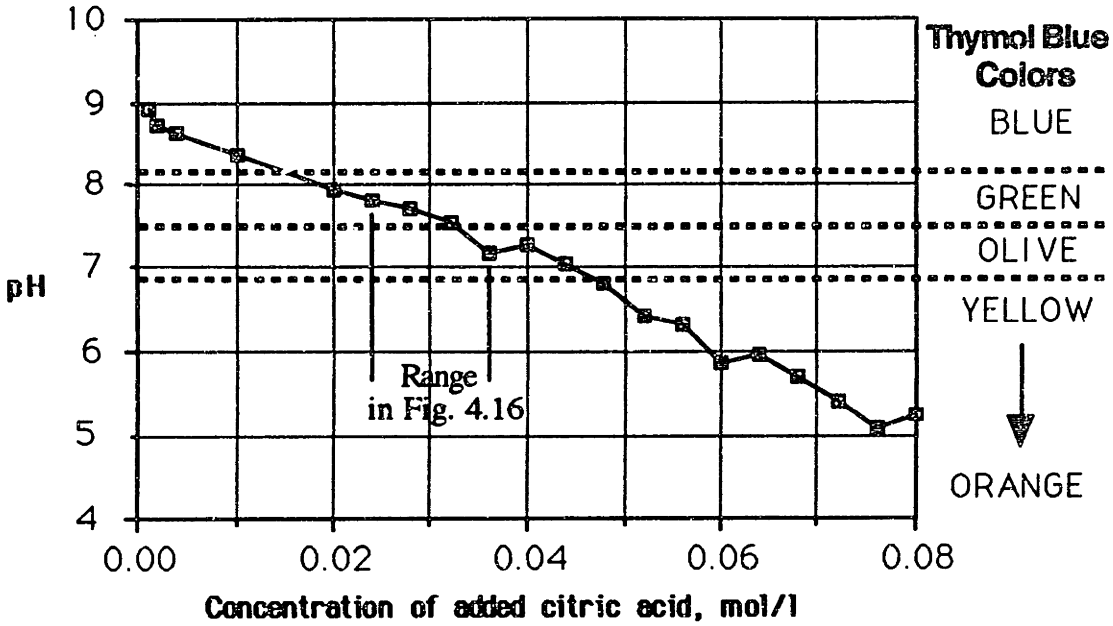

Figure 4.18 Titration curve for Binder "proto-B" with citric acid.

From these data is can be concluded that Binder "B" that is blue is uncoagulated, the state of binder that has been neutralized to a color of green is indeterminate (depending on the age) and binder that has been neutralized to a yellow or orange color must be solid. This is a very important tool for monitoring the state of gelation in printed power in process on the 3-D Printing machine. The critical concentration of citric acid is approximately 0.03 mol/l, depending on the time allowed for gelation. The concentration of citric acid in the powder bed is about three times this level at 0.5% citric by weight of powder, and it can be seen in figure 4.14 that there is no pathological restabilization at low pH.

4.5.2 Gel Growth Rate

a. Method

When binder is printed on powder containing crystals of citric acid, the gelled binder forms first on the surface of the crystals, and citric acid must diffuse through a growing film of gel to reach uncoagulated binder. To measure the rate of gel growth, a thin layer cell was designed. This is illustrated below.

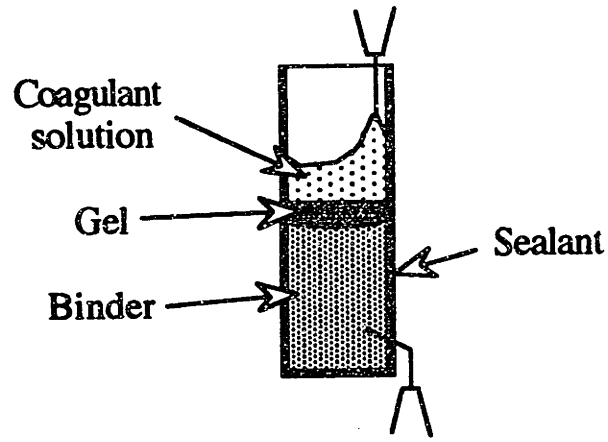

Figure 4.19 Gel Growth cell. Binder introduced first through hypodermic needle from below, then coagulant introduced from above. Film of gel grows at interface.

The cells were constructed from glass microscope slides. Two slides were clamped together with a loop of 40-Ga. "wire-wrap" wire in between. The edge was sealed with latex hot-melt glue. The wire loop was pulled out, leaving a reproducible 0.5 mm gap between the slides. A hypodermic needle was inserted near the bottom to feed in binder, and the coagulant was later introduced from above. The cell was placed, at about a 10° inclination under a stereomicroscope and the growth of the gel was videotaped. By backlighting the cell, it was possible to take advantage of the much higher scattering efficiency of the gel over that of the uncoagulated sol.

b. Results

The growth of gel of two binder formulas, one consisting of 2% TEA and 0.1% PEG (MW 3400) and another consisting of 10% TMAH, both containing 17.5% by volume silica, was measured using a 1-mol/l solution of citric acid as a coagulant. The gel thickness in plotted logarithmically with respect to the time elapsed after the introduction of the coagulant. The magnification of the microscope made the video frame about 3 mm high, and it was possible to resolve gel films as thin as 30 microns. After a little practice, it was possible to introduce the fluid in such a way that a mostly planar interface would be established in about 1/2 second.

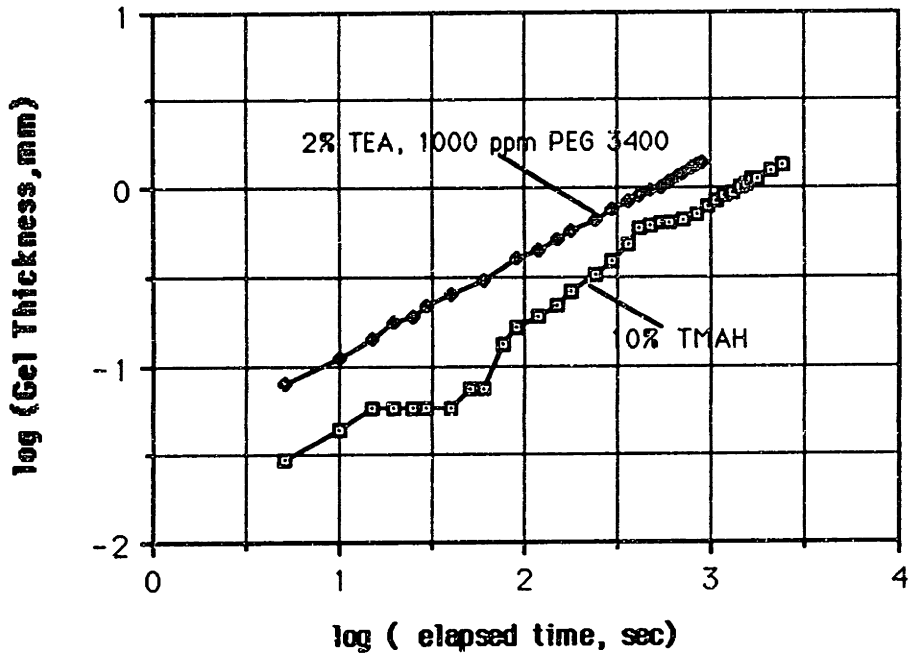

Figure 4.20 Gel thickness vs. elapsed time for two binders against 1 molar citric acid.

The lower rate of gel growth in the TMAH formula is most likely because a higher acid concentration is necessary to initiate coagulation. From the transmittance data, the 10% TMAH concoction required the addition of a .1 molar solution to coagulate. The TEA required only .036 molar citric acid to coagulate in 1 second. The curves are generally linear on the logarithmic plot: indication a constant exponent of approximately 0.55. The TMAH gel cracked during growth, and this caused the surge in growth rate after about 6 minutes. The lag in growth at a thickness of 50 μm cannot be explained.

Polyacrylic acid was, at the time, a candidate coagulant for binder. The results of Alan Lauder (see sect. 8.6.2) suggested that feature size and accuracy could be improved by using this polymeric acid to control bleeding. In section 4.4.2, it was found that polyacrylic acid was about 1/3 as effective, mole for mole, as citric acid in coagulating binder by neutralizing acid. It was found that the gel growth rate was roughly one third as great when a polyacrylic acid was used in the gel growth cell. This is shown in figure 4.21, below. The lag in growth rate for the PAA gel could be due to a lower diffusivity of the polymer in the gel. The rate accelerated after a few minuted because the gel cracked, admitting acid though channels that formed. This shrinkage of the gel could be what caused warpage in parts printed using powder containing PAA instead of citric acid.

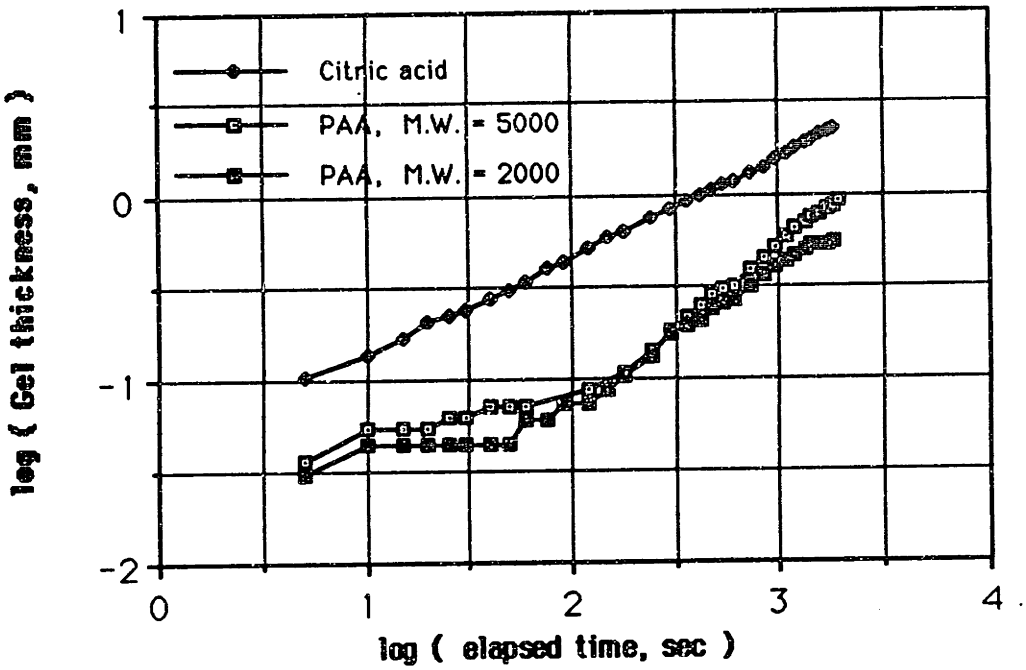

Figure 4.21 Gel growth rate for polyacrylic acid compared to citric acid. Concentration of coagulant: 1 mol/liter; PAA conc. by monomer.

The variation of growth rate with the volume percentage of silica was examined for binder with 2% TEA and .1% PEG. Five samples were prepared, with silica content varying from 11.3 % by volume to 25.5% by volume. The results are shown below; there was no significant difference between the growth rates. This suggests that the presence of the silica does not affect the diffusivity of citric acid through the gel.

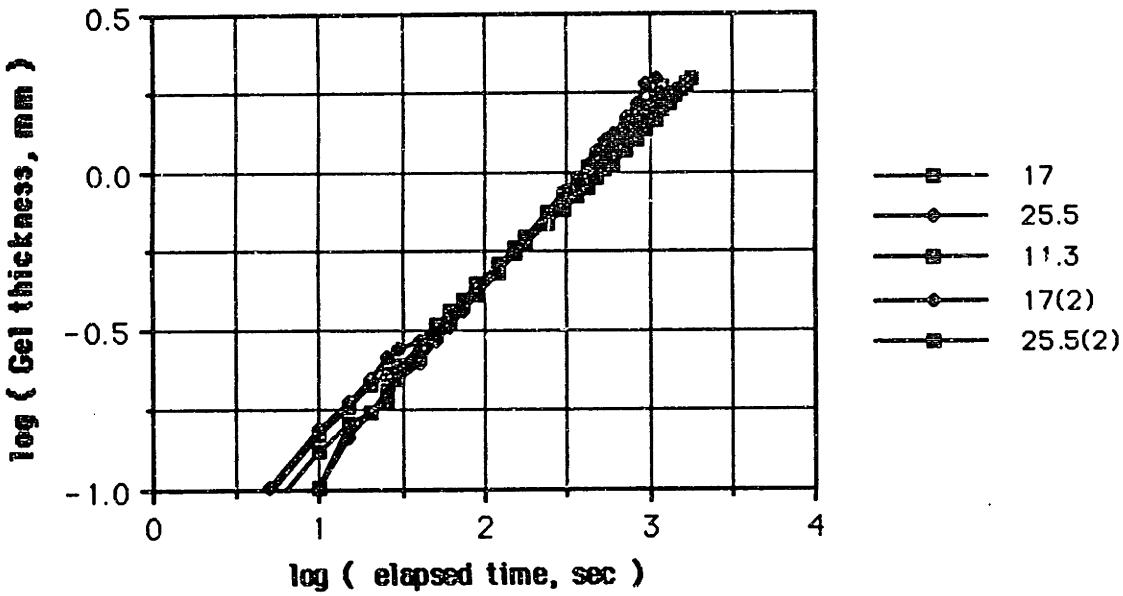

Figure 4.22 Growth rate of colloidal silica with 2% TEA, .1% PEG, various volume fractions of silica. Coagulated with 1 mol/l citric acid.

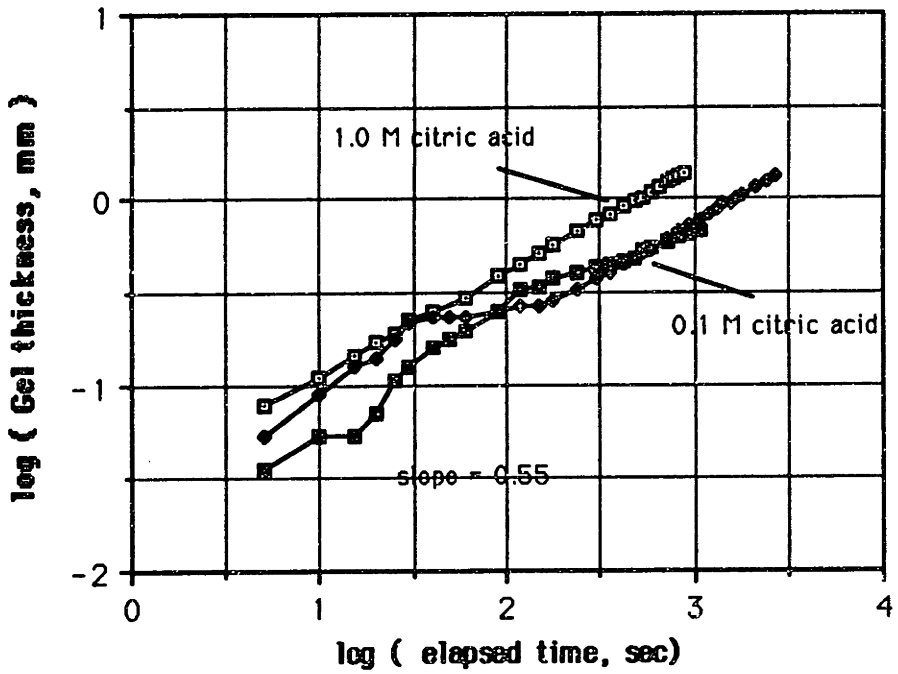

Figure 4.23 Growth rate of colloidal silica with 17.5 vol.% silica using different concentrations of coagulant: 1 mol/l citric and 0.1 mol/l citric acid. The curve for the lower concentration corresponds to the ambient conditions in the powder bed. This is used in the rate calculations in section 6.1.4 and in figure 4.26.

c. Discussion: Calculation of Diffusivity of Citric Acid in Gel

Since the exponent for the gel thickness is very close to 0.5, it suggests that the growth can be described by a simple diffusion model. The solution of coagulant over the gel is modelled as a source at fixed concentration. The coagulant begins to diffuse into the binder at t=0, and the concentration profile is given by

$$c(x) = c(0)\,\mathrm{erfc}\left(\frac{x}{2\sqrt{Dt}}\right) \qquad 4.1$$

where c(0) is the concentration in the bulk coagulant solution, D is the diffusivity of the coagulant in the colloid, and t is the time elapsed after the introduction of the coagulant. The plane at which the concentration is the critical coagulation concentration is the advancing gel front. This concentration profile is illustrated below.

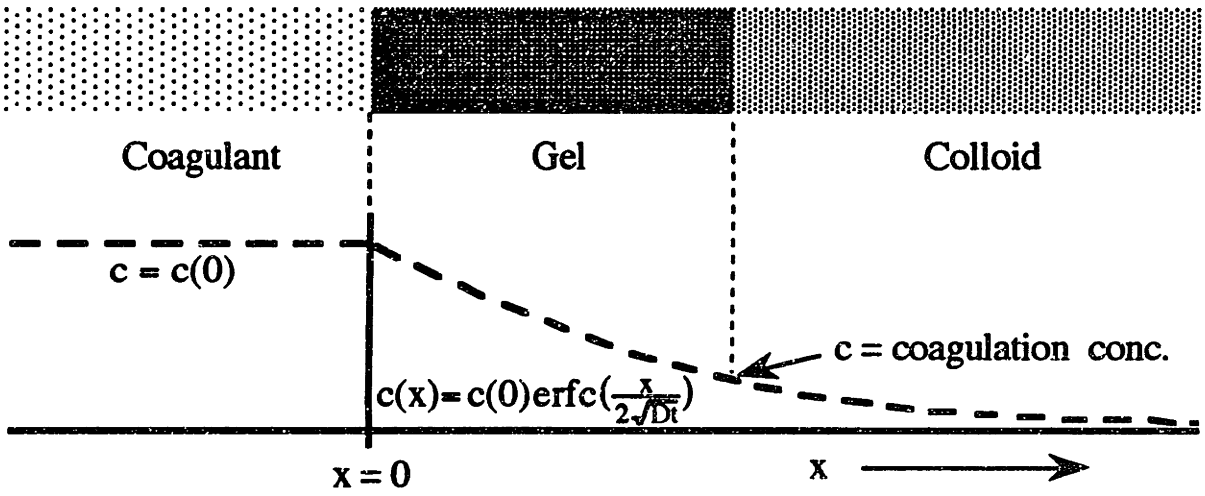

Figure 4.24 Model for gel growth.

Using the data shown in figure 4.23, the gel film grew to a thickness of 1 mm after 510 seconds with the 1 mol/l citric acid, and 1650 seconds with the 0.1 mol/l citric acid. This is enough data to calculate both the diffusivity and the coagulation concentration.

$$\begin{aligned} \text{c.c.c.} &= 1.0\ \mathrm{erfc}\left(\frac{1\text{mm}}{2\sqrt{510D}}\right) \\ &= 0.1\ \mathrm{erfc}\left(\frac{1\text{mm}}{2\sqrt{1660D}}\right) \end{aligned} \qquad 4.2$$

$$\text{erfc}\left(\frac{0.0221 \text{ mm sec}^{-1/2}}{\sqrt{D}}\right) = 0.1 \text{ erfc}\left(\frac{0.0122 \text{ mm sec}^{-1/2}}{\sqrt{D}}\right) \qquad 4.3$$

The task is to find a pair of arguments to the complementary error function whose ratio is (.0221/.0122) = 1.81 for which the value of the function differ by a ratio of 10. By inspecting a table of the complementary error function, the solution is approximately

$$\text{erfc}\,(1.60) \approx 0.1 \text{ erfc}\,(.85) \approx 0.023 \qquad 4.4$$

so

$$1.60 \approx \text{erfc}\left(\frac{0.0221 \text{ mm sec}^{-1/2}}{\sqrt{D}}\right). \qquad 4.5$$

This leads to $D \approx 1.9 \times 10^{-6}$ cm^2/sec and c.c.c. ≈ 0.023 mol/l. The result for the critical coagulation concentration agrees approximately with the value obtained in section 4.5.1 so this diffusivity for citric acid in binder gel must be approximately correct.

4.5.3 Gel Strength Measurement

The gel formed by neutralizing the binder with 2% TEA and .1% PEG had a strength approximately like yogurt. As a follow-up to the characterization of the gelation rate, a jig was constructed to measure the gel strength. A standard mixture, consisting of colloidal silica with 2% TEA, 5% ethylene glycol, 0.1% PEG-3400 was gelled with citric acid by adding 4% by volume of 1 mol/l citric acid solution. This thixotropic gel could be injected through a syringe and reform into a solid gel with approximately the same strength of the original material.

The jig consisted of a 1/2" steel coarse threaded rod which was suspended horizontally by fine cotton thread so it swung freely through the center of a 3/4" steel nut, also with coarse (steel) threads. Removable baffles were placed over the ends of the nut to form a closed cavity that could be filled with the gel. After allowing the gel to set for 2 hours, the baffles were carefully slid off, leaving a plug of gel that was locked into the threads of the rod and nut.

When the rod was pulled horizontally, the gel yielded on a cylindrical plane around the outer diameter of the threaded rod. A pull of 0.83 N (85 grams) was measured on a

number of attempts, allowing the gel to reset between pulls. The nut was 4 cm long and the shear plane had a diameter of 1.27 cm.

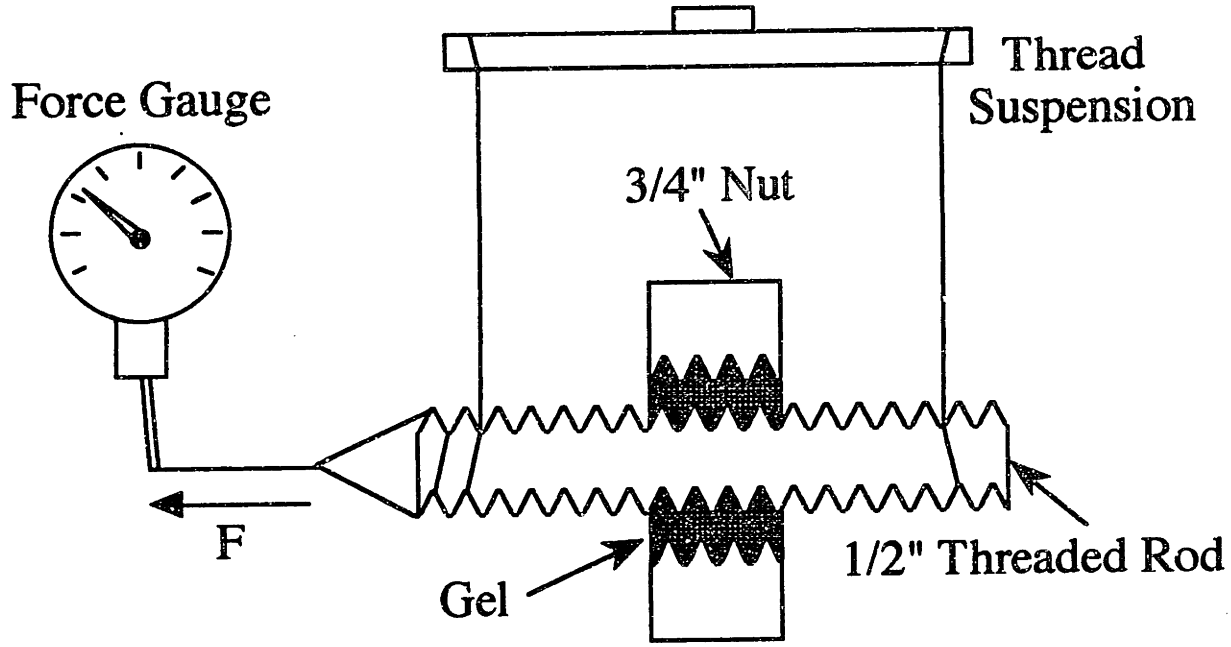

Figure 4.25 Gel shear jig. Gelled binder was injected into space between 3/4" nut and 1/2" threaded rod and allowed to set with temporary baffles in place. Breakaway force was measured with hand-held force gauge hooked onto thread loop on end of rod.

The strength of the gel is given by the relation below.

$$\tau_Y = \frac{(\text{Breakaway Force})}{(\text{Nut Length}) \times (\text{Circumference of Shear Plane})} \approx 520 \text{ Pa.} \qquad 4.6$$

Besides estimation of the green strength of 3-D Printed parts, this strength could be used to estimate the equilibrium size of binder flocs in shear flow (see sect. 2.2.9.b) A calculation is done in section 6.4 below of the strength required of the gel to resist gravitational loading.

4.6 Conclusion

The result of this experimental program was the introduction, in March 1993, of a binder formula, named "Binder B" . "Binder A" was the formula with 16 vol.% silica and 10% TMAH that had been used previously. The has been some slight modifications to the

formula in the time that followed; listed below is the formula for the binder "B" that is presently used (12/94) at MIT for the Three Dimensional Printing of ceramic shells.

385.9 cc = 385.9 g Distilled Water
58.4 cc = 65.1 g Propylene Glycol [CAS# 4254-15-3]
= 1-2 Propanediol
21.7 cc = 24.4 g Triethanolamine (TEA) [CAS# 102-71-6]
= 2-2'-2" Nitrilotriethanol
12.6 cc = 12.2 g Diethylene Glycol Monobutyl Ether [CAS# 112-34-5]
= Butyl Carbitol
= 2-(2-Butoxyethoxy)ethanol
(solid) **1.0 g Polyethylene Glycol** (PEG) MW 20,000 [CAS# 25322-68-3]
= Polyethylene oxide (PEO)
= Polyoxyethylene (POE)
(solid) **0.5 g Thymol Blue** [CAS# 76-61-9]

(Mix these components thoroughly to dissolve the solids. The PEG is the slowest to dissolve: it comes in solid flakes which sink. Then add:)

525.0 cc = 735.0 g Nyacol 9950 (prefiltered to 5 μm) [CAS# 7631-86-9]

The specific gravity of the mixture should be 1.21 for 17.5 vol.% silica. The pH should be between 9 and 9.5. The viscosity was found to be approximately 2 -3 cP (.002 to .003 Pa-s.) The surface tension was found to be 54 dyn/cm (.054 Pa-m). The butyl carbitol gives it a faint fruity odor, and it tastes like chicken. [Christopher Shutts, private communication]

The reagents are available from the following locations:

Distilled Water: Belmont Springs $3.50/ 5 gal
Propylene Glycol: Lab Supplies Solvents Rm $14.50 / kg
Aldrich: Cat.# 13,436-8 $24.90 / 3 kg
PPG: Aldrich: Cat# 20,230-4 $28.90 / 500 g
Fluka: Cat. # 81360 $30.60 / 1 kg
TEA: Aldrich: Cat# T5,830-0 $32.60 / 4 kg
Butyl: Aldrich: Cat# 11,031-0 $11.50 / liter
PEG: Fluka: Cat# 81300 (= 20,000 MW) $23.50 / kg
Aldrich Cat # 20,244-4 (=3,400 MW) $7.60 / 250g (works almost as well)
Thymol Blue: Aldrich: Cat# 11,454-5 $34.60 / 25g
Nyacol: Nyacol # 9950 $ 0.94 / lb, $15 repacking = $62 / 50 lbs

4.6.1 Functions of the Components

The **Nyacol/Water** balance is to maintain 17.5 vol.% silica.

Glycol (ethylene or propylene) seems to perform several functions. As a humectant, it slows down catcher buildup and enables the printhead to be stopped and restarted within a few minutes without difficulty. It also seems to soften the binder gel which aids cleaning and may reduce distortion during printing. As a cosolvent, its presence probably improves the binders' solubility for organic impurities which can contribute to jet instability.

Over prolonged recycling, diluting water tends to accumulate in the binder. To adjust the density upward, add Nyacol 9950. Over a very long period, the glycol will get diluted, so it may be necessary to make that up a little: the first symptom of glycol depletion seems to be catcher buildup.

TEA is a weak base and serves to hold the pH of the binder at about 9 - 9.5. The quantity added has been selected on the basis of the "normal" level of citric acid in the powder being sufficient to drop the binder pH to 7 or lower. TEA is advantageous because it does not precipitate or evaporate when the binder dries. Therefore, the dried binder still has a high pH and is easy to redisperse on drying. This aids cleanup.

The sum of the glycol and TEA components amounts to 10% of the liquid component of the sol. These together act as the humectant.

The **Butyl Carbitol** is a cosolvent to keep organic impurities from precipitating onto the printhead components. One impurity in particular is an ion exchange resin that comes in the Nyacol 9950. This additive reduces the surface tension somewhat and leads to foaming. It screws up the multijet printhead that Soligen uses, so a modification leaving out this component is dubbed Binder "C". Carbitol seems to deflocculate the silica a little bit, because the binder is easier to filter when this has been added and aged for a few days.

At this writing, an additive has been found to reduce the tendency to foam. Dow Corning "Antifoam 1500" is an emulsion which contains methylated silica and polydimethylsiloxane. Christopher D. Shutts, whose observations we value like pearls, reports that 10 ppm makes the region of jet impact in the catcher "like Alka-Seltzer instead

of like Mr. Bubble." Since too much foam can labor the pumping apparatus which returns binder from the printhead, leading to printhead failure, it is recommended to use several times this level.

PEG is the polymer that sticks the silica particles together when the pH is lowered below about 7.5. Silica below this pH has a substantial amount of hydrogen ions adsorbed onto it. The PEG has a lot of oxygen in its ether bonds, and these are attracted to the hydrogen. The phenomenon is fairly reversible: if binder pH is increased, it can be (mostly) redispersed. A cleaning solution consisting of $\approx$ 1% ammonia is currently used as a cleaning solution. It only requires a vanishingly small amount of PEG to gel the binder: the 0.1% that is added is at least 10 times the minimum required. Therefore, only massive dilution will affect the binder's ability to coagulate.

The optimum molecular weight of the PEG component was found to be 14,000-20,000. The results shown in figure 4.15 indicate that the higher the molecular weight, the less is needed to coagulate the binder. Experiments were done with formulas with higher molecular weights, and it was found that those with molecular weights of 35,000 and higher inhibited the breakup of the jet due to the viscoelastic "string-of-beads" phenomenon illustrated in Richard Yu's MS thesis on page 52.

Thymol Blue is a pH indicator that is blue above pH 8 and turns yellow at pH 7 or so. Its purpose is to monitor the condition of the binder during storage and recycling (it should always be blue) an to asses the citric acid content of the powder bed: The printed layers should be yellow or red. If they are green or blue, then not enough citric acid is present. The ideal mix is yellow with red polka-dots (around citric acid granules.) The quantity that is specified here is on the high end: I chose it so the color of the binder would match the ink on my business cards. It is just as good to use one-half or one-quarter as much.

4.6.2 Performance of Binder "B" in Service

In twenty months of use there have been few problems with this formula. It is very compatible with the fluid handling system and most printhead components: the chief success of this program was to remove the issue of printhead reliability from the top of the list of engineering problems on the project.

The largest problem encountered with this formula was that it required filtration after mixing. In order to condition the material for use, it must be pumped in a closed circuit through a five micron filter for a period of time. The filter does not load up, and this appears to be unnecessary if the binder has been allowed to stand some time after mixing. There is no quantitative data on this phenomenon, but it is evidently due to flocculation of the silica during mixing. The flocs appear to redisperse after some time, so the fluid can be cycled over and over through the same filter without the filter loading up. Possibly, the formula is inherently stable, and mixing procedure simply needs modification. [Christopher Shutts, private communication]

The interaction with the printhead is critical in the operation of 3-D Printers. This binder proved that it could be recycled with little degradation after the initial filtration cycle. There is a slight amount of solid buildup on the printhead components. The main cause of this is that binder droplets can occasionally receive levels of charge that cause them to land in unusual places. These "exceptional" droplets sit by themselves for long periods and dry out. They can be eliminated either by slowing down the drying rate still further or by synchronizing the electronic system more accurately.

Another printhead interaction led to the introduction of binder "C" for Soligen. When a jet of this binder breaks up in a gradient electric field, there appears to be a mist of droplets approximately 1-2 μm in size that collect on the printhead near the breakoff point. This effect was reduced by eliminating the wetting agent (Butyl Carbitol) from the formula. It is possible that this phenomenon is a consequence of the low viscosity of the binder: it is about 2 cP, while more conventional ink-jet inks have viscosities around 8 cP.

The color change of the binder in the powder bed gives a very useful way to asses the acid content of the powder and the rate of acid diffusion through the printed areas in the powder. Qualitative observations confirmed that the time for acid to migrate through a freshly printed layer confirmed that the time to coagulate can be as long as one minute (longer if the powder is depleted of acid.)

Printed material with this formula distorts very little after printing. There is no curling of layers as is observed with other binders, and what distortion occurs during processing, seems to happen during the heat treatment. The strength of printed but unfired material is quite low: parts cannot be removed from the powder bed before firing. Since it

is not ordinarily needed to do this, the low strength is not a problem. It is possible that the low strength prevents distortion, and the low strength certainly aids cleaning.

The organic content of the binder makes the parts smoke during the early stages of firing. This is not a big problem, except if large parts are to be fired without adequate ventilation.

4.6.3 Significance of Gel Growth Rate

The binder can take several minutes to fully coagulate after printing. The consequence of this is that there is sufficient time for the capillary attraction of the powder to exert a great deal of influence on the distribution of binder in the powder bed. Moisture spreads rapidly in the powder used in 3-D Printing, and a realization that the rate of gelation was too slow to influence the migration caused this research program to be directed towards a thorough study of the capillary interactions between the binder developed above and the powders used. A much more detailed discussion of the rates is pursued in section 6.1, below.

The rate of capillary migration can be estimated by the rate of imbibition of a liquid by a porous sample. This is done in section 7.10, and these data are compared below with the coagulation rate measured in section 4.5.2, above. The solidification event which causes the binder to immobilize in the powder can vary from a minimum if the citric acid is distributed as a coating on the surfaces of the powder grains. The gel only must grow across a characteristic pore size to stop binder flow. The upper limit to the solidification time comes if the acid is very poorly distributed. In this case, the gel must grow upward from the previously printed layers across a characteristic layer thickness, about 50 times further.

The migration rate was found to be sufficiently rapid that liquid binder could potentially migrate as much as 1 mm from the point of impact. This causes a conceptual difficulty, since the typical line size is on the order of 200 μm, and the features are nearly fully saturated. To explain this property of Three Dimensionally Printed features, it is necessary to develop a model for feature formation based on the percolation of binder through a network of pores in the porous powder bed.

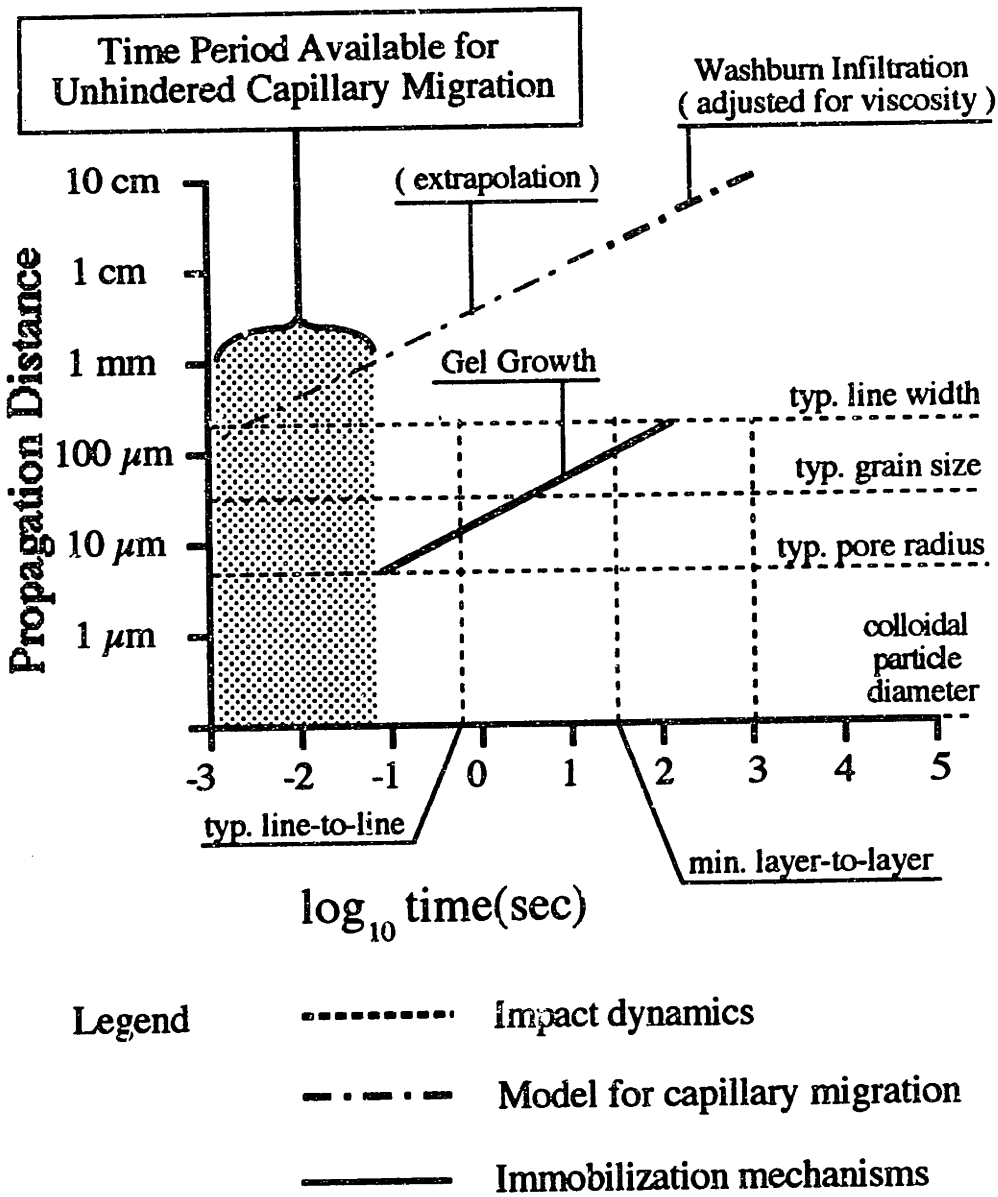

Figure 4.26 Improved time line for feature formation. See figure 1.10. Line labelled "Washburn Infiltration" corresponds to dat gathered in section 7.10, below. "Gel Growth" is the lower curve in figure 4.23.

Chapter 5.
Capillary Migration in Porous Materials: Foundations and Review of the Literature

5.0 Introduction

The interaction between binder and powder in Three Dimensional printing is dominated by capillary, and to a lesser extent, gravitational forces. In this chapter, the literature dealing with capillary effects in porous materials are reviewed, with special attention paid to the migration of liquids in porous media. Most of the literature that covers porous materials deals with soil hydrology, although some of the sources discuss the issues of oil recovery. Since the structures under consideration in these fields are quite large, the ale of the pores in quite small, and the theories generally lead to continuum models that have solutions which are not bounded in time. It was shown at the end of the last chapter that if fluid migration were not limited, the size of printed features would tend to be very much larger than that which is observed in practice. Although the continuum models discussed in this chapter are destined to be rejected in developing a model for feature formation, the general concepts are still valuable for the untutored reader, and are collected here for educational purposes.

For a more general discussion of the fundamental concepts of capillarity, see Appendix A. In Appendices B, and C, the theory of capillarity is developed with special attention to the primary phenomenon that occurs during feature formation in 3-D Printing: the migration of fluid from saturated regions to unsaturated regions in the establishment of an equilibrium configuration.

5.1 The Porous Structure of the Powder Bed in 3-D Printing

The medium that constitutes the receiving surface in Three Dimensional Printing is a level bed of powder particles that are to be bonded together by the fluid binder dispensed by the printhead. The powder bed is a porous medium which may be rigid under some conditions, but is usually somewhat deformable. In the basic textbooks on the subject

[Bear]; [Scheidegger]; [Dullien] the properties of porous media are defined on a length scale much larger than the mean pore size. In this view, a porous body can be treated as a continuous medium, and the equations of motion of a fluid can be developed along a continuum model. The powder bed in 3-D Printing consists of a chaotic pile of grains of generally irregular shape and different sizes. A cross section of a powder bed is illustrated in Figure 5.1 below.

Although the particle size is listed as 30μm, it is quite apparent that most of the grains are much smaller on one axis than on the other. This powder is sold as an abrasive. The 30μm product was the largest grain size available of this material, and grain sizes down to 1/4 μm are available. It is described in Alan Lauder's and John Lee's theses as "lamellar". The size distribution of the powder is discussed in greater detail in Appendix F.

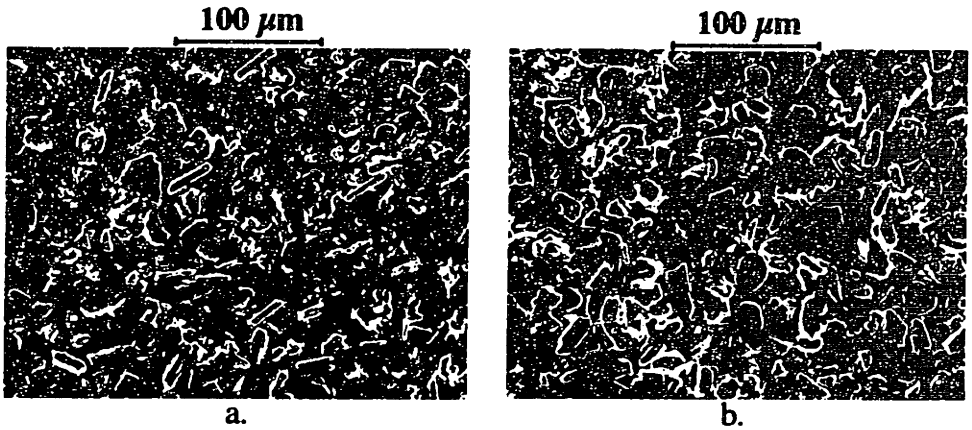

Figure 5.1 SEM micrograph of 30 μm Norton 7920 alumina powder. M=200x
Fractional densities: a. 0.33; b. 0.49.

The pore structure is not uniform. Cavities as large as 50μm in diameter are relatively common. The mean pore radii are 4.3 μm for the low density sample and 3.3 μm for the high density sample, measured by mercury porosimetry.

Discussions of the pore structure of porous media are as many and varied as the materials themselves. [Greenkorn p. 11, 23-30] claims that only two parameters are necessary to describe pore size distribution and develops an interesting stochastic model but does not pursue the interpretation. Brooks and Corey [Bear 465] ; [Greenkorn 123] proposed an empirical model to fit data for capillary pressure and permeability. Pore geometry can be deduced from micrographic data [Greenkorn 16-19] but interpretation of image data can be tricky. Various pore geometries and corresponding porosimetry data are surveyed in [Johnson & Sen] along with the acoustics of porous materials.

The most convenient way to define the pore structure of a porous material is in regards to the way the capillary pressure varies when it is saturated to different levels with a liquid. It is especially convenient if capillary properties are of interest, although it is shown (Appendix C) that little direct information about the pore size distribution can be obtained from capillary pressure methods. This provides empirical information about the geometry of the fluid meniscus in contact with the pores. Since the flow of liquid in a porous medium is driven by gradients in this pressure, knowledge of this sort is quite useful, even if it does not specifically address the dimensions of the cavities present between the particles in the powder.

5.2 Bulk Properties of Porous Powder

5.2.1 Porosity

The powder bed is composed of particles with a density ρ_{powder} which is packed at a density ρ_{bed}. The **fractional density** of the powder bed, also called the **packing density**, is defined by

$$f_{powder} = \frac{\rho_{bed}}{\rho_{powder}} . \qquad 5.1$$

The packing density is somewhat difficult to control. It typically varies from batch to batch and can change from day to day for a given batch, depending on such variables as the ambient humidity or powder additives that affect the cohesive strength of the powder of the condition of the powder handling system. While the packing density of the powder bed is difficult to control, is is relatively easy to measure. In the normal machine cycle of 3-D printing, the powder layering process is used to build a series of dry layers containing no binder. The volume is known to a high accuracy, the only measurement needed is the weight of the powder in the bed. If a particular packing density is desired, the machine settings can be iterated to approach it as long as patience holds out.

The **porosity** is defined as the space not occupied by solid grains in the powder bed. This is, in a simplified view, the space available for the binder to occupy. It is

$$\text{porosity} = 1 - f_{powder} . \qquad 5.2$$

(This view is complicated by the possibility of **closed porosity**. This is porosity that is sealed inside solid grains. It affects the fractional density of the powder bed, but is not available for fluid. The presence of closed porosity is quite unusual in the feed materials used in 3-D printing, although it can easily exist in the material after printing.)

[Perloff & Baron, 196-257] devote an entire chapter to the consolidation of granulated materials (soil) under load and develop a mechanics of dry powder based on the empirical relation

$$d\left[\frac{1 - f_{powder}}{f_{powder}}\right] = C_e \, d[\log \sigma_{MAX}] \qquad 5.3$$

where the quantity in the brackets on the left side of the equation is called the **void ratio**; C_e is called the compression index, and σ_{MAX} is the historical maximum applied stress.

5.2.2 Saturation

The **saturation** is the fraction of available space that is filled by a liquid:

$$S = \frac{f_{liquid}}{1 - f_{powder}} \qquad 5.4$$

where f_{liquid} is the volume fraction of liquid in a region of the powder bed.

The saturation, as defined, cannot exceed unity. [German ch. 5] describes the condition in a slurry of powder suspended in liquid where the powder grains touch one another and the body acts like a solid. He defines this condition as the **critical loading** f_{crit} of solid in liquid. At lower solid fractions, the material behaves like a slurry, while at higher solid fractions, the body behaves like a partially saturated porous solid. The system is actually a ternary system, and the air content is relatively independent of the liquid content. Since German is interested in the slurry state, he does not discuss the partially saturated state, but the transition between porous solid and slurry is a fundamental one that is of interest from either direction.

[Perloff and Baron pp. 306-309] relate that the hydrostatic pressure of a fully saturated porous medium increases as a result of an externally applied load. If the porous medium is composed of loose particles and is compressible, then the water occupying the pores can be subjected to elastic compression. This load-bearing capability is probably

only relevant when the large loads encountered in structural engineering, and certainly is not significant in unsaturated media: the fluid accommodates deformation of the solid medium by filling an increasing fraction of the available pore space.

5.2.3 Capillary Pressure in Porous Media

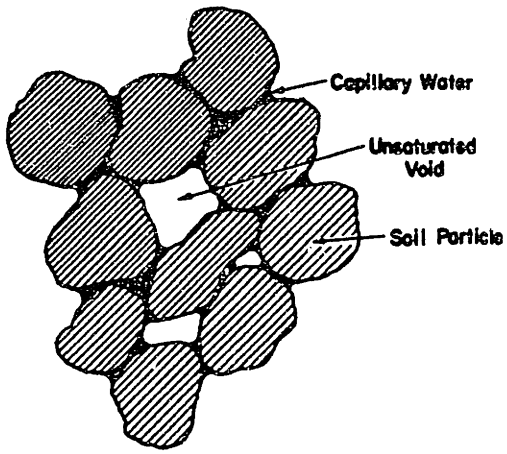

Figure 5.2 Diagram of a wetting fluid in a porous medium. From [Perloff & Baron, 278]

A wetting fluid in a porous medium distributes itself in the spaces between grains and contacts the powder surface with a local wetting angle of θ determined by the surface energies of the solid, liquid, and vapor phase boundaries. (See Appendix A for a more detailed discussion of capillary pressure). The shape of the meniscus is exceedingly complicated, but possesses a mean curvature and capillary pressure, defined uniquely everywhere in the fluid. Since fluid migration is driven by gradients in pressure, it is highly desirable for modelling purposes to establish a functional dependence of capillary pressure on saturation. One caveat is that saturation is not defined conveniently on scales smaller than the pore size of the medium.

5.2.4 Dependence of Capillary Pressure on Saturation

Jacob Bear, one of the most ubiquitous writers on the subject, considers saturation to be an independent variable in a continuum model of a porous body. Capillary pressure is considered to depend on the saturation:

$$P_C = P_C (S, f_{powder}, \sigma_{LV}, \theta). \qquad 5.5$$

This a convenient mathematical form, since it permits a classical flux law to be derived assuming constant values for the powder packing density f_{powder}, fluid surface tension σ_{LV}, and contact angle θ. Such a flux law can only express fluid motion across length scales larger than the pore size since that is the scale over which the saturation is defined. This is not a problem in soil water hydrology, but is a problem in considering the lower limits of feature size in Three Dimensional Printing. A typical curve of capillary pressure as a function of saturation from Bear is shown below

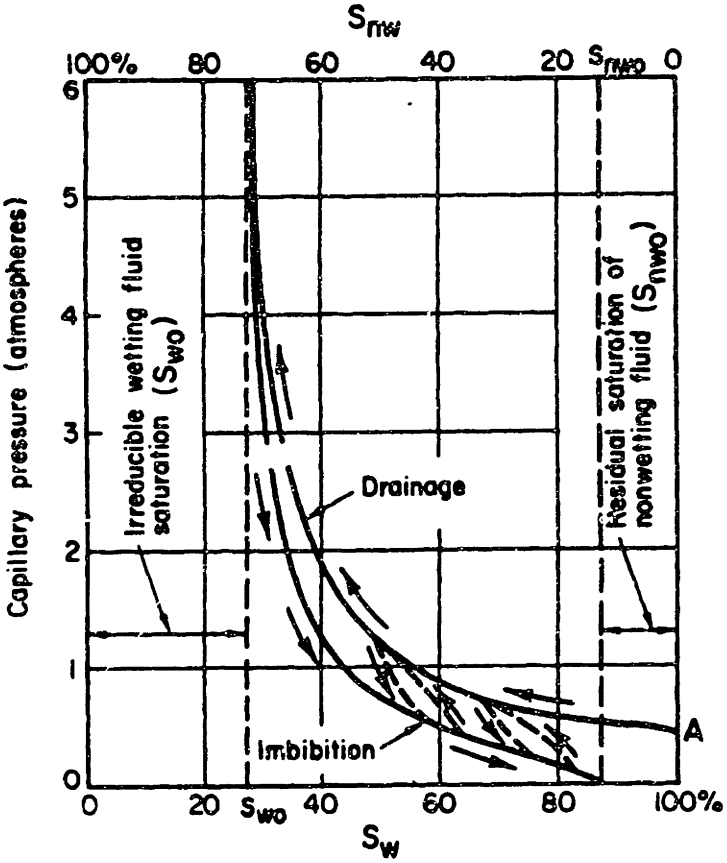

Figure 5.3 Typical capillary pressure-wetting fluid saturation curves in sandstone illustrating hysteresis [Bear, 451] The capillary pressure is defined in soil mechanics to be positive for suction. In this work, a suction pressure is always negative. The saturation of the wetting phase is the scale on the bottom.

In spite of the long times allowed for "equilibration" (see Appendix C), the curve follows different paths depending on whether the wetting fluid is entering (**imbibition**) or leaving (**drainage**) the sample. To make matters even more complicated, [Dullien 351] differentiates between wetting imbibition and nonwetting drainage because different fluids enter at a higher or lower pressure than the fluid being displaced. This distinction is relevant inasmuch as the rate of infiltration affects the pressure distribution in the two phases. See, for example[Lenormand] or [Scheidegger.]

The hysteresis in the capillary pressure curve is a result of irreversibility in the fluid flow through porous media. During feature formation in Three Dimensional Printing, binder is delivered to essentially one point on the powder surface which becomes fully saturated. This region is initially surrounded by dry powder. As fluid migration progresses, the saturated regions drain and the dry regions imbibe until the capillary pressure of both regions become equal. Since each region traverses along different curves in figure 5.3, in the final state, the two regions can exist at equilibrium with different fluid contents.

5.2.5 Critical Features in the $P_C(S)$ Curve

There are two important features on this figure that characterize the pore structure of the medium. There exists a critical wetting fluid saturation, S_{wo}, at which the fluid mobility in the medium becomes zero. A fluid cannot migrate if the saturation is so low the fluid cannot reach from one pore to the next. This state is called [German 292]; [Bear 476] the **pendular** state. The saturation at the transition from this state to the **funicular** state (when fluid has finite mobility) is quite low; approximately 0.3 [Bear, 451] but is variable depending on pore geometry. Geometrically, this corresponds to the fluid content at which the fluid meniscus between particles becomes discontinuous. Below this saturation, no continuous fluid path exists between the surface and the interior of the body, so fluid can only leave the body through evaporation. This is the **irreducible wetting saturation** S_{WO}. The capillary pressure does not tend to infinity as the graph implies, but references that explicitly say otherwise are difficult to find [Petre & Sanfeld p. 83.] The capillary pressure at the irreducible wetting saturation is a critical property in determining the migration of binder during feature formation in 3-D Printing. This pressure is called P_0, the **dry suction pressure**, and is treated in detail in Appendices B and C.

A second feature in figure 5.3 is the point labelled "A" on the right margin of the graph. Bear calls it the **bubbling pressure** P_B of the medium and it corresponds to the pressure at which a nonwetting fluid (e.g., air) must be forced into a saturated porous medium before fluid can be displaced. The positive pressure required to blow a bubble of a given radius depends, through Laplace's equation (equation A.33, Appendix A), on the mean curvature of the bubble. A bubble of a given radius cannot pass through a pore of a smaller radius, so bubbles cannot penetrate into a porous medium until their radius becomes smaller than a certain critical size at which a continuous path percolates into the body. [Lenormand] discusses immiscible displacements in porous media and describes

conditions under which fluid migrates through percolation clusters with a **fractal** structure. Pores of various sizes are connected in a space-filling network and the bubbling pressure corresponds to the **percolation threshold** of the population of the largest pores. The cluster of pores at this threshold has a fractal dimension of approximately 2.5 but the network rapidly approaches dimension 3 as more pores are infiltrated. [see, for example, Sapoval, Rosso, & Gouyet, pp. 227-245 in Avnir]

A wetting fluid occupying the tightest corners in the pore structure loses its ability to communicate from pore to pore at saturations below the irreducible saturation S_{WO}. It is asserted in Appendix C that pores cannot easily communicate fluid through the network until they are fully saturated, the approach to full saturation being gained as a catastrophic collapse of the meniscus at a critical pressure P_0. Since this, too is a percolation phenomenon, the fractal dimensions of the fluid network at this threshold must be similar. The literature, e.g. [Bear] suggests that S_{WO} is typically about 0.2-0.3. This is approximately the same as the percolation threshold in three dimensions. Obviously, the disordered structure of porous media makes the correspondence only approximate.

5.2.6 Empirical Model for $P_C(S)$

Brooks and Corey [Bear p.465] offer a convenient model for capillary pressure as a function of saturation to fit data of capillary pressure of a wetting fluid with respect to saturation obtained experimentally:

$$P_C = P_B S_e^{-1/\Lambda} \qquad 5.6$$

where S_e is the **effective saturation** and Λ is a parameter that describes the pore size distribution. The effective saturation varies from zero to one over the range of finite fluid mobility.

$$S_e = \frac{S - S_{wo}}{1 - S_{wo}} \qquad 5.7$$

The pore structure of microporous materials is the subject of a generous amount of literature. Most of the studies are based upon gas adsorption [Everett 1973] These methods are only suitable for pore sizes smaller than 100 nm, [Everett 1973, p. 126] which exists in the silica gel that forms upon gelation of binder, but is very far below the pore size of the powder bed before printing. [Feder, p. 236] discusses the fractal geometry of microporous surfaces and describes methods for measuring the fractal geometry of a microporous medium by Small--Angle Neutron Scattering (SANS).

There are a number of experiments for measuring the capillary pressure of a porous medium under laboratory or field conditions [Bear 453-457]. These are described in greater detail later. Briefly, the hydraulic pressure of a liquid partially saturating a porous sample is allowed to come to equilibrium with a pressure transducer of some sort. The measured pressure is tabulated as a function of the saturation. These experiments are somewhat tricky to perform, at least in part because the mobility of fluid decreases rapidly as the saturation departs from unity. The time for the liquid to come to hydraulic equilibrium with the transducer can become prohibitively long. Bear tells of experiments taking 10 to 40 days to complete.

5.3 Mechanics of Partly Saturated Powders

The mechanics of deformation of dry and wet powder is of great interest in Three Dimensional Printing. An understanding of powder mechanics would give some clues to the control of part distortion and control of the powder density during printing.

[Onoda 264] discusses the mechanics of clay with various levels of porosity, all fully loaded with fluid. Clay particles are colloidal in size. If they are flocculated, they will behave as a solid over a fairly wide range of moisture contents. [Onoda 366] also discusses the mechanics of partially saturated porous solids and gives the remarkably simple expression

$$\sigma_Y = S P_C \qquad 5.8$$

as an upper bound to the tensile strength of a partially saturated porous body. Data he gives for limestone powder is quite compelling. Similar data can be found in [Chiu & Cima.]

This picture is probably oversimplified. In [Perloff & Baron, pp. 51-80] the mechanics of dry and moist soils are considered, and a sophisticated method of failure analysis is discussed in detail, with entertaining case studies to illustrate. The mechanics of powders is quite complicated, particularly by the fact that powders tend to change their volume drastically when they deform. The consequences for partly saturated powder is that the capillary pressure can vary rapidly as a body of powder is deformed. If the simplified form of the yield strength in equation 5.8 is accepted on a local scale, the

equations of motion for powder under stress become cross-coupled in and extremely uninviting fashion.

Zimon calculates the force of adhesion between spherical particles as a function of contact angle and the volume of fluid contained in the neck. The force is equal to the sum of the capillary pressure times the area of the neck plus the surface tension times the circumference. In the limit as S -> 0, the adhesion force tends to a maximum of $2\pi r\sigma_{LV}\cos\theta$ where r is the radius of the sphere. As the diameter of the neck departs from zero, the adhesion force decreases slowly in a way that varies with contact angle. This is shown qualitatively in the figure below.

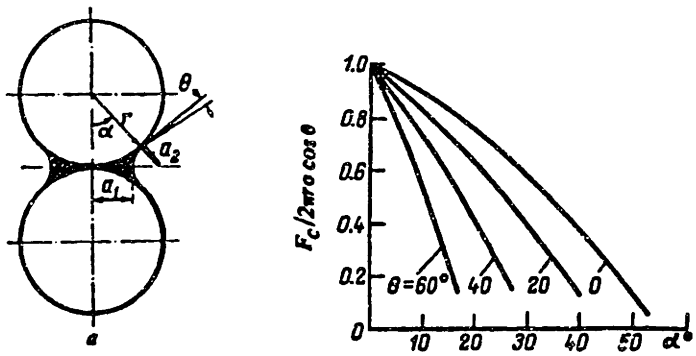

Figure 5.4 Adhesive force between two spherical particles of radius r. [Zimon 109-111]

[Perloff & Baron p. 239] describe a fascinating experiment in which the compressibility of clay samples was compared between samples saturated with water and carbon tetrachloride. The nonaqueous liquid increased the friction between particles because the electrostatic repulsion between particles was removed (See section 2.3.4 .) This effect increased the yield strength of the clay by roughly three times.

5.4 Hydraulic Permeability

5.4.1 Darcy's Law

Fluid inside a porous body flows under a gradient in pressure. Darcy's Law describes the flow of homogeneous fluids in continuous, isotropic media. The derivation of Darcy's law is covered widely, a very good treatment is given in [Scheidegger, Ch.4]:

$$J = \frac{-k(S)}{\eta} \nabla P \qquad 5.9$$

where J is a volumetric flux per unit are with dimension (length/time)

k(S) is the hydraulic permeability with dimension $(\text{length})^2$

η is the fluid viscosity

∇P is a pressure gradient in the fluid, e.g. imposed by a gradient in saturation.

5.4.2 Empirical Models for Hydraulic Permeability

The flux in equation 5.9 is inversely proportional to the viscosity of the fluid, and proportional to the hydraulic permeability. For a fully saturated porous bed, various models relating the permeability to the pore size have been devised. The permeability depends very strongly on particle size and porosity. [Bear 161-176] goes over several different theoretical derivations. One of the simplest for a completely saturated bed is:

$$k_{sat} = \frac{\left(1 - f_{powder}\right) R_{pore}^2}{24} \qquad 5.10$$

where R_{pore} is the "mean" pore radius. Another model is the Kozeny equation which can be used if the pore size is not known:

$$k_{sat} = \frac{d_{grain}^2}{180} \frac{\left(1 - f_{powder}\right)^3}{\left(f_{powder}\right)^2} \qquad 5.11$$

where d_{grain} is the hydrodynamic diameter of the particles in the bed.

Direct measurement of the hydraulic permeability of a porous sample is considerably easier than the measurement of capillary pressure. Most books on the subject (e.g. [Bear 119]) describe apparatus in which fluid is forced through a saturated porous sample and the flow rate is measured as a function of applied pressure. [Bear 459] and [Levine and Neale] suggest that a significant amount of air can be trapped during imbibition, which effectively reduces the porosity.

5.4.3 Permeability in Unsaturated Media

As the fluid content of the powder bed decreases from complete saturation, the hydraulic permeability decreases rapidly. Air that replaces liquid tends to occupy the largest pores, which were the ones that permitted the easiest flow of fluid. As the saturation decreases further, the fluid paths through the medium become less and less connected, until at S_{W0}, the liquid cannot percolate at all through the medium and the permeability is zero for saturations below this level. This is illustrated in the figure below, taken from Bear.

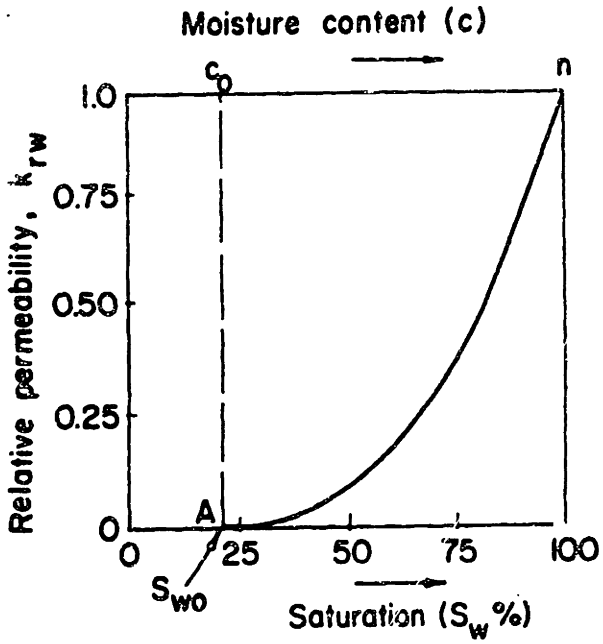

Figure 5.5 The variation of permeability in unsaturated sand [Bear 491.]

The relative permeability for a wetting fluid, k_{rw} is defined as the ratio

$$k_{rw} = \frac{k(S)}{k_{sat}} \qquad 5.12$$

where k(S) is the hydraulic permeability at some intermediate saturation S.

In [Bear 465] an empirical model permeability as a function of saturation is derived using the parameter Λ, also from Brooks and Corey:

$$k_{rw} = S_e^{(1+2/\Lambda)} \qquad 5.13$$

The capillary pressure and the hydraulic permeability both depend on the pore size, so this led Leverett [Scheidegger p.58]; [Bear 446] to suggest the fundamental form

$$J(S) = \frac{P_c(S)}{\sigma_{LV}\cos\theta}\left(\frac{k_{sat}}{(1-f_{powder})}\right)^{1/2} \qquad 5.14$$

5.5 Fluid Migration in Partially Saturated Porous Media

5.5.1 The Washburn Equation

A porous material can be idealized (more realistically that the skeptic might imagine, as shown in Appendix B) as a bundle of cylindrical capillaries with a distribution of diameters. [Greenkorn 13] The equation derived by Washburn [Levine & Neale] can be applied to the imbibition of a wetting fluid by this porous material fed by a flat pool of liquid.

Darcy's Law can be rewritten in this problem as a differential equation in x and t:

$$\frac{dx}{dt} = \frac{k_{sat}P_0}{(1-f_{powder})\eta x} \qquad 5.15$$

where x(t) is distance of the infiltration front from the point of liquid feed
P_0 is the capillary suction of dry powder for the liquid.

the solution for which is

$$\frac{x^2}{t} = \frac{2k_{sat}P_0}{(1-f_{powder})\eta} \qquad 5.16$$

If the porosity of the sample and the liquid viscosity are known, one can use a measurement of the rate of imbibition to estimate the product $k_{sat}P_0$. If the permeability is known, the capillary suction of dry powder can be estimated. Since dry powder cannot transmit hydraulic pressure, the value of P_0 is a good estimate for the capillary pressure at the minimum saturation at which fluid migration can occur. This model assumes that there is little pressure drop in the partially saturated migration front. [Levine and Neale] reported that a dynamic model that accounts for the effects of high Reynold's number converges on Washburn's equation at times greater than

$$t \sim \frac{10k_{sat}\rho_{liquid}}{\eta} \qquad 5.17$$

(ρ_{liquid} is the fluid density.)

5.5.2 The Richards Equation

A more general situation is described by a time-dependent form of Darcy's law for capillary pressure and permeability both variable with saturation derived by Richards [Sposito]; [Dullien 395]

$$\frac{d}{dt}(S) = \frac{-1}{\eta\left(1 - f_{powder}\right)} \nabla \cdot \left[k(S) \nabla P_C(S) \right] \qquad 5.18$$

The Richards equation is useful for modelling the transport of fluid in porous media that are partially saturated everywhere and the pressure gradients are small enough that the flow is gradual. [Boloutas] treated the problem of inhomogeneous permeability in soil water percolation by computer modelling very successfully. This approach is especially necessary in natural formations which contain a distribution of porosities [Greenkorn 56].

Empirical models for $P_C(S)$ and $k(S)$ invite analytic solution. Using the empirical models of Brooks and Corey [Bear 465]:

$$\frac{d}{dt}(S_e) = \frac{-P_B k_{sat}}{\eta \Lambda \left(1 - f_{powder}\right)} \nabla \cdot \left[S_e^{1+2/\lambda} \nabla S_e \right] \qquad 5.19$$

[Chang] pursued this in modelling the formation of features in ink-jet printing on porous paper. He solved the Richards equation analytically for an empirical model of the form

$$\frac{d}{dt}(S) = -D_M \nabla \cdot \left[S^n \nabla S \right] \qquad 5.20$$

for rectangular, cylindrical, and spherical geometries for the case of ink droplets impacting on porous paper. For the cylindrical geometry, for example, he finds that the invasion front advances as

$$r(t) = r_0\left(\frac{n+1}{n}\right)^{1/2}\left(\frac{4D_M t}{r_0^2}\right)^{1/(n+2)} \qquad 5.21$$

where r_0 = the initial radius of the pool formed by the droplet,

n = (1+2Λ)/Λ after Brooks and Corey [Bear 465]

$$D_M = \frac{P_B k_{sat}}{\eta\Lambda\left(1-f_{powder}\right)} \qquad 5.22$$

= the **moisture diffusivity** for the saturated medium.

P_B is the bubble pressure of the medium,

k_{sat} is the hydraulic permeability of the saturated medium,

η is the fluid viscosity,

Λ is the pore size distribution index (from equation 5.6)

($1-f_{powder}$) is the porosity of the powder bed.

For powders that have a narrow pore size distribution, which is the case in the monomodal powders used in 3-D Printing, the parameter Λ tends to be a number between 4 and 8. (See, for example, [Bear 449].) In the limit of large Λ, n = 2 and the time dependence of ink spreading in a cylindrically symmetric feature is $t^{1/6}$. The spread of a constant dose of liquid in a cylindrical geometry is shown below. The liquid starts at t=0 as a spot of radius a. The pore size distribution is assumed to be quite narrow. The cylindrical geometry used in this derivation might apply to single line features, as it does with circular ink spots on thin paper.

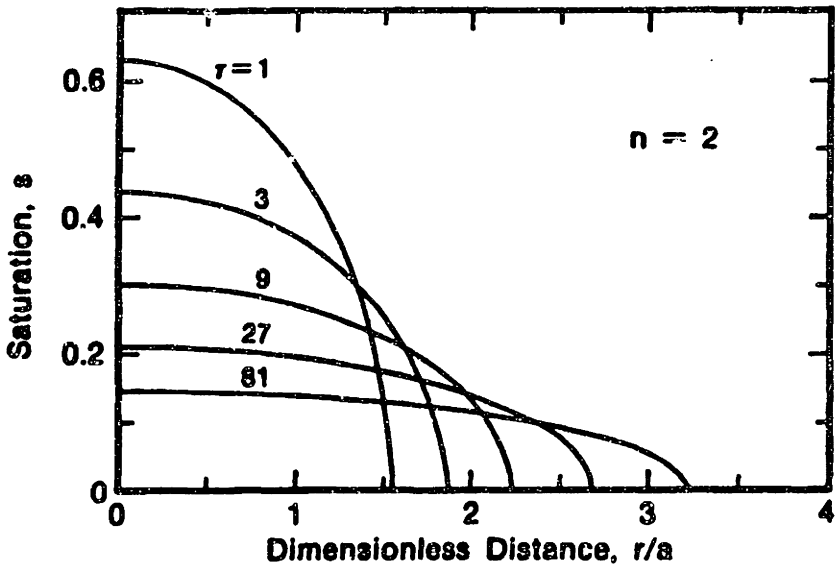

Figure 5.6 Radial migration of ink in paper [Chang]
n = 2 (limit Λ→∞) the dimensionless time variable $\tau = a^2 t / D_M$.

5.5.3 Other Continuum Treatments

There exists a huge amount of literature dealing with the continuum treatment of fluid migration in porous materials. [Muskat] gives a classical treatment of potential flow solutions to boundary value problems in the context of soil hydrology. Technical books are replete with models for water flow in soil. (see, for example, ASAE Advances in Infiltration, 1983 p.102 for the "Green-Ampt" model for surface water infiltration of soil). [Bear & Corapcioglu] model gravitationally driven flows and consolidation (i.e. densification) in partially saturated media. [Corapcioglu] develops a highly abstract mathematical model and applies it to flow instabilities in magnetic fluids. Petroleum recovery motivates quite a bit of study in the problems of gas-forced oil migration (secondary oil recovery) and water-forced oil migration (tertiary.) [Greenkorn] dwells on this at length, with an interesting section specialized to vapor-liquid equilibria in secondary recovery. [Scheidegger] discusses very clearly the instability of the water-oil interface when the less viscous fluid is used to force the more viscous in tertiary recovery. The subject of solute dispersion is treated very well by [Greenkorn], who also presses on through migration of viscoelastic fluids.

5.5.4 Discontinuous Fluid Flow

If the migration of fluids in porous media is observed on the pore level, the flow is observed to be very irregular. This flow is called **Haines jumping** [Greenkorn 122.] [Everett 1975] and [Shaw, T.] discuss the stability of liquid menisci in concave pores and conclude that sudden, dissipative collapse of the meniscus is a direct consequence of the geometry of the pores. This is discussed in detail in Appendix C. [Lenormand] discusses the geometry of fluid displacement in porous materials in terms of two dimensionless groups: the ratio of viscosities of the two fluids and the capillary number, given by

$$Ca = \frac{\eta_i u_i}{\sigma_{ij}} \qquad 5.23$$

where η_i is the viscosity of the fluid being injected

σ_{ij} is the interfacial tension between the two fluids

and u_i is the local velocity of fluid i.

The capillary number is the ratio between capillary forces and viscous forces during fluid flow. For a fluid flowing freely under the influence of capillary pressure, the capillary number can be approximated by combining equations 5.10 and 5.15:

$$Ca \approx \frac{R_{pore}}{12x} \qquad 5.24$$

where R_{pore} is the mean pore diameter from equation 5.10, and x is the characteristic distance across which the capillary pressure varies from zero to $P_0 \approx \frac{2\sigma_{LV}}{R_{pore}}$. During impact of a fluid droplet at a speed of 10 m/s, the capillary number starts at a value of about 40 and drops to zero when the fluid comes to rest.

When the fluid being displaced is air (generally the case in 3-D Printing during feature formation) the viscosity ratio favors a stable planar invasion front except in the limit of very low Ca (creeping flow). For capillary numbers less than 10^{-6} the flow is determined entirely by surface tension. The characteristic of the fluid migration under these conditions is that pores infiltrated are the finest dry pores in contact with the network of filled pores. Lenormand calls this phenomenon **invasion percolation**. He built a 2-dimensional model by photolithography of pores with a distribution of sizes on a flat substrate and sealed the pores with a transparent plate. He observed the fluid migration from pore to pore microscopically as one fluid was injected into an edge of the network to displace another fluid. The fractal dimension for the invasion percolation cluster on a square 2-D lattice is 1.89, and for a 3-D cubic lattice the dimension is 2.5. (Sapoval, Rosso, Gouyet, in [Avnir p. 232]) .

When the viscosity ratio is unfavorable, (e.g. for air displacing a liquid during drying) the geometry of the invasion front is highly dependent on capillary number. In the limit of very low capillary number, the geometry is that of invasion percolation. As capillary number increases, the percolation cluster becomes increasingly delicate and their fractal dimension decreases. The consequence of this is a lower volume fraction of the infiltrating fluid at percolation. This is studied primarily to express the inefficiencies encountered in tertiary oil recovery, but it has important implications on the drying or debinding of ceramic bodies [Cima, Lewis, & Devoe]. The distribution of air in a drying green body is more homogeneous at high capillary numbers because the percolation network forms very early and is able to conduct air to the surface of the body without causing much macroscopic distortion.

The literature of fractal geometry contains several subjects that are of interest in Three Dimensional Printing. There exist many, many computer simulations: for example, [Pietronero] contains papers discussing the mathematics and results of computer

simulations of coagulation, viscous fluid displacements and percolation. Dullien carries a network model of pore infiltration all the way to a prediction of capillary pressure curves. There exist many collections of papers that discuss the kinetics of coagulation and viscous fingering in fluid displacement.

5.6 Conclusion

There are two reasons to pursue a model of capillary migration on the pore level for modelling feature formation in 3-D Printing. The first reason is that the feature size in 3-D Printing approaches the dimensions of the pores in the powder bed. Compare 230 μm for the diameter of a printed line with 50 μm for the largest cavities in the powder bed.

The second reason to pursue a pore-scale model is that the continuum model for fluid migration usually predicts that the saturation will approach S_{W0} asymptotically in time. One of the earliest observations in 3-D Printing research was that printed regions of the powder bed retained their moisture in contact with a nearly infinite supply of dry powder.

5.6.1 Combined Variation of Capillary Pressure and Permeability

The mobility of fluid in a porous medium is a combination of the permeability and the capillary pressure, as exemplified by the moisture diffusivity defined in equation 5.22, above. As the saturation decreases from unity, the capillary pressure increases and permeability decreases, so the variation of their product kP_C, which characterizes the mobility of the liquid in the unsaturated medium, is somewhat indeterminate, and is quite sensitive to the pore size distribution of the powder.

In the illustration below, a somewhat iconic representation of the fluid distribution of fluid in a porous medium is shown at different saturations. Fluid is assumed to fill pores catastrophically (see Appendix C) so as fluid is added at one point to a fully dry sample, pores fill only adjacent to the point of addition. The local saturation is not uniform throughout the sample, and fluid cannot be transmitted across the whole body, so the permeability is effectively zero. At a saturation corresponding to the percolation threshold, the permeability departs slowly from zero (see figure 5.5) and the capillary pressure must necessarily have some finite value. This is different from what is implied by the experimentally derived curve in figure 5.3. The large measured capillary pressures

measured in figure 5.3 must be a consequence of the near-zero permeability at the percolation threshold. If a sample is drained from a fully saturated state to the percolation threshold, it is possible to exert a large capillary suction and not extract any additional fluid. This is a kinetic limit, however, not an equilibrium state.

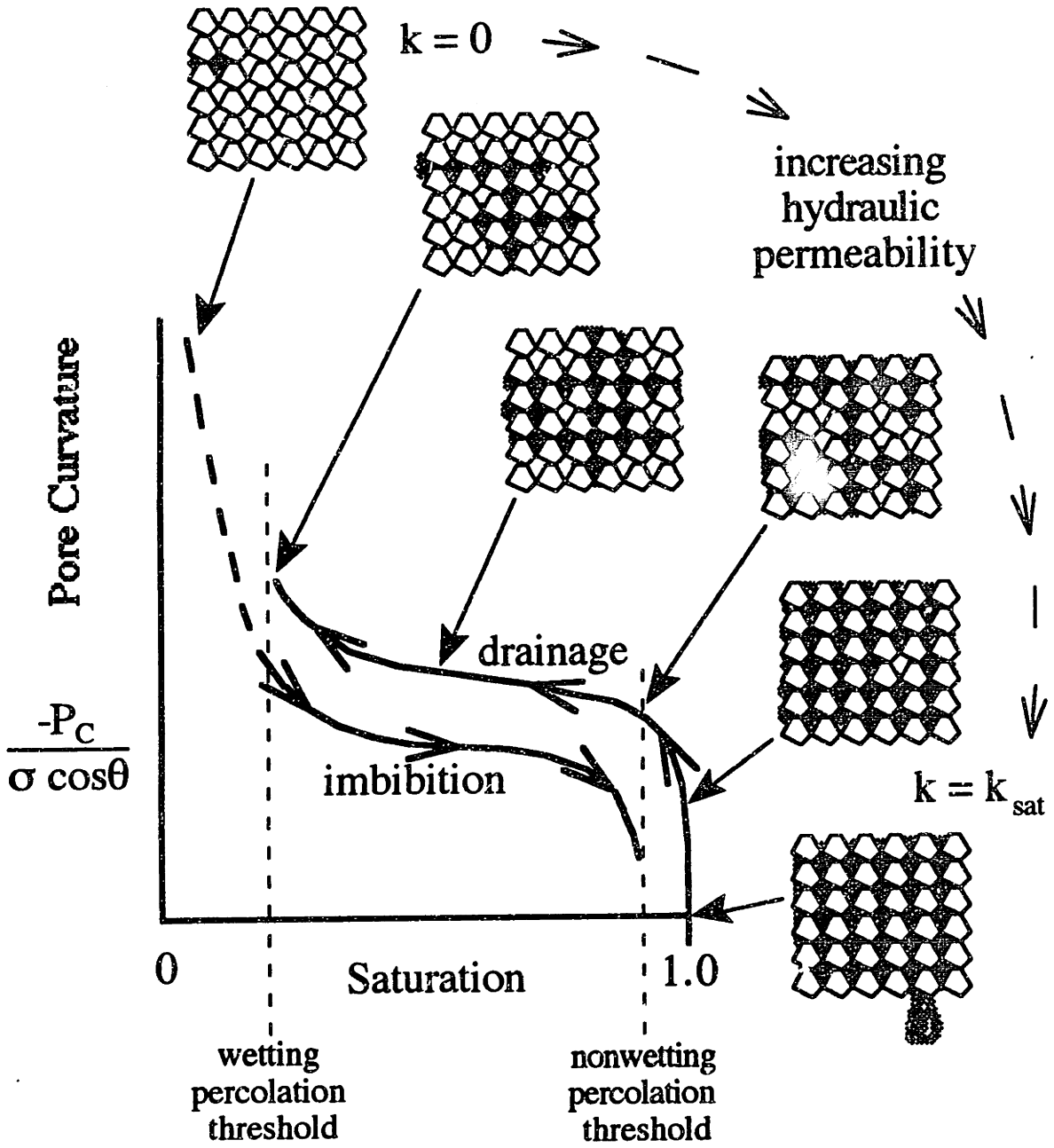

Figure 5.7 Combined variation of capillary pressure and permeability with saturation.

For saturations above the percolation threshold, the network of saturated pores traversing the sample becomes increasingly connected, and the permeability increases towards the upper limit of k_{sat}. In this range of intermediate saturations, the bulk mean saturation is approximately equal to the local saturation averaged across a few grain sizes. The capillary pressure exhibits the hysteresis effect that is characteristic of capillary media. The discontinuity in permeability that occurs at the wetting percolation threshold limits the capillary suction that can be exerted by the dry powder surrounding a printed feature. This limit suction can be measured experimentally, and techniques are described in Chapter 7.

Chapter 6. Feature Formation in Three Dimensional Printing

6.0 Introduction

In 3-D Printed features are a region of powder that has been infiltrated with binder . The spread of the binder in the powder bed in the course of the formation of a feature is driven by the capillary attraction of the liquid for the pores in the powder. The binder used in Three Dimensional Printing must make contact with the material comprising the powder at an angle considerably less than 90°: a contact angle of 30° can be considered large. The fluid is most strongly attracted to the smallest pores in the powder, and the largest pores most easily surrender their fluid in drainage.

The continuum model for capillary migration of a fluid necessarily leads to time-dependent solutions that are unbounded e.g. in [Chang] the fluid migrates outward with increasing time until some other mechanism arrests the migration. One physical limitation to the spread of a wetting fluid in a porous body is the irreducible wetting saturation S_{wo}. [Shaw, T.] discusses the occurrence of inhomogeneous saturation in a porous body as a result of geometric instability of the fluid meniscus (see Appendix C). It is possible, in the system that Shaw modelled, for fully saturated regions of a body to rest in equilibrium with dry regions. By considering the geometric instability of the liquid meniscus over a range of intermediate bulk saturations, the liquid is found to migrate in a series of discontinuous jumps as pores make the transition from nearly unsaturated to fully saturated. These discontinuities are called **Haines jumps** in the literature[Greenkorn 122] and network models for certain types of flow have been developed [Lenormand]

6.1 Rate Calculations in the Formation of Printed Features

From the instant of binder impact on the powder bed, there are a number of physical processes that take place which result in the formation of a printed feature. It is extremely important to have a reasonable estimate of the time scales over which these processes evolve: one process, e.g. coagulation, can arrest another, capillary migration, and it is important to know whether the migration has sufficient time to resolve itself before coagulation arrests it.

What follows is a collection of order-of-magnitude calculations based on approximate values of the relevant kinetic parameters of the powder\binder interaction. Although some of the parameters are known with fairly good precision, the approximate nature of this comparison and the lack of precision to which other parameters are known make it unnecessary to go into great detail here. The phenomena that lead o the formation of 3-D Printed features are discussed below in approximately the order of time that they develop.

6.1.1 Jet Impact

a. Deceleration

Droplets of binder impact the powder bed at a velocity of 10 m/sec. The jet is observed to penetrate a distance of approximately 500 μm. Since the liquid decelerates to rest across this distance, the deceleration time is roughly 10^{-4} sec. The deceleration is 10^5 m/sec^2, or about 10,000 g. During this time, if the printhead is depositing straight lines, approximately six more droplets impact the powder bed at a spacing of about four per droplet diameter. These droplets surely coalesce before coming to rest. Accordingly, the formation of features in 3-D printing is primarily the formation of linear features, not single droplet primitives, unless the droplets are spread out so they do not land on top of one another.

6.1.2 Line Coalescence

a. Damped Capillary Oscillator

High-speed photographs suggest that the flat binder stripe coalesces into a cylindrical line in a time of approximately 2 x 10^{-3} sec after impact. The mass of the feature is assumed to be concentrated at the edges of the stripe and the surface tension of the liquid draws the edges together.

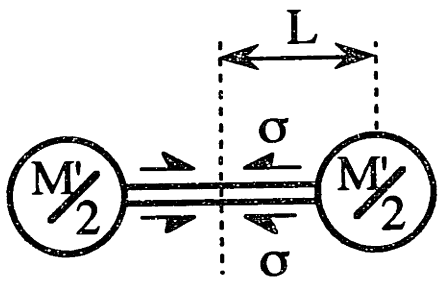

Figure 6.1 Dynamics of feature coalescence

The acceleration of the mass at the edge is given by

$$\frac{d^2x}{dt^2} = \frac{4\sigma_{LV}}{m'} \approx \omega_n{}^2 L \qquad 6.1$$

where x is the coordinate across the coalescing stripe,

σ_{LV} is the surface tension of the binder $\approx$ 50 dyn/cm

M' is the mass per unit length $\approx 5.4 \times 10^{-4}$ g/cm

L is the half-width of the stripe $\approx$ .025 cm

ω_n is the natural frequency of the (undamped) oscillator.

The natural frequency of the undamped system is approximately 4×10^3 sec^{-1}. If we assume that the system is critically damped, the settling time is approximately

$$t_s \approx 4/\omega_n = 10^{-3} \text{ sec.} \qquad 6.2$$

It is likely that powder densification, if it occurs in the system under consideration, occurs during this period, since this is the primary rearrangement of the material comprising the feature. Since the capillary coalescence time is an order of magnitude longer than the impact time, the impact can be assumed to be ballistic.

6.1.3. Capillary Migration

a. Washburn Infiltration

The rate of imbibition was measured in a Washburn-type arrangement using binder and powder. The Washburn rate is given by

$$\frac{x^2}{t} = \frac{2k_{sat}P_0}{(1-f_{powder})\eta} \qquad 5.16$$

and was measured to be 0.3 cm^2/sec in powder with a packing density of 0.44. (see section 7.10.) The time for migration from a standing pool (which might exist immediately after impact) to a distance 250 μm from the point of impact is 2 x 10^{-3} sec. Although this time is well below the asymptotic limit derived by Levine and Neale, this will serve as an approximate estimate of the rate of imbibition of the liquid directly following impact. This rate directly competes with the rate of capillary coalescence derived above, and most likely prevents the phenomenon of "balling" described below in section 6.2.1.

(From this measurement, we obtain the estimate of 2.5 x 10^{-4} Pa-cm^2 for the product $k_{sat}P_0$. The suction pressure of powder for binder is approximately 20,000 Pa, so the hydraulic permeability can accordingly be estimated: $k_{sat} \approx 1.2 \times 10^{-8}$ cm^2.)

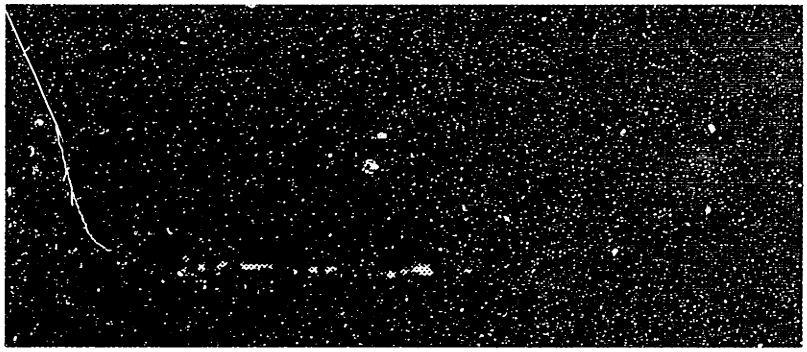

Figure 6.2 Binder trail on locked 20 μm stainless powder. Liquid pools on the powder surface can be clearly seen because they reflect light from source behind jet. Trail is about 2 mm long, and the printhead speed was 1.65 m/s. The imbibition time was accordingly 1.2 x 10^{-3} sec. Photo courtesy of Steven Michaels.

In the photograph above, a liquid trail is seen behind a travelling jet. This powder is the same material as that shown in figure 6.4, below, except that the powder has been locked in place to prevent coalescence of the printed line into a cylinder.

b. Chang Infiltration

Using the equation developed by Chang (see section 5.5.2) for cylindrical fluid migration in a capillary medium with saturation-dependent permeability:

$$r(t) = r_0\left(\frac{n+1}{n}\right)^{1/2}\left(\frac{4D_M t}{r_0^2}\right)^{1/(2n+2)} \qquad 5.21$$

where r_0 = the initial radius of the pool formed by the droplet, ≈ .01 cm
$n = (1+2\Lambda)/\Lambda$ after Brooks and Corey [Bear p.465]

$$D_M = \frac{P_B k_{sat}}{\eta\Lambda\left(1-f_{powder}\right)} \qquad 5.22$$

P_B is the bubble pressure of the medium, ≈ 20,000 Pa
k_{sat} is the hydraulic permeability of the saturated medium, ≈ 1.2×10^{-8} cm^2
η is the fluid viscosity, ≈ 3×10^{-3} Pa-s
Λ is the pore size distribution index (from equation 1.6) ≈ 4
($1-f_{powder}$) is the porosity of the powder bed. ≈ 0.6

we obtain a value of $D_M = 3.4 \times 10^{-2}$ cm^2/sec for the moisture diffusivity, and

$$r(t) = 1.2\, r_0\left(\frac{4D_M t}{r_0^2}\right)^{0.154} \approx .036\ (t)^{.154} \qquad 6.3$$

where r is in centimeters and t is in seconds.
The greatest distance to which a line of initial radius 100 μm could reasonably spread is a radius of about 250 μm, and it would spread this far in approximately 0.09 sec.

c. Pressure Equilibration

As a final estimate of the rate at which capillary pressure is equilibrated across large distances in a fully saturated feature, we can use the value of the moisture diffusivity to estimate the propagation rate of capillary pressure gradients in the medium:

$$t_K = \frac{x^2}{4D_M} \qquad 6.4$$

The time to propagate 250 μm is 4.6×10^{-3} sec; and the time to propagate 1 mm is sixteen times longer.(.074 sec .)

6.1.4 Coagulation

The immobilization of the binder in the powder bed after a moderate time is used to prevent bleeding due to gravitational head. This phenomenon is discussed in detail in section 6.4, below. The requirement is that the binder in a given layer be immobilized before several layers can be built over it.

a. Homogeneous Flocculation

The characteristic time for the formation of particle pairs by diffusion-limited aggregation is approximately $t_{½} = 6 \times 10^{-4}$ sec for the binder composition that is presently used. (equation 2.30) A computer model by Meakin [Avnir, p. 154] suggests that flocs in a homogeneous suspension grow proportional to $t^{1.45}$ in number, and to $t^{0.68}$ in size. The aggregation of flocs in a homogeneous suspension proceeds with a low time exponent because the diffusivity of flocs decreases with increasing size, and the space between them increases. (See section 2.2.9 a.) From equation 2.9, it was estimated that in binder, when the flocs contain about 70 particles, they are large enough to bump into one another, effectively forming a space-filling gel. The homogeneous gelation time can thus be calculated:

$$t_{70} \approx t_{½}(70)^{1.45} \approx 10^{-2} \text{ sec.} \qquad 6.5$$

This is the time to coagulate if the turbulence of jet impact is sufficient to dissolve enough citric acid to initiate coagulation. This assumes that the citric acid is evenly distributed in the powder bed, and constitutes an lower bound to the gelation time

b. Gel Growth

The binder gel growth rate was measured in section 3.5.2. The ordinary concentration of citric acid in the powder was approximated by the curve obtained with a citric acid solution of 0.1 mol/l: the rate was 0.00122 cm/√sec, and the diffusivity of citric acid through gelled binder was calculated to be 1.9×10^{-6} cm²/sec.

If the citric acid is poorly distributed in the powder bed, the acid must diffuse upward from the previously printed layer. The time for a film of gel to grow across a 200 μm layer is 270 sec.

If the citric acid is very well distributed in a thin coating over the surface of all of the powder grains, the distance across which the gel must grow is approximately equal to the pore radius, about 4 μm. The time for a film of gel to grow to this depth is 0.1 sec.

In practice, the distribution of citric acid is probably somewhere between these two extremes. If the gel must grow a distance on the order of the grain size, the time to gel is 6 sec.

6.1.5 Drying

a. Mass Transfer Rate

The rate of evaporation of water from an exposed surface without forced ventilation is approximately 1.3×10^{-4} g/sec-cm^2. [Gendler & Sporer] The rate per unit length is accordingly 2.6×10^{-6} g/sec per cm of line length. A typical printed line contains 1.6×10^{-4} g/cm of binder, of which approximately 60% of the weight is water. Since binder "B" is diluted approximately 50% with water, binder should coagulate when 30% of its volume has evaporated. The time for this to occur is

$$\frac{.3 \times 1.6 \times 10^{-4}}{2.6 \times 10^{-6}} = 18 \text{ sec.} \qquad 6.6$$

This period is far to long for evaporation to affect the migration of binder in the powder bed, but it is in the range of time over which the machine operates. The evaporation of water continues after the binder has coagulated, and water can condense in dry powder, causing the appearance of moist powder surrounding the part after sufficient time has elapsed. This phenomenon is different from bleeding, but if the powder moistened by condensation approaches a saturation of S_{WO}, this could affect the migration of binder during printing before coagulation.

6.1.6 Machine Operations

The printhead typically travels at a rate of 1.5 m/sec over the powder bed, and returns to print adjacent lines in a minimum of 0.5 sec. The time to print an entire layer can vary from 10 sec to 300 sec, and the spreading operation typically takes about 20 sec. A typical small part can take as little as 1000 sec and a large part can take > 10^5 sec.

Following printing, the part is baked in an oven which takes approximately 3000 sec to raise the temperature above the boiling point of water. The remainder of the firing schedule can take from 10,000 to 20,000 sec.

The thermal diffusivity of freshly printed material can be estimated by assuming that the material is 50% alumina and 50% water by volume, and the thermal diffusivity is the volume-weighted average of thermal diffusivities of the components. The rationale for doing this is that heat cannot conduct directly from particle to particle, but must pass through liquid to bridge between particles. The diffusivity of water is about .02 cm2/sec and for alumina it is about 0.6 cm2/sec. The approximate thermal diffusivity of freshly printed material is accordingly 0.3 cm2/sec. The unprinted powder surrounding the part must be at least an order of magnitude less.

6.1.7 Time Line for Feature Formation

The most convenient way to compare the rates at which the various phenomena described above is to make a graph of propagation distance for a given phenomenon versus the time after jet impact over which it could be active. For example, the various forms of infiltration and coalescence cannot begin until the binder has come to rest after impact. The line for gel growth starts at the earliest point at which is could potentially arrest binder migration if it is coating the surfaces of the powder grains. Homogeneous flocculation can arrest the binder migration only if the citric acid is dissolved and mixed with the binder during impact. It is more typical for the citric acid to be mixed as coarse granules, so the characteristic time for gel growth tends to the upper extreme.

Of the two models proposed for capillary migration, both are sufficiently rapid to have fully matured before any of the three proposed mechanisms for arresting migration can prevent binder from migrating outside of the observed size of printed features. The capillary time is also much faster than the time for the printhead to reciprocate. It can therefore be concluded that 3-D Printed features are linear features, and the distribution of binder within them reflects the equilibration of capillary forces.

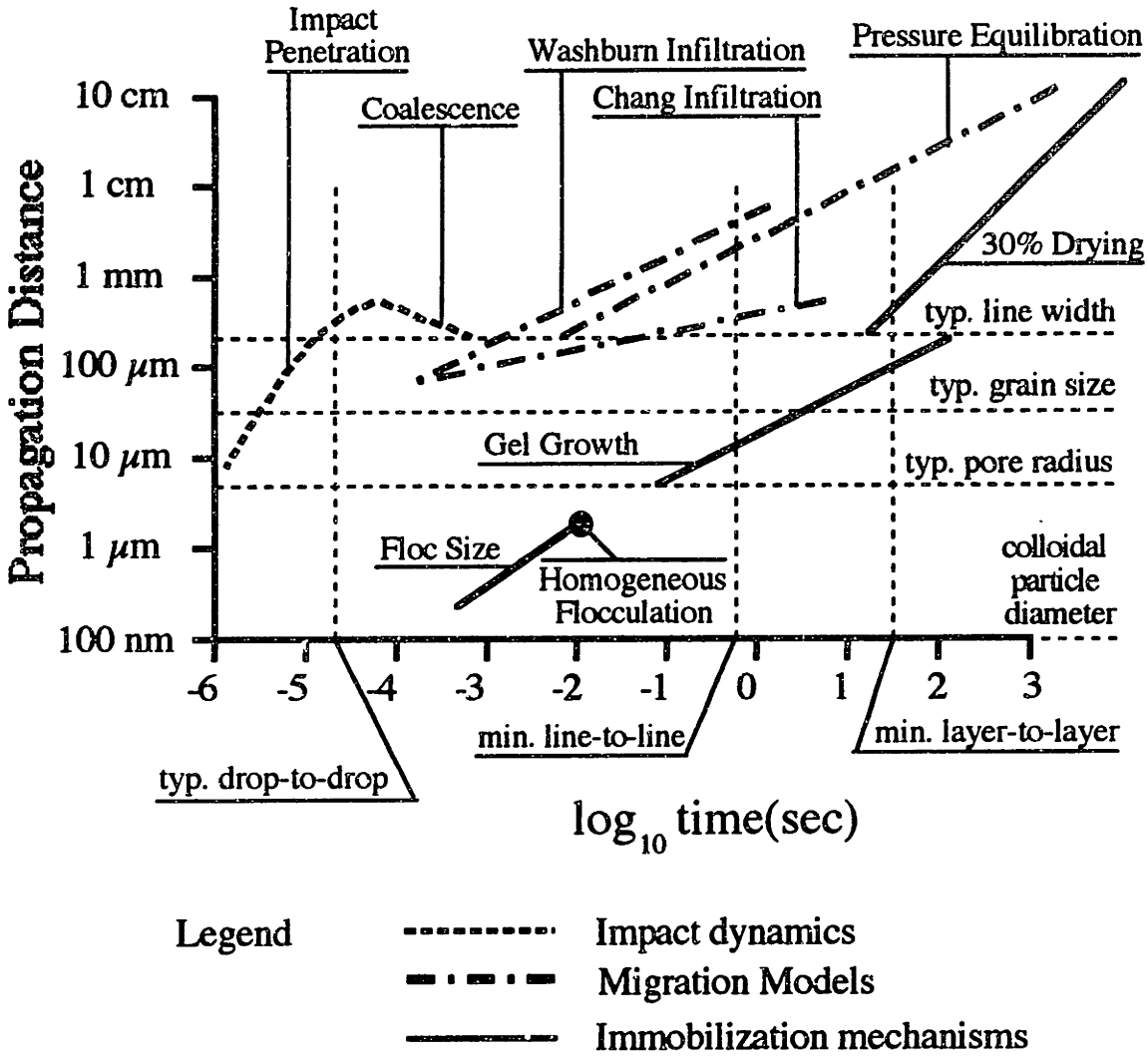

Figure 6.3 Time line for feature formation. Rates are calculated assuming a line diameter of 200 μm printed into lamellar alumina. The rates of capillary migration tend to scale proportional to the grain size. Time for gel growth to arrest capillary migration depends on the degree to which the gelling agent is dispersed in the powder. These are approximate calculations, any of which could vary by as much as a factor of two.

The gelation rate is just barely fast enough in the worst case to prevent gravitational bleeding. If layers are generated at a rate of two per minute, then six layers can be produced before the gel can grow the thickness of one layer. If problems are observed, two strategies to solve it are to increase the citric acid content of the powder (which increases the growth rate) or to distribute the additive more evenly in the powder bed (which decreases the thickness of gel necessary to immobilize the binder.) In recent results with multijet printheads, it has been found necessary to increase th cid content to alleviate some bleeding. It is likely that the compression exerted by the ler can squeeze binder out of printed material if several layers are present that have not yet gelled.

The flip-side to this problem is that the deformation probably improves the knitting of layers.

The rate of homogeneous coagulation is potentially fast enough to limit the migration of binder. This is the time it would theoretically take for flocks of binder to form which intersect with one another and form a space-filling network. If the citric acid is sufficiently well distributed in the powder, this rate could successfully compete with the later stages of capillary migration.

The rate of drying is shown to reflect one-dimensional drying from an exposed face; the propagation distance given is the depth to which the binder would be 50% depleted in water at a uniform drying rate. This is somewhat artificial, since the drying affects the capillary pressure, and the capillary equilibration rate is quite fast enough to transport liquid to the surface. Also, the evaporation rate of pure water has been used in the calculation: the presence of humectants reduces this somewhat. This makes distortion due to drying less important until the binder gels and reduces the transport rate.

6.2 Definition of a Hydraulic Feature

A model for feature formation requires a very specific definition of a feature that makes sense in the context of capillary migration. Since the model that follows depends on a pressure balance, a **hydraulic feature** is defined as a region of moistened powder across which fluid pressure can be transmitted. This necessarily requires that the fluid be in the pendular state, above the irreducible saturation S_{W0}. The feature can be at equilibrium if the fluid pressure is uniform. If a gradient in pressure exists, fluid can redistribute within the feature to neutralize the gradient. Areas out of hydraulic contact with each other cannot be considered part of the same feature.

6.2.1 Feature Size and Migration Phenomena

Under this definition, all portions of a 3-D Printed part that are connected by liquid bridges constitute a single feature. In discussing the accuracy of 3-D Printing, the term **feature size** is used to describe the smallest detail that can be printed by a given machine. The minimum size of a hydraulic feature in a given machine corresponds to this feature size, whether it has time to equilibrate or not. The feature size depends on two parameters:

the quantity of liquid deposited by the printhead and the degree to which the liquid spreads in the powder away from the point of impact. Feature size is distinct from **accuracy** in a printer. Features of a given size can be placed by the machine with a positioning error considerably smaller than their size. Feature size is influenced by the inhomogeneities of the powder bed, so the accuracy is limited by the uncertainty in feature size imposed by the pore structure and particle size of the powder.

Assuming that crisply defined spots or lines are delivered by the printer to the upper surface of the powder bed, further movement of printed binder is influenced by the distribution of fluid in the powder surrounding it. Two migration phenomena have been defined in 3-D Printing: **bleeding** is the macroscopic flow of binder in droplike features at high saturation that usually hang off the bottom of a large part. This effect was studied by Chris Harris in his SB Thesis. It is distinguished form **feathering** which is the microscopic spread of binder from the point of impact and is observed as a broadening and softening of printed lines. In both cases, fluid travels down a gradient of pressure, but the driving force for the former is evidently gravitational pressure, and for the latter, capillary attraction. A third phenomenon, that of **balling** results from failure of the binder to soak into the powder bed, curling up into a supersaturated ball on the printed surface.

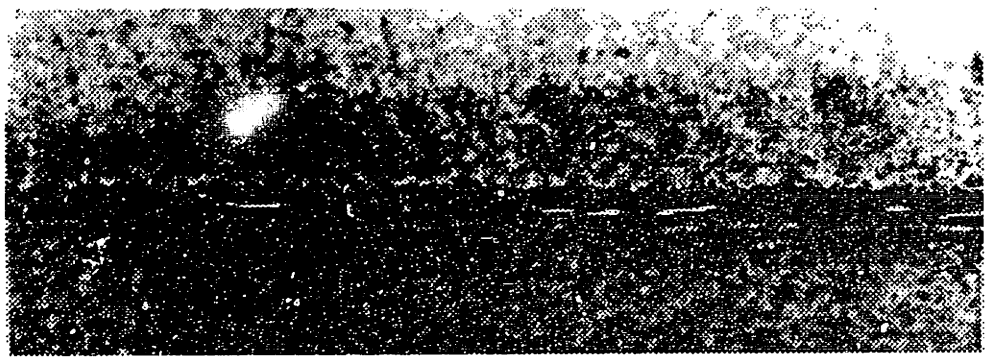

Figure 6.4 Ball formation in 20 μm stainless powder. [Michaels, 36]

The cylindrical lines that form in the capillary coalescence that occurs immediately after impact are mechanically unstable in the same way as the liquid jet emerging from the printhead nozzle. If the rate of capillary migration is not sufficiently high, the fully saturated cylindrical features will break up into spherical balls before binder can migrate into the powder. This phenomenon was caught in process by Steve Michaels by high-speed photography of feature formation in stainless powder. In figure 6.4, a printed line of latex binder is seen breaking into segments approximately .01 sec after the passage of the jet.

6.2.2 Real Porous Bodies and the Fantasy of "Pore Size".

In an actual bed of powder, particles are stacked at random, and there exists a random distribution of pores in a range of sizes. In the micrograph below, the powder bed is comprised of so-called "lamellar" particles with a hydrodynamic diameter of 30μm. Pores can be distinguished, but the concept of "pore size" is deceptively simple. In the experiments normally done to characterize the pore size of a material, the capillary pressure is measured as the fluid content is varied. In a granulated powderbed, the space not occupied by particles is an exceedingly complicated network of channels, gaps, nooks, corners, holes, etc.

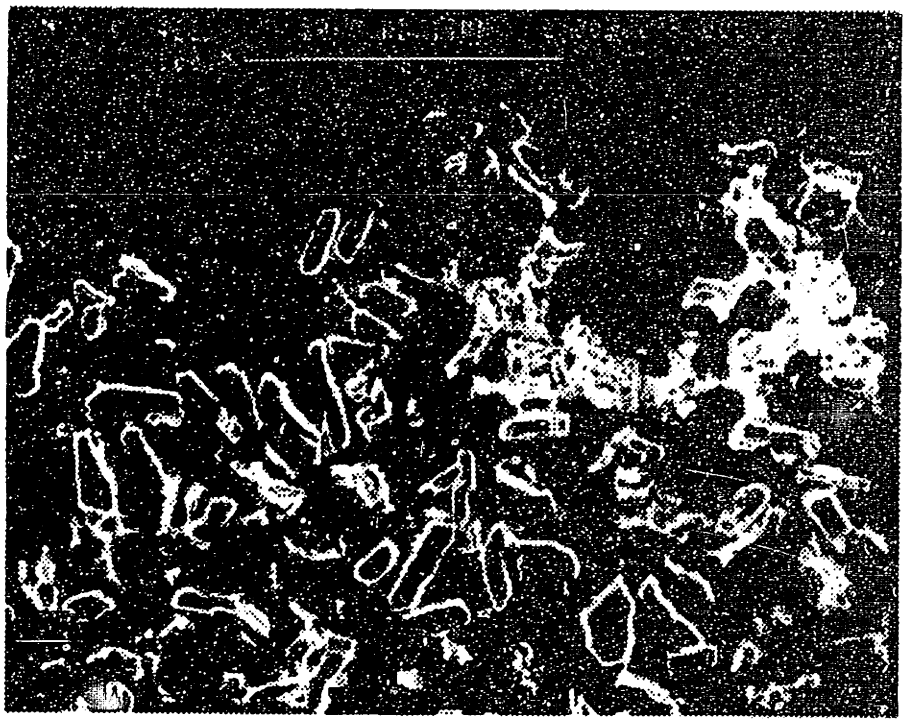

Figure 6.5 SEM micrograph of a line section in sintered powder. M = 354 x (S1)
Particles outlined in white: Norton 30 μm 7920 alumina, packing density 37%.
Bright white splat: Silica deposit from a single trace of colloidal silica under "standard" printing conditions. Silica dose: 0.0193 mm2 of silica (Volume/Length).
Binder "A"(16 vol.% 100 nm SiO_2 in 90%-H_2O/10%-TMAH, Biocide to taste).
Saturation on printing was near 100%; silica remaining has "saturation" near 15%.

Different fluids occupy different spaces in this structure. The wetting fluid shown above is the bright white right of center of the picture, and the particles are highlighted polygons filling the lower 2/3 of the frame. The upper surface of the powder bed is a line that traces the upper extent of the particles in the field of view. The spidery structure of the liquid

splat is a result of the attraction of the liquid to the tightest corners between grains in a region roughly 200 μm across and 100μm deep.

6.2.3 Pore Curvature as an Analog for Pore Size

The meniscus is curved in a very complicated way in this feature, and it is difficult to estimate its magnitude by direct measurement. The capillary pressure is the easiest (though not particularly easy) quantity to measure that can be unambiguously related to a pore size. For the purposes of modelling 3-D printing, it is the capillary pressure that is the driving force for fluid migration. There is, in fact, no reason whatsoever to introduce a pore "radius" except for illustrative purposes. The appropriate state variables in the hydrodynamics of porous materials are the fluid volume and the capillary pressure, and the pore "radius" is simply a derived quantity from the capillary pressure:

$$P_c = \frac{-2\sigma_{LV}\cos\theta}{r} = -K\sigma_{LV}\cos\theta \quad . \qquad 6.7$$

The difference in capillary pressure between imbibition and drainage of a fluid defines two characteristic pore curvatures for a single pore and for an ensemble of pores. The critical nonwetting curvature, K_{NW} is defined by the the bubble pressure, P_B, which is the suction pressure necessary to pull air through saturated powder. The critical wetting curvature K_W is defined by P_0, the suction pressure exerted by the dry material on a fluid source at the lower limit saturation S_{W0}.

$$K_W = 2/R_W = \frac{-P_0}{\sigma_{LV}\cos\theta_{adv}} \qquad 6.8$$

and

$$K_{NW} = 2/R_{NW} = \frac{-P_B}{\sigma_{LV}\cos\theta_{rec}} \qquad 6.9$$

where θ_{adv} is the advancing contact angle, and θ_{rec} is the receding contact angle.

The connection between the critical pore radii for a single pore with those for a pore network is made by assuming that fluid cannot communicate from one pore to the next until the pore is completely saturated. The transition from the unsaturated to saturated state is a Haines jump. Fluid is prevented from passing into the bulk of a porous material until the pressure reaches the critical pressure for a sufficient population of pores to form a percolating cluster. The same explanation holds equally for both wetting and nonwetting fluids.

6.3 Equilibrium Capillary Pressure in a Hydraulic Feature

The quantities R_W and R_{NW} characterize the pore geometry of the powder bed in a way that is relatively independent of the surface tension and contact angle of the binder. These two radii are the dimensions of analogous cylindrical capillaries that exert the same capillary pressure as the dry powder and the saturated feature, respectively. The feature is in hydraulic contact with the dry powder that surrounds it, so fluid can be drawn out into the dry powder from the feature. A fully saturated hydraulic feature can be modelled as a cavity penetrated by with two capillaries, one with radius R_W that represents the trail of dry pores that lead out into the bulk powder bed, and the other with a radius R_{NW} that represents the trail of saturated pores that guide air into the feature. (See Appendix C, section C.4.2)

There is always dry powder outside the feature, so the pressure exerted by the surroundings remains constant. The pressure of the liquid within the feature depends on the state of saturation and the drainage characteristics of the powder. For a fully saturated feature the pressure is greater than or equal to $P_B = -K_{NW}\sigma_{LV}\cos\theta_{rec}$. but as drainage proceeds, the pressure decreases (i.e. the suction becomes stronger.)

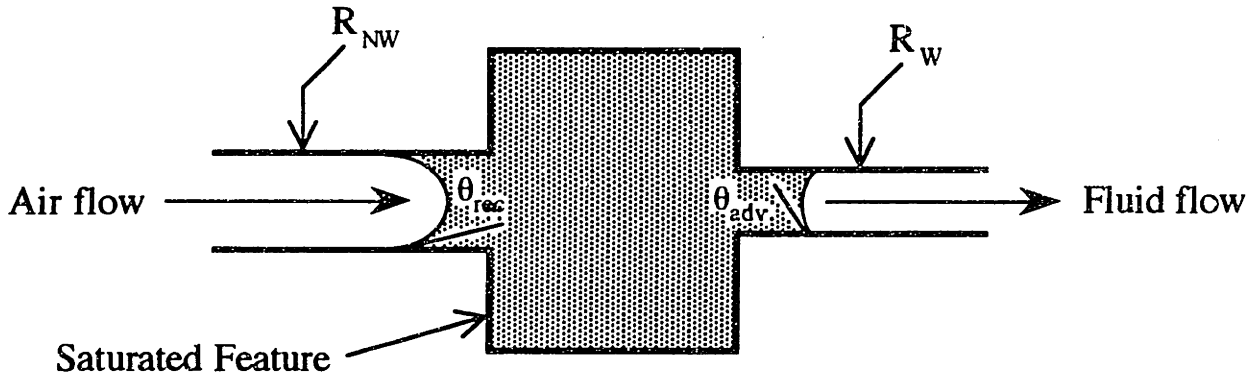

Figure 6.6 Metastable equilibrium of a liquid in a hydraulic feature.

Liquid pressure can be transmitted across this feature. The boundaries of the feature are a little bit unclear in this illustration: all portions that come to pressure equilibrium with one another are included. Besides fully saturated portions, pores that have been drained but are still in hydraulic contact are included, as are the pores that form

the boundary between dry and moist powder. It is convenient to view these hypothetical capillaries as chains of pores in the powder with the characteristic radii.

6.3.1 Excess Pressure in a Fully Saturated Feature

If the pressure within the smaller capillary is lower than the pressure in the larger capillary in figure 6.6, fluid will spontaneously migrate from left to right down the chain of narrow pores out into the dry powder surrounding the feature. One can express the excess pressure in the feature as the difference in capillary pressures between the fluid outlet path and the air inlet path:6.10

$$\Delta P = - P_0 + P_B \qquad 6.10$$

which in terms of the critical radii becomes

$$\Delta P = 2\sigma_{LV}\left[\frac{\cos\theta_{adv}}{R_W} - \frac{\cos\theta_{rec}}{R_{NW}}\right] \qquad 6.11$$

or alternatively,

$$\Delta P = \sigma_{LV}\left[K_W \cos\theta_{adv} - K_{NW} \cos\theta_{rec}\right]. \qquad 6.12$$

If this excess pressure is zero, there is no driving force for binder to depart from saturated regions into unsaturated regions of the powder bed. It is most frequent that the binder is highly wetting to the powder, and that $\cos\theta_{adv} \approx \cos\theta_{rec} \approx 1$. Under these conditions, the difference (K_W-K_{NW}) defines the driving force for binder migration away from a fully saturated feature. The convenience of using this representation with pore curvatures K_W and K_{NW} is that measurements of the critical capillary properties can be made with any liquid, and the results converted directly into capillary pressures.

6.3.2 Equilibrium Condition

In any local region of the powder bed, the fluid content changes monotonically: saturated regions tend to drain, and dry regions tend to become more moist. As a feature becomes less than fully saturated, the excess capillary pressure is proportional to the difference [$K_W\cos\theta_{adv}$-$K_{drainage}\cos\theta_{rec}$] where $K_{drainage}$ is variable with saturation. The condition for hydrostatic equilibrium of a feature is

$$K_{drainage}(S^*) = K_W \qquad 6.13$$

at the equilibrium saturation S* within a feature surrounded by an infinite quantity of dry powder.

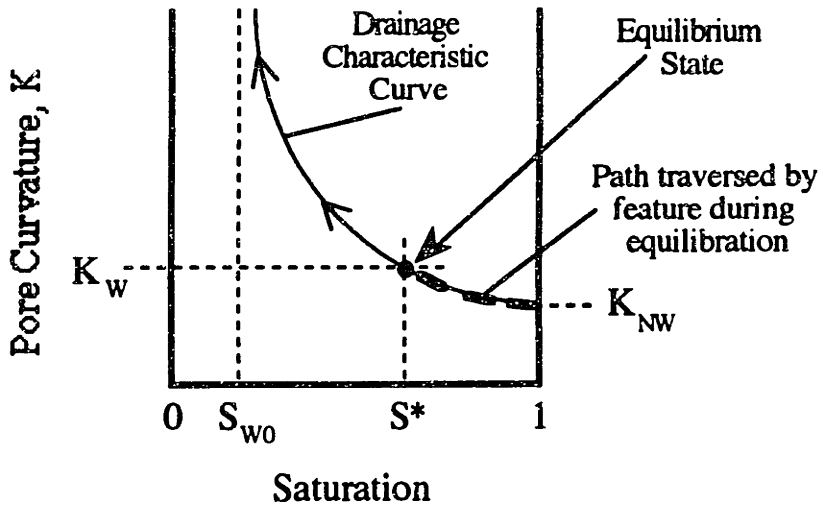

Figure 6.7 Pore Curvature/Saturation characteristic of a porous powder bed in drainage. K_W is proportional to P_0, K_{NW} is proportional to P_B. Shown is the equilibrium condition for a feature when $\cos\theta_{adv} \approx \cos\theta_{rec} \approx 1$.

The dependence of capillary pressure on saturation is illustrated above for a porous material. The capillary pressure within a feature is fixed by P_0, the capillary suction of the dry material surrounding the part. The equilibrium state is the saturation at which the pressure is equal to P_0.

6.4 Gravitational Bleeding

The effect of gravity on the hydrostatic pressure within a feature can cause fluid to flow downward out of the boundaries of the feature. This is generically referred to as **bleeding** in 3-D Printing, and was first studied by Chris Harris, in his SB thesis. The effect may be accounted for by adding the gravitational head to the expression for excess pressure in a feature

$$\Delta P = gh\rho_{liquid} + \sigma_{LV}\left[K_W \cos\theta_{adv} - K_{NW} \cos\theta_{rec}\right] \qquad 6.14$$

assuming that the entire printed part to a depth of h constitutes a single hydraulic feature. If the excess pressure is positive, the quantity of fluid available for bleeding is a substantial fraction of the total volume of the part. Some quite large positive volume defects can be formed by gravitational bleeding. Solving for h at $\Delta P = 0$:

$$h = \frac{-\sigma_{LV}\left[K_W \cos\theta_{adv} - K_{NW}\cos\theta_{rec}\right]}{g\rho_{liquid}} \qquad 6.15$$

Since the quantity in the square brackets in equation 6.15 is usually positive, gravitational bleeding will always be a problem unless some mechanism is provided to immobilize the fluid in the powder bed soon after each layer is printed. This can be explained by the following argument. The minimum capillary suction everywhere in a feature is set equal to P_0 by the suction of the dry powder. The gravitational field induces a pressure gradient from the top to the bottom of the feature, so the fluid at the top has a higher suction imposed on it than that imposed by the dry powder. New saturated regions that are printed at the top feed binder downward which percolates out into the dry powder surrounding the bottom of the feature.

Immobilization of the binder is accomplished in some cases by drying the binder between printing each layer, and in other cases by coagulating the dispersed solids in the binder. Strategies that merely increase the fluid viscosity only slow the rate of bleeding, but this delay could allow the part to dry before substantial bleeding takes place.

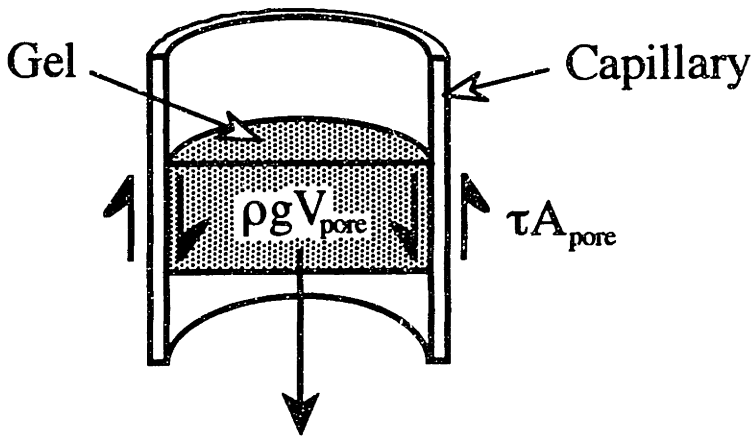

Figure 6.8 Force balance on a plug of gel in a capillary.

The strength requirement of the immobilized binder can be estimated by considering a force balance on a plug of gel in a model vertical capillary:

$$\rho g V_{pore} = \tau A_{pore} \qquad 6.16$$

A_{pore} is the surface area of the capillary and V_{pore} is the volume of the capillary. The ratio

$$\frac{(1-f_{powder})A_{pore}}{V_{pore}} = \textbf{specific surface area} \qquad 6.17$$

is the same order of magnitude as the reciprocal of the grain size of the powder. For 30 μm powder packed to 50% density infiltrated with water, the minimum gel strength necessary to resist gravity is ~ 0.1 Pa. The strength of binder gel has been measured (see section 4.5.3) to be on the order of 500 Pa: roughly the strength of yogurt. It is difficult to imagine a material that could have a "strength" of 0.1 Pa.

The capillary suction of dry powder for binder is roughly 20 kPa, well above the yield strength of the gel, but it has been shown above that the liquid has sufficient time to come to capillary equilibrium before gelation can occur. The onset of gravitational bleeding occurs after several layers have been built, with takes a few minutes with current hardware. The water contained within the gelled binder is free migrate through the gel, but the gel has a very small permeability.

6.5 The Bulk Properties of Single Lines

6.5.1 Binder and Power Dose, Saturation, Porosity, and Line Diameter

The dependence of pressure and saturation has heretofore been discussed considering "bulk" material, without directly considering the geometry of the formation process. The kinetics of feature formation have been shown above (section 6.1.1) to constrain the capillary migration of the binder into linear "primitives" in which the fluid binder is distributed evenly in one dimension (x) along the top surface of the powder bed, and fluid is constrained to migrate in the semi-infinite y-z plane below the powder surface. This is a slight oversimplification, since the jet penetrates the bed slightly and forms a trench in the powder. The geometry of line formation is illustrated below. The printhead moves with a velocity V_x over the powderbed and dispenses binder at a mass flow rate of $\dot{m}$. If the density of the binder is ρ_{liquid}. We can define the **binder dose**

$$A_{liquid} = \frac{\dot{m}}{V_x \rho_{liquid}} \qquad 6.18$$

which corresponds to the binder volume per unit line length. Each of the quantities used to calculate the dose are controlled by the machine operator to a very high accuracy, so the

dose is usually known to an accuracy of ±1% or better. The impact of the jet scatters the liquid and powder on a local scale, and such properties as the isotropy of the part strength can be directly related to the structure. For the purposes of this research, however, the binder dose will be assumed to be homogeneous.

It is possible to define an analogous quantity for the powder , A_{powder} , which corresponds to the volume per unit length of powder grains contained in a line.

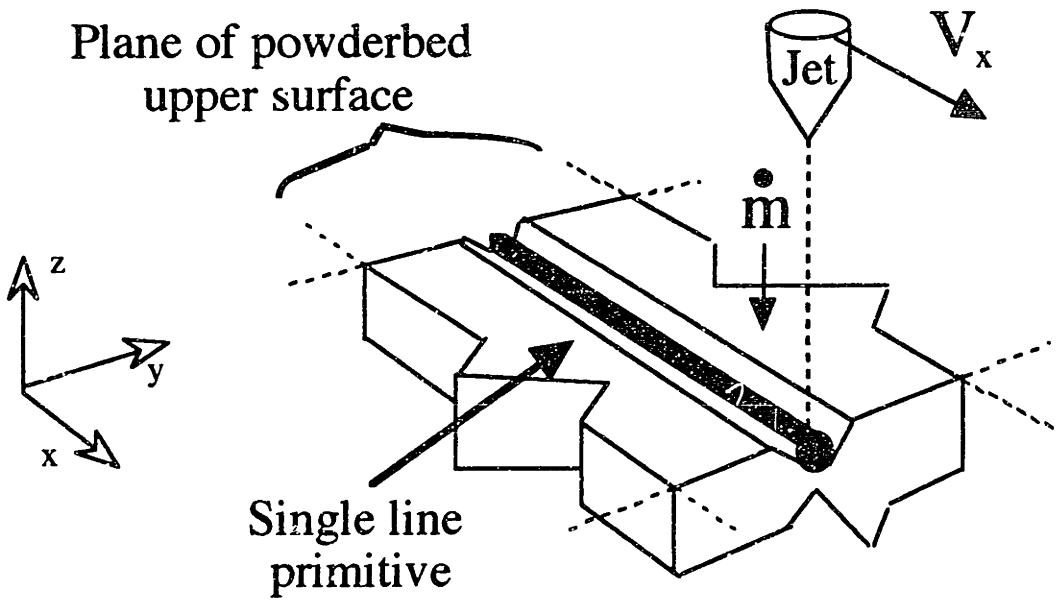

Figure 6.9 A simplified view of line printing.

The powder bed has a fractional density given by

$$f_{powder} = \frac{\rho_{bed}}{\rho_{powder}} . \qquad 5.1$$

and

$$porosity = 1 - f_{powder} . \qquad 5.2$$

The saturation has been defined earlier as the fraction of the pore space filled by liquid:

$$S = \frac{f_{liquid}}{1 - f_{powder}} \qquad 5.4$$

Where f_{liquid} is the local volume fraction of liquid in the powder bed. In one-dimensional features:

$$f_{liquid} = \frac{A_{liquid}}{A_{feature}} . \qquad 6.19$$

In a bulk part, a certain volume is allotted for each line by the rasterization algorithm. If the distance between lines is Δy and the layer thickness is Δz, then the mean saturation in a macroscopic part is completely defined:

$$S_{bulk} = \frac{A_{liquid}}{(1 - f_{powder})\Delta y \Delta z} \quad . \qquad 6.20$$

The packing density of the powder after printing can be different from the density of the powder as spread. Two major contributors to this change are the shock of the jet impact and consolidation of the powder under the capillary stress that exists within a partially saturated feature. The packing density is found from the powder dose, A_{powder}, by

$$f_{powder} = \frac{A_{powder}}{\Delta y \Delta z} \quad . \qquad 6.21$$

In a single line feature, the space surrounding the saturated region is unbounded, and the cylindrical diameter d_{line} is determined by the balance of capillary forces within the feature.

$$\frac{\pi d_{line}^2}{4} = \frac{A_{liquid}}{(1 - f_{powder})S_{local}} = \frac{A_{powder}}{f_{powder}} \quad . \qquad 6.22$$

The quantities A_{liquid} and A_{powder} are the easiest to measure accurately in a laboratory because they can be deduced from weight measurements. To measure the equilibrium binder saturation, it is necessary to independently measure either the porosity or the line diameter of a feature. Since the porosity could change from the bulk value in the course of printing, the most accessible quantity is the line diameter. The complications with this strategy will be discussed below.

6.5.2 Equilibrium Saturation Defines the Operating Point

Since a bulk part is composed of single line features, there is a potential conflict in the functional dependence of the binder saturation. For single features, the saturation is determined by the capillary forces (section 6.3). This must be the saturation determined by machine parameters as well, otherwise the bulk feature will not be stable with a stationary interface between saturated and unsaturated regions. If the equilibrium saturation is much smaller than the machine-imposed saturation, binder will tend to migrate out of the boundaries of the part during the time that it is mobile. If the equilibrium saturation is much higher than that imposed by machine operating parameters, unsaturated regions of powder will divide the lines from one another, resulting in poor knitting of features.

This provides the motivation for measuring the equilibrium saturation of primitive features and relate it to measurements of the capillary properties of the powder and binder. The saturation can be calculated from the powder and binder doses and the porosity or the line diameter:

$$S_{local} = \frac{A_{liquid}}{A_{powder}} \frac{f_{powder}}{\left(1 - f_{powder}\right)} = \frac{A_{liquid}}{\left(\pi d_{line}^2 / 4\right) - A_{powder}} \quad . \qquad 6.23$$

6.6 The Dilemma of Line Diameter

There is a complication in measuring the "diameter" of printed lines. Since the lines are representative "surface" features their surface texture is characteristic of the surface finish of larger "bulk" components. This surface texture is often very irregular on the scale of the grain size. The profile of a single line is shown below with the contrast enhanced, and the surface roughness can be clearly distinguished. The accuracy of diameter measurements from single lines is highly suspect due to the surface roughness.

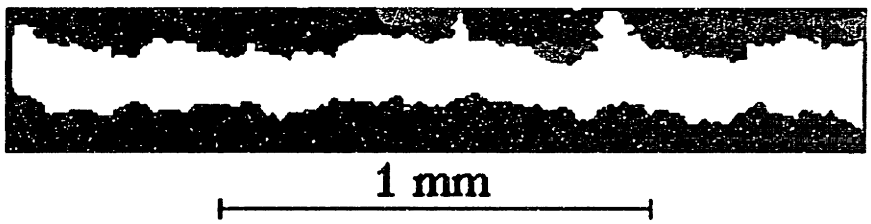

Figure 6.10 A magnified view of a single line (88.7). Grain size: 28μm. Measured diameter: 153 μm ; Std. Dev: 24 μm; (by occlusion) Same as fig. 8.2

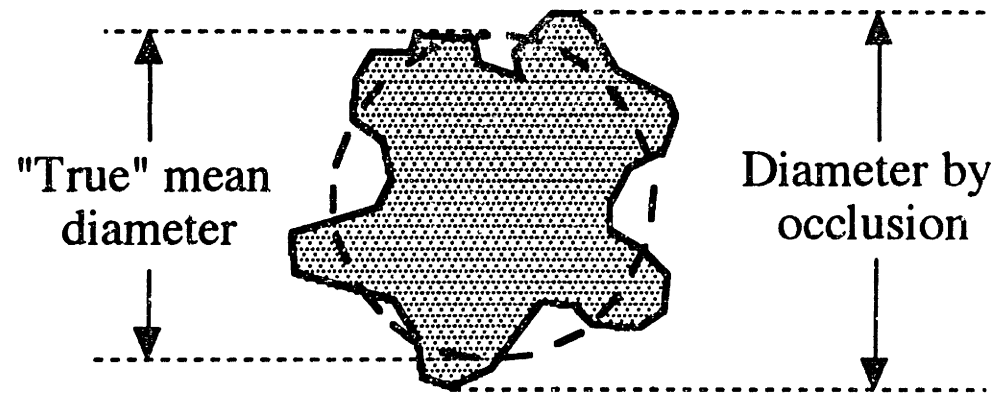

Figure 6.11 Bias on diameter measurement by occlusion.

6.6.1 Occlusion Measurement Bias

A most obvious technique for measuring the line diameter is to measure the width of a microscopic image such as that in figure 6.10. This can be described as measurement by **occlusion,** since one is looking at a projection, not a section. Measurements of the apparent diameter by the occlusion of light will tend to overestimate the mean diameter because particles projecting off of the surface will be visible while pits in the surface will not. This is illustrated in Figure 6.11, above. The density of single line features can be calculated if one has a good estimate of δ, the amount of the bias:

$$\rho_{appar} = \frac{4M'}{\pi d_{occl}^2} \qquad 6.24$$

and

$$\rho_{true} = \frac{4M'}{\pi(d_{occl} - \delta)^2} \quad . \qquad 6.25$$

where $M' = \rho_{liquid}A_{liquid} + \rho_{powder}A_{powder}$. This bias can be estimated by printing lines with different binder doses, measuring the apparent density ρ_{appar}, and enforcing the assumption that ρ_{true} must be constant for single lines printed with different binder doses, but at the same powder packing density.

6.6.2 Compact and Fractal Features

Assuming that this problem can be worked out adequately, there exists the additional problem that infiltration fronts in porous media are sometimes, but not always, **fractal** (see, for example, Lenormand). A fractal structure can be expected if binder migration proceeds outward along a minimally percolating network of pores to the lower limit of saturation. The fractal nature of the invasion of liquids into porous media has been studied by many workers particularly in the study of tertiary oil recovery. See Sapoval, Rosso, & Gouyet in [Avnir pp. 227-245]; [Lenormand] ; or [Feder, ch. 7.] Fractal structures have surface texture that occupies a substantial fraction of their volume, and density that is variable with their size. The classic fractal equation relates the mass M of the structure with its apparent diameter:

$$M' \propto d_{line}^{\partial} \quad [\text{ Feder, p. 135}] \qquad 6.26$$

where ∂ is the fractal dimension, not necessarily an integer. For a fractal,

$$\rho_{appar} \propto d_{line}^{\partial-2}. \qquad 6.27$$

The fractal dimension cannot exceed the dimension of the space it is embedded in, which in this case is 2, the Euclidean dimension for fluid migration imposed by the line geometry. Therefore, the apparent density of a fractal line should decrease as the apparent diameter increases. This is in contrast for the situation described above (equation 6.25), where a constant bias to the diameter measurement causes the apparent line density to increase with diameter, and converge on the true value. Features that do not possess fractal structure will henceforth be called **compact features**.

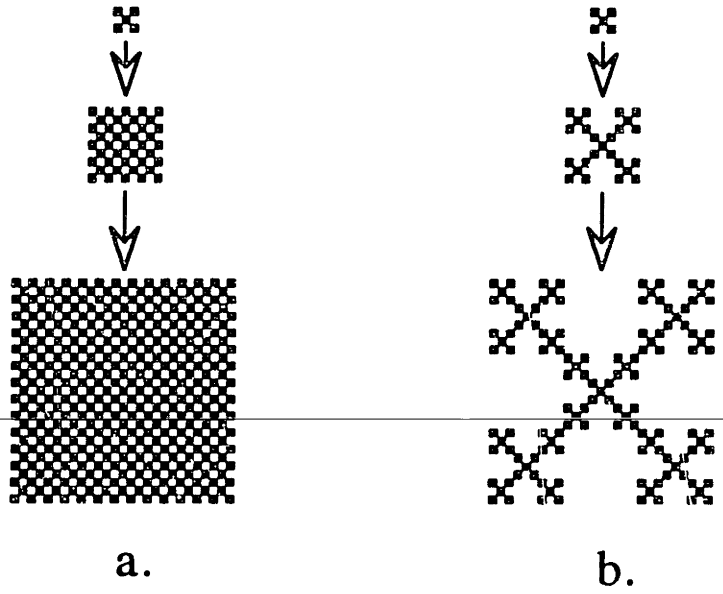

Figure 6.12 a. A compact feature $\delta = 2$; b. A fractal feature $\partial \approx 1.46$.
See [Mandelbrot]

In Figure 6.12 above, a compact feature is contrasted with a fractal feature. As the size of the compact feature is increased, the mean size of the gaps in the feature stays constant and the density stays constant. The fractal feature possesses gaps that increase in size as the apparent diameter of the feature increases, and its apparent density decreases by approximately 50% for each increase in scale.

6.7 Conclusion

The rate at which liquid binder is imbibed by dry powder is very rapid; much faster than evaporation or any diffusion-controlled process that could arrest the flow of fluid. Since it is frequently observed that the fluid is fairly localized in 3-D Printed features, a

theory is needed which predicts the conditions for capillary equilibrium of partly saturated powder in contact with dry powder.

For the purposes of modelling binder migration in 3-D Printed features, an entity called a hydraulic feature is introduced. It is a volume of moistened powder in which hydraulic pressure is transmitted throughout the fluid in the pores. The quantity defined in 3-D Printing as feature size corresponds to the smallest hydraulic feature that can be created by a particular printing engine.

The driving force for fluid migration is caused by the capillary suction of the dry powder surrounding a feature. The capillary pressure of the fluid in the feature must be equal to the pressure at the surface of the feature, which is in contact with the dry powder at its characteristic suction pressure. The strength with which a premoistened feature is capable of hanging onto its moisture is determined by the bubble pressure of the saturated powder. The excess pressure of a completely saturated feature in contact with dry powder is equal to the difference

$$\Delta P = - P_0 + P_B = \sigma_{LV} (K_W \cos\theta_{adv} - K_{NW}\cos\theta_{rec}). \qquad 6.10, 6.12$$

where P_0 is the suction pressure of dry powder and P_B is the bubble pressure of saturated powder. For the fluids most often used in 3-D Printing, it can be assumed that $\cos\theta_{adv} \approx \cos\theta_{rec} \approx 1$ and so the driving force is proportional to the difference ($K_W - K_{NW}$) which expresses the geometric characteristics of the pores in the powder bed in a way that is relatively independent of the properties of the fluid.

If the difference ($K_W - K_{NW}$) is positive, fluid will spontaneously migrate out of saturated areas in a feature into the dry surrounding powder. The capillary pressure in the feature will tend to decrease (become a stronger suction) until it equals the suction pressure P_0 of the dry powder, which is assumed to extend without bound in the powder bed. Thus, the capillary pressure will follow the characteristic drainage curve for the fluid in the powder until the bulk saturation of the feature is S^* at equilibrium such that

$$K_{drainage}(S^*) = K_W . \qquad 6.13$$

Powder that tends to consolidate when moistened will exude moisture until the internal stress caused by the capillary pressure equals the compressive stress to consolidate the powder to the higher density. The pore size of the densified powder will be smaller than the undensified powder, so densified features should be fully saturated.

Gravity will cause the top surface of a feature in a gravitational field to be less saturated than the bottom surface due to the difference in hydrostatic pressure. For large parts that constitute a single hydraulic feature, the quantity of fluid available from this saturation gradient can be enough to make macroscopic pools in the powder in regions never intended to be infiltrated. This phenomenon has been observed in 3-D Printing and is called bleeding. To alleviate this affect, it is necessary to immobilize the binder in the powder before too many layers have been printed and the effect becomes noticeable. This can be done by drying the liquid from each layer after printing, by turning the binder to a gel by a chemical reaction, or by introducing an additive to the powder bed that itself forms a gel. The gel strength required to support the binder is ridiculously small for reasonable grain sizes of powder, but it must be finite.

The rate of fluid imbibition into powder is much slower than the rate of impact of individual droplets from the binder stream, but much faster than the frequency at which complete lines are deposited. Thus, 3-D Printed features form as lines, and the knitting between these lines is determined by the agreement between the binder distribution determined by the capillary equilibrium and the binder distribution imposed by the motion of the printhead. The binder dose, or volume of binder per unit line length, is the machine parameter that determines the diameter of printed lines, through the equilibrium saturation.

The measurement of line diameter is complicated by the surface roughness of individual printed lines. If the diameter is measured by occlusion, a positive bias of approximately one grain size is expected. This bias can be estimated by enforcing the assumption that the bulk density of printed lines is independent of binder dose, under otherwise constant process conditions.

The assumption that the density of single lines is constant with increasing size may not be correct if the lines possess a fractal structure. The consequence of having a fractal structure is that the apparent density of the lines should decrease with increasing apparent diameter. Otherwise, the apparent density should increase slowly, and converge on the true value if and only if the features are compact.

Chapter 7. Experimental Characterization of Powder Pore Structure

7.0 Introduction

The migration of binder in the powder bed is driven by capillary forces. There exist several experimental techniques for measuring the capillary properties of porous materials, and it is up to the experimenter to decide which ones are relevant and what the results mean. In the theory of feature formation developed here, the primary characteristics of the powder bed are expressed by two parameters: P_0, the suction pressure of dry powder for liquid and P_B, the bubble pressure of fully saturated powder. This is the minimum amount of information necessary to asses the driving force for binder migration in the powder bed between 10^{-3} sec and 1 sec after the binder impacts the powder.

There are two extremes in the spread of binder in the powder bed. If the suction pressure of dry powder is insufficient to drain saturated powder adjacent to it, binder will not migrate at all, and the features will be found to be fully saturated. The opposite extreme occurs if the suction pressure greatly exceeds the bubble pressure and the liquid spreads to the greatest degree that is possible. Since the permeability of the powder bed decreases rapidly for unsaturated powder, the rate of spreading should decrease until some other phenomenon (e.g. drying or coagulation) arrests the liquid. Between these two extremes, there exists a continuous range at which a partially unsaturated feature comes to equilibrium with the surrounding powder.

Experiments were chosen that conveniently yielded accurate estimates of the two parameters P_0 and P_B. Two experiments in measuring the capillary pressure under conditions equivalent to drainage of a wetting liquid (sections 7.2 - 7.5), one measuring the suction pressure of dry powder for a wetting liquid (section 7.6) were developed extensively. Measurements of advancing contact angles were made using a simple setup (section 7.7.) These data are collected, in section 7.8, into calculations of the excess fluid pressure in a fully saturated feature following equation 6.12. Two more experiments were done which provided estimates of the powder permeability (sections 7.9 & 7.10).

7.1 Preparation of Powder Samples for Experimentation

To test the pore structure of powder used in 3-D Printing it was necessary to lock its structure so the arrangement did not change during the measurement, and multiple experiments could be performed on the same specimen. Samples were prepared by spreading loose powder with the layering mechanism on the prototype 3-D printer (built 1990-1991, presently located in 35-020) over alumina wafers 3"x3"x.025". Alumina with a mean particle size around 30 μm could be sintered into a solid (though loosely bound) network by firing at 1450°C for two hours. Smaller particle sizes sintered at lower temperatures, owing to the increased surface energy. Bimodal powder with 10% 3.0 μm and 90% 30μm could be effectively sintered at 1200°C, as could 9 μm powder.

This preparation constrains the powder against deformation during testing, but in actual practice, the powder is loose. The effects of this compromise can be minimized by taking measurements at different packing densities. The capillary stresses in the powder exert forces on the powder network, but the mechanics of moist powder densification is so little understood that this knowledge does not allow one to predict the magnitude or rate of deformation that may occur during or at any stage after printing. By measuring the density of single features, powder compaction can be measured after the fact, and the capillary characteristics of partially saturated features can be well documented.

7.2 Direct Measurement of Capillary Pressure in Drainage

[Bear pp. 453-456, 474-478] describes a device called the Haines apparatus which permits the capillary pressure to be measured as a wetting fluid is drained from a saturated porous sample or from saturated loose powder. It is a type of **tensiometer** which allows the sample to come to hydrostatic equilibrium with a pressure transducer, e.g. a manometer. The Haines apparatus is shown in Figure 7.1 below.

7.2.1 Design of the Haines Apparatus

The porous membrane at the top of the apparatus was saturated with a test liquid. When the sample was placed in contact with the membrane, the capillary pressures in the two objects tended to equalize. A mercury manometer served both to measure the suction pressure exerted by the sample and to control the amount of liquid in the sample. In

principle, any liquid could be used in the apparatus, but certain practical problems limited the choices somewhat.

The design of the apparatus took into account the expected range of pressure measurements and the rate at which the samples equilibrated. For testing 30 μm particles with a mean pore radius of approximately 4 μm a maximum suction pressure of 20 cm Hg (27 kPa) was deemed sufficient. The pore size of the membrane was substantially smaller than the pore size of the sample to avoid draining water from the membrane and allowing air to invade the system. This meant that P_B of the membrane had to be much larger in magnitude than the limiting suction of the apparatus. The time required for the sample to equilibrate at lower and lower saturations was long enough for some water to evaporate from the samples, so the sample cell was enclosed in a shroud to prevent evaporation. The apparatus was constructed from rigid material in order to measure the volume of test fluid drained from the sample on a scale along the column.

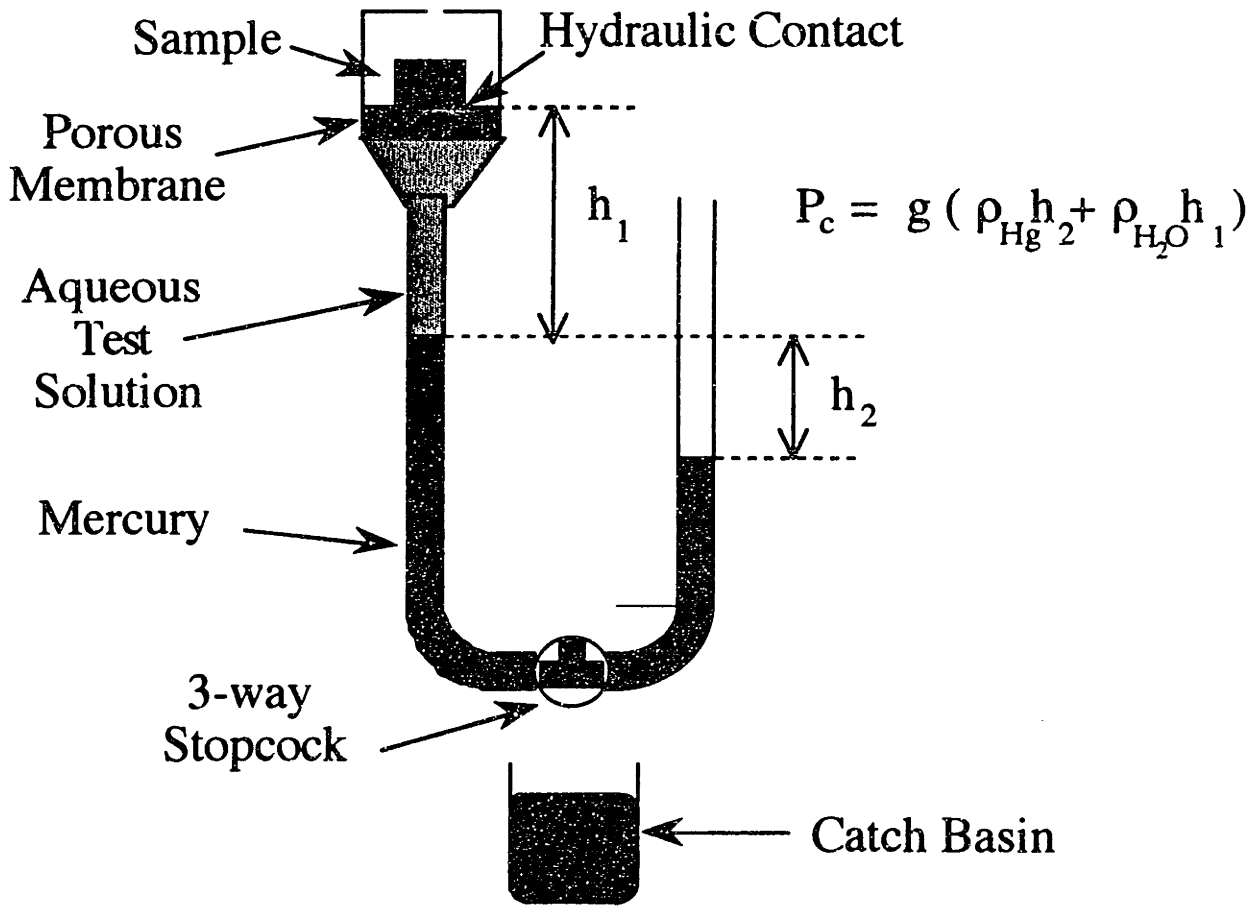

Figure 7.1 Haines' apparatus. (After Bear, p.478)

The test fluid used in the apparatus must possess a surface tension that is robust to the presence of impurities in the sample. This is not true of pure water, but it is true for strong soap solutions above the c.m.c. The formation of micelles in the soap solution buffers the concentration of soap in the solution. This makes the solution robust to impurities or dilution. The test fluid that was chosen was 0.1% Triton X-100 (a nonionic surfactant whose c.m.c. is about 0.025%) and 0.1% KOH in distilled water. This solution was judged to have a stable surface tension of .031 Pa-m. The alkalai was added to mimic the alkalinity of the colloidal silica that is used in the printing of ceramic. It was slightly corrosive to the liquid mercury, but caused no serious problems.

As a support for the membrane, a pyrex funnel with a fritted glass baffle was adapted. For the membrane, a slurry of 3 μm alumina powder (the same used in experiments with bimodal powders) was poured over the frit. The remainder of the apparatus was constructed from pyrex tubing and pyrex three-way stopcock. The funnel was fitted onto the tubing with a rubber stopper. A lucite cover was loosely fitted over the funnel to retard evaporation. The sample chamber must be ventilated to the atmosphere to allow the manometer to equilibrate.

It was very difficult to exclude air from the space behind the membrane. To account for the presence of an expansible air bubble in the top of the manometer, a pressure/displacement curve was measured for the empty apparatus at the beginning of each run and the volume change of the air bubble at different pressures could be subtracted out of the measurement

7.2.2 Procedure

The porosity and volume of sintered powder samples was measured at the beginning of each run by weighing the sample before and after infiltration with the test fluid. The skeletal volume of powder in the sample was calculated from the dry weight, and the pore volume was the difference between the dry and saturated weight. If the infiltration was performed carefully, virtually all the air could be excluded from a porous sample. If the sample initially had a weight W_o and gained ΔW during imbibition, the fractional density was

$$f_{powder} = \frac{W_0}{W_0 + \frac{\Delta W \rho_{powder}}{\rho_{liquid}}} \qquad 7.1$$

(and the porosity was 1 - f_{powder}.)

The experiment commenced with the manometer limbs filled with mercury up to a reference mark near the top of the U. Excess solution above the membrane was removed with a syringe until only a small amount of water stood at atmospheric pressure in the cup. At this point the sample was pressed slightly into the soft membrane. Good hydraulic contact was ensured because the membrane conformed to the lower surface of the sample.

Mercury was drained in small increments, and the heights of the mercury meniscus were measured in the two limbs of the apparatus, after a suitable equilibration time had elapsed. For an empty apparatus in a calibration run, a minute was sufficient for complete equilibration. For samples comprised of 30 μm alumina with thicknesses up to 1 cm, roughly 1 hour was necessary for substantial equilibration, although at the extreme lower limits of saturation, it is doubtful that equilibrium was approached in less than several hours.

7.3 Mercury Porosimetry

One of the most widely used methods for measuring the pore size distribution of porous materials is mercury porosimetry. [Bear, 48], [Everett 1973 p.149] Since mercury has a contact angle with most solid materials that exceeds 90°, positive pressure is required to force the liquid metal into a porous sample. The volume intruded into an evacuated sample is measured as a function of the applied pressure. Since mercury infiltrates the largest pores first, the infiltration of mercury proceeds along virtually the same path that air follows during drainage of a wetting liquid from the sample.

7.3.1 Procedure

The drainage characteristics of porous powder samples were measured on an Autopore 9220 manufactured by Micromeritics Corp in Hialeah, Fla. A dry, weighed porous sample was sealed in a glass bulb called a **penetrometer** and the assembly

weighed a second time to determine the tare weight. The penetrometer was then inserted into a vacuum port on the porosimeter. After it was evacuated to a pressure below 50 μm Hg, the penetrometer was backfilled with mercury at a pressure of 3 psia. The volume of mercury in the penetrometer was fixed at this pressure: the stem of the penetrometer served as a reservoir that fed the sample. Fifteen seconds was allowed for equilibration before the displace volume was measured. The displacement of the mercury in the stem was measured capacitively: the outside of the stem of the penetrometer was metallized, and the glass of the stem formed the dielectric in a capacitor for which the mercury itself was the other electrode. As the pressure was increased from the initial fill pressure, any displacement of the mercury corresponded to infiltration of the pores of the sample.

There are two stages in this apparatus: a dry low-pressure stage and a hydraulic high-pressure stage. Once the full pressure range of the low pressure system was traversed, the penetrometer was removed and weighed. The bulk volume of the sample was found by subtracting out the tare weight, dividing by the density of mercury at ambient temperature, and finding the difference from the calibrated volume of the penetrometer. This volume was calibrated by running an empty penetrometer on the system.

The remainder of the pore size distribution was measured by placing the penetrometer in one of the high pressure (hydraulic) ports. The system was closed, and air bled out. The pressure could be gradually increased to as high as 60,000 psi, but 1,000 psi was sufficient for complete infiltration of the samples tested. Further mercury intrusion was measured capacitively as the pressure was scanned upward and then back down to atmospheric. The skeletal volume was found by subtracting the volume of mercury intruded from the bulk volume.

7.3.2 Interpretation of the Data

There has been considerable effort expended in the interpretation of the infiltration curve to deduce the pore size distribution of porous samples. See, for example, [Dullien, 203-232] and [Everett 1973 pp.149-155]. The difficulty with dealing quantitatively with the irreversible filling of "ink-bottle" pores during mercury infiltration is a substantial obstacle in extracting pore size distributions from the data. For the purpose of this research, knowledge of the pore size "distribution" is superfluous: the analogy between mercury infiltration and binder drainage allows the data to be used to estimate the

pressure/saturation characteristics of the powder. The intrusion pressures of the mercury were used to calculate pore curvatures through the identity

$$K_{drainage} = \frac{-P_{Hg}}{\sigma_{Hg}\cos\theta_{adv}} \quad . \qquad 7.2$$

where $\sigma_{Hg} = 485$ dyn/cm, the surface tension of mercury and $\theta_{adv} = 130°$, the contact angle between mercury and alumina. Accordingly,

$$K_{drainage}(\mu m^{-1}) = \frac{P(psia)}{45.2} \quad . \qquad 7.3$$

It has been shown in Appendix B that K_W, the critical curvature for imbibition, is nearly independent of the contact angle of the liquid on the powder surface but the independence of K in drainage is more difficult to demonstrate theoretically. By measuring the drainage characteristics of powder samples with fluids with drastically different wetting characteristics, it was hoped that the independence of K in drainage could be demonstrated experimentally. The data from mercury porosimetry can be expected to diverge from data collected with a wetting fluid at the largest pressures because the infiltration of liquid mercury is not affected by the irreducible saturation S_{W0}, while the kinetics of wetting fluid migration become very slow as the pressure approaches S_{W0}.

Since the apparatus for performing mercury porosimetry was a commercial machine, the technical issues for gathering data are fairly well documented. Accurate data could be gathered once the operator had sufficient experience with the hardware. The principal difficulty was in the assembly of the penetrometer and establishing a vacuum seal. Handling liquid mercury is hazardous as a rule.

This method possessed the advantages of having automated operation and data collection. Also, most of the impurities present in ceramic materials do not alter the surface tension of mercury or its contact angle. The chief disadvantage was the drastic difference between mercury and the binder used in 3-D Printing. The question of whether data collected with mercury accurately reflected the properties of the porous material with respect to aqueous liquids motivated the construction of the Haines apparatus for comparative purposes.

7.4 Results of Drainage Measurements

Mercury porosimetry is overwhelmingly easier to perform than experiments with the Haines apparatus, but data for the capillary properties of alumina powders depend on the geometric similarity between imbibition of a nonwetting liquid (mercury) and drainage of a wetting liquid (binder). This assumption may not be justified (see [Dullien 341-353]) so it is necessary to check the data gathered using mercury against data gathered in drainage of a wetting fluid.

7.4.1 Results for Drainage of a Wetting Fluid

The Haines apparatus constructed for this purpose was used to test samples of some of the same powder packs that were measured by mercury porosimetry. The size of the samples tested in this apparatus was approximately ten times that which the porosimeter would accommodate, and the increased size helped to improve the accuracy of the measurements.

The drainage curves are shown in Figure 7.2, below for three powder samples, 30 μm Norton 7920 alumina, with packing densities of 0.33, 0.46, and 0.49. These samples had bulk volumes between two and three cc's and the volume of fluid in the pores was typically between one and two cc's. The bulk densities measured during the infiltration with test solution (equation 7.1) agreed exactly with the density measurements taken during the building of the samples on the "prototype" machine, taken under identical conditions with different powder samples. Samples began completely saturated with test solution (0.1% KOH, 0.1% Triton X-100 in dist. H_2O) and the pressure was measured with a mercury manometer after small quantities of liquid were drained out.

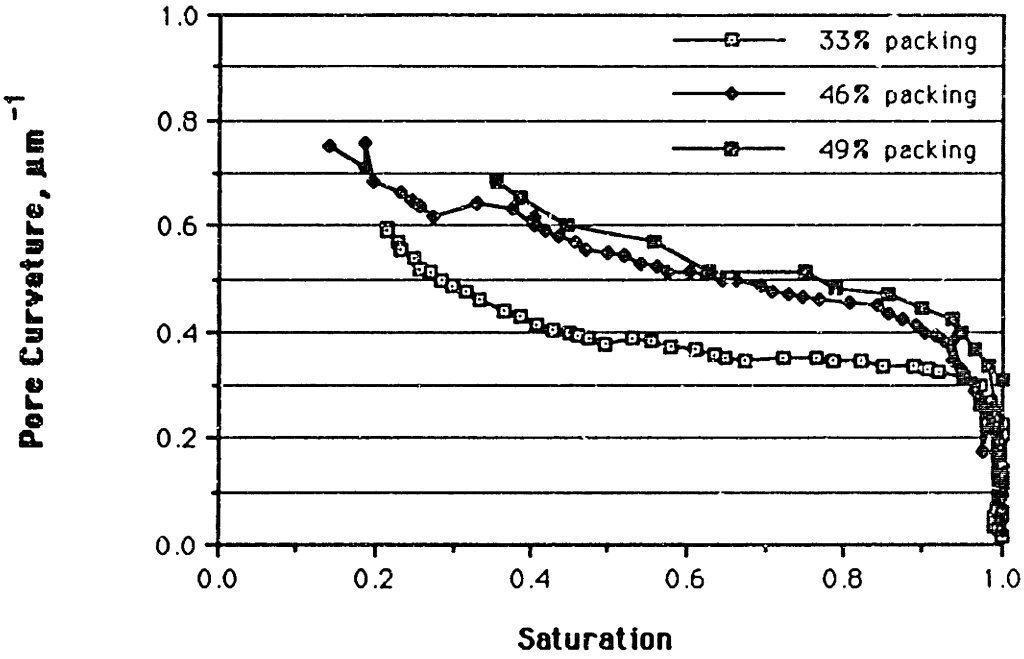

Figure 7.2 Pore Curvature vs. saturation for drainage of aqueous test solution from sintered Norton 30 μm 7920 alumina.

The measured pressures have been converted to equivalent pore curvatures to facilitate comparison with mercury porosimetry data. The general trend is that with higher packing density, the pore curvature increases. This is consistent with intuition, which suggests that the pore size, proportional to the reciprocal of the curvature, should decrease as packing density increases.

These curves can be used empirically, following the method outlined in figure 6.7. To compare the characteristics with data collected for different powders at different densities, two points along the curves are used to represent the characteristic. These two data are K_{90} and K_{50}, the pore curvatures at 90% and at 50 % saturation. The pore curvature K_{90} can be considered an estimate of the critical curvature K_{NW} while K_{50}, provides extra information about the slope of the drainage curve.

Packing Density	K_{50} μm^{-1}	K_{90} μm^{-1}
0.33	0.34	0.39
0.46	0.40	0.55
0.49	0.44	0.59

Table 7.1. Drainage curvatures from Haines' apparatus, 30 μm 7920 alumina, sintered at 1450 °C, various packing densities.

7.4.2 Porosimetry Results for Porous Sintered Powders.

Powder samples with weights ranging from 0.1 to 0.3 g were of appropriate size for measurement in the mercury porosimeter Samples were broken off the sintered powder packs, and care was taken to keep the fracture surfaces clean.

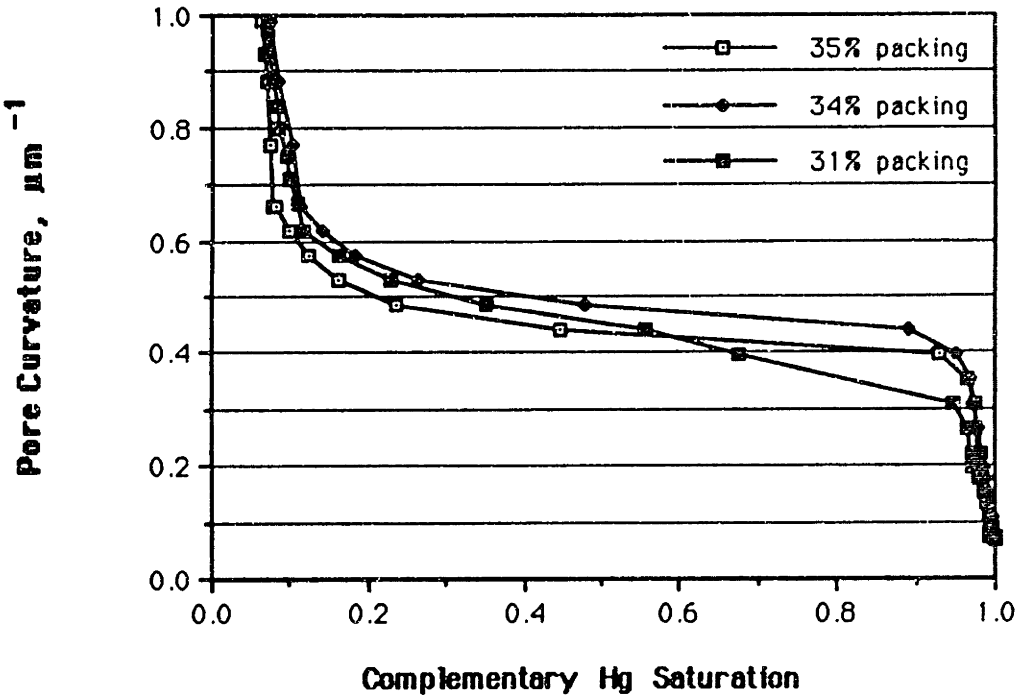

Figure 7.3 Pore curvature vs. complementary mercury saturation for 30 μm lamellar alumina with packing densities ≤ 35%.

Several samples of sintered 30 μm lamellar alumina, with bulk densities of 0.33, 0.37, 0.39, 0.46, and 0.49 were used, and at least two runs were done from each sample. Because of the miniscule size of the fragments tested in the porosimeter, the packing density of the sample varied, usually by one or two percent, from the mean density of the original compact. Infiltration curves were generated by converting the infiltration pressures to pore curvatures, and plotting them with respect to the complement of the mercury saturation, so as to resemble the drainage curves of a wetting fluid.

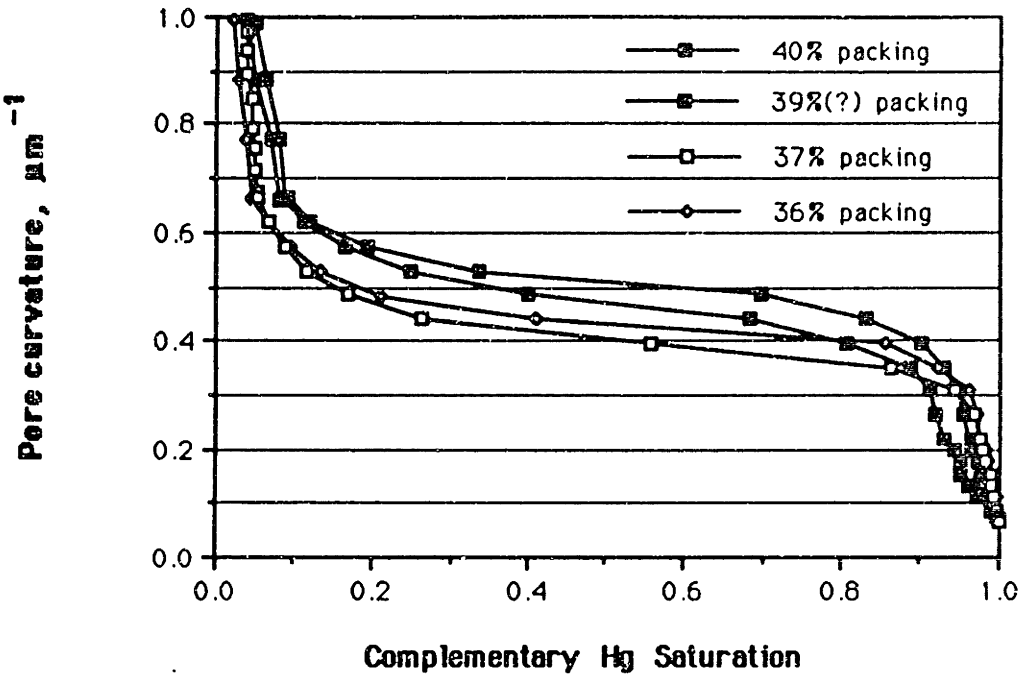

Figure 7.4 Pore curvature vs. complementary mercury saturation for 30 μm lamellar alumina with packing densities > 35% and ≤ 40%.

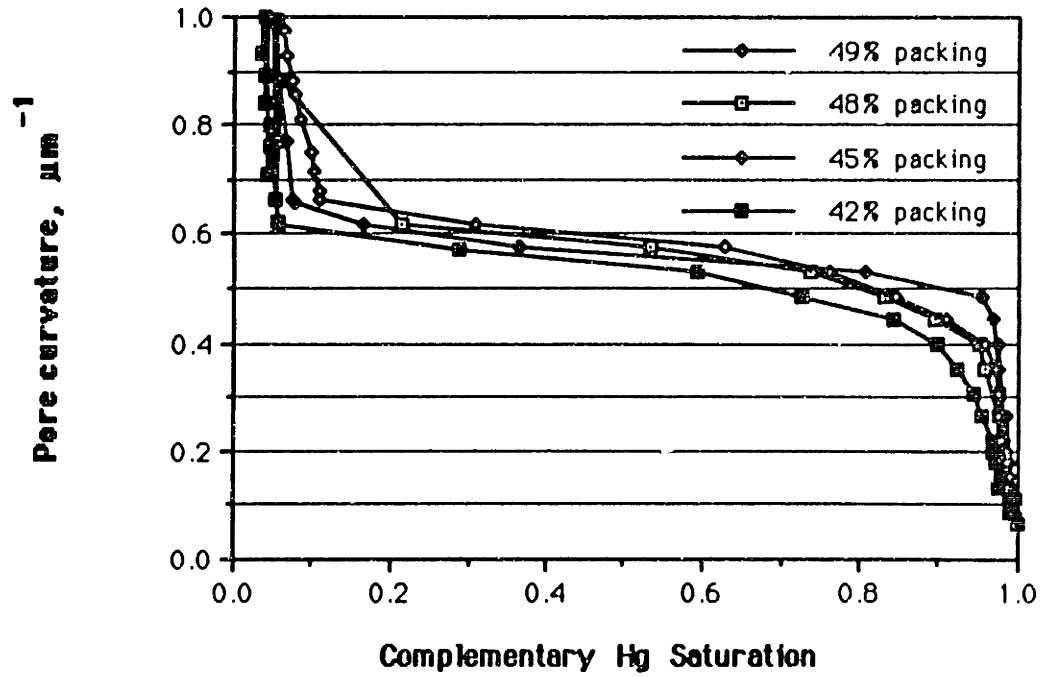

Figure 7.5 Pore curvature vs. complementary mercury saturation for 30 μm lamellar alumina with packing densities > 40%.

These curves strongly resemble those acquired with the Haines apparatus, except the data extend almost all of the way to zero saturation. The curves are relatively broad and flat, but a direct comparison between all of the curves is difficult to make with this raw data. The data for K_{50} and K_{90} are tabulated below for mercury porosimetry.

Packing Density	K_{50} μm^{-1}	K_{90} μm^{-1}
0.35	0.44	0.32
0.31	0.45	0.40
0.35	0.48	0.43
0.37	0.41	0.33
0.36	0.43	0.37
0.39	0.47	0.33
0.40	0.51	0.40
0.42	0.54	0.39
0.48	0.58	0.44
0.49	0.59	0.45
0.45	0.56	0.50

Table 7.2. Drainage curvatures from mercury porosimetry, 30 μm 7920 alumina, sintered at 1450 °C, various packing densities.

7.4.3 Comparison Between Aqueous Drainage and Mercury Infiltration

The data for K_{90} can be used as an approximation for the critical curvature K_{NW} for the sample. In neither of these experiments was it possible to detect the instant at which percolation occurred, but all of the curves exhibited an inflection point very close to a saturation of 90%. Values of K_{90} and K_{50} are plotted as a function of packing density below to facilitate direct comparison.

It can be seen from these data that the pore curvatures measured with the Haines apparatus group very well with the bulk of the porosimetry data. Three of the points in the porosimetry series lie far outside the group of other points. The two rogue points at the lower packing densities were collected during a period shortly before a defective pressure sensor was replaced, so these were likely out of calibration. The point at 45% packing was collected much later. Although there is no definite reason to exclude it, it stands so far outside the remainder of the K_{90} points that something must have gone wrong.

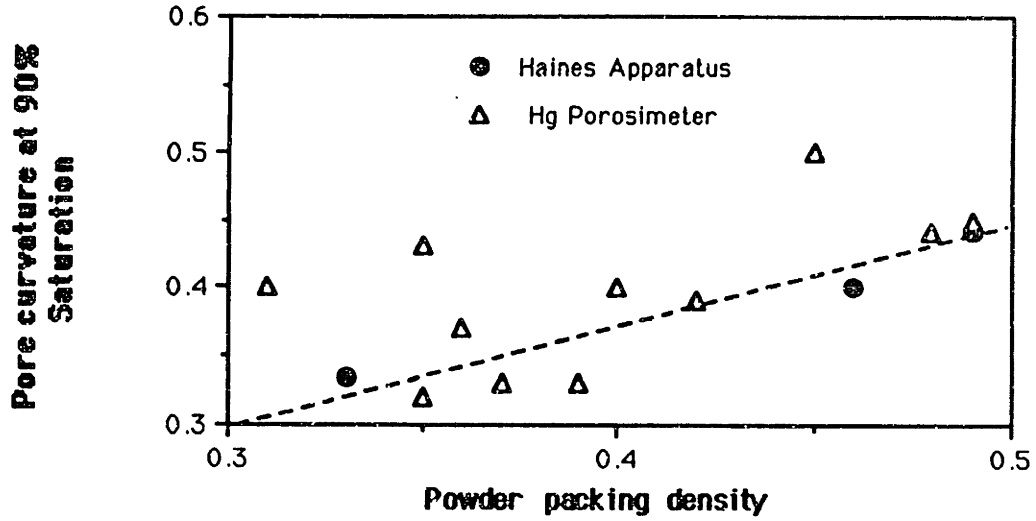

Figure 7.6 K_{90} vs. f_{powder} for Haines and porosimetry curves. Linear fit to data with three rogue points excluded: $K_{90} = .073 + .750\, f_{powder}$, $R^2 = 0.83$.

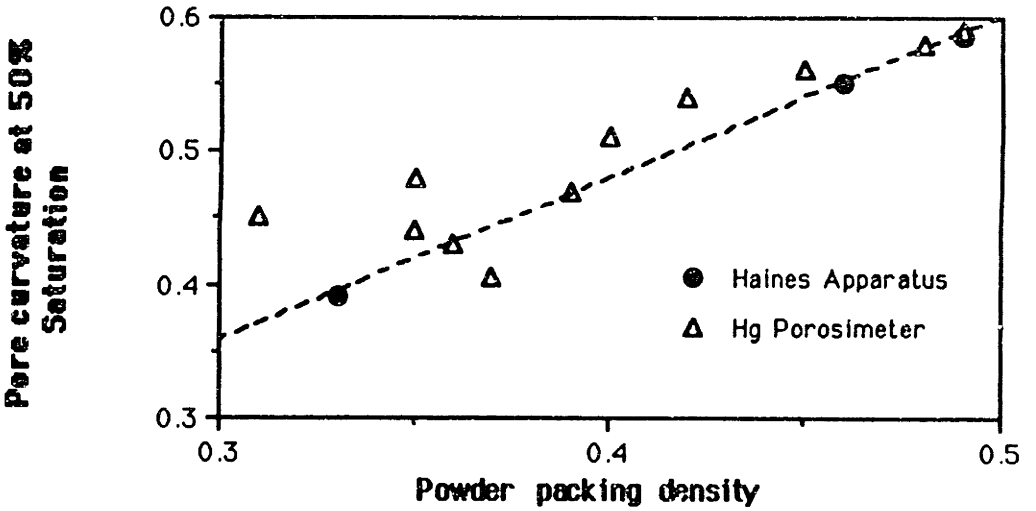

Figure 7.7 K_{50} vs. f_{powder} for Haines and porosimetry curves. Linear fit to data with three rogue points excluded: $K_{50} = -.007 + 1.228\, f_{powder}$, $R^2 = 0.93$.

The substantial agreement between data collected with mercury and soap solution, with contact angles of 140° and 0° respectively, should provide sufficient experimental justification for the assertion that $K_{drainage}$ is independent of θ (Appendix B, section B.5.) This evidence is at least as strong as the theoretical justification (Appendix B, section B.3.) for K_W being in dependent of θ.

The scatter of the data around the fitted lines is enigmatic. The scatter around the fitted line is much larger for the porosimetry data than for the Haines data. It is probably some consequence of the fact that the samples used for porosimetry were approximately 1/20 the size of the samples tested in the Haines apparatus. It is possible that this scatter reflects local variations in the pore size distribution at different points in the powder bed.

7.4.4 Spherical and Fine Powders

Other powders were tested, and their capillary characteristics are compared below in Figure 7.8. Two compacts containing finer grains were substantially more difficult to infiltrate with mercury than the larger grain size compacts. The capillary pressure of Norton 7920 9μm alumina was barely double the pressure of 30μm 7920 alumina at virtually the same packing density. Spherical powder, in spite of its very high packing density, had the lowest capillary pressure of any powder tested, owing to the more regular and open packing of the spherical particles relative to the flattened platelets comprising the lamellar product Norton 7920.

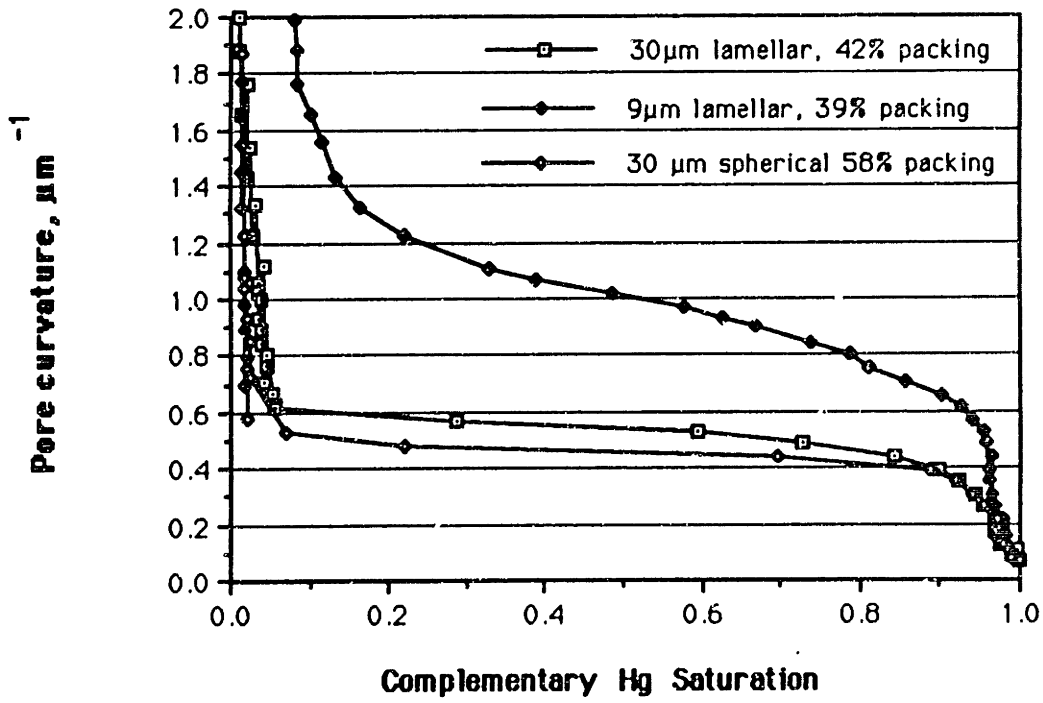

Figure 7.8 Pore Curvature vs. saturation for three alumina powders with different geometries. (Spherical powder: Showa Denko 30μm "alunabeads". Other powders Norton 7920.)

The characteristic curvatures K_{90} and K_{50} for these two powders were:

Powder	K_{50}	K_{90}
30 μm spherical	0.46	0.38
9 μm lamellar	1.01	0.66

Table 7.3

7.5 Capillary Measurements of Bimodal Powders

7.5.1 Introduction

In powder metallurgy, it is very common practice to use mixtures of powders with two grain sizes that are approximately an order of magnitude apart. [German 33-59] discusses bimodal and multimodal mixtures of spherical powders in considerable detail in the context of achieving high packing density for P/M parts so sintering can be done efficiently. The rationale behind bimodal powders is that the fine grains can fit in the spaces between the large grains. This is illustrated below.

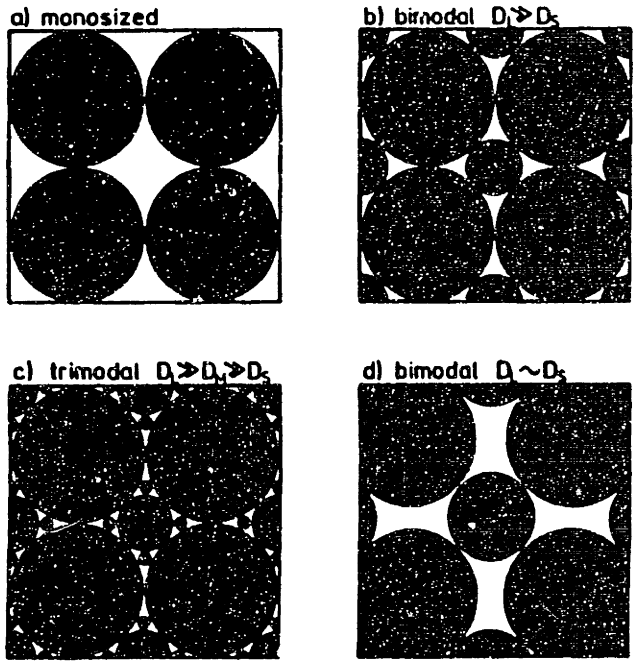

Figure 7.9 2-D Representation of various packings of different-sized circular particles. From [German p.36]. See figure 9.25 for an image of a real sample.

There is both an optimum fraction of fines and an optimum size ratio for bimodal powders: the fines must be small enough so that the packing of the coarse particles is not affected, and there must be approximately the same number of fine particles as holes for them to fit into. German gives data showing that the fines must be ten or more times smaller than the coarse particles in order to gain the full benefit. The fraction of fines to add depends on how densely the coarse particles pack by themselves. He discusses the effects of surface roughness on the packing density of powders, and clearly spherical powders are preferred.

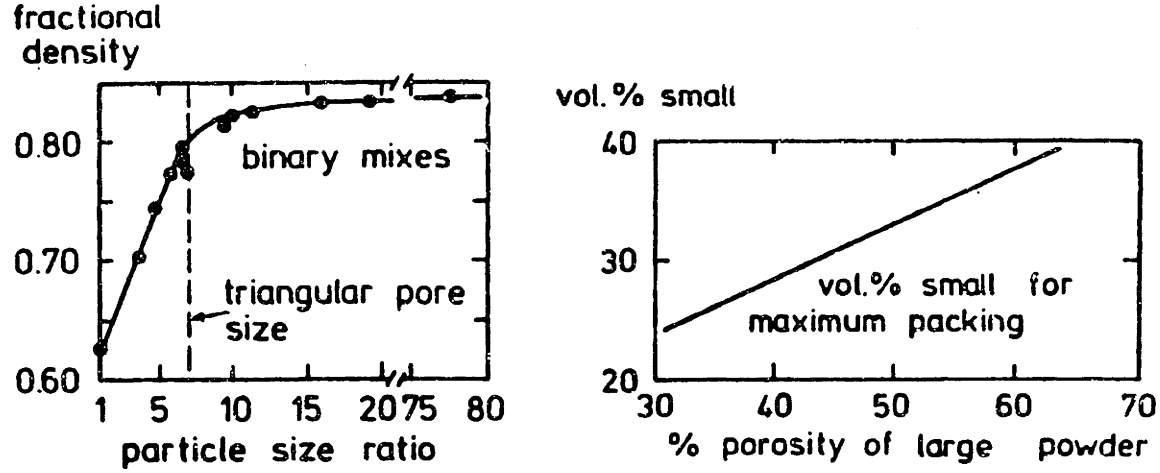

Figure 7.10 Packing efficiencies of bimodal powders. (a.) Maximum fractional density as a function of particle size ratio; (b.) Optimum composition of fines as a function of the packing density of the coarse component. From [German, p.40].

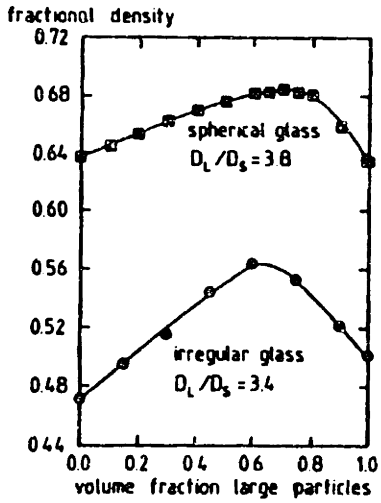

Figure 7.11 Fractional packing density vs. composition for spherical and irregular particles. [German p. 46]

Also, it is important that the fines be distributed homogeneously in the mixture. If the fines are highly agglomerated, the agglomerates behave like large particles, and the packing density is no better than that basic powder.

7.5.2 Formulation of Bimodal Powders

It was decided that the experimentation with bimodal ceramic powders would be done as a variation of the existing ceramic shell process. Accordingly, the coarse component of the powder was selected as a 28-μm lamellar alumina (Norton 7920) that self-packed to 46-48% density and for the fine component, a 3-μm version of the same product was obtained. To remove the sodium silicate which is present in this product, the powders were rinsed with distilled water and decanted.

It was found that the slurry of 3 μm particles could not be dried down without forming a solid, cohesive mass. The particles were stored under water, and redispersed by tumbling when they were needed. A slurry composed of 64% solids by volume in distilled water exhibited a shocking amount of shear thickening. The slurry could be sloshed around in the bottle like a syrupy liquid, but the liquid appeared to come alive (and was not happy) when it was poured. It was named magic liquid and had great entertainment value. This slurry was used in the Haines apparatus to form the soft porous membrane on top of the fritted glass baffle. The slurry lost its dilatant property if the suspension was acidified. This presumably increased the interparticle repulsion and allowed the lamellar particles to dodge one another when the slurry was sheared.

The fines were dispersed in the coarse component by demystifying the magic liquid with a small amount of nitric acid and mixing with the appropriate amount of dry coarse powder. The paste was stirred until the saturation appeared uniform and the paste was dried at 110 °C in an oven. Four mixtures were formulated, about 200 g each containing 10%, 20%, 30%, and 40% by weight of fine powder. The two with the lowest fines content were mixed i none step; the higher fines contents were too moist if all the magic liquid was added at once, so these were mixed by making a large quantity of 20% powder and adding more fines to samples of it.

After drying, the powders were weakly agglomerated, but they were easily broken up by sieving to 120 mesh. There was no good way to asses the state of dispersion of the fines with respect to the coarse grains. By design, the sieving procedure was insufficient

to break up the agglomerates in the combined hope of keeping down the evolution of dust and preventing the fines from segregating. These mixtures all packed very close to 40% of theoretical density. Since the coarse component by itself packed to 48% density, there was no doubt that the powders were agglomerated.

7.5.3 Results of Porosimetry Measurements in Bimodal Powders

These powders were found to densify greatly when moistened. Two samples of each powder were sintered: one sample layered by the "proto" 3-D Printer, and another that was moistened with distilled water as near to the critical loading as possible, and cast onto a paper towel. These samples were sintered and measured by mercury porosimetry. Data from mercury infiltration are presented below, each graph for one powder composition, with curves for the two packing conditions.

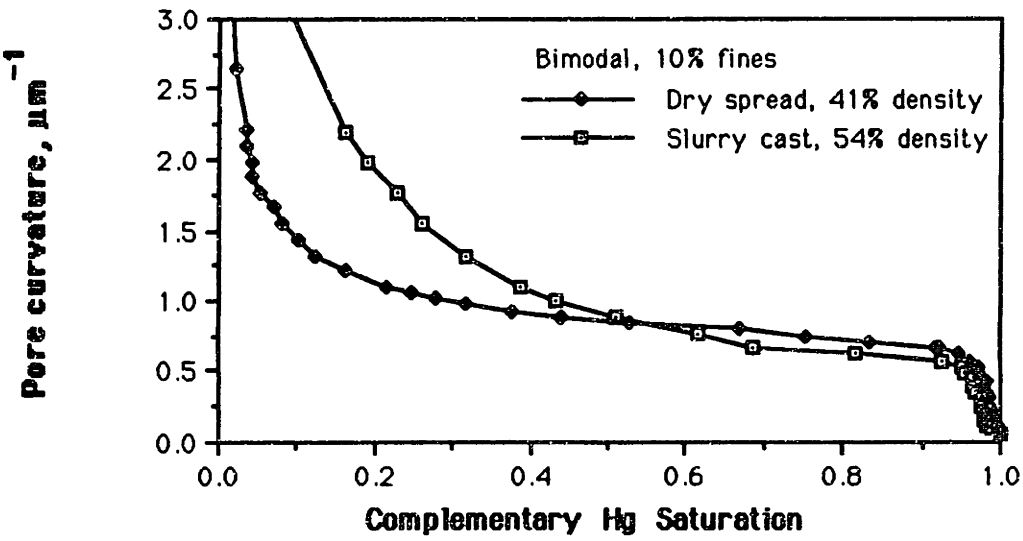

Figure 7.12 Drainage characteristics for bimodal powder, 90% 28 μm ; 10% 3 μm lamellar alumina, packed under different conditions (see text.)

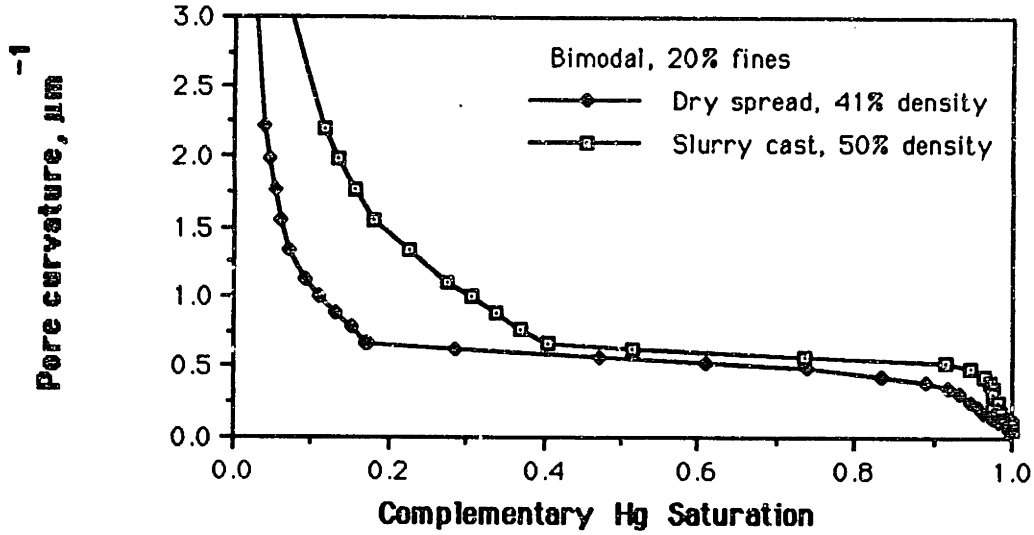

Figure 7.13 Drainage characteristics for bimodal powder, 80% 28 μm ; 20% 3 μm lamellar alumina, packed under different conditions (see text.)

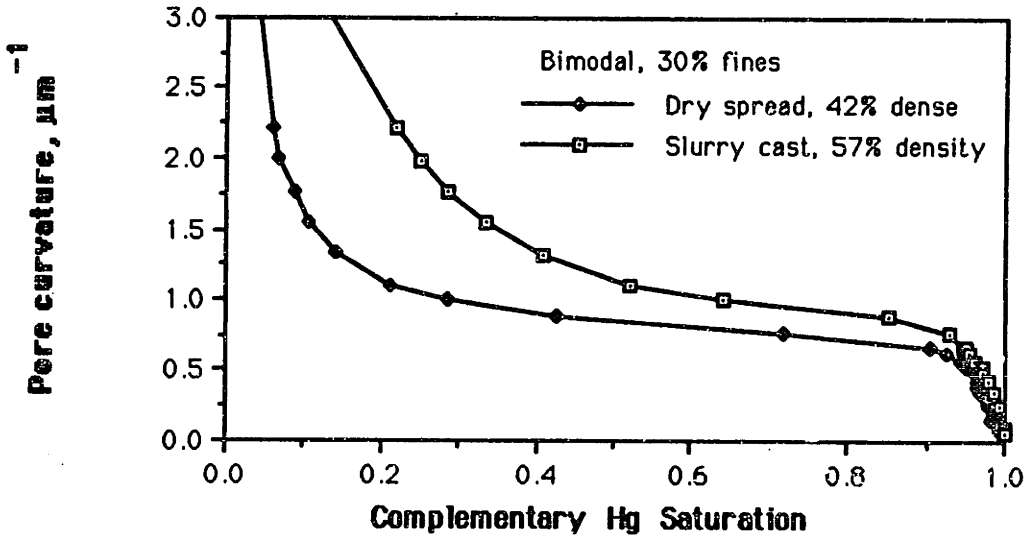

Figure 7.14 Drainage characteristics for bimodal powder, 70% 28 μm ; 30% 3 μm lamellar alumina, packed under different conditions (see text.)

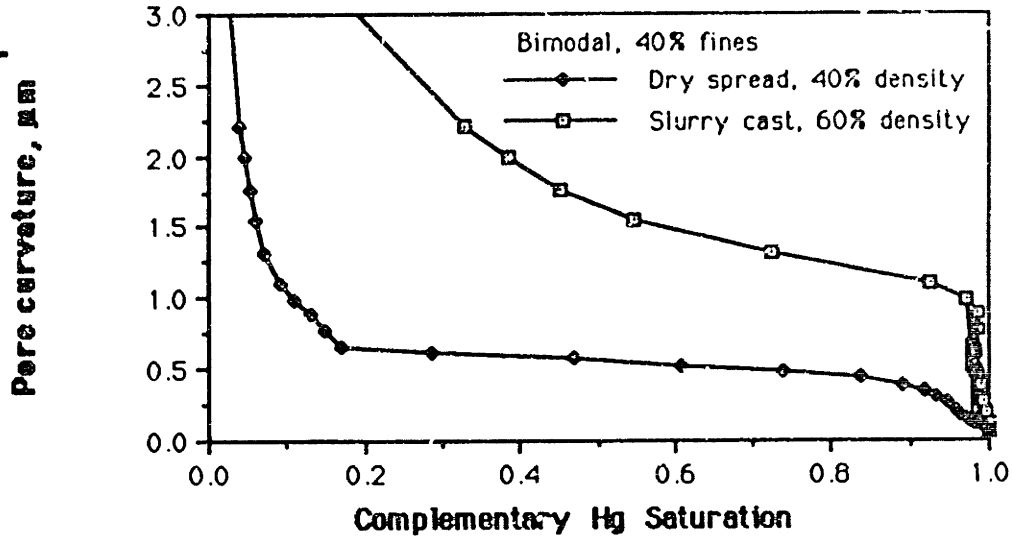

Figure 7.15 Drainage characteristics for bimodal powder, 60% 28 μm ; 40% 3 μm lamellar alumina, packed under different conditions (see text.)

Fines content	spread	packing density	K_{50} μm^{-1}	K_{90} μm^{-1}
10%	dry	0.41	0.86	0.59
	wet	0.54	0.90	0.67
20%	dry	0.41	0.57	0.38
	wet	0.50	0.62	0.54
30%	dry	0.42	0.88	0.66
	wet	0.57	1.14	0.81
40%	dry	0.40	0.57	0.38
	wet	0.60	1.66	1.13

Table 7.4 Characteristic pore curvatures for bimodal powders.

The densification of the powder during slurry casting is a result of the loose agglomerates of powder being dispersed by the added water. This is almost exclusively due to the presence of the fines. To compare, a sample of monomodal 30 μm powder that packed to 42% density dry, densified to only 46% when it was slurry cast in the same manner.

The slurry cast powders have consistently smaller pores than the dry spread samples, although the magnitudes of pore sized do not correlate well with the percentage of fines in the sample. This is easiest to see by studying figure 7.16, below. The characteristic curvature K_{90}, which approximates K_{NW}, is sensitive to the state of dispersion and agglomeration of the powders, as well as the packing density. The dry-

spread samples had virtually the same packing density, but the pore curvature does not correlate at all with the fines content. This clearly indicates that the powders were agglomerated and segregated to differing degrees.

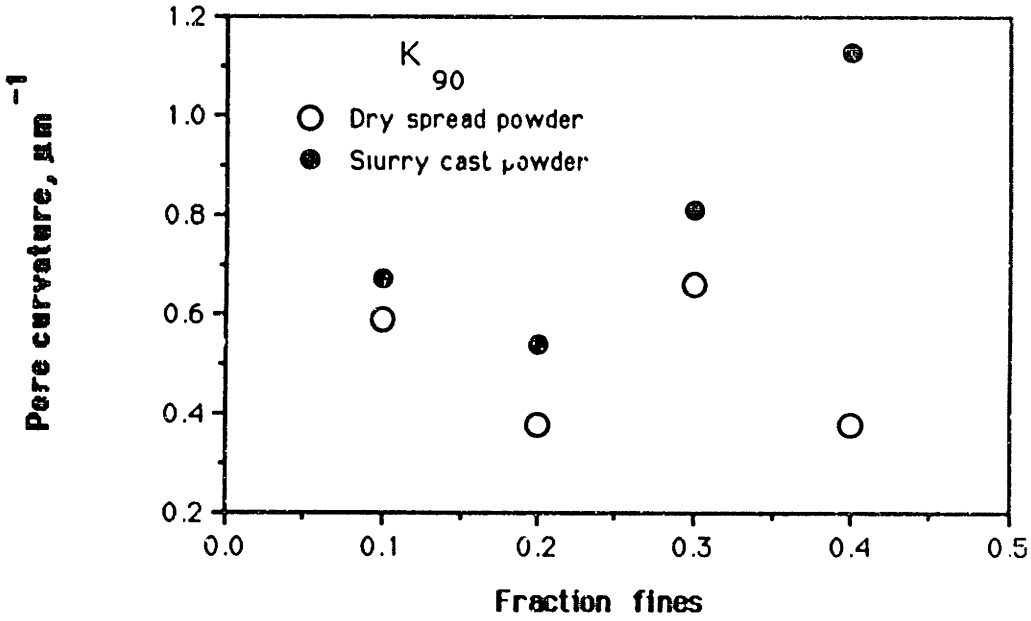

Figure 7.16 Pore curvature at 90% saturation for bimodal powders, plotted against fines content for mixture of 3 μm and 28 μm lamellar Norton 7920 alumina.

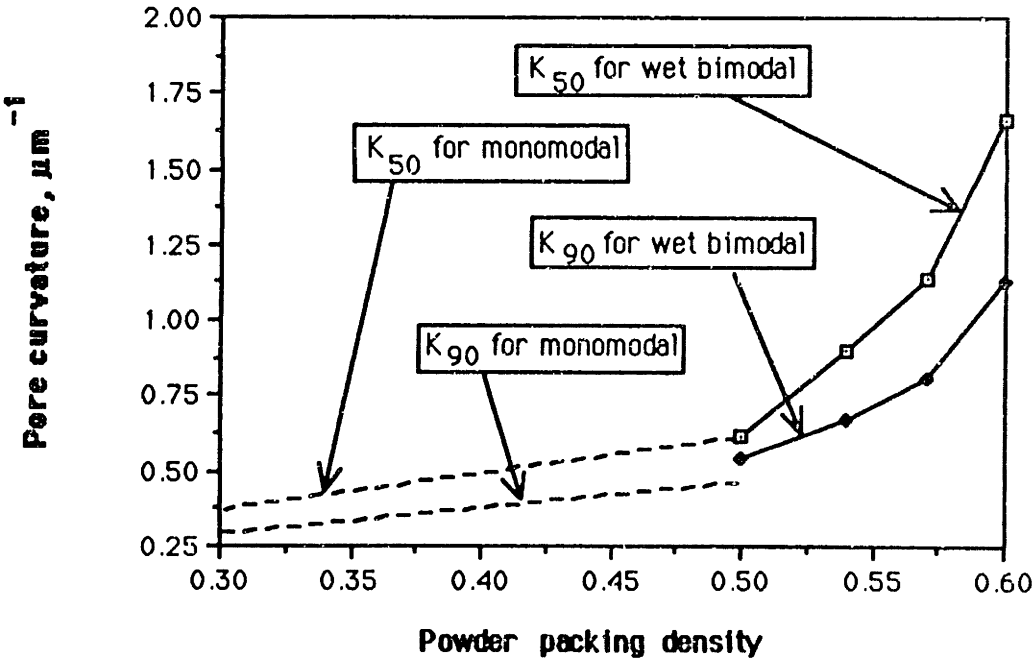

Figure 7.17 Pore curvature vs. packing density for slurry cast bimodal powders. Dashed lines are linear fits to curvatures for monomodal powders that packed to lower densities.

The pore curvatures for the slurry cast samples correlate slightly better with the fines content, but the best correlation is obtained when the data are plotted with respect to the as-cast packing density. This is done in figure 7.17, above.

The pore curvature increases rapidly with packing density. The process of slurry casting breaks up agglomerated particles and probably improves the quality of dispersion. The characteristic curvatures match up approximately with the data for dry spread monomodal powders. Since the powders densify immediately on the addition of moisture, the pore curvature K_{90} of the slurry cast powders probably approximates the value of K_{NW} for printed features in the bimodals.

7.6 Tensiometry of Dry Powder

7.6.1 Method

A tensiometer (see [Bear, 478]) was devised to measure the suction pressure of dry powder. Starting with a dry sample of sintered powder, the soapy test fluid used in the Haines apparatus was allowed to enter the sample from a syringe and an air bubble with a known volume at STP expanded under the partial vacuum caused by the capillary suction of the sample. The purpose of this experiment was to simulate, on an accessible scale, the infiltration of fluid into dry powder in the space immediately surrounding the impact point of the binder jet during 3-D printing. The liquid was assumed to propagate outward under the action of the suction pressure of the dry powder and come to rest without retraction.

Using a 3-ml syringe and a 1.0-ml graduated pipet, an air bubble with a volume of 1-2 ml at STP was trapped by a small quantity ($\approx$ 1 ml) of water. The porous plug was fabricated by packing powder into the pipet tip to form a porous plug, and a small excess of powder outside the tip forms the contact to a sample of fixed powder. The powder used was alumina powder with a grain size of 9 μm, which had a smaller pore size than the samples tested. The pipet was pressed vertically down onto the sample and held there until the liquid meniscus ceased falling. The volume in the pipet was measured during the infiltration as a function of time, to permit a more accurate extrapolation to zero flow rate.

If the volume of the bubble at atmospheric pressure was v_0, then the pressure P_i at some different volume v_i was found from the ideal gas law:

$$P_i = \frac{P_{atm} v_0}{v_i} \qquad 7.4$$

The flow rate through the plug into the sample can be assumed to obey Darcy's law, provided the permeability of the plus is lower than the permeability of the sample:

$$\left(\frac{dv}{dt}\right)_i \propto \left(P_{atm} + P_0 - P_i\right) . \qquad 7.5$$

The pressure difference between the inside and the outside of the pipet is (P_{atm} - P_i) and when that difference is equal to P_0, the capillary suction on the liquid, the flowrate through the plug should be zero:

$$P_0 = (P_{atm} - P_i)_{zero\ flow} \qquad 7.6$$

Since the saturation of liquid at the infiltration front is fairly low, the permeability of the sample is quite small, so the time to equilibrate can be fairly long. Early experiments were performed using a pack of 30 μm powder for the porous plug. The equilibration time was found to be 15 min to one hour but the mortality rate was high. Tests run using 9 μm powder as the plug still had measurable flow after a few hours, so the timing of these runs was essential. The total volume of liquid transferred into the sample with this apparatus was typically about 0.3 - 0.6 ml.

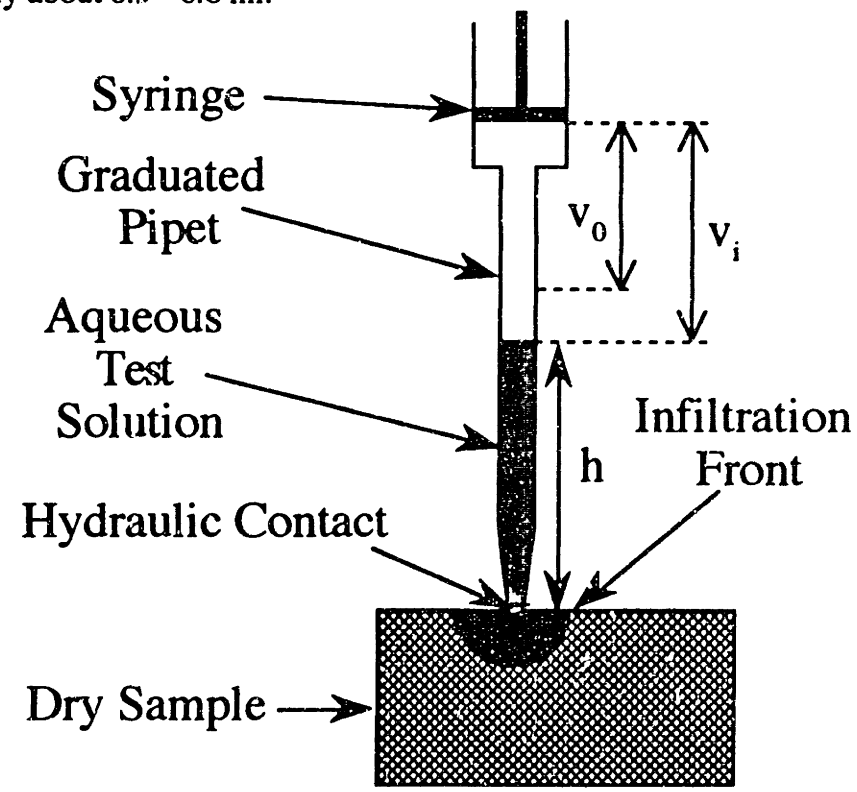

Figure 7.18 Benchtop tensiometer for measuring suction pressure of dry powder.

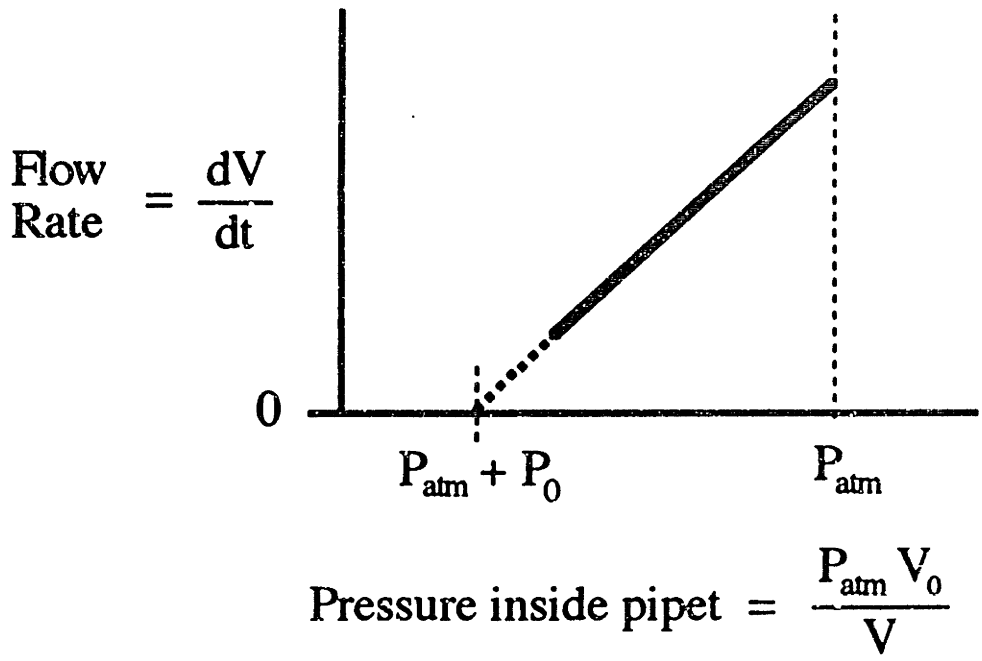

Figure 7.19 Extrapolation of imbibition rate to find limit pressure.

It was essential that the sample be completely dry at the beginning of the experiment and the volume of water that transferred to the sample during equilibration be small, otherwise the time to equilibrate was be prohibitively long. This is not a "true" equilibrium in the classical sense, because the system is not reversible. (See Appendix C.) Difficulties that were encountered with this device caused substantial variation in the measurements of the suction pressure for a given sample. Since the plug was held together by friction, it would frequently come loose, allowing air to relieve the vacuum in the pipet and halting the experiment. This technique could be used to test loose powder, although the effects of powder densification might be difficult to account for. The pressure measured by this technique, K_W, is a characteristic of loose, unprinted powder, so it is not necessary to measure densified powder.

7.6.2 Results

There was a great deal of scatter in the results of the tensiometry measurements. Data for monomodal powders are shown in figure 7.20 below. Two different strategies were pursued in taking these measurements. The data labelled "static" were collected using a coarse powder as the porous plug on the pipet. These tests were found to equilibrate in 15 min to 1 hr., so the capillary pressure could be measured in a single reading. The data

labelled "timed" were made with a finer porous plug, which took several hours to equilibrate. These data were obtained by measuring the volume change in the pipet over time and extrapolating the pressure readings to zero flow rate.

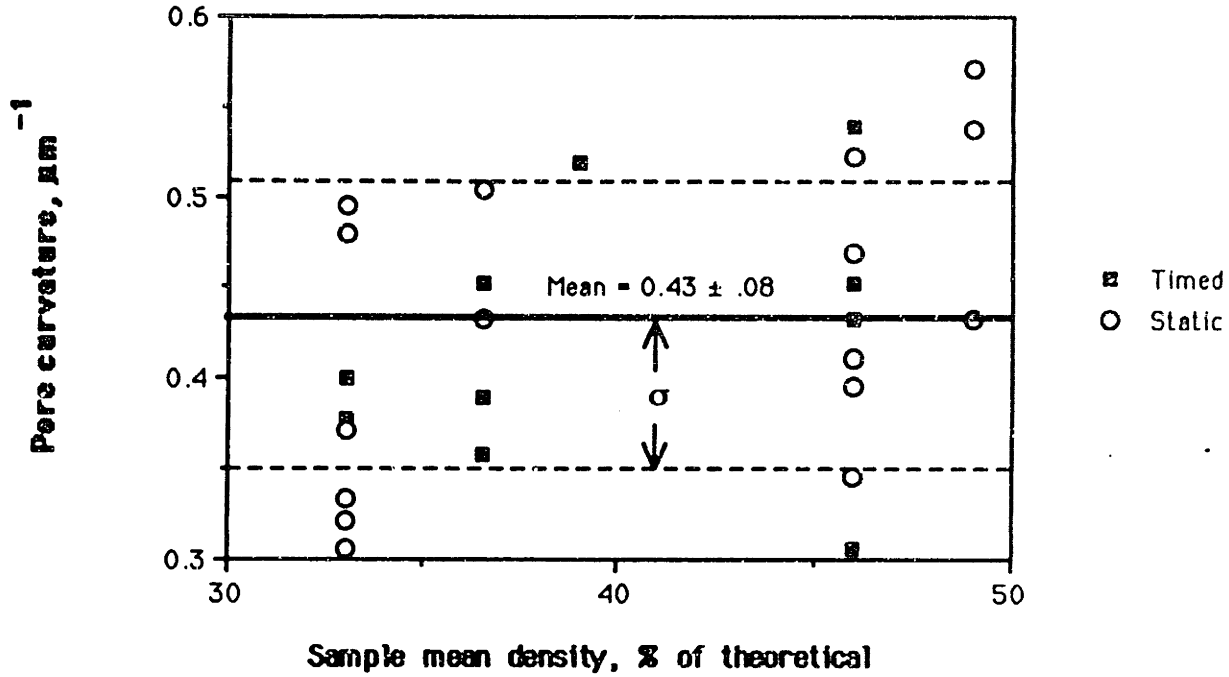

Figure 7.20 Suction pore curvatures for dry, sintered monomodal 30 μm lamellar alumina. See text for explanation of different experimental techniques.

The two techniques basically agree with one another, both in the average value measured, and in the scatter of the data. It seems unlikely that both methods could have been subject to the same level of inaccuracy, so perhaps much of the scatter could be attributed to local differences in the pore structure of the powder itself. There is perhaps a slight positive trend in K_W with packing density, but it is lost in the noise. For monomodal powders, the critical curvature for imbibition can be assumed constant: $K_W = 0.43 \pm 0.08$ μm^{-1}. The real standard deviation of the data is reported here, assuming that it reflects real variation in the structure of the samples. If the scatter were due simply to experimental error, the standard deviation could be reduced by a factor of $\sqrt{n}$, where n is the number of measurements. Large bulk parts can be assumed to sample a large volume of powder, so the effect of this standard deviation would be much less. For this reason, the value calculated here can be used with some confidence to predict saturations applicable to bulk parts. The uncertainty arises when the scale of parts becomes small enough that local variations of the powder properties become significant in determining the saturation. The

effects of this will be quite obvious in the following section, where the saturation of single line primitives is discussed.

Data for other powders are given in tabular form below.

Powder	KW μm-1	std. dev μm-1
30 μm spherical	0.26	0.10
9 μm lamellar	0.82	*
bimodal 10%	1.11	0.15
bimodal 20%	0.83	0.07
bimodal 30%	1.39	0.12
bimodal 40%	1.34	0.02

Table 7.5. Pore curvatures in dry suction. (* One measurement only for 9 μm.)

7.7 Contact Angle Measurement

There exist an interesting diversity of methods for measuring contact angles, largely because of the difficulties in obtaining consistent, accurate results. [Johnson and Dettre] review several methods, all of which involve placing a solid body in contact with a liquid and observing the meniscus in profile. The method used for measuring contact angles was taken from p. 119 of this reference. The advancing contact angle was of primary interest, the receding contact angle was presumed to be approximately zero for the short times of capillary equilibration.

7.7.1. Method

A drop of the liquid to be measured was placed on a cleaned, flat substrate composed of the same material as the powder (alumina.) Using a video camera with a microscope objective, the downhill edge of the slowly creeping droplet was viewed edge-on with lighting from behind. The arrangement is shown in figure 7.21, below.

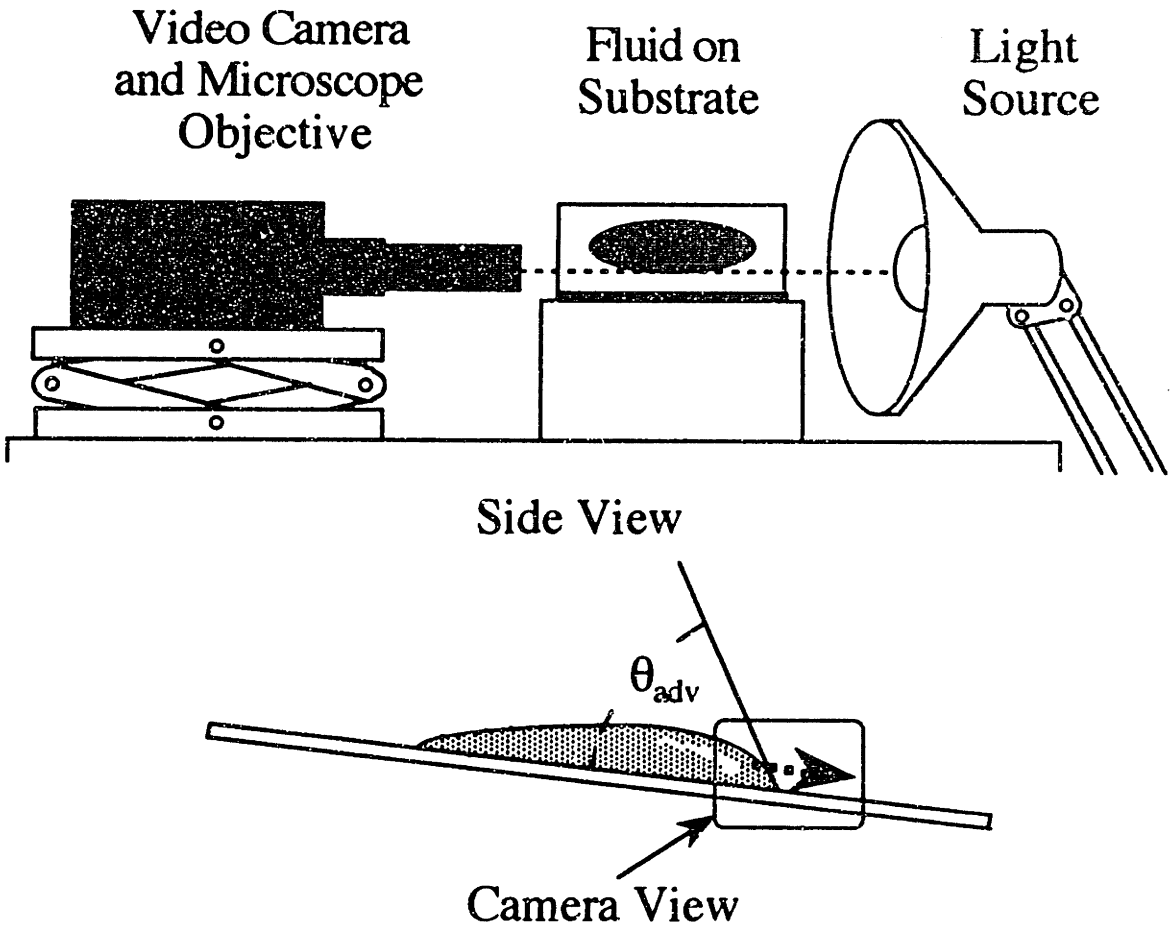

Figure 7.21 Arrangement for measuring advancing contact angles. Tilt of substrate shown greatly exaggerated.

Because of the short depth of focus of the video camera, it was impossible to simultaneously view the point of contact of the leading edge of the liquid drop and the edge of the substrate. To account for this, separate photographs were made of the edge and the droplet. Sample images of an advancing front and the substrate edge are shown below. The point of contact of the fluid droplet with the substrate was interpreted as the intersection between the profile and the reflection; the inclination of a tangent to this point was compared to the inclination of the substrate edge.

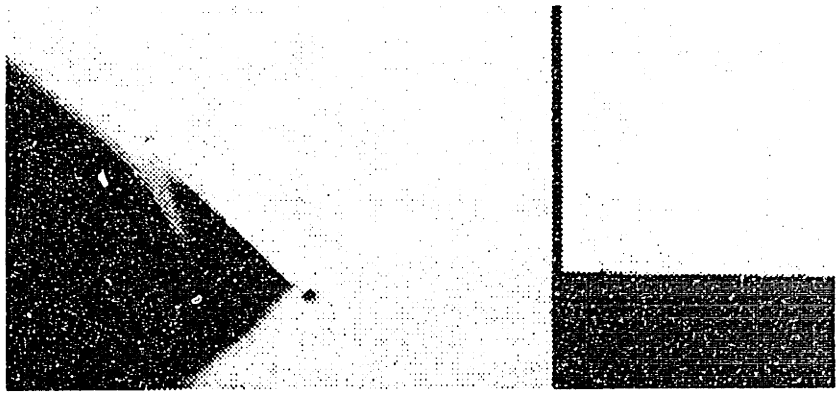

a. b.

Figure 7.2 2 (a.) Advancing front of colloidal silica binder, Formula "B" on alumina surface coated with PMMA.; (b.) Calibration shot of substrate edge. Inclination of liquid surface = 44.9°; inclination of substrate, 1.2°; Contact angle θ = 43.7°.

The difficulty of gaining pictures of a moving droplet at high magnification that were in focus was tricky. The best technique was to use a video frame-grabber and monitor connected to the camera. Two operators worked together: one watched the monitor and attempted to pan the camera along with the advancing front, and told the other when to grab frames on the computer. There was a high mortality of out-of-focus images, but the rate at which they were acquired made this process fairly efficient.

Several different binder compositions were measured, with varying concentrations of surfactant to alter the contact angle. Two surface preparations were used for the alumina substrates: One set was selected from a new shipment, and carefully baked at 700 °C to desorb water. Another set was coated with approximately 50 nm of PMMA to render it hydrophobic. Care was taken not to touch the upper surfaces of any of the substrates before measurement, and any surface was used only once.

7.7.2 Results

The contact angles measured with the video setup in figure 7.21 are shown below. The contact angles of all of the liquids on clean alumina were very small, and the cosine of the contact angle was ≥ 0.95 in all cases. This supports the assumption (section 6.3.1.)

$$\cos\theta_{adv} \approx \cos\theta_{rec} \approx 1 \qquad 7.7$$

Contact angles on the hydrophobically modified surface were substantially larger. Powder was treated in the same way and single line primitives were printed with them to

test the effects of variable contact angle on the equilibrium saturation of single line primitives.

Liquid	Solid	σ_{LV} dyn/cm	Contact angle degrees	Std. Dev. degrees	$\cos\theta_{adv}$
Dist. H_2O	Al_2O_3	72	8.6	0.4	0.99
Binder "B"		47	11.0	2.2	0.98
Binder "C"		58	12.3	2.0	0.98
Binder "X"		31	10.2	1.3	0.98
Acrysol WS-24		?	18.9	0.8	0.95
Dist. H_2O	PMMA	72	50.0	*	0.64
Binder "B"	coated	47	43.7 §	*	0.72
Binder "31"	Al_2O_3	31	43.3	*	0.73
Binder "X"		31	17.9	*	0.95

Table 7.6. Contact angles of binder formulas on alumina surfaces.
* All colloidal silica formulations 17.5 vol.% solids. Acrysol emulsion 15% solids

Notes:
§ see figure 7.22.
* only one frame was needed for large contact angles.
Binder formulas: Approx. quantities for 1 liter. Specific gravity 1.21 in all cases.
B: 735.0 g Nyacol 9950; 385.9 g water, 61.0 g propylene glycol; 24.4 g triethanolamine; 12.2 g diethylene glycol monobutyl ether; 1.0 g polyethylene glycol M.W. 20,000; 0.2 g Thymol Blue.
C: same as B without the diethylene glycol monobutyl ether.
X: same as B with 0.5% Triton X-100.
31: same as C with 0.025% Triton X-100
PMMA coating on Al2O3: 3 x 10^{-4} g PMMA dissolved in 1 cc MEK was spread evenly on a 3"x3" alumina wafer and dried. Result was a coating averaging 50 nm thick.
Surface tensions were measured with a Wilhelmy Plate tensiometer in the Ceramics Processing Research Lab in Building 12.

7.8 Calculation of the Driving Force for Binder Migration

With the assurance that the contact angles are all approximately zero, it is possible to combine the capillary pressure measurements into a calculation of the excess pressure in a fully saturated feature immediately after printing according to the model developed in the previous chapter.

$$\Delta P = \sigma_{LV}\left[K_W \cos\theta_{adv} - K_{NW} \cos\theta_{rec}\right]. \qquad 6.12$$

where $\cos\theta_{adv} \approx \cos\theta_{rec} \approx 1$ and $\sigma_{LV} = 50$ dyn/cm for a typical binder formulation.

Calculations for 30 μm, 9 μm and bimodal lamellar, and 30 μm spherical alumina powders are given below, using data collected from the previous sections. The difference $[K_W - K_{NW}]$ is proportional to the driving force. The excess pressure is calculated, assuming the surface tension is 50 dyn/cm. The value of the saturation at the meniscus curvature determined by K_W has been derived from the porosimetry data for each powder. Note that conditions that give a small or negative excess pressure lead to predictions of high saturation, while high positive excess pressure leads to a prediction of low saturation.

Packing Density f	$K_{90} \approx K_{NW}$ μm^{-1}	K_W μm^{-1}	$[K_W - K_{NW}]$ μm^{-1}	Excess pressure kPa at 50 dyn/cm	$S(K_W)$
Hg, monomodal					
0.35	0.32	0.43	0.11	5.5	0.58
0.31	0.40	0.43	0.03	1.5	0.59
0.35	0.43	0.43	0	0	0.91
0.37	0.33	0.43	0.1	5	0.34
0.36	0.37	0.43	0.06	3	0.53
0.39	0.33	0.43	0.1	5	0.72
0.4	0.40	0.43	0.03	1.5	0.85
0.42	0.39	0.43	0.04	2	0.86
0.48	0.44	0.43	-0.01	-0.5	0.91
0.49	0.45	0.43	-0.02	-1	0.92
0.45	0.50	0.43	-0.07	-3.5	0.97
fit to data	0.07 + .75 f	0.43	0.36 - .75 f	18.0 - 37.5 f	
Haines, mono					
0.33	0.34	0.43	0.09	4.5	0.38
0.46	0.40	0.43	0.03	1.5	0.87
0.49	0.44	0.43	-0.01	-0.5	0.93
Hg, bimodal					
10% fines	0.67	1.11	0.44	22	0.38
20% fines	0.54	0.83	0.29	14.5	0.35
30% fines	0.81	1.39	0.58	29	0.39
40% fines	1.13	1.34	0.21	10.5	0.71
Other					
30 µm spherical	0.38	0.26	-0.12	-6	0.96
9 µm lamellar	0.66	0.82	0.16	8	0.76

Table 7.7 Critical curvatures and feature excess pressure for various alumina powders.

The linear fits to the data for K_{50} and K_{90} permit one to derive an empirical relation for the saturation as a function of packing density for this powder. The slope of the K(S) curve can be estimated from the difference between K_{50} and K_{90} (see figure 7.23). This leads to the approximation

$$\frac{dK}{dS} = 0.2 - 1.195 f_{powder} \qquad 7.8$$

The saturation at some pressure K_W can be approximated by

$$S(K_w) \approx 0.9 + \frac{K_w - K_{90}}{\left(\frac{dK}{dS}\right)} \qquad 7.9$$

from which (assuming $\cos\theta = 1$):

$$S(K_w) \approx 0.9 + \frac{0.36 - 0.75 f_{powder}}{0.2 - 1.195 f_{powder}} \qquad 7.10$$

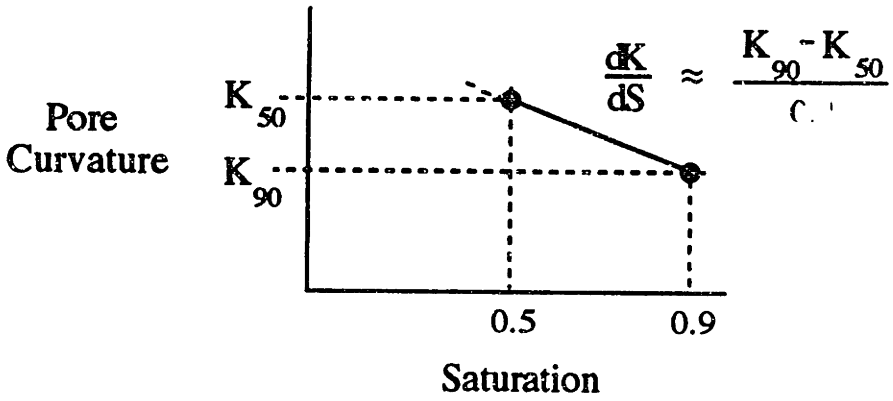

Figure 7.23 Derivation of slope of graph K(S).

The data for $S(K_W)$ derived from the experimental curves are plotted in figure 7.24 below, along with the line corresponding to equation 7.10.

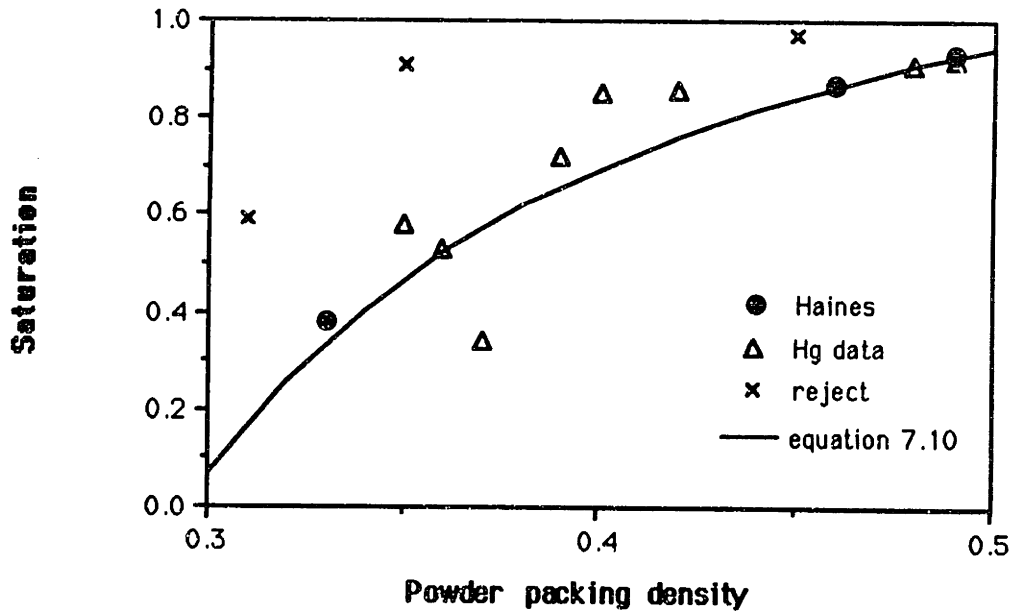

Figure 7.24 Predictions of binder saturations for various powder packing densities, derived from porosimetry and Haines data. Curve derived from linear fits to K_{90} and K_{50} (section 7.5.3) at $K_W = 0.43$ (section 7.7.2). Points designated with "X" were rejected from the fit in that section.

7.9 Washburn Infiltration

7.9.1 Method

If the pore size of a sample is very small, the capillary suction of the dry sample might be too high to measure directly. If this is the case, a dynamic measurement of the suction pressure could be used. The Equation of Washburn describes the rate of imbibition of a cylindrical capillary. The theory was revised and expanded by Levine and Neale. If a block of dry porous material is dipped into a wetting fluid, liquid will be imbibed under the dry suction pressure, P_0, but limited by the pressure gradient and permeability of the sample. A similar form of Washburn's equation can be derived for this situation using Darcy's Law:

$$\frac{x^2}{t} = \frac{2k_{sat}P_0}{(1-f_{powder})\eta} \qquad 5.16$$

where x(t) is distance of the infiltration front from the point of liquid feed

k_{sat} is the permeability of the saturated sample

$(1-f_{powder})$ is the porosity of the sample

η is the viscosity of the liquid.

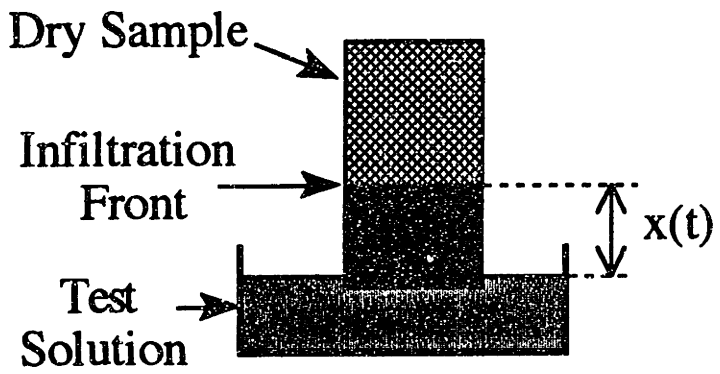

Figure 7.25 Washburn infiltration of a porous sample.

It is somewhat difficult to see the infiltration front unless the test solution is dyed very deeply. It is quite difficult to fabricate sintered powder samples with constant cross section and a great enough length to permit measurements to be made. As a substitute, 3-D Printed ceramic bars, left over from dimensional control experiments, were used. The

porosity of these samples was approximately 46%. This is somewhat higher than what is normal for powder, owing to the volume of silica holding the grains together.

If the porosity of the sample and the liquid viscosity are known, one can use a measurement of the rate of imbibition to estimate the product $k_{sat} P_0$. A discussion of this result can be found in section 5.5.1.

Estimates of capillary properties using this technique depend on accurate knowledge of the porosity and permeability of the sample. Both of these are strongly affected by the presence of residual air in the saturated region of the sample. Also, the measurement assumes that the sample is homogeneous and has a uniform cross section. Since sintered powder samples can become cracked if sintered too long, and uniform samples are difficult to fabricate, this can confound the test. Furthermore, the fluid at the invasion front will tend to concentrate soluble impurities from the specimen, which can drastically affect the surface tension unless the test fluid is chosen carefully.

Since the hydraulic permeability decreases as the square of pore size and the capillary pressure increases only linearly as the pore size, this technique slows down linearly as the pore size decreases. Samples with a large pore size may imbibe too quickly to yield accurate results, but as the pore size decreases, this method may be preferable to other methods that depend on long equilibration times.

7.9.2 Results

Three of these measurements were performed. One measurement was performed on dry powder with a packing density of 44%. The powder was tapped into a slender glass cell (similar in construction to the gel growth cells in section 4.5.2.a.) This cell was infiltrated with binder. This test resulted in an infiltration rate $x^2/t = 30.3$ mm^2/sec. This gives the value of the permeability calculated in section 6.1.3.a.

Infiltration curves for two other runs, made with 3-D Printed bars, are shown below in figure 7.26.

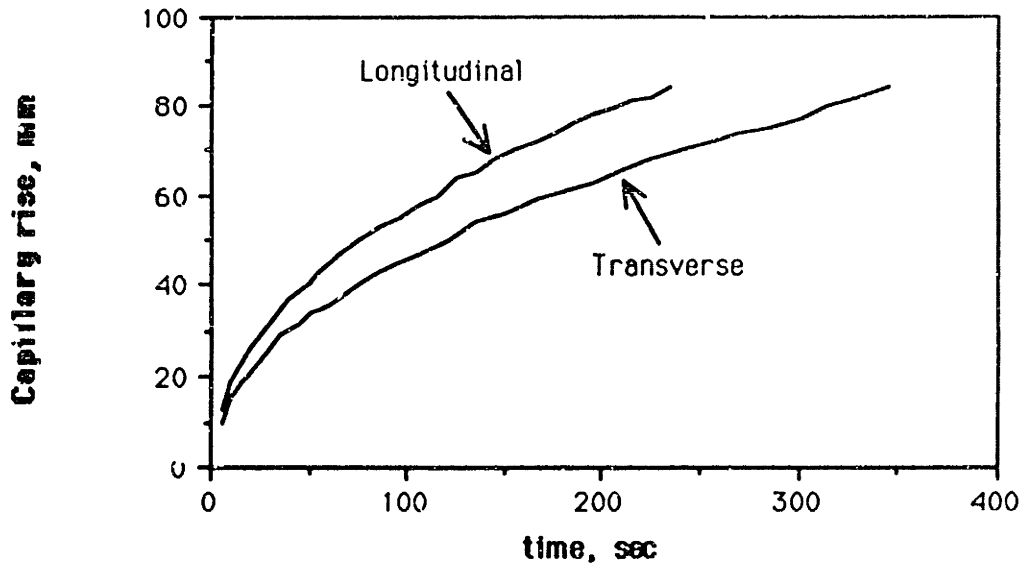

Figure 7.26 Height of infiltration front during free imbibition of soapy test solution (0.1% Triton X-100; 0.1% KOH) by 3-D Printed rectangular bars 10mmx10mmx100mm.

These experiments were under somewhat better control. The bars were printed in different directions, and the difference in infiltration rates reflect the anisotropy of the pore structure of 3-D Printed material. The lines along the longitudinal direction have long, narrow pres between them which affect both the permeability and the strength. The infiltration rate in the transverse direction is probably more characteristic of the permeability of the bulk powder.

The rates for these tests were 31.7 and 22.8 mm^2/sec for the longitudinal and transverse directions, respectively. From these measurements, the product $k_{sat}P_0$ is 7.3 x 10^{-5} and 5.2 x 10^{-5} Pa-cm^2. If we assume $K_W \approx 0.43\ \mu m^{-1}$, $P_0 \approx 13$ kPa. This gives a permeability of 5.6 x 10^{-9} cm^2 for the longitudinal and 4.0 x 10^{-9} cm^2 for the transverse specimens.

7.10 Hydraulic Permeability

The hydraulic permeability of powder is an important parameter on which to base calculations of the kinetics of binder migration. (see sect. 6.1) To measure permeability, it is necessary to establish a pressure difference across a sample and measure the flow rate of a fluid through it. See section 5.4.1 for a discussion of Darcy's Law. Air or water can

be used for this measurement. In both cases, care must be taken to seal the sample so all the fluid passes though the sample. If air is used, the flow must be kept slow to avoid effects due to turbulence and the compression of the gas.

Loose powder can travel with the fluid, so it is necessary to use fixed powder. With fixed powder, care must be taken to avoid crack formation during processing. Also, air trapping in the pores must be avoided unless that is taken into account as part of the measurement. One must be careful that the sample, which acts like a filter, does not become clogged with particles an affect the permeability.

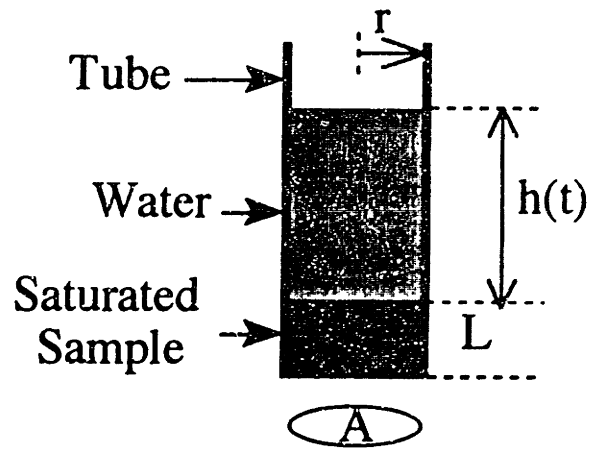

Figure 7.27 A simple setup for measuring permeability

A simple setup for measuring the hydraulic permeability of a small sample is shown above. The sample is sealed in the bottom end of a tube and the tube filled with a liquid. The pressure drop across the sample is determined by the height of the fluid in the tube, so if the height is measured over time, an equation of the following form is obtained

$$\frac{dh}{dt} = -nkh(t) \qquad 7.12$$

where k is the permeability and n is a geometrically determined constant. If the sample has a thickness L and a cross section A and the tube has an inside radius r, $n = A/\pi r^2 L$. The boundary condition is $h = h_0$ @ $t = 0$. The solution is

$$h = h_0 e^{-nkt}. \qquad 7.13$$

The permeability can be found by collecting data of h(t) as the tube drains through the sample, plotting $\ln\left(\frac{h}{h_0}\right)$ vs. t and fitting a line to the curve.

One measurement was made with a sample that had a fractional density of 0.33. The permeability was 2.0×10^{-8} cm^2. Three estimates have been made of the permeability of powder. Different methods were used on powder with different porosities. These are tabulated below and plotted in figure 7.28.

fractional density	permeability cm2	reference section
0.33	2 x 10-8	7.10
0.44	1.2 x 10-8	6.1.3.a.
"0.56"	5 x 10-9	7.9

Table 7.8 Hydraulic permeability of alumina powder.

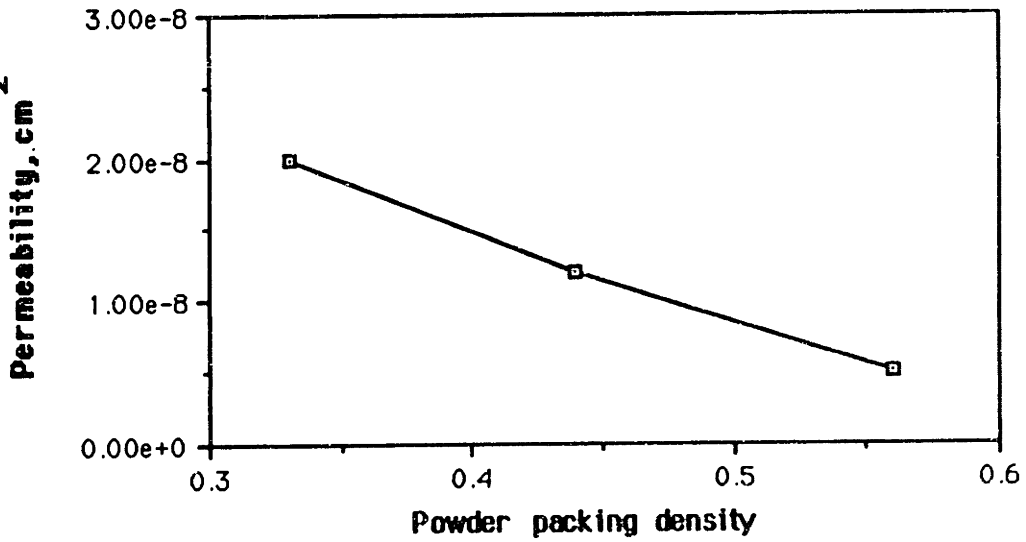

Figure 7.28 Hydraulic permeability of alumina powder vs. packing density.

7.11 Conclusion

By combining data from mercury porosimetry with measurements of the dry suction pressure of sintered powder, it is possible to arrive at an estimate of the equilibrium saturation of single printed lines. These saturations are very much higher than the saturation corresponding to the wetting percolation threshold, about 0.3 for most

materials,predicted as the limit saturation for the continuum models for fluid migration. It remains to measure the saturation in practice to see if it agrees with the theory.

Primitive, single line features are generally in contact with the dry powder that surrounds them, and have a very large ratio of surface area to volume. The migration rate of liquid through the powder samples tested indicate that there is more than sufficient time for the liquid in single line features to come to capillary equilibrium (see calculations in section 6.1.) A program for printing and measuring the liquid saturation in single line features was developed, and the results are presented in the following chapter.

Chapter 8. Experimental Measurement of Binder Saturation in Single Printed Lines

8.0 Introduction

Before a detailed theory can be developed for Three Dimensional Printing of general shapes, one must have a thorough understanding of the formation of "primitive" features. Following the rate calculations in section 6.1, the rate at which binder droplets impact the powder is very much faster than the rate at which binder migrates into the powder, which in turn is faster than the rate at which the binder coagulates. Before the printhead reciprocates, the features have sufficient time to come to equilibrium, so the best candidate for a "primitive" capillary feature is a linear feature formed by a single pass of the printhead. With single lines, the hydrodynamics of feature formation can be separated from the forces imposed by the layering process.

Single, isolated lines surrounded by unprinted powder on all sides are exposed to conditions similar to those that exist on the surface of a bulk 3-D Printed part. The dry powder surrounding the line exerts a capillary attraction on the binder in the line, and the liquid will assume a saturation determined by the attraction. It is likely that if a bulk part is printed at this characteristic saturation, the lines at the surface of the part will be in equilibrium with the dry powder surrounding the part, and the lines buried within the bulk of the part will be at equilibrium with the lines on the surface.

The question of whether the fluid has sufficient time to come to rest before it coagulates can be answered with single line experiments. By comparing results from powders with and without citric acid in the powder, the relative densities of lines will reflect differences in saturation. Predictions of the equilibrium saturations have been derived from capillary pressure measurements in the preceding chapter, and it remains to compare these predictions with experimentally measured saturations in primitive features that probably approach the equilibrium state most closely.

8.1 Sample Preparation

A test pattern was designed which consisted of 50 x 5 cm of single lines, with all segments separated by 1 mm of unprinted powder. The printhead speed and binder flowrate were adjusted to cover a range of binder doses per unit length. The patterns were printed into powder that had been spread, with a number of foundation layers beneath, over alumina wafers. After printing, the wafers were transported to a furnace and fired at 900 °C for two hours. Lines were sieved out of the unprinted powder after firing with an 80-mesh (170 μm) sieve. The sieved lines were weighed on a Mettler analytical balance to the nearest .0001 gram. To measure the diameter, samples of the lines were placed on a black felt background and photographed under a stereomicroscope. The digitized images were measured by an image analysis program to calculate the mean and variance of the apparent diameter.

8.2 Data Collection

8.2.1 Weight Measurements

The most accurate data for measuring the binder saturation is acquired form the analytical balance. While the diameter measurements discussed below have a standard error of about 10% of the mean, the weight measurements are made ±.0001 grams, so the accuracy for the samples measured was typically better than one part in 200.

The accuracy of the weight measurements depends on the selection of the line features and the exclusion of the unprinted powder. There are a number of effects that could cause errors in this measurement. If the agitation of the sieve is not sufficient, loose powder could be retained and transferred to the balance. This could be further aggravated by the strengthening effect of the powder during firing. The lines printed in "ordinary" 30-μm lamellar powder were not subject to this problem, but the bimodal powders that contained fractions of 3 μm fines were difficult to separate from the unprinted powder because of the strengthening phenomenon. The opposite to this problem is if the sieve must be agitated very much to separate them, the lines could be burnished, removing some of the positive texture

The binder dose is calculated directly from the machine settings.

$$A_{liquid} = \frac{\dot{m}}{V_x \rho_{liquid}} \qquad 6.18$$

where $\dot{m}$ is the mass flow rate of liquid binder in the printhead, V_x is the printhead traverse speed, and ρ_{liquid} is the density of the binder. The "normal" printing conditions are .02 cm^3/sec flow rate, and V_x = 150 cm/sec, so A_{liquid} = .0133 mm^2 is the "normal" binder dose. The weight per unit length of silica left after firing is given by

$$W'_{SiO_2} = \frac{\dot{m} f_{WSiO_2}}{V_x} \qquad 8.1$$

where f_{WSiO_2} is the weight fraction of silica in the binder. The weight per unit length of alumina in the sample is found by subtracting the weight of silica from the total weight:

$$W'_{Al_2O_3} = \frac{W_{line}}{L_{line}} - W'_{SiO_2} \qquad 8.2$$

and the powder dose is the volume per unit length of powder in the line features.

$$A_{powder} = \frac{W'_{Al_2O_3}}{\rho_{Al_2O_3}} \qquad 8.3$$

The binder saturation in the powder is calculated from

$$S_{local} = \frac{A_{liquid}}{A_{powder}} \frac{f_{powder}}{(1 - f_{powder})} = \frac{A_{liquid}}{\left(\pi d_{line}^2 / 4\right) - A_{powder}} \qquad 6.23$$

where d_{line} is the measured diameter of the line. The packing density, f_{powder}, can be measured before printing:

$$f_{powder} = \frac{\rho_{bed}}{\rho_{powder}} . \qquad 5.1$$

and it can be estimated after printing:

$$f_{powder} = \frac{4A_{powder}}{\pi d_{line}^2} . \qquad 8.4$$

Differences between these two values could be due to powder densification, but the effect might be difficult to separate from the errors in measurement of line diameter.

A given series of experiments generally consisted of five sets of lines, 2.5 m long. Plots of the powder dose with respect to the binder dose were found to be very linear, so the ratio between the two (the P\B ratio) has been treated as a dimensionless variable:

$$\textbf{powder / binder volume ratio} = \frac{A_{powder}}{A_{liquid}} . \qquad 8.5$$

8.2.2 Diameter Measurements

The diameter of the lines were measured by optical microscopy. After weighing, samples of the lines were placed on a black felt background, and video images were acquired via a frame grabber. An example of one of the images is shown below. The magnification was calibrated at 6.4 μm per pixel. At 72 pixels/inch, the magnification is about 55x. The image as acquired had 16 gray levels. Each image was approximately 400 pixels wide. In order to separate the feature from the background, pixels with a brightness higher than a given threshold were counted inside the feature. This threshold was most often 10, where zero is white and 16 is black. A thresholded image generated from this picture is shown in Figure 8.2, below.

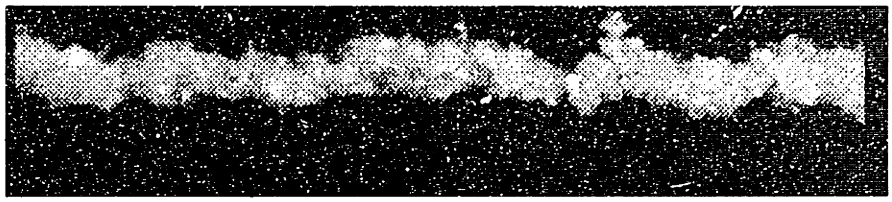

Figure 8.1 A magnified view of a single line (88.7). Grain size: 28μm.
Measured diameter: 153 μm ; Std. Dev: 24 μm; (by occlusion)

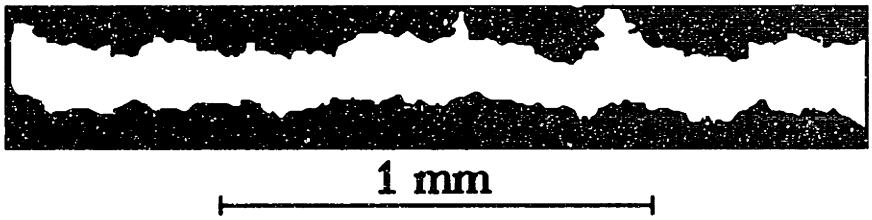

Figure 8.2 Figure 8.1, with data thresholded at darkness = 10/16. (same as figure 6.10)

The thresholded images were compared visually with the source image to verify that the thresholded contour accurately represented the apparent horizon of the line. If the image was accepted, white pixels were counted in vertical columns across the picture, and the mean and variance of the width were calculated. Typically, four to eight different images were taken from different portions of the lines in each sample. In all, over 1300 pictures were created electronically and examined for 225 different experimental conditions. These conditions are given in Table 8.1, below. The data collected during these experiments is given more completely in Appendix E.

Ser.	sample #s	binder formula	contact angle °	powder	powder treatment	spread density
1a	1,2,3,4,13	E	15	30μ 7920	no rinse	0.32
1b	5,6,7,12	E	15	30μ 7920		0.32
1c	8,9,10,11	E	15	30μ 7920	0.2% cit.	0.31
2	14-28	E	15	30μ 7920		0.34
3	29-34	E	15	28μ 7920		0.46
4a	35-40	E	15	28μ 7920		0.44
4b	41-47	E+.5% Triton	0	28μ 7920		0.42
5a	48-51	B	10	28μ 7920		0.46
5b	52-57	B	10	30μ 7920		0.34
5c	58-62	B	10	28μ 7920		0.46
6	64-68	B	10	10% bim.**		0.41
7a	69-73	B	10	28μ 7920		0.49
7b	74-78	B	10	28μ 7920	.5%cit.coat	0.35
7c	79-83	B	10	28μ 7920	.2%cit.coat	0.38
8	84-91	B	10	28μ 7920		0.48
9a	92-97	B	10	28μ 7920		0.36
10a	98-101	B	10	28μ 7920	.5%cit.coat	0.30
11a	102-106	B	10	30μ sph.S		0.53
9b	107-111	C+.35% hexyl	10	28μ 7920		0.36
10b	112-116	C+.35% hexyl	10	28μ 7920	.5%cit.coat	0.30
11b	117-121	C+.35% hexyl	10	30μ sph.	S	0.53
9c	122-5,136	C+.2% hexyl	10	28μ 7920		0.36
10c	126-130	C+.2% hexyl	10	28μ 7920	.5%cit.coat	0.30
11c	131-135	C+.2% hexyl	10	30μ sph.	S	0.53
9d	137-141	C+.025% Triton	10	28μ 7920		0.36
10d	142-146	C+.025% Triton	10	28μ 7920	.5%cit.coat	0.30
11d	147-151	C+.025% Triton	10	30μ sph.	S	0.53
11e	152-155	C	12	30μ sph.	S	0.53
10e	156-160	C	12	28μ 7920	.5%cit.coat	0.30
9e	161-165	C	12	28μ 7920		0.36
12a	166-168	B	10	28μ 7920		0.39
13a	169-173	B	44	28μ 7920	1%acr.coat	0.35
14a	174-178	B	44	28μ 7920	1%ac.lock	0.35
12b	179-183	C+.025% Triton	10	28μ 7920		0.39
13b	184-188	C+.025% Triton	44	28μ 7920	1%acr.coat	0.35
14b	189-193	C+.025% Triton	44	28μ 7920	1%ac.lock	0.35
12c	194-198	B + .5% Triton	0	28μ 7920		0.39
13c	199-203	B + .5% Triton	18	28μ 7920	1%acr.coat	0.35
14c	204-208	B + .5% Triton	18	28μ 7920	1%ac.lock	0.35
15a	209-213	B	10	20% bim.**		0.40
15b	214-217	B	10	30% bim.**		0.39
15c	218-221	B	10	40% bim.**		0.39
16	222-225	B	10	30% bim.**	slurry	0.57

Table 8.1. Conditions for line saturation experiments

Notes:

Binder formulas: Approx. quantities for 1 liter. Specific gravity 1.21 in all cases.

B: 735.0 g Nyacol 9950; 385.9 g water, 61.0 g propylene glycol; 24.4 g triethanolamine; 12.2 g diethylene glycol monobutyl ether; 1.0 g polyethylene glycol M.W. 20,000; 0.2 g Thymol Blue.

C: same as B without the diethylene glycol monobutyl ether.

E: 750 g Nyacol 9950; 386.3 g water; 122.5 g propylene glycol, 48.5 g "TRIS" = tris(dimethylamino)aminomethane; 1 g polyethylene glycol ; 0.5 g Thymol Blue.

Triton is Triton x-100; **hexyl** is diethylene glycol monohexyl ether. These additives were used to modify the surface tension and contact angle.

Contact angles measured by photographing sessile drops on alumina substrates. (sect. 7.7)

* alumina powder was washed with distilled water and decanted.

bim.** bimodal powder: 28 mm and 3 μm lamellar 7920 alumina, washed. Percentage is weight percent fines. (see sect. 7.5.2)

§ spherical powder: Showa Denko 30 μm "Alunabeads"

cit.coat: Rinsed powder coated by adding dilute citric acid solution to powder such that saturation ≈10%. Dried at 100°C. Percentage given is by weight w.r.t. powder .

acr.coat: Rinsed powder coated with 1% PMMA by weight Al_2O_3 dissolved in MEK using similar procedure for citric coating.

acr. lock Powder coated with acrylic prepared by spreading on alumina wafers, and locked by heating to 250°C.

Powder packing density measured by weighing 72 cc of powder spread in the printing machine.

8.3 Experimental Discussion: Powder\Binder System with No Additives.

The experiments were structured in such a way that data from a complete series could be used to extract information about the density and binder saturation. Throughout the experimental program, many control series were run on unmodified powder using ordinary binder. These series were used to characterize the basic process over variable packing density. The data used in the following discussion came from series 1b,2,3,4a,5c,7a,8,9a,9b,9c,9d,9e,12a, and 12b. Although the precise composition of the binder used varied slightly over all of these series, differences between performance were primarily due to contact angle, and not directly correlated to the differences in composition.

8.3.1 Direct Examination of Line Density

The data shown below are for two different batches of powder, nominally the same, that packed to different densities under the same processing conditions. By varying the printhead speed across the powder bed, lines of different diameters were printed. For each set of lines in a 2.5 m sample, both the weight and the diameter were measured. The weight was measured on a Mettler analytic balance with an accuracy of ±.0001 g and the diameter was measured by the mean width of images gathered on a stereomicroscope. The accuracy of the weight measurements should be assumed to be an order of magnitude more accurate than the diameters. The data presented are combined results. The line labelled "44-46%" combines results from series 3 and 4a. The line labelled "32-34%" is combined from series 1b and 2.

These data are plotted logarithmically for the purpose of observing whether or not the features might have fractal structure. The mass is seen to vary as the square of the line diameter across approximately half an order of magnitude. From these results, it can be concluded that these features are compact. (sect. 6.6.2)

Pictures of representative lines from these samples are shown in Figures 8.4 and 8.5 below.

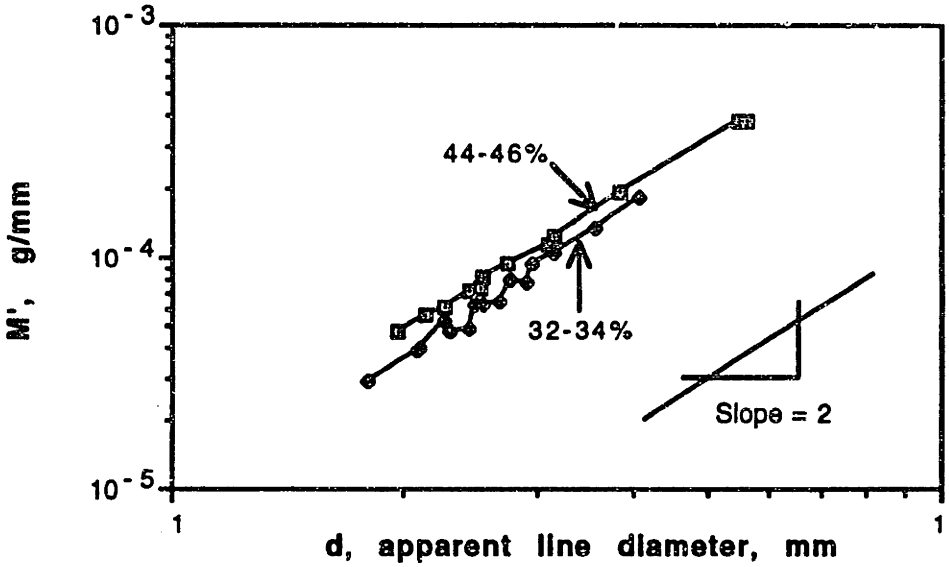

Figure 8.3 Line weight per unit length vs. line diameter, mm, measured optically. Data is for binder "E" (54 dyn/cm) and 7920 alumina with no additives: high density: series 3 & 4a; low density: series 1b & 2.

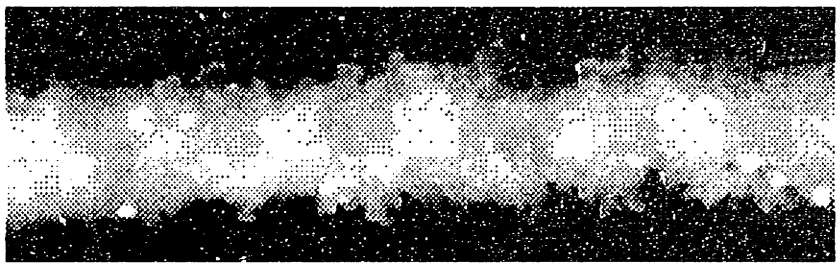

a.

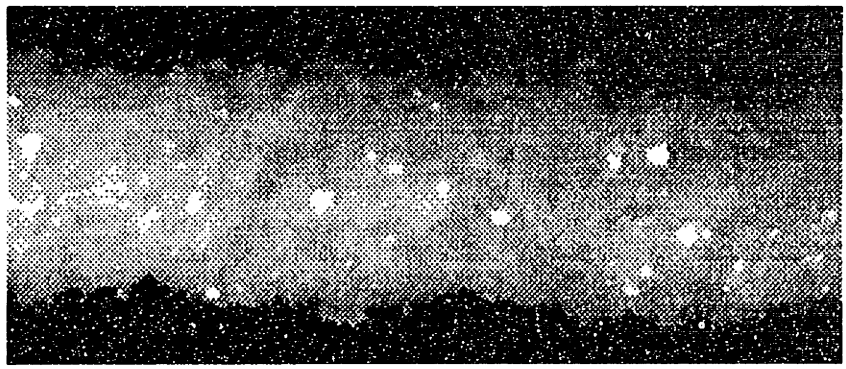

b.

Figure 8.4 powder: 30 μm 7920 alumina, 34% packing, no additives.
a.) Sample 26.2, Binder "E", 1.50 cc/min, printhead speed 1.65 m/s.
M = 73x, diam = 246 ± 19 μm. (optical)
b.) Sample 21.6, Binder "E", 1.40 cc/min, printhead speed 0.38 m/s.
M = 73x, diam = 424 ± 27 μm. (optical)

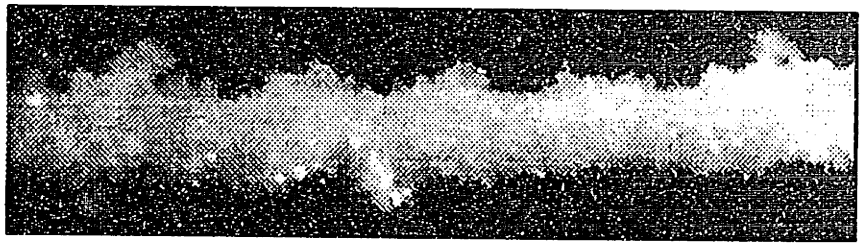

a.

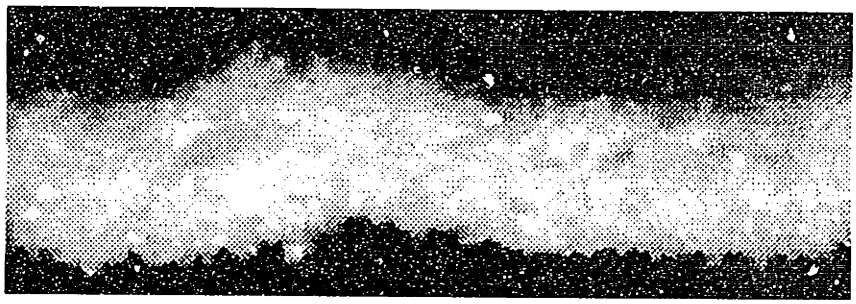

b.

Figure 8.5 powder: 28 μm 7920 alumina, 46% packing, no additives.
a.) Sample 29.3, Binder "E" 1.12 cc/min, printhead speed 1.65 m/s.
M = 73x, diam = 188 ± 26 μm. (optical)
b.) Sample 34.7, Binder "E", 1.60 cc/min, printhead speed 1.02 m/s.
M = 73x, diam = 318 ± 28 μm. (optical)

All of the lines have quite rough surfaces, and the standard deviations of the line diameters are roughly the same: approximately equal to the grain size of the powder used. Highlights reflecting off of planar facets of individual grains can be distinguished, but the morphology is very difficult to see. The enhanced edge contrast of the SEM permits a little better view. For more SEM views, see Alan Lauder's MS thesis.

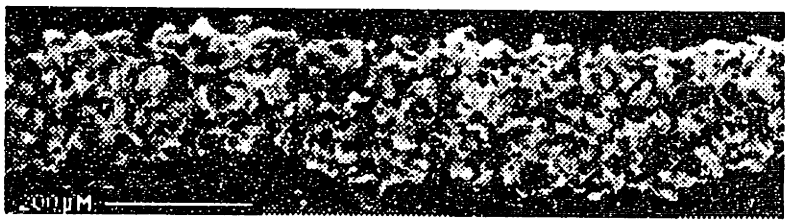

Figure 8.6 Scanning Electron Micrograph of a single line. (Sample 9)
powder: 28 μm 7920 alumina, 31% packing, 0.2% citric acid.
Binder "E" 1.41 cc/min, printhead speed 1.50 m/s.
M = 80x; diam = 233 ± 17 μm (optical)

Individual grains can be easily resolved on the scanning electron microscope. The structure does not appear to be permeated with large pores, but it is reassuring that the weight data supports the conclusion that the features are compact.

8.3.2 Observations of Powder\Binder Volume Ratio

For any set of lines, the quantity of silica per unit length is known from the process conditions. The quantity of alumina present can be calculated by subtracting the weight per unit length of silica from the measured weight per unit length of the sample (eqn. 8.2). Data for alumina without additives, at various packing densities are shown below. The weights have been divided by the densities of the components to give cross-sectional areas.

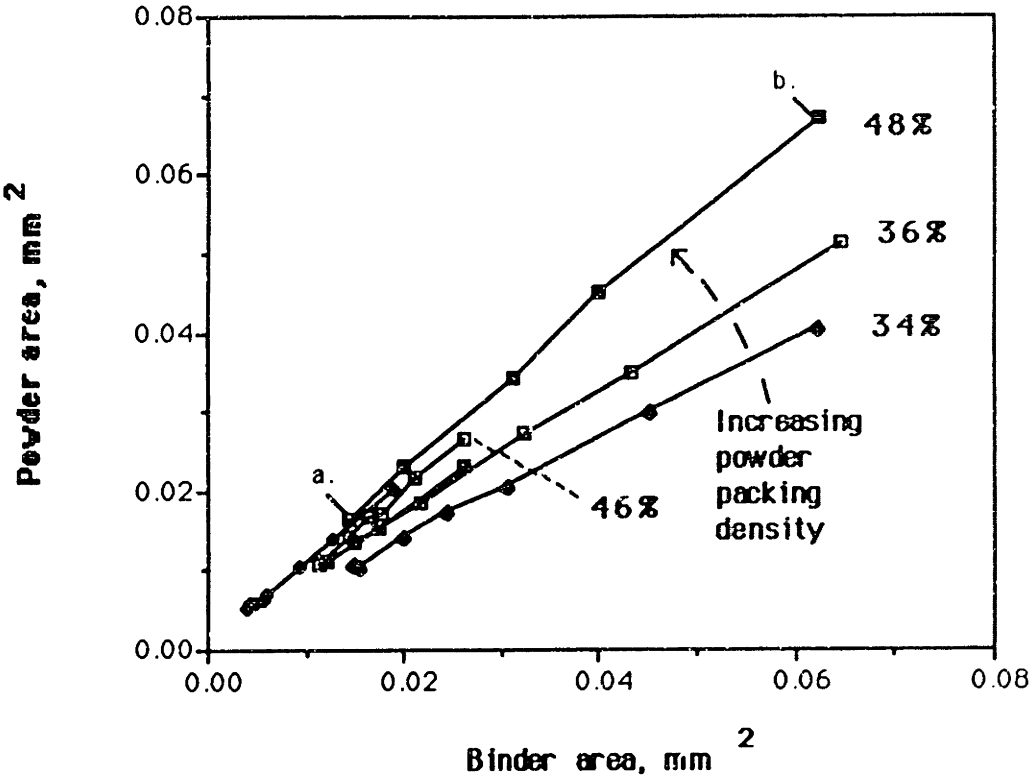

Figure 8.7 Powder area vs.binder area in single lines for 7920 powder at various packing densities. a. and b. are samples 69 and 71, respectively, shown in figure 8.14, below. These samples were printed into densely packed powder and exhibited a great deal of surface roughness. A binder dose of 0.0133 corresponds to "normal" conditions.

These data are strongly linear, radiating from the origin. These indicate that a fundamental quantity for a given series is the ratio of the powder and binder volumes for a given test condition. The important parameter of the powder packing density has been left off of this graph to avoid confusion. The slope of these lines shows how the incremental addition of binder in a feature increases the amount of powder incorporated into the lines. If powder is assumed to be distributed equally in the space surrounding the point of impact of the jet, the uniformity of this slope suggests that a fixed volume of liquid binder is needed to invade a particular region in order to incorporate a quantity of powder. This rate

is variable with packing density: the amount of binder needed decreases as the packing density increases. The Powder\Binder volume ratio is plotted below as a function of powder packing density for 7920 alumina.

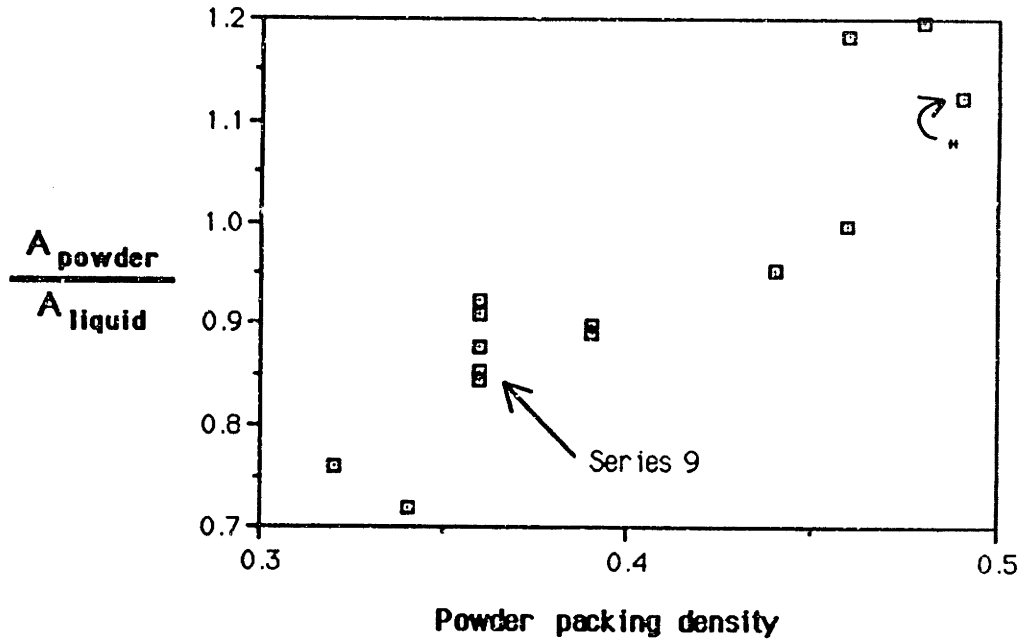

Figure 8.8 Powder\Binder volume ratio as a function of powder packing density. Data from series 1b,2,3,4a,5c,7a,8,9a,9b,9c,9d,9e,12a, and 12b. * indicates series 7a containing samples 69 and 71 illustrated in Figure 8.14, below. Note that this point is unexceptional, even though these lines had very irregular surfaces. In Series 9, the binder surface tension was varied. The contact angle varied between 0° and 10°, so there was little change in $\cos\theta$. The variation in P\B ratio did not correlate with the surface tension, so this is treated simply as scattered data.

It can be clearly seen that this ratio depends strongly on the packing density and the relationship can be further simplified by plotting the slope of the line from each point to the origin as a function of packing density, shown below. This slope is equal to the quantity A_{powder} / f_{powder} which represents the cross sectional area of the bulk line, $\pi d^2/4$, assuming that the powder packing density does not change during printing.

The ratio plotted in figure 8.9 is scattered evenly around a mean of 2.37 with a standard deviation of 0.16. These data suggest very strongly that the **volume fraction filled by binder in single lines is nearly a constant fraction** (0.42 ± 0.03) **of the total volume of the line.** This qualitative expression reflects the competition between two effects that cancel each other out in this range of packing density. These two effects are the lower saturation at lower packing densities due to the higher bubble pressure

of the powder, and the larger amount of space available at the lower packing densities which must be filled at a given saturation.

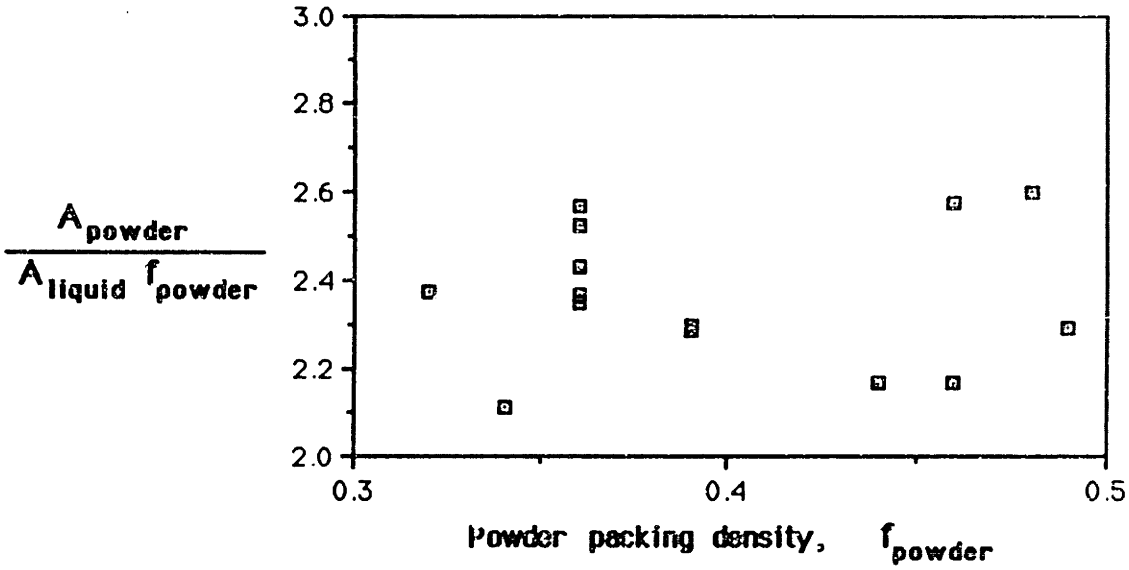

Figure 8.9 Line\Binder volume ratio vs. packing density.
Data from series 1b,2,3,4a,5c,7a,8,9a,9b,9c,9d,9e,12a, and 12b.

8.3.3 Appeal to Optical Measurements

Observations based on the P\B ratio alone depend on some assumption about the porosity of the powder in the sample. For convenience, it was assumed that **the packing density of the powder in features after printing was equal to the packing density before printing.** It is very important to verify whether or not this assumption is well founded. To answer this question it is necessary to appeal to the microscopic measurements of line diameter. Since these data are somewhat suspect we will compare them to an estimate of the line diameter, given by (see eqn. 6.22)

$$d_{est'd} = \sqrt{\frac{4A_{powder}}{\pi f_{powder}}} \quad . \qquad 8.6$$

The optical diameter is plotted as a function of the estimated diameter below for the series of lines used to generate Figures 8.8 and 8.9. The data are too thick to derive any quantitative conclusions, but from this plot it is easy to see that the diameters measured optically are slightly larger than the diameters estimated from the line packing density. Two possibilities to explain this discrepancy are that the optical measurements place a positive bias on the diameter or that the powder is expanded by the impact of binder when the lines

are formed. There is a good reason to suspect the former (section 6.6.1) and little reason to suspect the latter [Jain Charnnarong, private communication].

If the discrepancy is due to the powder changing density, it would be variable with line scale: the error caused by assuming a high value for the packing density would become larger with larger lines . It is shown below that this is not the case.

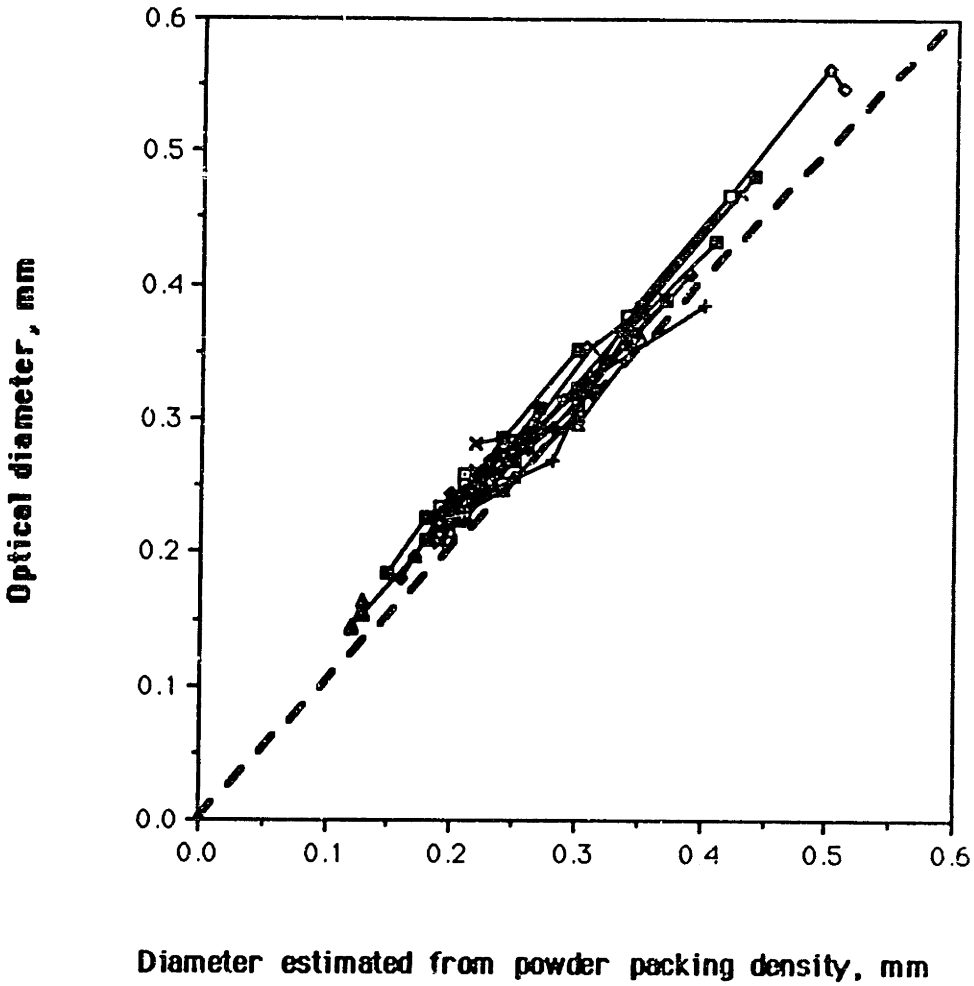

Figure 8.10 Optically measured line diameter vs.line diameter estimated from line weights for alumina 7920 with no additives at various packing densities.

The difference between the estimated and optical diameters is plotted below as a function of packing density . From these data it can be easily seen that there is no trend in the errors of the optical measurements with respect to powder packing. In fact, the

apparent bias of the optical measurement is 26 μm with a standard deviation of 14 μm which is almost identical to the dimensions of the powder grains.

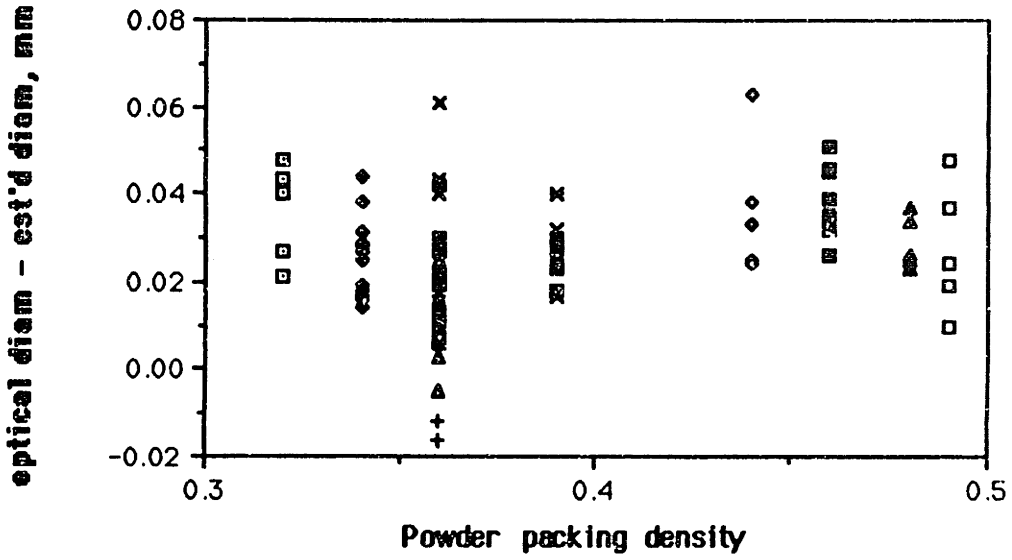

Figure 8.11 Bias in optical measurement as a function of powder packing density.

8.4 Calculation of Equilibrium Saturation of Single Line Features

It has been shown earlier that there is a very good reason for the optical measurements to place a positive bias on the diameter of the lines, and this bias is, in fact, very close in magnitude to the grain size of the powder. Thus it can be concluded that there is no significant change in the powder packing density during printing, and one can convert the P\B ratio directly into a binder saturation by:

$$S_{local} = \frac{A_{liquid}}{A_{powder}} \frac{f_{powder}}{\left(1 - f_{p...}\right)} \qquad 6.23$$

and

$$f_{liquid} = \frac{S_{local}}{\left(1 - f_{powder}\right)} \qquad 8.7$$

is the volume fraction of binder in the entire bed. The measured values for saturation are shown in the table below for the "control" series printed with ordinary binder into rinsed, unmodified powder.

Series	packing density	P\B ratio	saturation measured	volume fr. binder	contact < degrees	$K_W\cos\theta - K_{NW}$ μm^{-1}
1b	0.32	0.76	0.63	0.43	15	0.102
2	0.34	0.72	0.71	0.47	15	0.087
3	0.46	1.00	0.86	0.46	15	-0.003
4a	0.44	0.95	0.85	0.48	15	0.012
5c	0.46	1.19	0.74	0.40	10	0.005
7a	0.49	1.12	0.85	0.44	10	-0.017
8	0.48	1.20	0.80	0.42	10	-0.010
9a	0.36	0.88	0.65	0.41	10	0.080
9b	0.36	0.91	0.62	0.40	10	0.080
9c	0.36	0.92	0.61	0.39	10	0.080
9d	0.36	0.85	0.66	0.42	10	0.080
9e	0.36	0.85	0.67	0.43	12	0.078
12a	0.39	0.89	0.72	0.44	10	0.058
12b	0.39	0.90	0.71	0.44	10	0.058

Table 8.2. Results of saturation measurements for unmodified 7920 alumina. Data in last column derived from porosimetry measurements.

The measured values of saturation show the same trend as the data estimated from the capillary pressure data in section 7.8: Low packing density in the powder leads to a low saturation. The data can be more easily be compared graphically, below:

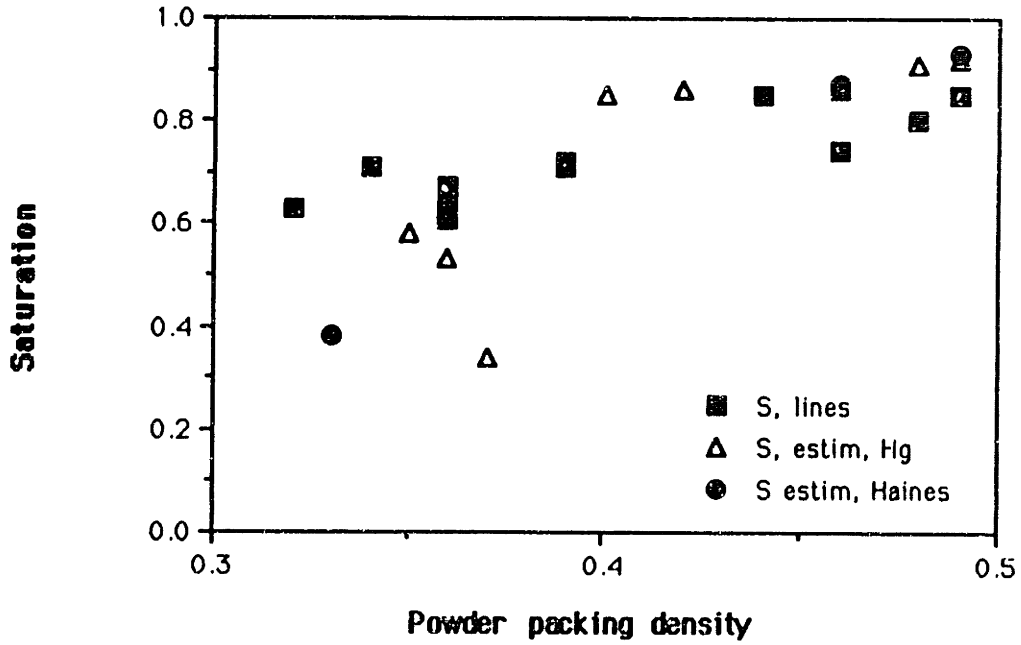

Figure 8.12 Saturation vs. packing density, real data for single line primitives and theoretical predictions derived from capillary pressure measurements.

The correspondence between the experimental measurements and the estimates from capillary pressure measurements is less than perfect: the saturations at low packing density are significantly higher than the prediction based on the capillary pressure measurement.

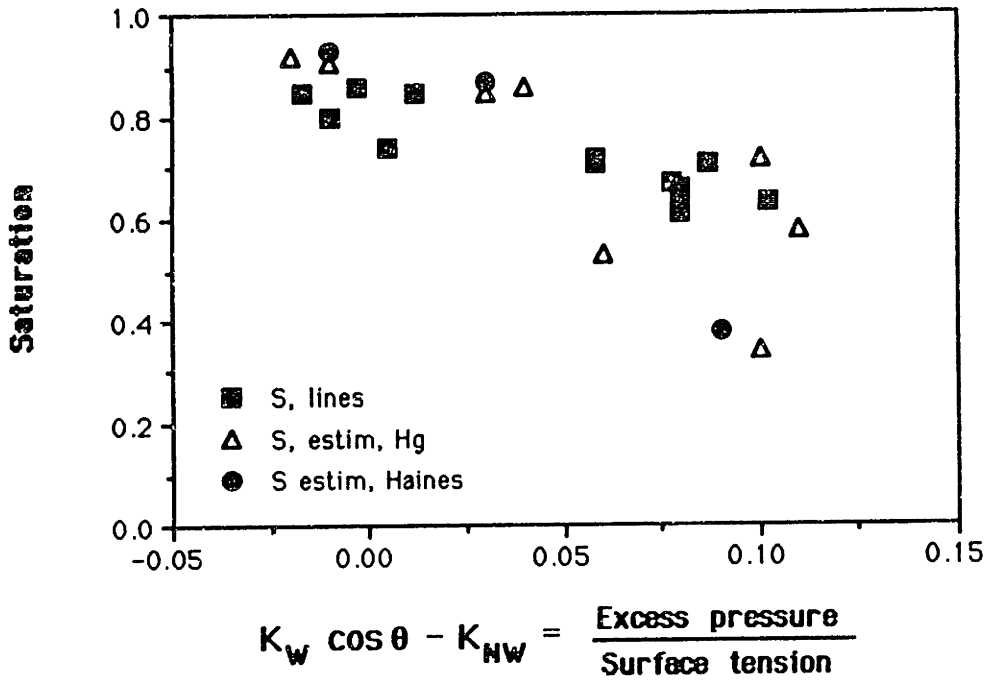

Figure 8.13 Saturation vs. $[K_W\cos\theta - K_{NW}]$ for single line primitives and $S(K_W)$ from capillary pressure measurements.

In figure 8.13, the saturation data is plotted with respect to the group $[K_W\cos\theta - K_{NW}]$ for the powder samples. This is proportional to the driving force for binder migration, following the derivation in section 6.3. Again, the agreement between the experimental data and the estimates from capillary pressure measurements is marginal, at best. Regrettably, the scatter in the data is far too large to base any quantitative conclusions.

8.5 Comment on Surface Finish

Two extreme situations where binder arrived outside the desired boundaries of a line are illustrated in Figure 8.14, below. These points are designated a. and b. in figure 8.7. Figure 8.14.a shows a line of a small diameter ($\approx 200\ \mu m$) that is otherwise relatively smooth except that it has a "wart" poking out of its side at periodic intervals. This is in contrast to Figure 8.14.b, which shows a surface modified

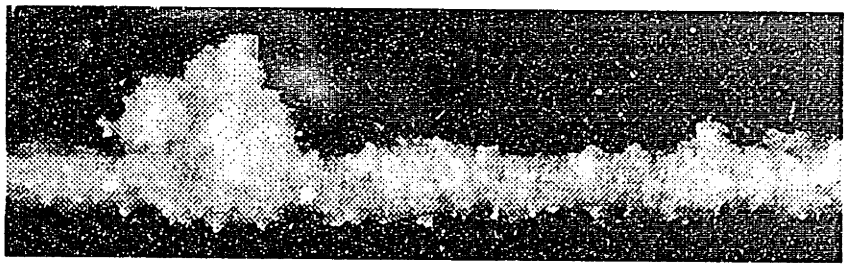

a.

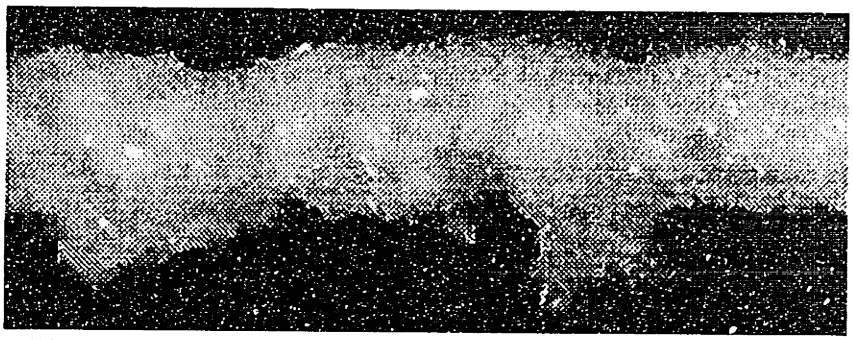

b.

Figure 8.14 Single line primitives showing odd surface features.
Binder "B" 1.43 cc/min powder: 28μm 7920 , no additives, 49% packing
a) Sample 69.7: printhead speed 1.65 m/s; M = 55x; diam = 230 ± 83 μm (optical)
b) Sample 71.5, printhead speed 0.38 m/s; M = 55x; diam = 466 ± 75 μm (optical)

binder bleeding out into the powder surrounding the area initially wetted by the impact of the jet. These samples are indicated on Figure 8.7 and the P\B volume ratio for this series is indicated with an asterisk in Figure 8.8. Referring to these graphs, those very irregular lines do not particularly stand out in the weight data. It must be that the areas infiltrated by binder outside of the cylindrical limits of the line had very nearly the same density as the rest of the line, so their presence does not affect the overall powder\binder volume ratio.

The surface finish of 3-D Printed material depends on the surface finish of the lines comprising it. It was evident that the texture on the line in figure 8.14.b was due to fluid migration. These samples (series 7) had a measured saturation of 0.85, so it does not necessarily follow that highly saturated material necessarily has better surface finish. The origin of the wart in figure 8.14.a is unknown. These features were found regularly spaces, about 3-4 mm apart along the sample.

8.6 Conclusion: The Performance of the Basic Process

8.6.1. Conclusions from this Chapter

In order to explore the change of the process when conditions are varied, it is necessary that the basic process be characterized very well. The foregoing analysis is an attempt to do this for the combination of 7920 alumina with a grain size of approximately 30 μm and no additives into which binder is printed containing 30.5 wt.% silica with a nominal surface tension of 45 - 60 dyn/cm. For this combination of materials the following conclusions can be drawn:

1. There is practically no densification of the powder upon printing of single lines into dry powder with no additives. This conclusion had to be inferred from comparison between optical and weight measurements. The bias of the optical measurements was constant only if it was assumed that the powder did not change in density when printed. If any densification exists, it must change the diameter 10 μm or less in lines up to 400 μm in diameter. The change in powder density must therefore be less than 5% of the mean; e.g. powder of 40% density compacts by less than 2% on printing. This conclusion has been supported by other measurements taken by Jain Charnnarong on bulk printed parts.

2. The features are compact: i.e. they do not possess a fractal structure that affects their size or density significantly. This conclusion is supported by comparing the weight of lines with their diameter over a range of binder contents at constant packing density (fig. 8.3) If the lines were fractal, their density would decrease with increasing diameter.

3. The measurement of line diameter by the optical technique developed in this thesis overestimates the line diameter by approximately 26 μm. Since this is approximately the grain size, it can be assumed that this effect is due to the random arrangement of individual grains attached to the surfaces of the lines. In other words, the camera sees single grains standing on the surfaces of the lines, but cannot see grain-sized holes that penetrate the surface.

4. Binder printed into 7920 alumina with no additives appears to fill 42% of the space in the powder bed with a standard deviation of about 3% regardless of how the remaining volume is divided between solid powder and air. This condition holds for a range of packing densities from 32% to 49%. This observation is supported qualitatively by the

measurements of capillary pressure from chapter 6. AS the powder packing density decreases, the saturation should decrease, but the amount of space that must be saturated increases. The competition between these two effects keeps the volume fraction of fluid constant over this range of packing density.

5. The saturation of binder in the features is marginally in agreement with estimates based on capillary pressure measurements. The scatter in both data sets makes close comparison difficult, but there appears to be more divergence at lower packing densities. The reason behind this could be the slowing of the migration rate that occurs at lower saturations: the lines may not have had sufficient time to equilibrate before drying.

8.6.2 Discussion of Earlier Data

a. **Marcos Esterman** reported data taken be Alain Curodeau on the widths of single-line walls in 325-mesh alumina powder. These widths were measured optically, and correspond to the widths of walls at the top of the part.

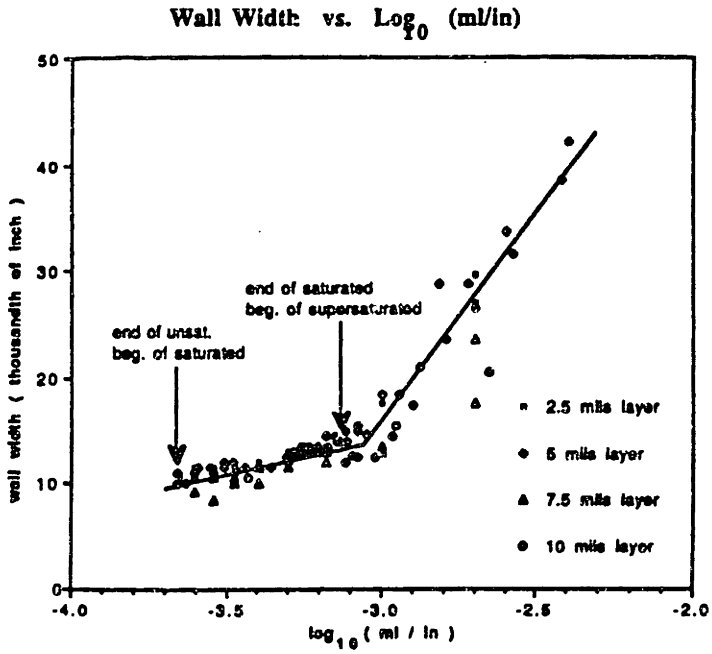

Figure 8.15 Wall widths vs. binder dose for colloidal silica in 325 mesh alumina. Data by Curodeau [Esterman, p. 36]

These parts were printed with unmodified colloidal silica, and consequently, the parts at higher doses bled ferociously. The point labelled "beg. of supersaturated" corresponded to a binder dose of .031 mm^2, about 2.3 times the "normal" binder dose. This graph is primarily of historical interest, because it helped to decide to fix the "normal" dose approximately at the point labelled "beg. of saturated". The problem of bleeding was solved shortly after this work, with the introduction of binder "A" (see sect. 4.4.2)

Speculating for a moment on the form of the graph, the knee of the curve corresponds closely to a binder dose that would fill 50% of the volume of a rectangular region 250μm square along the fast axis. The lower limit, about .01 mm^2, corresponds to a line containing 40% per unit volume binder, with a diameter of 180 μm (7 mils). A possible explanation for this form is that the binder jet penetrated approximately 250 μm on impact, independent of the spread layer thickness. If the dose was less than .031 mm^2, the spread was approximately the same as the penetration depth (250 μm $\approx$ 10 mils.) Quantities in excess of this critical does spread out to the sides of the line of impact, so a twice the dose, the wall was twice as wide, at three times the dose, the line was three times as wide, and so on.

b. **Alan Lauder** reported more data for wall widths. By this time, binder "A" was in use, and Lauder looked at the degree of spread of the liquid as a function of binder dose. He did little with the data, but he noted that the lines printed into powder containing citric acid were highly distorted by the spreading mechanism, while the features containing polyacrylic acid were compact. Lauder concluded that the features printed with polyacrylic acid had a high enough green strength to support the forces imposed by the spreading mechanism. His micrographic evidence is quite convincing. While these highly distorted features are not necessarily comparable to undistorted cylindrical lines, it is evident in figure 8.16 that the concentration of citric acid does not greatly affect the size of the lines.

The undistorted lines containing polyacrylic acid had a fluid content of approximately 50% of the volume of a homogeneous wall. since they were nearly cylindrical, the volume fraction of liquid was roughly 64%, corresponding to 100% saturation. Besides gelling the binder, the polymer must have increased the viscosity to the point where the liquid could not migrate before gelation. As the binder dose increases towards the right margin of the graph, the saturation of all of the lines tend to approach the line corresponding to 40% binder per unit volume: the empirical result found in section 8.3. At the highest binder doses, the quantity of liquid added would overwhelm the acid in the

powder right around the impact point, so the approach to capillary equilibrium could proceed further. Some experimentation was done with polyacrylic acid here; see sections 4.4.2 and 4.5.2.

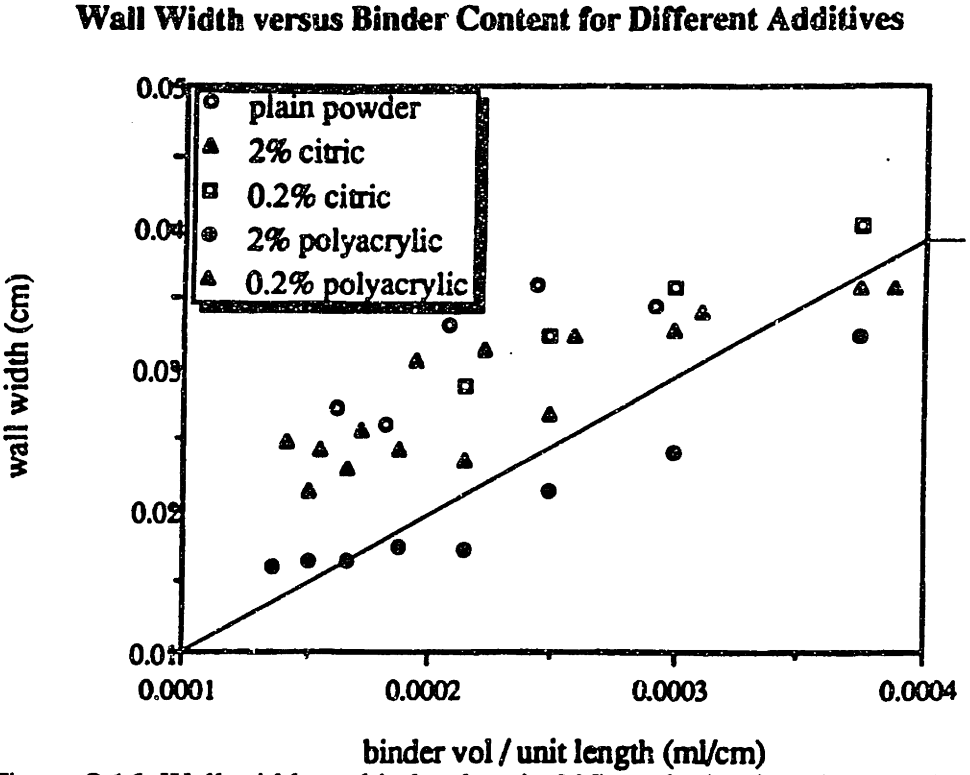

Figure 8.16 Wall width vs. binder dose in 325-mesh alumina. Layer thickness = 250 μm. From Lauder, p. 65. Concentrations of acid additives are weight percent in 325-mesh alumina, 35% packing. Binder composition: Nyacol 830 + 2% TMAH. Line corresponds to a volume fraction of liquid binder equal to 40%.

Following the acquisition of these results, some printing was done using polyacrylic acid as a coagulant. Unfortunately, this materials combination proved to be unacceptable for printing due to distortion of the parts. Experience has shown that materials combinations with weaker gel strength are less prone to distortion caused by layers drying during the printing process.

Chapter 9. Variation of Process Conditions

9.0 Introduction

In the previous chapter, experiments were discussed that were designed to characterize the 3-D Printing of ceramic shells using "ordinary" processing conditions. This mostly regards the condition of the powder, which consisted of unmodified lamellar alumina, Norton #7920, with a grain size on the order of 30 the binder flow rate covered the normal operating range, and the surface tension, while subject to wide variation in different tests, didn't noticeable alter the contact angle with the powder. The chief variable was the packing density of the powder, and it was found that, subject to the large amount of scatter in the measurements, that the migration of binder in unmodified powder agrees with the model derived from the assumption that the binder comes to capillary equilibrium with the surrounding powder.

In this chapter, experiments are discussed in which the processing conditions are pushed to various extremes, to determine the limits of the model and of the process itself. In the first set of experiments discussed, an attempt was made to find the lower limit in feature size that could be obtained using available hardware. The greatest success was obtained by using a 30-μm diameter nozzle that dispensed smaller droplets than usual. In the following section, a set of experiments were done to see whether the presence of citric acid has any affect on feature size. It has been shown earlier that the rate of gelation or the binder formula in use is slow enough that it was unlikely that there would be any kinetic effect: i.e. the binder gelling before it could come to equilibrium. In these experiments, the effect of citric acid addition was found to influence feature formation insofar as the citric acid affects the packing density of the powder during printing, which in turn affects the migration of binder.

In the remainder of the experiments discussed in this chapter, different powder formulations were tested. Spherical powder was tested in one series. In another set, the effects of powder locking and variable contact angle were investigated. The results did not diverge from the predictions based on the model.

In the last set of experiments, bimodal powders containing 3 μm and 30 μm grain sizes were tested. These powders were found to diverge substantially from the predictions based on the model. The divergence could have been caused in part by the extreme amount of densification that occurred in the powder upon moistening with the binder, and in part because of the low permeability resulting from the smaller mean pore size which slowed down the capillary equilibration to the point where the binder gelled by drying before it had sufficient time to migrate.

9.1 Line Formation at the Extreme Lower Limit of Binder Dose

The feature size of the printer is the primary determinant of the accuracy of the printer. There exist many schemes of arranging features of a given size to give a resolution better than the feature size, but all must address the feature size as a fundamental quantity. To explore the lower limits of ordinary feature size, two series of experiments were performed. In series 5, a TTL switching circuit was built into the path of the electronic signal between the computer and the charging amplifier. A diagram of this circuit is given in Appendix G. This permitted lines to be printed using one of every four droplets emitted by the printhead; the remaining three were charged and caught by the catcher. In series 8, a 30 μm nozzle was substituted for the standard 50 μm nozzle in the printhead. This resulted in a flowrate three times smaller than that obtained under ordinary conditions.

9.1.1 1:4 Circuit, Standard 50μm Nozzle

The maximum speed available on the standard 3-D Printing equipment at MIT was 1.65 m/sec. Since the breakoff frequency for the 50 μm Kodak nozzles was 77 kHz, this translated to a maximum droplet spacing on the powderbed of 21 μm per droplet. Droplets are approximately 80 μm in diameter, so a pattern in which one droplet in every four is printed would correspond to a droplet spacing approximately equal to their diameter.

Following the analysis in the previous chapter, we can examine the structure of the lines by looking at the weight/unit length of the sets of printed lines. The weight per unit length of the silica from the binder is known from process conditions, and the weight per unit length of alumina is found by subtracting the silica weight from the total weight of the samples. The data are converted to cross-sectional areas (volume per unit line length) of

liquid binder and powder to make the results relate more closely to the original printing conditions. A graph of powder area vs. binder area is shown below in figure 9.1 for Series 5, with two packing densities of powder using the 1:4 switching circuit. There is some indication of a deviation from ordinary linear behavior for the range of binder doses below .005 mm^2. This deviation is, in fact, a complete breakdown of the continuity of the single lines.

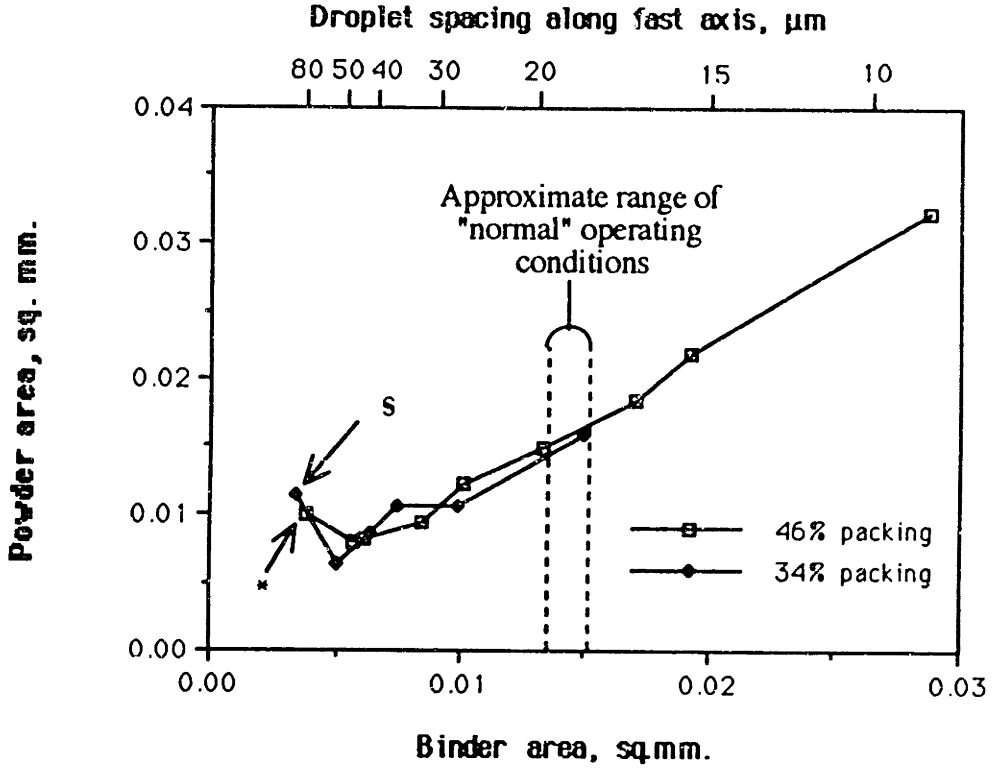

Figure 9.1 Powder area vs. binder area for printing binder at low flow rates into 7920 powder with no additives. * Sample 47 ; § Sample 52. Binder distribution varied at constant flow rate by varying printhead speed. Droplet spacing calculated assuming breakoff frequency 75 kHz, printhead speed 1.5 m/sec.

Ordinarily, lines were collected in a sieve with 180 μm openings (80 mesh) which was sufficient to collect lines with a minimum of shock. It was found that significant mass was passing through this screen for these samples, so a second sieve with 90 μm openings (170 mesh) was used to collect the disconnected powder\binder aggregates. The fraction of the total weight collected by the smaller screen is shown in figure 9.2 below. Since single binder droplets create primitives 120 μm in size or larger ([Lauder 46], see figure 9.7) the 90 μm sieve was sufficient to collect all powder moistened by binder. Only line segments shorter than 180 μm could pass through the 180 μm sieve, and since single droplet primitives are already 120 μm across, these features must be composed of only a couple of droplets of binder plus the powder they accumulated on impact.

The result of this breakdown in continuity is that more powder is incorporated into the features because the features become spherical instead of cylindrical. One of these primitive features can be seen in figure 9.3, below, next to a short linear segment for the lowest binder dose in the denser packing powder. Sample number 52, designated in these figures with the symbol § is especially interesting because was composed almost entirely of disconnected spherical primitives.

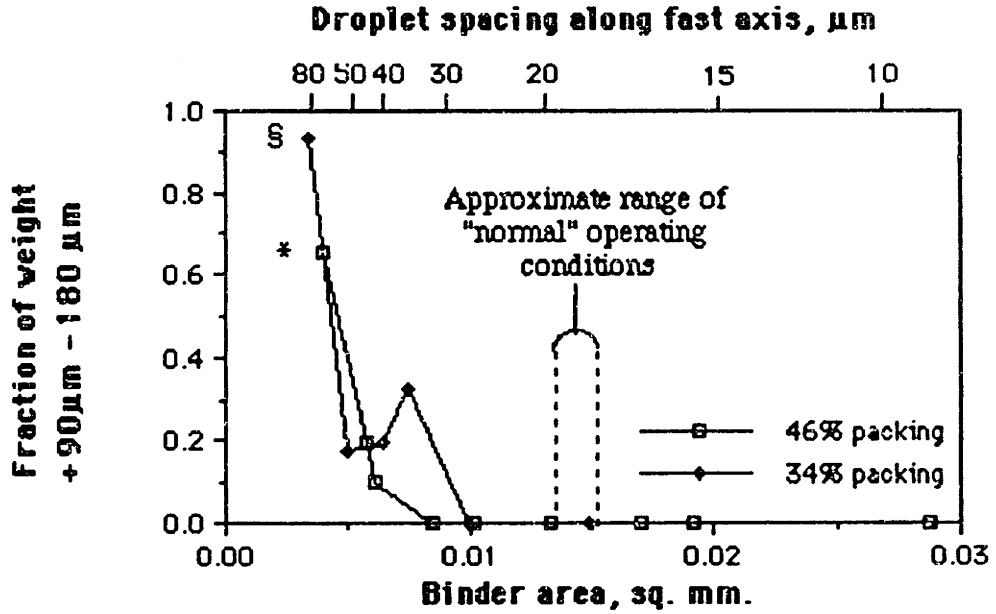

Figure 9.2 Fraction of total mass collected -180 µm +90 µm vs. Binder dose for series 5. * Sample 48; § Sample 52.

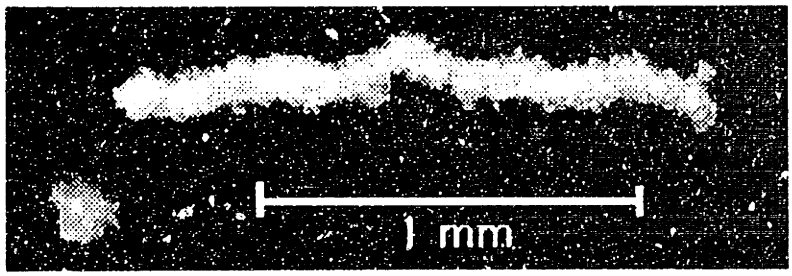

Figure 9.3 Tiny single line primitive. Sample 48.5: Powder: 28 µm 7920 alumina, 46% packing, Binder "B", 0.39 cc/min (with 1:4 circuit) printhead speed 1.65 m/s; diam = 139 ± 13 µm. (optical) ; M = 48 x. Also shown is a primitive formed of 2-3 droplets. major axis ≈ 170 µm Point designated with * in graphs in this section.

This breakdown is further amplified when the powder\binder volume ratio is plotted versus binder area in figure 9.4, below. Please note that at these very low binder doses, the P\B volume ratio asymptotically approaches a value of approximately 1.1-1.2 for both 34% packing and 46% packing. The binder saturation is accordingly 44-47% for the low packing density and 77-84% for the high packing powder. The sample consisting predominantly of spherical primitives (§) had a P\B ratio of 3.3, about three times as much powder as the other samples printed at the same packing density, but with the droplets more closely spaced.

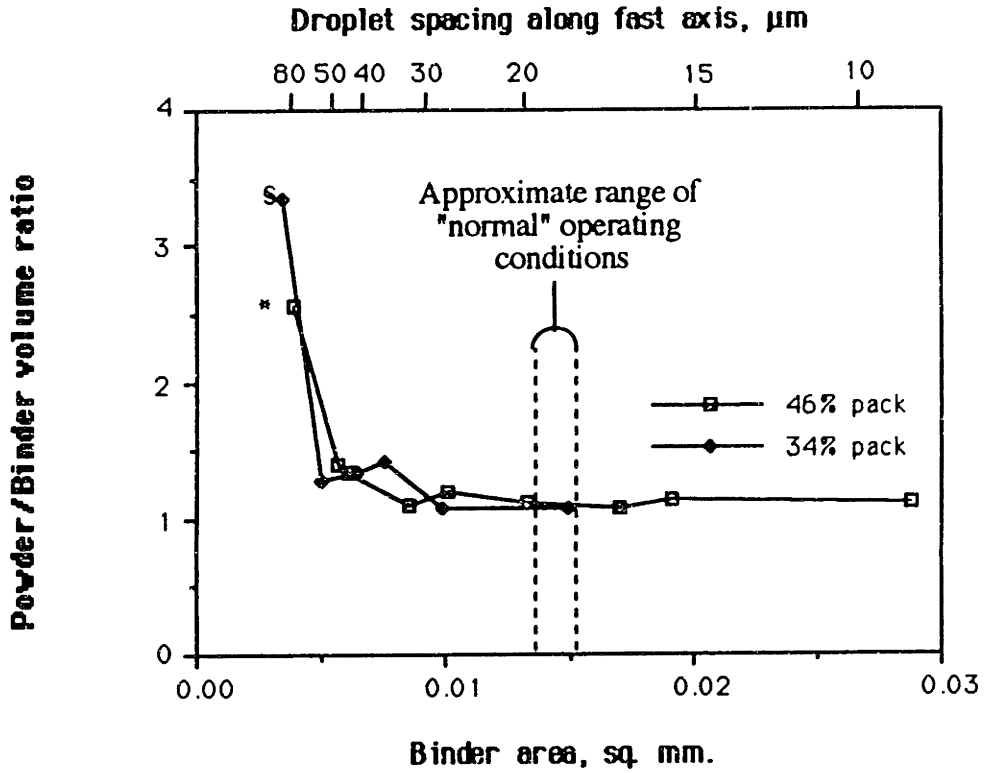

Figure 9.4. P\B volume ratio for individual samples in series 5. * Sample 48; § Sample 52. (See Appendix E)

There are a few possible explanations for this extreme increase in density of the features when the droplets are disconnected. Spherical droplets posses 1.5 times the surface area of a cylinder of the same diameter and volume, this increases the effect of powder grains adhering to the surface by point-contact to binder-wetted portions. It is very difficult to see how this effect alone could account for all of the difference. Another likely effect is that the kinetic energy of the impact of a single droplet in isolated, dry powder causes the droplet to moisten more powder (per unit volume) than it ordinarily would when the droplets overlap. When droplets overlap, each succeeding droplet lands on powder that

is already moist, and so additional powder grains are incorporated by capillary migration. Since grains initially wetted are not easily dewetted, this results in a structure for single droplet primitives that is not governed by the capillary equilibrium.

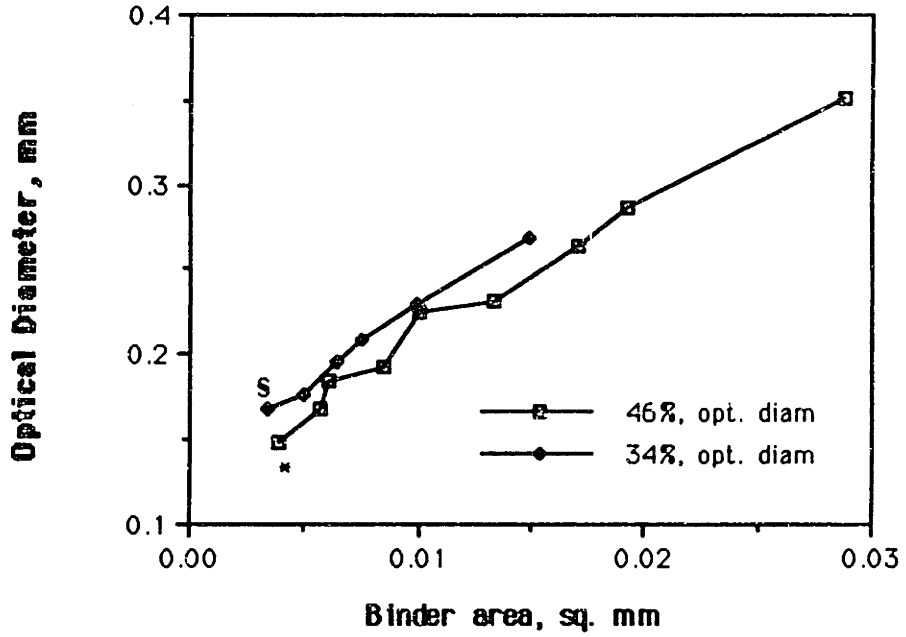

Figure 9.5. Optical diameter for lines at low binder dose. * Sample 48; § Sample 52. Measured from fraction +180 μm. * 34.5% of sample weight +180μm; § 6.5% of sample weight +180 μm.

The fractions that were caught by the 180 μm screen could be measured optically. The diameters could also be estimated from the weight of powder contained in the samples. If the diameter measured optically is compared with the estimated diameters, as shown in figure 9.6, it can be seen that the optical measurement consistently overestimates the line diameter by about 30 μm in the same way as in the previous chapter, except in the pathological cases in samples 48 and 52. In sample 52 in particular, 93.5% of the material passed through the 180 μm screen, but the optical measurement was made on the remaining 6.5% which were cylindrical. The diameters of the lines were very much smaller than the estimated values because the higher density of the disconnected spherical primitives skewed the calculation.

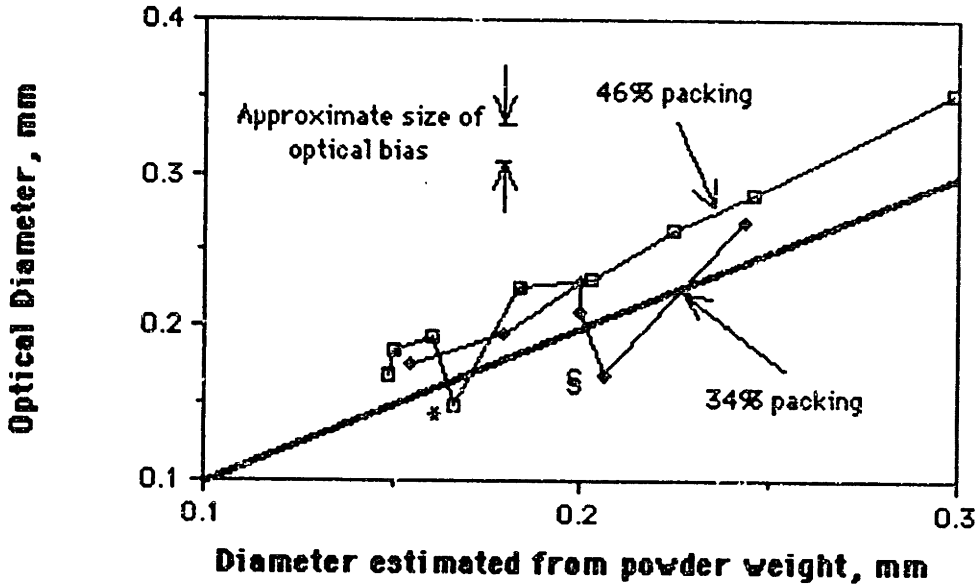

Figure 9.6 Optical diameter vs. estimated diameter for Series 5.* Sample 48,§ Sample 52.

Lines as small as 150 μm in diameter can be printed with a 50 μm orifice. The lower limit of line integrity appears to correspond to the condition where the droplets impact the powderbed at a spacing of one droplet diameter.

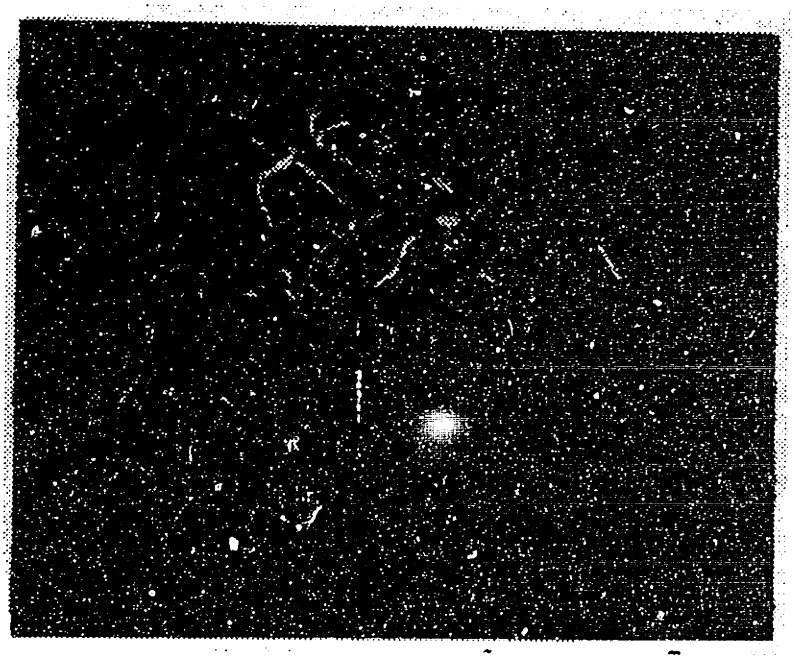

Figure 9.7 Single droplet primitive. [Lauder 46]

9.1.2 Feature Formation Using a Smaller, 30 μm Nozzle.

To experiment with low binder doses using smaller droplets, wire-bonding tools were obtained from Gaiser Tool Co. with an orifice diameter of 30 μm (1.2 mils) (See Dave Brancazio's thesis for a discussion of the assembly of wire-bonding tools into a printhead.) At a fluid pressure of 40 psi, the flowrate was found to be 0.41 cc/min. The corresponding jet velocity was theoretically 9.7 m/s: consistent with normal operation of a 50 μm nozzle at 0.9 cc/min. The optimum stimulation frequency was found to be 122 kHz. At this frequency and flowrate, the droplet diameter was 47 μm. At 1.65 m/s the droplets landed every 14 μm. The stream was charged in a 26-mil charging cell at 30 V and deflected in a 60-mil deflection cell with a high voltage of 800 volts. A series of lines (Series 8) were printed into 28μm 7920 alumina with no additives which, on that day, packed to 48% of theoretical density.

The performance of this nozzle in the printing of single lines can be most compactly expressed by plotting the powder\binder volume ratio as a function of binder dose and comparing the curve with that for a "standard" 50 μm nozzle, printing 80 μm droplets every fourth cycle.

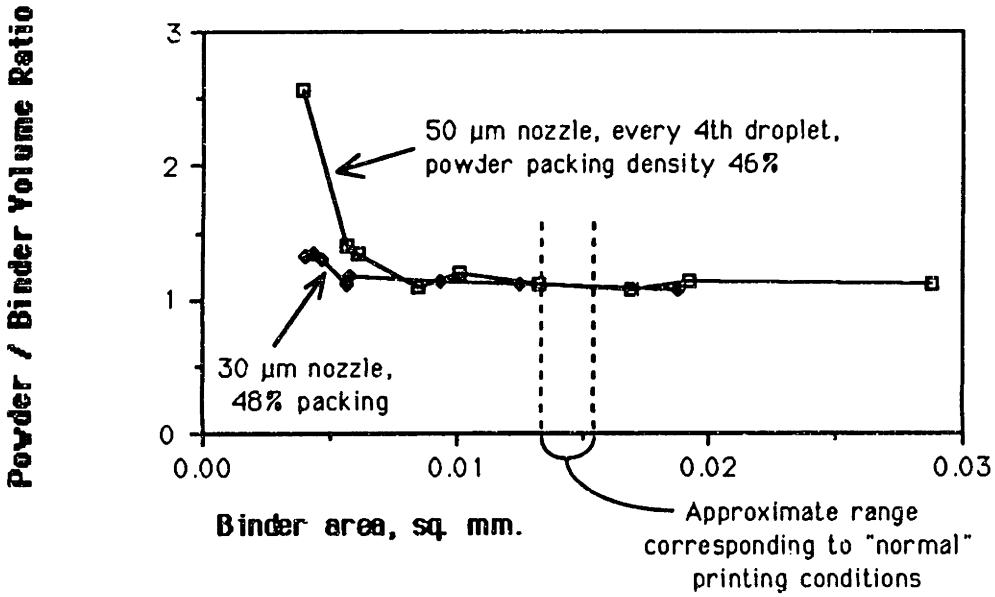

Figure 9.8 P\B volume ratio vs. binder dose, comparing 30 μm and 50 μm nozzles. Data for 50 μm nozzle same as in Figure 9.4.

The onset of line breakdown can be detected on this graph, and it is further amplified by examining the weight fraction of the sample collected between 180 μm and 90 μm screens in figure 9.9, below. The variation of optical diameter with binder dose is

shown in figure 9.10. It should be understood that the optically measured diameters are consistently 26 μm over the true diameter. The finest lines produced by any 3-D printer, in sample 85, are illustrated in figure 9.11, below. (To see the exact experimental conditions, see Appendix E.

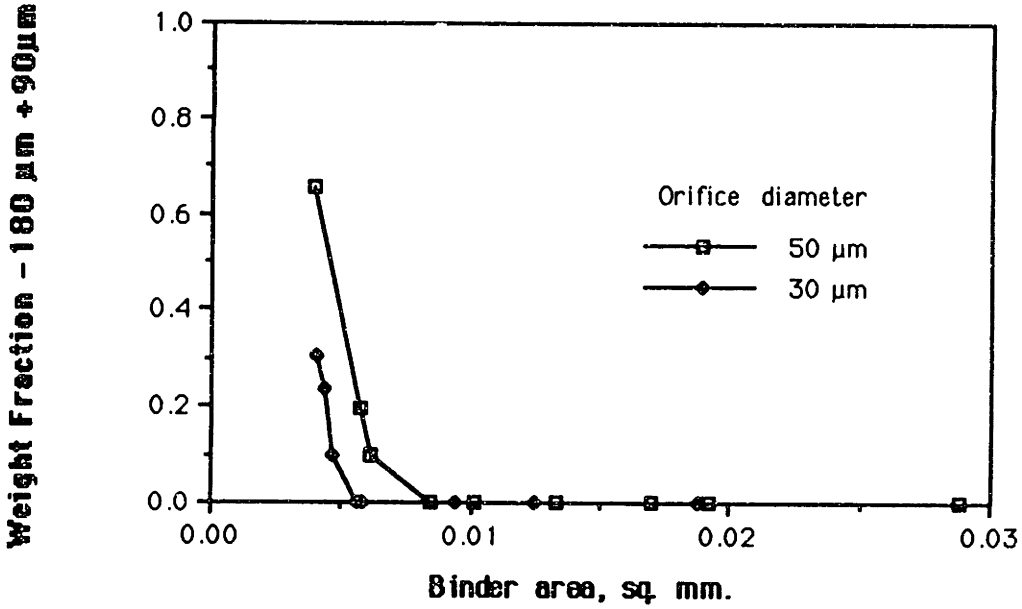

Figure 9.9 Weight fraction of sample -180 μm + 90 μm vs. binder dose. Series 5a,5c,8. (50 μm nozzle, 1:4 switched; and 30 μm nozzle)

The graph of the weight fraction that passed through a 180 μm screen is a direct indicator of the quality of knitting of the primitives. The 30 μm droplet generator ran at 120 kHz, while the 50 μm droplet generator ran at 75 kHz. The higher frequency droplets were more closely spaced along the fast axis, besides having a smaller size. Because of this, the binder could be spread more thinly along the fast axis before the droplets became disconnected. For the points on both curves at which 10% of the mass of the sample was in the form of disconnected spherical primitives, the larger droplets were spaced about 40 μm apart along the fast axis. This corresponds approximately to the radius of the droplets. For the smaller droplets, the spacing was approximately 15 μm along the fast axis. These droplets were about 45 μm in diameter. The degree of overlap of the smaller droplets was larger at the threshold where the droplets became disconnected, but the smaller size of the droplets still yielded finer features.

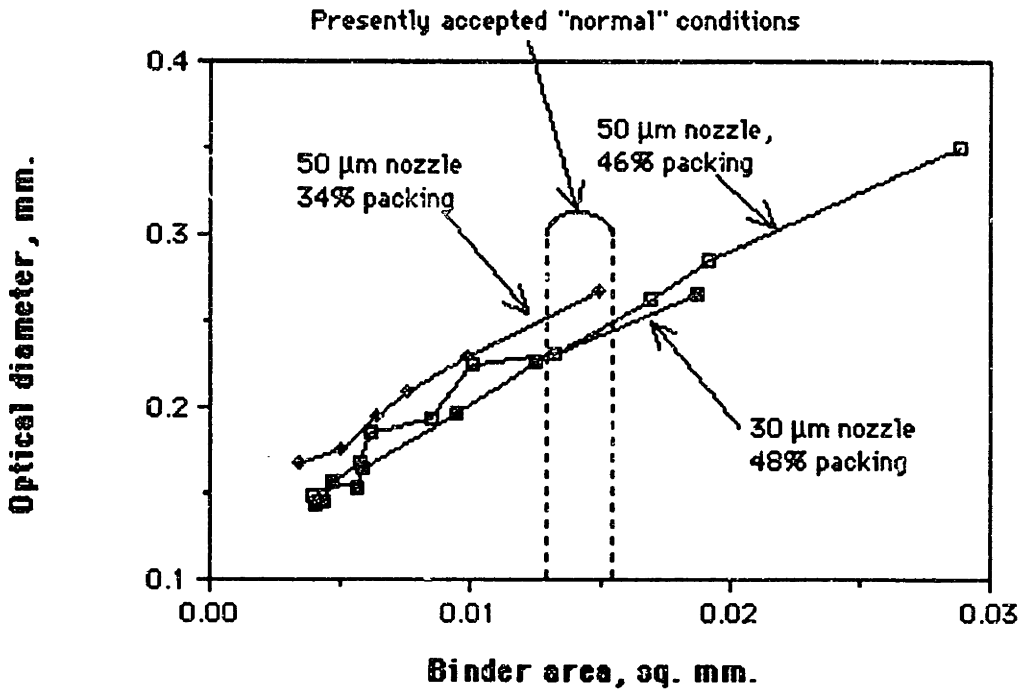

Figure 9.10 Optical diameter vs. binder dose for 30 and 50 µm nozzles. Note: Actual diameters are approximately .026 mm smaller than data indicate.

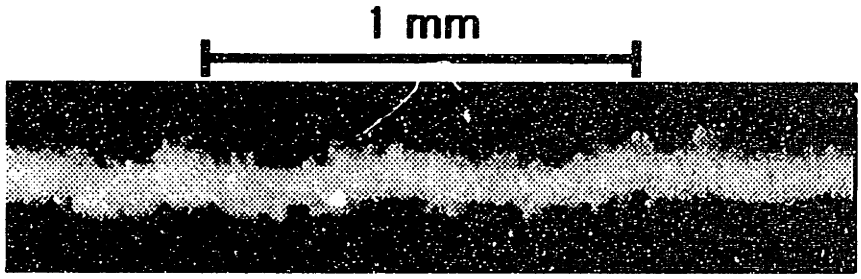

Figure 9.11 Tiny single line primitive, printed with 30 µm nozzle. Sample 85.5: Powder: 28 µm 7920 alumina, 48% packing, Binder "B" 0.41 cc/min (30 µm nozzle) printhead speed 1.65 m/s; M = 55x, diam = 140 ± 18 µm (optical)

Although the lines in sample 85 (30 µm nozzle) are almost identical to those in sample 48 (50 µm nozzle), the lines produced with the smaller nozzle had much better integrity. To see experimental conditions, see Appendix E.

9.1.3 Conclusion

The optimum printing conditions that have been used for years in Three Dimensional Printing were arrived at by trial and error. This optimum corresponds to the maximum possible translation speed and the minimum possible binder flowrate. Presently, lines approximately 200 µm in diameter are accepted as standard. These conditions are a

binder flow rate of 1.2 cc/min and the printhead speed of 1.5 m/s across the powder bed. This yields a binder dose of .0133 mm^2, but variation in flowrate causes this value to fluctuate by roughly 10% . This study has shown that this dose is double the value that produces coherent lines with a 50 μm nozzle. The present accuracy of Three-Dimensional Printing is limited by the mechanics of the machine, not the materials being used.

The lower limit to the feature size must in some way be determined by the grain size. Features that are 120 μm in diameter are still 4-5 grain sizes in diameter. It seems highly likely that the lower limit possible for 28 μm powder is less than 100 μm, although such tiny features would need to be printed with a nozzle smaller than 30 μm. Such features could be interdigitated in 50 μm layers, and the "stairstepping" defects which are presently the most visible defects on 3-D Printed parts could be reduced in scale to approximately the same scale as the grain size, effectively smoothing them out. If the features illustrated in figure 1.6 represent the smallest coherent features that can be created by the process, reducing the feature size from 200 μm to 100 μm would make it possible to build these elements 1/2 the size, or build them the same size with more control over the designed shape.

9.2 Does Citric Acid Affect Feature Size?

9.2.1 Method

The addition of citric acid to the powder used in the Three Dimensional Printing of colloidal silica is necessary to prevent the migration of the binder outside of the boundaries defining the part. The most egregious defects occur in parts with depth greater than approximately 5 mm in which the binder, if not gelled by acid, dribbles downward beneath the part, colonizing areas of powder never intended in the design. The reaction between the acid and the binder is discussed elsewhere in the context of the binder formulation, and the rate of gelation has been measured experimentally. The question of how the content of citric acid with its control over the mobility of silica in the powder bed affect the size of printed lines was addressed in a series of experiments.

No special differences were designed into the printing apparatus or the binder for these experiments. The powder was prepared in a way that differs from normal practice,

however. In order that the binder encounter a uniform distribution of acid in the powder, the powder was coated with acid. To coat powder with any solute, the solute is dissolved in a solvent with a volume 5% - 10 % of the bulk volume of the powder sample. The solution is mixed with the powder thoroughly so the powder becomes a fluffy, moist but not soaked body. It is essential to keep the fluid saturation low so that the solvent will evaporate out through the pores in the powder without migrating to the surface. This eliminates the tendency of the solute to segregate on the surface of the powder sample. If the solubility of the solute is limited, the process can be repeated. When coating powder with citric acid, the solvent was water and the powder was dried at 70°C. In a subsequent series of experiments, powder was coated with PMMA using MEK as a solvent, and the high viscosity of the solution required the process to be repeated three times with dilute solutions to coat the powder with enough polymer to have the desired effect. Following drying, the powder must be sieved to break up agglomerates. Milling should not be necessary if the saturation of the powder sample was low enough.

9.2.2 Results

Powder with a dry spread density of 39% was divided into three samples. One sample was printed as is. The other two were coated with 0.2% and 0.5% by weight of citric acid. The powder with .2% citric spread to 38% density and the .5% citric powder spread to 35% density. The powder\binder volume ratios for each condition are given below, and scale approximately with the spread densities.

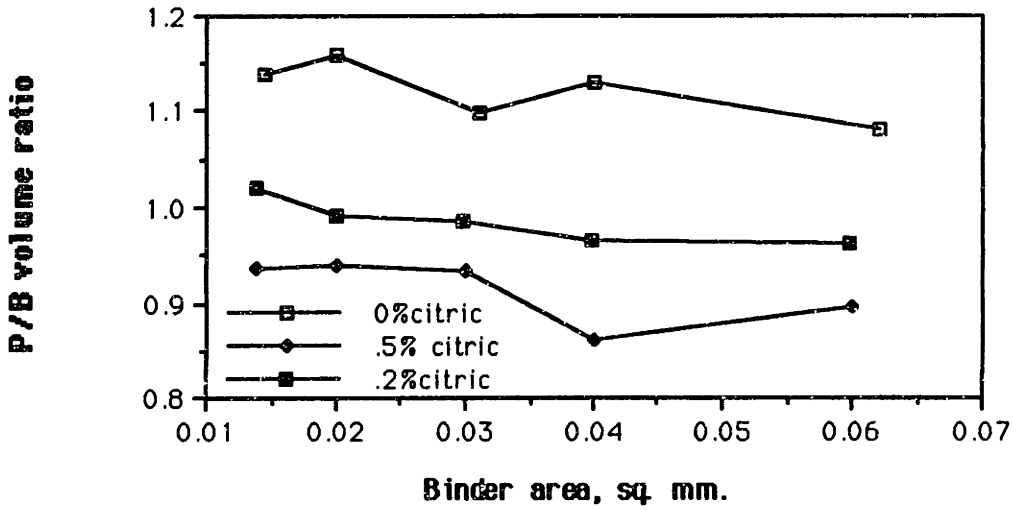

Figure 9.12 P\B volume ratio vs.binder dose for Series 7: powder treated with citric acid.

The powder\binder volume ratios can be combined with the packing density data to estimate the binder saturation. This is done in figure 9.13, below. The binder saturation is fairly well disposed within the scatter of the data without citric. It is possible that it is slightly lower than the trend.

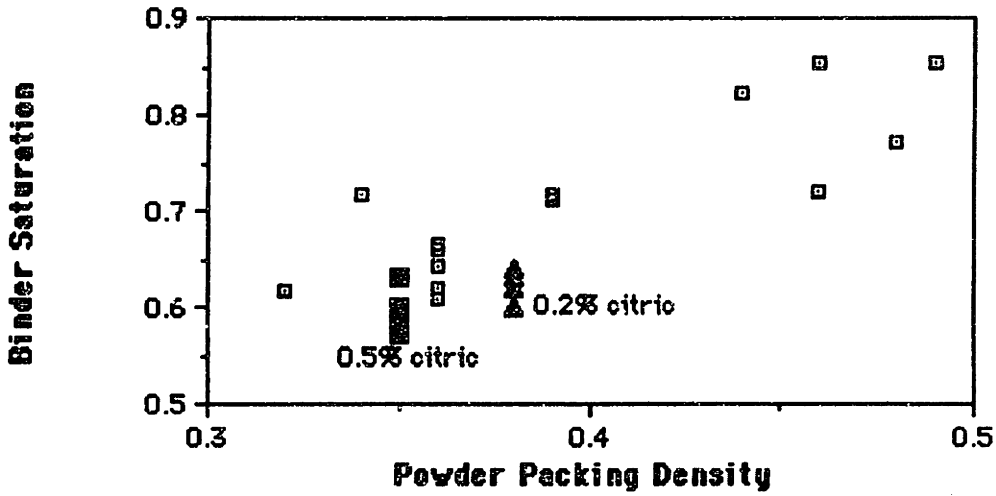

Figure 9.13 Binder saturation vs. packing density. Data for powder with citric acid is compared to the data for powder without citric (fig. 8.12)

If the powder content of the lines and the respective packing densities are used to estimate the line diameters, they compare very favorably with the diameters measured optically. This is shown in figure 9.14.

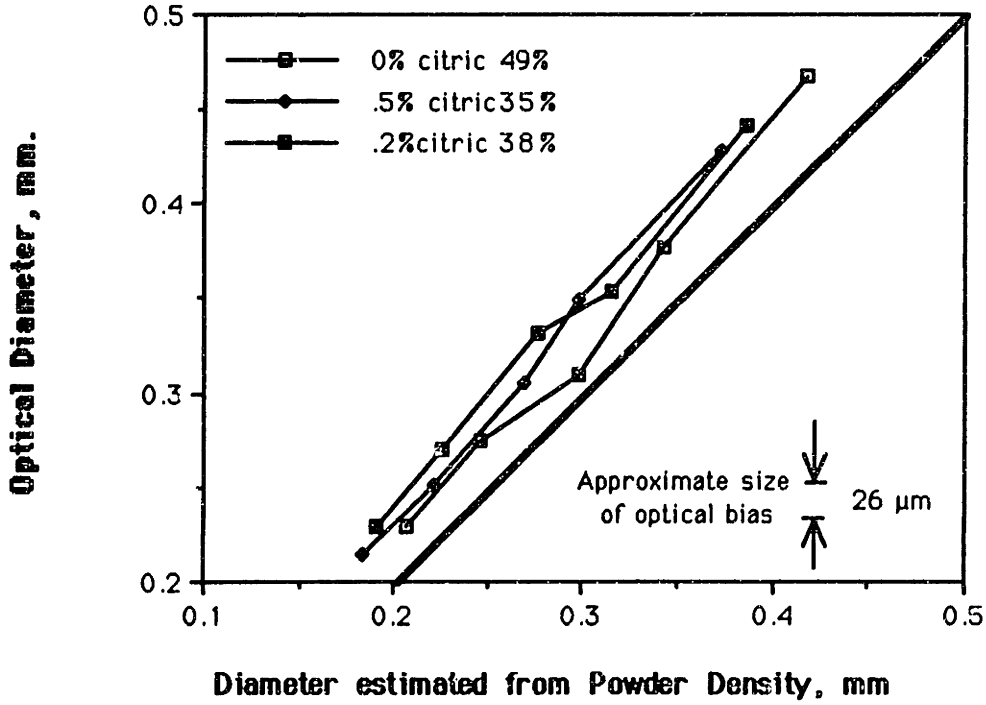

Figure 9.14 Optical diameter vs. estimated diameter for powder with citric acid.

9.2.3 Conclusion

The addition of citric acid to powder does not appreciably affect the feature size in 3-D Printing of colloidal silica onto aluminum oxide, except insofar as it affects the packing density of the powder in the powder bed.

Since there is no measurable effect from powder coated with citric acid, the migration of binder that occurs during feature formation must occur over a time period much less than the time for a gelation front to propagate a distance approximately equal to the pore size in the powder bed. The propagation rate has been measured to be approximately 20 μm in one second with a $t^{1/2}$ dependence. Since the pore size is on the order of 10 μm, the coagulation time for coated powders must be on the order of 0.25 sec and the capillary migration time must be much faster than this.

9.3 Spherical Powder

A sample of alumina powder was obtained from Showa Denko that had particles which were spherical in shape, and had a diameter narrowly distributed around 30 microns. The powder was found to pack at a density of 53% of theoretical. Five sets of lines were printed in this series (Series 11), using binder formulations with surface energies that varied from 31 to 58 dyn/cm with additions of various surfactants. Although there was considerable variation in the surface tension, the contact angle remained 10°-12° for all combinations. The data for the powder cross-sectional area as a function of binder dose are plotted in figure 9.15 below.

The line saturations, based on the powder\binder volume ratio, varied from 0.77 to 0.82 across the series. A prediction of the equilibrium saturation can be made by measuring the suction pressure of the powder for liquid, and setting that pressure equal to the capillary pressure for drainage. This is done in figure 9.16, below. The distinct lack of any difference between the powder\binder ratio for these samples shows that the variation of surface tension had no significant effect on the equilibrium saturation.

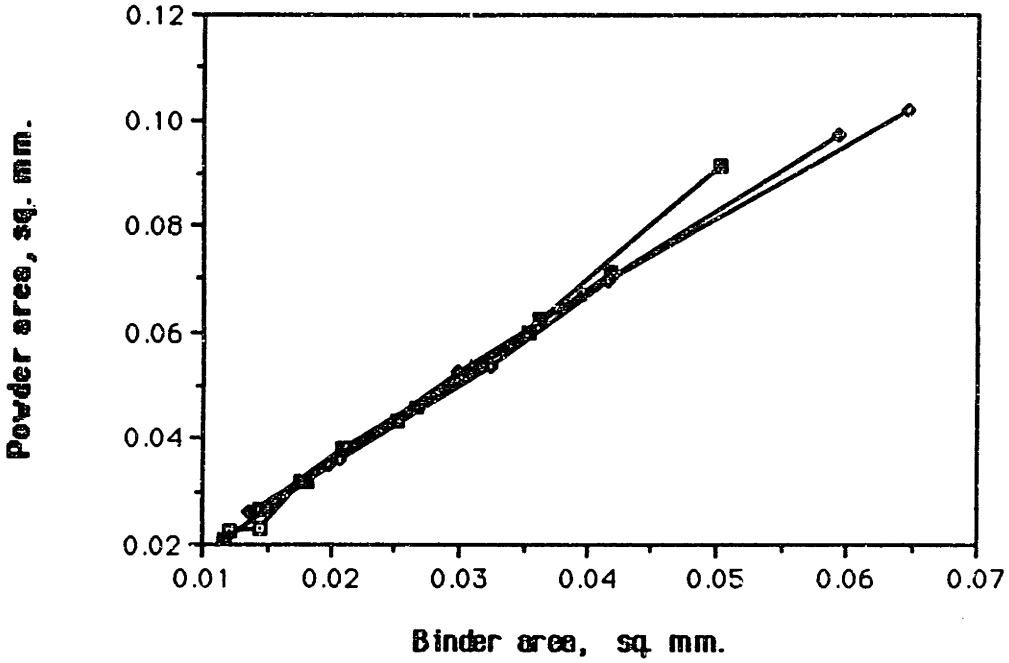

Figure 9.15 Powder dose vs. binder dose for series 11, 30 micron spherical powder.

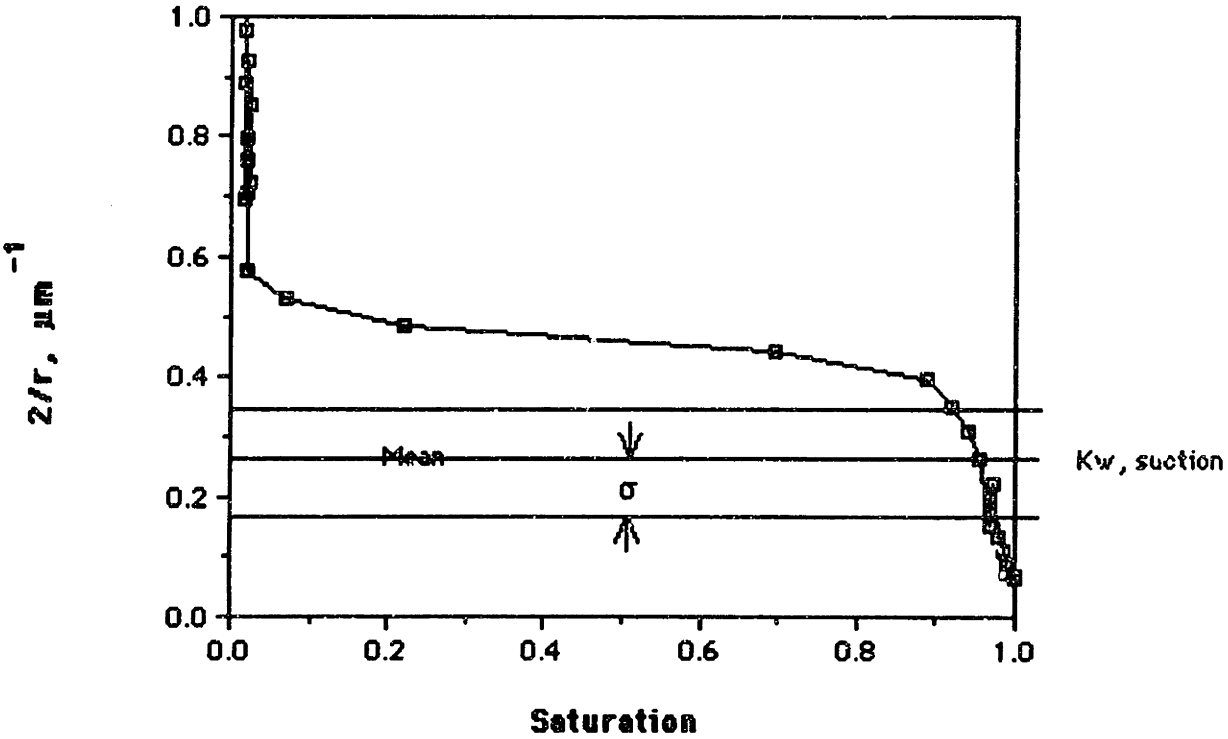

Figure 9.16 Pore curvature in drainage (derived from mercury porosimetry) as a function of saturation for spherical powder. Line labelled Kw is the mean pore curvature for dry imbibition, derived from three pipet measurements of the suction pressure. The error bars are set at a distance of one standard deviation from the mean.

Capillary pressures have been converted into pore curvatures:

$$K \equiv \frac{-P_c}{\sigma_{LV} \cos\theta} \qquad \text{(see Appendix B, section B.4.)}$$

which make the data independent of surface tension and contact angle. The prediction from the capillary measurements is that the saturation should be above 90%. The actual measured value of 80% differs slightly from this prediction, but is still quite close enough.

The morphology of the lines provided few surprises, aside from the ease in resolving the silica necks joining alumina particles.

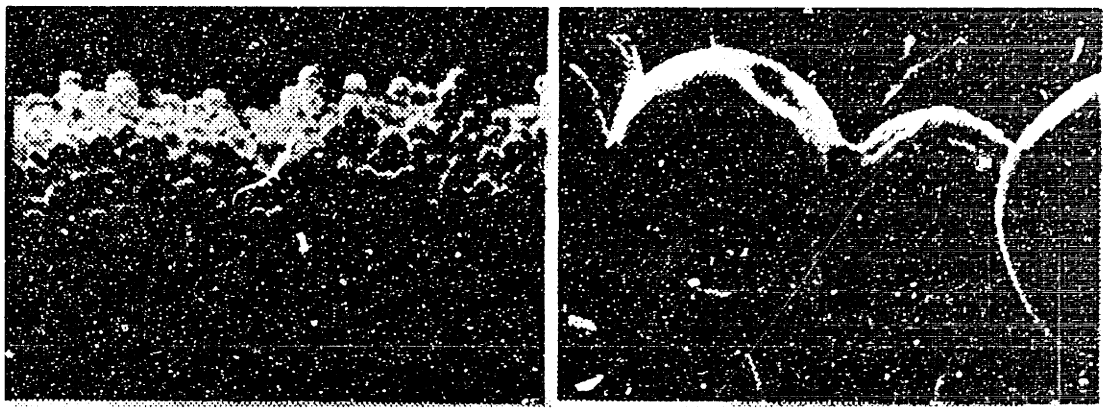

a. b.

Figure 9.17 Lines printed with spherical powder Sample #102; Binder "B" 1.48 g/min, printhead speed 1.65 m/s; packing density 0.53. a.) M = 173 x; b.) M = 1860 x.

9.4 Variation of Line Saturation with Wetting Angle and Effect of Powder Locking

The migration of binder into powder in the period following the impact of the binder jet is driven by capillary pressure, which is quite sensitive to the contact angle between the binder and the surface of the powder grains. At the very least, the contact angle between binder and powder must be less than 90° for the binder to be spontaneously imbibed by the powder. A test was devised to simultaneously check the effects of variation of the binder contact angle and the effects of mechanical locking on the printing.

The issue of powder rearrangement is a difficult one to address. For the monomodal powders tested in this study, the packing density did not change substantially on printing. By printing on loose powder that did not densify, but did rearrange, and comparing that with lines printed on powder that was locked and did not rearrange, the effect of powder rearrangement could be separated from the effect of powder densification. In the situation of powders that densify on printing, the effect of powder rearrangement is to both reorient and compact the powder grains. This is a much more complicated situation and it has yet to be addressed in a thorough fashion.

In series 12, 13, and 14, a "conventional" 28 μm lamellar Norton 7920 powder was used. The unmodified powder was printed in series 12 as a control, and it packed to a density of 39% of theoretical. To lock the powder together so it wouldn't deform during printing, the powder was coated with PMMA with a composition of 1% by weight. The polymer powder was dissolved in a solvent (MEK) and mixed with the dry powder to form a relatively dry, crumbly paste, with a saturation of about 10%. The strategy was to keep the saturation of the solvent in the powder low enough so that the liquid could not migrate through the powder, but a high enough saturation that mechanical stirring would homogenize the powder. The paste was kept dry and crumbly to keep it porous, so the solvent could evaporate from deep cavities, rather than migrating to a surface to escape. The powder was dried in an oven at 50 °C and the agglomerated powder was easily ground down to pass through a 120-mesh screen. The powder after this procedure packed to a density of 35% of theoretical, indicating that is was still slightly agglomerated.

Series 13 was a set of lines printed on the coated powder without any treatment to lock it. In series 14, powder samples were layered onto alumina substrates in the printing machine and the samples were heat treated at 450 °F (230 °C) in a toaster oven. This made the powder cohesive enough that it did not rearrange when the binder jet passed over it.

This treatment corresponded to a polymer thickness of approximately 50 nm if it were distributed evenly over the grains. To measure the contact angle, a dose of this magnitude was deposited via solvent on the surface of a flat alumina substrate and the contact angles of the three binders tested were measured on this substrate. The three binders tested had varying amounts of the nonionic surfactant Triton X-100 added to them: sample "a" had none, sample "b" had .025%, and sample "c" had 0.5%. The contact angles on clean alumina were approximately as follows:

Triton X-100 composition	surface tension dyn/cm	contact angle clean	coated
0	47	10°	44
0.025%	31	10°	44
0.5%	32	0°	18

Table 1. Contact angles on clean and coated alumina.

The measured saturations for the lines in these series are shown in figure 9.18, below, plotted against the cosine of the contact angle.

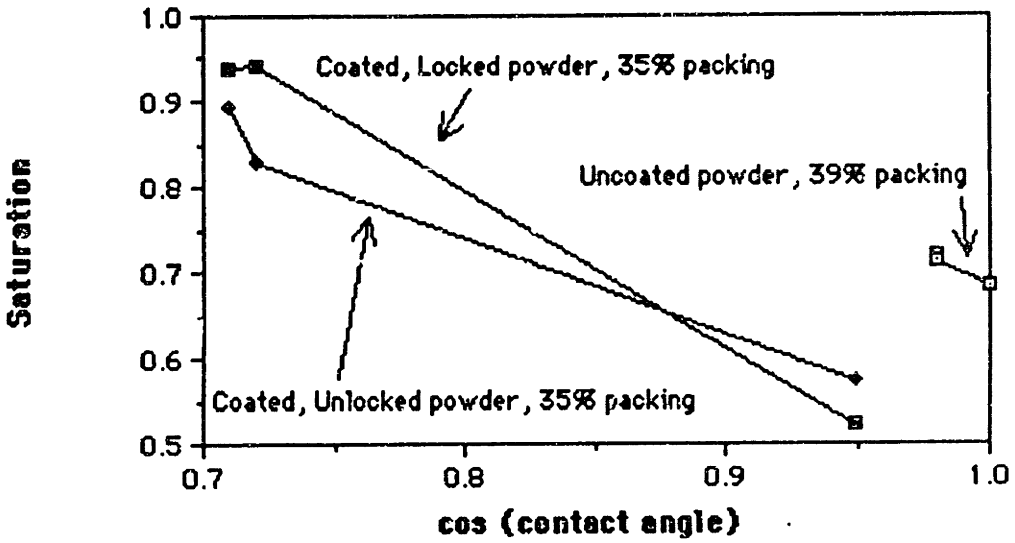

Figure 9.18 Line saturation for 28 μm alumina coated with PMMA as a function of binder contact angle.

Although the data are somewhat sparse, there is a clear trend towards higher saturation as the contact angle increases (and its cosine decreases.) There is little effect of the powder having been locked. The uncoated powder has a higher saturation as the contact angle approaches zero, but that is to be expected for a powder with a higher packing density. Estimates of the expected saturation may be gained from porosimetry and suction data for powder with 36% packing density. These data were collected from an uncoated sample, but thus example serves to illustrate how different contact angles are accounted for in the graphical method.

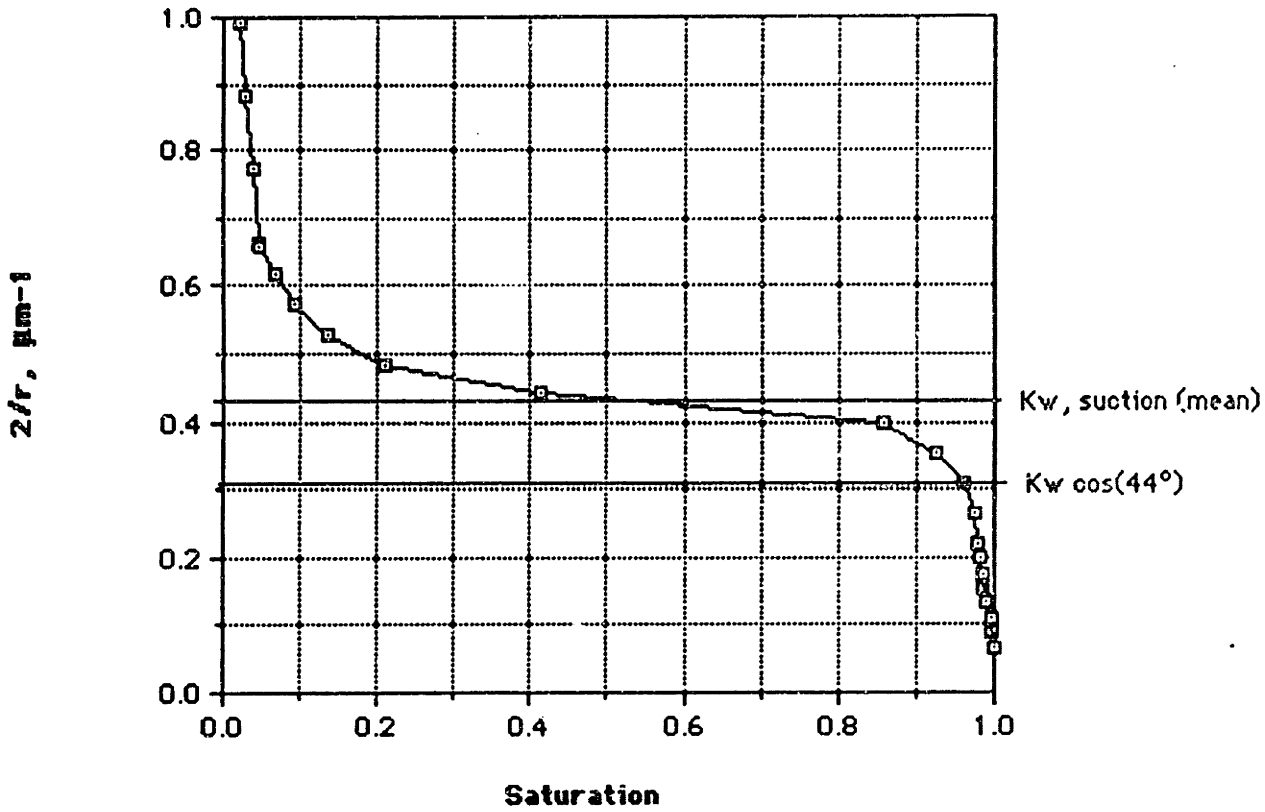

Figure 9.19 Pore curvatures from capillary pressure and suction data for 30 μm 7920 alumina, 36% packing, and calculated curvature for a fluid with a contact angle of 44°.

The saturation at zero contact angle is found as before from the intersection of the capillary pressure curve with the horizontal line corresponding to K_w, the meniscus curvature from the dry suction. The saturation at large contact angle θ is found from the intersection of the capillary pressure curve with the horizontal line at a reduced suction pressure of $K_w \cos\theta$. The values predicted from these data are 0.53 for the perfectly wetting case, and 0.96 for the contact angle of 44°. These values correspond almost exactly to the values measured for the locked powder samples in figure 9.18.

The "Pore curvature" is the quantity

$$K = \frac{-P_c}{\sigma_{LV} \cos\theta}$$

where P_C is the measured capillary pressure, σ_{LV} is the measured surface tension of the liquid and θ is the contact angle. This is equal to the curvature of a spherical meniscus at zero contact angle in a cylindrical capillary with a diameter equivalent to the "pore size" of the powder at that saturation. The mercury porosimetry data is collected at a contact angle of 140°, for which the cosine is -0.76 and simulates the drainage of a moistened porous

body, for which the contact angle has been assumed to be equal to zero (this is the assumption that powder, once wet, does not dewet.) During imbibition, it has been shown in the quasi-analytic model for the double-funnel pore that the meniscus curvature in a pore of a given geometry has a strong dependence on cosθ. This experiment is the only one in this document for which cosθ has differed substantially from unity.

Although there was little effect in the equilibrium saturation from having locked the powder in these experiments, there was some observable effect in the morphology of the printed lines. Due to the spreading of the liquid on impact, the lines were approximately semi-cylindrical with a flat face corresponding to the upper surface of the powder bed and a width roughly twice the depth. The SEM micrograph below shows two views of one of these lines; some flattening of the line can be seen in the end view.

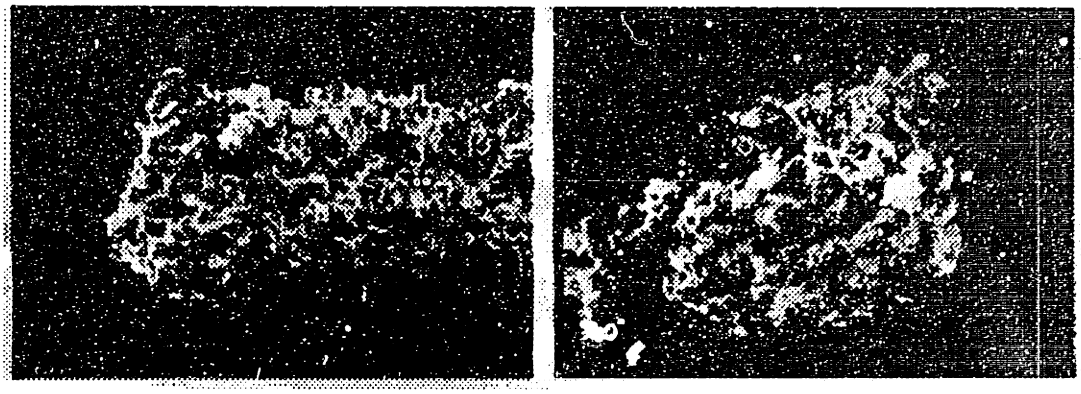

a. b.

Figure 9.20 Scanning Electron Micrograph of a line printed into locked powder.
Sample 174: Binder "B" 1.31 g/min; printhead speed 1.65 m/s; powder: locked PMMA coated 28 μm lamellar alumina; packing density 35%.
(a.) side view, 163x; (b.) end view, 209 x.

9.5 Bimodal Powders

9.5.1 Measurement of Equilibrium Saturation

Bimodal lamellar alumina was formulated for experiments. For background and description of the formulation process, see section 7.5.2. Sets of lines were printed into four bimodal compositions, consisting of 28 μm and 3 μm lamellar alumina (Norton 7920) with 10%, 20%, 30%, and 40% fines by weight. The packing density for all four samples was between 39% and 41% for the powders. These samples were series 6, 15, and 16. Printing conditions were the same as those used for the monomodal powders.

The samples were fired at 750 °C to reduce the effect of sintering of the fine powders. In spite of this caution, the samples were quite difficult to separate from the unprinted powder, which became clumpy in the furnace.

The assumption that the powder does not densify on printing cannot hold for these powders. The severe compaction of these powder samples was measured by forming a slurry of samples of the powders and pouring them onto a paper towel to draw out the moisture. The densities of the powders were measured by mercury porosimetry and the results are given in table 7.4. Using the higher, slurry-cast packing densities, the line weights were used to estimate the diameters of the lines from

$$d_{est'd} = \sqrt{\frac{4A_{powder}}{\pi f_{powder}}} \quad . \qquad 8.6$$

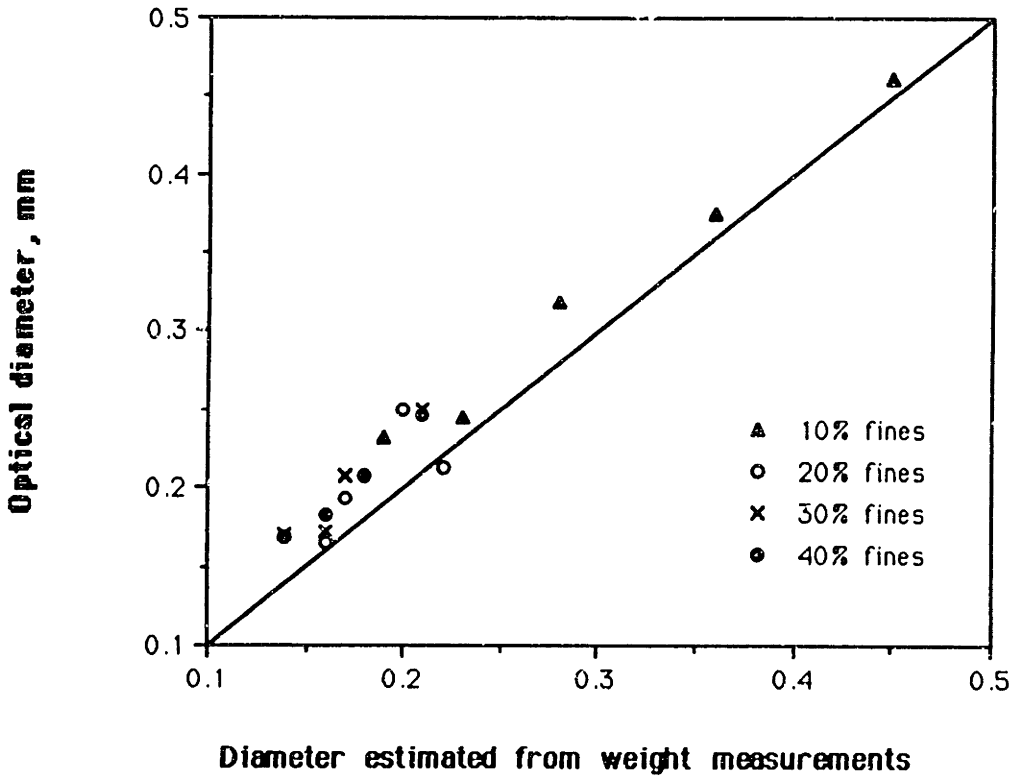

Figure 9.21 Diameters of bimodal lines measured optically plotted against diameters estimated from their weight and slurry-cast packing density.

The difference between the optical and estimated diameters is on the order of the coarser grain size, and this seems to support the assumption that the powder density in the

lines had increased to the density of the slurry cast samples. Assuming that this conclusion is correct, one can proceed to calculate the saturation from

$$S_{local} = \frac{A_{liquid}}{A_{powder}} \frac{f_{powder}}{\left(1 - f_{powder}\right)} \quad . \qquad 6.23$$

These saturations are graphed in figure 9.22 below for comparison with estimates of $S(K_W)$ from the porosimetry and dry suction measurements reported in table 7.7. The measured saturations cluster between 0.6 and 0.7, while three of four estimated saturations are below 0.4, and one is about 0.7. The one sample for which the estimated value of the saturation agrees with the measured value is the one with the highest content of fine powders. The biggest difference between this sample and the others was in the porosimetry curves: The curve for the slurry cast sample with 40% fines had a very much higher bubble pressure than all the other samples: slurry cast and not. The most likely explanation for this difference is that the other slurry cast samples segregated in such a way that they had entry pores similar to the entry pores of the dry spread, sintered samples.

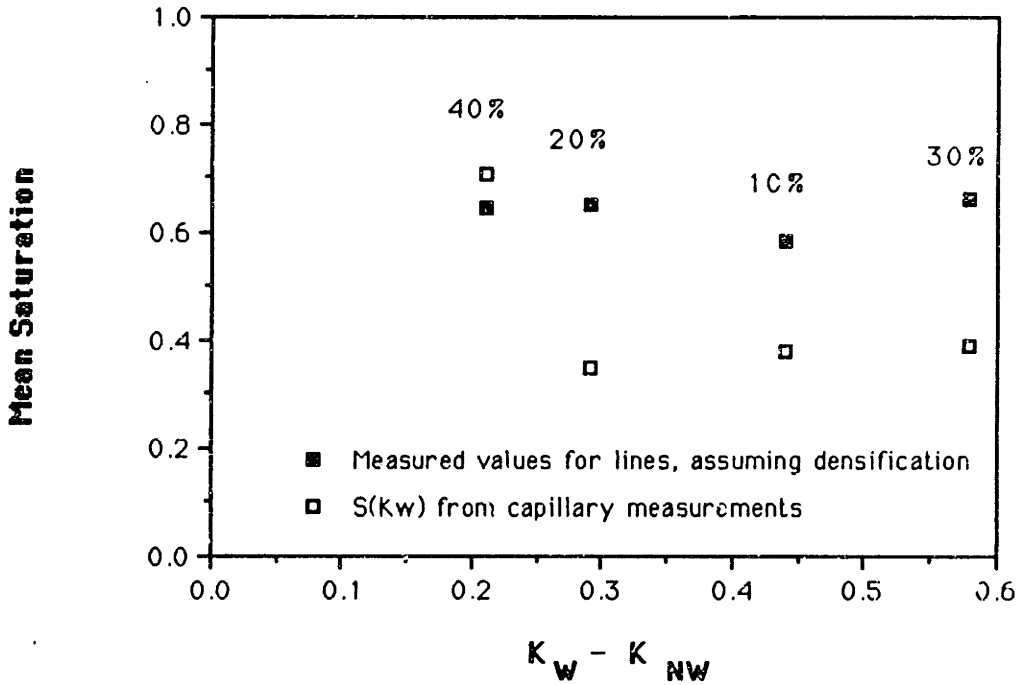

Figure 9.22 Binder saturation vs. excess pressure for bimodal powders. The open boxes correspond to calculations from the porosimetry data for slurry-cast samples, to simulate the effect of powder densification on wetting.

9.5.2 Microscopic Analysis of Lines Printed in Bimodal Powders

The difficulties with characterizing the bimodal powders give a clue that they must be fairly complex. This complexity is borne out by microscope inspection. The following figures show scanning electron micrographs of single line primitives made with the sample containing 10% fine powders.

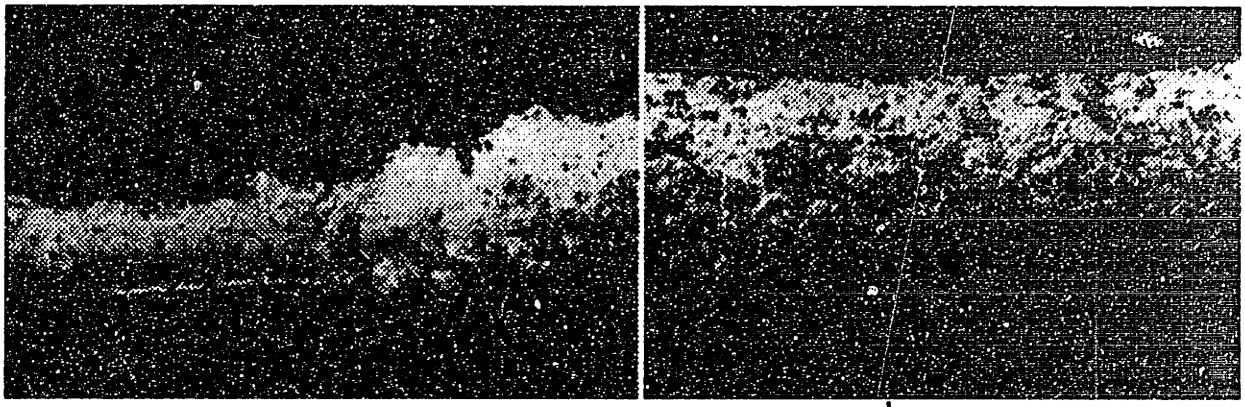

a. b.

Figure 9.23 SEM micrographs of bimodal lines. Sample 64: Powder: 90%- 28 μm, 10% 3 μm alumina Norton 7920. Binder "B", 1.64 g/min; printhead speed: 1.65 m/s; dry powder density: 41%; slurry cast density: 54%. a.) M= 105x; b.) M = 270 x.

In figure 9.23, above, two views of the same line show a combination of very smooth and very rough surface finish. The very rough surface in figure 9.23.a is probably the location of a point of contact between the freshly printed, densified line and the dry powder. The densification of the powder so distorts it that very likely the feature comes out of contact with the rest of the powder over most of its circumference. It must touch in a few points, and at these points, the feature will drain binder. Because the smaller pore size probably reduces the permeability of the powder, the combination probably prevents the feature from coming to complete equilibrium before it dries.

a. b.

Figure 9.24 Comparison between bimodal and monomodal surface finish. a.) same sample as above, M = 1160x. ; b.) Sample 41: Powder: 30 μm lamellar alumina (same as the coarse grains in (a), packing density 0.42, same magnification.

In figure 9.24, the surfaces are magnified of a bimodal line with 10% fines and another line consisting of monomodal powder that was the same as the coarse component of the bimodal. The higher density of the bimodal feature is clearly evident. The fine grains of the powder tend to fill the pores between the coarse component, but a relatively large (≈ 10 μm) entry pore can still be found. The ideal practical structure for a bimodal powder is illustrated below.

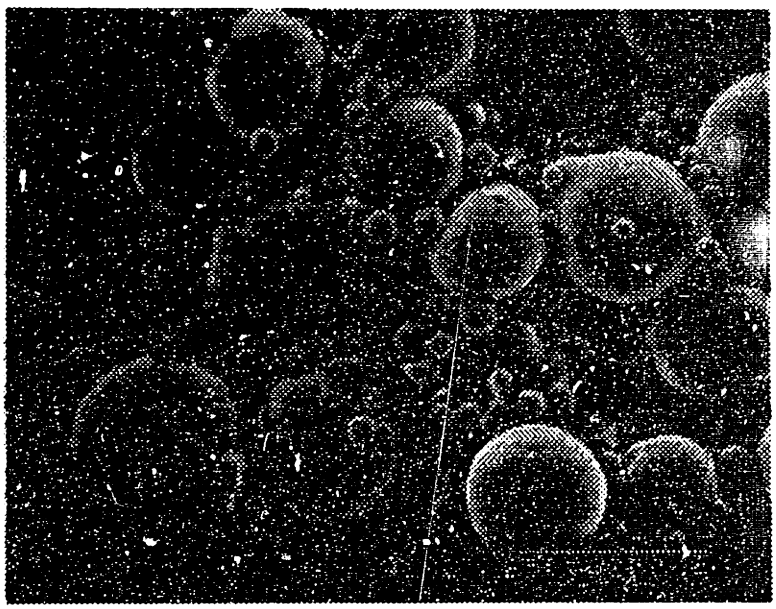

Figure 9.25 Bimodal spherical stainless steel powder (100 μm / 20 μm) [Michaels, 79]

9.5.3 Whither Bimodals?

The bimodal powders exhibit quite interesting properties of very high density and a tendency towards very good surface finish. Figure 9.23.b. alone calls for further study. Whether or not feature formation adheres to the capillary equilibrium cannot be concluded from these data. The chief problem with the modelling work was that the slurry casting process was not controlled well enough to adequately simulate the densification of the powder.

The distribution of the fine grains with respect to the coarse grains must be kept under control: if the fines segregate into large agglomerates, they will behave like large grains, with a corresponding deterioration of the small pore size and high capillary pressure. The control of the fines also includes the control of dust in the workplace: over the five year duration of the 3-D Printing project, there have been numerous problems, particularly with computer disk drives, from the 30 μm powders used. The fine component of the bimodals was even loftier, and very likely these problems would be greatly amplified unless some solution can be found to the problem.

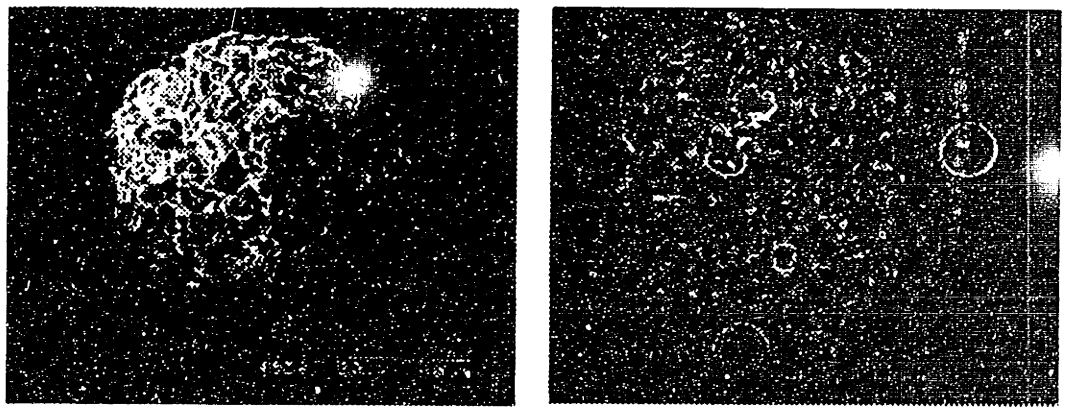

a. b.

Figure 9.26 Single Droplet primitives produced by infiltration from a syringe. [Lauder 49,50].

Alan Lauder observed some particle rearrangement when he infiltrated powder with binder from a syringe. The primitives produced had a relatively smooth surface finish, owing to the reorientation of the powder grains be the surface tension of the binder parallel to the surface. The internal structure shows an interesting pattern of the grains: the binder entered from the upper left of this image (fig. 9.26.b) and added powder grains as the invasion front travelled diagonally down to the right. It is quite probable that powder

densification is the key to smooth surface finish: The movement of powder grains during densification causes them to reorient into a low energy configuration, which is necessarily parallel to the advancing fluid meniscus.

9.6 Conclusion

1. The "standard" printing conditions do not represent the finest features that can be produced with easily available hardware. The smallest features were obtained using a 30 μm nozzle that dispensed 50 μm droplets. The finest lines had an optical diameter of 140 μm (which overestimates the diameter by approximately 26 μm). The "true" diameter of the lines printed was likely less than 120 μm, approximately half the diameter of lines printed under "ordinary" conditions with a 50 μm orifice, jetting at 1.2 cc/min, and travelling at 1.5 m/s.

2. Citric acid does not appreciably affect the size or saturation of printed features. The gelation rate from the citric acid is very much slower than the rate of capillary equilibration in the monomodal 30 μm powders. In fact, it was shown in section 6.1 that the gelation rate can be slower than the rate of layer generation for a multijet printer. In this case, the printing can get far ahead of the gelation, and bleeding can occur. The solution to this problem is to increase the citric acid content which increases the gelation rate. The added citric acid may cause other problems, such as the strengthening of unprinted powder. It may be necessary, in the future, to find another gelling agent that acts more quickly to keep up with accelerated printing rates.

3. Spherical powders pack to a very high density and the binder saturation in features made with this powder tends to be very high. The large pore size of the powder ensures that the permeability is high enough for the liquid to equilibrate.

4. Powders that have been rendered hydrophobic by surface treatment with a polymer exhibit a higher equilibrium saturation than unmodified powder. The difference is entirely attributable to the change in contact angle, and the dependence of the dry suction pressure P_0 on $\cos\theta$. This dependence is modelled theoretically in Appendix B, and demonstrated experimentally here.

5. The bimodal powders tested exhibited a large amount of densification during printing. This reduced the size of the nonwetting entry pores to a level where the dry powder could

not drain them very far. Accordingly, the saturation of the bimodal features remained relatively high. The lines exhibited very smooth surface finish in most areas, with occasional spots that were very rough. These rough spots were probably points of contact to the dry powder.

The properties of the bimodal powders are very sensitive to processing conditions, and the method pursued here was not sophisticated enough to control all of the important variables. Some of these variables were segregation and agglomeration of the fines, and packing of the loose powder in the printing machine.

Chapter 10 Conclusions

10.1 Overall

Three Dimensional Printing is a process for forming solid objects by printing a liquid binder onto a dry powder. Binder is deposited though an ink-jet printhead and solid parts are formed by the sequential bonding of thin layers. The binder most usually consists of a dispersion of an adhesive in an aqueous medium. To obtain sufficient mechanical strength of printed objects, it is usually necessary that the adhesive form approximately 6-10% of the volume of the final component. The binder from the printhead fills only the pore space in the powder bed, so the fraction of adhesive in the binder must be relatively high to provide the necessary final loading. The strength, accuracy, and isotropy of 3-D Printed material depends crucially on both the quantity of adhesive delivered in the binder and the distance across which the binder spreads after printing. If this distance is known, machine operating parameters can be adjusted to assure proper knitting of features

The stability of the binder is paramount in gaining reliability of the hardware. In the research situation that pertains at present, the long-term stability of the binder is probably less of a concern than hardware compatibility and the ease of handling and cleanup. Printhead reliability is of overwhelming importance, and the binder characteristics that promote this are low drying rate, low foaming, and a soft gel.

In developing binder formulations for 3-D Printing, it is necessary to control the evaporation rate of the solvent in the binder. When the solvent is water, this can adequately be done by adding 10% glycol per unit volume of the liquid phase. The primary function of this is to retard the buildup of solid material on the printhead, both during normal operation and during service.

The hydrostatics of 3-D Printed features requires that the adhesive component of the binder be immobilized (gelled) in the powder in a time comparable to the time to print a layer. If parts greater than a few millimeters in height remain liquid, the hydrostatic pressure can cause binder to leak out of the boundaries of the part, causing positive surface defects of macroscopic dimensions. This phenomenon is generally referred to as "bleeding". The kinetics of feature formation permit a wide variation of the time over

which gelation can manifest, but a clear mechanism for immobilization must be designed into the material system.

in the formation of printed features, the distribution of liquid is an equilibrium configuration, arrived at by a balance between the capillary suction of the dry powder surrounding the feature and the attraction of moisture to the powder in the partially saturated regions. The pressure/saturation characteristic of the powder during drainage can be measured, and the equilibrium saturation is that which corresponds to the suction imposed by the dry powder. The time to equilibrate was found to be much less, for primitive features, than the time for the binder to gel and halt further migration.

10.2 Binder Stability

The kinetic characteristics of colloidal dispersions seem to favor large particles. The primary characteristic is the diffusion rate of particles through the dispersion and this decreases with particle size. The upper limit of particle size is probably determined either by sedimentation or by abrasion of the orifice. these phenomena were demonstrated by Satbir Khanuja with alumina suspensions up to 800 nm in particle size, but neither have been observed in colloidal silica of 100 nm size.

Colloidal silica possesses a level of stability that is anomalous for inorganic sols in aqueous media. This stability can be attributed to the attraction of water to the hydroxylated silica surface. This enables silica sols to be manufactured with solids loading greatly exceeding that for dispersions of other inorganic pigments, e.g. TiO_2. Since the solids loading of the binder must be greater than 10% by volume, this feature is very important. A similar attraction also exists between hydroxylated silica and the ether oxygen in polyethylene glycol. This attraction forms the basis of a robust gelation mechanism developed for this process. The concentration of PEG required to cause gelation can vary from 100 ppm up to about 1%, so substantial variation in binder composition can be tolerated and still effect gelation.

Binder "B" developed in this research consists of colloidal silica with a 100 nm primary particle size and a solids loading of 17.5% by volume. The gelling agent is 0.1% PEG with a molecular weight typically around 20,000. The long-term stability is maintained by holding the pH at a level between 9 and 9.5 with 0.2 mol/l TEA in the aqueous phase. Additional humectant effect is provided by 5% by weight of propylene

glycol. The gelation is effected by neutralizing the base with a minimum of 0.03 mol/l citric acid; typically about three times this quantity is added to the powder in the powder bed. A pH indicator added to the binder serves to verify that the pH in the stock is correct and that the acid content in the powder is sufficiently high to cause gelation. An organic cosolvent is added to solubilize oily impurities, and an antifoam additive had been introduced.

The acid and base combination were chosen because they possessed long-term stability after formulation prior to printing, could be easily burned out of the printed material, were nonvolatile at ambient conditions, and did not pose any severe health hazard. By themselves, TEA and citric acid in the concentrations used are insufficient to effect gelation. Polyethylene glycol is the necessary necessary ingredient.

The rate of binder gel formation depends on the concentration of acid present and the degree to which it is dispersed in the powder. A film of gel forms at the interface between the liquid binder and an acidic region, and the rate of growth of the film can be related to the diffusivity of the acid in the gel. The diffusivity of citric acid in a gel of Binder "B" was measured to be 2×10^{-6} cm^2/sec. The shear strength of the gel was also measured: it was found to be approximately 500 Pa.

10.3 Time Domain of Feature Formation

Droplets of binder impact the powder bed with such frequency that they merge before coming to rest. Binder comes to rest in the form of a stripe of liquid which is not at mechanical equilibrium about 10^{-4} sec after impact. The surface tension of the stripe causes it to coalesce in roughly 10^{-3} seconds into a cylindrical feature.

The minimum time required for binder to gel is approximately 10^{-2} seconds if the binder were neutralized by the acid at the instant of impact. It is more common for the acid to be segregated in the powder, and the time for binder to be immobilized is determined by the gel growth rate from acidic regions. The gelation time can vary accordingly from 10^{-1} sec to 10^{2} sec., depending on the mean distance between acid grains.

For the powder an binder that are normally used in the process, between 10^{-2} and 10^{-1} sec is sufficient for the liquid to reach an equilibrium distribution determined purely by the pore geometry of the powder and the wetting characteristics of the binder for the

powder. The rate of migration is determined primarily by the product $k_{sat}P_0$ where k_{sat} is the hydraulic permeability of the saturated powder, and P_0 is the suction exerted by the dry powder surrounding the feature.

Binder migration is arrested by the balance of capillary pressure between the moist feature and the dry powder surrounding it. It can be seen in the figure below that single lines require only a few thousandths of a second to come to equilibrium across their own diameter. The pressure has sufficient time to equilibrate across macroscopic dimensions of the part before the binder has a chance to gel. This tends to homogenize the parts, but cannot make them completely isotropic. The process of coalescence rearranges the powder grains in the bed and can lead to the formation of large cavities between lines. Some of these cavities are shown below. These cavities are a result of printing of lines in a square array: with lines on later layers printed directly over lines on previous layers. Subsequent research has shown that alternating the lines in a close-packed pattern eliminates much of this effect (Hon Tang, private communication.)

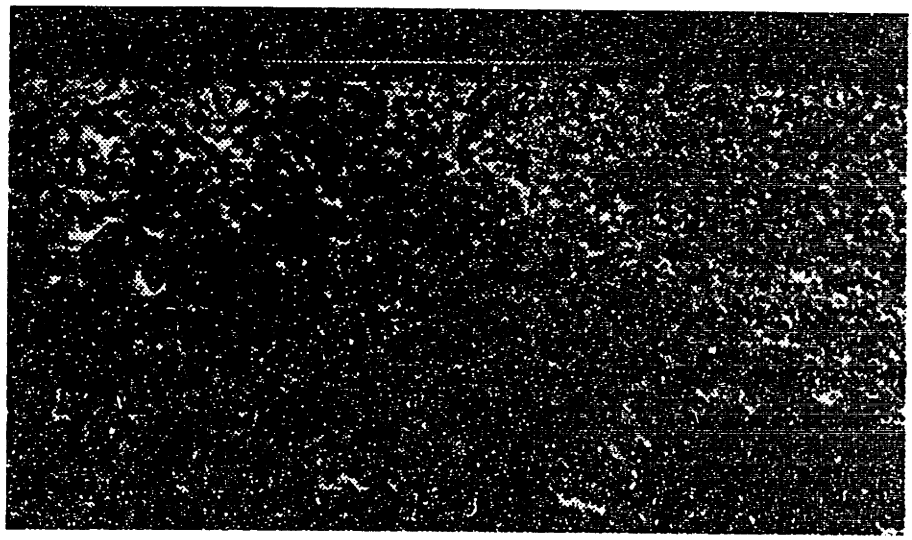

Figure 10.1 Transverse section through 3-D Printed ceramic shell material.

A final version of the time line for feature formation is given below, reflecting the capillary equilibration of the liquid with respect to the dry powder. The very brief time over which capillary migration takes place causes the features to widen from the diameter of the fully saturated, coalesced feature to a diameter perhaps only 20% larger in most cases. Some amount of capillary migration is necessary to anchor the feature to the powder and prevent balling. The time to gel is determined by the distribution of the acid in the powder:

the minimum gelation time pertains to the condition where the acid coats the surface of the powder grains: gel need only grow across a characteristic pore size. The maximum gelation time corresponds to very poor distribution of acid: it must diffuse through the previously printed layers up to the just-printed surface. The same quantity of acid can be present in both cases, but the distance over which it must act causes drastically differing performance

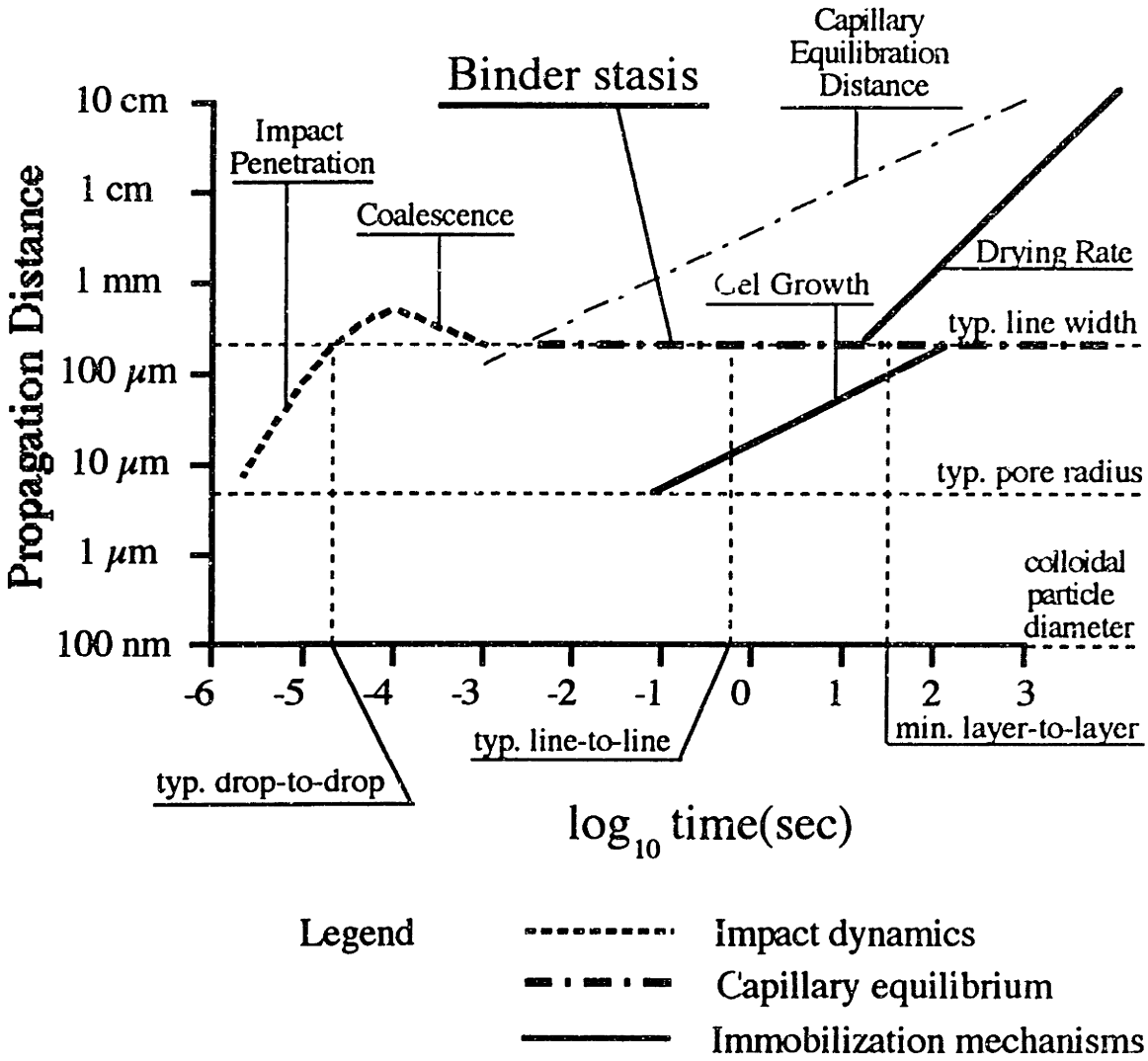

Figure 10.2 Time line for feature formation.

10.4 Capillary Model for Feature Formation

A model for feature formation based on a balance of capillary pressures was developed. Because the scale of primitive features is close to the scale of the grain size of

the powder, a pore-network model was developed. The network model predicts the existence of two critical pressures, P_0 and P_B that correspond to two percolation thresholds of the pores in the network. The dry suction pressure, P_0, is the capillary pressure at the threshold where a wetting fluid advancing into a dry network is able to communicate from pore to pore across the network, and therefore communicate capillary pressure. The bubble pressure, P_B, is the capillary pressure at which air, displacing a wetting fluid from a saturated network, is able to communicate from pore to pore across the network. Furthermore, there is strong evidence that these two critical pressures are proportional to $\cos\theta$ where θ is the contact angle between the fluid in the network and the solid surfaces of the pores. This permits the derivation a quantity called pore curvature

$$K \equiv \frac{-P_C}{\sigma_{LV} \cos\theta} \qquad 10.1$$

where P_C is the capillary pressure, a negative quantity (suction) for a wetting fluid; σ_{LV} is the surface tension of the liquid, and θ is the contact angle between the liquid and the pore surface. Pore curvature is a geometric property of a porous material and does not depend on the properties of the liquid present. This permits data taken with different liquids to be related to one another. The critical curvatures for a network of pores are

$$K_W \equiv \frac{-P_0}{\sigma_{LV} \cos\theta_{adv}} \quad \text{and} \quad K_{NW} \equiv \frac{-P_B}{\sigma_{LV} \cos\theta_{rec}}. \qquad 10.2,\ 10.3$$

where θ_{adv} is the contact angle of an advancing meniscus, and θ_{rec} is the contact angle of a receding meniscus.

In the formation of 3-D Printed features, binder is initially concentrated in the immediate area of jet impact, and is surrounded by dry powder. It is assumed that a substantial quantity of dry powder surrounds the feature and attracts binder away from the saturated feature. The excess pressure of the fluid within the feature is given by the difference

$$\Delta P = -P_0 + P_B . \qquad 10.4$$

If this pressure is positive, binder will drain from the saturated region. As the drainage proceeds, the excess pressure decreases until the equilibrium condition, defined by

$$K_{drainage}(S^*) = K_W \qquad 10.5$$

is obtained at the equilibrium saturation S^*. Saturation is the fraction of the pore volume filled by liquid.

The force of gravity increases the excess pressure at the bottom of a feature with respect to the top of the feature. If a large region containing mobile,liquid binder exists, then this pressure difference can cause significant amounts of liquid to migrate downward into unprinted regions. This is the bleeding bleeding phenomenon described above.

10.5 Capillary Measurements

The pore-network model for feature formation indicates a minimum set of data to characterize the powder\binder interaction sufficiently to predict the equilibrium saturation of binder in 3-D Printed features. The dry suction pressure P_0 can be measured directly. The capillary pressure variation during drainage is most conveniently measured by mercury porosimetry, and the pressure data converted to pore curvatures by equation 10.1. The contact angles between the various fluids involved can be measured by microscopic examination, and the surface tensions can be measured by any of a variety of well-documented methods.

The powder that is currently used in the ceramic shell process has flattened lamellar grains with a mean size of approximately 30 μm. Samples were prepared by layering powder in a 3-D Printer and sintering the grains together to form a cohesive body with the same pore structure as the loose powder. Spherical powder with a 30 μm grain size was also tested, as were bimodal powders containing predominantly 30 μm lamellar with smaller amounts of 3 μm lamellar.

The drainage curves generated from mercury porosimetry data on the monomodal lamellar powder gave nonwetting critical pore curvatures (K_{NW}) between 0.3 and 0.6 μm^{-1}. These correspond approximately to a mean pore diameters between 7 μm and 12 μm. The larger curvature and smaller pore diameter were for the more tightly packed powders. The packing density of powder was found to be very difficult to control, varying between 30% and 50% with significant changes occurring on a daily basis, subject to the vagaries of ambient humidity and condition of the spreading apparatus.

The dry suction measurements gave $K_W \approx 0.4\ \mu m^{-1}$. for 30 μm lamellar alumina across the range of packing density. These data showed considerable variation among measurements taken with the same sample, as well as variation from sample to sample. Some of this variation could have been a result of experimental error, but some was

probably due to variation in homogeneity of the powder as a result of the spreading mechanism.

The rearrangement of powder in a feature can strongly influence the pore structure of the powder and thereby affect the distribution of binder. If the powder within the features is much more tightly packed that the unprinted powder, the distortion could cause the lines to separate from the surrounding powder and not approach capillary equilibrium during the available time. The bimodal powders were the only powders that were found to change substantially in density when moistened.

10.6 Equilibrium Saturation Measurements

To measure the density of the tiny single line features, two different techniques were used to estimate the mean diameters of the lines. One technique was to measure the width of microscopic images of the features. The other technique was to calculate the weight of powder contained within the features and to estimate the diameter assuming that the powder was packed to the same density in the lines as it was in the bulk of the powder bed. This derived quantity is given below.

$$d_{est'd} = \sqrt{\frac{4A_{powder}}{\pi f_{powder}}} \quad . \qquad 10.6$$

where A_{powder} was the cross sectional area filled by the powder in the lines (calculated from the weight) and f_{powder} was the packing density of the bulk powder bed before printing. It was found that the two sets of measurements could only be reconciled by assuming that the optical measurements overestimated the line diameters by approximately 26 μm. Subsequent measurements by Jain Charnnarong confirmed that the "standard" powder does not significantly change in packing density after printing. The saturation of binder in single line primitives could be calculated as the ratio of the amount of binder deposited per unit line length and the available pore space in the line with the estimated diameter and assumed packing density.

$$S_{local} = \frac{A_{liquid}}{A_{powder}} \frac{f_{powder}}{(1 - f_{powder})} \qquad 10.7$$

where A_{liquid} was the binder volume per unit line length.

The density and binder saturation of single line primitives was measured under a variety of process conditions. The surface tension of binder and the packing density of "standard" powder were varied to asses the performance of the ceramic shell process as it is currently practiced. It was found that the measured saturations conformed reasonably well with the values predicted by the model using capillary pressure data. Citric acid added to powder was found to affect the packing density of the powder, and the equilibrium saturation was found to reflect that change in packing density. No effect could be detected due to any kinetic effect of gelation limiting the approach to equilibrium.

The volume of binder per unit length of line was varied from a level several times higher to a level roughly 1/4 the present norm. In nearly all cases, the formation of lines was found to agree with the capillary equilibrium model. The exception was when binder droplets were separated by such distance that they did not overlap on impact, and they tended to form single-droplet primitives instead of lines. Printing with nozzles with a diameter of 30 μm, at a flow rate roughly 1/4 the "standard" value resulted in lines that are approximately 110 μm in diameter. These lines could be interdigitated between 50 μm layers, reducing the "stairstepping" lamination defect to a magnitude the same as the grain size of the powder.

Primitive features were generally linear, except at the very lowest extremes of binder dose. When binder droplets were distributed at a spacing somewhat larger than the droplet radius, significant amounts of the printed material formed as disconnected, spherical primitives. These primitives has anomalously high density. A method of printing a pattern of drops that are widely dispersed could be a very good strategy for increasing part density and improving the isotropy of printed material.

Spherical powder with a much different pore structure form the conventional lamellar powders was found to agree with the capillary model. Lamellar powder was coated with polymer and fused after spreading to inhibit the rearrangement of powder during jet impact. The morphology of the lines was found to be noncircular, but tne equilibrium saturation was found to agree with the capillary model if proper account was taken of the contact angle of the binder against the polymer-coated surface.

Bimodal powders were the only materials tested that did not substantially agree with the capillary model. The lines printed were found to have a packing density very much larger than the density as spread. To account for this, the drainage behavior of densified

samples of powder were measured by mercury porosimetry. The capillary pressure measurements suggested that the dry powder surrounding the lines should have been capable of draining a large fraction of the binder from the features, but in all cases the fluid content of the features was found to be roughly 60% of the available pore space. It could not be determined if the discrepancy was due to a kinetic limitation of the binder migration through the smaller pores or due to improper sample preparation for porosimetry.

The distribution of fine particles in the bimodals depends very much on the processing steps in their formulation, which in turn affects their capillary properties in ways that are difficult to predict. The mixtures increase in packing density substantially during printing. This drastically changes the structure of the powder within the features, and adds to the difficulty of modelling their formation. Qualitatively, single lines printed with bimodal powders appear to have very smooth surface finish. This is likely to be a result of the powder rearrangement during densification: the fine grains plug the gaps between larger grains, and grains generally tend to reorient themselves in low-energy configurations, parallel to the feature surface.

The mechanics of powder packing is a topic that must be investigated in detail before a thorough understanding of the process of 3-D Printing is to be understood in any great depth. Particularly in the case of materials that require a high packing density in order to properly achieve their required properties, control of the density and uniformity of powder layering is crucial. Some of the scatter in the measurements of capillary pressure and feature density were probably due in part to nonuniformity of the properties of the powder bed: aspects that are presently completely unmeasured and uncontrolled. It may not be necessary to understand powder packing in all its aspects, but a coherent strategy for controlling it is definitely needed.

A table summarizing the theoretical predictions and experimental results is given below.

Theoretical			Experi mental	
Packing Density f Hg, monomodal	Excess pressure kPa at 50 dyn/cm	predicted saturation	dry spread density monomodal	measured saturation
0.35	5.5	0.58	0.30	0.511
0.31	1.5	0.59	0.31	0.621
0.35	0	0.91	0.32	0.626
0.37	5	0.34	0.34	0.709
0.36	3	0.53	0.35	0.591
0.39	5	0.72	0.36	0.639
0.4	1.5	0.85	0.38	0.622
0.42	2	0.86	0.39	0.705
0.48	-0.5	0.91	0.41	0.584
0.49	- 1	0.92	0.42	0.625
0.45	-3.5	0.97	0.44	0.848
Haines, mono			0.46	0.796
0.33	4.5	0.38	0.48	0.804
0.46	1.5	0.87	0.49	0.85
0.49	-0.5	0.93		
Hg, bimodal				
10% fines	22	0.38	0.41	0.6
20% fines	14.5	0.35	0.4	0.63
30% fines	29	0.39	0.39	0.64
40% fines	10.5	0.71	0.39	0.63
Other				
30 μm spherical	- 6	0.96	0.58	0.82

Table 10.1 Predicted values of equilibrium saturation and experimentally determined values.

10.7 Final Conclusions

Three dimensional printing has the potential to change the way people think about manufacturing. The success of the process in the marketplace depends as much on reliability as it does on accuracy. Both these issues depend on the interaction between the printing hardware and the materials: one must treat the two as a complete system, rather than improving just one or the other.

The experience of working on the 3-D Printing project has been very similar to the experience of working for startup companies. A large group of people were focused on

constructing interacting systems that, as a whole, forms the goal of the project. This is completely opposite to conventional academic research, in which each researcher seeks knowledge, the results of which do not directly affect other people with whom they might be associated. The former method is much more difficult than the latter, but the rewards are far greater. Much of the discussion in this thesis has been directed to readers who, themselves, wish to develop materials systems for Three Dimensional Printing. These efforts cannot enjoy any lasting success unless they are integrated with the whole system, and designed to be convenient enough so other personnel involved with the process can work with them.

Appendix A. Thermodynamics and Capillary Phenomena

A.1 Stability

The general condition for equilibrium [Gibbs, p. 61] is that there should be no decrease in energy in a thermally isolated system for any admissible variations in the state of the system. This expressed by the inequality $(\delta E)_S \geq 0$. (If the system is not thermally isolated, a more convenient criterion might be $(\delta S)_E \leq 0$: No increase in entropy for a system of fixed energy.) If a variable that defines the state of the system is z, for any admissible variation dz, the condition for equilibrium is exactly

$$\left(\frac{dE_T}{dz}\right)_S = 0 . \qquad \text{A.1}$$

There are three conditions, defined by the second derivative:

$$\left(\frac{d^2E_T}{dz^2}\right)_S > 0 \text{ for a stable equilibrium;} \qquad \text{A.2}$$

$$\left(\frac{d^2E_T}{dz^2}\right)_S = 0 \text{ for a neutral equilibrium;} \qquad \text{A.3}$$

and

$$\left(\frac{d^2E_T}{dz^2}\right)_S < 0 \text{ for an unstable equilibrium.} \qquad \text{A.4}$$

where E_T is the "total" energy: the sum of all the energy terms that change with a change in z. "Admissible" variations in the total energy are determined by the constrains on the system in question. A fourth type of equilibrium is defined by

$$(\delta E)_S > 0 . \qquad \text{A.5}$$

This corresponds to a discontinuity in the state equation E = E(z) e.g. at some system limit. It is not completely clear that this condition is different from a stable equilibrium, since at a high enough magnification, every energy curve should appear continuous. These four conditions are illustrated below:

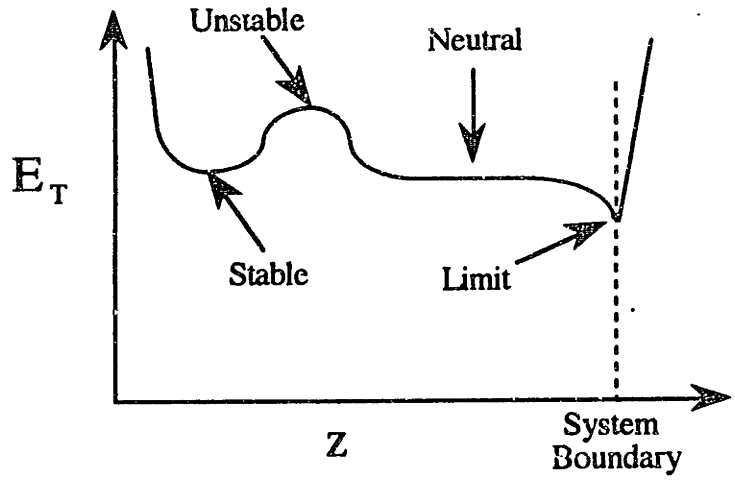

Figure A.1. Energy curves showing different forms of equilibrium.

A.2 A Quick Review of Classical Thermodynamics

Although a great deal of complexity can be developed for incompressible fluids that are thermally isolated from their surroundings, there are conditions under which a change of volume occurs and heat interactions might occur. In general, the fluid systems under consideration will be immersed in an atmosphere with ambient pressure P_0 and ambient temperature T_0. All heat and work interactions between a fluid and its surroundings change its **internal energy**, U, according to the **First Law of thermodynamics**:

$$dU = \delta Q - \delta W \qquad \text{A.6}$$

where δQ is the heat absorbed and δW is the work done. Since both heat and work are forms of energy, this equation is somewhat redundant. People have an intuitive understanding of heat, which often leads to misconceptions about energetics. Work is an abstract quantity that can be defined in a wide variety of convenient ways. For fluids that perform work by changing volume,

$$\delta W = P\, dV. \qquad \text{A.7}$$

Heat interactions are universally expressed in terms of the **Second Law of Thermodynamics** which defines the work equivalent of heat for a reversible transformation

$$\delta Q = T\, dS \qquad \text{A.8}$$

where S is **entropy**. The nature of reversible heat interactions is usually defined in terms of a reversible cyclic heat engine, or Carnot engine, which extracts the greatest possible

amount of work from a given quantity of heat. The reader is invited to browse the enormous literature on reversible processes to develop a better understanding of entropy. Substituting these expressions into the First Law:

$$dU = TdS - PdV. \qquad A.9$$

In an expression such as this, the quantities are usually understood to be molar quantities, but they can be defined in any convenient units as long as consistency is maintained.

The internal energy is like the accounting book that keeps track of energy transformations. For a homogeneous fluid at equilibrium with itself, U is a function of temperature only, and corresponds to the sum of the kinetic energy of all the molecules in the fluid and the potential energy of forces of attraction between molecules. If heat is added to a fluid contained in a vessel of fixed volume, the internal energy increases by a corresponding amount, and the temperature increase defines the **constant volume heat capacity** C_V:

$$\delta Q_V = dU = C_V dT . \qquad A.10$$

Quite often a fluid is contained in some apparatus, or it is otherwise constrained by its surroundings. If a fluid is constrained in such a way that it cannot exchange heat with its surroundings, it is **adiabatically** confined. The converse of that is such perfect thermal communication with the surroundings that the temperature is always constant. That is an **isothermal** constraint. A process that occurs at constant volume is **isochoric**, and the converse, an **isobaric** process, occurs at constant pressure.

A compressible fluid can undergo a change in volume in a time too fast for thermal equilibrium to be maintained. Rapid processes are frequently adiabatic. Work is performed on the atmosphere in the volume change at the constant ambient pressure:

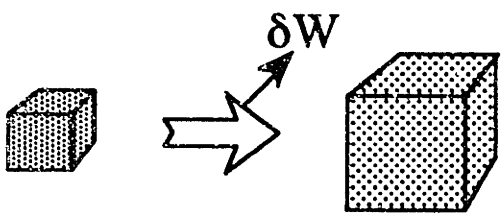

$P = P_0$

$dU = \delta Q - \delta W$

$= -P_0 dV$

V_0 $\quad V_1 = V_0 + dV$

U_0 $\quad U_1 = U_0 + dU$

$(U+PV)_0 = (U+PV)_1$

Figure A.2 Adiabatic work of a gas as a change in enthalpy.

IF a fluid expands in some way that performs no work on its surroundings, the expansion is called a "free" expansion. The work is dissipated internally and increases the internal energy U of the fluid such that the quantity (U+PV) remains constant. (U+PV) is the **enthalpy** of the fluid. The enthalpy expresses the work that is available from a fluid that can only be expanded adiabatically. This is the case, for example, in a steam turbine, where the available energy is the change in enthalpy between the inlet steam and outlet steam.

The First Law can be expressed in terms of enthalpy as

$$dH = d(U + PV) = TdS + VdP. \qquad \text{A.11}$$

If heat is added to a fluid whose volume is free to vary at constant pressure, the temperature of the fluid changes as a result of the increase in enthalpy. The constant **pressure heat capacity** of the fluid is defined by

$$dQ_P = dH = C_p dT \qquad \text{A.12}$$

because the fluid is able to expand when its temperature increases, it takes more energy to raise its temperature than when the volume is fixed: $C_P > C_V$ except when the fluid has zero thermal expansion.

In cases where a thermal equilibrium exists, the temperature is fixed at the ambient temperature of the surroundings, and heat can be exchanged during a change of state of the fluid. This characterizes equilibrium changes of phase of a simple substance, e.g. during evaporation of a fluid or dissolution of a solute into a saturated solution. Under these conditions, the quantity (U-TS+PV) is constant for all phases at equilibrium. This is the **Gibbs free energy** function.

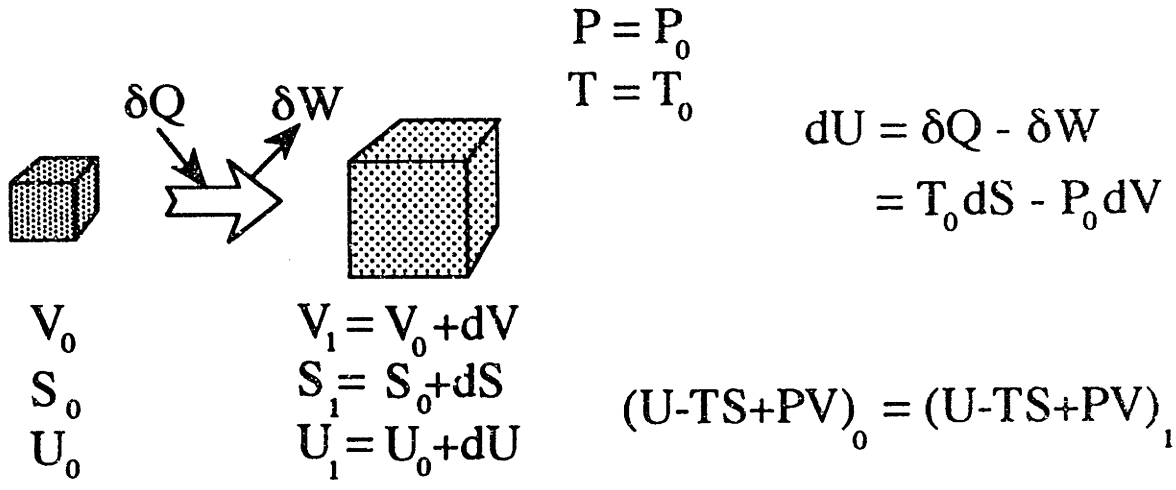

Figure A.3 Available energy as a change in the Gibbs function.

The Gibbs function describes the amount of work that can be gained from a fluid which can come to thermal equilibrium with its surroundings. This function is especially useful in chemical systems, where the pressure is generally constant and thermal equilibrium usually pertains. The First Law, expressed in terms of the Gibbs function is

$$dG = -SdT + VdP \qquad A.13$$

Gibbs [p. 37] discusses rather elegantly the conditions necessary for two substances to coexist at equilibrium in contact with one another. If the internal energy U of a substance is taken to be a function of is entropy and volume then the temperature and pressure are defined by

$$T = \left(\frac{\partial U}{\partial S}\right)_V \text{ and } P = -\left(\frac{\partial U}{\partial V}\right)_S . \qquad A.14$$

Gibbs considers a graph of U(S,V) and notes that T and -P are the slopes of the surface in the S and V directions, respectively. When a body consists of a mixture of two phases, the energy of the aggregate is determined by the center of gravity between the points on the U(S,V) surface that corresponds to the states of the two phases. In order for the two phases to coexist at equilibrium, they must occupy points on the surface that have the same tangent plane. If this were not true, then one phase transfer heat or work to the other and lower the energy of the aggregate. The generic equation for a plane in the {U,S,V} space is $(U - TS + PV)$ = a constant, and so all phases in equilibrium must have the same value

of $G = (U - TS + PV)$. It also follows that phases in equilibrium must be at the same temperature and pressure.

Finally if a fluid is constrained to constant volume but is in thermal equilibrium with its surroundings, the quantity (U-TS) expresses the energy content of the system. Work interactions with such a system change the value of this quantity. This is the case in the surface of a phase boundary which, in Gibbs' original derivation, cannot change in volume. (U-TS) is the Helmholtz free energy function, F, and its form of the First Law is

$$dF = -SdT - PdV . \qquad A.15$$

A.3 Irreversibility

When a system traverses reversibly from one state to another, all the states it occupies during the transformation are equilibrium states. In general, real systems never occupy an equilibrium state, but frequently they can be close enough that the difference is negligible. When a system finds itself in a non-equilibrium state, it will tend to spontaneously approach the equilibrium state by dissipating energy until its energy reaches a minimum. This energy might be dissipated in a number of ways: the most common being the generation of noise or the production of excess heat. The process is irreversible in the sense that the heat generated cannot be converted into work equal to the amount of energy dissipated.

One classic example of an irreversible process is the conduction of heat from a hot body into its colder surroundings. The heat that is dissipated corresponds to a quantity of energy that cannot be recovered. Alternatively, the heat could be used to drive a reversible Carnot engine and derive the maximum amount of useful work possible. The engine is reversible because the work derived from the engine can be used to drive a second Carnot engine in reverse to pump the same quantity of heat back up to the original temperature. A Carnot engine cannot usually be obtained before heat dissipates from a hot body to its surroundings (since Carnot engines do not really exist) so every process that involves heat incorporates some degree of irreversibility.

The capillary migration of an incompressible fluid represents a case where all pressure and temperature gradients are dissipated irreversibly. When the fluid is at rest, its equilibrium is defined by a reversible balance of forces, but kinetic energy from fluid

motion is entirely dissipated in heat, and the heat produced is dissipated by conduction to the surroundings. The bulk fluid occupying the cavities of a porous medium may be considered separate from a surface phase that divides the fluid from the solid particles. The surface phase exchanges work by changing its surface area and state of wetting, and the bulk phases exchange work by changing shape and lifting against the force of gravity. All equilibrium configurations are defined by the geometric properties of the system.

The phenomenon of irreversibility permits one to ignore all thermal effects for virtually every system of interest in Three Dimensional Printing.

A.4 Surface Energy

The surface energy of the boundary between two phases at equilibrium is defined as

$$\sigma_{ij} = \left(\frac{\partial}{\partial a_{ij}} \left(U_s - TS_s \right)_{ij} \right)_{T,V,m_1,m_2,\ldots} \qquad \text{A.16}$$

[Gibbs p. 231. but [Hunter 242-250] is rather clearer. See also [Guggenheim,194] where the subscript ij denotes the boundary between two phases i and j, a_{ij} is the area of the boundary and $(U_S\text{-}TS_S)_{ij}$ is the Helmholtz free energy of a thin region containing the surface discontinuity separating the two phases. Gibbs [226] assumes this region to have a fixed volume, and so the Helmholtz free energy expresses the "available" energy of the surface phase. The differential is taken at constant temperature and masses of the components in phases i and j.

Other workers, e.g. [Adamson,p.76], regard the surface discontinuity to have a volume that is variable, but with a constant thickness d. This makes somewhat more sense, since changes in volume at constant thickness are identical to changes in area. The "pressure" in the surface phase must therefore be resolved into tangential and normal components:

$$\sigma_{ij} = \left(\frac{\partial}{\partial a_{ij}} \left(U_s - TS_s + PV_s \right)_{ij} \right)_{T,P,\delta,m_1,m_2,\ldots} \qquad \text{A.17}$$

where the quantity $(U_S\text{-}TS_S\text{+}PV_S)_{ij}$ is the Gibbs free energy of the surface region. The difference is almost purely academic for ordinary systems at atmospheric pressure.

It is assumed that surface is created and destroyed reversibly in deformations of the interface between two phases. The available energy is converted completely to work and the equation

$$\delta W = -\sigma_{ij} da_{ij} = -dG \qquad A.18$$

expresses the work done by the phase boundary when the interface is deformed by an arbitrary amount which changes the area by Δa_{ij}.

A liquid in a partially saturated porous medium is a three-phase system and there are accordingly three phase boundaries, each with their own surface energies. The tern σ_{LV} is the surface energy of the liquid phase in contact with the gaseous phase (in equilibrium with the vapor of the liquid and solid phases) and is normally designated "the surface energy of the liquid." The terms σ_{SV} and σ_{SL} are the energies of the dry and wet solid surfaces respectively. The situation becomes considerably more complicated when mall concentrations of surfactants are present, contributing partial monolayers of adsorbed molecules. See, for example, [Adamson ch.2].

In a bulk body of fluid, molecules are attracted to one another. Because of this force of attraction, the free energy of molecules surrounded by other molecules is lower than molecules that are only partly surrounded. For a fluid body at equilibrium, this excess free energy will be minimized, subject to the geometrical constraints on the fluid. The tendency for the free energy to be minimized causes the surface to contract, and the strength of the contraction can be measured by a variety of methods (Adamson, 16-36; Hunter, 310-311)

The surface tension of a liquid is normally measured in a static arrangement, e.g. the Wilhelmy Plate experiment, in which a rectangular plate is withdrawn from a fluid and the adhesive force on the edge is measured with a balance. [Defay & Petre] report that the static value of surface tension in newly formed surfaces is the same as that of the pure solvent until sufficient time has elapsed for solutes to diffuse to the surface and possibly overcome an activation energy. For 1-8 octanediol at 7×10^{-3} M for example, the time constant is approximately 4×10^{-3} sec. They used a method based upon the observation of droplet oscillations in a fluid jet. Similar results are discussed by [Adamson, p.35]

Because of the underlying assumption of thermodynamic equilibrium, one must assume that the gas phase is saturated with the vapor of both the solid and liquid phases respectively. For most practical purposes, this is merely a semantic convention.

A.5 Young's Equation

Adamson [p. 340] derives Young's equation from the condition of equilibrium for a fluid droplet that makes a contact angle of θ with a flat solid surface:

$$\lim_{\Delta A \to 0} \frac{\Delta G_s}{\Delta A} = 0 \qquad \text{A.19}$$

where ΔG_s is the net surface free energy when the boundary of the fluid drop encroaches over a dry area ΔA of the solid plate. This arrangement is illustrated below. A fluid surface makes contact with a solid surface at an angle of θ. We consider a virtual displacement of the interface across an arbitrary area ΔA. In this displacement an area ΔA of the solid surface is converted from dry to wet, and the change in liquid surface area is found by translating the fluid surface perpendicular to itself and calculating the extra area needed to reach to the surface:

$$\Delta G_s = \Delta A \, (\sigma_{SL} - \sigma_{SV} + \sigma_{LV}\cos\theta) \qquad \text{A.20}$$

And Young's Equation follows directly:

$$\sigma_{SV} - \sigma_{SL} = \sigma_{LV}\cos\theta \qquad \text{A.21}$$

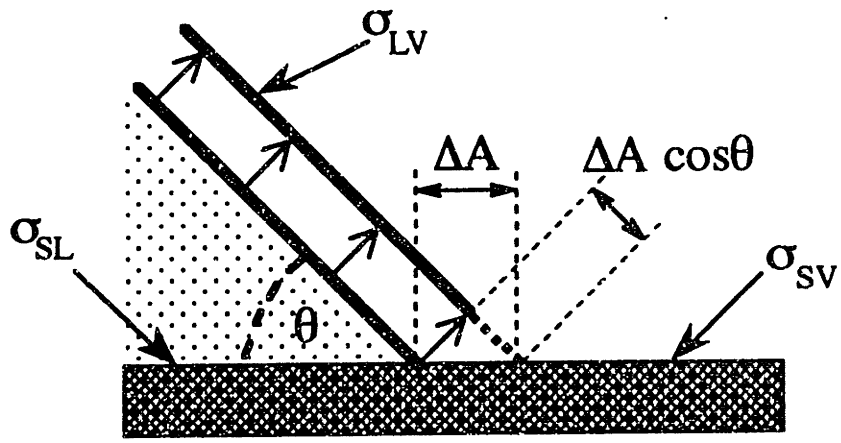

Figure A.4 Contact between a liquid and a flat solid surface.

In 1805 Thomas Young derived his famous equation from a force balance at the three-phase boundary illustrated below. The three-phase boundary is a one-dimensional boundary, so this illustration could be a side view of the edge of a pool of liquid standing on a flat surface.

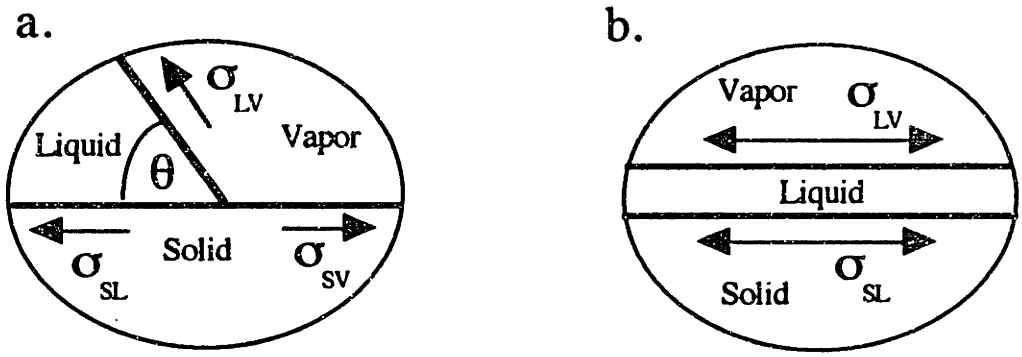

$$\sigma_{SV} - \sigma_{SL} = \sigma_{LV} \cos\theta \qquad \sigma_{SV} \geq \sigma_{SL} + \sigma_{LV}$$

Figure A.5 a. Surface Tension components: partially wetting condition and Young's equation. c. Fully wetting condition.

If σ_{LV} is sufficiently large that $1 > \cos\theta > -1$ in (a.), the liquid/vapor interface intersects the solid surface at a contact angle given by θ. If the inequality shown in (b) is true, the fluid spontaneously spreads over the entire available solid surface. If the angle $\theta < 90°$ the fluid is called **wetting** to the surface. If $\theta > 90°$ the fluid is **nonwetting**. For porous powder in particular this is far from an arbitrary distinction. For fluid to spontaneously soak into powder, the fluid must be wetting to the powder. This spontaneous process is called **imbibition** and the quantity $\cos\theta$ is sometimes called the wetting coefficient [Probstein, 275 .]

A.6 Contact Angle Hysteresis

One complication of this model is **contact-angle hysteresis**. This is discussed in great detail by [Johnson & Dettre] It is observed that the contact angle changes depending on whether the liquid/vapor interface is moving: the contact angle of an advancing front tends to be larger than the contact angle of a receding front. Johnson and Dettre associate this effect with roughness of the solid surface. The advancing contact angle is usually closer to the stationary value than the receding one, which frequently tends to zero. Qualitatively, this means that it is easier to wet surfaces than it is to dewet them. (

The term **dewetting** implies the fluid leaving a solid surface as a liquid, reversing the process of **wetting**, while the term **drying** implies removal by evaporation.)

A.7 The Classic Example: A Cylindrical Capillary

The interaction between a wetting fluid and a solid cylindrical capillary is used widely to represent the capillary properties of disordered porous material. The justification for doing this will be clarified later, but for the present, consider the energetics of a system consisting of a solid, cylindrical capillary and a body of fluid which wets the capillary. We assume for simplicity that the capillary has negligible weight and when the fluid wets the capillary, the meniscus has negligible weight and does not significantly alter the area of the liquid surface. This is illustrated below.

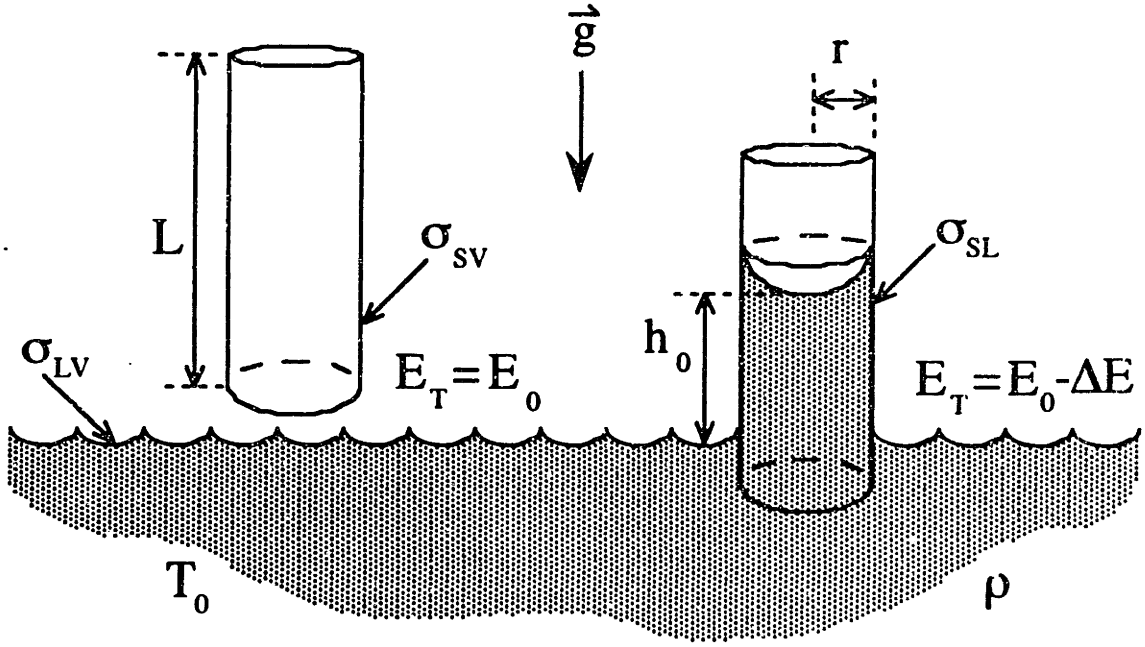

Figure A.6 Liquid rise in a cylindrical capillary.

We define the total energy of the system conveniently to include the surface energy at the inside surface of the capillary and the gravitational potential energy of any fluid (except the negligible quantity contained in the meniscus) that is lifted above the level surface of the liquid pool. Initially, the capillary is dry and the total surface energy given is

$$G_0 = 2\pi r L \sigma_{sv}. \qquad \text{A.22}$$

(Please note that the subscript zero refers to the initial state, while the superscript zero refers to the standard state.)

When the tip of the capillary is brought in contact with the surface of the liquid, the capillary becomes wet, and the energy, σ_{SL}, of the wet surface is lower than σ_{SV}, the energy of the dry surface. As dry surface is replace by wet surface, the energy liberated serves to raise water from the liquid pool. At any instant during the imbibition, when the liquid rises from z to z+dz, the change in surface energy is

$$dG_s = 2\pi r(\sigma_{SL} - \sigma_{SV})dz \qquad A.23$$

and the change in gravitational energy is

$$dE_G = \pi r^2 \rho g z\, dz. \qquad A.24$$

These are the only energy terms that change reversibly with z, so the total energy is the sum of these two terms:

$$dE_T = \pi r^2 \rho g z\, dz + 2\pi r(\sigma_{SL} - \sigma_{SV})dz. \qquad A.25$$

These expressions can all be integrated from z = 0 and the results are graphed in the figure below.

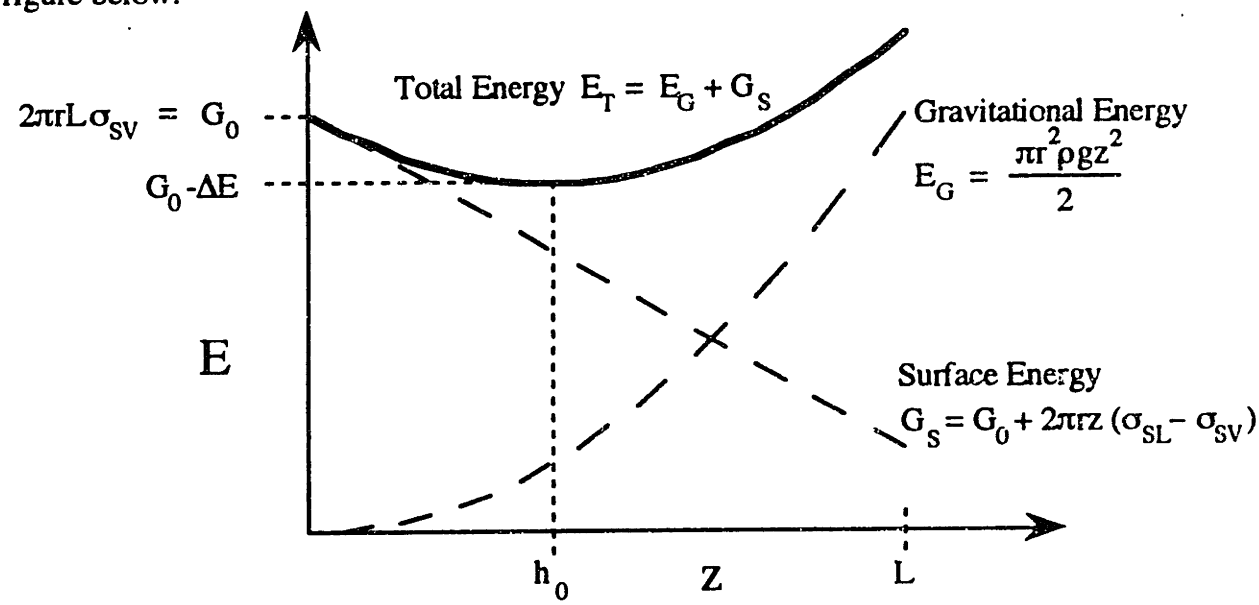

Figure A.7. Energy functions during capillary rise of a liquid.

The equilibrium position of the liquid meniscus is the point at which the total energy is minimum:

$$\frac{dE_T}{dz} = \pi r^2 \left[\rho g h_0 + \frac{2(\sigma_{SL} - \sigma_{SV})}{r} \right] = 0. \qquad A.26$$

If the difference in surface energies (σ_{SL} - σ_{SV}) is negative, the capillary rise is positive, if it is negative, the meniscus is pushed below the surface of the liquid. From Young's Equation (A.21)

$$(\sigma_{SL} - \sigma_{SV}) = - \sigma_{LV} \cos\theta . \qquad \text{A.21}$$

The hydrostatic pressure of the liquid at the top of the capillary is

$$P_{liq.} = P_{ATM} - \rho g h_0 = P_{ATM} - \frac{2\sigma_{LV} \cos\theta}{r}. \qquad \text{A.27}$$

The difference in pressure between the that hydrostatic pressure and the ambient pressure is caused by the interaction of the fluid with the capillary. Accordingly, the quantity

$$P_c = - \frac{2\sigma_{LV} \cos\theta}{r} \qquad \text{A.28}$$

is called the **capillary pressure** of the fluid in the tube. The capillary pressure can be derived directly from the surface free energy G_S:

$$P_c = \frac{dG_s}{dV} \qquad \text{A.29}$$

$$= \frac{-2\pi r(\sigma_{LV} \cos\theta) dz}{\pi r^2 dz} \qquad \text{A.30}$$

The irreversibility of this system can be characterized by the magnitude of the quantity ΔE in figure A.7. If the fluid were inviscid, ΔE would be converted into kinetic energy, and the meniscus would oscillate around the equilibrium point. Since the system is dissipative, the meniscus might oscillate a few times, but this excess energy is ultimately lost through friction in the liquid. The fluid is heated slightly, but nothing is done with the heat. The condition of reversibility is applicable at the equilibrium state **only**: changes in energy as the system passes through nonequilibrium states are irreversible, and one cannot expect the books to balance.

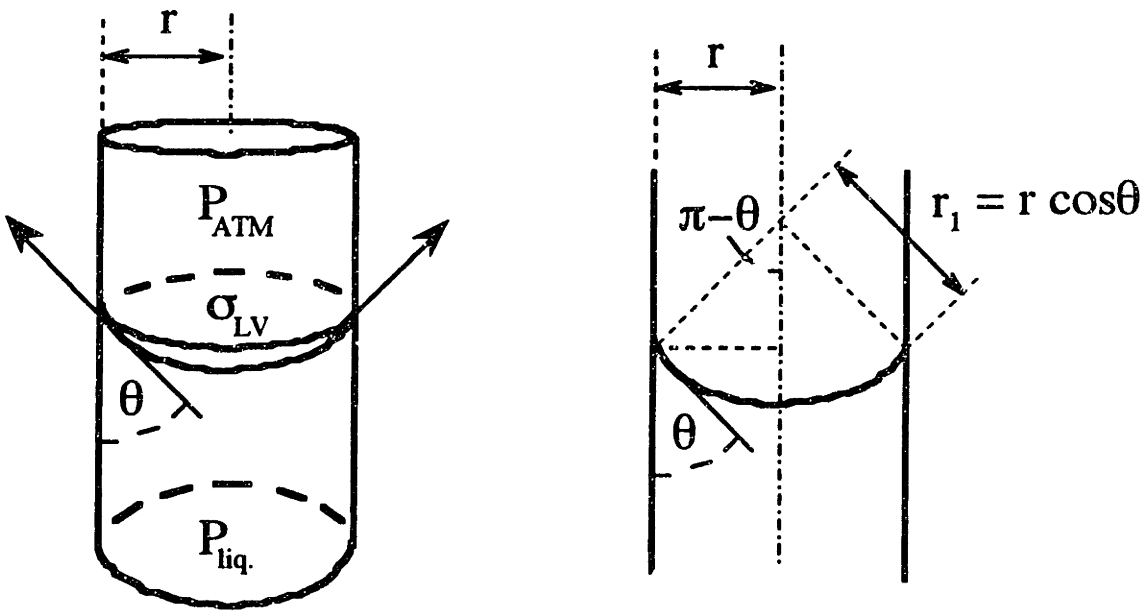

Figure A.8 Cylindrical capillary with a spherical meniscus.

Looking more closely at the liquid surface, the fluid forms a **meniscus**, or curved interface between the fluid and vapor phases. The free surface of the liquid is approximately spherical (in the absence of gravity, it would be exactly spherical) with a radius of $r_1 = \frac{r}{\cos\theta}$. The vertical component of the tensile force exerted by the meniscus on the wall of the capillary is balanced by a pressure difference between the fluid and vapor phase:

$$0 = 2\pi r\sigma_{LV}\cos\theta + \pi r^2(P_{liq.} - P_{ATM}) \qquad \text{A.31}$$

$$P_C = (P_{liq.} - P_{ATM}) = \frac{-2\sigma_{LV}\cos\theta}{r}. \qquad \text{A.32}$$

In the absence of gravitational forces, the meniscus in this capillary is spherical, and the mean curvature of the meniscus is $C = -2\cos\theta / r$. The curvature is negative if the center if curvature is outside of the fluid. A larger pressure always exists on the side containing the center of the radius of curvature. This leads to Laplace's equation [Everett 1975]:

$$P_c = P_1 - P_2 = C\sigma_{LV} \qquad \text{A.33}$$

On a curved surface that is nonspherical,

$$C = \frac{1}{r_1} + \frac{1}{r_2} \qquad \text{A.34}$$

where r_1 and r_2 are the **principal radii** of curvature.* P_c is called the **capillary pressure** of the fluid in the capillary. If the fluid is wetting to the capillary, P_c is a negative quantity; i.e. it is a suction pressure. Fluids that can serve as binders in Three Dimensional Printing must spontaneously infiltrate the porous powder bed, so the capillary pressure must be negative, and θ must be smaller than 90°.

*(For a more general surface given in cartesian coordinates: $z = f(x,y)$ with derivatives f_x, f_y, f_{xx}, f_{yy}, f_{xy}:

$$C = \frac{\left(1+f_y^2\right)f_{xx} - 2f_x f_y f_{xy} + \left(1+f_x^2\right)f_{yy}}{\left(1+f_x^2+f_y^2\right)^{3/2}} \qquad \text{[Morgan, 19]} \quad \text{A.35}$$

A.8 A Last, Lingering Look at Reversibility: The Kelvin Equation

We consider a fluid that is in equilibrium with its vapor. For the standard state at the reference altitude h_0 the equilibrium vapor pressure is P^0. The vapor undergoes a free expansion when it changes in altitude, and the change in enthalpy is equal to the work to raise the vapor against the force of gravity:

$$dH = TdS + VdP = -mg\,dh\,. \qquad \text{A.36}$$

For the adiabatic change considered, TdS=0. For convenience, we consider a molar mass of fluid and assume that the vapor obeys the ideal gas law. We can integrate this expression from h_0 to h_1:

$$\int_{P^0}^{P_1} V'dP = RT\int_{P^0}^{P_1}\frac{dP}{P} = RT\ln\left(\frac{P_1}{P^0}\right) = -m'g(h_1 - h_0) \qquad \text{A.37}$$

where m' and V' are the molar mass and volume, respectively and R is the universal gas constant.

Since the vapor pressure at height h_1 is less than at h_0 we can propose the following perpetual motion machine: Use a capillary with radius

$$r = \frac{2\sigma_{LV}\cos\theta}{\rho g(h_1 - h_0)} \qquad \text{A.38}$$

to lift the fluid to an altitude of h_1. The vapor in equilibrium with the liquid at the top of the capillary should have a higher pressure than the vapor at a high altitude, so we should be able to drive a turbine at the top of the capillary. The fluid that evaporates from the top of the capillary falls and condenses at the liquid surface and subsequently is replaced by fluid pumped up be the capillary attraction.

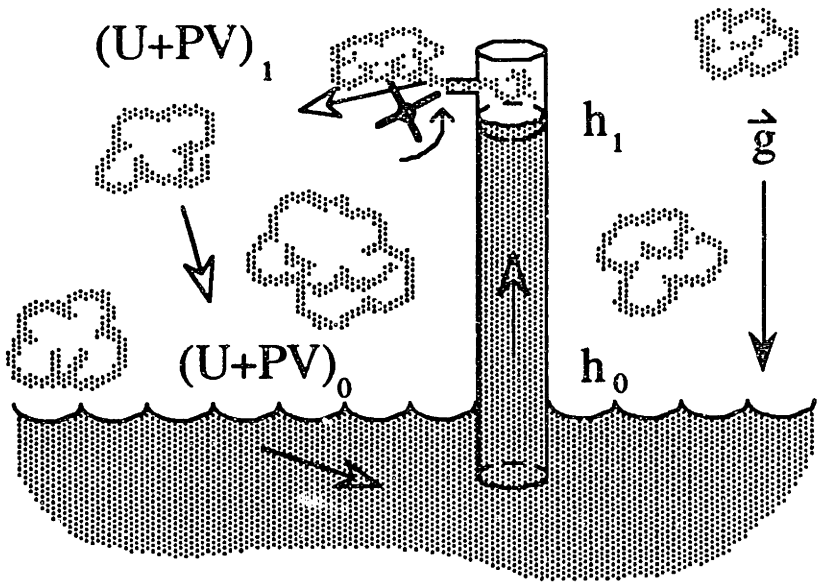

Figure A.9. A proposed perpetual motion machine (After [Adamson, p.93])

This amusing proposal is used by Adamson as a problem at the end of one of his chapters. Instead of seriously proposing perpetual motion, one is expected to smugly declare the impossibility of perpetual motion and assert that the pressure of the vapor over the liquid meniscus at the top of the capillary is equal to the pressure at the height h_1.

$$RT \ln\left(\frac{P}{P^0}\right) = -m'g(h_1 - h_0) = -\frac{m'}{\rho}\cdot\frac{2\sigma_{LV}\cos\theta}{r} \qquad \text{A.39}$$

and we can substitute

$$V' = \frac{m'}{\rho} \qquad \text{A.40}$$

so

$$RT \ln\left(\frac{P}{P^0}\right) = \frac{-2V'\sigma_{LV}}{r} \qquad \text{A.41}$$

where V' is the molar volume, this time of the liquid phase. This is the Kelvin equation and it expresses the variation in vapor pressure with hydrostatic pressure in a liquid.

In the equilibrium between the liquid and its vapor, the Gibbs function is constant. The Gibbs function is basically the available energy from a system, and the available energy of vapor in a gravitational fluid is given by the quantity $\Phi = (U-TS+PV+m'gh)$ which is uniform throughout the system illustrated above. For a rare good discussion of availability, see [Van Wylen, 231-247]. The Gibbs function of the liquid is given by

$$\Phi = G + m'gh = \text{a constant} \qquad \text{A.42}$$

$$\Delta\Phi = \Delta G + m'g\Delta h = 0 \qquad \text{A.43}$$

$$\Delta G = G_h - G^0 = -\rho V' g (h - h_0) = V'\left(P_h^{fluid} - P^{0,fluid}\right). \qquad A.44$$

while the Gibbs function for the vapor is

$$\Delta G = RT \ln\left(\frac{P_h^{vapor}}{P^{0,vapor}}\right) = V'\left(P_h^{fluid} - P^{0,fluid}\right). \qquad A.45$$

where $P^{0,vapor}$ is the vapor pressure of the liquid at ambient pressure $P^{0,fluid}$; and P_h^{vapor} is the vapor pressure over the fluid at some different hydrostatic pressure P_h^{fluid}.

Kelvin's equation is used as the basis for a method for measuring the surface area in a porous material. The equilibrium vapor pressure is measured over a porous material as the quantity of liquid in the pores is varied. (see, for example, [Hunter, 277-281] or [Scheidegger]) This technique is widely used for measuring microporous materials, but it is quite limited for studying powders used for Three Dimensional Printing, which have pores that are too large. Adamson gives the vapor pressure ratio $\left(\frac{P_h^{vapor}}{P^{0,vapor}}\right)$ of water as 1.001 over pores of 1 μm in radius, and 1.114 over pores 10 nm in radius.

[Everett 1975] deals with the equilibrium of a fluid in a porous medium with respect to capillary pressure and vapor pressure. In general for the short times involved in the formation of features during 3-D Printing, the fluid is considered nonvolatile.

Appendix B. Geometric Model of an "Ink-Bottle" Pore

B.0 Introduction

There is a widespread convention in the literature to express the capillary attraction of porous materials in terms of the properties of cylindrical capillaries. For a cylindrical capillary of radius r, the capillary pressure is

$$P_c = \frac{-2\sigma_{LV}\cos\theta}{r} \quad . \qquad \text{B.1}$$

In mercury porosimetry, for example, the pore size is calculated from this equation, with the contact angle $\theta > 90°$ for most materials; e.g. 130° for Hg on Al_2O_3. There seems to have been little work done to justify the use of equation B.1 to describe materials that do not contain cylindrical capillaries. The most critical issue is how the contact angle affects the capillary pressure in geometrically complicated pores. The model that is generally proposed for real porous materials is an entity called an "ink-bottle" pore which exhibits an instability of its meniscus during filling. In the following appendix, a geometric model will be developed for an ink-bottle pore in three dimensions and the dependence of the capillary pressure on the contact (or "wetting") angle will be explored qualitatively.

It is hoped that this derivation will provide not only sufficient justification for the use of equation B.1 to describe complicated porous materials, but will elucidate the conditions under which it can reasonably be applied.

B.1 Dullien's Two Dimensional Model

The cavities in a real porous material are geometrically different from cylindrical capillaries. To examine the effects of this difference, consider a simple geometric model for a three-dimensional pore. [Dullien, ch.3] proposed an angular pore geometry to represent the structure of pores in granular material, at least in the early stages of imbibition. This is illustrated below:

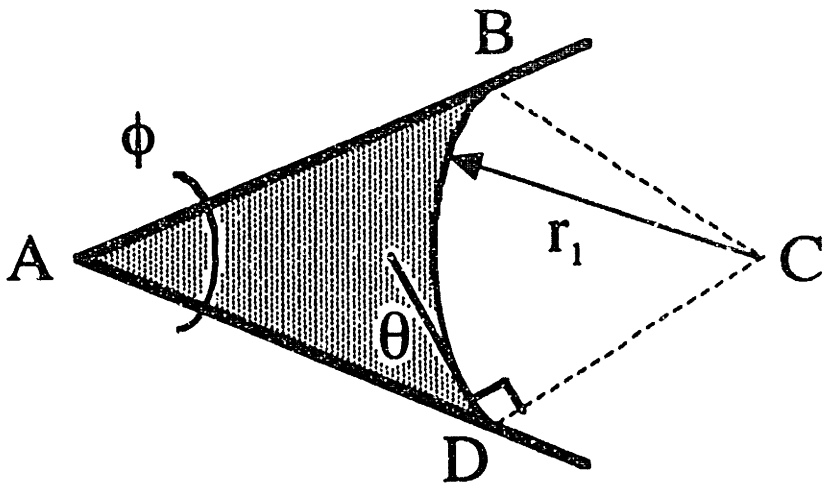

Figure B.1 Angular cavity in a porous body, after [Dullien ch. 3]

The angle BAD represents a point or line of contact between two prismatic particles. The angle ϕ is a characteristic angle of the porous body on which Dullien's derivation does not depend strongly. Assuming the fluid wets the solid with a contact angle of θ, the area shaded is equal to the area of the quadrilateral ABCD minus the area of the circular sector BCD. These two areas are given by:

$$A_{quad} = r_1^2 \frac{\cos\theta \cos(\phi/2 + \theta)}{\sin \phi/2} \qquad \text{B.2}$$

and

$$A_{sector} = r_1^2(\pi/2 - \phi/2 - \theta) \qquad \text{B.3}$$

from which one can calculate the total area of the shaded portion:

$$A_{fluid} = r_1^2\left[\frac{\cos\theta\cos(\phi/2 + \theta)}{\sin \phi/2} - (\pi/2 - \phi/2 - \theta)\right] . \qquad \text{B.4}$$

This analysis admits the possibility that $(\phi/2 + \theta) > \pi/2$ but this is a practical limit to the physical sensibility of the derivation because there must be a negative capillary pressure within the pore.

Dullien assumes that the capillary pressure is $-2\sigma_{LV}/r_1$ and the fluid volume in the porous body is proportional to r_1^2 Dependence on ϕ in Dullien's treatment is simply in an arbitrary constant of proportionality, and he considers the variation of capillary pressure as the volume of fluid varies. This approach has an advantage over models based on

cylindrical capillaries, e.g. in [Greenkorn 23-30], because variation of Pc with S comes as a consequence of a single geometric entity that resembles the structure in question.

B.2 A Three Dimensional Model

This model can be pushed into the third dimension in the following way: The pore shown in figure B.1 is swept out in a circular path about an axis in the vertical direction on the page. If the axis passes through point A, it can be shown that the fluid volume varies as r_1^3 . The more interesting case is where the axis passes through a point to the right of A. This is shown below:

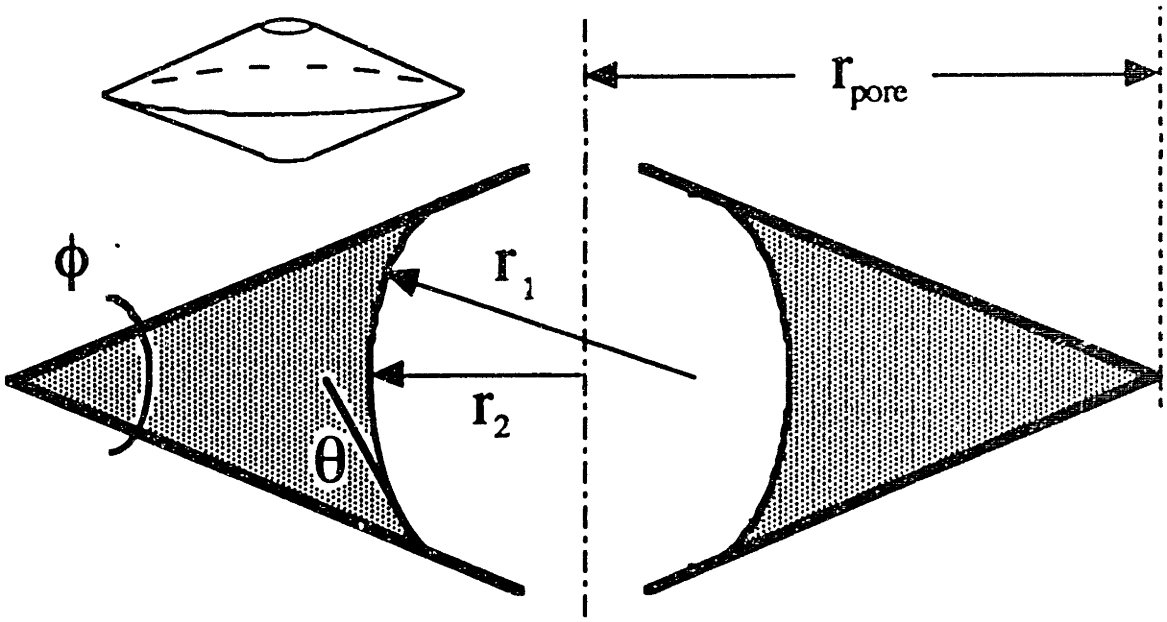

Figure B.2 Fluid meniscus in double-funnel pore.

The circular sweep creates a pore that consists of two conical funnels welded together at the rims. The major axis of the pore is r_{pore} , and r_2 is the radius of curvature of the meniscus in the plane perpendicular to the axis of the sweep. The apex of the two funnels is shown as a pair of circular holes to make the analogy of a pore. Their size is assumed to be relatively small compared to the cavity of the pore. Fluid is assumed to occupy a fillet filling the corner at the circumference of the pore, although it will be shown below that at some critical point this configuration becomes unstable.

The volume of the pore is

$$V_{pore} = \tfrac{2\pi}{3} r_{pore}^3 \sin\tfrac{\phi}{2} \qquad \text{B.5}$$

and the fluid volume is the difference between the volumes of the two toroids created by sweeping the quadrilateral and the circular sector from Figure B.1 about the axis. These volumes can be found by Pappus' theorem [Mark's p.2•22]:

$$V_{quadtorus} = 2\pi\left(r_{pore} - x_{quad}\right)A_{quad} \qquad B.6$$

and

$$V_{sector\ torus} = 2\pi\left(r_{pore} - x_{sector}\right)A_{sector} \qquad B.7$$

where x_{quad} and x_{sector} are the centroids of the quadrilateral ABCD and sector BCD, respectively, in Figure B.1 measured from the apex of the pore.

The centroids of these two figures may be derived from Figure B.1 [Mark's p. 3•17]:

$$x_{quad} = \tfrac{1}{3}r_1\left(\frac{\cos\left(\phi/2 + \theta\right)}{\tan\phi/2} + \sin\left(\phi/2 + \theta\right)\right) \qquad B.8$$

and

$$x_{sector} = r_1\left(\frac{\cos\theta}{\sin\phi/2} - \tfrac{2}{3}\frac{\cos\left(\phi/2 + \theta\right)}{\pi/2 - \left(\phi/2 + \theta\right)}\right) \qquad B.9$$

And finally, $$V_{fluid} = V_{quadtorus} - V_{sector\ torus}\ . \qquad B.10$$

This model leads to an expression for the fluid volume contained in the pore which has the form

$$V_{fluid} = c_2 r_{pore} r_1^2 + c_3 r_1^3 \qquad B.11$$

where c_2 and c_3 are functions of θ and ϕ only:

$$c_2 = 2\pi\left[\frac{\cos\theta\cos\left(\phi/2 + \theta\right)}{\sin\phi/2} - \pi/2 + \left(\phi/2 + \theta\right)\right] \qquad B.12$$

and

$$c_3 = 2\pi\left[\left(\frac{\cos\theta}{\sin\phi/2} - \frac{2}{3}\frac{\cos(\phi/2+\theta)}{\pi/2-(\phi/2+\theta)}\right)\left(\pi/2-(\phi/2+\theta)\right)\right] - 2\pi/3\left[\left(\frac{\cos(\phi/2+\theta)}{\tan\phi/2}+\sin(\phi/2+\theta)\right)\left(\frac{\cos\theta\cos(\phi/2+\theta)}{\sin\phi/2}\right)\right] \qquad \text{B.13}$$

for which the solution [Mark's p.2-29] is

$$r_1 = \sqrt[3]{\frac{V_{fluid}}{2c_3} - \left(\frac{c_2 r_{pore}}{3c_3}\right)^3 + \sqrt{\left(\frac{V_{fluid}}{2c_3}\right)^2 - \frac{V_{fluid}}{c_3}\left(\frac{c_2 r_{pore}}{3c_3}\right)^3}} + \sqrt[3]{\frac{V_{fluid}}{2c_3} - \left(\frac{c_2 r_{pore}}{3c_3}\right)^3 - \sqrt{\left(\frac{V_{fluid}}{2c_3}\right)^2 - \frac{V_{fluid}}{c_3}\left(\frac{c_2 r_{pore}}{3c_3}\right)^3}} - \left(\frac{c_2 r_{pore}}{3c_3}\right) \qquad \text{B.14}$$

in the range where $$V_{fluid} > 4c_3\left(\frac{c_2 r_{pore}}{3c_3}\right)^3 . \qquad \text{B.15}$$

The mean curvature of the meniscus C, which determines the capillary pressure, is

$$C = \frac{-1}{r_1} + \frac{-1}{r_2} \qquad \text{B.16}$$

($C < 0$ if the centers of curvature are outside the fluid.)

where $$r_2 = r_{pore} - r_1\left(\frac{\cos\theta}{\sin\phi/2} - 1\right) . \qquad \text{B.17}$$

B.3 Dependence of the Critical Curvature on Contact Angle

We define a dimensionless curvature function and the saturation as

$$C^* = Cr_{pore} \qquad \text{B.18}$$

and $$S = \frac{V_{fluid}}{V_{pore}} \qquad \text{B.19}$$

respectively. The function $C(S,\phi,\theta,r_{pore})$ has been solved above, and the capillary pressure of the fluid in the pore is $P_c = C\sigma_{LV}$. and the pore curvature has been defined elsewhere as

$$K = \frac{-P_c}{\sigma_{LV}\cos\theta} = \frac{-C}{\cos\theta} = \frac{2}{R} \qquad \text{B.20}$$

where R is the radius of an equivalent cylindrical capillary that has the same capillary pressure with the same fluid.

By examining the the relationship between C* and S for the double-funnel pore we shall now see that the pore curvature K expresses the capillary properties of these pores in a way that is relatively independent of the contact angle θ. In the graphs that follow, values for C* and S have been calculated fro various values of r_1/r_{pore}, ϕ, and θ and the results graphed to show C* as a function of S. This has been done to circumvent the limitations of the analytic solution described in equation B.14, above.

In this graph, in figure B.3, below, the meniscus curvature is plotted as a function of fluid content for different contact angles θ in a double-funnel pore with a corner angle ϕ of 40°. At the lowest limit of saturation, the meniscus curvature tends to negative infinity. It can be shown, in fact, that $C^* \propto -S^{-1/2}$ as $S \rightarrow 0$. As the contact angle increases from zero, the magnitude of the curvature decreases (becomes closer to zero.) This is also true in a cylindrical capillary for which $P_c \propto \cos\theta$. Qualitatively, the large contact angle permits the meniscus to bridge between the walls of the pore more easily. At a zero contact angle, the meniscus must be tangent to the pore walls, but as θ increases, this constraint is relaxed.

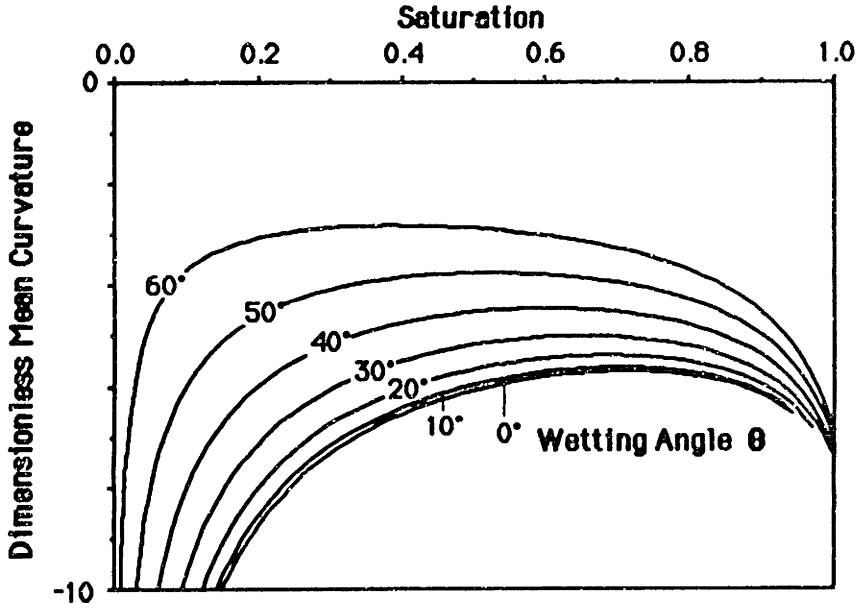

Figure B.3 Dependence of meniscus curvature on saturation and contact angle θ for a double-funnel pore with a corner angle ϕ of 40°.

In the intermediate range of saturation, the meniscus curvature is relatively constant, and passes through a maximum and begins to get more negative. The point of zero slope on each curve is a critical point at which the meniscus becomes unstable. After passing through the maximum, the meniscus begins to detach from the walls of the pore and more closely resemble a contracting bubble than a swelling fillet. This instability will be discussed in greater detail below, but for the moment, we shall examine the dependence of this critical point on the contact angle. This is shown in figure B.4, below, for values of the corner angle on the circumference of the pore, ranging from 10° to 90°. The lines on the graph terminate where the combination of corner angle and contact angle leads to a positive meniscus curvature, leading to a nonwetting condition: not relevant to this model.

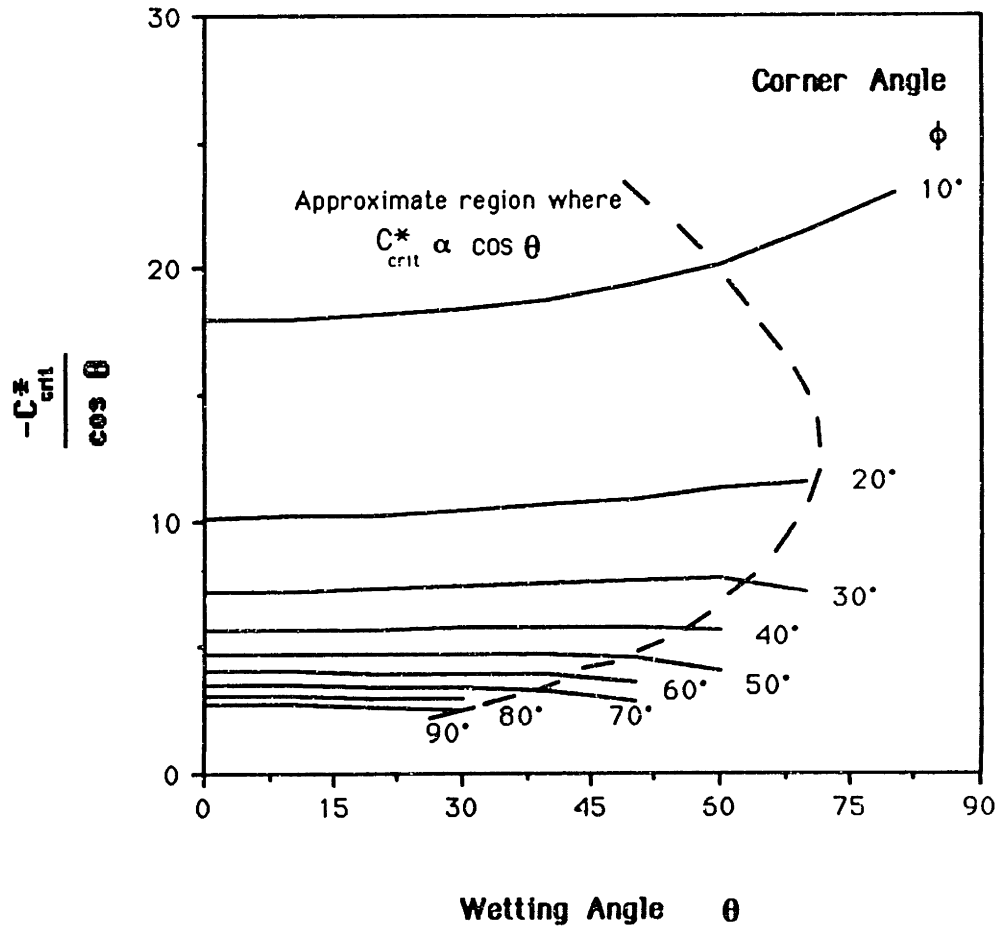

Figure B.4 Dependence of the critical value of the mean curvature on the wetting angle.

The dimensionless group $\frac{-C^*_{crit}}{\cos\theta}$ is plotted versus θ. Regions where the graph is nearly horizontal are where the meniscus curvature is proportional to cosθ. In these regions, the value of the pore curvature

$$K_{crit} = \frac{-P_c}{\sigma_{LV}\cos\theta} = \frac{-C_{crit}}{\cos\theta} \qquad \text{B.21}$$

will be independent of contact angle and surface tension, and is therefore a universal measure of the capillary property of the pore at this critical point. The empirical relation

$$K_{crit} \approx \frac{(3.5 \pm 0.2)}{r_{pore}\sin\phi} \qquad \text{B.22}$$

is correct for $20° < \phi < 60°$ and $\theta < 50°$. This covers most of the range of interest in 3-D Printing.

B.4 Pore Curvature

The double-funnel pore derived above is designed to approximate an angular cavity that might exist between five or six lamellar particles with a grain size approximately equal to $2r_{pore}$. During imbibition, the curvature in the mid range of saturation remains relatively close to the maximum value across a wide range of saturation, and this maximum value has been shown to have a strong dependence on cosθ. This dependence justifies an analogy to be made between this angular pore and a cylindrical capillary, at least in the case of imbibition. The equivalent radius of a cylindrical capillary can be defined as:

$$R_W = \frac{-2\sigma_{LV}\cos\theta_{adv}}{P_0} \qquad \text{B.23}$$

and an associated mean curvature, called the **pore curvature:**

$$K_W = \frac{2}{R_W} \qquad \text{B.24}$$

where P_0 is the limiting capillary pressure in the pore during imbibition of a fluid with surface tension σ_{LV} and advancing contact angle θ_{adv}. These two parameters are geometric properties of the porous medium and are relatively independent of the properties of the fluid used to measure them.

Measurements of the capillary pressure of powder samples during imbibition the pore curvature in powder with a grain size of 28 μm is approximately 0.4 μm^{-1}. Using the

empirical relation B.22 for pore curvature, $\phi \approx 40°$, quite a reasonable number, and supplies the reason for the choice in figure B.3.

B.5 Pore Curvature in Drainage

To develop a consistent system, it is highly desirable to obtain a relationship between pore geometry and capillary pressure for the entry of air through a gap between particles into a saturated pore. A simplified geometry is shown in figure B.5 below

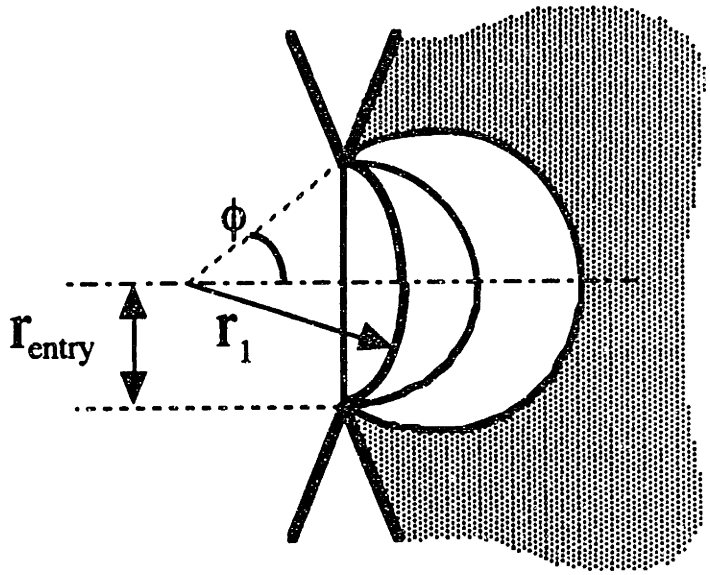

Figure B.5 The entry of a bubble through a sharp circular gap of radius r_{entry}. (Wetting fluid is assumed to be on the right)

The curvature of the meniscus is negative, implying that the pressure in the liquid on the right is lower than the pressure in the air on the left. The meniscus starts at the planar surface that bridges the gap directly. As it bows to the left, its curvature increases, passes through a maximum, and begins to decrease. It is very easy to show that the maximum curvature occurs for a hemispherical surface with radius r_{entry}.

From the geometry of the meniscus shown in figure B.5, the radius r_1 of the meniscus is given by

$$r_1 = \frac{r_{entry}}{\sin\phi} \qquad \text{B.25}$$

where ϕ is the included angle of the meniscus, shown in figure B.5. the radius of curvature is a minimum, and the pressure difference is a maximum if $\sin \phi = 1$. This occurs if the meniscus is hemispherical.

The geometry shown in figure B.5 represents a somewhat unlikely condition where the edges of a number of grains line up exactly to form an aperture. It is much more probable for the throats to pores to be formed by misaligned grains (the angular geometry of grains being assumed.) The angular edges are expected to pin the meniscus more effectively than the planar surfaces of the grains.

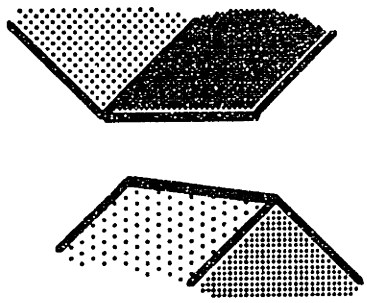

Figure B.6 The edges of two misaligned cubes.
(The solids are assumed to be lit by a diffuse light source coming from the upper right.)

A hypothetical entry pore geometry can be derived from the misaligned edges illustrated in figure B.6. Following the procedure used to transform the two-dimensional angular pore in figure B.1 to the three dimensional pore in figure B.3, these two lines are used to generate a figure of rotation about an axis through the midpoint of the line of closes approach of the two edges. This procedure generates a hyperbolic trumpet and it is hoped that this geometry approximates the geometry of the aggregate of pores that contribute to the characteristic entry pressure during drainage. This geometry is illustrated in figure B.7, below. It can reasonable be assumed that the principal radii of curvature of the hyperboloid, r_2 is approximately equal to the grain size of the powder, and r_{entry} is much smaller.

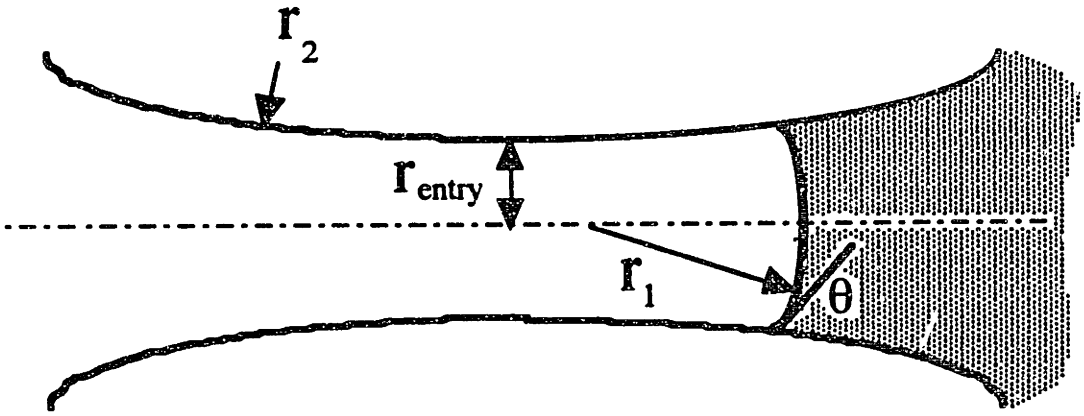

Figure B.7. Hyperboloidal entry pore showing critical meniscus at a nonzero contact angle.

This pore resembles a cylindrical capillary more closely than that shown in figure B.5. Although both these geometries are somewhat arbitrary and approximate, for flat grains that pack closely, it seems likely that many of the entry pores will be long and tapered, yielding an approximate dependence of the entry pressure on $\cos\theta$.

In Figure B.2, the pore was drawn with a small mouth to allow the air displaced by the imbibed fluid to leave. This mouth must also be the entry point for air that enters the pore when fluid is drained. This gap is also the hole through which mercury would enter in mercury porosimetry. It is unclear whether this argument provides sufficient justification to use a cylindrical capillary as an analog for a porous material during drainage. Since this is the convention, however, we shall assume that if the entry pressure of a pore is P_B after the "bubble pressure" in [Bear, 451-452]that defines a characteristic radius

$$R_{NW} = \frac{-2\sigma_{LV}\cos\theta_{rec}}{P_B} \qquad \text{B.26}$$

and corresponding pore curvature

$$K_{NW} = \frac{2}{R_{NW}} \qquad \text{B.27}$$

for the drainage of a wetting fluid from a pore. For the infiltration of a nonwetting fluid, one must substitute the advancing contact angle for the nonwetting fluid.

B.6 Conclusion

A model for the imbibition of a wetting fluid into an angular pore has been developed, and the solution for the capillary pressure as a function of saturation shows that there is a characteristic critical pressure for these pores that exhibits a strong dependence on the cosine of the contact angle of the fluid to the medium. This dependence justifies the analogy between the capillary pressure of an angular pore and a cylindrical capillary during imbibition. The analogy for drainage is more qualitative, but there are still reasons for preserving it.

The analogy between an angular pore and a cylindrical capillary permits one to derive a characteristic pore curvature:

$$K = \frac{-P_c}{\sigma_{LV} \cos\theta} \qquad \text{B.28}$$

that describes the capillary properties independent of the fluid, and permits measurements made with one fluid to be compared with measurements made with another fluid. The analogy is only approximate, and as yet only applies to a single pore. In the following appendix, the analogy will be extended to a network of pores with a distribution of sizes, and it will be shown that a porous material possesses two critical pore curvatures, K_W and K_{NW}, which determine, in large part, the capillary properties of the material in a way that is relatively independent of the nature of the fluid under consideration.

Appendix C. Meniscus Instability in Networks of Ink-Bottle Pores

C.0 Introduction

In the preceding appendix, a geometric model for an ink-bottle pore was developed, and it was shown that there existed a critical meniscus curvature during imbibition. When the saturation was below this critical point, the curvature approached zero from a large negative value. At the critical point, the curvature passed through an extreme value, and began to become more negative with increasing saturation. Qualitatively, this critical point corresponded to the point at which the meniscus ceased to behave like a swelling fillet in the corner of the pore, and began to behave like a contracting bubble in the center of the pore.

A dependence of this critical curvature on the contact angle justified the derivation of a characteristic pore curvature K_W that was a geometric property of the pore, but independent of the fluid saturating it. A similar critical value, K_{NW}, corresponding to drainage, was derived, on more qualitative grounds.

C.1 Qualitative Representation of an Ink-Bottle Pore

The behavior of the capillarity of the double-funnel pore is characteristic of a pore called an "ink-bottle" pore in the literature, e.g. [Bear, 447]. The cross section of an idealized ink bottle is shown in figure C.1 below. Gravity can be ignored in this picture because the pore under consideration are on the order of the grain size of the powder. The disposition of the fluid in the bottle is therefore determined by the contact angle between the liquid and the solid and the need to minimize the liquid/vapor interfacial area. In the more general case, the fluid is not fully wetting to the pore, so the liquid contacts the solid surface with a contact angle of θ at a line that divides wet surface from dry surface.

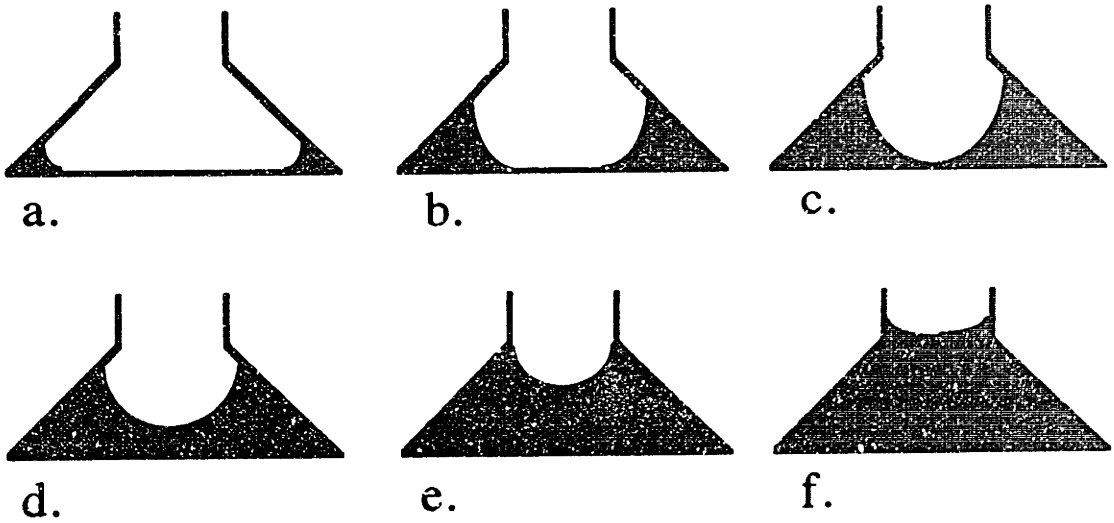

Figure C.1 Progressive stages of filling of an "ink-bottle" pore.
(a),(b): Stage I filling; (c),(d),(e): Stage II filling; (f): Stage I filling.

In this figure, fluid is added to the pore in progressively. In part (a) the fluid meniscus is confined to a fillet in the lower corner of the bottle. As more fluid is added from (a) to (b) the meniscus moves further from the angular corner, with the result that its mean curvature decreases. In (c), the meniscus detaches from the floor of the bottle and takes on the character of a bubble. From (c) through (d) to (e), addition of fluid causes its surface to become more tightly curved as the confining wall of the bubble converges. Finally, the bubble exits through the neck of the bottle, and the meniscus flattens out from (e) through (f).

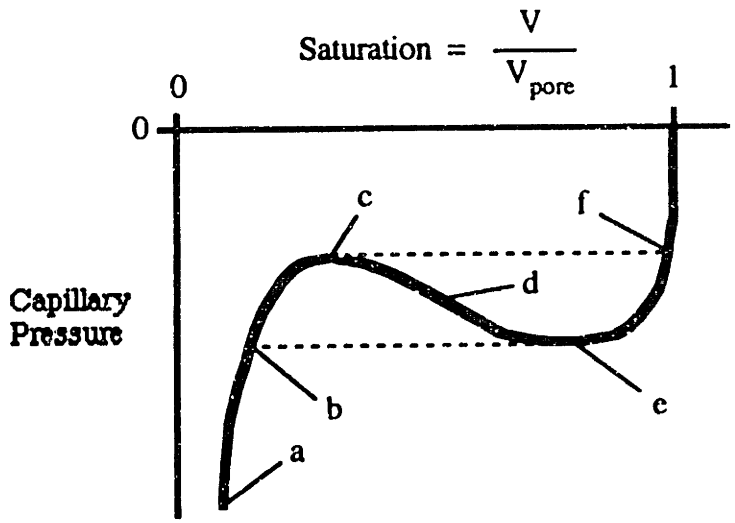

Figure C.2. Meniscus curvature vs. saturation for the ink-bottle shown in Fig. C.1.

In figure C.2, above, the capillary pressure of the fluid in the bottle is plotted empirically as a function of the fraction it is filled. At the lower end of the curve, between (a) and (d), the capillary pressure behaves similarly to the curvature derived for the double-funnel pore in figure B.3 above. Beyond that point, the capillary pressure must remain continuous for a single pore, and it must approach zero for a fully saturated pore. This restrict the remainder of the curve to a path similar to that shown from (d) to (f). By inspection of figure C.1, it can be seen intuitively that the meniscus converges as it approaches the neck of the bottle, and then flattens out as it passes out through the neck.

[Shaw, T.] has distinguished two stages of filling of the pores in a porous network by a wetting liquid ($\theta < \pi/2$). Shaw developed a geometric model of a porous network based on a hexagonal array of circular particles in two dimensions. As fluid is added to an isolated pore, the early stages of filling are characterized by a steady decrease in the capillary pressure. In other words,

$$\frac{d^2G_s}{dV^2} = \frac{dP_c}{dV} \geq 0 \qquad \text{for stage I filling.} \qquad \text{C.1}$$

In later stages of filling, the menisci begin to converge upon each other, and the peculiar situation where the capillary pressure becomes stronger (i.e. becomes more negative) with increases in the fluid content. Thus, the free energy passes through an inflection point at some critical level of saturation and

$$\frac{d^2G_s}{dV^2} = \frac{dP_c}{dV} < 0 \qquad \text{for stage II filling.} \qquad \text{C.2}$$

E_T is the total energy of the system, here defined as the surface energies of the phases in contact in the system. Although Shaw derived his analytic results for two-dimensional networks, this behavior has been amply demonstrated in Appendix B for three-dimensional geometries. For a discussion of the connection between surface energy, capillary pressure, and meniscus curvature, see Appendix A, especially section A.7.

C.2 Geometric Instability of the Meniscus During Stage II Filling

The second derivative of the energy defines the stability of a system at equilibrium with its surroundings. This implies that the pressure and temperature are fixed by ambient conditions. The ink-bottle pore illustrated in figure C.1. is stable for all fluid contents if it is an isolated system, but it is unstable if it is placed in contact with a fluid supply at

ambient pressure in a range of saturation characterized by equation C.2. This is understood easily by the thought experiment illustrated by figure C.3, below.

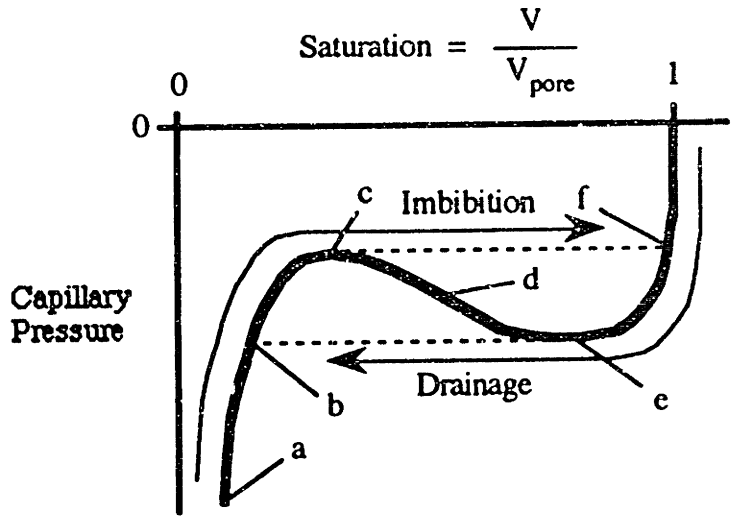

Figure C.3 Hysteresis in capillary pressure due to meniscus instability.

Imagine that the ink-bottle in figure C.1 is connected to a reservoir of liquid at a pressure that we control. If the fluid pressure starts out at a large, negative pressure, the bottle will start with only a small quantity of fluid in it. As the pressure of the fluid is raised by a small amount, a small amount of liquid flows into the bottle until the capillary pressure in the bottle increases to the same pressure. As the pressure is raised further, from (a) to (b) and approaching (c) in figure C.2, the pore will gradually imbibe fluid and gradually increase in pressure along with the reservoir. At the saturation passes the critical point at point (c) a further increase in the quantity of fluid contained in the pore results in a **decrease** in the fluid pressure in the pore. This makes the fluid flow in faster. As more fluid enters, the pressure decreases still further, causing more fluid to enter. This continues until the bottle is nearly full, at point (f) where the pressure in the pore once again equals the pressure of the supply. This is called a **Haines jump** [Greenkorn 122.]

Starting from a full bottle at zero capillary pressure, we can drain fluid by lowering the pressure of the reservoir. The fluid drains gradually, with the meniscus trapped by the angle of the lip, and the pressure becoming more negative until point (e) is reached. If fluid is drained past this point, fluid leaving the bottle causes the pressure in the bottle to increase, causing more fluid to be squirted out into the reservoir. This continues spontaneously until the point (b) is reached where the liquid fillet has a curvature equal to the curvature of the bubble at the point of instability.

This catastrophic collapse of the fluid meniscus leads to the hysteresis shown in figure C.3 as the saturation is cycled between points (b) and (f). This collapse is irreversible, sudden, and involves the transfer of a substantial fraction of the fluid in the pore at a pressure determined by either of the two critical points in the capillary pressure curve. These are the points used to derive the critical pore curvatures K_W and K_{NW} in Appendix B.

C.3 Behavior of a Network of Ink-Bottle Pores

Porous bodies are made up of an ensemble of pores connected together in a network. The significance of the network is that is pore "A" is connected to pore "B" and not pore "C" ; and "B" is connected to both "A" and "C", then fluid must flow from "A" through "B" in order to get to "C"; unless there is another pore "D" also connected to both "A" and "C" through which the fluid can flow more easily. All this may sound rather trivial, but the constraints to fluid flow imposed by a network structure are not admitted by an equilibrium.

Consider a network of identical, connected ink-bottle pores. If we assume that all the pores can communicate with one another, then the fluid in the body can come to a form of equilibrium. Fluid is added in increments from a point source and the pressure is not controlled. Starting with a dry network, the first increment of fluid enriches the pore that is directly under the point of addition with respect to the others. With Stage I filling, that slight enrichment causes the local pressure to be higher than the surroundings, so some of the fluid will flow outward to the other pores until the network is at a uniform pressure. P_C. Note that since the capillary pressure is defined by the meniscus curvature, it is defined locally, on a scale very much smaller than the pore size of the material.

The fluid spreads outward from the point of addition uniformly as long as all of the pores are in a state defined by equation C.1. As the capillary pressure reaches the critical point defined by K_W for the (identical) pores, the pressure ceases to increase with further addition of fluid. Instead, the pore at the point of addition is enriched past the point of stability. As a result, the local capillary pressure decreases with the fluid addition. This decrease draws fluid inward from the surrounding pores until the pore has filled to the saturation defined by point (f) in figure C.3.

If the critical saturation is S* during imbibition, then before the first pore collapses, all of the pores have a saturation slightly below S*. If the first pore then collapses to a saturation of unity and there are N_{pore} pores in the network, then the transformation in the network is illustrated by the diagram in figure C.4.

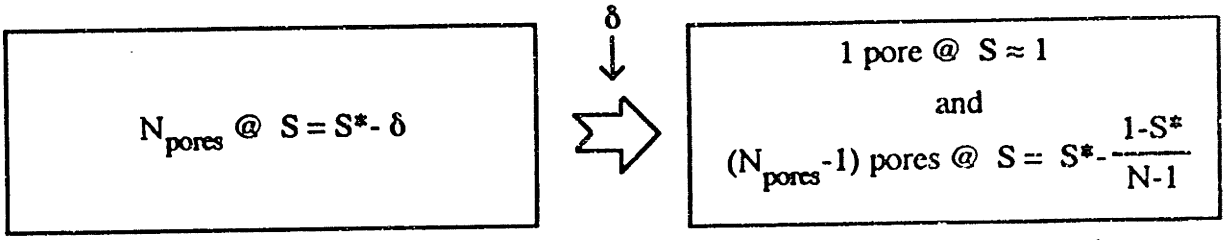

Figure C.4 State of saturation before and after first pore collapse in a network.

After the first pore collapses, the capillary pressure falls slightly below the critical point, so further addition of fluid spreads outward until the critical pressure is obtained once again. After a number of pores have collapsed, the remaining uncollapsed pores supply fluid to each subsequently collapsing pore. It is assumed that after collapse, the slope of the capillary pressure curve is relatively steep.

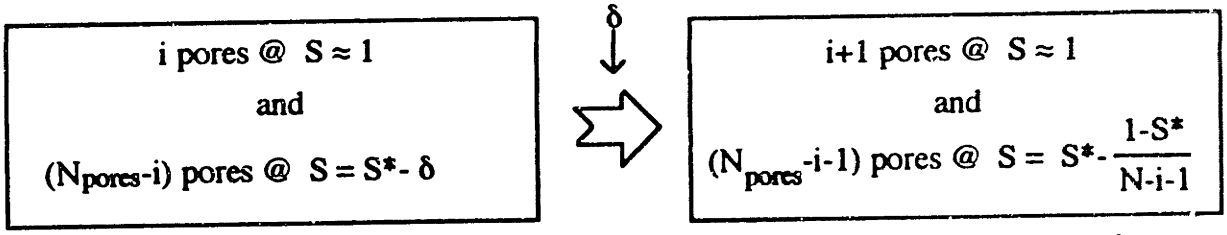

Figure C.5 State of saturation before and after the i-th pore collapse in a network.

The magnitude of the drop in capillary pressure with each pore collapse depends on the number of pores remaining and the curvature of the capillary pressure curve in the vicinity of point (c) on the capillary pressure curve (Figure C.3). If there are many, many pores in the network, then the decrease in saturation of the uncollapsed pores will be negligible and the capillary pressure will remain constant. The change in pressure is in any case second order with respect to the change in saturation. This critical pressure for the network is equal to the critical pressure of the individual pores, and is called the **dry suction pressure**, defined as P_0. The reason for calling P_0 the dry suction pressure will be explained in detail in section C.4 below.

If the same body is drained from the fully saturated state, the same type of instability is obtained, and the capillary pressure remains nearly constant at the critical

pressure for the pores in drainage. This critical pressure is called the **bubble pressure**, P_B.

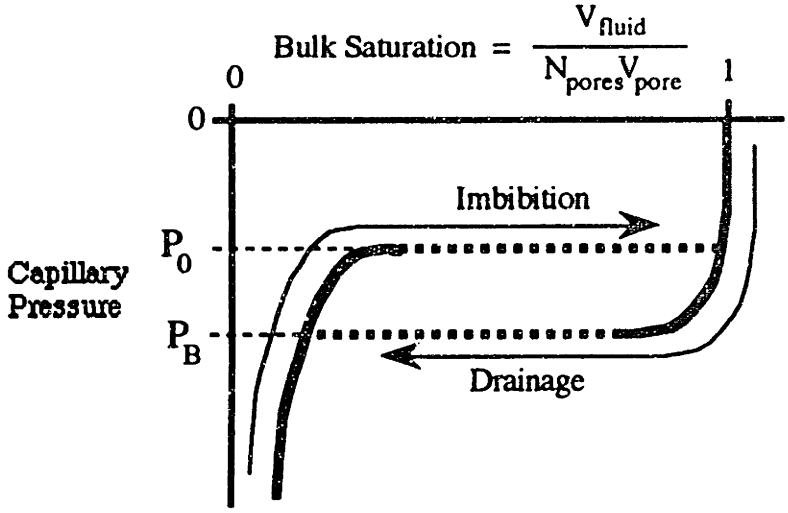

Figure C.6. Capillary pressure as a function of saturation in a bulk porous sample containing a large number N_{pores} of ink-bottle pores with critical pressures P_0 and P_B.

Hysteresis curves of this sort are given by [Barrier, McKenzie,& Reay.]

Following the analogy developed earlier to represent the capillary pressure of a porous material in terms of pore curvatures, the two critical curvatures are here defined for a bulk porous medium:

$$K_W = \frac{-P_0}{\sigma_{LV}\cos\theta_{adv}} \quad \text{for imbibition;} \qquad \text{C.3}$$

and

$$K_{NW} = \frac{-P_B}{\sigma_{LV}\cos\theta_{rec}} \quad \text{for drainage;} \qquad \text{C.4}$$

which are geometric properties of the medium, relatively independent of the properties of the fluid saturating it. There are corresponding radii, defined below:

$$R_W = \frac{2}{K_W} \qquad \text{C.5}$$

$$R_{NW} = \frac{2}{K_{NW}} \qquad \text{C.6}$$

R_W is the larger of the two radii and is determined by the pressure during imbibition at which the bubble inside the pore begins to collapse. If the pore were perfectly spherical

its radius would equal R_W. More generally, it corresponds to the surface of minimum constant curvature that can exist inside the pore. The smaller radius is determined by the pressure required to force air into the pore, and corresponds to the radius of the largest gap through which air can enter the pore. This gap must necessarily be smaller than the upper radius, since this is the radius of the pore itself. The only geometry for which these two radii are equal is a cylindrical pore. This may be found in certain structures, but generally not in the porous powder beds that are used in 3-D printing. In an array of geometrically similar pores, some of which are saturated, the unsaturated ones will be incapable of draining the saturated ones. This is a direct consequence of the irreversibility of the system. In a body containing a distribution of pores, pores that have R_W smaller than the R_{NW} of another pore will be capable of draining it.

C.4 Network Properties of the Medium

C.4.1 Distinction Between Pores and Ducts

The pore mouth shown in Figure C.1 is arbitrary size: it could possibly have a radius larger than the critical radius for imbibition. If this is true, then the structure exhibits no instability during imbibition or drainage. One could call such a structure a **duct** to distinguish it from a **pore**, which exhibits at least one local maximum in its capillary pressure/saturation curve. A duct must necessarily fill from the tightest corner to the largest hole. The space in a duct cannot widen forever: once the meniscus leaves through the mouth of a duct, before too long it will encounter a particle that blocks the divergence of the duct; and it will arrive at a situation where the meniscus begins to close up. Therefore, every duct that does not reside on the surface of the porous body must actually comprise a portion of a pore.

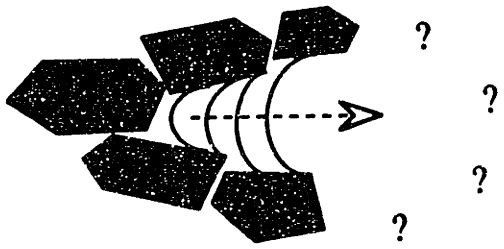

Figure C.7 Ducts cannot diverge forever unless they intersect the surface of the body of porous material. Here, the meniscus propagates from right to left during imbibition, but the meniscus must eventually encounter a blockage or else leave the surface of the porous body. Blockages of diverging ducts cause the meniscus to converge and initiates Phase II filling: causing the meniscus to cease behaving like a swelling fillet, and begin behaving like a collapsing bubble.

Pores can be thought of as collections of ducts that converge. The ducts do not collapse catastrophically when they fill individually and this characterizes Stage I filling, but the pore traps a bubble that collapses when the menisci from the various ducts converge and intersect with one another. The critical point of meniscus collapse defines the point at which the ducts communicate with one another across a given pore. This leads to the assertion that **fluid is not freely communicated from one side of a pore to the other until the pore has passed its critical saturation.** This assertion can hold only in systems where the fluid is not volatile.

The only geometry that is comprised entirely of ducts is a body containing only straight or uniformly tapered capillaries. For this body, $K_W = K_{NW} = K$. Capillaries of a given radius fill or drain entirely at a pressure $P_C = -K\sigma_{LV}\cos\theta$. There is no critical saturation. Imbibition and drainage are both completely reversible for a cylindrical capillary.

C.4.2 Consequence of the Assertion

If fluid cannot communicate between pores that are not fully saturated, then fluid will stay localized until the capillary pressure reaches the critical pressure for the medium. At that point, the fluid will percolate throughout the body, and pores will fill one by one until the body is completely saturated. Individual pores will only fill if two conditions are met: First, that the capillary pressure exceeds the critical value P_0 for that pore; Second, that there exists a trail of saturated pores leading back to the fluid reservoir.

In a body with pores that are distributed in size, fluid will remain localized until a percolating network of pores become saturated. This network is the collection of smallest pores that form a continuous trail across the body. [Lenormand] calls this type of fluid flow **invasion percolation**. The fractal geometry of invasion percolation is amply discussed by Sapoval, Rosso, and Gouyet in [Avnir p. 232 ff] and by Feder et. al. in [Pietronero, p. 307 ff]. The transition from a nonpercolating to a percolating network is a sudden one, even when the pore sizes are broadly distributed. If this property is accepted for a general porous body, then no fluid will be communicated below the critical pressure P0 for the percolating network of pores. The porous body below this pressure will act like an impermeable block.

If fluid is fed from a source to a dry porous body, then the suction pressure that the body will exert will initially be the critical pressure for the percolating network: not higher suction can be transmitted by the medium. For this reason, the critical pressure P_0 is called the dry suction pressure of the medium.

The situation for drainage is similar: air cannot infiltrate deeply into a saturated porous medium until its pressure reaches the critical bubble pressure for the collection of largest pores that form a percolating network. The critical pressure for drainage P_B is called the bubble pressure because that is the pressure at which bubbles of air can be forced through a saturated sample.

The two percolating networks: one composed of the population of pores with the smallest R_W, and one composed of the population of pores with the largest R_{NW}, will generally not contain any of the same pores. It is likely that, given a broad pore size distribution, R_W will be smaller than R_{NW} for the network, even though R_W is strictly larger than R_{NW} for a single pore. The processes of imbibition and drainage cannot occur simultaneously in the same portion of material, so the two networks cannot interfere. It is possible, though, that a region of dry material will be in contact with another region of saturated material. If R_W of the dry network is less than R_{NW} of the saturated network, fluid can spontaneously migrate into into the dry network. This forms the basis of a model for feature formation, developed in Section 6.3.

C.4.3 Pathology in Pore-Size Distribution

Since pores are characterized by two radii, one which is meaningful during imbibition and the other during drainage, the distribution of pore sizes will be different depending on which operation is being performed.

If we imagine that all the pores in a porous body possess geometric similarity, then the first pores to be filled during imbibition will also be the last ones to drain during drainage. In general this would not be the case, and an extreme example could be found in a bed composed of spherical agglomerates of fine powders that are hollow. Structures of this sort are encountered in spray-dried powders. This bed will contain two types of pores: ones between agglomerates, with both characteristic radii relatively close together, and others in the centers of agglomerates, large, but only accessible through the fine pores at the surfaces of the agglomerates. This geometry is illustrated below.

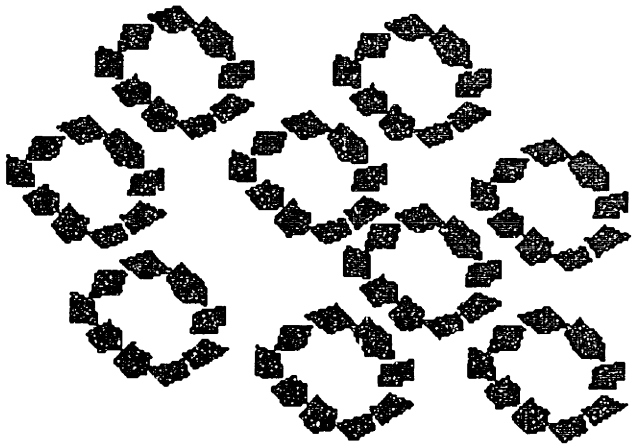

Figure C.8 Pore geometry possible with spray-dried powder with two types of pores: one population for which $R_W \approx R_{NW}$ and another for which $R_W >> R_{NW}$.

If the pores between the agglomerates were smaller than the pores within the agglomerates, those pores will be the first to fill. Since the entry holes to them are much larger than the entry holes into the agglomerates, these pores would also be the first to drain. If we assume that capillary equilibrium exists throughout a porous body and the fluid is completely wetting, then pores will fill in increasing order of R_W, and drain in decreasing order of R_{NW}. It is highly possible that the centers of the agglomerates may never fill. The air contained within them will be trapped when the pores surrounding the agglomerates. Once filled, however, these pores are unlikely ever to drain.

C.5 Conclusion

This appendix has treated the energetics of capillary migration of fluids in a porous medium. From this examination, a number of conclusions have been drawn that may be used as theorems upon which to base a theory for the capillary migration in the special situation of feature formation during 3-D Printing.

1. Capillary pressure P_c is defined as dG/dV and is uniform across a feature at equilibrium.
2. **Pores** are structures in the porous medium for which $d^2G/dV^2 < 0$ for some range of saturation. These structures fill catastrophically at a critical pressure if fluid is supplied at a controlled pressure.

3. The irreversibility causes hysteresis in the pressure/saturation curve between imbibition and drainage.
4. The hysteresis defines two characteristic radii, R_W and R_{NW} or similarly two curvatures K_W and K_{NW} that correspond to the critical values of capillary pressure at the points of instability during imbibition and drainage.
5. R_W is larger than R_{NW} in a given pore. If this is not true, then both R_W and R_{NW} are undefined and there is no hysteresis. Structures that do not exhibit hysteresis may be called **ducts** to distinguish them from pores.
6. During imbibition, available pores are filled in increasing order of R_W.
7. Pores drain in decreasing order of R_{NW}.
8. There exists strong empirical evidence that pore curvature K is defined only by the geometry of the pore and is largely independent of the surface tension and contact angle of the fluid saturating the pore.

9. Fluid is not easily communicated across a pore that is below its critical saturation. This saturation very likely defines the irreducible saturation S_{W0} for a given pore.

Appendix D. The Physics of Our Printhead

D.0 Introduction

What follows are a collection of derivations of various aspects of printhead physics which have been useful at various times throughout the duration of the project. They are not meant to be a complete theoretical development of continuous-jet printing, but they are intended as tools for future workers to use in such development.

D.1. Approach to the Orifice

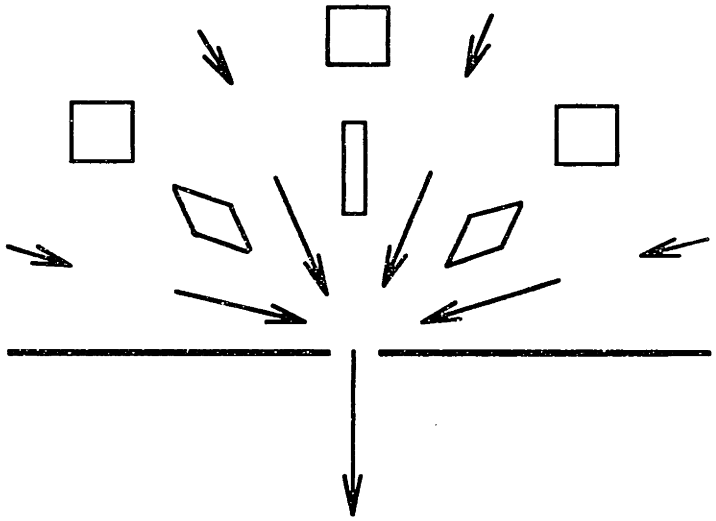

Figure D.1. Extensional flow in the approach to the orifice.

During the approach of the fluid to the orifice in the fractions of a second before being incorporated into the jet, the fluid undergoes a large, transient deformation. Assuming the volumetric flow rate is Q, the fluid velocity is given by:-

$$\vec{v} = v_r \hat{r} \quad ; \quad v_r = \frac{-Q}{2\pi r^2} \qquad \text{D.1, D.2}$$

This flow is a type that is called **extensional** in the literature [Boger & Waters, 6-7] Looking at the strain rate in the vicinity of the nozzle axis,

$$v_x = \frac{v_r x}{r} \quad ; \quad \frac{dv_x}{dx} = \frac{-Q}{2\pi r^3} \qquad \text{D.3, D.4}$$

$$v_y = \frac{v_r y}{r} \quad ; \quad \frac{dv_y}{dy} = \frac{-Q}{2\pi r^3} \qquad \text{D.5, D.6}$$

$$v_z = v_r \quad ; \quad \frac{dv_z}{dz} = \frac{Q}{\pi r^3} \qquad \text{D.7, D.8}$$

[Petrie 26-41] gives the strain rate in extensional flows as

$$e = \begin{vmatrix} \dot{\gamma} & 0 & 0 \\ 0 & -\dot{\gamma}/2 & 0 \\ 0 & 0 & -\dot{\gamma}/2 \end{vmatrix} \qquad \text{D.9}$$

and the stress in the fluid is given by

$$\sigma_{zz} - \sigma_{xx} = \sigma_{zz} - \sigma_{yy} = \dot{\gamma}\eta_T \qquad \text{D.10}$$

where η_T is the Trouton viscosity. For Newtonian fluids, $\eta_T = 3\eta$.

So the strain rate, $\dot{\gamma}$ which can be used in the calculation of orthokinetic coagulation, is

$$\dot{\gamma} = \frac{Q}{\pi r^3}. \qquad \text{D.11}$$

A normal flow rate for a 50 μm nozzle is Q = 20 mm^3/sec. At a distance of 50 μm from the orifice, conventional nickel orifice plates have rounded corners, so this redirects the flow downward.. At this point, the strain rate is $\dot{\gamma} \approx 5 \times 10^4$ sec^{-1}. If the orifice has a sharp rim, the flow must converge all the way to the rim, and so $\dot{\gamma} \approx 2 \times 10^5$ sec^{-1} at the rim. The total strain in a volume of liquid in approaching the orifice is a measure of the degree of shock to the colloid. We must assume finite limits of integration, otherwise the stain is infinite:

$$\gamma = \left| \int \dot{\gamma}\, dt \right| \approx \left| \int_{50\mu m}^{1mm} \frac{\dot{\gamma}\, dr}{v_r} \right| = \int_{50\mu m}^{1mm} \frac{2\, dr}{r} = 2\ln(20) = 5.99 \qquad \text{D.9}$$

and for an inner radius of 25 μm, the strain is 7.38. Compare this to the strain that occurs in a tube:

$$\bar{\dot{\gamma}} = \frac{8\bar{v}}{3r_{tube}}. \qquad 2.39$$

where for a tube of 0.5 mm inside radius 2 cm in length, the mean strain is 107. Therefore, the degradation that might occur in the shear zone near the orifice is 15 times less than what occurs in the nozzle body approaching the orifice. Since the fluid system consists of several meters of tubing, the strain at the orifice is negligible, assuming that the fluid is newtonian and there are no unexpected effects at high strain rate. One effect is discussed by Van de Ven: at high strain rates, the ionic atmospheres of the charged colloidal particles can be stripped away, increasing the likelihood that particle interactions will lead to merging. The Peclet number is the ratio between strain rate and diffusion rate:

$$Pe = \frac{\dot{\gamma}a^2}{D} \qquad \text{D.10}$$

the diffusivity of electrolytes in water is on the order of 10^{-5} cm^2/sec [Hunter 60] and if particles are 50 nm in radius, a strain rate of 4×10^5 sec^{-1} is required to strip the ion atmospheres from the particles. For colloidal silica, the particles have high stability because of adsorbed water, so stability is virtually guaranteed.

D.2 Action of the Resonator

Diconix (now part of Kodak) designed a stainless steel block that feeds fluid to a nickel orifice plate glued to one face. The block carries several PZT elements, two which stimulate the block to oscill..te, and one that is used to monitor the amplitude. The block oscillates in a fundamental extension mode, with the longest axis of the block corresponding to one-half of the wavelength of sound at the resonant frequency. (See fig. D.2.)

The vertical motion of the orifice plate stimulates the jet to break up into uniform droplets. This subject is reviewed quite satisfactorally in section 5.2.1 of Paul Williams' thesis. For an inviscid jet, the breakoff length is given by:

$$\frac{z_{bo}}{d_0} = 1.03\sqrt{We}\ \ln\left(\frac{d_0}{2\delta}\right) \qquad \text{D.11}$$

where z_{bo} = breakoff length,

d_O = jet diameter = orifice diameter

δ = amplitude of disturbance on jet surface $\approx \frac{\pi d_0 A f}{2u}$

f = resonator frequency

A = amplitude of resonator vibrations (distance)

u = jet velocity

We = Weber number = $\frac{\rho u^2 d_0}{\sigma_{LV}}$.

ρ = fluid density

σ_{LV} = fluid surface tension.

To estimate δ from the amplitude of the resonator motion, consider a volume ΔV that passes through the orifice in a time increment Δt. If the orifice plate is stationary, this volume element will have a cross sectional area $\Delta V/u\Delta t = \pi d_o^2/4$. If the orifice plate moves downward due to its vibration when ΔV is emitted, then the cross sectional area will be $\Delta V/(u-v)\Delta t$; slightly greater than in the stationary case (See Figure D.3). The difference in cross sectional areas between the stationary case and the moving case will be $\pi d_o^2/4$ ((u/(u-v)) -1) which is approximately equal (for v << u) to $\pi d_o^2 v/4u$. Since this change in area is added to a cylinder with diameter d_O, this quantity must be equal to $\pi d_o \delta$. Thus, $\delta = d_o v/4u$. All that remains is to estimate v from A, the resonator

amplitude. Since the resonator oscillates according to $X = A \sin (2\pi f t)$ the velocity goes as $2\pi f A \cos (2\pi f t)$. The maximum velocity is therefore $v = 2\pi f A$. (Note that amplitude is defined as one-half the peak-to-peak distance)

For a 50μm jet to break up in 3 mm, using relevant parameters for the machine, $\delta \sim 400$ Å and $A \sim 600$Å. This is really only an order of magnitude calculation, because small changes in surface tension or density can drastically alter the breakoff length.

The Diconix resonators are very efficient, and achieving a breakoff length of 3 mm is no problem. They do not, in general, create satellite drops unless the stimulation is too low or too high.

Sketch of Diconix Resonator

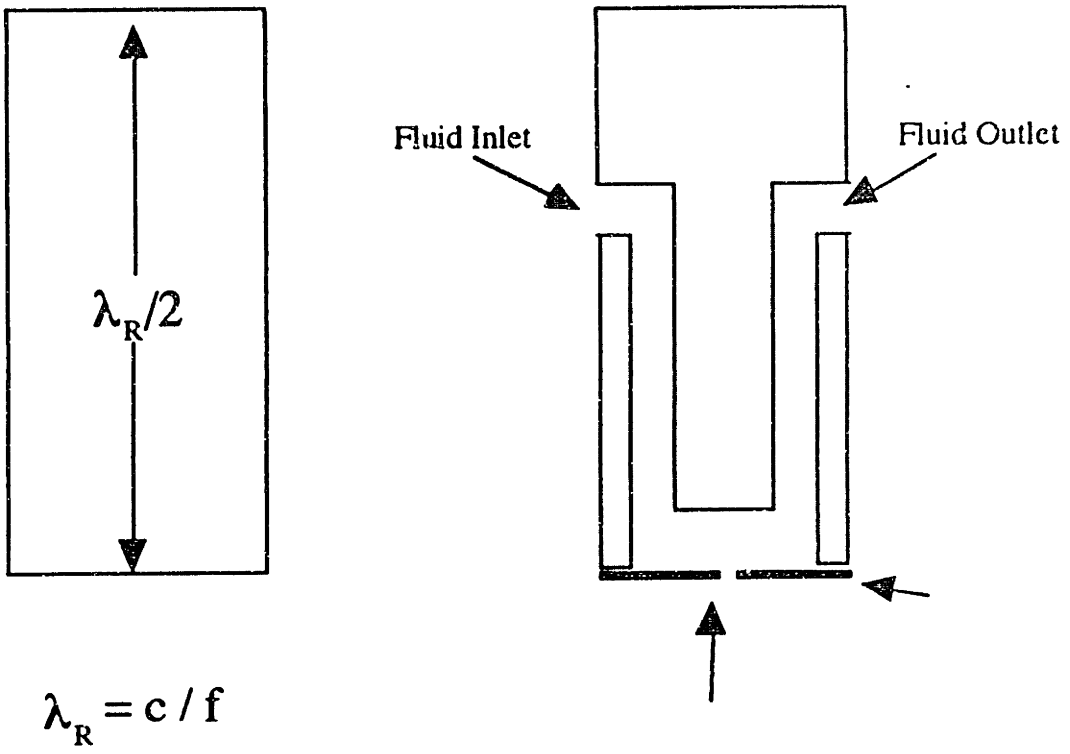

$$\lambda_R = c / f$$

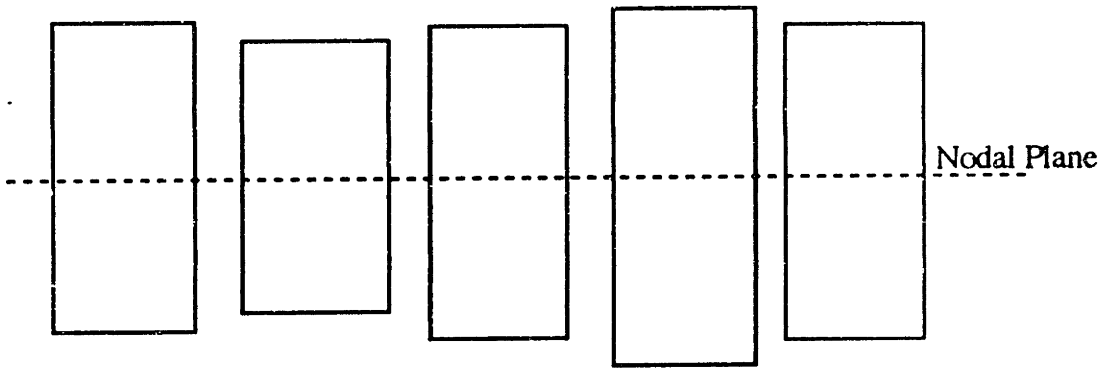

Figure D.2 Diagram of the Resonator.

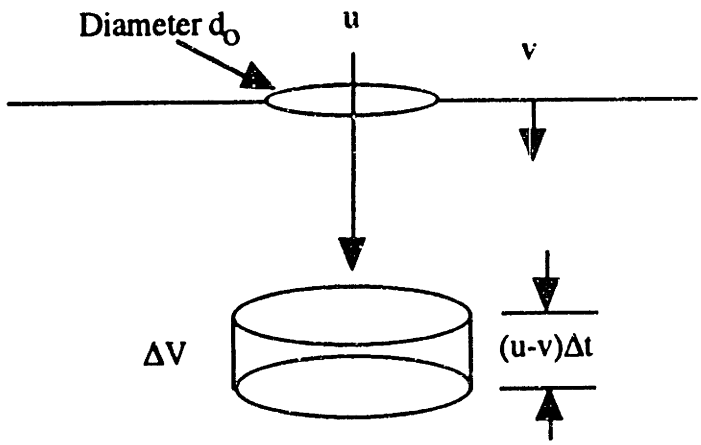

Figure D.3. Derivation of Jet Disturbance.

D.3 Flow through the Orifice

In the preceding derivation, the jet velocity u was assumed known. In actuality, all that is known is the mass-flow rate m' and possibly the time-of-flight between the breakoff point and the powder bed (See Jill Milner's thesis).

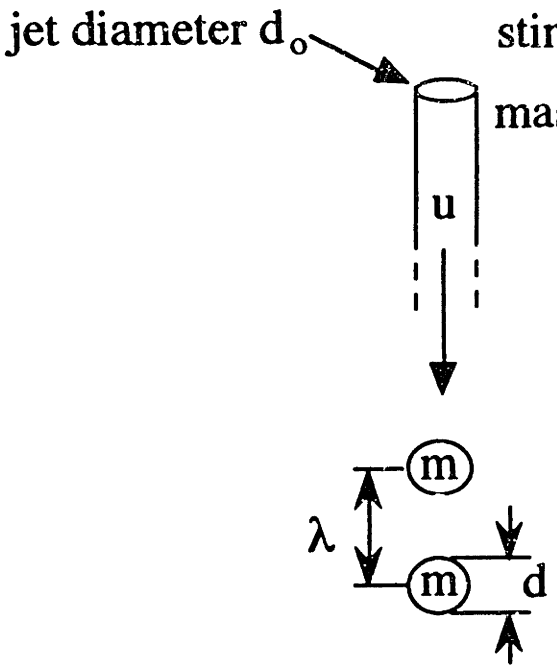

$$u = \frac{4\,m'}{\pi d_0^2 \rho} \qquad \text{D.12}$$

$$\lambda = \frac{u}{f} \qquad \text{D.13}$$

$$m = \frac{m'}{f} \qquad \text{D.14}$$

$$d = \left(\frac{6\,m'}{\pi \rho\, f}\right)^{1/3} \qquad \text{D.15}$$

Figure D.4 Derivation of u, λ, m, and d as a function of input parameters m', d_O, ρ, and f.

D.4. The Charging Cell

In order for the computer to control the jet, the droplets must be charged electrostatically. Since the jet is continuous from the nozzle up to breakoff point, it is in electrical contact with the printhead. Below the point at which the jet breaks up, the droplets are isolated from one another. Thus, any charge that exists on a droplet at the instant of breakoff is carried with it all the way down to the powder bed. The electrode configuration that we use essentially forms a capacitor with the jet itself constituting one of the "plates". In our setup, the jet is grounded, and the charging cell has a positive voltage applied to it. This induces a negative charge in the jet.

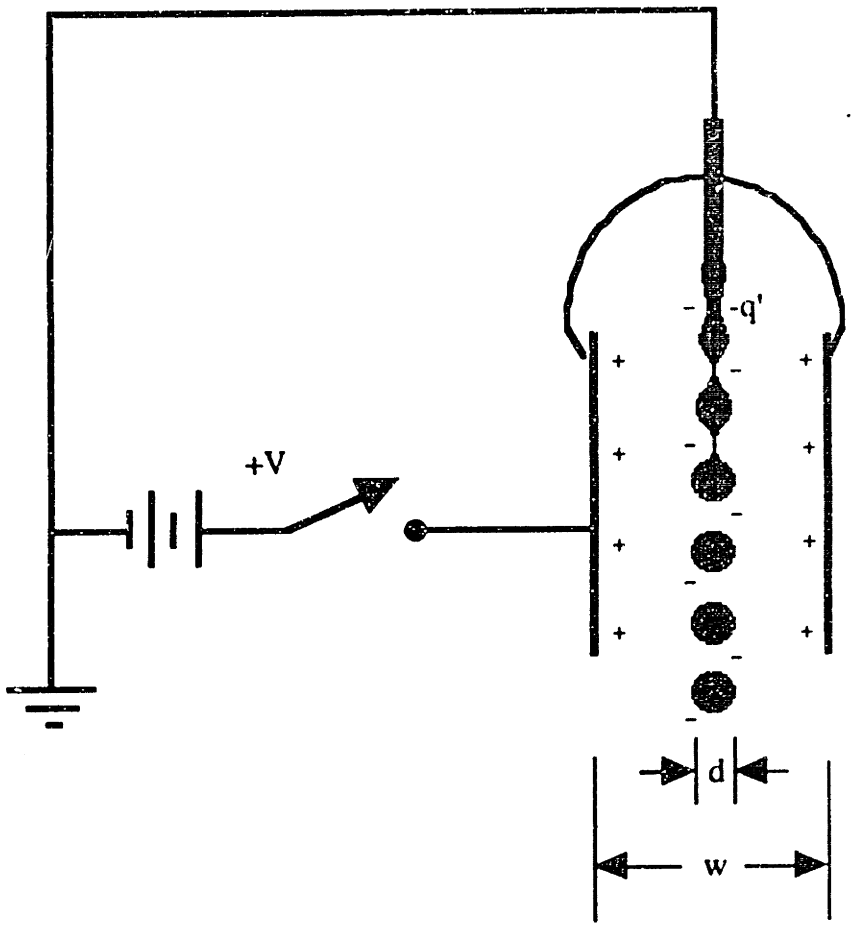

Figure D.5 Schematic of the charging cell.

D.4.1 Capacitance of Centered Jet in a Cylindrical Cell

The jet can be assumed to be a continuous line of charge, and so it makes sense to derive a capacitance per unit length of the jet. The electric field around a line of charge is derived in every textbook on electrostatics:

$$E = \frac{q'}{2\pi\varepsilon_0 r} \qquad \text{D.16}$$

Where q' = charge per unit length

ε_0 = 8.84 pF/m (Permittivity of free space)

r = distance from line.

The capacitance per unit length $C' = q'/V$. The potential difference between the jet and the plates can be found by integrating the electric field strength from the surface of the jet

to the electrode. For a cylindrical charging cell, this follows directly from the above expression:

$$V_{12} = \frac{q'}{2\pi\varepsilon_0} \ln\left(\frac{r_2}{r_1}\right) \qquad \text{D.17}$$

where r_2 = the radius of the cylindrical charging cell.

r_1 is chosen to be the radius of the droplets at breakoff = d/2

If the above figure were a section of a cylindrical charging cell,

$$C' = \frac{2\pi\varepsilon_0}{\ln\left(w/d\right)} \qquad \text{D.18}$$

D.4.2 Capacitance of Centered Jet in Parallel-Plate Cell

The capacitance of a charging cell with two parallel plates is not very much different from the cylindrical case. It can be calculated using a very clever invention called the **Method of Images** [Frank, pp. 45-67]. A grounded conducting plane affects the electric field near a charged body in the same way as a mirror image of the body with an opposite charge. For example, as shown in figure 5a, a point charge casts an electric field around a grounded plane in the same pattern as though there were an oppositely charged point behind the plane in the same place a reflection would be.

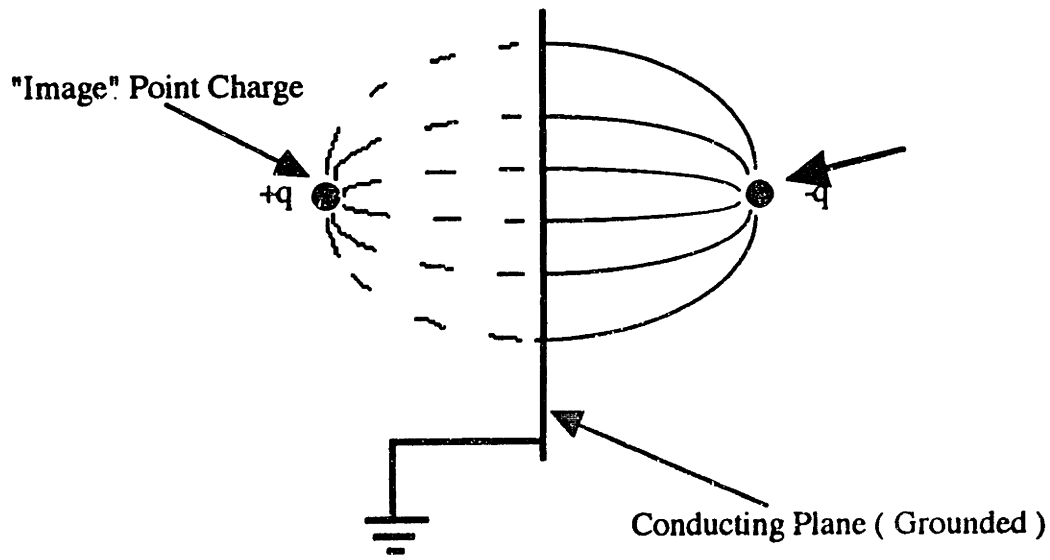

a. Image of point charge in a single conducting plane

Figure D.6 The method of images:

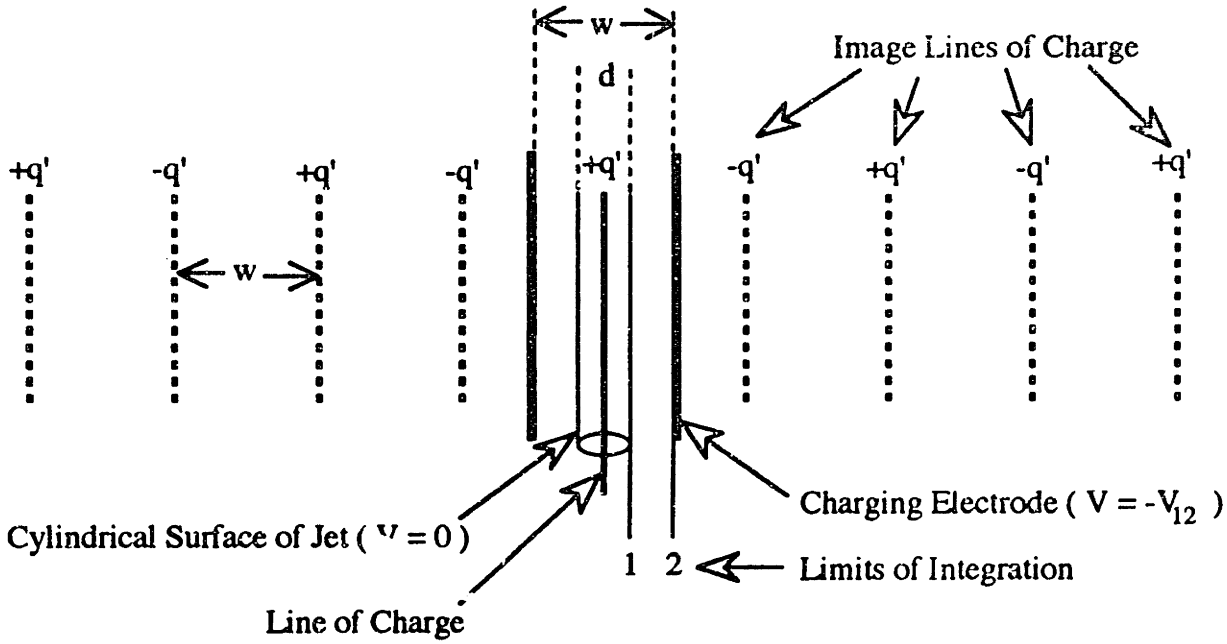

Figure D.6 The method of images: (b.) Image of line charges from two planar electrodes.

The parallel plate charging cell acts like two mirrors facing each other, engendering an infinite number of images, all spaced by a distance w, the charging cell gap. The electric field from each image contributes additively to the total electric field, and the potential difference between points 1 and 2 is a line integral of the electric field from 1 to 2. This leads to an infinite series expression for the potential difference:

$$V_{12} = \frac{q'}{2\pi\varepsilon_0}\left[\ln\left(\frac{w}{d}\right) + \ln\left(\frac{2w-d}{d}\right) - \ln\left(\frac{3w}{2w+d}\right) - \ln\left(\frac{4w-d}{3w}\right) + \ln\left(\frac{5w}{4w+d}\right) + \ldots\right] \quad \text{D.19}$$

Jill Milner gives a reduced expression for this series in her thesis. If d << w, the terms resulting from the image charges converge to 0.216. Accordingly,

$$C' = \frac{2\pi\varepsilon_0}{0.216 + \ln\left(w/d\right)} \; . \quad \text{D.20}$$

This may seem like a lot of froth for a small correction to the equation for a cylindrical cell, but the method of images is quite powerful, and it could also be used to derive expressions for other electrode configurations. It will be used below as the starting point for a derivation of an off-axis jet in a similar cell.

It can be seen that as w/d -> 1, the cell capacitance increases rapidly. Assuming that d = 3 mils, the capacitance of the 26-mil charging cell on the proto machine had a

capacitance of 23 pF/m. The alpha machine has a 10-mil charging cell, which should have a capacitance of 39 pF/m. This is an important figure of merit for a printhead, because the higher the capacitance, the lower the voltage necessary to obtain a given charge-mass ratio on the droplets. Presently, the op-amp that drives the charging cell is the most expensive single component in the controller. This is reasonable for a single or even eight-jet printhead, but could be prohibitive for more jets. There is everything to be gained by building the charging cell as narrow as possible.

D.4.3 Capacitance of Off-Center Jet in Parallel-Plate Cell

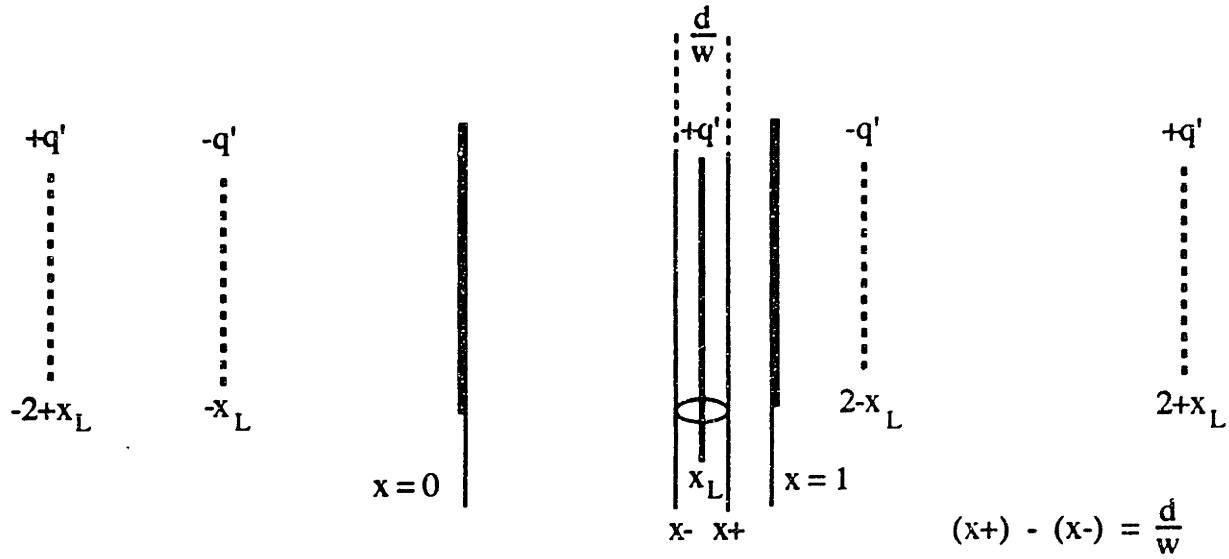

Figure D.7 Image charges and limits of integration for off-axis jet.

Perusing a derivation similar to the one developed for the centered jet, an approximate solution is desired for the capacitance of the jet using the "real" line of charge and the first four images in the series.The cell is nondimensionalized, with with equal to 1, the diameter of the jet is accordingly d/w. We derive the potential difference between the limbs of the cylindrical, equipotential surface surrounding the hypothetical line of charge +q' at $x = x_L$. The limbs of the jet are located at x- and x+ and we calculate two potentials, that between the left-hand limb at x=x- and the left-hand electrode at x=0, and the potential difference between the right-hand limb at x=x+ and the right-hand electrode at x=1.

$$V(x^-) = \frac{q'}{2\pi\varepsilon_0}\int_0^{x^-} dx\left[\frac{1}{x_L - x} + \frac{1}{x_L + x} - \frac{1}{2-(x_L + x)} - \frac{1}{2-(x_L - x)} + \frac{1}{2+(x_L - x)}\right] \quad \text{D.21}$$

and

$$V(x^+) = \frac{q'}{2\pi\varepsilon_0}\int_{x+}^{1} dx\left[\frac{1}{x - x_L} + \frac{1}{x + x_L} - \frac{1}{2-(x + x_L)} - \frac{1}{2-(x - x_L)} + \frac{1}{2+(x - x_L)}\right] \quad \text{D.22}$$

. from which we obtain

$$\frac{2\pi\varepsilon_0 V(x^-)}{q'} = \ln\left(\frac{x_L + x^-}{x_L - x^-}\right) + \ln\left(\frac{2 - x_L - x^-}{2 - x_L + x^-}\right) + \ln\left(\frac{2 + x_L}{2 + x_L - x^-}\right) \quad \text{D.23}$$

and

$$\frac{2\pi\varepsilon_0 V(x^+)}{q'} = \ln\left(\frac{x^+ + x_L}{x^+ - x_L}\right) + \ln\left(\frac{2 - x^+ - x_L}{2 - x^+ + x_L}\right) + \ln\left(\frac{3 - x_L}{2 + x^+ - x_L}\right). \quad \text{D.24}$$

To simplify the algebra, we define the function $\Phi(x)$ such that

$$\exp\left(\frac{2\pi\varepsilon_0 V_{jet}}{q'}\right) = \frac{2 + x_L}{\Phi(x^-)} = \frac{3 - x_L}{-\Phi(x^+)} \quad \text{D.25}$$

because $V(x-) = V(x+) = V_{jet}$.

Now we wish to invert $\Phi(x)$ into $x(\Phi)$. This is done approximately by linearizing Φ about $x = x_L$.

$$\left(\frac{d\Phi}{dx}\right)_{x=x_L} = \frac{-1}{(x_L - x_L^2)} \quad \text{D.26}$$

so

$$\Phi(x) \approx \frac{x_L - x}{(x_L - x_L^2)} \quad \text{D.27}$$

which is inverted very easily to

$$x(\Phi) \approx x_L - (x_L - x_L^2)\Phi \quad \text{D.28}$$

The identity for the width of the jet is

$$\frac{d}{w} = x^+ - x^- = (x_L - x_L^2)\left[\Phi(x^-) - \Phi(x^+)\right] \quad \text{D.29}$$

substituting equations D.25, and D.29,

$$\exp\left(\frac{2\pi\varepsilon_0 V_{jet}}{q'}\right) \approx \frac{5\left(x_L - x_L^2\right)w}{d} \qquad \text{D.30}$$

Now we have an expression in terms of the artificial coordinate x_L which is not the same as the axis of the jet:

$$x_{jet} = \frac{x^+ + x^-}{2} = x_L - \frac{\left(x_L - x_L^2\right)\left[\Phi\left(x^-\right) + \Phi\left(x^+\right)\right]}{2} \qquad \text{D.31}$$

from which we obtain

$$x_{jet} \approx x_L + \frac{\left(1 - 2x_L\right)}{10}\frac{d}{w} \qquad \text{D.32}$$

and so

$$x_L = \frac{x_{jet} - \frac{1}{10}\frac{d}{w}}{1 - \frac{2}{10}\frac{d}{w}} \qquad \text{D.33}$$

All that now remains is to assert the identity $C' = q'/V_{jet}$:

$$C' = \frac{2\pi\varepsilon_0}{\ln\left[5\left(x_L - x_L^2\right)\frac{w}{d}\right]} \qquad \text{D.34}$$

The accuracy of this expression is subject to the approximations of the linearization of $\Phi(x)$, the inclusion of only the first five terms of the series, and the implicit approximation that the cylindrical geometry accurately represents the shape of the jet in the vicinity of the breakoff point. Please note that if $x_{jet} = 0.5$, this expression reduces to

$$C' \approx \frac{2\pi\varepsilon_0}{0.2231 + \ln\left(\frac{w}{d}\right)} \qquad \text{D.35}$$

which approximately reproduces the expression above for the centered jet.

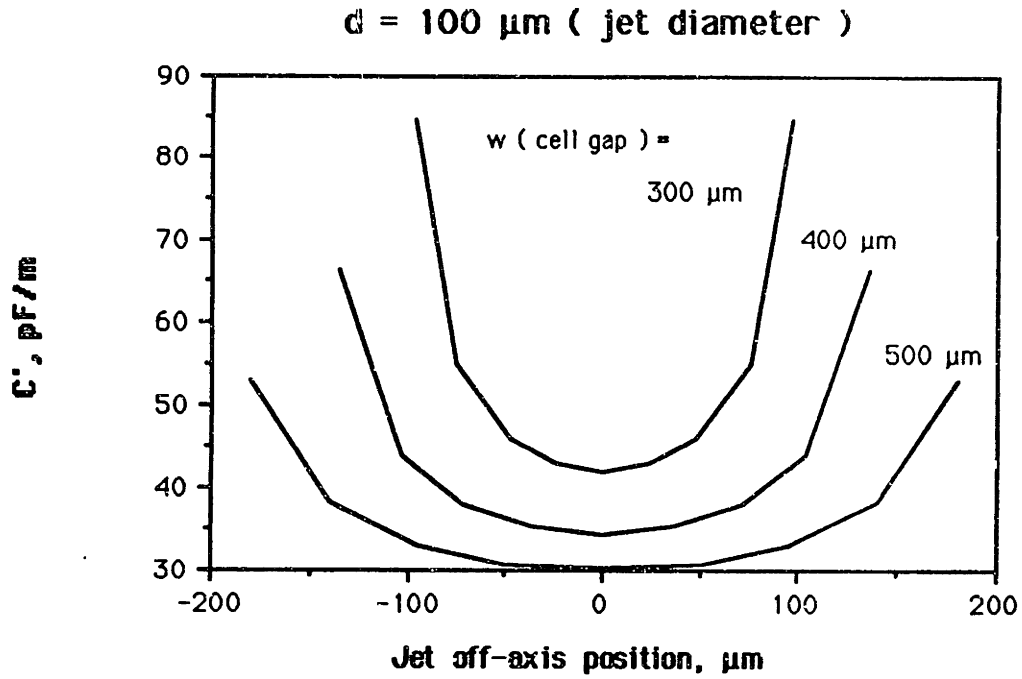

Figure D.8 Jet capacitance as a function of distance off center for cells of various gap widths.

D.5 Charge/Mass Ratio

The amount that a droplet is deflected in the deflection cell depends on the charge-mass ratio of the droplet. This ratio is given by:

$$\frac{q}{m} = \frac{C' V\lambda}{m} = \frac{C' Vu}{m'} = \frac{4C' V}{\pi d_0 \rho} \quad . \qquad \text{D.36}$$

The charge-mass ratio of the jet is independent of the flow rate and the stimulation frequency. It will be seen below that the deflection is strongly dependent on the flowrate. The independence of deflection from stimulation frequency is not complete, since the capacitance of the charging cell depends on the droplet diameter, which is a function of the frequency.

The drift current is $$i_d = \frac{qm'}{m} = C' Vu \qquad \text{D.37}$$

D.6 Jet Deflection

Jill Milners' description of the deflection of the jet in the charging cell bears no improvement:

(Here is her appendix A3, verbatim)

This section describes the forces applies to charged droplets as they pass through the deflection cell and the corresponding displacement of the droplets.

Normal Operating Parameters:

$V_d \approx$ -1200 V (Voltage applied to deflection cell during normal operation)

$w_d =$ 0.060" (width of deflection cell)

$l_d =$ 8 mm (length of deflection plate)

$l_p =$ 0.700" (distance between deflection plate/powder bed)

$l_r =$ 0.370" (distance to recycling catcher)

Acceleration of a droplet in the deflection cell (a_y):

The negatively charged droplets will experience an acceleration in the positive y-direction (along the slow axis) due to the electric field set up from the high voltage applied to the deflection plate. The acceleration is found from

$$a_y = \frac{q\, V_d}{m\, w_d} \qquad \text{D.38}$$

Note that the acceleration does not depend strongly on the flowrate of the binder. Under normal operating conditions the acceleration is equal to 1680 m/s^2.

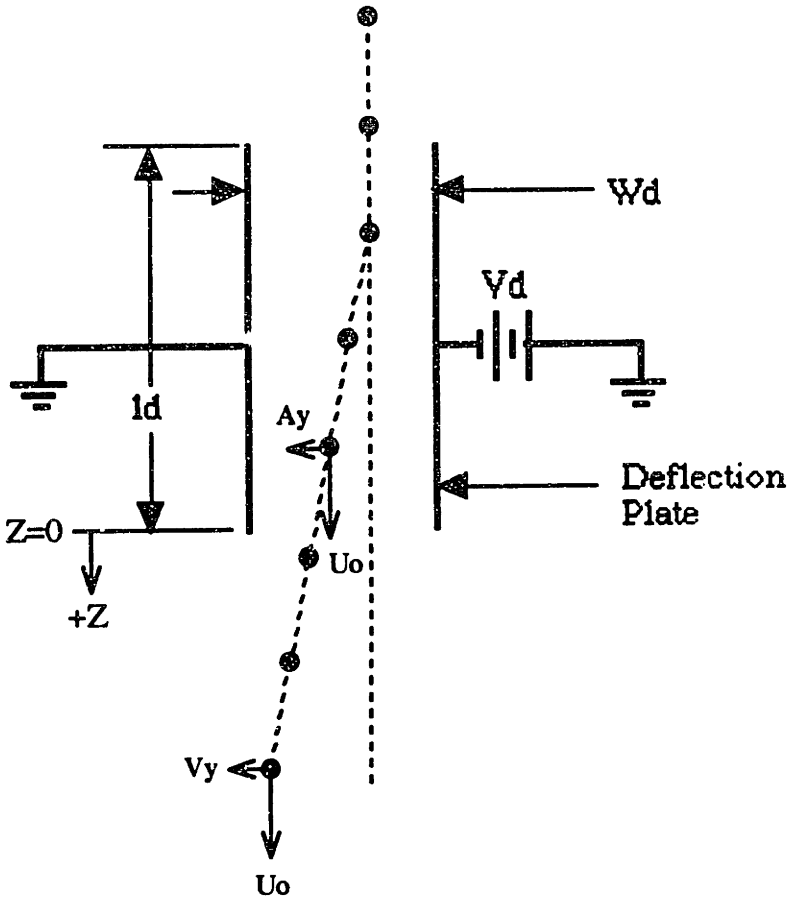

Figure D.9 Deflection of the droplets in the deflection cell.

Y-Deflection of a droplet as a function of Z (y_{defl}):

Assuming that the velocity of the jet entering the deflection plate is equal to the exit velocity of the jet, u_o (no drag), and the bottom edge of the deflection plate is considered to be the point z=0 (z is positive down), then the y-deflection at any point z is equal to:

$$y_{defl}(Zl) = \frac{a_y}{u_o^2}\left(\frac{l_d^2}{2} + l_d z\right) \qquad \text{D.39}$$

under normal operating conditions:

$$y_{defl}(z) = 10.62 \times 10^{-3}(32 + 8z)) \qquad \text{D.40}$$

where y_{defl} and z are both in millimeters. The electrostatic deflection of drops is dependent on the flowrate (or exit velocity of the jet). If the flowrate changes during operation, the deflected droplets may miss the catcher. Under normal operating conditions the deflection at the catcher (z = 9.4 mm) is 1.14 mm.

D.7 Conclusion

The preceding section has been included to help propagate the theoretical development of the printhead. This is in no way a complete theoretical development; merely a pile of relatively isolated derivations presented here to help later workers.

Appendix E. Data from Single Line Primitives

Ser.	sample #s	binder formula	contact angle °	powder	powder treatment	spread density
1a	1,2,3,4,13	E	15	30µ 7920	no rinse	0.32
1b	5,6,7,12	E	15	30µ 7920		0.32
1c	8,9,10,11	E	15	30µ 7920	0.2% cit.	0.31
2	14-28	E	15	30µ 7920		0.34
3	29-34	E	15	28µ 7920		0.46
4a	35-40	E	15	28µ 7920		0.44
4b	41-47	E+.5% Triton	0	28µ 7920		0.42
5a	48-51	B	10	28µ 7920		0.46
5b	52-57	B	10	30µ 7920		0.34
5c	58-62	B	10	28µ 7920		0.46
6	64-68	B	10	10% bim.**		0.41
7a	69-73	B	10	28µ 7920		0.49
7b	74-78	B	10	28µ 7920	.5%cit.coat	0.35
7c	79-83	B	10	28µ 7920	.2%cit.coat	0.38
8	84-91	B	10	28µ 7920		0.48
9a	92-97	B	10	28µ 7920		0.36
10a	98-101	B	10	28µ 7920	.5%cit.coat	0.30
11a	102-106	B	10	30µ sph.§		0.53
9b	107-111	C+.35% hexyl	10	28µ 7920		0.36
10b	112-116	C+.35% hexyl	10	28µ 7920	.5%cit.coat	0.30
11b	117-121	C+.35% hexyl	10	30µ sph.	§	0.53
9c	122-5,136	C+.2% hexyl	10	28µ 7920		0.36
10c	126-130	C+.2% hexyl	10	28µ 7920	.5%cit.coat	0.30
11c	131-135	C+.2% hexyl	10	30µ sph.	§	0.53
9d	137-141	C+.025% Triton	10	28µ 7920		0.36
10d	142-146	C+.025% Triton	10	28µ 7920	.5%cit.coat	0.30
11d	147-151	C+.025% Triton	10	30µ sph.	§	0.53
11e	152-155	C	12	30µ sph.	§	0.53
10e	156-160	C	12	28µ 7920	.5%cit.coat	0.30
9e	161-165	C	12	28µ 7920		0.36
12a	166-168	B	10	28µ 7920		0.39
13a	169-173	B	44	28µ 7920	1%acr.coat	0.35
14a	174-178	B	44	28µ 7920	1%ac.lock	0.35
12b	179-183	C+.025% Triton	10	28µ 7920		0.39
13b	184-188	C+.025% Triton	44	28µ 7920	1%acr.coat	0.35
14b	189-193	C+.025% Triton	44	28µ 7920	1%ac.lock	0.35
12c	194-198	B + .5% Triton	0	28µ 7920		0.39
13c	199-203	B + .5% Triton	18	28µ 7920	1%acr.coat	0.35
14c	204-208	B + .5% Triton	18	28µ 7920	1%ac.lock	0.35
15a	209-213	B	10	20% bim.**		0.40
15b	214-217	B	10	30% bim.**		0.39
15c	218-221	B	10	40% bim.**		0.39
16	222-225	B	10	30% bim.**	slurry	0.57

Table 8.1. Conditions for line saturation experiments

Notes:

Binder formulas: Approx. quantities for 1 liter. Specific gravity 1.21 in all cases.

B: 735.0 g Nyacol 9950; 385.9 g water, 61.0 g propylene glycol; 24.4 g triethanolamine; 12.2 g diethylene glycol monobutyl ether; 1.0 g polyethylene glycol M.W. 20,000; 0.2 g Thymol Blue.

C: same as B without the diethylene glycol monobutyl ether.

E: 750 g Nyacol 9950; 386.3 g water; 122.5 g propylene glycol, 48.5 g "TRIS" = tris(dimethylamino)aminomethane; 1 g polyethylene glycol ; 0.5 g Thymol Blue.

Triton is Triton x-100; **hexyl** is diethylene glycol monohexyl ether. These additives were used to modify the surface tension and contact angle.

Contact angles measured by photographing sessile drops on alumina substrates. (sect. 7.7)

* alumina powder was washed with distilled water and decanted.

bim.** bimodal powder: 28 mm and 3 μm lamellar 7920 alumina, washed. Percentage is weight percent fines. (see sect. 7.5.2)

§ spherical powder: Showa Denko 30 μm "Alunabeads"

cit.coat: Rinsed powder coated by adding dilute citric acid solution to powder such that saturation ≈10%. Dried at 100°C. Percentage given is by weight w.r.t. powder .

acr.coat: Rinsed powder coated with 1% PMMA by weight Al_2O_3 dissolved in MEK using similar procedure for citric coating.

acr. lock Powder coated with acrylic prepared by spreading on alumina wafers, and locked by heating to 250°C.

Powder packing density measured by weighing 72 cc of powder spread in the printing machine.

The following table contains the data and calculated results for the measurements of the single line primitives discussed in chapters 8 and 9, for which the experimental conditions are outlined in table 8.1, above. Samples were numbered sequentially in chronological order. All consisted of a total of 2.5 m of isolated single line primitives. The quantities given are as follows:

M' = weight of sample / length of sample.

$A_{liquid} = \frac{\dot{m}}{V_x \rho_{liquid}}$ = Binder area within line features.

where $\dot{m}$ = mass flow rate of binder;

V_x = printhead speed;

ρ_{liquid} = binder density = 1.21 g/cm^3.

$A_{powder} = \frac{1}{\rho_{Al_2O_3}} \left[M' - \frac{\dot{m} f_{WSiO_2}}{V_x} \right]$ = Powder area in line features.

where $\rho_{Al_2O_3}$ = density of alumina = 3.98 g/cm^3;

f_{WSiO_2} = weight fraction of silica in liquid binder = 0.305 .

$f_{powder} = \frac{\rho_{bed}}{\rho_{Al_2O_3}}$ = Powder packing density.

where ρ_{bed} = bulk density of powder bed; measured at run time.

$d_{est'd} = \sqrt{\frac{4A_{powder}}{\pi f_{powder}}}$ = line diameter estimated from density measurements.

M_{opt} = scale of optical images of samples (microns per pixel). Bitmapped images archived at MIT 3-D Printing project. Scales calibrated by photographing a strand of 40-Ga wire and measuring wire on a toolmaker's microscope to an accuracy of ± 2.5 μm

d_{opt} = diameter measured from optical images, averaged from 4-8 images.

σ_{local} = standard deviation of line diameter within an image, averaged over all images of the sample.

$S = \frac{A_{liquid}}{A_{powder}} \frac{f_{powder}}{(1 - f_{powder})}$ = Binder saturation within features.

sample No.	M' g/mm	A_{liquid} mm^2	A_{powder} mm^2	f_{powder}	$d_{est'd}$ mm
1	3.89E-05	0.0130	0.0098	0.32	0.197
2	3.59E-05	0.0118	0.0090	0.32	0.189
3	4.66E-05	0.0155	0.0117	0.32	0.215
4	4.31E-05	0.0143	0.0108	0.32	0.207
5	3.58E-05	0.0118	0.0090	0.32	0.188
6	3.92E-05	0.0130	0.0098	0.32	0.197
7	4.36E-05	0.0144	0.0110	0.32	0.208
8	3.47E-05	0.0118	0.0087	0.31	0.186
9	3.78E-05	0.0130	0.0095	0.31	0.194
10	4.17E-05	0.0143	0.0105	0.31	0.204
11	4.13E-05	0.0141	0.0104	0.31	0.203
12	4.29E-05	0.0141	0.0108	0.32	0.206
13	4.35E-05	0.0141	0.0109	0.32	0.208
14	3.60E-05	0.0113	0.0091	0.34	0.185
15	4.75E-05	0.0156	0.0119	0.34	0.213
16	5.50E-05	0.0197	0.0138	0.34	0.229
17	6.99E-05	0.0260	0.0176	0.34	0.258
18	9.31E-05	0.0312	0.0234	0.34	0.297
19	1.19E-04	0.0449	0.0299	0.34	0.336
20	8.21E-05	0.0302	0.0206	0.34	0.279
21	1.61E-04	0.0621	0.0405	0.34	0.391
22	5.61E-05	0.0186	0.0141	0.34	0.231
23	2.57E-05	0.0091	0.0065	0.34	0.156
24	3.53E-05	0.0122	0.0089	0.34	0.183
25	4.35E-05	0.0146	0.0109	0.34	0.203
26	4.20E-05	0.0151	0.0106	0.34	0.200
27	5.64E-05	0.0197	0.0142	0.34	0.231
28	6.98E-05	0.0241	0.0175	0.34	0.257
29	4.30E-05	0.0113	0.0108	0.46	0.173
30	5.65E-05	0.0144	0.0142	0.46	0.198
31	6.82E-05	0.0177	0.0171	0.46	0.218
32	6.63E-05	0.0162	0.0167	0.46	0.215
33	8.63E-05	0.0210	0.0217	0.46	0.245
34	1.06E-04	0.0262	0.0266	0.46	0.271
35	5.07E-05	0.0138	0.0127	0.45	0.190
36	7.57E-05	0.0200	0.0190	0.45	0.232
37	1.15E-04	0.0304	0.0289	0.45	0.286
38	1.74E-04	0.0456	0.0437	0.45	0.352
39	3.46E-04	0.0892	0.0869	0.43	0.510
40	3.51E-04	0.0912	0.0882	0.46	0.496
41	6.11E-05	0.0140	0.0154	0.40	0.221
42	1.09E-04	0.0233	0.0273	0.40	0.296
43	8.33E-05	0.0186	0.0209	0.44	0.246
44	1.52E-04	0.0310	0.0383	0.42	0.341
45	2.32E-04	0.0466	0.0583	0.42	0.421

sample No.	M_{opt} µm/pixel	d_{opt} mm	σ_{local} mm	S	S series avg.
1	1.92	0.237	0.019	0.63	0.63
2	1.92	0.232	0.017	0.62	0.63
3	1.92	0.266	0.020	0.63	0.62
4	1.92	0.253	0.021	0.63	
5	1.92	0.223	0.017	0.62	
6	1.92	0.227	0.015	0.63	
7	1.92	0.258	0.019	0.62	
8	1.92	0.217	0.016	0.62	
9	1.92	0.233	0.017	0.62	
10	1.92	0.250	0.017	0.62	
11	1.92	0.257	0.017	0.62	
12	1.92	0.250	0.017	0.63	
13	1.92	0.264	0.018	0.62	
14	4.81	0.211	0.023	0.63	0.71
15	4.81	0.226	0.021	0.66	
16	4.81	0.248	0.023	0.72	
17	4.81	0.277	0.020	0.75	
18	4.81	0.314	0.023	0.68	
19	4.81	0.356	0.024	0.76	
20	4.81	0.294	0.019	0.74	
21	4.81	0.407	0.027	0.78	
22	4.81	0.255	0.037	0.67	
23	4.81	0.179	0.019	0.71	
24	4.81	0.208	0.026	0.70	
25	4.81	0.244	0.039	0.68	
26	4.81	0.231	0.019	0.73	
27	4.81	0.268	0.020	0.71	
28	4.81	0.289	0.022	0.70	
29	4.81	0.197	0.028	0.89	0.86
30	4.81	0.226	0.027	0.87	
31	4.81	0.252	0.026	0.88	
32	4.81	0.244	0.021	0.83	
33	4.81	0.274	0.027	0.83	
34	4.81	0.309	0.028	0.84	
35	4.81	0.214	0.028	0.89	0.85
36	4.81	0.255	0.038	0.86	
37	4.81	0.314	0.036	0.86	
38	4.81	0.383	0.055	0.85	
39	4.81	0.548	0.057	0.76	
40	4.81	0.563	0.057	0.87	
41	4.81	0.241	0.050	0.61	0.63
42	4.81	0.320	0.074	0.56	
43	4.81	0.271	0.040	0.70	
44	4.81	0.368	0.081	0.59	
45	4.81	0.481	0.103	0.58	

sample No.	M' g/mm	A_{liquid} mm^2	A_{powder} mm^2	f_{powder}	$d_{est'd}$ mm
46	6.09E-05	0.0139	0.0153	0.42	0.216
47	4.48E-05	0.0107	0.0113	0.42	0.185
48	3.99E-05	0.0039	0.0100	0.46	0.167
49	3.68E-05	0.0085	0.0093	0.46	0.160
50	7.30E-05	0.0170	0.0183	0.46	0.226
51	3.20E-05	0.0057	0.0080	0.46	0.149
52	4.54E-05	0.0034	0.0114	0.34	0.206
53	4.26E-05	0.0075	0.0107	0.34	0.200
54	6.33E-05	0.0149	0.0159	0.34	0.244
55	4.24E-05	0.0099	0.0107	0.34	0.200
56	3.41E-05	0.0064	0.0086	0.34	0.180
57	2.57E-05	0.0050	0.0064	0.34	0.156
58	4.87E-05	0.0101	0.0122	0.46	0.184
59	3.25E-05	0.0061	0.0082	0.46	0.150
60	5.93E-05	0.0133	0.0149	0.47	0.202
61	8.67E-05	0.0192	0.0218	0.47	0.244
62	1.28E-04	0.0288	0.0322	0.47	0.297
63	lost	0.0576	-	0.47	-
64	5.81E-05	0.0137	0.0146	0.42	0.186
65	1.35E-04	0.0296	0.0340	0.42	0.283
66	3.35E-04	0.0593	0.0843	0.42	0.446
67	2.20E-04	0.0395	0.0552	0.42	0.361
68	9.00E-05	0.0198	0.0226	0.42	0.231
69	6.53E-05	0.0144	0.0164	0.49	0.207
70	1.36E-04	0.0311	0.0342	0.49	0.298
71	2.68E-04	0.0622	0.0672	0.49	0.418
72	1.80E-04	0.0399	0.0451	0.49	0.344
73	9.25E-05	0.0200	0.0232	0.49	0.247
74	5.12E-05	0.0138	0.0129	0.35	0.216
75	1.11E-04	0.0299	0.0279	0.35	0.319
76	2.13E-04	0.0599	0.0536	0.35	0.442
77	7.47E-05	0.0200	0.0188	0.35	0.261
78	1.36E-04	0.0399	0.0343	0.35	0.353
79	5.62E-05	0.0138	0.0141	0.38	0.217
80	1.17E-04	0.0298	0.0294	0.38	0.314
81	2.29E-04	0.0597	0.0575	0.38	0.439
82	7.85E-05	0.0199	0.0197	0.38	0.257
83	1.53E-04	0.0398	0.0384	0.38	0.359
84	2.75E-05	0.0058	0.0069	0.49	0.134
85	2.09E-05	0.0040	0.0053	0.49	0.117
86	2.33E-05	0.0043	0.0058	0.49	0.123
87	2.44E-05	0.0047	0.0061	0.49	0.127
88	2.48E-05	0.0056	0.0062	0.49	0.127
89	4.21E-05	0.0094	0.0106	0.49	0.166
90	8.04E-05	0.0188	0.0202	0.49	0.229

sample No.	M_{opt} µm/pixel	d_{opt} mm	σ_{local} mm	S	S series avg.
46	4.81	0.255	0.082	0.66	0.63
47	7.32	0.234	0.082	0.69	
48	7.32	0.148	0.016	0.33	
49	7.32	0.193	0.022	0.78	
50	7.32	0.264	0.027	0.78	
51	7.32	0.168	0.019	0.60	
52	7.32	0.168	0.022	0.16	
53	7.32	0.209	0.037	0.36	
54	7.32	0.269	0.029	0.48	
55	7.32	0.230	0.026	0.48	
56	7.32	0.195	0.026	0.38	
57	7.32	0.176	0.020	0.39	
58	7.32	0.225	0.023	0.71	0.74
59	7.32	0.185	0.020	0.64	
60	7.32	0.232	0.025	0.78	
61	7.32	0.286	0.028	0.77	
62	7.32	0.351	0.048	0.78	
63	7.32	-	-	-	
64	7.32	0.232	0.032	0.67	0.58
65	6.38	0.319	0.064	0.62	
66	6.38	0.462	0.083	0.50	
67	6.38	0.375	0.071	0.51	
68	6.38	0.244	0.027	0.62	
69	6.38	0.229	0.051	0.84	0.85
70	6.38	0.310	0.049	0.87	
71	6.38	0.468	0.061	0.89	
72	6.38	0.377	0.061	0.84	
73	6.38	0.274	0.050	0.81	
74	6.38	0.215	0.025	0.58	0.59
75	6.38	0.306	0.022	0.58	
76	6.38	0.428	0.028	0.60	
77	6.38	0.251	0.026	0.57	
78	6.38	0.350	0.026	0.63	
79	6.38	0.230	0.033	0.60	0.62
80	6.38	0.332	0.051	0.62	
81	6.38	0.441	0.032	0.64	
82	6.38	0.270	0.037	0.62	
83	6.38	0.354	0.033	0.63	
84	6.38	0.164	0.021	0.80	0.80
85	6.38	0.143	0.020	0.73	
86	6.38	0.145	0.020	0.71	
87	6.38	0.156	0.021	0.74	
88	6.38	0.153	0.020	0.87	
89	6.38	0.196	0.019	0.85	
90	6.38	0.267	0.022	0.89	

sample No.	M' g/mm	A_{liquid} mm^2	A_{powder} mm^2	f_{powder}	$d_{est'd}$ mm
91	5.57E-05	0.0125	0.0140	0.49	0.191
92	4.63E-05	0.0140	0.0116	0.36	0.203
93	5.81E-05	0.0182	0.0146	0.36	0.227
94	7.12E-05	0.0228	0.0179	0.36	0.251
95	1.00E-04	0.0252	0.0251	0.36	0.298
96	1.03E-04	0.0282	0.0258	0.36	0.302
97	1.38E-04	0.0376	0.0347	0.36	0.350
98	4.34E-05	0.0130	0.0109	0.30	0.196
99	5.30E-05	0.0154	0.0133	0.30	0.217
100	6.61E-05	0.0188	0.0166	0.30	0.242
101	9.53E-05	0.0282	0.0239	0.30	0.291
102	8.96E-05	0.0122	0.0225	0.58	0.222
103	9.20E-05	0.0144	0.0231	0.58	0.225
104	1.27E-04	0.0176	0.0319	0.58	0.264
105	1.83E-04	0.0265	0.0460	0.58	0.318
106	2.38E-04	0.0353	0.0599	0.58	0.363
107	5.13E-05	0.0137	0.0129	0.36	0.214
108	1.06E-04	0.0297	0.0265	0.36	0.306
109	2.14E-04	0.0594	0.0537	0.36	0.436
110	1.41E-04	0.0396	0.0354	0.36	0.354
111	7.23E-05	0.0198	0.0182	0.36	0.253
112	4.75E-05	0.0137	0.0119	0.30	0.205
113	9.81E-05	0.0297	0.0247	0.30	0.295
114	1.81E-04	0.0594	0.0454	0.30	0.401
115	1.28E-04	0.0396	0.0321	0.30	0.337
116	6.68E-05	0.0198	0.0168	0.30	0.244
117	1.04E-04	0.0137	0.0262	0.58	0.240
118	2.09E-04	0.0297	0.0525	0.58	0.340
119	3.86E-04	0.0594	0.0970	0.58	0.461
120	2.68E-04	0.0396	0.0674	0.58	0.385
121	1.39E-04	0.0198	0.0350	0.58	0.277
122	4.25E-05	0.0107	0.0107	0.36	0.194
123	8.95E-05	0.0232	0.0225	0.36	0.282
124	1.10E-04	0.0309	0.0276	0.36	0.312
125	5.78E-05	0.0155	0.0145	0.36	0.227
126	4.55E-05	0.0121	0.0114	0.30	0.201
127	8.97E-05	0.0262	0.0225	0.30	0.282
128	1.68E-04	0.0525	0.0423	0.30	0.387
129	1.13E-04	0.0341	0.0285	0.30	0.317
130	5.87E-05	0.0171	0.0148	0.30	0.228
131	8.44E-05	0.0116	0.0212	0.58	0.216
132	1.72E-04	0.0252	0.0431	0.58	0.308
133	3.65E-04	0.0503	0.0917	0.58	0.449
134	2.50E-04	0.0362	0.0627	0.58	0.371
135	1.27E-04	0.0181	0.0319	0.58	0.264

sample No.	M_{opt} µm/pixel	d_{opt} mm	σ_{local} mm	S	S series avg.
91	6.38	0.227	0.020	0.86	
92	7.38	0.216	0.021	0.68	0.65
93	7.38	0.255	0.023	0.70	
94	7.38	0.257	0.020	0.72	
95	7.38	0.303	0.021	0.56	
96	7.38	0.295	.027	0.61	
97	7.38	0.360	0.037	0.61	
98	7.38	0.229	0.038	0.51	0.50
99	7.38	0.249	0.031	0.50	
100	7.38	0.268	0.034	0.49	
101	7.38	0.340	0.038	0.50	
102	7.38	0.240	0.028	0.75	0.80
103	7.38	0.264	0.021	0.86	
104	7.38	0.282	0.025	0.76	
105	7.38	0.345	0.031	0.79	
106	7.38	0.378	0.023	0.81	
107	7.38	0.223	0.020	0.60	0.62
108	7.38	0.321	0.028	0.63	
109	7.38	0.482	0.062	0.62	
110	7.38	0.380	0.039	0.63	
111	7.38	0.269	0.038	0.61	
112	7.38	0.249	0.022	0.49	0.52
113	7.38	0.317	0.025	0.52	
114	7.38	0.400	0.028	0.56	
115	7.38	0.349	0.026	0.53	
116	7.38	0.275	0.023	0.51	
117	7.38	0.260	0.025	0.72	0.79
118	7.38	0.382	0.028	0.78	
119	7.38	0.487	0.033	0.85	
120	7.38	0.413	0.032	0.81	
121	7.38	0.315	0.027	0.78	
122	7.38	0.220	0.040	0.56	0.61
123	7.38	0.268	0.029	0.58	
124	7.38	0.332	0.039	0.63	
125	7.38	0.247	0.053	0.60	
126	7.38	0.231	0.026	0.45	0.50
127	7.38	0.306	0.024	0.50	
128	7.38	0.406	0.029	0.53	
129	7.38	0.347	0.025	0.51	
130	7.38	0.260	0.025	0.50	
131	7.38	0.247	0.027	0.76	0.78
132	7.38	0.321	0.023	0.81	
133	7.38	0.489	0.026	0.76	
134	7.38	0.417	0.027	0.80	
135	7.38	0.295	0.022	0.78	

sample No.	M' g/mm	A_{liquid} mm^2	A_{powder} mm^2	f_{powder}	$d_{est'd}$ mm
136	1.79E-04	0.0542	0.0449	0.36	0.398
137	4.92E-05	0.0135	0.0124	0.36	0.209
138	1.02E-04	0.0293	0.0255	0.36	0.301
139	1.93E-04	0.0586	0.0484	0.36	0.414
140	1.28E-04	0.0390	0.0322	0.36	0.337
141	6.46E-05	0.0195	0.0162	0.36	0.240
142	5.48E-05	0.0154	0.0138	0.30	0.221
143	1.12E-04	0.0334	0.0282	0.30	0.316
144	2.13E-04	0.0668	0.0536	0.30	0.435
145	1.44E-04	0.0445	0.0363	0.30	0.358
146	7.55E-05	0.0223	0.0190	0.30	0.259
147	1.07E-04	0.0149	0.0268	0.58	0.242
148	2.14E-04	0.0323	0.0537	0.58	0.343
149	4.06E-04	0.0646	0.1021	0.58	0.473
150	2.78E-04	0.0414	0.0698	0.58	0.392
151	1.44E-04	0.0207	0.0361	0.58	0.282
152	1.07E-04	0.0144	0.0268	0.58	0.242
153	2.15E-04	0.0312	0.0539	0.58	0.344
154	2.84E-04	0.0417	0.0713	0.58	0.396
155	1.52E-04	0.0208	0.0383	0.58	0.290
156	5.05E-05	0.0144	0.0127	0.30	0.212
157	1.06E-04	0.0323	0.0266	0.30	0.307
158	2.00E-04	0.0646	0.0504	0.30	0.422
159	1.45E-04	0.0431	0.0364	0.30	0.359
160	7.42E-05	0.0215	0.0186	0.30	0.257
161	5.40E-05	0.0149	0.0136	0.36	0.219
162	1.08E-04	0.0323	0.0271	0.36	0.310
163	2.05E-04	0.0646	0.0515	0.36	0.427
164	1.40E-04	0.0431	0.0351	0.36	0.352
165	7.41E-05	0.0215	0.0186	0.36	0.257
166	4.45E-05	0.0121	0.0112	0.39	0.191
167	9.15E-05	0.0262	0.0230	0.39	0.274
168	6.10E-05	0.0175	0.0153	0.39	0.224
169	3.38E-05	0.0120	0.0085	0.35	0.176
170	4.61E-05	0.0174	0.0116	0.35	0.205
171	6.54E-05	0.0260	0.0164	0.35	0.244
172	8.47E-05	0.0330	0.0213	0.35	0.278
173	1.20E-04	0.0495	0.0301	0.35	0.331
174	2.98E-05	0.0114	0.0075	0.35	0.165
175	7.88E-05	0.0165	0.0086	0.35	0.177
176	3.43E-05	0.0234	0.0136	0.35	0.223
177	5.42E-05	0.0312	0.0198	0.35	0.268
178	9.30E-05	0.0469	0.0234	0.35	0.292
179	4.06E-05	0.0110	0.0102	0.39	0.183
180	8.48E-05	0.0239	0.0213	0.39	0.264

sample No.	M_{opt} µm/pixel	d_{opt} mm	σ_{local} mm	S	S series avg.
136	7.38	0.384	0.029	0.68	
137	7.38	0.229	0.028	0.62	0.66
138	7.38	0.306	0.034	0.64	
139	7.38	0.432	0.038	0.68	
140	7.38	0.367	0.028	0.68	
141	7.38	0.247	0.030	0.68	
142	7.38	0.244	0.024	0.48	0.51
143	7.38	0.343	0.024	0.51	
144	7.38	0.460	0.028	0.53	
145	7.38	0.408	0.030	0.53	
146	7.38	0.312	0.027	0.50	
147	7.38	0.284	0.027	0.77	0.82
148	7.38	0.433	0.023	0.83	
149	7.17	0.524	0.027	0.87	
150	7.17	0.457	0.029	0.82	
151	7.17	0.325	0.025	0.79	
152	7.17	0.276	0.026	0.74	0.78
153	7.17	0.411	0.029	0.80	
154	7.17	0.464	0.023	0.81	
155	7.17	0.339	0.024	0.75	
156	7.17	0.265	0.024	0.49	0.51
157	7.17	0.353	0.026	0.52	
158	7.17	0.466	0.026	0.55	
159	7.17	0.400	0.031	0.51	
160	7.17	0.301	0.038	0.50	
161	7.17	0.281	0.026	0.62	0.67
162	7.17	0.353	0.025	0.67	
163	7.17	0.470	0.022	0.71	
164	7.17	0.382	0.029	0.69	
165	7.17	0.290	0.023	0.65	
166	6.12	0.207	0.027	0.69	0.72
167	6.12	0.295	0.039	0.73	
168	6.12	0.260	0.030	0.73	
169	6.12	0.184	0.025	0.76	0.83
170	6.12	0.213	0.030	0.81	
171	6.12	0.263	0.026	0.85	
172	6.12	0.292	0.037	0.83	
173	6.12	0.333	0.038	0.88	
174	6.44	0.210	0.028	0.82	0.94
175	6.44	0.299	0.034	1.03	
176	6.44	0.233	0.029	0.93	
177	6.44	0.275	0.031	0.85	
178	6.44	0.351	0.032	1.08	
179	6.44	0.208	0.034	0.69	0.71
180	6.44	0.283	0.031	0.72	

sample No.	M' g/mm	A_{liquid} mm^2	A_{powder} mm^2	f_{powder}	$d_{est'd}$ mm
181	1.66E-04	0.0477	0.0416	0.39	0.369
182	1.12E-04	0.0318	0.0281	0.39	0.303
183	5.78E-05	0.0159	0.0145	0.39	0.218
184	2.77E-05	0.0107	0.0070	0.35	0.159
185	5.69E-05	0.0232	0.0143	0.35	0.228
186	1.01E-04	0.0464	0.0255	0.35	0.305
187	7.13E-05	0.0309	0.0179	0.35	0.255
188	3.84E-05	0.0155	0.0096	0.35	0.187
189	2.86E-05	0.0111	0.0072	0.35	0.162
190	3.78E-05	0.0161	0.0095	0.35	0.186
191	5.40E-05	0.0241	0.0136	0.35	0.222
192	6.83E-05	0.0312	0.0172	0.35	0.250
193	9.84E-05	0.0469	0.0247	0.35	0.300
194	4.57E-05	0.0118	0.0115	0.39	0.194
195	9.18E-05	0.0256	0.0231	0.39	0.274
196	1.17E-04	0.0318	0.0294	0.39	0.310
197	1.80E-04	0.0477	0.0453	0.39	0.385
198	5.93E-05	0.0159	0.0149	0.39	0.221
199	9.17E-05	0.0234	0.0230	0.35	0.290
200	1.57E-04	0.0456	0.0394	0.35	0.379
201	4.24E-05	0.0115	0.0107	0.35	0.197
202	1.01E-04	0.0289	0.0254	0.35	0.304
203	7.26E-05	0.0174	0.0182	0.35	0.258
204	2.50E-04	0.0521	0.0628	0.35	0.478
205	6.72E-05	0.0174	0.0169	0.35	0.248
206	9.84E-05	0.0260	0.0247	0.35	0.300
207	1.43E-04	0.0341	0.0358	0.35	0.361
208	4.77E-05	0.0118	0.0120	0.35	0.209
209	5.52E-05	0.0121	0.0127	0.40	0.202
210	4.48E-05	0.0093	0.0104	0.40	0.163
211	6.50E-05	0.0150	0.0149	0.40	0.195
212	8.34E-05	0.0201	0.0191	0.40	0.220
213	5.16E-05	0.0120	0.0118	0.40	0.174
214	3.75E-05	0.0090	0.0086	0.39	0.138
215	5.98E-05	0.0146	0.0137	0.39	0.175
216	8.49E-05	0.0195	0.0195	0.39	0.209
217	5.17E-05	0.0117	0.0119	0.39	0.163
218	3.82E-05	0.0090	0.0088	0.39	0.136
219	6.35E-05	0.0146	0.0146	0.39	0.176
220	8.72E-05	0.0195	0.0201	0.39	0.206
221	5.00E-05	0.0117	0.0115	0.39	0.156
222	2.00E-04	0.0115	0.0492	0.57	0.332
223	1.66E-04	0.0166	0.0401	0.57	0.299
224	3.08E-04	0.0250	0.0749	0.57	0.409
225	1.56E-04	0.0115	0.0382	0.57	0.292

sample No.	M_{opt} µm/pixel	d_{opt} mm	σ_{local} mm	S	S series avg.
181	6.44	0.388	0.037	0.73	
182	6.44	0.323	0.030	0.72	
183	6.44	0.249	0.033	0.70	
184	6.44	0.200	0.035	0.83	0.90
185	6.44	0.248	0.028	0.87	
186	6.44	0.311	0.030	0.98	
187	6.44	0.256	0.025	0.93	
188	6.44	0.206	0.025	0.86	
189	6.44	0.198	0.029	0.83	0.94
190	6.44	0.232	0.027	0.91	
191	6.44	0.245	0.030	0.96	
192	6.44	0.294	0.030	0.98	
193	6.44	0.338	0.034	1.02	
194	6.44	0.220	0.288	0.66	0.68
195	6.44	0.291	0.298	0.71	
196	6.44	0.314	0.031	0.69	
197	6.44	0.377	0.030	0.67	
198	6.44	0.187	0.030	0.68	
199	6.44	0.331	0.072	0.55	0.58
200	6.44	0.404	0.044	0.62	
201	6.44	0.230	0.039	0.58	
202	6.44	0.331	0.035	0.61	
203	6.44	0.280	0.039	0.51	
204	6.44	0.513	0.049	0.45	0.52
205	6.44	0.354	0.046	0.55	
206	6.44	0.336	0.044	0.57	
207	6.44	0.437	0.043	0.51	
208	6.44	0.245	0.030	0.53	
209	6.44			0.63	0.65
210	5.29	0.165		0.59	
211	5.29	0.250		0.67	
212	5.29	0.212		0.70	
213	5.29	0.194		0.67	
214	5.29	0.170		0.67	0.66
215	5.29	0.208	0.030	0.69	
216	5.29	0.250		0.64	
217	5.29	0.172		0.63	
218	5.29	0.168		0.66	0.64
219	5.29	0.207		0.64	
220	5.29	0.246		0.62	
221	5.29	0.183		0.65	
222				0.31	0.43
223				0.55	
224				0.44	
225				0.40	

Appendix F. Material Specifications

F.1 Colloidal Silica

Nyacol Corporation, of Ashland MA was acquired by Eka-Nobel in the beginning of 1995. Prior to this event, all material were shipped from Ashland, MA. After this point, all materials were shipped from Atlanta, Georgia. There is every reason to believe that the product quality will remain comparable.

Prior to the takeover, the material specifications were as follows:

Nyacol 9950:

Particle size: 100 nm (SiO_2)
Solids loading: 50% by weight.
Specific gr ity: 1.40
pH as shipped: 8 - 8.5
Alkalai content ≈ 0.5% by weight as Na_2O.

According to private communications with Nyacol employees, the material also contains traces of "Giv-Guard" biocide (Givaudan) and can contain substantial amounts (≈ 1%) of hydrolyzed ion-exchange resin. This resin impurity appears as an oily film on the surface of the liquid, and can gradually come out of solution as a waxy, yellow precipitate. Other fibrous black inclusions have eluded identification. To remove these large inclusions, it is recommended that the product be filtered to 5 μm on receipt. As a precaution, the formulation of Binder "B" includes the cosolvent diethylene glycol monobutyl ether which appears to solubilize the traces of resin when added at a concentration of 1% by weight.

F.2 Alumina Powder

John Lee, in his master's thesis, compared the packing characteristics of various powders, and selected a powder from Norton which is normally sold as a grinding media. The powders are sized by air classification, and the largest fraction has a mean grain size of approximately 30 μm. This material, Norton 7920, is nearly identical to another product, Norton 7921; the difference being in the amount of sodium silicate added as a flowing agent. Since sodium silicate melts during the firing process, it contributes to difficulties in

removing powder from finished shells. To alleviate this problem, a procedure was instituted at MIT of rinsing the powder with distilled water and decanting off the soluble additives.

The morphology of the powder grains is shown below in a micrograph obtained by Alan Lauder. The morphology can perhaps best be described as "tiny bathroom tiles" which are lamellar, generally hexagonal and ar about 1/5 as thick as they are in diameter.

Figure F.1 Scanning electron micrograph of 30 μm Norton 7920 "EGPA" alumina (Lauder, p.29)

Although the particles are oblate, their size can be characterized by the equivalent spherical diameter, derived from Coulter Counter measurements below. In the coulter counter, a suspension of particles in electrolyte is pumped through a capillary, and the transconductance of the capillary drops by an amount proportional to the volume of any particles passing through the capillary. By counting the frequency and magnitude of voltage pulses, the device can measure the number and size of particles in a suspension. Results, obtained from Norton, for two different batches of powder are shown below.

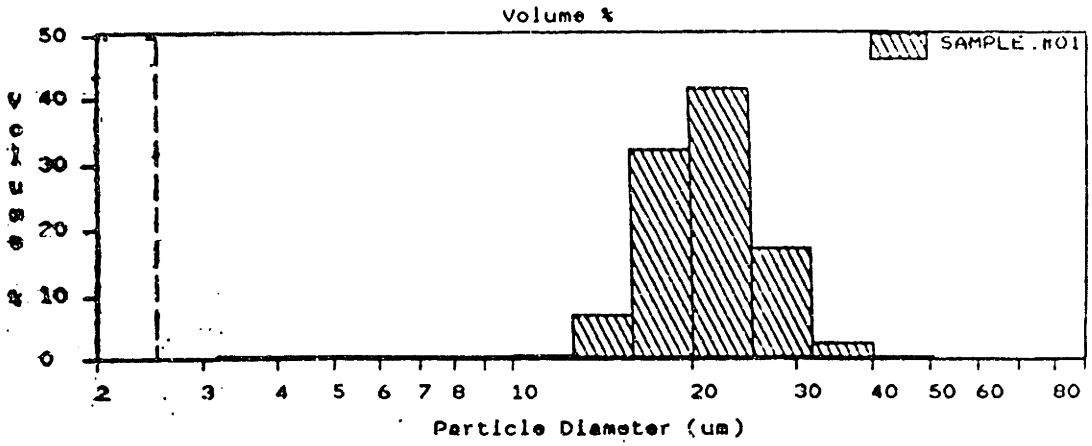

Figure F.2 Particle size distribution for 30 µm Norton 7920 "EGPA" alumina (used prior to Feb. 94.)

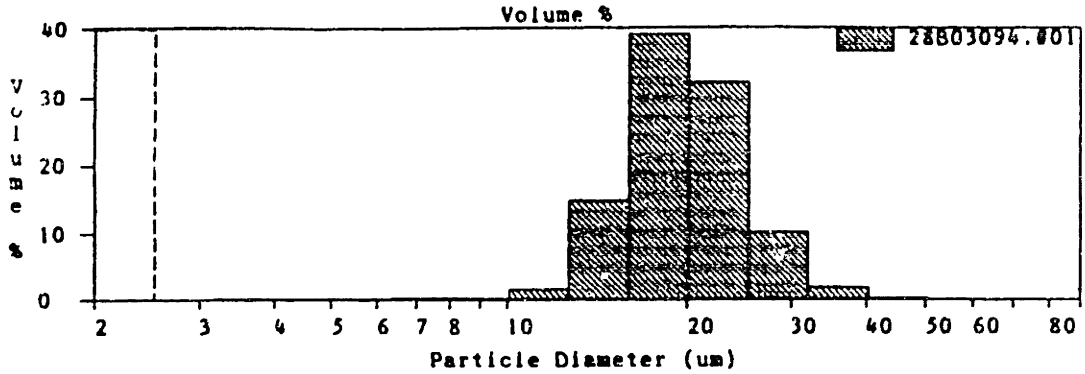

Figure F.3 Particle size distribution for 28 µm Norton 7920 "EGPA" alumina. (used after Feb. 94.)

Appendix G. Schematic of 1:4 Switching Circuit for Printing at Low Binder Dose

G.0 Introduction

In order to distribute binder extremely thinly along single lines, a logic circuit was constructed which printed only one out of every four droplets generated by the printhead.

G.1 Description of the Circuit

The circuit used a TTL output of the nozzle stimulation oscillator to synchronize a two-bit counter to the droplet breakoff. The switching signal from the computer that controlled the printhead was combined (Boolean "and") with the output of a flip-flop that gave a pulse on every fourth stimulator cycle. The location of the 1:4 circuit in the system is diagrammed below. This circuit was designed by Timothy Anderson.

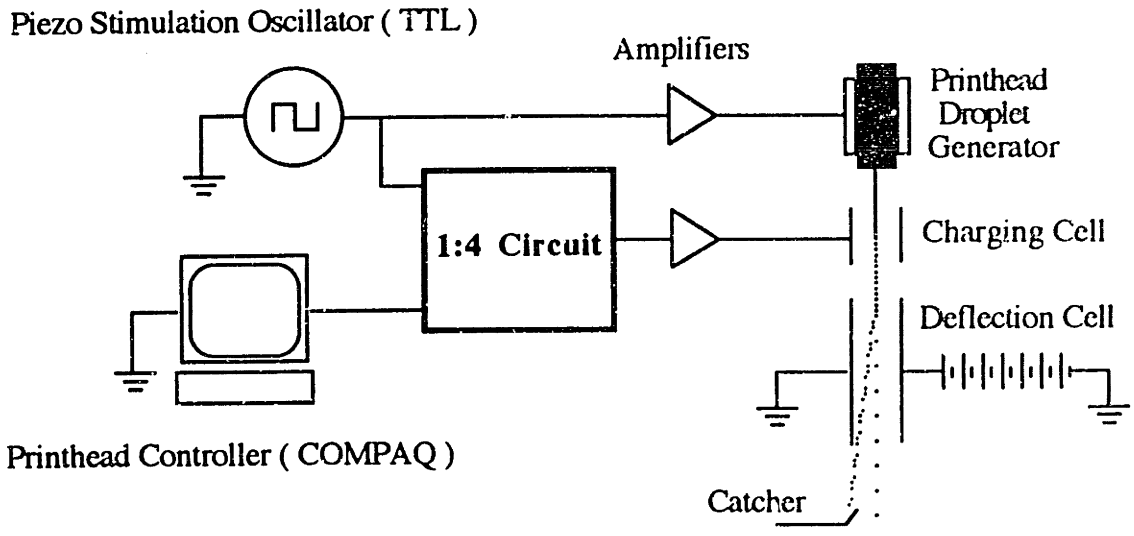

Figure G.1 Configuration of 1:4 circuit in printhead control path.

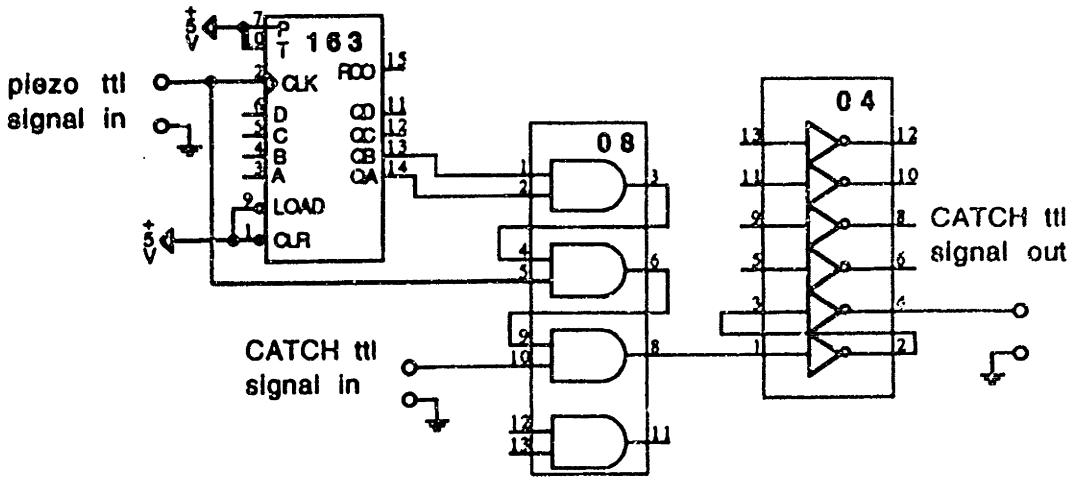

Figure G.2 Schematic of 1:4 circuit. 163: Flip-Flop; 08: Quad "AND"; 04: Hex Inverter.

Bibliography

Adamson, Physical Chemistry of Surfaces, Wiley,1976,

Ashley, C.T. Edds, K.E., & Elbert, D.L., "Development and Characterization of Ink for an Electrostatic Ink Jet Printer", IBM J. Res Dev., **21** 1, 69-75.

Allen, L.W., and Matijevic, E., "Stability of Colloidal Silica; I. Effect of Simple Electrolytes" J. Coll. Interf. Sci, **31** (3) 287 (11/69) ; "III. Effect of Hydrolyzable Cations" JCIS **35** (1) 66 (1/71).

Avnir, D., ed., The Fractal Approach to Heterogeneous Chemistry, Wiley, 1992

Barrier, R.M., McKenzie, N., and Reay, J.S.S., "Capillary Condensation in Single Pores", J. Colloid Sci. **11**, 479-495 (1956).

Bear, Jacob, Dynamics of Fluid in Porous Media, Elsevier, 1972, available in a Dover edition, 1988. Page citations will be in the Dover ed.

Bear, J., and Corapcioglu, M.Y., eds, Fundamentals of Fluid Transport in Porous Media NATO Advanced Study Institute on Mechanics of Fluids in Porous Media, 1982, Newark, Del.

Blackley, D.C., High Polymer Latices, vol. 1, MacLaren, 1966

Boccara, N., and Daoud, M., Physics of Finely-Divided Matter, Springer-Verlag, 1985

Boger, D.V. and Waters, K., Rheological Phenomena in Focus, Elsevier, 1993

Boloutas, E., "Improved Numerical Methods for Modelling Flow and Transport Processes in Partially Saturated Porous Media", Ph.D. Thesis, Civil Eng., MIT 1989.

Bolt, J.Phys.Chem **61**, 1166 1957

Chang, L.S.,"Spreading of Ink Drops on Paper: A Kinetic Model" 4th SPSE Proc. Non-Impact Printing, pp. 320-324

Chiu, R., and Cima, M., " Drying of Granular Ceramic Films: II, Drying Stress and Saturation Uniformity", JACS **76** 11, 2774.

Cima, M.J., Lewis, J.,A., and Devoe, A.D., Binder Distrbution in Ceramic Greenware During Thermolysis, JACS **72** (7) 1192-99 (1989)

Clark, M.M., and Flora, J.R.V.,"Floc Restructuring in Varied Turbulent Mixing" JCIS **147** 2, pp.407-420.

Corapcioglu, M.Y., ed, Advances in Transport Phenomena in Porous Media NATO Advanced Study Institute on Mechanics of Fluids in Porous Media, 1985, Newark, Del.

Defay, R., & Petre, G., "Dynamic Surface Tension", Ch. 3 in Surface and Colloid Science vol. 3, E. Matijevic, ed., Wiley, 1973

Dullien, F.A.L. Porous Media, Fluid Transport and Pore Structure, 2d. Ed., 1992

Everett, D.H. Colloid Science, Vol. 1, The Chem. Soc., 1973, pp. 125-136.

Everett, D.H., "Thermodynamics of Multiphase Flow in Porous Media", JCIS 52 (1) 189-198 (1975)

Feder, J., Fractals, Plenum, 1988, p.236

Feder, J. in Weitz, D., & Huang, J., Aggregation Gelation, F.Family & D.P. Landau, eds., North-Holland, 1984, pp.19-28.

Fillmore, G.L., Buehner, W.L., & West, D.L., "Drop Charging and Deflection in an Electrostatic Ink Jet Printer", IBM J. Res. Dev., Jan. '77, pp 37-47.

Frank, N.H., Introduction to Electricity and Optics, McGraw-Hill, 1950

Gendler, P.L., and Sporer, A.H., "Membrane Ink Technology", in 4th S.P.S.E. Proc. Int'l Cong. on Adv. in Non-Impact Printing Technol., A. Jaffee, ed., 1988, pp. 289-297.

German, R.L., Powder Injection Molding, Metal Powder Industries Federation, 1990

Gibbs, J.W., Collected Works, Longmans, Green & Co. 1906 ed., p. 61

Greenkorn R.A., Flow Phenomena in Porous Media, M. Dekker, 1983

Gregory, P., High-Technology Applications of Organic Colorants, Plenum, 1991, Ch. 9, "Ink-Jet Printing"

Guggenheim, E, Thermodynamics, North-Holland, 1959.

Gums and Stabilizers for the Food Industry , Biennial Intl'l Conference , Pergamon, 1 982, 6 vols.

Hiemenz, P., Principles of Colloid and Surface Chemistry, Dekker, 1977

Hunter, R.J., Foundations of Colloid Science, Vol. 1, Clarendon Pr., 1991.

Hirst, E., The Chemistry and Rheology of Water-Soluble Gums and Colloids, Soc. Chem. Ind. 1966

Iler, R.K., The Chemistry of Silica, Wiley/Intersci 1979

Jefferies, H.D., "Dispersion of Inorganic Pigments", Ch. 9, in [Parfitt]

Johnson, D.L., and Sen, P.N., eds, Physics and Chemistry of Porous Materials, AIP, 1984

Johnson, R.E., and Dettre, R.H., in "Wettability and Contact Angles", pp. 85-153 in Surface and Colloid Science, E. Matijevic, ed., vol. 2, 1969.

Kingery, W.D., Bowen, H.K, and Uhlmann, D.R., Introduction to Ceramics, Wiley/Intersci., 1976.

Kirk-Othmer Encyclopedia of Chemical Technology, 3d Ed., Wiley, 1978.

Leach, R.H., and Pierce, R.J., The Printing Ink Manual, 5th ed., Blueprint Pr., 1993, Ch. 12, "Ink-jet Inks"

Lee, H.C., "Boundary Layer Around a Liquid Jet", IBM J. Res. Dev., Jan. '77, pp 48-51.

Lenormand, R. " Flow Through Porous Media: Limits of Fractal Patterns" AIP Conf. Proc. 154 Physics and Chem of Porous Materials II

Levine and Neale "A Theory of the Rate of Wetting of a Finely Dispersed Random Porous Network", in Wetting,Spreading, and Adhesion, Padday, J.F., Ed., Acad. Pr., 1978, p. 241-260.

Maltesh and Somasundaran, JCIS **153** (1) 298-301.

Mandelbrot, B.B., The Fractal Geometry of Nature. Freeman, 1983

Mark's Mechanical Engineers' Handbook, McGraw-Hill, 6th Ed., 1958.

Melrose, J.R., and Heyes, D.M.,"Rheology of Weakly Flocculated Suspensions: Simulation of Agglomerates in Shear" JCIS **157** pp. 227-234

McGee, H. On Food and Cooking, Collier, 1988

Morgan, F., Rhiemannian Geometry, A Beginner's Guide, Jones & Bartlett, 1993.

Muskat, M., The Flow of Homogeneous Fluids through Porous Media, J.W.Edwards, publ. 1946

Myers, D., Surfactant Science and Technology, VCH Publ. 1988

Myers, R. Treatise on Coatings, Dekker, 1967

Nelson, R.D., Jr., Dispersing Powders in Liquids, Elsevier 1988

Onoda, G., Ceramic Processing Before Firing, Wiley, 1978

Overbeek, J.T.G., "Stability of Lyophobic Colloids and Emulsions" in Kruyt, H.R., Colloid Science Vol. 1, pp.302-341.

Parfitt, G.D., Dispersion of Powders in Liquids, 3d Ed., Applied Sci. 1981

Parker, D.H., Principles of Surface Coating Technology, Wiley/Interscl 1965.

Perloff, W., and Baron, W., Soil Mechanics, Ronald Pr., 1976.

Perram, J.W., "Structure of the Double Layer at the Oxide/Water Interface", J. Chem. Soc. Faraday II **69** (7) 993 (1973).

Petre, G., and Sanfeld, A., eds., Capillarity Today : Proceedings of an Advanced Workshop on Capillarity (1990 : Brussels, Belgium)

Petrie, C.J.S., Elongational Flows, Pitman Pr., 1979

Pietronero, L., Fractals' Physical Origin and Properties Plenum, 1988.

Poitanin, A.A., "On the Computer Simulation of the Deformation and Breakup of Colloidal Aggregates in Shear Flow" JCIS **145** 1, 140-157]

Probstein, R.M., Physicochemical Hydrodynamics, Butterworths, 1989

Pynn, R., and Riste, T., Time Dependent Effects in Disordered Materials, Plenum, 1987

Rusher, R.L., "Strength Factors of Ceramic Shell Molds", Cast Metals Research Journal, 12/74 pp.149-153; 3/75 pp.21-26.

Russel, W.B., and Schowalter, W.R., "Simulations of Coagulation in Viscous Flows"JCIS **145** 1, pp.51-73]

Sachs, E., Haggerty, J., Cima, M., & Williams, P.,"Three Dimensional Printing Techniques", U.S. Patent # 5204055, 4/28/93

Sachs, E., et.al., "CAD-Casting: Direct Fabrication of Ceramic Shells and Cores by Three Dimensional Printing," Manuf. Review, 5 2, 6/9

Scheidegger, A.E., The Physics of Flow Through Porous Media, 3d Ed., U.Toronto Pr., 1974

Shaw, D.J., Introduction to Colloid and Surface Chemistry, Butterworths, 1989

Shaw, T.M., "Liquid Redistribution During Liquid-Phase Sintering", J.Am.Ceram.Soc. **69**(1) 27-37.

Sposito, G., "The Physics of Soil Water Physics", Water Rsrc. Res. **22** 9, 83S-88S, 8/86.

Sweet, Richard L. "High Frequency Oscillography with Electrostatically-Deflected Ink Jets" Stanford Electronics Lab Tech. Report #1722-1, March 1964.

Tadros, T.F., and Lyklema, J, J Electroanal. Chem **17**, 267-275 (1968)]

Tomkiewicz, M., and Sen, P.N., Symp. on The Chemistry and Physics of Composite Media, The Electrochemical Society, 1985

Van de Ven, Th., Colloidal Hydrodynamics, Acad. Pr., 1989

Van Wylen, G., Thermodynamics, Wiley, 1959

Wong, K. et.al., "Intermediate Structures in Equilibrium Flocculation" JCIS **153** 1, pp. 55-72

Zimon, A.D., Adhesion of Dust and Powder, second ed., (R.K.Johnson, transl.) Consultants Bureau, NY 1982

Three Dimensional Printing Theses

Brancazio, David, "Development of a Robust Electrostatically Deflecting Printhead for Three Dimensional Printing", MS Thesis, MIT 5/91.

Curodeau, Alain, "Three Dimensional Printing: Machine Control from CAD Model to Nozzles", MS Thesis, Mech. E., MIT 8/91.

Esterman, Marcos, "Characterization of the Powder/Binder Interaction in the Three Dimensional Printing Process", MS Thesis, Mech. E. MIT 8/90

Galla, Matthew, "Process Development for Three Dimensional Printing of Metal Slurries", MS Thesis, Mat'l Sci., 5/94

Harris, Christopher, "Characterization of Dimensional Variability and Part Bleeding Using the Three Dimensional Printing Process" SB Thesis, Mech. E., MIT 5/91

Lee, Sang-Joon John,"Powder Layer Generation for Three Dimensional Printing" MS Thesis, Mech. E., MIT 5/93

Lewis, Portia, and Shiu, Leung, "Three Dimensional Printing Using Stencils", BS Thesis, Mech. E., 5/93

Lauder, Alan, "Microstructure and Particle Arrangement in Three Dimensional Printing", MS Thesis, Mat'ls Sci., MIT 9/92

Michaels, Steven, "Production of Metal Parts Using the Three Dimensional Printing Process", MS Thesis, Mech. E., MIT 11/93.

Milner, Jill, "Time of Flight Controller and Stream Position Compensation System for the Three Dimensional Printing Process", MS Thesis, Mech. E., MIT 5/93

Perrin, Susan, "Control of Thin Layer Powder Packing Density Effects of Applied Vibration", BS Thesis, MIT 5/91

Williams, Paul, "Three Dimensional Printing: A New Process to Fabricate Prototypes Directly from CAD Models", MS Thesis, MIT 5/90

Yu, Richard, "Development of a Co-Dispersion Binder for the Three-Dimensional PRinting Process to Facilitate Handling of Ceramic Casting Shells in the Green State", MS Thesis, Mech. E., MIT 5/94.

Zapata, Elizabeth, "Methods for Densification of Powder During Spreading Using the Three Dimensional Printing Process", BS Thesis, Mech. E., MIT 5/94